Formation of C_3 and C_2 in Cometary Comae

vorgelegt von
Dipl.-Phys. Alexander Hölscher

Von der Fakultät II – Mathematik und Naturwissenschaften
der Technischen Universität Berlin
zur Erlangung des akademischen Grades

Doktor der Naturwissenschaften
– Dr. rer. nat. –

genehmigte Dissertation

Promotionsausschuss:

Vorsitzender:	Prof. Dr. M. Dähne
Berichter:	Prof. Dr. H. Rauer
	Prof. Dr. O. Dopfer

Tag der wissenschaftlichen Aussprache: 05. März 2015

Berlin 2015
D 83

Diese Arbeit wurde im Institut für Planetenforschung am Deutschen Zentrum für Luft und Raumfahrt e.V. in Berlin-Adlershof in der Abteilung 'Extrasolare Planeten und Atmosphären' unter Betreuung von Prof. Dr. rer. nat. Heike Rauer angefertigt.

Abstract

Comets are remnants from the Solar System formation. They reside at large distances from the Sun and are believed to store deep freeze imprints of the chemical and physical conditions at the time the Solar System formed. The main ice component of a comet is H_2O followed by CO and CO_2 with additional small amounts of molecules with varying complexity. Comets also contain large amounts of dust. If a comet approaches the Sun the ices begin to sublimate giving rise to the cometary coma.

The molecules producing the coma can be observed in the infrared, the radio wavelength range and at optical wavelengths. To constrain the formation of the Solar System, models require knowledge of the composition for a statistically significant number of comets. This favors optical observations of e.g. C_3 (tricarbon) and C_2 (dicarbon) since these species allow observations even of relatively faint comets and do not require space missions (infrared observations). However, one has to link these observed photodissociation product species (daughter species) to the molecules that originally sublimated from the comet nucleus surface, i.e. the so-called parent molecules, as e.g. C_2H_2 (acetylene) for C_2. However, for C_3 no parent molecules have been identified so far.

This thesis investigates the formation of C_3 and C_2 radicals in cometary comae due to photodissociation of observed and in the literature proposed hydrocarbon parent molecules. For this purpose a one-dimensional multi-fluid coma chemistry model has been improved and applied. This work added new photo reactions to the model, updated the hydrocarbon photo rate coefficients and quantified their uncertainty. A sensitivity analysis has been carried out to determine the reactions whose uncertainty most affect the model output uncertainty. Special attention should be paid to these so-called key reactions in future laboratory experiments and quantum chemical computations to reduce the model output uncertainty more effectively. This will allow to better constrain which parent molecules are responsible for the observational C_3 and C_2 column densities. Based on observations of the four sample comets C/2001 Q4 (NEAT), C/2002 T7 (LINEAR), 9P (Tempel 1) and C/1995 O1 (Hale-Bopp), this work investigates which combination of the following proposed parent molecules C_4H_2 (diacetylene), $CH_2C_2H_2$ (allene), CH_3C_2H (propyne), C_2H_4 (ethene) and observed parent molecules C_2H_2 and HC_3N (cyanoacetylene) can best reproduce the observational C_3 and C_2 column densities in cometary comae, taking into account the uncertainties in photodissociation rate coefficients.

It was found that the investigated photodissociation rate coefficients have large uncertainties and also a significant effect on the C_3 and C_2 model column densities. The responsible key reactions were determined with the sensitivity analysis. The important result of this thesis is that one can reasonably well reproduce the observations of comets with the improved model at $r_h = 1.00$ AU (NEAT) and $r_h = 3.78$ AU (Hale-Bopp), within the photodissociation uncertainties using realistic parent molecule production rate ratios and by various combinations of the investigated parent molecules. To confirm the agreement (NEAT, Hale-Bopp) and to clearify remaining discrepancies (LINEAR, Tempel 1) between model and observations requires additional observations of parent and daughter molecules in the coma of comets as well as in situ measurements of cometary ices (Rosetta).

Zusammenfassung

Kometen sind Überreste aus der Entstehungszeit des Sonnensystems. Da sie sich weit entfernt von der Sonne befinden, vermutet man, dass die physikalischen und chemischen Bedingungen zu dieser Zeit in ihrem Eis konserviert sind. Der Hauptbestandteil des Eises ist H_2O, gefolgt von CO, CO_2 und Spuren von verschieden komplexen Molekülen. Des Weiteren enthalten Kometen große Mengen an Staub. Wenn sich ein Komet der Sonne nähert, sublimiert das Eis und bildet dadurch die Kometenkoma.

Moleküle der Koma werden im infraroten, im Radio- und im optischen Wellenlängenbereich beobachtet. Um Randbedingungen der Entstehung des Sonnensystems zu erhalten, benötigt man die Zusammensetzung einer statistisch signifikanten Anzahl von Kometen. Am Besten dafür geeignet sind optische Beobachtungen z.B. von C_3 (Trikohlenstoff) und C_2 (Dikohlenstoff), die auch für relativ leuchtschwache Kometen und vom Boden aus beobachtet werden können. Man muss jedoch die beobachteten Photodissoziationsprodukte (Tochtermoleküle) C_3 und C_2 den von der Kometenoberfläche sublimierten sogenannten Elternmolekülen zuordnen, z.B. C_2H_2 (Ethin) für C_2. Für C_3 sind bislang keine Elternmoleküle identifiziert worden.

Die vorliegende Arbeit untersucht die Entstehung von C_3- und C_2-Radikalen in der Kometenkoma durch die Photodissoziation von beobachteten und in der Literatur vorgeschlagenen Elternmolekülen. Zu diesem Zweck wurde ein eindimensionales Multi-Fluid-Model der Komachemie verbessert und angewendet. In dieser Arbeit wurden dem Model neue Photoreaktionen hinzugefügt, die Ratenkoeffizienten aktualisiert und deren Unsicherheiten zum ersten Mal umfassend berechnet. Es wurde eine Sensitivitätsanalyse durchgeführt, um die Reaktionen zu bestimmen, deren Unsicherheiten den größten Einfluss auf die Unsicherheit der C_3- und C_2-Modelergebnisse haben. Diese sogenannten Schlüsselreaktionen sollten bevorzugt in zukünftigen Laboruntersuchungen und quantenchemischen Berechnungen untersucht werden, um die Modelunsicherheiten effektiv zu reduzieren. Dadurch kann man besser eingrenzen, welche Moleküle für die beobachteten C_3- und C_2-Säulendichten verantwortlich sind. Basierend auf Beobachtungen der 4 Kometen C/2001 Q4 (NEAT), C/2002 T7 (LINEAR), 9P (Tempel 1) and C/1995 O1 (Hale-Bopp) untersucht diese Arbeit welche Kombination der in der Literatur vorgeschlagenen Elternmoleküle C_4H_2 (Diacetylen), $CH_2C_2H_2$ (Allene), CH_3C_2H (Propin), C_2H_4 (Ethen) und der beobachteten Elternmoleküle C_2H_2 und HC_3N (Cyanoacetylen) die C_3- und C_2-Beobachtungen im Rahmen der Unsicherheiten der Photodissoziationsratenkoeffizienten am Besten reproduzieren kann.

Es wurde ermittelt, dass die Unsicherheiten der Photodissoziationsratenkoeffizienten zu signifikanten Unsicherheiten der C_3- und C_2-Modelsäulendichten führen. Die dafür verantwortlichen Schlüsselreaktionen wurden mit der Sensitivitätsanalyse bestimmt. Das wichtige Ergebnis dieser Arbeit ist, dass mit dem verbesserten Model die Beobachtungen von Kometen bei den Abständen $r_h = 1.00$ AU (NEAT) und $r_h = 3.78$ AU (Hale-Bopp) innerhalb der Unsicherheiten der Photodissoziation angemessen gut reproduziert werden können, mit realistischen Elternmolekülproduktionsraten und mit verschiedenen Kombinationen der untersuchten Elternmoleküle. Um die Übereinstimmungen (NEAT, Hale-Bopp) zu bestätigen und verbleibende Abweichungen (LINEAR, Tempel 1) zwischen Model und Beobachtungen aufzuklären, werden weitere Messungen von Eltern- und Tochtermolekülen in der Koma von Kometen und in situ Messungen von Kometeneis (Rosetta) benötigt.

Contents

List of Abbreviations

1D	one-dimensional
alr	additive-logratio
Churyumov-Gerasimenko	67P
clr	centred-logratio
COSAC	Cometary Sampling and Composition
COSIMA	Cometary Second Ion Mass Analyser
Diut	'uniform truncated Dirichlet distribution'
EC	ecliptic comet
ED	experimental design
EUV	extreme-ultraviolet
FIR	far-infrared
FUSE	Far Ultraviolet Spectroscopic Explorer
FUV	far-ultraviolet
GSA	global sensitivity analysis
Hale-Bopp	C/1995 O1
HFC	Halley family comet
HIFI	Heterodyne Instrument for the Far Infrared
HM	harmony memory
HST	Hubble Space Telescope
HS	harmony search
Halley	1P
Hartley 2	103P
Hyakutake	C/1996 B2
IC	internal conversion
IDL	Interactive Data Language
IDP	interplanetary dust particle
ilr	isometric-logratio
IOM	insoluble organic matter
IRAS	Infrared Astronomical Satellite
IR	infrared
ISC	intersystem crossing
ISM	interstellar matter
IUE	International Ultraviolet Explorer
IVR	intramolecular / internal vibrational energy redistribution

JFC	Jupiter family comet
KBO	Kuiper belt object
KB	Kuiper belt
LPC	long period comet
LSA	local sensitivity analysis
LSODE	Livermore solver for ordinary differential equations
LTE	local thermodynamic equilibrium
LUP	local uncertainty propagation
Lα	Lyman-alpha
LINEAR	C/2002 T7
Lulin	C/2007 N3
Machholz 1	96P
MAB	main asteroid belt
MC	Monte Carlo
MIR	mid-infrared
MMMC	microcanonical metropolis monte carlo
MUV	mid-ultraviolet
NIC	nearly isotropic comet
NIR	near-infrared
NPP	nominal production path
NUV	near-ultraviolet
OAT	one factor at a time
OCC	Oort cloud comet
OC	Oort cloud
ODE	ordinary differential equation
ODE	ordinary differential equation
PAH	polycyclic aromatic hydrocarbon
PDF	probability density function
POM	polyoxymethylene
PPD	protoplanetary disk
PPN	protoplanetary nebula
PP	production path
PSN	protosolar nebula
PST	phase space theory
NEAT	C/2001 Q4
RCC	rank correlation coefficient
ROSINA	Rosetta Orbiter Spectrometer for Ion and Neutral Analysis
RRKM	Rice-Ramsperger-Kassel-Marcus
SACM	statistical adiabatic channel model
SA	sensitivity analysis
SC	sensitivity coefficient
SDO	scattered disk object
SD	scattered disk
SFG	signal flow graph
SIMS	second ion mass spectrometer
SPC	short period comet
Schwassmann-Wachmann 1	29P
Schwassmann-Wachmann 3	73P
TMC-1	Taurus molecular cloud 1
TNO	trans-Neptunian object
TOF	time of fly

Tempel 1	9P
UV	ultraviolet
VIRTIS	Visible and Infrared Thermal Imaging Spectrometer
VSMOW	Vienna standard mean ocean water
VUV	vacuum-ultraviolet
Wild 2	81P
Wolf-Harrington	43P

Part I

Introduction

CHAPTER 1

Introduction

Figure 1.1: *Comet C/2012 S1 (ISON) in a montage of images taken between 24th of September and 15th of November 2013 ($r_h = 1.78 - 0.62$ AU). On 14th of November 2013 (far right) comet ISON abruptly increased in brightness due to an outburst. Source: Peach (2014).*

Comets are remnants of our Solar System's formation and (although they are rather small astronomical objects of several 100 m to several tens of km) they contain valuable information on the processes that prevailed at those times. Comets are a mixture of different ices and dust. These materials have a complex history. These were partly produced in old stars, arrived in the Solar System's parent molecular cloud where they were processed and mixed with molecules produced during the formation phase as well as the following protosolar nebula **(PSN)** and protoplanetary disk **(PPD)** phases. These materials then agglomerated into icy planetesimals from which the giant planets formed. The structure and chemical composition of the comets is believed to be the most pristine (Mumma and Charnley, 2011, Crovisier and Encrenaz, 2000, Altwegg, 2009).

Comets contain large amounts of water and a part of Earth's water content may be of cometary origin. Comets are also rich in carbon and numerous organic compounds (prebiotic) which may have favored the emergence of life (Jewitt et al., 2008, Despois and Cottin, 2005).

If a comet comes close enough to the Sun the ices sublimate and release the dust - leading to the fascinating object seen in Figure 1.1, which shows a montage of different images of comet ISON taken between 24th of September and 15th of November 2013, at heliocentric distances $r_h = 1.78 - 0.62$ astronomical units (AU). A neutral gas coma is established, typically extending to cometocentric distances of several 10^5 km. The sublimating molecules are dissociated by solar photons into various radicals. The greenish color of the coma of comet ISON in Figure 1.1 is due to fluorescence of the C_2 radical (note that some images appear blue due to image

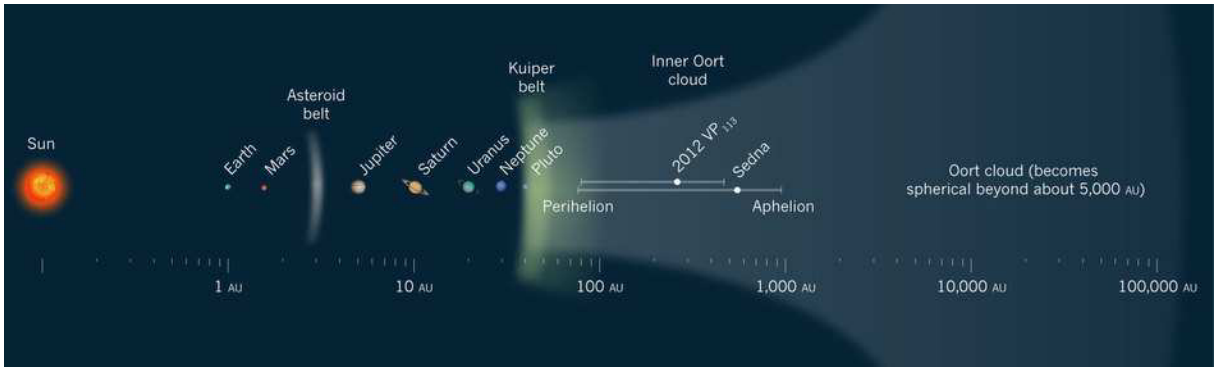

Figure 1.2: *Structure of the Solar System including the Kuiper belt* ***(KB)*** *(and scattered disk* ***(SD)****, both making up the trans-Neptunian objects* ***(TNOs)****) and the Oort cloud* ***(OC)****. Source: Schwamb (2014), Stern (2003).*

processing. Additionally comet ISON increased in brightness on 14th of November 2013 due to an outburst). The released dust is shaped into a dust tail by interaction with the Sun's gravitation and radiation pressure. Ionized particles leaving the coma are forced by the solar magnetic field into the shape of an ion tail which points radially away from the Sun. The name 'comet' was derived long ago from the Greek word $\alpha\sigma\tau\eta\rho\ \ \kappa o\mu\acute{\eta}\tau\eta\varsigma$, aster' come'tes, which means 'hairy star'.

Central questions in comet science are (Jewitt et al., 2008):

- Where, when and how did comets form?
- How pristine is the cometary material?
- What is the composition of comets?
- How diverse are comets?

Today, two main reservoirs of comets exist in the Solar System, namely the trans-Neptunian objects **(TNOs)**, consisting of the Kuiper belt **(KB)** and the scattered disk **(SD)**, and the Oort cloud **(OC)**, see Figure 1.2. The SD lies beyond the KB. Comets are believed today to be transferred from the SD to shorter orbits via interaction with the giant planets (the SD objects have more eccentric orbits than the rather stable Kuiper belt objects **(KBOs)**). The Jupiter family comets **(JFCs)** are so-called short period comets **(SPCs)** with orbital periods of around $T = 5$ years and with aphelion close to the heliocentric distance of Jupiter. These are termed ecliptic comets **(ECs)** today due to their small inclination to the ecliptic plane. The observation of long period comets **(LPCs)** ($T > 200$ years) and comets with hyperbolic orbits with various inclinations have led to the assumption that these originate in the OC - a spherically shaped reservoir located at $r_h > 10^4$ AU. These comets are termed nearly isotropic comets **(NICs)** nowadays (Jewitt et al., 2008, Levison, 1996).

Today it is believed that the Oort cloud comets **(OCCs)** formed much closer in, i.e. in the formation region of Jupiter and Saturn ($5-14$ AU) and were expelled by the migration of these giant planets into the OC and to an outer disk, i.e. an intra-Neptune region ($15-35$ AU), see Figure 1.3. The SD is also believed to be a result of the ejection of comets from the intra-Neptune region to orbits beyond Neptune (Gomes et al., 2005, Morbidelli et al., 2005). The different formation regions (at different distances from the Sun) may be reflected in the composition of comets, e.g. the depletion of volatile ices. It is unknown where exactly the two comet classes, i.e. the comets from the Oort cloud **(OC)** and the comets from the scattered disk **(SD)**, formed and to what extent these are compositionally different (Crovisier, 2007). Furthermore, Levison et al. (2010) suggested that 90 % or more of the OCCs were not formed in the Sun's PPD but

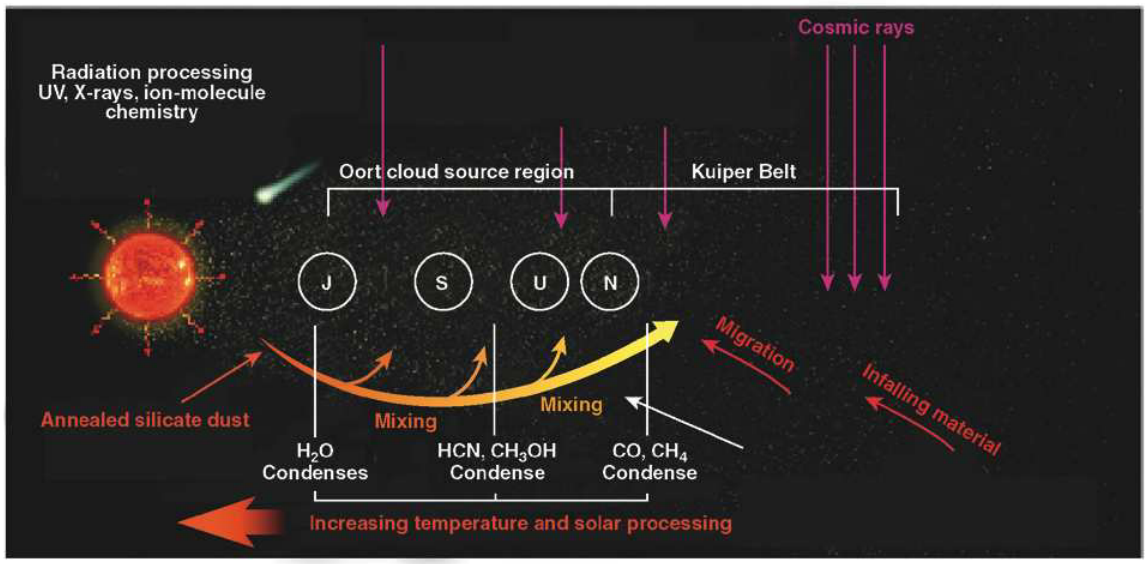

Figure 1.3: *Sketch of the formation regions of comets with respect to the formation regions of the giant planets Jupiter (J), Saturn (S), Uranus (U) and Neptune (N) in the PPD. The OCCs are believed to have formed closer to the Sun than the TNOs (including the KB and the SD). Source: Dello Russo et al. (2006a).*

were captured from the PPDs of nearby stars, which were part, at that time, of their common birth cluster.

Several space mission have been undertaken to investigate the chemistry and physics of comets. The *Giotto* and *Vega* missions to comet 1P **(Halley)** took the first close-up image of a comet nucleus (Keller et al., 2004). The *Giotto* mission detected many new molecules and passed Halley at a distance of 596 km on 14th of May 1986. The *Stardust* mission collected interstellar dust between 2000 and 2002 as well as dust from comet 81P **(Wild 2)** in January 2004 and returned these samples in January 2006. The investigation of the dust samples indicate a rich chemical inventory of presolar and solar origin. The existence of ices and refractory organics in comets indicates that parts of the cometary material were not exposed to temperatures $T > 30 - 150$ K. However, the high temperature minerals (> 1100 K) detected must have formed in the hot inner Solar Nebula, which substantiate the view of large-scale mixing (Bockelée-Morvan et al., 2002, Sandford et al., 2006, Brownlee et al., 2006, Wooden et al., 2007, Zolensky et al., 2008, Westphal et al., 2009).

The *Deep Impact* mission featured the impact of a projectile into comet 9P **(Tempel 1)** to release gas and dust from subsurface layers together with a concerted observation campaign around the impact event. This mission gave valuable information on surface sublimation layers and subsurface material, as well as the homogeneity of upper and lower layers (Meech et al., 2005, A'Hearn et al., 2005, A'Hearn, 2011), see also Section 2.2. The *Rosetta* mission investigates the outgassing evolution of comet 67P **(Churyumov-Gerasimenko)** from November 2014 to December 2015 (it entered the comet's orbit in August 2014). It aims to gather insight into the chemical processes at work in the coma between neutral molecules, cations and anions. It investigates in detail also the composition of the dust and its role as a possible source of molecules in the coma. The *Rosetta* lander *Philae* landed on the comet on 12th November 2014 and probed the chemical and physical properties of the cometary material in situ (Gulkis and Alexander, 2008, Schulz, 2009).

Different observational techniques with ground-based telescopes are used to investigate compositional characteristics and differences among comets. In the infrared **(IR)** one probes the

abundance of various amorphous dust grains (interstellar origin) and crystalline dust grains. Wooden et al. (2007) found a higher amorphous to crystalline silicate dust ratio in OCCs suggesting large-scale mixing in the PPD (heating close to the Sun) and/or the presence of accretion shocks in the comet forming zone.

The composition of cometary ices is probed on the one hand in the optical wavelength range by the detection of radicals such as C_3, C_2, CN, NH and OH. Optical observations additionally allow the investigation of even rather faint comets in contrast to IR and radio observations, therefore facilitating the observation of a statistically significant number of comets for compositional studies. A chemical diversity among comets has been detected in the optical wavelength range (A'Hearn et al., 1995, Schleicher, 2008, Fink, 2009, Langland-Shula and Smith, 2011, Cochran et al., 2012). The study of A'Hearn et al. (1995) showed that most of the comets depleted in C_2 radicals with respect to CN are JFCs although not all JFCs are depleted. See for example Figure 2.4 in the more detailed Section 2.3.3. A similar though a bit less clear depletion pattern was apparent for C_3. These results were argued to be a primordial characteristic of the comet formation region in the PPD. In this view the so-called 'typical' comets, i.e. comets with a moderate C_2/CN abundance ratio, formed in the Uranus-Neptune region of the PPD, of which the bulk were expelled into the OC and a fraction were scattered into the KB.

On the other hand the IR and radio wavelength ranges are used to detect relatively large complex molecules, e.g. C_2H_2, C_2H_6, HC_3N, CH_3OH, HCN, H_2O, which partly constitute the so-called parent molecules of the observed radicals. Parent molecules are those molecules which sublimate directly from the comet nucleus ices and dissociate into smaller molecules, e.g. HCN to CN or C_2H_2, C_2H_6 and HC_3N to C_2. There are also proposed C_2 parent molecules like C_2H_4 which may provide clues to the formation of C_2H_6, e.g. via subsequent H addition to C_2H_2 on icy grains or dimerization of CH_3 (Kobayashi and Kawakita, 2010, Kobayashi et al., 2013). Investigations of Biver et al. (2002), Crovisier et al. (2009a,b), Disanti and Mumma (2008) indicate a chemical diversity of the comets. However, no correlations with the so-called dynamical classes ECs and NICs, i.e. with their source regions in the Solar System, have been found so far. For the C_3 radical no parent molecule has been detected up until now, but various species have been proposed such as e.g. C_4H_2 and C_3H_4. The C_4H_2 isomer CH_2C_3 and the C_3H_4 isomer propyne CH_3C_2H (but not its isomer allene $CH_2C_2H_2$) were detected in the interstellar matter **(ISM)**, see e.g. Kawaguchi et al. (1991) and Snyder and Buhl (1973), respectively. It is also not known if C_3 and C_2 in cometary comae are linked by a common source or if these have distinct origins, i.e. sublimating hydrocarbon molecules which are dissociated and/or dust which releases molecules of different size containing C_3 and/or C_2. The following questions arise in this context:

- Are there compositional differences between the nearly isotropic comets **(NICs)** from the Oort cloud **(OC)** and the ecliptic comets **(ECs)** from beyond Neptune?
- Can one explain the C_3 and C_2 observations in cometary comae with the destruction of hydrocarbon molecules which sublimate from the comet nucleus?
- Which parent molecules can explain the C_3 and C_2 observations?

1.1 The Formation Chemistry of C_3 and C_2

Helbert (2002) and Helbert et al. (2005) were the first to model the formation of C_3 and C_2 from parent molecules and to compare with the observations of the NIC C/1995 O1 **(Hale-Bopp)** at large $r_h > 2.8$ AU. That work included the already in cometary comae oberved parent molecules C_2H_2 and C_2H_6 and assumed C_3H_4 as the C_3 parent molecule. In that work a complex 1D coma chemistry model (ComChem) was used with a hydrodynamical coma description and a large chemical reaction network which included e.g. photodissociation, ion-molecule and electron

impact reactions. However, they required some estimations in the reaction network, e.g. the rate coefficient of $C_3 + e^- \rightarrow C_2 + C + e^-$ as well as that of $C_3H_2 + \gamma \rightarrow C_3 + H_2$ were estimated by adjusting the rate coefficient to fit the observed C_3 and C_2. In that work the C_3 and C_2 observations of Hale-Bopp were fitted satisfactorily using as parent molecules C_3H_4, C_2H_2 and C_2H_6.

Weiler (2006) investigated the formation of C_3 and C_2 in three comets observed at small heliocentric distances $r_h = 1.0 - 1.5$ AU, namely the ecliptic comet **(EC)** Tempel 1 and the nearly isotropic comets **(NICs)** C/2001 Q4 **(NEAT)** and C/2002 T7 **(LINEAR)**. That work constructed a 1D coma chemistry model (as the ComChem model was no longer available), adopted the reaction network of Helbert (2002), Helbert et al. (2005), assumed the parent molecules C_2H_2, HC_3N, C_3H_4 and C_4H_2 and updated hydrocarbon electron impact reaction rate coefficients. Additionally, photodissociation rate coefficients of several species had to be estimated due to a lack of sufficient data on absorption cross sections and dissociation quantum yields. Their work showed that electron impact reactions are not an important hydrocarbon destruction process in cometary comae, i.e. photodissociation remained as the main process.

Weiler (2006) could not reproduce the observations of the comets with C_3H_4 as the sole C_3 parent molecule. However, on including additionally C_4H_2 and assuming the formation of C_3 from this parent molecule in one step Weiler (2006) could then reproduce the C_3 column densities. That work also included the C_2 parent molecules C_2H_2 and HC_3N. However, the C_2 column densities could only be reproduced reasonably well for comet NEAT. For the comets LINEAR and Tempel 1 the C_2 model profiles featured a smaller slope in the intermediate to outer coma than the observations. Moreover, this reaction network did not reproduce the C_3 and C_2 observations of comet Hale-Bopp at $r_h = 3.78$ AU. Since the photodissociation rate coefficients were partially estimated it was not possible to determine whether the estimated photodissociation rate coefficients were the reason for the discrepancy or whether this was due to the parent molecules assumed. The main scientific questions are:

1.2 Aim of this Thesis

Regarding the results of the previous works of Helbert (2002) and Weiler (2006) the present work aims at further constraining and analysing the C_3 and C_2 photochemistry in the cometary comae of the comets NEAT, LINEAR, Tempel 1, observed around $r_h = 1 - 1.5$ AU, and comet Hale-Bopp observed at $r_h = 3.78$ AU. In this regard this work addresses the following scientific questions in order to determine if the C_3 and C_2 radicals in cometary comae can be explained by the photodissociation of the already detected C_2 producing hydrocarbon molecules C_2H_2, C_2H_6 and HC_3N and the proposed C_3 and C_2 producing parent molecules C_4H_2, $CH_2C_2H_2$, CH_3C_2H and C_2H_4. For this purpose a 1D coma chemistry model is adapted from the work of Weiler (2006)

Which photodissociation reactions' rate coefficient uncertainties have to be reduced primarily in order to determine if the observed and proposed parent molecules can account for the observed C_3 and C_2?

To answer the above question this work updates the photochemical part of the reaction network relevant to the C_3 and C_2 chemistry. This work investigates and quantifies different sources of uncertainties affecting the accuracy of the photodissociation rate coefficients. The distributions of the photo rate coefficients are computed by the Monte Carlo **(MC)** method. To pinpoint the so-called *key reactions*, i.e. the reactions that most affect the uncertainties of the model output for C_3 and C_2, this work carries out a sensitivity analysis **(SA)**. This SA is also carried out with respect to the observations of the four comets NEAT, LINEAR, Tempel 1 and Hale-Bopp

available for the present work. Knowing these reactions will allow to reduce the model output uncertainties much more efficiently by reducing the uncertainties of these *key reactions*.

Can one account for the C_3 and C_2 observations with the investigated parent molecules within the uncertainties of the photodissociation rate coefficients?

This question is examined by investigating various combinations of the proposed parent molecules C_4H_2, $CH_2C_2H_2$, CH_3C_2H, C_2H_4 and the observed parent molecules C_2H_2, HC_3N to account for the C_3 and C_2 observations of the four analysed comets by optimizing the parent molecule production rate ratios with respect to water (composition) for each comet and by optimizing the photodissociation rate coefficients within their estimated uncertainties, using the presented coma chemistry model.

1.3 Outline of this Thesis

Chapter 2 gives a deeper introduction to cometary composition, source regions and their classifications as well as an overview of the early and recent investigations on the origin of C_3 and C_2 in cometary comae.

Chapter 3 introduces the basic physics and chemistry of cometary comae with a special focus on photodissociation which is the major destruction process of volatiles in cometary comae and therefore important for the formation of C_3 and C_2.

Chapter 4 provides an overview of observations of parent molecules in the IR and radio wavelength ranges as well as the observation of the radicals C_3 and C_2 in the optical wavelength range. This section also gives details about the C_3 and C_2 observational data set investigated in this work. This data set comprises three sample comets from the Oort cloud **(OC)**, i.e. the nearly isotropic comets **(NICs)** C/2001 Q4 **(NEAT)**, C/2002 T7 **(LINEAR)**, C/1995 O1 **(Hale-Bopp)**, and one comet from beyond Neptune, i.e. the ecliptic comet **(EC)** 9P **(Tempel 1)**.

Chapter 5 describes the one-dimensional coma chemistry model used in this work to model the formation of C_3 and C_2 from hydrocarbon parent molecules. This chapter also discusses the assumptions and the validity range of the model.

Chapter 6 validates the model used in this work against models of previous works.

Chapter 7 discusses the uncertainty of the parameters required to compute photodissociation rate coefficients and presents a method to estimate their uncertainty including up-to-date molecular data.

Chapter 8 carries out a sensitivity analysis **(SA)** of the C_3 and C_2 photochemistry of the coma chemistry model to determine the reactions which most affect the model output uncertainty.

Chapter 9 analyses whether modelling different combinations of C_3 and C_2 parent molecules can account for the observations of C_3 and C_2 of the four investigated sample comets by optimizing the parent molecules' production rate ratio with respect to water for each comet and the involved photodissociation reactions' rate coefficients within their uncertainties.

Chapter 10 summarizes the results and conclusions of this work. The chapter closes with an outlook for future works in this research field.

The Appendix gives details of Dirichlet distributions, transformations between absorption cross section units and of ab initio electronic oscillator strengths as applied in this work. It also discusses the molecular data on absorption cross sections, quantum yields, fragmentation branching ratios and threshold wavelengths used to compute the photodissociation rate coefficients. This Appendix also introduces the used heuristic global search algorithm and the adjusted χ^2 to optimize the model (photodissociation rate coefficients within their uncertainties) and the individual parent molecule production rate ratios of the investigated comets simultaneously for the C_3 and C_2 observations of the four investigated comets. The complete reaction network of the coma chemistry model is also listed.

CHAPTER 2

Comets

Section 2.1 presents an overview of the composition of comets. Section 2.2 discusses the evolution and homogeneity of the comet nucleus as well as how its chemical composition relates to the coma composition. Section 2.3 provides a description of the source regions of comets in the Solar System and the modern classification schemes. As this work focuses on the C_3 and C_2 formation chemistry in cometary comae, Section 2.4 introduces to early and recent investigations on the origin of C_3 and C_2 in cometary comae.

2.1 Composition

To obtain constraints on the physical and chemical properties that prevailed during the protosolar nebula **(PSN)** and the protoplanetary disk **(PPD)** phases it is useful to compare the composition of interstellar matter with that of comets. Organic molecules synthesized in different phases might also be important for the emergence of life on the Earth.

Cometary nuclei are a mixture of dust and ice with probably more dust than ice (Küppers et al., 2005). When the comet gets close enough to the Sun the ices begin to sublimate thereby releasing dust into the coma. The following summary on the dust and volatile components in cometary comae is mainly based on the reviews of Bockelée-Morvan (2011) and Mumma and Charnley (2011).

It is insightful to compare interstellar matter with cometary matter, since all cometary matter was once interstellar and was either modified in different ways (degree of modification unknown) or destroyed during the PSN and PPD phases, during the formation of our Solar System. Important indications as to the physical and chemical processes of these phases might be therefore obtained, by investigating the compositional differences and similarities of cometary and interstellar composition.

2.1.1 Volatile Ices

Cometary ices are much more sensitive to physical and chemical properties in the PSN/PPD than refractory solids, hence their existence and abundance carry important information. An overview of the range of the abundance of volatile species in comets is presented in Figure 2.1.

Water is the most abundant species in comets and therefore often used as a reference species for cometary activity (for $r_h < 3$ AU, where water sublimation is effective).

The next most abundant species are CO_2 and CO. In addition, CH_3OH, CH_4, H_2CO and many other organic species have been detected in comets up until today some of which have been found in interstellar sources.

C_2H_6 is an example of a species which has only been detected in comets and is suggested to be formed either by hydrogenation of C_2H_2 ice films on icy (dust) grains (Hiraoka and Sato, 2001) or via $2 \cdot CH_3 \rightarrow C_2H_6 + M$ (M = any species to carry away excess vibrational energy) in the gas phase. In summary the cometary volatile ices seem to be related to interstellar ices that have been processed. CH_3C_2H (propyne), a C_3H_4 isomer, has been detected in molecular clouds, e.g. Bergin et al. (1994), whereas only an upper limit has been determined for comet C/1995 O1 **(Hale-Bopp)** (Crovisier et al., 2004). Another isomer $CH_2C_2H_2$ (allene) exists, although this has not been searched for in comets up until now.

It is likely that also other species detected in the interstellar matter **(ISM)** may be found in comets in future investigations. The C_4H_2 isomer H_2C_4 was first detected in the Taurus molecular cloud 1 **(TMC-1)** by Kawaguchi et al. (1991). The diacetylene isomer HC_4H was first detected in the ISM by Cernicharo et al. (2001) in the protoplanetary nebula **(PPN)** CRL 618 but not in comets so far. In the TMC-1 e.g. C_4H was found to be even more abundant than the common species CH_3CHO, CH_3OH, HCOOH, CH_3CN, C_3H_2, C_4H_2, and HC_3N (Herbst and Leung, 1989, Lee et al., 1996, Graf et al., 2001).

Anions such as O^-, OH^-, C^-, CH^- and CN^- together with unidentified organic anion mass peaks in the range $22 - 65$ amu and $85 - 110$ amu were recorded during the 1P **(Halley)** flyby of the *Giotto* spacecraft in 1986 (at ≈ 2300 km distance to the nucleus) (Chaizy et al., 1991). These were interpreted as the anions of CHON (carbon, hydrogen, oxygen, nitrogen) containing particles in the coma of comet Halley (Altwegg et al., 1999). Anions such as C_nH^- and C_m^- ($n = 4, 6, 8, 10$; $m = 5 - 10$) have been detected in circumstellar shells and envelopes (McCarthy et al., 2006, Cernicharo et al., 2007, Remijan et al., 2007, Gupta et al., 2009, Cordiner et al., 2011) and even larger anions are predicted by models of molecular clouds and circumstellar envelopes (Millar et al., 2007, Harada and Herbst, 2008, Cordiner and Millar, 2009). These large molecules might contribute to the observed C_3 and C_2 in cometary comae. However, the determined anion densities in Halley have large uncertainties. This topic can be investigated in more detail when reliable data becomes available by the ongoing *Rosetta* space mission to comet 67P **(Churyumov-Gerasimenko)**.

From chemical models of interstellar clouds, treating also anion chemistry, species such as C_6O, C_7O, HC_6O and HC_7O have been reported to be formed (Cordiner and Charnley, 2012). Other molecules detected e.g. in the molecular cloud TMC-1 is e.g. $CH_2{=}C{=}CH{-}CN$ (cyano-allene) (Chin et al., 2006). Future cometary observations and especially the in situ measurements of the Rosetta space mission will clarify if such molecules are present in cometary ices.

2.1.2 Dust

Cometary dust is composed of refractory (temperature resistant) mineral particles containing the elements Mg, Si, Fe and Ca and organic particles containing the elements C, H, O, N, P, S in different amounts.

Mg-rich olivines and pyroxines, e.g. Mg_2SiO_4, $Mg_2Si_2O_6$, abundant in the Earth's crust, are the prevailing silicate component in comets (Hanner and Bradley, 2004). Both the amorphous and crystalline forms have been found in comets, with more crystalline silicates in *Stardust* samples (Zolensky et al., 2008, Westphal et al., 2009) contrary to the mainly amorphous form found in the ISM (only 2 % crystalline) (Kemper et al., 2004, 2005). However, the amount of crystalline silicates varies strongly among Oort cloud comets **(OCCs)** (Harker et al., 2002,

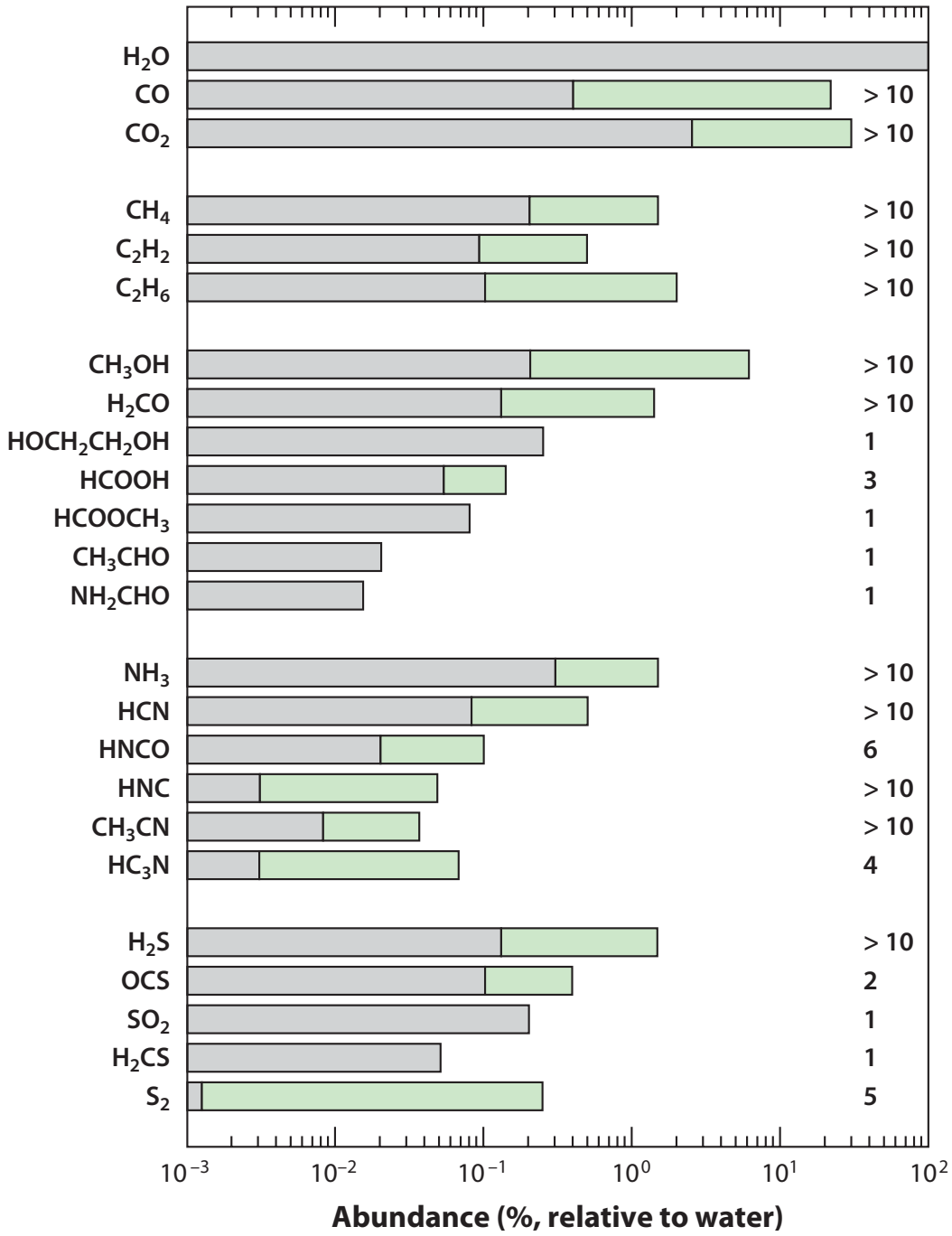

Figure 2.1: *Observed production rate ratios normalized by water* $c(\text{species}) = Q(\text{species})/Q(\text{H}_2\text{O})$*, shown as a % ([*$Q$*] = molecules* s^{-1}*), of cometary volatiles. Most of the species are regarded to sublimate directly from the comet nucleus ices.* HNC *is mainly a product species, whereas* H_2CO *and* CO *are both product and direct species. Plotted is the range of production rate ratios (green bar) and the number of comets in which the species has been detected (number shown on the right hand side). Grey indicates the nominal lower range. For six species only one detection exists, namely for comet Hale-Bopp. Source: Mumma and Charnley (2011).*

2004). These crystalline silicates are believed to have formed in the hot inner nebula. These were then transported to the colder comet forming regions (Wooden et al., 2007).

The organic component found in *Stardust* samples comprises only a small fraction of aromatics. The insoluble organic matter **(IOM)** contains aliphatic hydrocarbons, polycyclic aromatic hydrocarbons **(PAHs)**, fullerenes, heteropolymers and carbonyls (Becker et al., 2000, Pizzarello et al., 2006), from which the first three are also found in the ISM and in circumstellar envelopes (Tielens, 2008, Cami et al., 2010). Hence, there appear to be many more similarities between asteroids and comets than was previously supposed before the *Stardust* mission (Zolensky et al., 2006) and furthermore, there may exist a continuum between carbonaceous asteroids and comets regarding chemical and physical properties (Gounelle et al., 2008, Morbidelli et al., 2012).

Nevertheless, there are differences between the organic component in *Stardust* samples, carbonaceous meteorites, the ISM and interplanetary dust particles **(IDPs)**. For example aliphatic chains are larger in *Stardust* samples and IDPs than in carbonaceous meteorites and the ISM (Keller et al., 2006). The PAH content in *Stardust* samples is lower compared to ISM, where 10 to 20 % of carbon is locked into PAHs (Clemett et al., 2010). Also larger PAHs of more than 50 C atoms as in the ISM are not observed (Cody et al., 2008). The IOM investigated so far have all solar $^{12}C/^{13}C$ ratios which argues for a solar rather than an ISM origin. There must have been at least a strong processing of aromatics from the ISM to account for the above observations (Alexander et al., 2008).

Additionally, other larger molecules have been proposed to exist in comets, not observed in the ISM so far. For example polyoxymethylene **(POM)** was proposed by Fray et al. (2006) as an extended source to explain the observed formaldehyde (H_2CO) abundance in comets. However, this was later concluded to be an unrealistic source for H_2CO (Milam et al., 2006, measurements in three comets), since POM is not produced efficiently enough in the ISM and the PSN phase to account for the required high abundance of POM to explain the observed H_2CO. As a more likely explanation evaporation of H_2CO from organic material in grain matrices was proposed (Cottin and Fray, 2008).

2.2 Relation Between Nucleus Ice and Coma Abundances

It is currently a subject of research as to how coma and nucleus ice abundances are related or how much the nucleus composition reflects the composition of the formation region and the time within the protoplanetary disk **(PPD)**. Even comets that resided in 'deep freeze' in their reservoirs, i.e. Oort cloud **(OC)** or Kuiper belt **(KB)**, since their formation have likely experienced some degree of alteration, e.g. by cosmic rays and radioactive decay processes. Decay of short-lived radioactive species as well as visits of the comet close to the Sun may have provided sufficient heat for depletion of highly volatile species in the surface and subsurface layers. Such heating may lead to crystallization of amorphous ice, therefore providing additional heat for sublimation or even liquefaction of H_2O (Prialnik et al., 2008).

In addition, the nucleus may not be homogeneous but instead consists of an agglomeration of cometesimals formed at different regions of the PPD. Also accretion of material from different regions in the PPD may be reflected by inhomogeneous nucleus abundances. Indications of such properties have been obtained e.g. in Weiler et al. (2007).

Observations in the infrared **(IR)** of the B and C fragments of comet 73P **(Schwassmann-Wachmann 3)**, which split in 2006, showed depletion in most volatiles, except HCN, with respect to H_2O. Since processing due to evolution is assumed only to affect the upper cometary layers (Prialnik et al., 2004) and since the high depletion of CH_3OH with respect to HCN cannot be explained by thermal processing of the nucleus surface, the parent comet Schwassmann-Wachmann 3 was concluded by Dello Russo et al. (2007) to have been almost chemically

homogeneous. Similar results were obtained by Kobayashi et al. (2007), i.e. that C_2H_2 and C_2H_6 were depleted in all fragments. Schleicher and Bair (2011) found that the composition of pre-fragmented Schwassmann-Wachmann 3 as well as its fragments were the same with respect to C_3, C_2, CN and NH. C_3 and C_2 were depleted as well.

In July 2005 the projectile of the *Deep Impact* spacecraft hit the surface of comet 9P **(Tempel 1)** and allowed the comparison of the ambient outgassing from the surface and near subsurface (2 to 3 cm (Thomas et al., 2008)) with material released during the impact (at least 20 m below the surface). Cochran et al. (2007) found the same abundance ratios of the species NH, CN, CH, NH_2, C_3 and C_2 to OH before and after impact. Also HCN, CO, CO_2 and CS did not change within the uncertainties (DiSanti et al., 2007, Feldman et al., 2006, Feaga et al., 2007, Feldman et al., 2010). The exception was C_2H_6 which changed by a factor of 2.4 (DiSanti et al., 2007). Although uncertainties were in some cases of the order of several tens of percent the main conclusion is that nucleus and coma abundance ratios are similar and that remote observations of the coma can be used to deduce the composition of comet nuclei. The *Deep Impact* mission also showed heterogeneity in the outgassing of CO_2 relative to H_2O from different regions of the nucleus (A'Hearn, 2011).

2.3 Cometary Source Regions and Classifications

A central goal in cometary science is to provide constraints to models of PPDs, e.g. Gail (2002), Semenov and Wiebe (2011) and planet formation e.g. the Nice model (Gomes et al., 2005, Tsiganis et al., 2005, Morbidelli et al., 2005, Walsh et al., 2011). The protoplanetary disk **(PPD)** studies predict chemical differentiation in the disk material depending on the distance to the protosun, accretion shocks and mixing of disk material from different regions of the PPD. The Nice model links the formation regions of cometesimals in the PPD of our Solar System with their modern reservoirs from which they are transferred to the inner Solar System where they are observed.

2.3.1 Source Regions

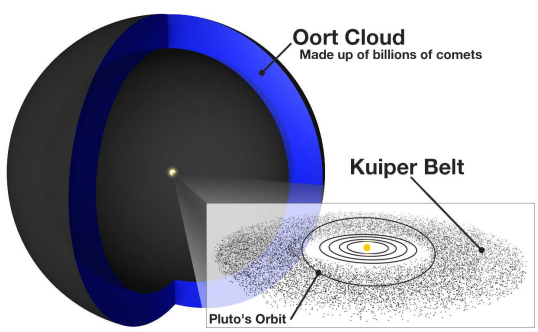

Figure 2.2: *The OC in the outermost region of the Solar System and the Kuiper belt **(KB)**. The KB is a sub population of the trans-Neptunian object **(TNO)**, which is closer to Neptune than the SD (not displayed). Source: Narciso Valle Campos.*

Comets are transferred to the inner Solar System from two reservoirs: the Oort cloud **(OC)** and the scattered disk **(SD)**.

The Oort cloud (OC) is a hypothetical, spherical shaped cluster of comets located between 50,000 AU and 150,000 AU from the Sun, see Figure 2.2. Its existence was suggested by Oort (1950) to explain the peak of cometary semi-major axes at $a \sim 2000$ AU for long period comets **(LPCs)** (period $T \geq 200$ years). Additional observables that had to be explained were the replenishment of LPCs in the inner Solar System, having arbitrary inclinations, including retrograde orbits and also the existence of very bright comets, interpreted as a sign of unprocessed ice surfaces due to the long storage at very low temperatures. Millions of comets are assumed to reside there in loosely bound orbits around the Sun.

Comets are transferred to the inner Solar System by interactions with molecular clouds, nearby stars or gravitational tides of the Milky Way. Comets escaping the OC into the inner Solar System undergo a change in their semi-major axis by Jupiter that is proportional to $a^{7/2}$ (Hills, 1981). LPCs ($T > 200$ years) can be subdivided into 'dynamically new' and 'returning' comets. 'Dynamically new' comets are those which enter the inner Solar System with a semi-major axis $a \gtrapprox 10,000$ AU. Due to the gravitational interaction with Jupiter the comet's a changes to $a < 10,000$ AU or the comet is expelled from the Solar System. Comets entering the Solar System with $a < 10,000$ AU once had $a > 10,000$ AU. They likely reduced their semi-major axis in several passages through the inner Solar System and are therefore denoted 'returning' comets (Levison, 1996).

The scattered disk (SD) together with the KB forms the TNOs beyond Neptune. The scattered disk objects **(SDOs)** have higher eccentricities e in contrast to the rather stable Kuiper belt objects **(KBOs)** (including Pluto) which is the reason that they are transferred by interactions with the giant planets to the inner Solar System to become short period comets **(SPCs)** with periods $T < 200$ years. The KB and the SD are part of the TNOs, see also Figure 2.2. These can be further subdivided into Halley family comets **(HFCs)** ($20 < T < 200$ years, mean inclination $i = 41°$) and Jupiter family comets **(JFCs)** ($T < 20$ years, mean inclination $i = 10°$) (Levison, 1996).

The main asteroid belt (MAB) denotes the region between Jupiter and Mars. It has been suggested to harbour objects showing continued outgassing behavior which may be intermediates between asteroids and comets (Hsieh and Jewitt, 2006, Jewitt, 2012).

2.3.2 Dynamical Classification - The Tisserand Invariant

The requirement of classifying comets by their modern source region (Oort cloud or scattered disk) is related to the so-called Tisserand invariant T_J. T_J conserves its value before and after an encounter with e.g. Jupiter - in contrast to the period of the comet which may be changed dramatically. T_J is also invariant in the restricted three-body-problem where two massive objects (e.g. the most massive Solar System objects, Sun and Jupiter) on circular orbits, moving around their common center of mass, act on a body with negligible mass (the comet). The Tisserand invariant with respect to Jupiter is defined as

$$T_J = \frac{a_J}{a_c} + 2\cos(i)\sqrt{\frac{a_c}{a_J(1-e^2)}}\,, \tag{2.1}$$

where a_J is the semi-major axis of Jupiter and a_c that of the comet with inclination i and eccentricity e. Comets can then be classified into nearly isotropic comets **(NICs)** with $T_J < 2$ including LPCs and HFCs and ecliptic comets **(ECs)** with $2 < T_J < 3$ including JFCs, see Figure 2.3 (Levison, 1996).

2.3.3 Compositional Classification

Comets have been divided into several compositional classes depending on the species which are being investigated in the coma. For example A'Hearn et al. (1995) investigated the coma abundances of the radicals C_3, C_2, CN, NH, and OH (optical wavelength range). More optical surveys were made by Fink (2009), Langland-Shula and Smith (2011), Cochran et al. (2012) with similar conclusions. These authors noted that different comets could be grouped into different compositional types as we will now discuss (of which some are subgroups of the C_2 depleted group). In the first large and detailed compositional survey of A'Hearn et al. (1995) a connection

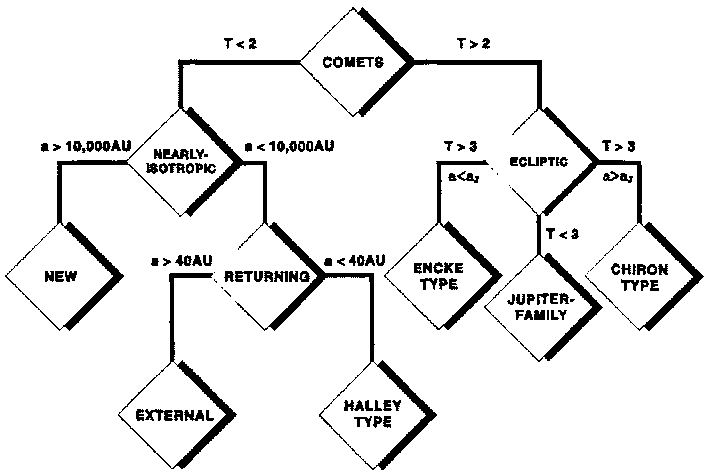

Figure 2.3: *Classification of comets with the Tisserand invariant T_J, see Equation* (2.1). *Source: Levison (1996).*

between composition and dynamical class was suggested. The JFCs $\subset$ ECs in their data set of 41 comets (with reasonable observational r_h coverage) included more carbon-chain depleted comets than the group of LPCs $\subset$ NICs. So-called carbon-chain depletion was measured with the C_2/CN coma abundance ratio, see right panel of Figure 2.4. This subset is also detectable in the left panel of Figure 2.4 in which the relative abundances of C_2 and CN (with respect to OH) are regarded, in which the carbon-chain typical comets seem to follow a slope of one. A less clear but still discernable characteristic was apparent for C_3. Additionally, it was found that the CN abundance and with a lesser degree the C_2 abundance is correlated with the dust to gas ratio leading A'Hearn et al. (1995) to suggest that CN is mainly, and C_2 partly released from dust. The carbon-chain depletion of comets was suggested to be a primordial characteristic of the comets rather than due to evolution, see also Section 2.2. However, a less significant correlation is found for the C_3 depletion and it is not known to which extent the C_3 and C_2 coma abundances are linked (Mumma and Charnley, 2011).

Radio observations of HCN, CH_3OH, CH_3CN, H_2CO, H_2S and CS were investigated in Crovisier et al. (2009a,b). Disanti and Mumma (2008) investigated CO, CH_4, C_2H_6, C_2H_2, HCN, CH_3OH combined with OH prompt emission as a proxy for H_2O in the IR. In these investigations chemical diversity is evident but no correlations with dynamical classes are discernable.

There are also compositionally exceptional comets like 43P **(Wolf-Harrington)**, which features extremely low C_3 and C_2 but strong CN emissions (Schleicher et al., 1993). Or, comet Yanaka (1988r, XXIV), with its low C_2 and CN but strong NH_2 emissions (Fink, 1992) and comet 96P **(Machholz 1)** with extremely low CN and depletion in C_2. Schleicher (2008) discusses that the comets Yanaka and Machholz 1 might have formed in a region of the Solar System with unusual conditions or that they have been captured from other star forming regions.

Clearly a statistically significant number of investigated comets is required to achieve a clearer and bias-free picture of the distribution of cometary composition. Also required is to identify the sources of C_3 and C_2, since these can be produced from different volatiles as well as from dust particles.

2.4 Formation Chemistry of C_3 and C_2

The first spectroscopic detection of cometary C_2 was made for comet Bronson (Donati, 1864, Huggins, 1867). Although known to be of carbonaceous origin, the carrier of the Swan bands

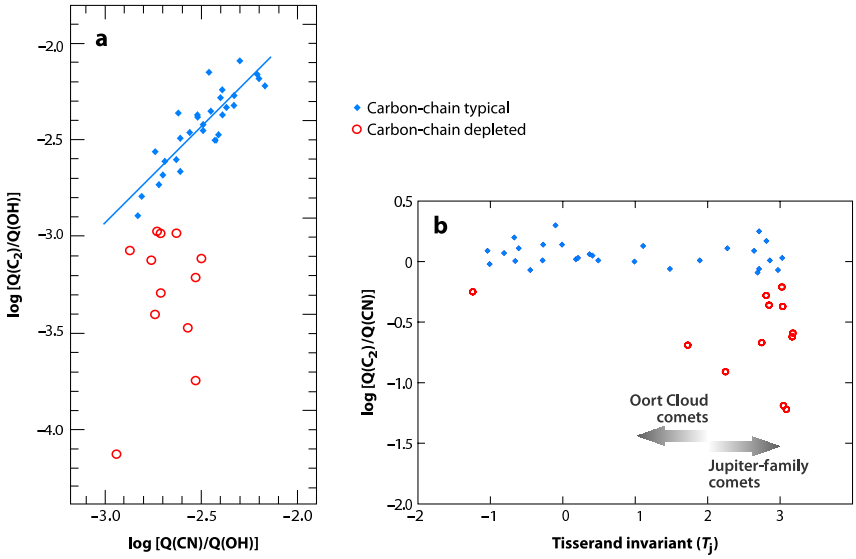

Figure 2.4: *Carbon-chain depleted comets and typical comets as found by A'Hearn et al. (1995). The left panel shows the two groupings of comets of which the upper group follows a slope of* ≈ 1. *The right panel shows the number of carbon-chain depleted and typical comets among the NICs (from the Oort cloud) and among the ECs including the Jupiter family comets* ***(JFCs)*** *(from the scattered disk* ***(SD)****). Source: Mumma and Charnley (2011).*

(fluorescence emission bands in the optical wavelength range of C_2) were only clearly identified as C_2 much later by Mulliken (1927). Donati (1864) and Huggins (1867) also detected emissions at 4050 Å in comet Bronson from the C_3 radical. Since then, these emissions have been detected in several other comets, though not in all. Douglas (1951) identified the C_3 radical as the source of such emissions (Grunenberg, 2010).

2.4.1 Early Investigations on the Origin of C_3 and C_2

Several parent molecules were suggested to be responsible for the observed C_3 and C_2. Stief et al. (1965) assumed a one-step formation of C_2 from C_2H_2. However, this was in disagreement with subsequent photodissociation experimental results of Okabe (1975) and observations of Yamamoto (1981), which led Jackson (1976) to propose a two-step formation: $C_2H_2 \xrightarrow{\gamma} C_2H \xrightarrow{\gamma} C_2$. Model calculations of Yamamoto (1981) and Cochran (1985) supported this idea. C_2H_2 (Brooke et al., 1996b, Tokunaga et al., 1996) as well as an additionally assumed parent molecule candidate, C_2H_6 (Mumma et al., 1996) were first detected in 1996 in comet C/1996 B2 **(Hyakutake)**. C_4H_2 was introduced by Swings (1965) to explain formation of C_3 in a two-step formation processes, e.g. $C_4H_2 \xrightarrow{\gamma} C_3H \xrightarrow{\gamma} C_3$. Stief (1972) proposed a one-step C_3 formation from CH_3C_2H (propyne) as it was already detected in the interstellar matter **(ISM)** (Snyder and Buhl, 1973) and since it is the simplest stable hydrocarbon containing C_3. Later, Jackson (1976) suggested a two-step formation of C_3 from CH_3C_2H via C_3H_2, also suggested by Yamamoto (1981) for comet Kohoutek.

Some authors discussed the possibility of C_3 and C_2 parent molecules being released from ices of different volatility, e.g. H_2O and CO_2, or being produced from photodissociation of different parent molecules with different volatility or even released from dust grains within the coma. A'Hearn and Cowan (1980) for example suggested that the parent molecules of C_3 and CN may sublimate directly from ices in the nucleus more volatile than water, e.g. CO_2, and that the parent molecules of C_2 would be released from H_2O icy grains, since effective H_2O sublimation is reduced at $r_h > 1.8$ AU. This was assumed to explain the increased reduction of C_2 at

$r_h \gtrsim 1.8$ AU in contrast to C_3 and CN (A'Hearn and Millis, 1980, A'Hearn and Cowan, 1980, Newburn Jr. and Spinrad, 1984), see also Krasnopolsky (1991).

Krasnopolsky (1991) explained this observation via the different sublimation temperatures of the following parent molecules: CH_3C_2H (propyne) and $CH_2C_2H_2$ (allene) as well as HCN, as being the main sources of C_3 and HCN at $r_h > 1.8$ AU, respectively, with a low production of C_2 (assuming low amounts of C_2H_2, which also has a very small sublimation temperature, like CH_3C_2H). At smaller r_h C_3H_2O (propynal) produces additional C_3 and the main part of C_2 with additional contributions from HC_3N and C_4N_2. However, at that time it was not known that C_2H_2 is a typical parent molecule in comets.

Combi and Fink (1997) discussed production of C_2 in cometary comae from CHON dust grains. These release either C_2 directly or via a species 'X$-C_2$', e.g. C_2H, which then dissociates to C_2. See e.g. Feldman et al. (2004a) for an overview.

Crovisier (1994) argued for CH_3C_2H and $CH_2C_2H_2$ and proposed C_6H_6 (benzene, an emission at $\lambda = 3.28$ mm in various comets) as being potential C_3 precursors. Benzene was argued to have a large photodissociation rate coefficient in view of the photodissociation measurements of Yokoyama et al. (1990) at 1930 Å and 2480 Å and would dissociate as $C_6H_5 \xrightarrow{\gamma} C_6H_4$ (phenyl to benzyne). Further photodissociation breaks the aromatic ring to form C_3 bearing molecules. However, in Yokoyama et al. (1990) two-photon processes occurred and newer measurements (Tsai et al., 2001, Kislov et al., 2004, Ni et al., 2007) showed a much less efficient photodissociation at the investigated wavelengths. The main dissociation pathway at the investigated wavelengths was $C_6H_6 \xrightarrow{\gamma} C_6H_5 \xrightarrow{\gamma} C_6H_4$. i.e. one additional reaction step before C_3 bearing molecules are produced, which may not be efficient in producing C_3. A similar case is the C_2 formation from C_2H_6, see further below.

Based on mass spectrometric detections of the *Giotto* spacecraft in comet Halley in 1986 of $C_4H_2^+$ which can be formed via $C_4H + H_3O^+ \rightarrow C_4H_2^+ + H_2O$, Geiss et al. (1999) suggested C_4H, produced or released close to the nucleus, as the main C_3 parent molecule. Their argument for this theory, instead of a C_4H_2 release, is the absence of a high $C_4H_3^+/C_4H_2^+$ ratio, which would have been detected due to C_4H_2's high proton affinity. Their estimated C_3H abundance is smaller than that of C_4H. Their estimate was $Q(C_4H) \approx (2.38 \pm 0.8) \cdot 10^{-3}$. They argue these findings to be a sign of interstellar cloud chemistry, where the so called odd-even effect is observable: even unsaturated carbon chains like C_4H are more abundant than odd carbon chains like C_3H.

$C_3H_3^+$ (Korth et al., 1989) and C_3H^+ (Marconi et al., 1989) were also argued to be detected by mass spectrometers in comet Halley by ion mass peaks at 39 amu and 37 amu, respectively. Those studies suggest a source of unsaturated hydrocarbon chains, released from CHON dust particles. $C_3H_3^+$ may result mainly from $C_3H_2 + H_3O^+ \rightarrow C_3H_3^+ + H_2O$ (Geiss et al., 1999).

2.4.2 Recent Investigations on the Origin of C_3 and C_2

Helbert (2002) and Helbert et al. (2005) successfully fitted observations from the longterm monitoring program of comet Hale-Bopp obtained in Rauer et al. (1997) and Rauer et al. (2003), i.e. at $r_h = 2.86$ AU to $r_h = 4.74$ AU assuming only parent molecules that sublimate directly from the nucleus ices. They applied a one-dimensional **(1D)** hydrodynamical model (ComChem) of the coma together with a complex chemistry scheme. C_2H_2 was the assumed main parent molecule of C_2, produced via photodissociation and electron impact dissociation - directly and via the intermediate C_2H. An important finding was the minor contribution of C_2H_6 to C_2 in the range 10^4 km to $\approx 3 \cdot 10^5$ km of the observations due to the long dissociation path $C_2H_6 \xrightarrow{\gamma} C_2H_4 \xrightarrow{\gamma} C_2H_2 \xrightarrow{\gamma} C_2H \xrightarrow{\gamma} C_2$. Electron impact dissociation rate coefficients for C_2H_6 were unknown at that time and not estimated in their work, but it was argued that these would have to be orders of magnitudes higher than the C_2H_6 photodissociation rate coefficients to be

significant.

The isomers CH_3C_2H (propyne) and $CH_2C_2H_2$ (allene) of C_3H_4 were combined into one molecule to produce C_3, since the isomers were argued to be indistinguishable by optical observations of C_3 and since molecular data was insufficient at that time. However, the absorption cross sections of both isomers differ (so that their total rate coefficient may differ as well) by one order of magnitude. HC_3N was not used to explain C_2, since this molecule would exceed the CN production in comet Hale-Bopp, which is already well explained by the photodissociation of HCN (Rauer et al., 2003).

In addition, the rate coefficient of $C_3H_4 + e^- \rightarrow C_3 + 2 \cdot H_2 + e^-$ was estimated in order to model the electron impact dissociation path ways. Photodissociation rate coefficients leading to the intermediate C_3H_3 were computed (Fahr et al., 1997). The C_3H_2 and the C_3 photodissociation rate coefficients had to be estimated by adjusting the rate coefficients to fit the observed reaction products. C_4H_2 was excluded as a potential parent molecule, since its estimated lifetime was higher than that of the assumed C_3 parent molecule for comet Halley as argued by Krasnopolsky (1991). However, Helbert (2002) stated: "Although the reaction network for the formation of C_3 shows a good agreement with the observed C_3 column density profiles it is still preliminary".

Weiler (2006) studied the C_3 and C_2 formation chemistry at smaller heliocentric distances, i.e. $r_h = 1 - 1.5$ AU, and for three different comets, i.e. C/2001 Q4 **(NEAT)**, C/2002 T7 **(LINEAR)** and Tempel 1. For this study a new coma chemistry model was constructed (ComChem model as used in Helbert (2002), Helbert et al. (2005) was no longer available). This new scheme successfully reproduced earlier studies (Helbert, 2002, Helbert et al., 2005) within a factor of two for the observations of comet Hale-Bopp at $r_h = 3.78$ AU and using the same reaction network.

The observations of the comets NEAT, LINEAR and Tempel 1 could not be reproduced by Weiler (2006) using their coma chemistry model and the reaction network of Helbert (2002), Helbert et al. (2005). As a consequence Weiler (2006) updated the hydrocarbon dissociation reactions, i.e. electron impact and photodissociation reactions of hydrocarbon species. The updated electron impact reactions were significantly smaller than in Helbert (2002), Helbert et al. (2005), so small that they played no significant role in the formation of C_3 and C_2.

The above mentioned overestimated electron impact rate coefficients were found in Weiler (2006) as follows. A rise of the modeled C_3 column densities appeared for the comets with a large water production rate $Q(H_2O)$, i.e. LINEAR and NEAT, due to electron impact reactions, whereas no such rise appeared in the C_3 column densities of comet Tempel 1 with smaller water production rates $Q(H_2O)$ than the comets LINEAR and NEAT. This rise is connected to a higher energy of the electron gas, when cooling by collisions with H_2O molecules is reduced, as the coma density decreases in the intermediate coma due to expansion. The contribution of reactions with a relatively large energy barrier for C_3 production is therefore increased. The rise is closer to the nucleus for comets with a relatively low $Q(H_2O)$, which was the case for Tempel 1 at $r_h = 1.51$ AU and also for Hale-Bopp at $r_h = 3.78$ AU. For these comets this onset is at $r_c < 10^3$ km, i.e. also below the observational range of the comets Tempel 1 and Hale-Bopp. The new electron impact dissociation rate coefficients (Alman et al., 2000, Woodall et al., 2007) removed the C_3 column density rise.

As Weiler (2006) could not reproduce the C_3 and C_2 observations of the comets NEAT, LINEAR and Tempel 1 using only the C_3 parent molecule C_3H_4 and the additional C_2 parent molecule C_2H_2 when applying their updated reaction network the molecules C_4H_2 and HC_3N were introduced in that work as additional parent molecules. Photodissociation rate coefficients were calculated for C_4H_2 and HC_3N. The reaction $C_4H_2 \xrightarrow{\gamma} C_3 + CH_2$ was assumed in order to produce C_3 very fast. Estimated were the photodissociation rate coefficients of the radicals C_3N, C_4H and C_4, in light of the missing absorption cross sections and quantum yields.

Weiler (2006) succeeded in reproducing reasonably well the C_3 and C_2 observations of comet

NEAT using the parent molecules C_3H_4, C_4H_2, C_2H_2 and HC_3N and the updated reaction network. However, unrealistically high production rate ratios for the investigated parent molecules C_3H_4 and HC_3N were required for this to achieve. For LINEAR and Tempel 1 only the C_3 observations could be reproduced, the modeled C_2 column densities were, however, flatter in comparison with the observations. Weiler (2006) could also not reproduce the observations of Hale-Bopp (at $r_h = 3.78$ AU). That study found that C_2H_6 has only a very little contribution to the observational C_2 of the investigated comets.

CHAPTER 3

Physics and Chemistry of Cometary Comae

This chapter describes the physics and chemistry of cometary comae. It starts by describing the sublimation of ices making up the coma and the interaction between the coma and the solar wind. After dealing with the characteristics of the neutral coma gas, important for this thesis. We then discuss the physical regimes, the hydrodynamics and the initial conditions. The coma chemistry section follows, with a focus on photochemistry, which is closely investigated in this thesis. This chapter also discusses the optical depth in cometary comae.

3.1 Physics

3.1.1 Sublimation of Ices

Sublimation of volatiles from the cometary nucleus depends on several properties of the nucleus: the volatility of the ices, their mixture with dust, the ratio of amorphous to crystalline ices, layers of dust preventing ice heating by re-radiation in the infrared **(IR)** and the heat conduction into the interior of porous ice-dust mixtures leading to sublimation from subsurface regions. The onset of sublimation is referred to as the point where the sublimation rate increases strongly, transitioning into a nearly r_h^{-2} dependence for smaller r_h, since nearly all energy is used for sublimation. The result for a comet with an albedo of $A = 0.04$ and emissivity $\epsilon = 0.9$ is shown in Figure 3.1a for the species H_2O, CH_3OH, NH_3, CO_2, C_2H_6, CH_4 and CO. CO starts to sublimate at 24 K or $r_h = 100 - 200$ AU whereas H_2O starts to sublimate at $r_h = 3 - 5$ AU. At this distance the surface temperature has exceeded $T = 150$ K (Jewitt et al., 2008). Nevertheless simple sublimation models, e.g. Meech and Svoren (2004), which solve the energy balance at the nucleus surface, Equation (3.14), for a pure ice layer neglecting heat conduction k_s, can provide estimates of each molecule's sublimation temperature and of the development of the sublimation rate with heliocentric distance.

3.1.2 Coma - Solar Wind Interactions

The solar wind consists mainly of H^+, He^{2+} and electrons, which stream radially away from the Sun with around 400 km s^{-1}. The imprint of the Sun's magnetic field is thereby carried by the solar wind and moves outward with it to larger distances. Since the Sun rotates, the magnetic field forms a so-called Parker-spiral around the Sun (Milone and Wilson, 2008).

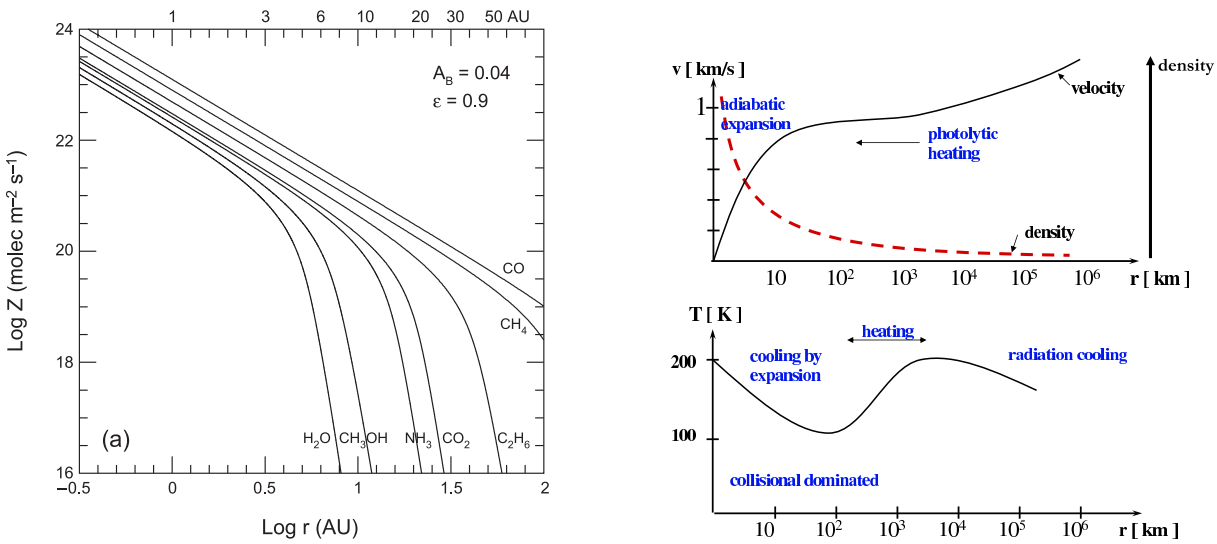

(a) *Change of sublimation rates with r_h.* **(b)** *Change of v, T, n with r_c.*

Figure 3.1: *(a) The change of sublimation rates Z with heliocentric distance r_h and log(r_h), calculated for pure ice surfaces, assuming an albedo $A = 0.04$, an emissivity $\epsilon = 0.9$ and neglecting heat conduction k_s. Source: Meech and Svoren (2004). (b) The principle change of mean velocity v, temperature T and density n of the gas in the coma with cometocentric distance r_c. Source: Jewitt et al. (2008).*

Ions are formed in the cometary coma by photodissociation, charge exchange reactions and collisional ionization. A large interaction zone between these ions and the solar wind establishes as the comet approaches the Sun and as its activity increases. The magnetic field of the solar wind picks up an increasing number of cometary ions via charge-exchange reactions, also called mass loading, with decreasing distance to the comet. This leads to a reduction of the solar wind speed. A bow shock can form at the boundary between the supersonic solar wind and the subsonic ions in the coma, e.g. located at the cometocentric distance of the cometary coma $r_c \approx 10^6$ km for a moderately active comet like 1P **(Halley)** at a distance to the Sun (r_h) of $r_h \approx 1$ AU, i.e. with a water production rate $Q(\mathrm{H_2O}) \approx 10^{30}$ s^{-1} (Combi and Feldman, 1993), see Figure 3.2.

With decreasing distance of the solar wind to the cometary nucleus, behind the cometary bow shock, the mass loading of the solar wind increases and its velocity decreases further until reaching the cometary ionopause (the pressure boundary between cometary and solar wind ions). Inside the ionopause pure cometary plasma exists besides neutral cometary species. Within the ionopause, in direction to the cometary nucleus, a magnetic field free cavity surrounds the inner coma, e.g. at about $3.5 \cdot 10^3$ km for a moderately active comet at $r_h = 1$ AU, for example comet Halley during the *Giotto* spacecraft encounter in 1986. This is also approximately the region where the electron temperature drops because the density of H_2O is high enough to efficiently cool via collisions. This also forms the transition region between the outer free molecular flow region and the inner collisional coma (Jewitt et al., 2008).

Due to the pile up of the solar magnetic field lines in front of the ionopause, arriving cometary ions are accelerated up to several hundreds of km s^{-1} and carried away, forming the cometary ion tail. Comets far away from the Sun, or with low activity, however, may lack a bow shock or even a magnetic cavity (Jewitt et al., 2008, Rodgers et al., 2004, Cravens and Gombosi, 2004).

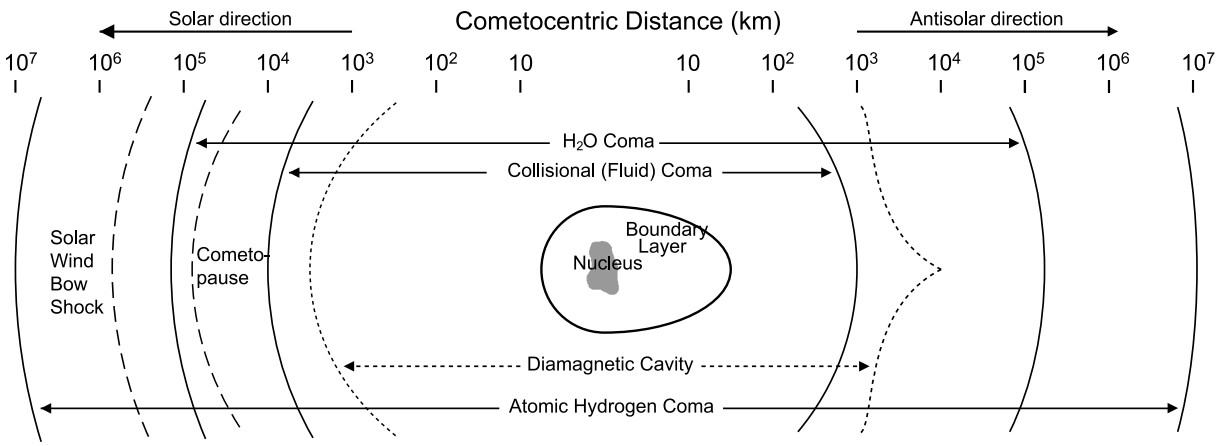

Figure 3.2: *Structure and physical regimes in a cometary coma of a moderately active comet like Halley at $r_h = 1$ AU. The cometocentric distance scale is logarithmic. Source: Rodgers et al. (2004).*

Figure 3.3: *Physical regimes of the coma of a moderately active comet like Halley at $r_h = 1$ AU. Shown are the Knudsen number K, expressing the deviation of the gas flow from local thermodynamic equilibrium conditions, and the deformation of the coma due to the pressure of the solar radiation. Adopted from Jewitt et al. (2008).*

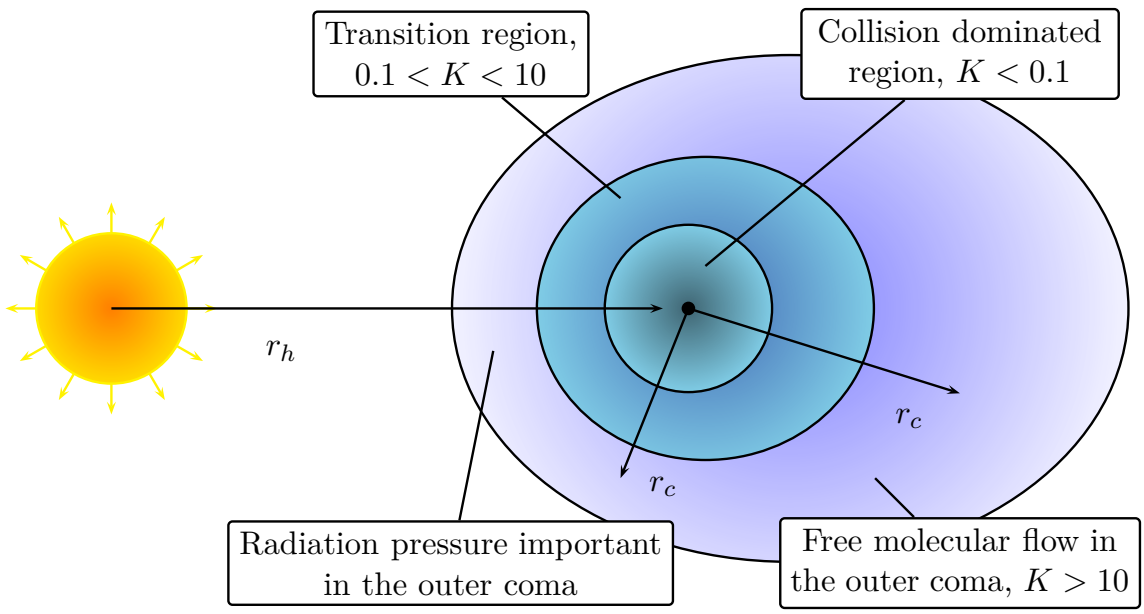

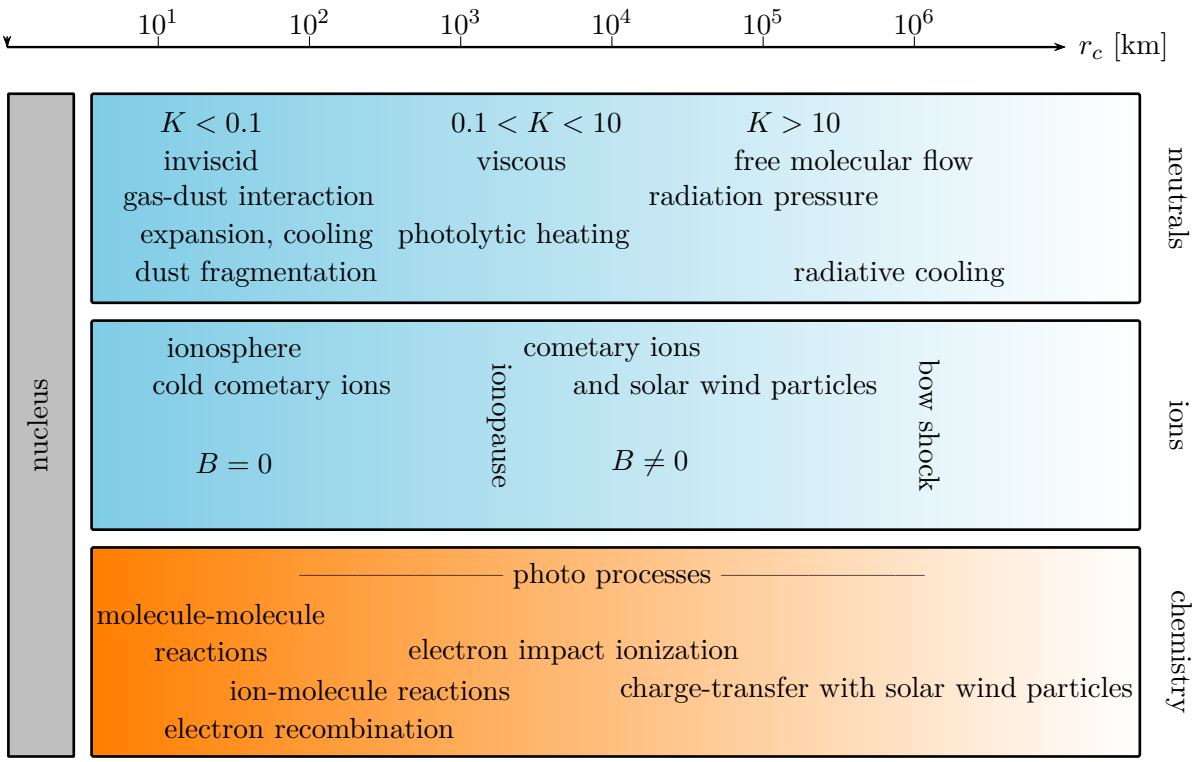

Figure 3.4: *Overview of the typical flow regimes in the coma of a moderately active comet like Halley at $r_h = 1$ AU. r_c is the cometocentric distance. Shown are also the physical and chemical processes. B denotes the magnetic field, which is zero in the inner coma, and K the Knudsen number, which describes the deviation of the gas flow from local thermodynamic equilibrium conditions. Adopted from Jewitt et al. (2008).*

3.1.3 Neutral Coma Characteristics

As the Sun heats the surface of a comet gas molecules sublimate from active surface regions into the coma. In the following description the evolution of the gas characteristics is regarded thereby starting at the nucleus surface then moving to the outer coma regions. An overview of the relevant physical processes and their associated regions is displayed in Figures 3.2, 3.3 and 3.4. For a Halley-type comet with a sublimation or production rate $Q(H_2O) = 10^{30}$ molecules s^{-1} at $r_h = 1$ AU the main acceleration of the cometary gas occurs at cometocentric distances r_c between the nucleus out to a few kilometers by adiabatic expansion into vacuum. The mean gas velocity increases further to $u \approx 1$ km s^{-1} within the first tens to a few hundreds of kilometers above the nucleus. The coma density decreases with r_c^{-2} assuming an isotropic expansion with velocity $u = 1$ km s^{-1}. Photolytic heating sets in at r_c of around a hundred kilometers, which leads to further acceleration of the gas beyond r_c of a few thousand kilometers.

The gas temperature of 200 K above active surface areas on the nucleus drops to around 100 K at $r_c = 10^2$ km to $r_c = 10^3$ km and down to 20 K for pure adiabatic gas expansion. However, higher temperatures have been observed which may be a result of re-condensation or gas-dust interactions. The photodissociation reactions $H_2O + \gamma \rightarrow OH + H$ and $OH + \gamma \rightarrow O + H$, in which γ denotes a photon which the molecule absorbs, H has average excess velocities of 18 km s^{-1} and 7 km s^{-1}, respectively, are the main heat source of the gas between $r_c = 10^3$ km and $r_c = 10^4$ km. However, other photolysis reactions contribute as well. At distances larger than $r_c = 10^5$ km radiative cooling becomes important as the density of the coma and therefore also the optical thickness drops further.

3.1.4 Physical Regimes

After a few molecular collisions above the surface the gas reaches a Maxwellian velocity distribution. From there to 10^3 km the gas flow is collisionally dominated, i.e. in local thermodynamic equilibrium and can be described by macroscopic properties. Beyond 10^4 km, i.e. after the transition region, the gas motion is an almost free molecular flow due to the low molecular density. Farther out the solar radiation pressure and the charged solar wind become important, compressing the coma by accelerating the gas into the anti-solar direction, see Figure 3.3.

The appropriate mathematical description of the coma, whether hydrodynamical for collision dominated conditions or a Monte-Carlo approach for free molecular flow conditions, can be determined using the Knudsen number K. This number compares the molecular mean free path length for collisions λ with a characteristic length L of the modeled system (Jewitt et al., 2008)

$$K = \frac{\lambda}{L} \,. \tag{3.1}$$

The molecular collisional mean free path λ is calculated via

$$\lambda = \frac{1}{\sqrt{2}\sigma n} = \frac{u}{\sqrt{2}\sigma Z_{\text{gas}}} \,, \tag{3.2}$$

where σ is the collisional cross section of the gas molecules, n the particle number density, Z_{gas} [molecules m^{-2} s^{-1}] the surface sublimation rate and u the velocity at the surface. A typical number density in the inner coma of $n = 10^{19}$ m^{-3} and collision cross section 10^{-19} m^2 for the most abundant cometary species water results in $\lambda \leq 1$ m, which is small compared to the cometary nucleus, e.g. $d = 1 - 50$ km or the cometary coma, e.g. $d \approx 10^6$ km, i.e. the scale at which physical properties change significantly (Huebner, 1990). As K expresses the number of collisions or degree of dilution of the medium it measures the deviation of the gas flow from local thermodynamic equilibrium, see e.g. Lockerby et al. (2009).

An inviscid hydrodynamical description, i.e. the Euler equations, can be applied for $K < 0.1$, where the medium can be described as being continuous using the macroscopic variables density, pressure, velocity and temperature. For cometary comae the collision dominated region having $K < 0.1$ extends up to around 10^3 km, when assuming L to be the nucleus' radius r_{nucleus}. Alternatively, the radial distance r_{c} to the nucleus can be used. The transition region, where the gas is still hydrodynamic but viscous having $0.1 < K < 10$ extends from about 10^3 km to 10^4 km. In this regime the Navier-Stokes equations have to be used, hence the Euler equations including terms describing internal friction. From 10^4 km to 10^5 km lies the transition region, and beyond 10^5 km the free molecular flow region. The properties of the gas in the free molecular flow region, where e.g. no temperature is defined, have to be modeled with a Monte-Carlo approach, i.e. a reduced number of particles is used to model the molecular trajectories and collisions (Jewitt et al., 2008).

3.1.5 Hydrodynamics - Basic Equations

Starting with the basic Euler equations the conservation equations for particle number, mass, momentum and energy density are given in Equations (3.3), (3.4), (3.5) and Equation (3.6), where n is the particle number density, N its source term, ρ the mass density and $\mathbf{u}$ is the velocity vector

$$\frac{\partial n}{\partial t} + \nabla \cdot (n\mathbf{u}) = N \,, \tag{3.3}$$

$$\frac{\partial \rho}{\partial t} + \nabla \cdot (\rho\mathbf{u}) = M \,. \tag{3.4}$$

M is simply the source by the gas production rate of the comet, e.g. by sublimation, and sources and sinks by chemical reactions. When chemical reactions are regarded each species has to be described by such a set of equations which are then coupled over the source terms.

The Equation

$$\frac{\partial}{\partial t}(\rho \mathbf{u}) + \nabla \cdot (\rho \mathbf{u} \otimes \mathbf{u}) + \nabla p = \mathbf{F}\,. \tag{3.5}$$

describes the acceleration of a fluid element via a pressure gradient ∇p and via an external force density $\mathbf{F}$, such as e.g. gravitation or interaction between gas and dust particles.

The term $\nabla \cdot (\rho \mathbf{u} \otimes \mathbf{u}) + \nabla p$ can also be written with the momentum flux tensor Π as $\nabla \cdot \Pi$ with the components $\Pi_{ij} = \rho u_i u_j + \delta_{ij} p$ in Cartesian coordinates (Landau and Lifschitz, 1991). In the energy conservation equation

$$\frac{\partial \rho e}{\partial t} + \nabla \cdot \mathbf{j}_e = Q \tag{3.6}$$

e denotes the specific energy

$$e = \epsilon + \frac{1}{2}\mathbf{u}^2 \tag{3.7}$$

Q its source term and $\mathbf{j}_e$ the energy flux density with

$$\mathbf{j}_e = \rho \mathbf{u}(\frac{\mathbf{u}^2}{2} + h)\,. \tag{3.8}$$

ϵ in Equation (3.7) denotes the specific internal energy and h in Equation (3.8) is the specific enthalpy, which is the specific internal energy ϵ plus the work done by expansion

$$h = \epsilon + \frac{p}{\rho} = \epsilon + pv\,, \tag{3.9}$$

where v is the specific volume, $v = \rho/m = 1/V$, and p the gas pressure. The mass density ρ can be calculated from the number density n by

$$\rho = \mu \cdot n \tag{3.10}$$

with μ the molecular mass. The equation of state for the cometary gas is usually assumed to follow that of an ideal gas

$$\epsilon = \frac{p}{\rho(\gamma - 1)} = \frac{R_g T}{\gamma - 1} \tag{3.11}$$

with the specific gas constant $R_g = k_B/m$ and the adiabatic exponent $\gamma = (f+2)/f = C_p/C_V$. f is the number of degrees of freedom of the regarded molecule, e.g. $\gamma(H_2O) = 4/3$ with $f(H_2O) = 6$ (3 kinetic, 3 rotational) at low temperatures, and C_p and C_V are the heat capacities at constant pressure and constant volume, respectively (Jewitt et al., 2008).

3.1.6 Gas - Dust Interactions

For dust an analogous set of equations has to be defined, which are usually furthermore subdivided for each particle size interval (Jewitt et al., 2008, p.194). As described in Rodgers et al. (2004), the interaction between gas and dust leads to a reduction of the outflowing gas to subsonic velocities near the nucleus by gas-dust drag (Marconi and Mendis, 1983). The gas then has a transition close to the nucleus from subsonic to supersonic flow. Weiler (2006) showed for comet 67P **(Churyumov-Gerasimenko)** that the effect of dust on the gas flow is negligible for dust-to-gas mass ratios of up to 8.5.

3.1.7 Initial Conditions at the Cometary Nucleus

Initial Velocity u_0

The initial velocity can be approximated by (Weiler, 2006)

$$u_0 \approx c_0 = \sqrt{\gamma R_g T_0}\,, \tag{3.12}$$

where γ is the adiabatic exponent, R_g is the specific gas constant and T_0 the initial gas temperature, which is computed below. On the one hand gas-dust interactions restrict the gas flow to subsonic velocities, on the other hand closely above the cometary nucleus the gas flow rapidly becomes supersonic due to the reduction of the local sonic speed, since the gas cools down to several tens of Kelvins due to adiabatic expansion. The gas dilutes approximately with r_c^{-2}.

Initial Temperature T_0

The initial gas temperature T_0 can be calculated using a simple sublimation model from Knollenberg (1993) in which a pure ice surface is considered. First the ice temperature T_s is calculated using the Clausius-Clapeyron equation, to relate the vapour pressure and the temperature of the sublimating ice (Fanale and Salvail, 1984), and then a reservoir outflow analogy (Knollenberg, 1993)

$$T_0 = \frac{T_s}{1 + \frac{1}{2}(\gamma - 1)} \tag{3.13}$$

is used to calculate the initial temperature T_0 from the ice temperature T_s. T_0 is only defined after some molecular collisions above the surface have taken place, hence when it may be assumed that a Maxwellian velocity distribution is reached. For $r_h < 3$ AU one can assume the adiabatic exponent of water $\gamma = 4/3$, the most abundant species in cometary comae at such distances.

To derive the surface temperature T_s the energy balance at the comet nucleus is required, approximated by a pure ice surface, which can be written as

$$\frac{F_\odot(1 - A_v)}{r_h^2}\cos(\phi) = \epsilon_{\mathrm{IR}}\sigma T^4 + H(T)Z_{\mathrm{gas}}(T) - k_s \left.\frac{\partial T}{\partial z}\right|_s\,, \tag{3.14}$$

with the visual albedo A_v, solar photon flux $F_\odot$, heliocentric distance r_h, solar zenith angle ϕ, infrared emissivity ϵ_{IR}, Stefan-Boltzmann constant σ, ice temperature T, latent heat of sublimation H, surface sublimation rate Z_{gas}, heat conduction k_s and temperature gradient at the surface $\partial T_s/\partial z|_s$. The energy which the comet's surface can absorb is the reduced solar photon flux at the comets distance r_h, reduced due to the mean solar zenith angle ϕ of 60°, and an assumed albedo $A = 0.04$ of the comet nucleus. Energy is emitted partly as thermal radiation with an assumed emissivity of around $\epsilon = 0.9$. Some of the energy leads to sublimation of material from the nucleus. The heat conduction of the ice into the nucleus is neglible for $r_h < 3$ AU, since the energy conducted into the interior is very small compared to the energy consumed by the sublimation of ices (Huebner et al., 2006, chapter 5).

3.2 Chemistry

Chemical reactions critically affect the abundances of key species in the coma. The influence of each reaction type depends inter alia on the nucleocentric distance r_c, e.g. proton transfer reactions in the inner coma, where gas densities are high enough, and the heliocentric distance r_h.

Table 3.1: *Reaction types in cometary comae.*

reaction type	example
photodissociation	$H_2O + \gamma \rightarrow OH + H$
photoionization	$H_2O + \gamma \rightarrow H_2O^+ + e^-$
photodissociative ionization	$CO_2 + \gamma \rightarrow CO^+ + e^- + O$
e^- impact dissociation	$C_2H_2 + e^- \rightarrow C_2 + H_2 + e^-$
e^- impact ionization	$CO + e^- \rightarrow CO^+ + 2e^-$
e^- recombination	$H^+ + e^- \rightarrow H + \gamma$
dissociative e^- recombination	$C_2H^+ + e^- \rightarrow C_2 + H$
neutral-neutral rearrangement	$H_2CO + H \rightarrow HCO + 2H$
charge exchange	$CO^+ + H_2O \rightarrow CO + H_2O^+$
neutral-ion rearrangement	$C_2H_6^+ + H_2O \rightarrow C_2H_5 + H_3O^+$
ionizative association	$CH + O \rightarrow CHO^+ + e^-$
e^- impact excitation	$CO + e^- \rightarrow CO^* + e^-$
radiative de-excitation	$CO^* \rightarrow CO + \gamma$

3.2.1 Reactions

Molecule-molecule, ion-molecule and electron recombination reactions become important close to the nucleus, i.e. $r_c < 10^2$ km, where densities are high, see also Figure 3.4. The density in the coma decreases with $\approx r^{-2}$. Photolytic reactions constitute key chemical processes throughout the coma, see Section 3.2.2. They may be reduced by high optical thicknesses in the inner coma, but only for very active comets. The main heat source for the neutral coma is the photodissociation of H_2O into H and OH, which possess an average excess speed of 18 km s^{-1} and 1 km s^{-1}, respectively. H atoms with an average excess speed of 7 km s^{-1} are produced by the dissociation of OH. These species heat the inner coma by collisions with other neutral molecules, mainly H_2O and CO. In the outer coma these species do not thermalize with the surrounding gas and therefore represent an energy sink. Neutral molecules are ionized by photons, electrons and solar wind particles. An overview of some reaction types in the cometary coma is presented in Table 3.1. The most important processes to initiate the complex chemistry in the coma are photodissociation and photoionization, in which radicals, ions and electrons are produced. Electron impact dissociation occurs in the inner coma where the electrons decouple from the water gas as the density of H_2O molecules decreases, so that more and more electrons are able to overcome reaction activation energies.

Chemical reactions are modeled by solving a set of reaction equations, e.g. for the reaction $A + B \longrightarrow C + D$, one has from the law of mass action (Jewitt et al., 2008)

$$\frac{\partial n_A}{\partial t} = \frac{\partial n_B}{\partial t} = -k n_A n_B, \qquad \frac{\partial n_C}{\partial t} = \frac{\partial n_D}{\partial t} = k n_A n_B\,, \tag{3.15}$$

with $n_A, \ldots, n_D$ the number densities of species A to D, where species A and B are replaced in the coma by species C and D. All reactions involving a species i may be summarized by (Schmidt et al., 1988)

$$N_i = \frac{dn_i}{dt} = \sum_{j=1}^{J} N_i^j = \sum_{j=1}^{J} \nu_{ij} k_j \prod_{l=1}^{S} n_l^{m_{lj}} = \sum_{j=1}^{J} \nu_{ij} R_j, \qquad i = 1, \ldots, S\,. \tag{3.16}$$

This equation expresses the net change N_i of the density n_i per time interval of species i by its production and destruction by J reactions. N_i^j describes therefore the destruction or creation

of species i by reaction j. ν_{ij} is the stoichiometric coefficient of species i in reaction j, giving the amount of species i produced or destroyed per reaction j, being negative for educts and positive for products. The reaction order m_{lj} is equal to $|\nu_{lj}|$ if ν_{lj} is negative, for those species l which are educts in reaction j, and zero otherwise, i.e. for products of reaction j or species not involved in reaction j (Schmidt et al., 1988). Therefore, also l runs from 1 to the number of species S regarded, as does the index i. R_j is the reaction rate.

The rate coefficients k_j of these reactions may be expressed in a general Arrhenius form

$$k_j = A_j \left(\frac{T}{300K} \right)^{B_j} \exp\left(\frac{-C_j}{T} \right). \tag{3.17}$$

The coefficients A_j, B_j and C_j are the fitting parameters for the T dependence of Equation (3.17), obtained in the laboratory or by ab initio calculations. The Arrhenius form is only valid for local thermodynamic equilibrium **(LTE)** conditions, i.e. the velocities are Maxwell-distributed. The dependency on impact energy $E_i \sim \sqrt{T}$ is described with the term $(T/300\text{ K})^{B_j}$. A possible dependency on an activation energy E_a is modeled via the term $e^{-C_j/T}$. The temperature T is that of the reactants, e.g. between neutral species (Jewitt et al., 2008). If ions and neutral molecules are treated as separate fluids, having different temperatures, an effective temperature has to be applied. This is described in more detail in the model description in Chapter 5 (p.63).

3.2.2 Photochemistry

Radical formation of tri- and dicarbon (C_3, C_2) is investigated in detail in this thesis. Photodissociation is the dominant chemical process in cometary comae. C_3 and C_2 are photodissociation products of carbonaceous molecules, where e.g. C_2H produces C_2. As this work also focuses on uncertainties of photodissociation rate coefficients, the following section gives details about the relevant processes.

Photodissociation can be subdivided into: direct photodissociation, the indirect photo processes predissociation and spontaneous radiative dissociation and unimolecular dissociation, see e.g. Herzberg (1966), Schinke (1993), van Dishoeck and Visser (2011). Whether a direct or an indirect photodissociation process dominates, varies from molecule to molecule. Direct photodissociation prevails for example in H_2O and OH, predissociation in CO and spontaneous radiative dissociation in H_2 ($E > 13.6$ eV or $\lambda < 900$ Å). The following description of these processes is based mainly on discussions summarized from van Dishoeck and Visser (2011), Schinke (1993) and Drake (2006, chapter 34).

Direct Dissociation

Absorption of a photon can excite a molecule AB into the excited molecule AB* which can be either unstable (repulsive state) or stable (bound, attractive state). These processes are denoted bound-free and bound-bound transitions, respectively.

In the case of direct dissociation a continuous absorption spectrum is observed as seen in the upper panel of Figure 3.5. This figure shows the three dissociation processes: direct dissociation, the indirect processes predissociation and spontaneous radiative dissociation and their typical absorption spectra, for a diatomic molecule (van Dishoeck and Visser, 2011). In the upper panel of Figure 3.5 the molecule AB is directly fragmenting since the molecule's energy is higher than its bond energy in its electronic ground state and since no potential well exists in this excited state, which hinders separation of the atoms.

Electronic transitions are much faster than the nuclear vibration according to the Born-Oppenheimer approximation, therefore the relative positions of the nuclei do not change, when the molecule transitions into an excited electronic state. The energy difference between the two

electronic states at equal internuclear distance is denoted the vertical excitation energy. For bound states in the vibrational ground state the molecule has the highest probability of being present at the equilibrium internuclear distance. Therefore the highest absorption occurs at the vertical excitation energy, where the largest overlap between the initial and final wave functions exists, as shown in Figure 3.6. Therein k =1, 2, 3 denote the ground, the first bound excited and the second repulsive excited states, respectively, $\Psi(E_f)$ is the continuum wavefunction, E_{excess} is the available energy to be distributed among the dissociation products' degrees of freedom. The absorption cross sections are drawn on the right side, i.e. discrete for the bound state and continuous for the repulsive state. $\hbar\omega_1$ denotes the photon energy for transition into the second vibrational level of the first excited state.

An example for direct dissociation apparent in an absorption spectrum is shown for the H_2O molecule in Figure 3.7a. Around $E = 7.5$ eV or $\lambda = 165$ nm the absorption continuum of the $\tilde{X}^1A_1 \rightarrow \tilde{A}^1B_1$ † electronic transition is clearly visible. Absorption peaks are thinner for steep repulsive potentials (van Dishoeck and Visser, 2011). For very steep repulsive potentials the absorption peaks become visible in the absorption spectrum, i.e. they do not overlap to form one smooth continuum since they are now less broad (Schinke, 1993, chapter 6).

Predissociation

In predissociation the molecule is excited to a bound state but then interacts with a repulsive state non-radiatively (van Dishoeck and Visser, 2011) as depicted in the middle of Figure 3.5. Predissociation can be subdivided into electronic, vibrational and rotational predissociation, also called Herzberg type I, II and III predissociation, see Herzberg (1966) or (Drake, 2006, chapter 34). In vibrational predissociation a potential well can be tunneled or it can be overcome by increasing the vibrational energy by supplying vibrational energy from other nuclear degrees of freedom, also called intramolecular / internal vibrational energy redistribution **(IVR)**, Figure 3.7b. This can only operate if the molecule has more than two atoms. In rotational predissociation the process is analogous but for a rotational state. In electronic predissociation the upper bound state interacts non-radiatively with an energetically nearby overlapping repulsive electronic state to which the molecule can transition and finally dissociate, see the middle left panel of Figure 3.5.

In a spectrum like in Figure 3.7a each electronic band consists of vibrational-rotational lines. These can only be observed with high-resolution spectrometers provided the density of states, i.e. the number of energetically close lying electronic states, is relatively low and the predissociated state does not have a short lifetime.

Each rotational line is broadened by the individual movement of each molecule (Doppler broadening) and by the natural lifetime of the excited state (natural broadening) by the Heisenberg principle. In the case of predissociation the lifetime of the excited state can be very short $\tau < 10^{-10}$ s and so natural broadening usually dominates. For very short lifetimes the rotational line structures cannot be resolved even in high resolution measurements. Broad bands are also observed in direct dissociation in the case of very shallow repulsive / dissociating states, see (Schinke, 1993, Figure 6.4, p.119), as mentioned for direct dissociation described above.

† Molecular term symbol of electronic state with general form ${}^{2S+1}\Lambda^{(+/-)}_{\Omega(\text{g/u})}$. S: total spin multiplicity, i.e. number of unpaired e^- times spin 1/2, Λ: projection of orbital angular momentum ($\Sigma, \Pi, \Delta, \ldots = 0, 1, 2, \ldots$), Ω: projection of total angular momentum, onto internuclear distance, respectively, g/u: parity (only for homonuclear diatomics), +/-: symmetry along an arbitrary plane containing internuclear axis. Example: C_2 ground state $X^1\Sigma_g$. An empirical notation of an electronic transition is $\tilde{X}^1A_1 \rightarrow \tilde{B}^1A_1$, which means ${}^1A_1 = {}^{2S+1}A_\Omega$, $\tilde{X}$: electronic ground state, all electronically excited states with the same Λ are denoted B, C, etc., ordered by energy above $\tilde{X}$. $\sim$ is added for polyatomics ($\neq$ diatomics). For states with different Λ than the ground state one uses a, b, c. Examples: C_3 excited state to ground state transition: $\tilde{A}^1\Pi_u - \tilde{X}^1\Sigma_g^+$, C_2 excited state to excited state transition $d^3\Pi_g - a^3\Pi_u$ (Demtröder, 2003, Section 2.4).

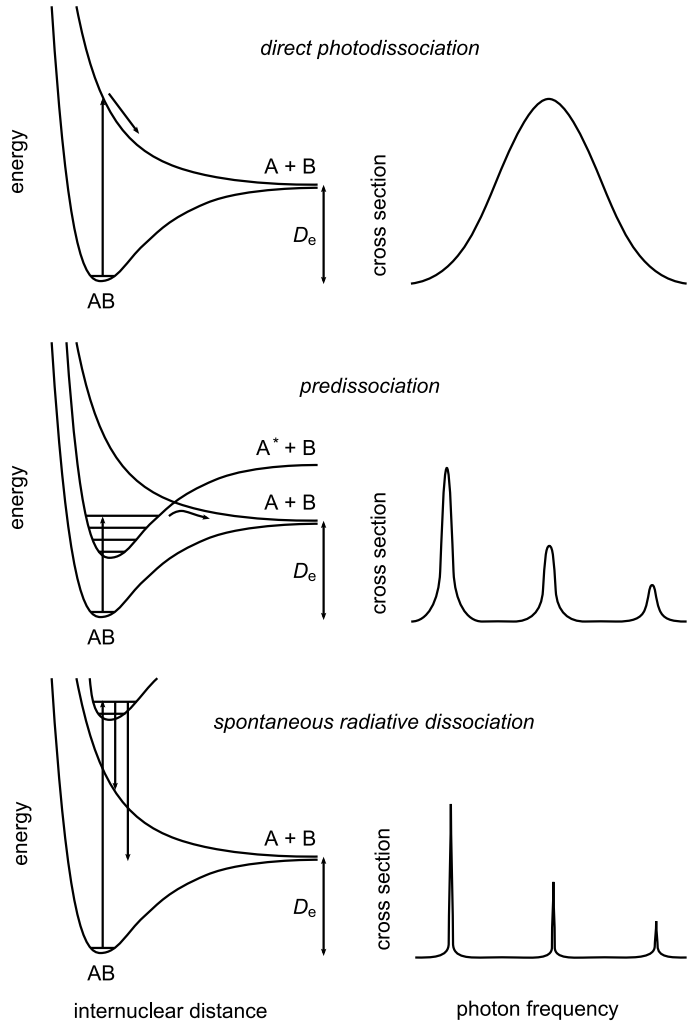

Figure 3.5: *Direct (continuous) dissociation and the indirect dissociation processes predissociation and spontaneous radiative dissociation, in the upper, mid and lower panel, respectively, illustrated for a diatomic molecule. D_e is the dissociation energy, i.e. the minimum energy to dissociate the diatomic AB into A and B. In the upper left Figure the absorption of a photon causes electronic excitation into the antibonding/repulsive potential of the ground electronic state. Source: van Dishoeck and Visser (2011).*

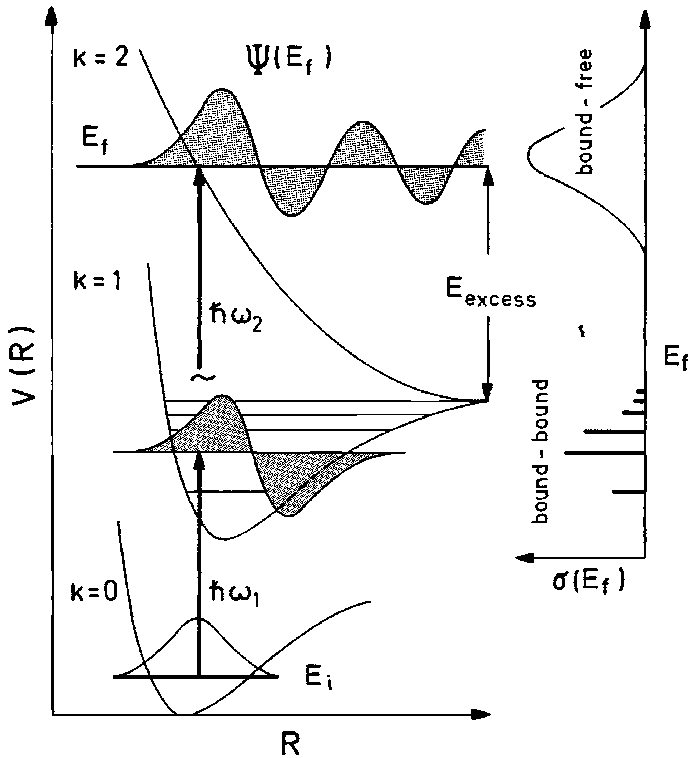

Figure 3.6: *Illustration of electronic transitions from the electronic and vibrational ground state ($k = 0$, $v = 1$) to the second vibrational level of a bound electronic state ($k = 1$, $v = 2$, $E_{photon} = \hbar\omega_1$) and from the electronic and vibrational ground state ($k = 0$, $v = 1$) into a repulsive (free) electronic state ($k = 2$, $E_{photon} = \hbar\omega_2$). R is the internuclear distance between e.g. two atoms of a diatomic molecule. Shown are also the vibrational and the free wave function for the bound and the repulsive excited state, respectively. The vertical arrow marks the vertical excitation, i.e. the Franck-Condon region. On the right panel the corresponding absorption cross sections are shown. Source: Schinke (1993).*

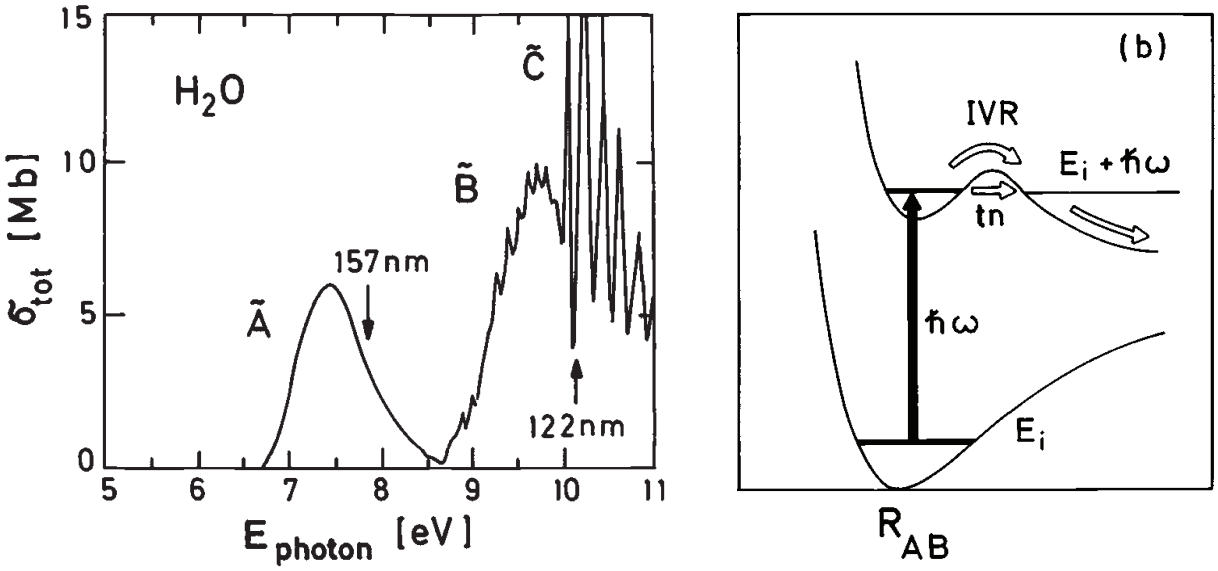

(a) $\sigma(E)$ *of* H_2O. **(b)** *Vibrational predissociation.*

Figure 3.7: *Absorption spectrum* $\sigma(E)$ *of* H_2O *shown in (a) and vibrational predissociation via intramolecular / internal vibrational energy redistribution* ***(IVR)*** *or tunneling (tn) shown in (b).* R_{AB} *is a general depiction of the internuclear distance of the fragments* A *and* B*.* E_i *is the parent molecule energy (initial state). In (a)* $\tilde{A}$*,* $\tilde{B}$ *and* $\tilde{C}$ *denote* H_2O *absorption bands abbr. the responsible transitions from the ground to these excited electronic states. Source: Schinke (1993)*

Doppler broadening is associated with radiative de-excitation, corresponding to lifetimes of $\tau \sim 10^{-8}$ s for allowed and $\tau \gtrsim 10^{-3}$ s for forbidden transitions. Additionally, predissociation with shorter lifetimes might be discernable in the spectrum at lower temperatures where the Doppler width is smaller than at higher temperatures.

In the $\tilde{B}$ band / electronic state of the $\tilde{X}^1A_1 \rightarrow \tilde{B}^1A_1$ transition in Figure 3.7a direct dissociation dominates over indirect dissociation, indicated by the broad continuum only superimposed by small undulations / peaks from excited states with lifetimes of one internal vibration. No rotational structures are identifiable in the lines of the $\tilde{X}^1A_1 \rightarrow \tilde{C}^1B_1$ transition above $E = 10$ eV or $\lambda \approx 122$ nm, where only indirect photodissociation can occur, since the excited states exist for several internal molecular vibrations (Schinke, 1993).

Note that especially for the $\tilde{B}$ band of H_2O, Figure 3.7a, the rather hybrid features (i.e. continuum plus peaks) suggest that the absorption cross sections may be highly averaged quantities resulting from several photodissociation processes (Schinke, 1993).

Spontaneous Radiative Dissociation

Spontaneous radiative dissociation manifests in very sharp absorption peaks as shown in the bottom panel of Figure 3.5. Spontaneous radiative dissociation can occur if the excited molecule radiates a photon through which it transitions into the continuum of a lower lying repulsive state (second arrow from the left) or into the dissociative vibrational continuum of a bound state (third arrow from the left) (van Dishoeck and Visser, 2011). The dissociation efficiency depends on the competition between transition into bound and into free states.

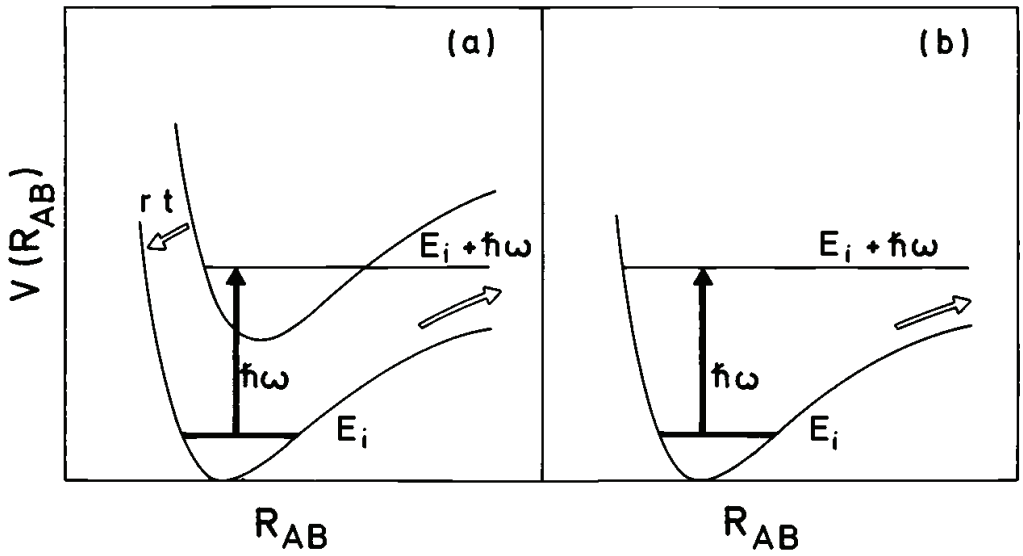

Figure 3.8: *Unimolecular dissociation (a) by internal conversion* ***(IC)*** *from an electronically excited bound state to a high vibrational-rotational quantum level above the dissociation threshold of the electronic ground state by radiationless transition (rt), e.g. for* H_2CO *and (b) by overtone pumping into a high vibrational-rotational quantum level above the dissociation threshold of the electronic ground state, e.g. for* H_2O_2*.* R_{AB} *is the internuclear distance of the two regarded fragments and* E_i *is the parent molecule energy. Source: Schinke (1993)*

Unimolecular Dissociation, Statistical Dissociation

As depicted in Figure 3.8 unimolecular dissociation can dissociate the molecule by two processes. In the left panel of Figure 3.8 the molecule is excited into a bound excited electronic state of equal spin-multiplicity Λ. From there it transitions, via radiationless transition (rt), into a high vibrational-rotational quantum level above the dissociation limit of the electronic ground state. In the right panel of Figure 3.8 a molecule is excited to a high vibrational-rotational level above the dissociation threshold of the electronic ground state via overtone pumping using e.g. IR photons (in the laboratory via a laser). As in both cases the vibrational-rotational excitation level lies above the dissociation threshold the molecule eventually dissociates. Example molecules are H_2CO and H_2O_2, respectively (Schinke, 1993).

For larger molecules the densities of electronically excited states is higher, which can lead to couplings among these states. For such molecules specific models for molecular dissociation, see below, assume that dynamical effects are negligible and that the molecule is excited into a bound state with a high and broad barrier for dissociation. Therefore, internal conversion **(IC)** to the ground state is faster than dissociation by intramolecular / internal vibrational energy redistribution **(IVR)** or tunneling, see e.g. Figure 3.7b These are described in so-called models of "statistical dissociation", like e.g. Rice-Ramsperger-Kassel-Marcus **(RRKM)** models, phase space theory **(PST)**, statistical adiabatic channel model **(SACM)** and the microcanonical metropolis monte carlo **(MMMC)** model. These theories assume that all available energy is used to uniformly populate all quantum states, which obey energy and angular momentum conservation. "Calculating final state distributions [...] basically amounts to counting of states rather than solving the quantum mechanical or classical equations of motion." (Schinke, 1993, p.250).

Mathematical Description of Photodissociation

The photo rate coefficient $k_i(r_c, r_h)$ of a reaction i at the cometocentric distance r_c of the comet and the heliocentric distance r_h is calculated following (Jewitt et al., 2008) via

$$k_i(r_c, r_h) = \int_0^{\lambda_0^i} \sigma(\lambda)\phi_i(\lambda)F_\odot(\lambda, r_h)\, e^{-\tau(\lambda, r_c)}\, d\lambda\,, \tag{3.18}$$

where $\sigma(\lambda)$ denotes the absorption cross section in cm^2, $\phi_i(\lambda)$ denotes the quantum yield, $\mathrm{F}_\odot(\lambda, \mathrm{r_h})$ the solar photon flux in photons s^{-1} cm^{-2} $\mathrm{Å}^{-1}$ at r_h and wavelength λ. λ_0^i denotes the threshold wavelength in Å, which corresponds to the minimum energy needed to break the molecular bond regarded in reaction i. $\tau(\lambda, r_c)$ is the optical depth at wavelength λ and at the cometocentric distance r_c. A description of the optical depth is given in Section 3.2.3.

After absorption of the photon a molecule can dissociate into reaction path i with a certain efficiency $\phi_i(\lambda)$. One may also find a further definition of quantum yield $\phi_i^{\mathrm{prod}}(\lambda) = n \cdot \phi_i(\lambda)$, with n the number of equal products. An example is $\phi_i^{\mathrm{prod}}(\lambda) = 2 \cdot \phi_i(\lambda)$ for the reaction $C_2H_6 + \gamma \rightarrow CH_3 + CH_3$, in which two CH_3 radicals are formed. Absorption cross sections and the quantum yields are also temperature dependent. The quantum yield $\phi_i(\lambda)$ therefore expresses the probability of a dissociation, ionization or dissociative ionization reaction to occur per absorbed photon. The sum of the quantum yields for the dissociation of a species into the different paths is lower or equal to one

$$\phi(\lambda) = \sum_{i=1}^{n} \phi_i(\lambda) \leq 1\,. \tag{3.19}$$

The equality holds in the case that no fluorescence or other de-excitation processes are involved, i.e. processes which do not lead to dissociation. The total dissociation rate coefficient of a molecule is the sum of all n dissociation rate coefficients

$$k = \sum_{i=0}^{n} k_i\,. \tag{3.20}$$

Note that the absorption cross sections $\sigma(\lambda)$ can include the absorption into several excited states.

Photodissociation Using Oscillator Strengths

The absorption cross section of a transition can be transformed into an oscillator strength f_{ul}, which describe the probability of an electronic transition to occur from a lower state l to an upper state u. Near unity values correspond to allowed, strong transitions, near zero values to forbidden, weak transitions. f_{ul} is defined by the ratio of an electronic transition strength in the molecule to that of an harmonic oscillator model, see e.g. Nieto-Gligorovski et al. (2009).

An oscillator strength f is calculated by integrating absorption cross sections over the wavelengths containing all bands of a transition system (Drake, 2006, eq. 84.77)

$$f_{\mathrm{abs}} = \frac{m_e c}{\pi e^2} \int \sigma_{\mathrm{abs}}(\nu)\, d\nu = \frac{m_e c^2}{\pi e^2} \int \sigma_{\mathrm{abs}}(\lambda) \cdot \frac{1}{\lambda^2}\, d\lambda \tag{3.21}$$

with frequency ν in s^{-1}, σ in cm^{-2} and $|d\nu| = c/\lambda^2\, d\lambda$. It is independent of the experimental band width and is therefore suitable for comparison among various experiments, see e.g. Cheng et al. (2006).

The oscillator strength is dimensionless and fulfills the summation rule for electric-dipole transitions, which states that the sum of all transition probabilities, from all lower states l to all upper states u, are equal to the number of electrons in the molecule

$$\sum_u f_{ul} = \text{number of electrons}\,. \tag{3.22}$$

Photodissociation rate coefficients can be approximated using electronic oscillator strengths via

$$k^{\text{line}}_{\lambda_{ul}}(r_h) = \frac{\pi e^2}{m_e c^2}\lambda^2_{ul} f_{ul}\phi_u x_l F_\odot(\lambda_{ul}, r_h)\,, \tag{3.23}$$

where the optical depth is neglected and $\pi e^2/m_e c^2 = 8.85 \cdot 10^{-21}$ cm^2 Å^{-1} for wavelengths in Å and $F_\odot$ in photons cm^{-2} s^{-1} Å^{-1}. This equation describes the dissociation by photoexcitation from a lower electronic state l to a specific bound or unbound upper electronic state u. ϕ_u is the total dissociation quantum yield of the upper electronic state u, i.e. the fraction of molecules that dissociate with respect to the molecules excited into this state. Corresponding to Equation (3.19), x_l is the occupation fraction of the lower electronic state l and λ_{ul} is the wavelength equivalent for the energy difference between state l and u (excitation energy $\Delta E_{ul} = E_u - E_l$). m_e is the mass of the electron. $F_\odot(\lambda_{ul}, r_h)$ is the solar photon flux at λ_{ul} in photons cm^{-2} s^{-1} A^{-1} and at the heliocentric distance r_h. Summation over all transitions below the ionization energy and above the lowest dissociation energy, i.e. $\lambda_{\text{ion}} < \lambda_{ul} < \lambda_0$, and assuming $\phi_u = 1$ for these transitions results in an upper limit of the total photodissociation rate coefficient (van Hemert and van Dishoeck, 2008)

$$k = \sum_{\lambda_{\text{ion}} < \lambda_{ul} < \lambda_0} k^{\text{line}}_{\lambda_{ul}}\,. \tag{3.24}$$

The photodissociation rate coefficient of a particular reaction path can be computed via

$$k_i = k \cdot bf_i \tag{3.25}$$

when the total branching ratios bf_i are known. The bf_i are independent of wavelength and describe the relative contribution k_i of path i to the total photodissociation rate coefficient k. An overview of the definitions of branching ratios is given in Section 3.2.2. For more details about the above photo rate coefficient computation and approximation of photodissociation rate coefficients see Appendix C.

Branching Ratio Definitions

Since the quantum yield of a reaction is more complicated to determine than its branching ratio, most often branching ratios are determined, either in experiments or by ab initio computations. A branching ratio $br_i(\lambda)$ may be simply defined as the quantum yield of reaction path i, see Equation (3.19), relative to the sum of the quantum yields of all (dissociation) reaction paths

$$br_i(\lambda) = \frac{\phi_i(\lambda)}{\sum_{k=1}^{n} \phi_k(\lambda)}\,. \tag{3.26}$$

Thereby, the sum of all branching ratios is always one and branching ratios have values between zero and one. With Equation (3.19) one also obtains

$$\phi_i(\lambda) = \phi(\lambda) \cdot br_i(\lambda)\,. \tag{3.27}$$

A full branching ratio bf_i for path i, which is independent of wavelength λ, is defined here to distinguish it from branching ratios $br_i(\lambda)$. It is the ratio of the rate coefficient k_i of reaction path i to the total dissociation rate coefficient k, defined in Equation (3.20),

$$bf_i = \frac{k_i}{k} \qquad \text{with} \qquad k_i = k \cdot bf_i \,. \tag{3.28}$$

From Equation (3.28) and (3.20) follows that

$$\sum_{i=1}^{n} bf_i = 1 \,, \tag{3.29}$$

which expresses that the sum of the dissociation from each photodissociation reaction path cannot be higher or smaller than the total dissociation of the molecule.

3.2.3 Optical Depth

Reduction of the solar photon flux by absorption and scattering of molecules and dust particles reduces the photon flux in the coma. This affects the photochemistry and excitation of molecules. In general, cometary comae are optically thin, as found by the observation of sublimating ices alone. Optically thick conditions have been observed only near the nucleus, e.g. around 500 to 1000 km calculated for comet C/1995 O1 **(Hale-Bopp)** at 1 AU (Combi, 2000), which featured a very high water production rate, in comparison to the typical molecular coma extension of 10^6 km. However, some strong resonance lines such as Lyman-alpha **(Lα)** might be optically thick.

The optical depth depends on the distance to the Sun, the number of active surfaces and the nucleus' water content. Higher optical depths shift the onsets and peaks of photodissociation product number densities outwards. Giguere and Huebner (1978) showed for comet Halley at $r_h = 1$ AU that the higher opacity reduces the production of photodissociation products in the coma only by less than a factor of two. The water production rates of the comets studied in this thesis have comparable or lower optical depths than Halley. The optical depth at the position r_c in the coma lying in the line of sight between the nucleus and the Sun can be calculated via

$$\tau(\lambda, r_c) = \sum_{i=1}^{n} \left(\int_{r_c}^{r_{\text{outer}}} n_i(R)\sigma_i(\lambda)\, dR \right) \,. \tag{3.30}$$

The densities n_i and the absorption cross sections $\sigma_i(\lambda)$ of wavelength λ are multiplied, integrated between the cometocentric distance r_c and an outer position r_{outer} in the coma, where the coma's density is negligible, and summed over all species. It is usually sufficient to calculate the optical depth from the densities of the most abundant species H_2O, CO and CO_2.

Part II

Observations and Model Description

CHAPTER 4

Observations of Cometary Comae and the Data Set

This chapter gives an overview of observations of volatile molecules in cometary comae obtained in different spectral wavelength regions. For example the hydrocarbon parent molecules C_2H_2 and HC_3N of the daughter species C_2 are observed in the infrared **(IR)** and the radio wavelength range, respectively. Also discussed is resonance fluorescence in the optical wavelength range which is critical for the observations of key species like C_3 and C_2. Thereafter comes an overview of the investigated observational data in Section 4.2 which comprises four sample comets, namely the three nearly isotropic comets **(NICs)** C/2001 Q4 **(NEAT)**, C/2002 T7 **(LINEAR)**, C/1995 O1 **(Hale-Bopp)**, i.e. from the Oort cloud **(OC)**, and one ecliptic comet **(EC)**, i.e. from beyond Neptune, 9P **(Tempel 1)**.

4.1 Observations of Volatile Molecules in Cometary Comae

Observations of coma species are possible over a wide range of wavelengths, from the ultraviolet **(UV)**, 100 - 3800 Å, over the optical, 3800 - 7800 Å, and infrared **(IR)**, 0.78 - 1000 μm, to the microwave, 1 mm - 1 m, and radio, 10 m - 10 km, wavelength range. The UV can be subdivided into vacuum-ultraviolet **(VUV)**, 100 - 2000 Å, comprising the extreme-ultraviolet **(EUV)**, 100 - 1210 Å, Lyman-alpha **(Lα)**, 1216 Å and the far-ultraviolet **(FUV)**, 1220 - 2000 Å followed by the mid-ultraviolet **(MUV)**, 2000 - 3000 Å and the near-ultraviolet **(NUV)**, 3000 - 3800 Å. The infrared wavelength range can be subdivided into near-infrared **(NIR)**, 0.78 - 5 μm, mid-infrared **(MIR)**, 5 - 30 μm and far-infrared **(FIR)**, 30 - 300 μ m.

4.1.1 Overview

The emissions originate from electronic, vibrational, rotational and mixtures of these transitions by excitation of the species in the coma by solar photons or by collisions. The emission frequency is proportional to the energy differences between each upper ($'$) and lower state ($''$) (Jewitt et al., 2008),

$$\nu \sim (E'_{\mathrm{el}} - E''_{\mathrm{el}}) + (E'_{\mathrm{vib}} - E''_{\mathrm{vib}}) + (E'_{\mathrm{rot}} - E''_{\mathrm{rot}})\,, \tag{4.1}$$

taking into account the energy difference of the electronic (el), the vibrational (vib) and the rotational (rot) states. Which particular wavelength range is better suited or available for observations depends on the species, i.e. whether it is a symmetric or asymmetric neutral molecule,

a radical or an ion. It depends on the strength of the emissions and if these may be observed from the ground or space.

Electronic transitions emit radiation in the UV, optical and NIR. Emissions of vibrational transitions of atoms and functional groups, e.g. R−CH_3, bonded to the main molecule R, occur in the NIR and MIR. Possible vibrational modes are the symmetric, antisymmetric stretching, scissoring, rocking, wagging and twisting modes. Pure rotational transitions have emissions mainly in the radio wavelength range but also in the FIR wavelength range. While electronic transitions of atoms are observable in the UV and optical wavelength range, radicals are mainly observable at optical wavelengths, because their upper electronic bands are excited.

An example for prominent UV observations is the electronically excited CO, produced during the photodissociation of CO_2, called the Fourth positive system, which emits radiation at 2050 Å and the OH emission at 3085 Å ($X^2\Pi \rightarrow A^2\Sigma^+$ transition), formed by H_2O photodissociation (Jewitt et al., 2008). These emissions are so-called prompt emissions of excited photo dissociation products, which de-excite immediately after production.

An example of emissions in the optical is the Swan band system of C_2 between 4400 Å and 6300 Å, see Figure 4.1 (p.57). For this radical the potential of the excited and the initial electronic state are similar both to each other as well as the C≡C equilibrium internuclear distance. Therefore, in emission, a mixed, 'group' spectrum is observable. This is due to the Born-Oppenheimer principle and the Franck-Condon principle, hence the internuclear distance (vibration) does not change during an electronic transition and an electronic transition between two vibrational levels is the more likely the more the two vibrational wave functions overlap (Haken and Wolf, 2005). See also Figure 3.6, where this effect is seen for absorption. Therefore, transitions between electronic states of C_2 with no change in the vibrational quantum number $\Delta v = 0$ are the most likely, denoted by $C_2(\Delta v{=}0)$. The band structure is due to the unresolved rotational transitions in each electronic-vibrational (vibronic) transition, i.e. a transition with a simultaneous change of the electronic and the vibrational quantum number.

An example of investigations of the structure and evolution of the H coma of comet Hale-Bopp at Lyman-alpha **(Lα)** is provided by Combi et al. (2000). Examples of investigations using optical observations are A'Hearn et al. (1995), the first larger statistical analysis of cometary composition, and Rauer et al. (2003), the long-term monitoring program of comet Hale-Bopp over a large range of heliocentric distances. These two studies focused, among other radicals, on C_3 and C_2.

Emissions of neutral molecules originate from excitation of their lowest rotational and rotational-vibrational states by collisions and solar photons. Optical emissions of neutral molecules are not observable, because these require an excitation of a binding electron and therefore usually lead to their dissociation into radicals (Jewitt et al., 2008). For symmetric molecules lacking a permanent dipole moment pure rotational transitions are forbidden. They can therefore not be observed at radio wavelengths.

Rotational-vibrational transitions can only be observed in the IR when a temporal dipole moment is established and the molecule becomes polar by breaking symmetry by bending vibrations. An example are the bending vibrations of CO_2 at 15 μm in which bond angles change. Electromagnetic radiation can only induce rotational transitions for molecules with a dipole moment. Two-atomic homonuclear molecules like e.g. N_2 and H_2 are non-polar molecules since these are symmetric and the atoms have equal electronegativity. An example of a two-atomic polar molecule is CH where both atoms have different electronegativity. CH_4 on the other hand has no permanent dipole moment as the dipole moments of each H connection compensate overall. When this molecule is excited vibrationally, however, the symmetry is lost and a temporal dipole moment results. Other examples of symmetric molecules are C_2H_2, C_2H_6, C_4H_2, C_6H_2 and the C_3H_4 isomer allene $CH_2C_2H_2$. These molecules can be observed in the IR by their ro-vibrational transitions. Present day measurements in the radio and IR range are sensitive

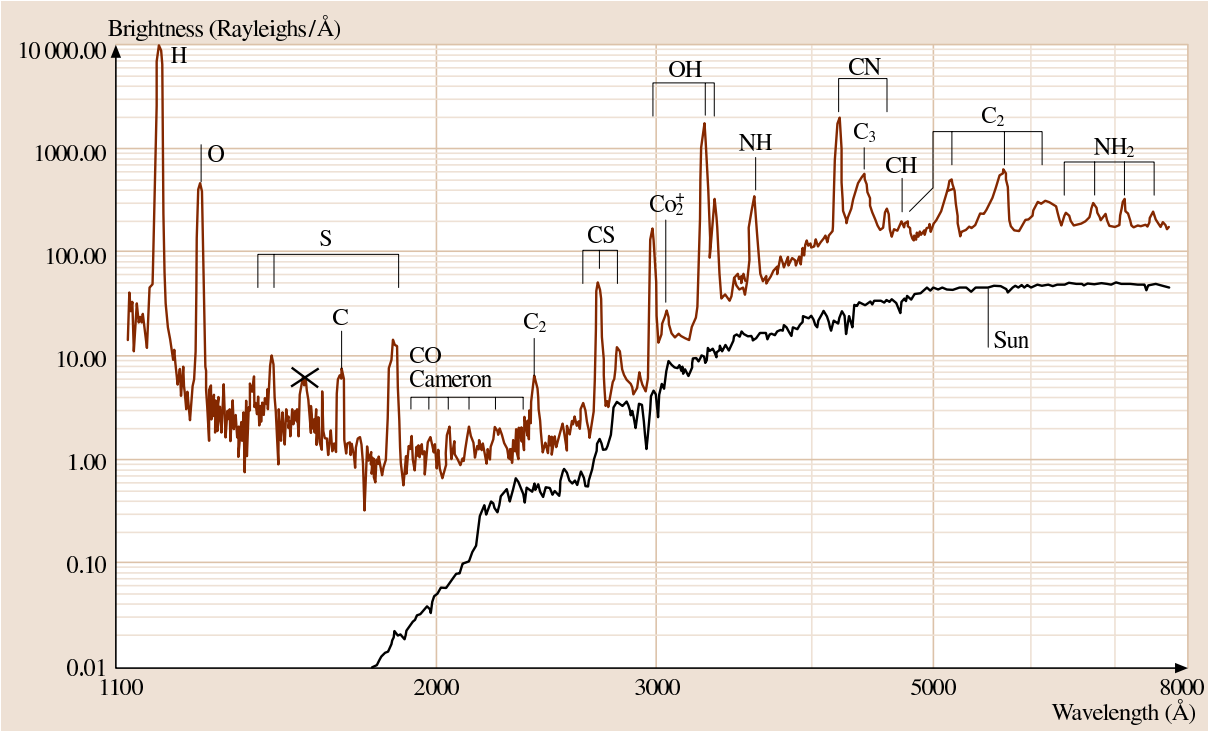

Figure 4.1: *Emission spectrum of comet Hartley 2 (brown) superimposed on the continuum of dust-scattered solar radiation (black), ranging from the VUV to the end of the optical wavelength range. The main source of the visible cometary coma and dust tail is the scattering of sunlight on dust. Therefore to obtain the pure emissions of atomic and molecular species the dust-scattered solar radiation has to be subtracted from the cometary emission spectrum. Figure taken from Drake (2006), original source is Weaver and Feldman (1992).*

enough to measure abundances down to 100 ppm level relative to water vapour (Mumma and Charnley, 2011).

Examples of asymmetric molecules are the main cometary ices H_2O, CO and possible parent species of C_3 and C_2, e.g. the C_3H_4 isomer propyne CH_3C_2H and HC_3N, respectively. Since rotational levels are often the only excited levels in parent molecules at very low temperatures such transitions are most suitable for observations of distant comets. An example is the detection of the $J(2-1)$ transition of CO at the frequency $\nu = 230$ GHz in 29P **(Schwassmann-Wachmann 1)** at $r_h = 6.08$ AU, where the CO gas temperature is $T \approx 20 - 80$ K (Senay and Jewitt, 1994). CO sublimates already at very low temperatures and therefore also at large r_h, see Section 3.1.1.

Intensities of vibrational and rotational transitions are in general low, requiring observations of very active comets or observations of comets at small r_h. For example, many new molecules were detected in comet Hale-Bopp, e.g. SO, SO_2, HC_3N, NH_2CHO, HCOOH, $HCOOCH_3$ (Bockelée-Morvan et al., 2000) and in comet C/1996 B2 **(Hyakutake)**, e.g. C_2H_6, CH_4 (Mumma et al., 1996) and C_2H_2 (Brooke et al., 1996b). See also Woon (2013) for an overview of detected molecules in comets.

4.1.2 Atmospheric Windows and Space Missions

The Earth's atmosphere is an efficient absorber of UV, mainly by O_2 and O_3, as well as IR radiation, mainly by water vapour and CO_2. Also parts of the radio wavelengths range are blocked by absorbing water molecules. In contrast to UV, which is very efficiently absorbed over all its wavelengths by Earth's atmosphere, observations in the IR are possible in small atmospheric

windows from the ground for which observations are conducted at dry and high-lying sites like Mauna Kea (Hawaii) or Paranal (Chile) - with fluctuating degrees of transmission due to the underlying atmosphere. Space telescopes avoid these problems, e.g. in the UV the International Ultraviolet Explorer **(IUE)** (Feldman et al., 1984), the Hubble Space Telescope **(HST)** (Weaver and Feldman, 1992), the Far Ultraviolet Spectroscopic Explorer **(FUSE)** (Feldman et al., 2002), and IR, e.g. the Infrared Astronomical Satellite **(IRAS)** (Feldman et al., 1984) and AKARI (Murakami et al., 2007, Ootsubo et al., 2012). Infrared observations of e.g. water in comets is aimed at with the SOFIA mission, an infrared telescope onboard a Boeing 747, operating at high scale heights above 99.8% of the Earth's water vapour (Gehrz et al., 2008).

Observations of H_2O at radio wavelengths are also prevented by the atmosphere's strong absorption of radiation by H_2O for which, e.g. the instrument HIFI onboard the space telescope Herschel is used (Hartogh et al., 2010). It is interesting to note that HIFI observations led to the spectacular finding of the first comet, namely the ecliptic comet Hartley 2, having Earth's mean ocean D/H ratio, i.e. corresponding to Vienna standard mean ocean water **(VSMOW)** (Hartogh et al., 2011).

4.1.3 Resonance Fluorescence

Fluorescence is the photo-excitation of an electronic and/or vibrational state in a molecule and the followed de-excitation by spontaneous emission of a photon of the same or lower energy to an electronic state of the same spin multiplicity, also called internal conversion **(IC)**. However, the upper state does not necessarily need to have the same spin multiplicity as the ground state. This is the case for the C_2 radical with a singlet $X^1\Sigma_g^+$ ground state, which is excited to the triplet state $d^3\Pi_g$. From there it transitions e.g. to the triplet state $a^3\Pi_u$, i.e. the Swan band system $d^3\Pi_g - a^3\Pi_u$. Transitions between states with different spin multiplicity is also denoted as intersystem crossing **(ISC)**. ISC is quantum mechanically forbidden and has therefore much lower transition probabilities than transitions between states of the same spin multiplicity. In the simple fluorescence of the $A^1\Pi_u - X^1\Sigma_g^+$ Philips band system, excitation and de-excitation occurs between the ground and excited state of equal spin multiplicity (Helbert, 2002, Rousselot et al., 2000). Nevertheless, C_2 fluorescence from the Swan band system is significant and can be used to obtain column densities of the radical in cometary comae, see also Section 4.1.4.

In resonance fluorescence the absorbed and the emitted photons have the same energy. Resonance fluorescence by the solar flux is the prevailing excitation mechanism for electronic-vibrational transitions in the NUV, optical and NIR. The emitted photon flux of a certain electronic-vibrational transition can be used to calculate column densities of the regarded species.

In the case of simple fluorescence with excitation from the ground state (and almost all molecules are in the ground state) one takes the absorption rate, exciting the molecule from the lower state l into the upper state u, in molecules per second, corresponding to the regarded resonance fluorescence wavelength λ_{lu}, see also Equation (3.23),

$$k_{lu} = B_{lu}\rho(\lambda_{lu}) = \frac{\pi e^2}{m_e c^2}\lambda_{lu}^2 f_{lu} F_\odot(\lambda_{lu})\,. \tag{4.2}$$

The branching ratio of the molecules emitting at the regarded wavelength to the molecules emitting at all lower wavelengths, i.e. de-excitation to higher vibrational energies of the ground state, needs also to be taken into account

$$b_{ul} = \frac{A_{ul}}{\sum_{k<u} A_{uk}}\,. \tag{4.3}$$

This leads to the g-factor, which has units photons s^{-1} molecule^{-1}, by using $g_{ul} = k_{lu} b_{ul}$ (3.28)

$$g_{ul} = \frac{\pi e^2}{m_e c^2}\lambda_{lu}^2 f_{lu} F_\odot(\lambda_{lu}) \frac{A_{ul}}{\sum_{k<u} A_{uk}}\,. \tag{4.4}$$

B and A are the Einstein coefficients for absorption and spontaneous emission, respectively, $\rho(\lambda_{lu})$ is the photon energy density, f_{lu} is the oscillator strength, $F_{\odot}(\lambda_{lu})$ is the solar photon flux at the regarded wavelength (Helbert, 2002, Jewitt et al., 2008). The computation of column densities with the g-factor and the fluxes from observations is described in Section 4.1.4.

Commonly the situation is more complex, as shown for the Swan band system of the C_2 molecule. In such cases no simple resonance fluorescence prevails and a significant amount of the molecule population is not in the ground state. In such cases radiative equilibrium between the molecule populations is assumed, hence the rate of change of molecules into and out of the state is equal. A set of balance equations can be set up to derive the g-factor in this case. See also Drake (2006, chapter 83), Jewitt et al. (2008, section 4.4) and Helbert (2002).

Swings and Greenstein Effects

For some species the fluorescence emission and therefore g-factors depend also on the comet's radial velocity $\dot{r}_h$ to the Sun, denoted as the Swings effect (Swings, 1941). Since for the comet the Fraunhofer lines in the solar photon spectrum can be Doppler-shifted these may coincide with the species excitation wavelength, e.g. CN at 3880 Å. Thereby e.g. the CN$(0,0)$ fluorescence efficiency can vary by a factor of 1.9 at $r_h = 1$ AU depending on the comet's radial velocity, having a strong minimum at $\dot{r}_h = 0$ km s^{-1} (Schleicher, 2010). When deriving radical column densities from fluorescence fluxes, see Section 4.1.4, this effect is important for CN, since comets can have velocities of several tens of km s^{-1}. Additionally the excitation of emission bands can vary with r_h (Schleicher, 2010) which has to be taken into account in excitation models. Further problems are due to the solar cycle, sunspots and the differing importance of collisional and radiative excitation with r_h (Jewitt et al., 2008) and cometary activity.

The Greenstein effect is similar to the Swings effect but is caused by the different radial velocities of the off-streaming species in the coma, instead of the radial velocity of the comet itself (Greenstein, 1958). This effect is important only for atoms, e.g. O or Na, or ions, which may reach very high velocities between several tenths and a hundred km s^{-1} (Jewitt et al., 2008).

Examples of Fluorescence Emissions in Comets

Examples of fluorescence emission in comet Hartley 2 observable in the UV by atoms and in the optical by radicals are shown in Figure 4.1, including also the reflection of sunlight by dust particles. Underlying in black is the solar photon flux. Emissions observable are e.g. the H Lα line at 1215 Å, the CO Cameron bands at 2050 Å (prompt emission from photodissociation of CO_2), the C_2 Swan band system, between approximately 4460 and 6185 Å, with the four bands $C_2(\Delta v{=}1)$, $C_2(\Delta v{=}0)$, $C_2(\Delta v{=}-1)$ and $C_2(\Delta v{=}-2)$ originating from one electronic transition but each having different vibrational quantum number changes Δv. The C_3 band is observable at 4040 Å. The CN band at 3875 Å has a high fluorescence efficiency making it suitable for detection of activity of faint or distant comets. Fluorescence of OH radicals at 3085 Å is used as a proxy of the water release which is the main cometary ice.

4.1.4 Conversion from Fluorescence Fluxes to Column Densities

To compare the C_3 and C_2 column densities of the coma chemistry model with the observations, the observations have to be converted from fluorescence fluxes to column densities. These conversions were carried out in this work for the comets NEAT, LINEAR, Hale-Bopp and Tempel 1. An overview of the observations investigated in this work is given in Table 4.2.

Table 4.1: *Fluorescence efficiencies g of the emissions from the indicated transitions. These are used to convert* C_3 *and* C_2 *fluorescence fluxes (Swan bands) for this work (and* CN *in general) to column densities. Values are given for* $r_h = 1$ *AU and can be scaled to other* r_h *by* $g \cdot r_h^{-2}$*. For* CN *the g-factor depends additionally on the radial component of the comet's heliocentric velocity* $\dot{r}_h$*. Values can be extracted from the table in Schleicher (2010). Here the value for* $\dot{r}_h = 0$ *is given.*

emission	electronic transitions	λ [Å]	$g \cdot 10^{-14}$ [erg s^{-1} molec. $^{-1}$]	reference
$C_2(\Delta v{=}0)$	$d^3\Pi_g - a^3\Pi_u$	4860 – 5185	44.7	Cochran et al. (1992)
C_3	$\tilde{A}^1\Pi_u - \tilde{X}^1\Sigma_g^+$	3975 – 4150	38.0	Cochran et al. (1992)
CN(0, 0)	$B^2\Sigma^+ - X^2\Sigma^+$	3830 – 3905	2.38	Schleicher (2010)

For pure resonance fluorescence one can calculate the column densities N with

$$N = \frac{4\pi}{g_{ul}} \frac{1}{\Omega} F \tag{4.5}$$

with Ω the aperture size of the telescope, F the emission flux in it and g_{ul} the g-factor of the used fluorescence transition, see Jewitt et al. (2008) or Helbert (2002, chapter 8). Fluorescence efficiencies used in this work are tabulated in Table 4.1. The g-factors for CN have been recalculated in Schleicher (2010). The g-factors in Cochran et al. (1992) for C_3 and C_2 assume an optically thin coma.

4.2 Data Set

This work studies the formation chemistry of C_3 and C_2 in cometary comae using available observations of the four comets NEAT, LINEAR, Tempel 1 and Hale-Bopp. Table 4.2 provides an overview of the used observations and the orbital parameters of the comets. These observations make it possible to study comets with different water production rates $Q(H_2O)$ and at different heliocentric distances r_h, i.e. at different intensities of the solar photon flux, the most important driver of the coma chemistry. Moreover, this data set comprises three sample NICs, i.e. from the OC, (NEAT, LINEAR, Hale-Bopp) and one EC, i.e. from beyond Neptune, (Tempel 1). The column densities of the four comets are shown in Figure 4.2.

For the analysis of comet Hale-Bopp, discovered 7-1995, observations done on 12-19/20-1997 are used. These observations are a part of the long-term monitoring programme of Hale-Bopp (Rauer et al., 2003), see also Helbert (2002), Helbert et al. (2005).

The comets NEAT and LINEAR were discovered in 8-2001 and in 10-2002, respectively. The observations of both comets were carried out at the ESO La Silla observatory (ESO 3.6-m telescope, EFOSC2 instrument). Comet NEAT was observed on 4-29/30-2004, with a high spatial resolution due to the small geocentric distance of $\Delta = 0.39$ AU, and comet LINEAR on 6-12/13-2004. Around the *Deep Impact* event (Meech et al., 2005) the periodic comet Tempel 1 was observed between 7-2/3-2005 and 7-10-2005 at the VLT (UT1/FORS2). The present work analyses observations taken on 7-3/4-2005, i.e. before the Deep-Impact projectile impacted and disturbed the coma. Due to the seeing effect, the inner parts of the C_3 and C_2 column densities of NEAT, LINEAR and Tempel 1 below 1500 km, 4000 km, and 3000 km are removed in this work, respectively, as also done in Weiler (2006).

Table 4.2: *Overview of the observational and orbital parameters of the comets Hale-Bopp, NEAT, LINEAR and Tempel 1 used in this work, which are taken from Helbert (2002) and Weiler (2006). Shown are the heliocentric distance r_h, the geocentric distance Δ, the covered spectral wavelength range (w.r.), the spatial scale Δx ($\Delta x'$ is the corresponding Δx in km at the cometary nucleus), the wavelength increment $\Delta\lambda$, the phase angle β, the perihelion distance q, the eccentricity e, the inclination i, the argument of perihelion w, the longitude of ascending node Ω and the Tisserand parameter T_J. $Q(H_2O)$ is the water production rate.*

parameter	Hale-Bopp	NEAT	LINEAR	Tempel 1
date	19/20-12-1997	29/30-4-2004	12/13-6-2004	3/4-7-2005
r_h [AU]	3.78	1.00	1.20	1.51
Δ [AU]	3.62	0.39	1.03	0.89
slit length [′]	4.5	5.0	5.0	6.8
slit width [″]	2.36	2.0	2.0	1.0
w.r. [Å]	3600-6800	3700-6100	3700-6100	3700-6200
Δx [″/pixel]	0.82 (7.38, binned)	0.158	0.316	0.252
$\Delta x'$ [km/pixel]	2158.8 (19429.2, binned)	44.7	235.8	163.2
$\Delta\lambda$ [Å/pixel]	1.89	1.5	3.0	1.5
β [°]	15.0	79.7	53.6	40.9
q [AU]	0.914	0.962	0.615	1.506
e	0.995112	1.000664	1.000561	0.517491
i [°]	89.43	99.643	160.583	10.530
w [°]	130.59	1.204	157.736	178.839
Ω [°]	282.47	210.279	94.859	68.937
T_J	0.21	-	-	2.97
orbital period [y]	4000	-	-	5.52
$Q(H_2O)$ [molec. s^{-1}]	$4 \cdot 10^{28}$ [a]	$2.6 \cdot 10^{29}$ [b]	$6.9 \cdot 10^{28}$ [c]	$3.4 \cdot 10^{27}$ [c]

[a] Calculated in Helbert (2002) using the sublimation model of Benkhoff and Huebner (1995) and Huebner and Benkhoff (1999).

[b] $Q(H_2O) = 2.6 \cdot 10^{29}$ s^{-1} is an average of all production rates from 4-29+30-2004 from Biver et al. (2009), taken from Weiler (2012). Weaver et al. (1999) gives $Q(H_2O) = 1.9 \cdot 10^{29}$ s^{-1}.

[c] Howell et al. (2004).

[d] Küppers et al. (2005). A higher $Q(H_2O) = 1.21 \cdot 10^{28}$ is reported by Mumma et al. (2005).

Used in this work are the spectra of comet NEAT, LINEAR and Hale-Bopp, having the slit oriented to the projected solar-antisolar direction. For comet Tempel 1 a mean spectrum of spectra with the slit positioned in the projected comet-Sun direction is used in this work. The slit is positioned onto the optocenter of the coma. For more information the reader is referred to Weiler (2006) for the comets NEAT, LINEAR, Tempel 1 and to Helbert (2002) and Rauer et al. (2003) for comet Hale-Bopp.

To compare the observations with the model outputs, C_3 and C_2 column densities were obtained in this work by converting the fluorescence fluxes of the four comets as described in Section 4.1.4. The used fluorescence efficiencies are given in Table 4.1.

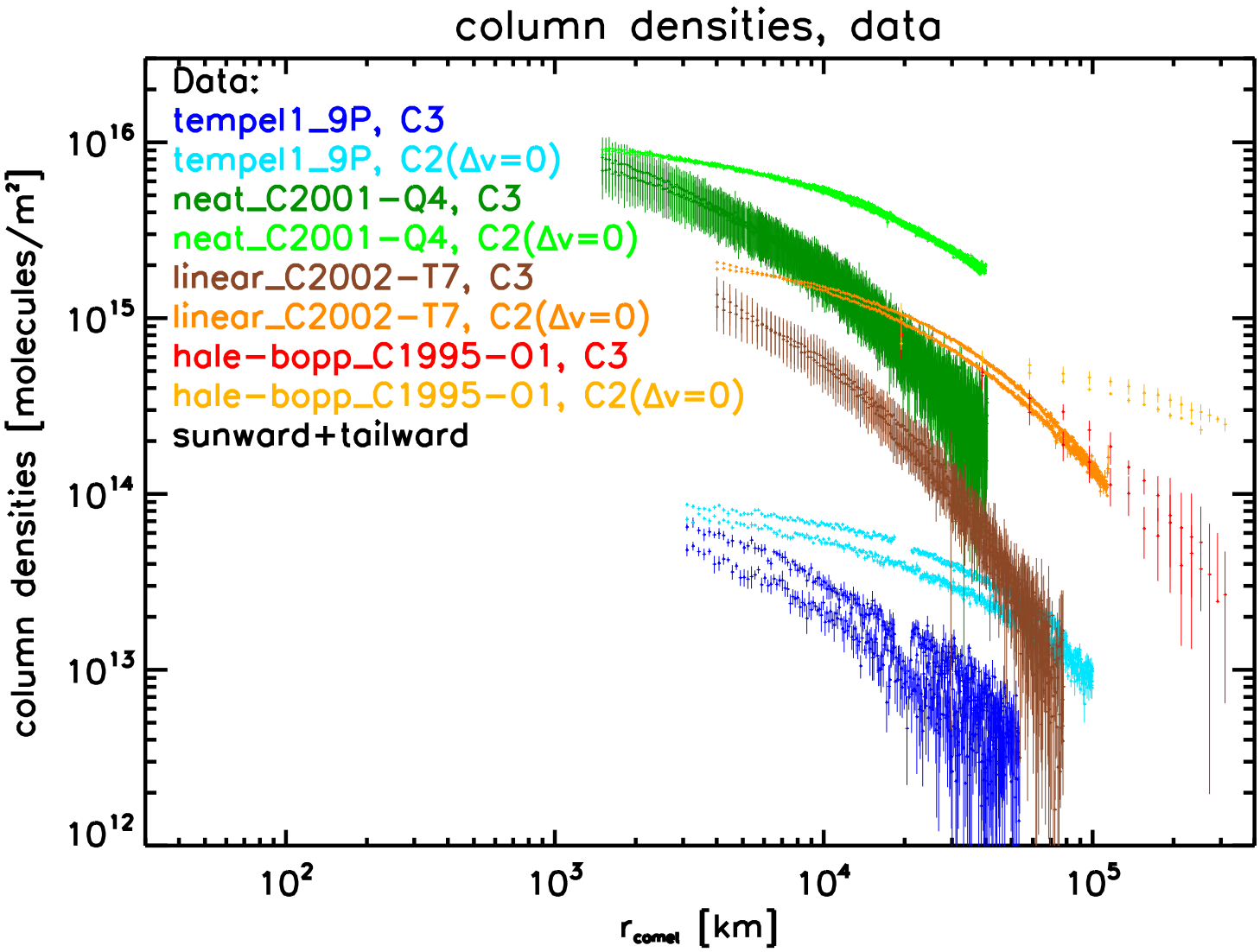

Figure 4.2: C_3 *and* C_2 *observations of the comets Tempel 1, NEAT, LINEAR, Hale-Bopp investigated in the present work. Both sunward and tailward column densities are shown.*

CHAPTER 5

Model Description

In order to model and interpret the observations of C_3 and C_2 in cometary comae, a numerical model is required to describe the coma hydrodynamics and chemistry. This Chapter introduces the complex coma chemistry model of Weiler (2006), which has been adapted for this work. The model used in the present work features some updates in the chemical reaction network, see Chapter 7, compared with Weiler (2006). The hydrodynamics of this model as well as the boundary conditions and initial values are described in Section 5.1. The energy sources terms for the chemistry and the collisional processes are described in Section 5.2. The treatment of the chemistry in the coma is provided in Section 5.3. The validity range and the assumptions of the model are presented in Section 5.4. The conversion from number densities to column densities, for the comparison with the observational column densities, is provided in Section 5.5.

5.1 Hydrodynamical Description

The model applied in this work was constructed by Weiler (2006) based on Rodgers and Charnley (2002) and Schmidt et al. (1988). The presented description of the model follows Weiler (2006) and in parts Rodgers and Charnley (2002).

The central, governing model equations are based on the conservation of number density, mass, momentum and energy for one fluid, i.e. the Equations (3.3), (3.4), (3.5) and (3.6). These equations are then modified by the following model assumptions: the gas is in steady-state, so that the partial derivative with respect to time is zero and only the divergence terms remain, and the coma is spherically symmetric, expressed by a transformation to spherical coordinates, in which equations then only the radial components are non-zero. The above assumptions result in the following equations

$$\frac{1}{r^2}\frac{d}{dr}\left(r^2 n u\right) = N\,, \tag{5.1}$$

$$\frac{1}{r^2}\frac{d}{dr}\left(r^2 \rho u\right) = M\,, \tag{5.2}$$

$$\frac{1}{r^2}\frac{d}{dr}\left(r^2 \rho u^2\right) + \frac{d}{dr}\left(n k_B T\right) = F\,, \tag{5.3}$$

$$\frac{1}{r^2}\frac{d}{dr}\left(r^2 \rho u \left(\frac{u^2}{2} + \frac{\gamma}{\gamma-1}\frac{k_B T}{\mu}\right)\right) = Q\,, \tag{5.4}$$

with the source terms N, M, F and Q for the number density, mass, momentum and energy, respectively, and r the cometocentric distance, see Figure 5.1. The specific enthalpy h was replaced in Equation (5.3) by

$$h = \frac{\gamma}{(\gamma-1)} pV = \frac{\gamma}{(\gamma-1)} \frac{k_B T}{\mu}\,, \tag{5.5}$$

where k_B is the Boltzmann constant, γ the adiabatic exponent and μ the molecular mass. An ideal gas is assumed so that the pressure p could be replaced in Equation (5.4) by

$$p = n k_B T\,. \tag{5.6}$$

Now the derivatives of the number density n, the velocity u and the temperature T are obtained by rearranging the Equations (5.1), (5.2), (5.3) and (5.4), respectively.

$$\frac{dn}{dr} = \frac{N}{u} - \frac{n}{u}\frac{du}{dr} - \frac{2n}{r}\,, \tag{5.7}$$

$$\frac{du}{dr} = \frac{1}{\rho u^2 - \gamma n k_B T}\left(Fu - (\gamma-1)G - Mu^2 + \frac{2u}{r}\gamma n k_B T\right), \tag{5.8}$$

$$\frac{dT}{dr} = \frac{(\gamma-1)T}{u}\left(\frac{G}{n k_B T} - \frac{2u}{r} - \frac{du}{dr} - \frac{N}{(\gamma-1)n}\right). \tag{5.9}$$

The source terms for the energy, the momentum and the mass are summarized into the thermal energy source term

$$G = Q - Fu + \frac{1}{2}Mu^2\,. \tag{5.10}$$

To describe the coma physics and chemistry, the system of ordinary differential equations **(ODEs)** (5.7), (5.8) and (5.9) generally has to be solved separately for each type of species in the coma, i.e. each type of species is treated as a separate fluid. The system of ODEs of each fluid are coupled by the chemical source term N and the thermal energy source term G, given in Equation (5.10), which describe the change of the number density, energy, momentum and mass of a species' fluid due to chemical reactions, collisional and other processes, respectively. The source term $M = \mu N$, with μ the molecular mass of the regarded species. Since such a treatment is computationally intensive, it is reasonable to reduce the calculations to a neutral, an ionic and an electronic fluid. Such a simplification is included in the model used in this work and is described in more detail in the next Section 5.1.1.

5.1.1 Hydrodynamics of Three Fluids With Simplifications

In the following three fluids are regarded, the neutral, the ionic and the electron fluid. The ODEs (5.7), (5.8) and (5.9) include a singularity at the sonic point c, due to the assumption of steady-state, i.e. $du/dr \to \infty$ if $u \to c$. For an ideal gas the speed of sound is defined as (Landau and Lifschitz, 1991, chapter 8)

$$c = \sqrt{\frac{\gamma P}{\rho}} = \sqrt{\frac{\gamma k_B T}{\mu}}\,, \tag{5.11}$$

with γ, P, ρ, k_B, T and μ the adiabatic exponent, pressure, density, Boltzmann constant, temperature and the mean molecular mass of the species combined in the regarded fluid, respectively. For the neutral species $u_n > c_n$ (supersonic) everywhere in the coma. This is because in the inner coma the temperature of the neutral fluid T_n (where a hydrodynamical description with one fluid is valid) drops due to adiabatic expansion. Therefore $c_n = \sqrt{\frac{\gamma k_B T_n}{\mu_n}}$ drops as well.

Due to the Coulomb force the electrons and ions always move with the same so-called plasma velocity u_p. For the plasma fluid however, i.e. a fluid containing all ions and the electrons, a singularity is reached within the intermediate to outer coma, i.e. around 10^4 km to 10^5 km for a moderately active comet like C/1996 B2 **(Hyakutake)** with a water production rate of $Q(H_2O) = 10^{30}$ molecules s^{-1} at $r_h \approx 1$ AU, which is due to the large temperature the electrons attain, up to $T_e = 10^4$ K and even higher. In that region of the coma the collisional cooling with neutrals and ions is reduced due to the decreased number densities, caused by the expansion of the coma. See the diverging energy term for inelastic collisional cooling of electrons $G_{e,n}^{\text{scatt.inelast.}}$ and for chemistry G_e^{chem} for comet Hyakutake between 10^4 km and 10^5 km in the bottom panel of Figure 6.1b. The plasma sonic velocity c_p is defined as

$$c_p = \sqrt{\frac{\gamma_i P_i + \gamma_e P_e}{\rho_i}} = \sqrt{\frac{k_B(\gamma_i T_i + \gamma_e T_e)}{\mu_i}} \,. \tag{5.12}$$

μ_i is the mean molecular mass of the ions and the mass of the electrons is assumed to be negligible (being $\approx$ four orders of magnitude smaller). As T_e increases in the outer coma, the singularity occurs (see following Equation (5.13)) when c_p reaches u_p. When c_p exceeds u_p the plasma becomes subsonic. This singularity at $u_p = c_p$ becomes apparent on combining Equation (5.12) applied for the plasma of ions and electrons with Equation (5.8)

$$\frac{du_p}{dr} = \frac{\psi}{u_p^2 - c_p^2} \tag{5.13}$$

with

$$\psi = \frac{1}{\rho_i}\left((F_i + F_e)u_p - (\gamma_i - 1)G_i - (\gamma_e - 1)G_e - M_i u_p^2 + \frac{2u_p \rho_i c_i^2}{r}\right) \tag{5.14}$$

A numerical integration across the singularity is not possible, because du/dr becomes infinite when $u_p \to c_p$. However, such a procedure would be possible if the numerator were also to tend to $u_p^2 - c_p^2$ or, if it were to tend to zero when $u_p \to c_p$, respectively. In this case the transition from supersonic to subsonic would be smooth and one would obtain du/dr via l'Hôpital's rule. But as pointed out by Rodgers and Charnley (2002) it is not possible to choose realistic initial conditions leading to such a behavior of ψ, since it is dominated by the electron heating term, which becomes high in the outer coma where the sonic transition occurs. To avoid these numerical challenges, the model assigns one common velocity for all three fluids.

As outlined by Rodgers and Charnley (2002) assuming one common velocity for all fluids corresponds to adding an additional drag force f and the corresponding energy term $f \cdot u$ to the external sources of momentum F' and energy Q' for each of the three fluids

$$F = F' + f \,, \tag{5.15}$$

$$Q = Q' + f \cdot u \,. \tag{5.16}$$

The f is an artificial drag force (not the actual physical one) so that the velocities of all three fluids remain equal. As stated before, the electrons and ions move with the same velocity, since the Coulomb force is strong, which means $f = n_i \, e \, E$ with n_i the number density of the ions, e the electric charge and E the electric field strength (Körösmezey et al., 1987). However, Marconi and Mendis (1986) reproduced with this approach the densities and the temperature of the electrons observed in comet Giacobini-Zinner within a factor of two.

5.1.2 Final Model Equations

When one assumes a common velocity for all three fluids, as discussed in Section 5.1.1, the central Equations (5.7), (5.8) and (5.9) become (with $s = 1, ..., S$ for the species and $k = n, i, e$

for the fluids of the neutrals, ions and electrons)

$$\frac{d(n_s r^2)}{dr} = \frac{N_s r^2}{u} - \frac{n_s r^2}{u}\frac{du}{dr}\,, \tag{5.17}$$

$$\frac{du}{dr} = \frac{-\sum_{k=1}^{3}(\gamma_k - 1)G_k + \frac{2u}{r}\sum_{k=1}^{3}\gamma_k n_k k_B T_k}{\sum_{k=1}^{3}\rho_k u^2 - \sum_{k=1}^{3}\gamma_k n_k k_B T_k}\,, \tag{5.18}$$

$$\frac{dT_k}{dr} = \frac{(\gamma_k - 1)T_k}{u}\left(\frac{G_k}{n_k k_B T_k} - \frac{2u}{r} - \frac{du}{dr} - \frac{N_k}{(\gamma_k - 1)n_k}\right). \tag{5.19}$$

These are the differential equations which must be solved in the coma model to obtain the velocity u, the three temperatures T_k for each of the three fluids and the number density n_j of each species j.

This work uses $\gamma_n = \gamma_i = \frac{4}{3}$ for the specific adiabatic exponent $\gamma = \frac{f+2}{f}$ (specific heat ratio) for the neutral and the ionic fluid, since the water molecules have at low temperatures only $f = 6$ degrees of freedom, namely 3 translational and 3 rotational. $\gamma(T)$ is nearly constant in the range of temperatures encountered in the coma, i.e. 1.33 at $T \leq 100$ K and 1.252 at $T = 1000$ K (Keenan et al., 1983). Therefore, the model assumes a constant γ. For the electrons $\gamma_e = \frac{5}{3}$.

In Equation (5.17) the number density n_j was replaced by $n_j \cdot r^2$ to decrease the strong dilution in fluid density with increasing r G_k is analogous to the energy source term G from Equation (5.10), but now for each fluid $k = n, i, e$

$$G_k = Q_k - F_k u + \frac{1}{2}M_k u^2\,, \tag{5.20}$$

which are further described in Section 5.2.

The total of the mass source terms and the total of the momentum source terms of each fluid are conserved

$$\sum_{k}^{3} M_k = 0\,, \tag{5.21}$$

$$\sum_{k=1}^{3} F_k = 0\,. \tag{5.22}$$

$\sum_k Q_k \neq 0$ due to endothermic and exothermic reactions. The number density n_k and the mass density ρ_k of each fluid are obtained by summation of the number density and mass density of each species belonging to fluid k, respectively,

$$n_k = \sum_{s_k} n_{s_k}\,, \qquad \rho_k = \sum_{s_k} \mu_{s_k} n_{s_k}\,, \tag{5.23}$$

where s_k are the species indices belonging to fluid k with $\sum_k^3 s_k = n$ the number of all species in the reaction network of the model. Again, the sinks and sources for number density of each fluid are obtained by summation over all species belonging to fluid k, using the Equation (3.16) of Chapter 3, by

$$N_k = \sum_{s_k} N_{s_k} = \sum_{s_k}\sum_{j=1}^{J} \nu_{s_k j} R_j\,, \tag{5.24}$$

which is required in Equation (5.19), $M_k = \sum_{s_k} \mu_{s_k} N_{s_k}$. To calculate the change in number density of species s, N_s, due to chemistry, one takes the net sum of all productions minus destructions by all involved reactions, described by the rate Equation (3.16).

Note that Equations (5.17), (5.18) and (5.19) are intercoupled by N_s for each species and the energy source terms G_k for each fluid, containing the chemical and the hydrodynamic energy source terms, see Section 5.2. To solve these equations first the source terms N_s for each species s are computed using the reaction network of the model, see Appendix F, and the rate Equation (3.16). In the next step the gradient of the common velocity is computed via Equation (5.18). In addition, the energy source term G_k is computed for each fluid k, see the general Equation (5.20) or the explicit Equations (5.28). Finally, the temperature gradient of the neutral, the ionic and the electron fluid, Equation (5.19), and the continuity Equation (5.17) are computed using the initial values for u, n_s, ρ_s and T_k. The initial values are described in the following Section 5.1.3 and the chemical energy source terms in Section 5.2.

T_k (for each fluid), u and n_s (for each species) are computed by numerical integration of the Equations (5.17), (5.18) and (5.19). The system of ODEs given by (5.17) is stiff, since the reaction network, described by the Equation (3.16), includes rate coefficients of different orders of magnitudes. For this reason the presented model uses the implicit integrator LSODE. The LSODE varies the integration step size dynamically (Radhakrishnan and Hindmarsh, 1993).

5.1.3 Boundary Conditions and Initial Values

Initial conditions have to be given at the nucleus' surface for each species' number and mass density, n_j and ρ_j, the velocity u and the temperatures T_k of the three fluids

$$n_j(r_0) = n_{j,0}\,, \qquad \rho_k(r_0) = \rho_{k,0}\,, \tag{5.25}$$

with $\rho_{k,0} = \sum_{s_k} \mu_{s_k} n_{s_k,0}$ according to Equation (5.23). The initial velocity and temperatures

$$u(r_0) = u_0\,, \qquad T_k(r_0) = T_{k,0}\,, \tag{5.26}$$

are calculated as described in Section 3.1.7 (p.43). For the comets investigated in this work T_0 varies between $T_0 = 165$ K and $T_0 = 172$ K and u_0 between $u_0 = 310$ m s^{-1} and $u_0 = 320$ m s^{-1}, see Table 8.3. This Table lists the boundary conditions, i.e. the heliocentric distance r_h, the nucleus radius r_0 and the production rate ratios of common cometary species $c(\text{species}) = Q(\text{species})/Q(\text{H}_2\text{O})$ with respect to the water production rate $Q(\text{H}_2\text{O})$. For these species one computes the initial number density at the comet nucleus surface (radius r_0) via

$$n_0(\text{species}) = \frac{c(\text{species}) \cdot Q(\text{H}_2\text{O})}{4\pi r_0^2 \cdot u_0}\,. \tag{5.27}$$

5.2 Energy Source Terms

The energy source terms, which are used in Equation (5.18) and Equation (5.19), are defined by

$$\begin{aligned} G_n &= G_n^{\text{chem}} + G_{e,n}^{\text{scatt-elast}} - G_n^{\text{rad}} + G_n^{\text{reabs-IR}}\,, \\ G_i &= G_i^{\text{chem}} - G_{e,i}^{\text{scatt-elast}}\,, \\ G_e &= G_e^{\text{chem}} + G_{e,i}^{\text{scatt-elast}} - G_{e,n}^{\text{scatt-inelast}} - G_{e,n}^{\text{scatt-elast}}\,, \end{aligned} \tag{5.28}$$

where the subscripts n, i, e denote the neutral, the ionic and the electron fluid, respectively.

5.2.1 Chemical Energy Source Terms

The chemical energy source terms G_n^{chem}, G_i^{chem} and G_e^{chem} are calculated with the formula for the mean thermal energy source terms per reaction, given in Table 5.3, by

$$G_k^{\text{chem},j} = \hat{G}_k^{\text{chem},j} \cdot R_j \,, \tag{5.29}$$

$$G_k^{\text{chem}} = \sum_j^J G_k^{\text{chem},j} = \sum_j^J \hat{G}_k^{\text{chem},j} \cdot R_j \,. \tag{5.30}$$

Here $\hat{G}_k^{\text{chem},j}$ is the mean energy change of fluid k by one reaction of reaction j and $G_k^{\text{chem},j}$ the mean energy change of fluid k per all occurring reactions of reaction j. R_j is the reaction rate [reactions cm^{-3} s^{-1}] of reaction j, G_k^{chem} is the net energy change of fluid k by all reactions in the chemical reaction network, where J is the number of reactions in the model (Rodgers and Charnley, 2002).

5.2.2 Energy Source Terms for Scattering Processes

The coma is heated due to photodissociation and photoionization. The temperature of the electron fluid can rise in the intermediate coma due to ionization of neutral molecules. However, collisions of electrons with the neutral and the ionic species can reduce the temperature and therefore cool the electron fluid. Elastic scattering transfers kinetic energy to the neutral and ion fluid. Inelastic collisions additionally transfer energy from the electrons to inner degrees of freedom, i.e. electronic, vibrational and rotational excitation of neutrals and ions. Scattering between neutrals can also lead to vibrational excitation. In the process of de-excitation energy escapes the coma in the form of photons. However, a part of these will be reabsorbed in the coma (radiative trapping). Collisions between neutral species and ions will transfer energy between the neutral and the ionic fluid. How these processes are modeled in the coma model of Weiler (2006) will now be described in this Section.

Elastic Scattering Between Electrons and Neutrals

Elastic scattering between electrons and neutrals is modeled only for water molecules, the most abundant molecule in the cometary coma. This was also applied in the model of Rodgers and Charnley (2002) by

$$G_{e,n}^{\text{scatt-elast}} = 1.1 \cdot 10^{-25}\, n_{\text{H}_2\text{O}}\, n_e\, T_e^{-1/2} (2T_e - 3T_n) \,, \tag{5.31}$$

which has units [erg s cm^{-3} s^{-}1]. n_e and $n_{\text{H}_2\text{O}}$ are the number density of the electron fluid and the water molecules, respectively. T_e and T_n are the temperatures of the electron and the neutral fluid, respectively. The equation is based on a measured collision cross section of H_2O.

Elastic Scattering Between Electrons and Ions

Draine (1980) provides a formula to describe elastic scattering between electrons and ions with units [erg s cm^{-3} s^{-}1],

$$G_{e,i}^{\text{scatt-elast}} = 1.37 \cdot 10^{-42}\, \frac{n_i^2}{\bar{\mu}_i}\, T_e^{-1.5} (T_i - T_e) \ln\left(1.24 \cdot 10^4 \sqrt{\frac{T_e^3}{n_i}}\right) , \tag{5.32}$$

with the mean ion mass

$$\bar{\mu}_i = \rho_i / n_i \,. \tag{5.33}$$

T_i and n_i are the temperature and the number density of the ion fluid.

Table 5.1: *Parameters from Cravens and Korosmezey (1986) for* $e^- - H_2O$ *cooling, used in the Equations* (5.36) *and* (5.37).

$W_1 = 0.198\,\mathrm{eV}$	$A_1 = -35.62$	$B_1 = -215.0$	$C_1 = -1.75 \cdot 10^4$	$D_1 = 5.25 \cdot 10^4$
$W_2 = 0.460\,\mathrm{eV}$	$A_2 = -33.91$	$B_2 = -297.0$	$C_2 = -6.11 \cdot 10^4$	$D_2 = 2.66 \cdot 10^5$

Inelastic Scattering Between Electrons and Neutrals

Inelastic collisions of electrons with neutral species lead to a loss of energy of the electronic fluid. H_2O is the most abundant molecule in cometary comae and has an electron collision cross section which is four magnitudes larger than the next most abundant molecule CO. This is because H_2O is a polar and CO a homopolar molecule (Ashihara, 1975). This makes it sufficient to calculate the electron-neutral inelastic scattering only for H_2O. The cooling rates of the electrons by rotational and vibrational excitation of H_2O,

$$G_{e,n}^{\text{scatt-inelast}} = G_{\text{rot}} + G_{\nu 1} + G_{\nu 2}\,, \tag{5.34}$$

have been obtained as analytical equations in Cravens and Korosmezey (1986). Cooling by rotational excitation is described by

$$G_{\text{rot}} = \left(a + b \ln\left(\frac{T_e}{T_n}\right)\right)(T_e - T_n)\, T_e^{-5/4}\, n_{\text{H}_2\text{O}}\, n_e\,, \tag{5.35}$$

with $a = 1.052 \cdot 10^{-8} + 6.043 \cdot 10^{-10} \ln(T_n)$ and $b = 4.180 \cdot 10^{-9} + 2.026 \cdot 10^{-10} \ln(T_n)$. G_{rot} has units [eV cm^{-3} s$^-$1]. Cooling by vibrational excitation is described by

$$G_{\nu j} = \left(8.37 \cdot 10^{13} W_j T_e^{-3/2}\right)\left(1 - \exp\left(W_j / k_B (T_e^{-1} - T_n^{-1})\right)\right) I_j T_e\, n_{\text{H}_2\text{O}}\, n_e\,, \tag{5.36}$$

where $j = 1, 2$ stand for the following vibrational transitions, $(000) \rightarrow (010)$ and the sum of $(000) \rightarrow (100), (000) \rightarrow (001)$, respectively. (ν_1, ν_2, ν_3) are the fundamental vibrational quantum numbers of H_2O. $G_{\nu j}$ has units [eV cm^{-3} s$^-$1], k_B is measured here in cgs units. I_j is defined as

$$I_j = \exp\left(A_j + B_j / T_e^{1/2} + C_j / T_e^{3/2} + D_j / T_e^2\right). \tag{5.37}$$

The parameters W_j, A_j, B_j, C_j and D_i for these equations are listed in Table 5.1.

A part of the radiated energy of de-exciting H_2O molecules may be reabsorbed by neutral molecules. This depends on the optical depth for infrared **(IR)** radiation. Therefore, this heating source of the neutral fluid is described by

$$G_n^{\text{reabs-IR}} = G_{e,n}^{\text{scatt-inelast}} \left(1 - \exp(-\tau_{\text{IR}})\right). \tag{5.38}$$

The optical depth at IR wavelengths τ_{IR} is approximated by (Schmidt et al., 1988)

$$\tau_{\text{IR}}(r) \approx 0.4 \cdot n_{\text{H}_2\text{O}}(r_0) \cdot r_0^2 \cdot \frac{\sigma_{\text{IR}}}{r} \tag{5.39}$$

with $\sigma_{\text{IR}} = 4 \cdot 10^{-19}$ m^2.

The electron fluid is also cooled by inelastic collisions with CO, which are modeled by chemical reactions in the model described here. A cooling by electronic excitation of CO (note that excited CO will be denoted CO*) is included by the first four chemical reactions displayed in Table 5.2 together with the next six reactions describing the de-excitation of CO*. The electron fluid is cooled via the first four reactions.

Table 5.2: *Cooling of the electron fluid by inelastic collisions of e^- with* CO *(upper four reactions). CO* de-excitation by emission of a photon is modeled by the lower six reactions. The coefficients A, B and C for the Arrhenius form Equation* (3.17) *are taken from Schmidt et al. (1988).*

reaction	A [cm^3 s^{-1}]	B	C	ΔE [eV]
$\mathrm{CO} + \mathrm{e}^- \rightarrow \mathrm{CO}(^1\mathrm{p}) + \mathrm{e}^-$	$4.46 \cdot 10^{-9}$	0.203	94940.0	-8.1
$\mathrm{CO} + \mathrm{e}^- \rightarrow \mathrm{CO}(^3\mathrm{p}) + \mathrm{e}^-$	$1.36 \cdot 10^{-7}$	-0.418	83840.0	-6.0
$\mathrm{CO} + \mathrm{e}^- \rightarrow \mathrm{CO}(^1\mathrm{s}) + \mathrm{e}^-$	$2.89 \cdot 10^{-9}$	0.107	91000.0	-6.9
$\mathrm{CO} + \mathrm{e}^- \rightarrow \mathrm{CO}(^3\mathrm{d}) + \mathrm{e}^-$	$8.22 \cdot 10^{-10}$	-0.040	99850.0	-7.7
reaction	A [s^{-1}]	B	C	ΔE [eV]
$\mathrm{CO}(^1\mathrm{p}) \rightarrow \mathrm{CO} + \gamma$	$9.79 \cdot 10^7$	0	0	0
$\mathrm{CO}(^3\mathrm{p}) \rightarrow \mathrm{CO} + \gamma$	$1.26 \cdot 10^2$	0	0	0
$\mathrm{CO}(^3\mathrm{s}) \rightarrow \mathrm{CO} + \gamma$	$1.00 \cdot 10^5$	0	0	0
$\mathrm{CO}(^3\mathrm{s}) \rightarrow \mathrm{CO}(^3\mathrm{p}) + \gamma$	$1.00 \cdot 10^5$	0	0	0
$\mathrm{CO}(^3\mathrm{d}) \rightarrow \mathrm{CO} + \gamma$	$1.00 \cdot 10^{-5}$	0	0	0
$\mathrm{CO}(^3\mathrm{d}) \rightarrow \mathrm{CO}(^3\mathrm{p}) + \gamma$	$2.37 \cdot 10^5$	0	0	0

Inelastic Scattering Between Neutrals

Energy from the neutral fluid can escape the coma by radiative de-excitation of excited neutrals via inelastic scattering. The empirical relation from Schmidt et al. (1988) takes only H_2O-H_2O collisions into account and is adopted in the model of Weiler (2006). The energy source term, in units [erg cm^{-3} s^{-1}], is

$$G_n^{\mathrm{rad}} \approx \frac{8.5 \cdot 10^{-19}\, T_n^2\, n_{\mathrm{H_2O}}^2}{n_{\mathrm{H_2O}} + 2.7 \cdot 10^7\, T_n} \exp(-\tau_{\mathrm{IR}}) \tag{5.40}$$

where τ_{IR} is the optical depth at infrared wavelengths, i.e. Equation (5.39), as in the case of inelastic electron-neutral scattering.

Elastic Scattering Between Neutrals and Ions

Exchange of energy between neutrals and ions by elastic collisions is taken into account by so-called pseudo reactions

$$\mathrm{A} + \mathrm{B}^+ \longrightarrow \mathrm{A} + \mathrm{B}^+ , \tag{5.41}$$

whereby only energy exchange is calculated and not a change in the number densities of A and B. H_2O, CO, CO_2 and H_3O^+, CH_4^+, H_2CO^+ are the most abundant neutral and ionic species and are used for the exchange of energy. The rate coefficients for these processes $A_j \approx 10^{-10}\mathrm{cm}^3\,\mathrm{s}^{-1}$ and $B_J = 0.5$ and $C_j = 0$ can be computed, using the hard-sphere collision theory (Connors, 1990), which has the Arrhenius form (3.17),

$$k = (r_A + r_B)^2 \sqrt{\frac{8\pi k_B T}{\mu}} \exp(-E/k_B T) , \tag{5.42}$$

assuming typical radii of neutrals and ions and an energy threshold $E = 0$. Here μ is the reduced molecular mass $\mu = (m_A \cdot m_B)/(m_A + m_B)$ of the species A and B, which exchange energy, r_A, r_B are their molecular radii.

Table 5.3: *Mean thermal energy source terms $\hat{G}_n^{chem,j}$, $\hat{G}_i^{chem,j}$ and $\hat{G}_e^{chem,j}$ per reaction used in Equation (5.30) of the model of Weiler (2006). The index j is the reaction in the reaction network. $\hat{G}_k^{chem,j}$ depends on the reaction type and the fluid k. $\Theta_n = \frac{3}{2}k_B T_n$, $\Theta_i = \frac{3}{2}k_B T_i$, $\Theta_e = k_B T_e$ is the thermal energy per particle of the neutral, ionic and electron fluid, respectively (equipartition theorem). M is the total mass of the reactants. ΔE is the average exothermicity or endothermicity per reaction. For neutral-neutral rearrangement and dissociative recombination reactions the source terms are also valid for reactions with more than two products, indicated by parenthesis. The sources are 1: Draine (1986), 2: Rodgers and Charnley (2002), 3: Weiler (2006), noted in the last column.*

reaction type	formula	$\hat{G}_n^{\mathrm{chem},j}$	$\hat{G}_i^{\mathrm{chem},j}$	$\hat{G}_e^{\mathrm{chem},j}$	
photodissociation	$\mathrm{A}+\gamma \rightarrow \mathrm{B}+\mathrm{C}$	ΔE	0	0	1
photoionization	$\mathrm{A}+\gamma \rightarrow \mathrm{A}^+ + \mathrm{e}^-$	$-\Theta_n$	Θ_n	ΔE	2
photodissociative ionization	$\mathrm{A}+\gamma \rightarrow \mathrm{B}+\mathrm{C}^+ + \mathrm{e}^-$	$-\frac{m_C}{m_A}\Theta_n$	$\frac{m_C}{m_A}\Theta_n$	ΔE	2
photodissociative ionization	$\mathrm{A}+\gamma \rightarrow \mathrm{B}+\mathrm{C}+\mathrm{D}^+ + \mathrm{e}^-$	$-\frac{m_D}{m_A}\Theta_n$	$\frac{m_D}{m_A}\Theta_n$	ΔE	3
neutral-neutral rearrangement	$\mathrm{A}+\mathrm{B} \rightarrow \mathrm{C}+\mathrm{D}\,(+\mathrm{E})$	ΔE	0	0	2,3
neutral-ion rearrangement	$\mathrm{A}+\mathrm{B}^+ \rightarrow \mathrm{C}+\mathrm{D}^+$	$\frac{m_A m_D + m_B m_C}{M^2}(\Theta_i - \Theta_n) + \frac{m_D}{M}\Delta E$	$-\frac{m_A m_D + m_B m_C}{M^2}(\Theta_i - \Theta_n) + \frac{m_C}{M}\Delta E$	0	1
neutral-ion rearrangement	$\mathrm{A}+\mathrm{B}^+ \rightarrow \mathrm{C}+\mathrm{D}+\mathrm{E}^+$	$\frac{m_A m_E + m_B m_{CD}}{M^2}(\Theta_i - \Theta_n) + \frac{m_E}{M}\Delta E$	$-\frac{m_A m_E + m_B m_{CD}}{M^2}(\Theta_i - \Theta_n) + \frac{m_{CD}}{M}\Delta E$	0	3
neutral-ion rearrangement	$\mathrm{A}+\mathrm{B}^+ \rightarrow \mathrm{C}+\mathrm{D}+\mathrm{E}+\mathrm{F}^+$	$\frac{m_A m_F + m_B m_{CDE}}{M^2}(\Theta_i - \Theta_n) + \frac{m_F}{M}\Delta E$	$-\frac{m_A m_F + m_B m_{CDE}}{M^2}(\Theta_i - \Theta_n) + \frac{m_{CDE}}{M}\Delta E$	0	3
charge-exchange	$\mathrm{A}+\mathrm{B}^+ \rightarrow \mathrm{A}^+ + \mathrm{B}$	$\frac{m_A^2 + m_B^2}{M^2}(\Theta_i - \Theta_n) + \frac{m_A}{M}\Delta E$	$-\frac{m_A^2 + m_B^2}{M^2}(\Theta_i - \Theta_n) + \frac{m_B}{M}\Delta E$	0	1
e^- impact dissociation	$\mathrm{A}+\mathrm{e}^- \rightarrow \mathrm{B}+\mathrm{C}+\mathrm{e}^-$	0	0	ΔE	2
e^- impact ionization	$\mathrm{A}+\mathrm{e}^- \rightarrow \mathrm{A}^+ + \mathrm{e}^- + \mathrm{e}^-$	$-\Theta_n$	Θ_n	ΔE	2
recombination	$\mathrm{A}^+ + \mathrm{e}^- \rightarrow \mathrm{A}+\gamma$	Θ_i	$-\Theta_i$	$-\Theta_e$	1
dissociative recombination	$\mathrm{A}^+ + \mathrm{e}^- \rightarrow \mathrm{B}+\mathrm{C}\,(+\mathrm{D}+\mathrm{E})$	$\Theta_i + \Theta_e + \Delta E$	$-\Theta_i$	$-\Theta_e$	1,3
ionizative association	$\mathrm{A}+\mathrm{B} \rightarrow \mathrm{C}^+ + \mathrm{e}^-$	$-2\Theta_n$	$2\Theta_n$	ΔE	3
dissociative e^- impact ionization	$\mathrm{A}+\mathrm{e}^- \rightarrow \mathrm{B}+\mathrm{C}^+ + \mathrm{e}^- + \mathrm{e}^-$	$-\frac{m_C}{m_A}\Theta_n$	$\frac{m_C}{m_A}\Theta_n$	ΔE	3
e^- impact excitation	$\mathrm{A}+\mathrm{e}^- \rightarrow \mathrm{A}^* + \mathrm{e}^-$	0	0	ΔE	3
radiative de-excitation	$\mathrm{A}^* \rightarrow \mathrm{A}+\gamma$	0	0	0	3

5.3 Chemistry

Chemical reactions are modeled by the Equation (3.16) for which the rate coefficients, parametrized in an Arrhenius form, are used. The reactions and the parameters A, B and C are adopted from Weiler (2006), whose values were mostly based on Huebner et al. (1992), Helbert (2002) and the UMIST astrochemistry database (Woodall et al., 2007).

5.3.1 Collisional Reactions

An effective temperature is defined for the collisional reactions to account for the different temperatures each fluid has (Flower et al., 1985), which is used in Equation (3.17),

$$T = \frac{m_k T_l + m_l T_k}{m_l + m_k} \,. \tag{5.43}$$

m_l, m_k, T_l and T_k is the mass and temperature of the species belonging to fluid l and k, respectively. For the electronic fluid m_e is the mass of an electron, therefore $T = T_e$ for electron collisions, due to the low mass compared to all other species.

5.3.2 Photochemistry and Optical Depth

The model is supplied with so-called unattenuated photo rate coefficients $k_i^0(r_h = 1 \text{ AU})$, i.e. rate coefficients for a zero optical depth $\tau = 0$, for each photo reaction, calculated via Equation (3.18) with the solar photon flux of Huebner et al. (1992) at a heliocentric distance of $r_h = 1$ AU.

The optical depth τ in Equation (3.30) requires knowledge of the number density of molecules between the cometocentric distance r in the coma and the outer coma region, where the solar photon flux is reduced only insignificantly due to the low number densities, see Figure 5.1. Since $n(r)$ is computed from $r = r_0$ to $r = 10^7$ km, $n(\tilde{r})$ with $\tilde{r} > r$ is in principle unknown at the computation step at r. However, $n(r)$ can be approximated to decrease with r^{-2}, which is the case for gas streaming off the nucleus with constant velocity and passively, i.e. without in situ chemistry. τ can be approximated by using only the most abundant species in the coma: H_2O, CO and CO_2. This leads to (Schmidt et al., 1988)

$$\tau(r, \lambda) = \sum_{i=1}^{3} n_i(r) \cdot \sigma(\lambda) \cdot r \,. \tag{5.44}$$

This can be further simplified to

$$\bar{\tau}(r) = \sum_{i=1}^{3} n_i(r) \cdot \bar{\sigma}_i \cdot r \,, \tag{5.45}$$

computed by summation of the products of the average absorption cross sections $\bar{\sigma}_i$, averaged over 175 λ bins between $\lambda = 0$ and $\lambda = 3525$ Å, times the number density of H_2O, CO and CO_2. The rate coefficient $k_i(r, r_h = 1 \text{ AU})$ is then calculated via

$$k_i(r, 1 \text{ AU}) = k_i^0(1 \text{ AU}) \cdot \exp(-\bar{\tau}(\mathrm{r})) \,. \tag{5.46}$$

The rate coefficient $k_i(r, 1\text{AU})$ is scaled to other r_h values by (Jewitt et al., 2008)

$$k_i(r, r_h) = \frac{k_i(r, 1 \text{ AU})}{r_h^2} \,. \tag{5.47}$$

In the current model of Weiler (2006) the rate coefficient can also be calculated with the Equation of the wavelength dependent $\tau(\lambda, r)$ (5.44), for 16 species. For these species the

integration in Equation (3.18) can be replaced by a summation over the above-mentioned 175 wavelengths bins.

This wavelength dependent optical depth treatment for some species is omitted in this work, especially in view of the photo rate coefficient variation applied in Chapter 8. The effect of this wavelength dependent treatment is very small, as shown in Section 6.2 of the model validation Chapter 6.

5.4 Validity Range and Simplifications of the Model

This section gives an overview and discussion of the simplifications included into the model of Weiler (2006).

5.4.1 Assumption of Hydrodynamic and Steady State Flow and a Spherically Symmetric Coma

The assumption of a hydrodynamic flow in the coma is only supported as long as the collisions between species lead to a Maxwellian velocity distribution. As described in Section 3.1.4 this assumption is no longer valid at cometocentric distances of $r \gtrapprox 10^4$ km for a Halley-type comet, i.e. a comet being at $r_h = 1$ AU and having a water production rate of $Q(\mathrm{H_2O}) = 10^{30}$ molecules s^{-1}.

Around $r = 10^4$ km the gas transitions from collisionally dominated to a free molecular flow due to the decrease of the coma density with r^{-2} (when assuming a constant gas velocity). This means that the collisional mean free path increases so that the particle's velocity distribution is no more a Maxwell distribution, i.e. a hydrodynamical description of the coma properties becomes less realistic. At such greater distances the trajectories and the velocity distributions of the particles have to be computed with a Monte-Carlo simulation. However, studies suggest that the computed number densities and temperatures can be described reasonably with a hydrodynamical model even in the free molecular flow region. For example Marconi and Mendis (1986) reasonably reproduced observations in this regime for comet 21P/Giacobini-Zinner within a factor of two. This is why the model in this work uses a hydrodynamical description.

The model assumes a steady state flow in the coma. Therefore, changes of the gas density with time, e.g. due to sudden outbursts or periodic variations due to e.g. active regions on a rotating nucleus, are not treated. Although the water production rate and therefore the coma densities do vary with the heliocentric distance r_h, significant changes are only observable over several weeks. The change of the solar insolation with r_h is not significant within the time a particle travels, e.g. with a mean velocity of $u = 1$ km s^{-1}, from the nucleus to the outer range of the observations used in this work, i.e. around $r = 10^5$ km.

The present model assumes a spherically symmetric coma since results of current 3D models suggest that asymmetries in the coma densities close to the nucleus are smoothed out beyond $r = 10^3$ km, see e.g. Crifo (1991), Crifo et al. (2004) and Rodgers and Charnley (2002) for a discussion, i.e. the smallest distance of the available observations used in this work. Such near nucleus asymmetries may be caused by an irregularly shaped comet nucleus and/or inhomogeneous outgassing of the nucleus (active and inactive nucleus surface areas) as well as the rotation of the nucleus. The shape of the nucleus has a smaller influence on the coma gas distribution the farther away from the nucleus whereas rotation of the nucleus may have a stronger influence on the symmetry of the coma even at larger distances due to a periodic change in the total gas production (Crifo et al., 2004). Generally, one would expect sublimation to occur only on the sunward side of the cometary nucleus.

5.4.2 Neglection of Magnetic Field, Superthermal Species and Dust Treatment

The neglection of the interaction of the coma plasma and the solar wind introduces a significant simplification for the ionic species. Beyond the magnetic cavity at around $r = 10^3$ km - 10^4 km, depending on the gas production rate of the comet, ions are accelerated by the solar wind, leading to an asymmetry in the densities of the ionic species. The formation of C_3 and C_2 in cometary comae is not affected significantly by this simplification, as ionic hydrocarbons are much less abundant than neutral hydrocarbons in the range of the observations investigated in the present work, i.e. beyond several 10^3 km. Therefore, these ions cannot contribute significantly to the C_3 and C_2 produced by photodissociation of hydrocarbons. Additionally, a 3-dimensional magnetohydrodynamic model would introduce additional, unconstrained input parameters, which may not result in an increased accuracy of the number densities.

In the photodissociation of e.g. H_2O into OH and H, the H obtains a large excess velocity of $\Delta u \approx 18$ km s^{-1} due to its much smaller weight compared to OH, which obtains $\Delta u \approx 1.09$ km s^{-1}. Due to the decrease of the coma density with r^{-2} (spherical expansion of the coma, assuming a constant gas velocity) the molecular collision mean free path increases, so that the excess energy of photodissociation products is no longer distributed among the other particles. The superthermal species H and H_2 (mainly via $H_2O + \gamma \rightarrow O + H_2$) tend to remove energy from the coma, since on the one hand such species require more collisions than heavier ones to distribute their kinetic energy among the other species, due to their small mass, and on the other hand H and H_2 are much more numerous than other species, since H_2O is the most abundant species in the coma. In contrast to the model of Rodgers and Charnley (2002) the model used in this work does not include a treatment of superthermal species. This leads to an overestimation of the temperature of the neutral fluid beyond the intermediate coma. However, at such distances, i.e. approximately the range of the observations investigated in the present work, the number densities are already so low that chemical reactions are not efficient in producing additional C_3 and C_2 containing hydrocarbons. The higher temperature of the neutral species causes the hydrodynamic gas velocity to be somewhat larger in the outer coma in comparison to models including a treatment of superthermal species. As a result the C_3 and C_2 model column density profiles are shifted to smaller values in the coma and feature a somewhat larger slope in the outer coma as when including this effect, e.g. by a parametrization as used by Rodgers and Charnley (2002). However, one has to keep in mind that the excess kinetic energy imparted to the H and H_2 species after photodissociation of H_2O is uncertain. Also the amount of excess energy going into internal energy by ro-vibrational excitation of the OH molecule and not into excess velocity of the H is uncertain (Huebner et al., 1992, Rodgers and Charnley, 2002). This uncertainty may also have an effect on the height and shape of the column density profiles. Therefore, inclusion of a correction for superthermal species does not necessarily increase the accuracy of the model outputs. Detailed modelling of this effect needs either the application of a Monte Carlo **(MC)** model (including modelling of the superthermal species H and H_2) and/ or a sophisticated parameter study, including e.g. a variation of the excess kinetic energy for H_2O photodissociation.

It is known that comets can release large amounts of dust into the coma, visible by the cometary dust tail. In Weiler (2006) it was shown, e.g. for comet 67P **(Churyumov-Gerasimenko)**, that even large dust-to-gas mass ratios as 8.5 only negligibly influence the gas flow in the coma for realistic dust size distributions. Therefore, the model in this work does not treat dust. Although there are studies assessing the possibility of dust grains to release C_2 into the cometary coma (Combi and Fink, 1997), these require the dust composition of the comet and laboratory data to model the C_2 release from the dust particles.

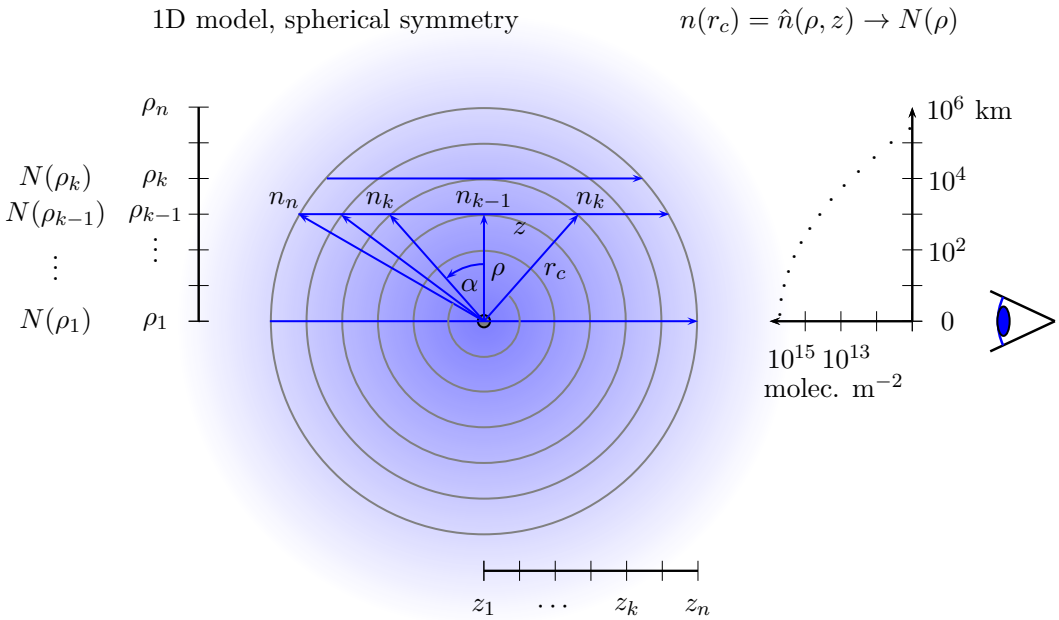

Figure 5.1: *Viewgraph illustrating the conversion from number densities $n(r)$ of a 1D model to column densities $N(\rho)$. r is the cometocentric distance.*

5.5 Conversion from Number Densities to Column Densities

To compare column densities derived from observations one has to convert the number densities $n(r)$, as calculated in the comet model, to column densities $N(\rho)$. The following conversion is illustrated in Figure 5.1. Under the assumption of a spherically symmetric coma, number densities are defined at each position in the displayed 2D coma. The density $n(r)$ is transformed into $\hat{n}(\rho, z)$ by transforming the cometocentric distance r into cylindrical coordinates using $r = \sqrt{\rho^2 + z^2}$. Then, at each distance ρ, the column density $N(\rho)$ is computed by integrating $\hat{n}(\rho, z)$ along z, the displayed line of sight, for each ρ (Weiler, 2006)

$$N(\rho) = \int_{-\infty}^{\infty} \hat{n}(\rho, z)\, dz. \tag{5.48}$$

On the right sight of Figure 5.1 a plot of the column densities is plotted logarithmically. Within the conversion routine used in this work, the number densities, $N(\rho_k)$ in the Figure, from a model are interpolated and the integration is performed from the center to a maximum ρ. The integration along z is performed to values high enough, i.e. $z = 10^7$ km, to attain the significant part of the density in the line of sight, i.e. increasing the integration to higher values of z does not significantly increase the column density values.

CHAPTER 6

Model Validation With Previous Work

The model used in this work is adapted from Weiler (2006), which is similar to the model of Rodgers and Charnley (1998) and Rodgers and Charnley (2002). Updates and improvements to the model used in this thesis comprise (a) the photochemical part of the reaction network important for the formation of C_3 and C_2 and (b) the neglection of the wavelength dependent optical depth for some species in favour of an integrated optical depth for all species. This chapter tests the numerics of the hydrodynamical part of the code by validating the model of this work against the model used in Weiler (2006) and also partly against the model of Rodgers and Charnley (1998, 2002), as done in Weiler (2006). The effect of the updated reaction network onto the model outputs is discussed in the framework of a sensitivity analysis **(SA)** in Chapter 8.

6.1 Energy Source Terms, Fluxes, Temperatures and Velocity

The model used in this work is validated with respect to the energy source terms, the flux densities of common coma species, the temperatures of the neutral and the ionic species and the electrons, i.e. T_n, T_i and $\mathrm{T_e}$, and their common velocity u.

6.1.1 Energy Source Terms

In this section the energy source terms of comet C/1996 B2 **(Hyakutake)** are compared with Weiler (2006). Table 6.1 gives the input parameters for comet Hyakutake at $r_h = 1.1$ AU. The energy source terms, see Section 5.2, computed in this work are given in Figure 6.1a and those computed in Weiler (2006) are given in Figure 6.1b. The energy source terms (and written here in parenthesis the corresponding terms in Weiler (2006)) are G_n^{chem} (G_n^c), G_i^{chem} (G_i^c), G_e^{chem} (G_e^c) the chemical source terms for the neutrals, ions and electrons, respectively, $G_{e,n}^{\mathrm{scatt.elast.}}$ (G_n^e), $G_{e,i}^{\mathrm{scatt.elast.}}$ (G_i^e) elastic scattering between electrons and neutrals and between electrons and ions, respectively, $G_{e,n}^{\mathrm{scatt.inelast.}}$ (G_e^{in}), G_n^{rad} (G_n^r) for inelastic scattering between electrons and neutrals and between neutrals, respectively, $G_n^{\mathrm{reabs\text{-}IR}}$ for reabsorption of infrared **(IR)** radiation by neutrals, for which $G_n^{\mathrm{reabs\text{-}IR}} = G_{e,n}^{\mathrm{scatt\text{-}inelast}}(1 - \exp(-\tau_{\mathrm{IR}})) \approx G_{e,n}^{\mathrm{scatt\text{-}inelast}}$ as the optical depth τ is usually very small. This is the reason why $G_{e,n}^{\mathrm{scatt\text{-}inelast}}$ (G_e^{in}) appears rather

than $G_n^{\text{reabs-IR}}$ in Figure 6.1a of Weiler (2006). Figure 6.1 suggests that the energy flux terms for comet Hyakutake computed in Weiler (2006) shows good agreement with this work.

6.1.2 Gas Fluxes

Regarding the gas fluxes the model of this work is compared to Rodgers and Charnley (1998) and Weiler (2006). The initial values are given in the right column of Table 6.1 taken from Rodgers and Charnley (1998).

The gas flux f, in units of molecules per second, is defined as

$$f = 4\pi u n r_c^2 \,, \tag{6.1}$$

with u the common gas velocity, n the particle number density of the species being considered and r_c the cometocentric distance. The gas flux corresponds to the number density of the gas corrected by the coma expansion. Therefore, the flux profile $f(r_c)$ describes the change of the number density only due to the chemistry in the coma.

Figures 6.2a, 6.2b and 6.2c compare the fluxes of the species H_2O, OH, H, HCN, HNC, H_3O^+, and NH_4^+ from Rodgers and Charnley (1998), Weiler (2006) and from this work. The main difference between this work and Weiler (2006) is for the HCN flux, which decreases slightly faster in Weiler (2006). Nevertheless, a model test computation with the adopted model from 2006 results in the same decrease for HCN as computed in this work. The reason for the discrepancy between this work an Weiler (2006) requires further investigations and could be due to a difference in the applied wavelength dependent optical depth for HCN used in Weiler (2006).

A comparison with Figure 6.2a from Rodgers and Charnley (1998) shows additionally the fluxes of the species $HCNH^+$ and $CH_3OH_2^+$ as these authors use a larger reaction network for the computation of the HCN and HNC chemistry. As already stated in Weiler (2006) there are large differences for HNC in comparison to Rodgers and Charnley (1998), which can be due to the different reaction networks and due to the treatment of super-thermal species like H, H_2, D and HD in Rodgers and Charnley (1998), important for the formation of HNC e.g. via $\text{HCN} + \text{H} \rightarrow \text{HNC} + \text{H}$. The differences at $r_c < 100$ km might be due to differences in the initial values for some daughter species.

6.1.3 Temperatures and Velocity

Regarding the temperatures and the common gas velocity the model of this work is compared to Weiler (2006) and Rodgers and Charnley (2002) using the initial values given in the left column of Table 6.1 taken from Rodgers and Charnley (2002). Figures 6.2d, 6.2e and 6.2f show computed temperatures of the fluids for the neutral species, the ionic species and the electrons together with the common gas velocity u, with the exception of Figure 6.2e.

The temperatures computed in this work are in agreement with Weiler (2006). A comparison to Rodgers and Charnley (2002) shows that T_n is higher in this work at $r_c > 10^3$ km. Also the velocity is slightly higher in this work due to this effect. This is consistent with the simplified treatment of the superthermal species like H and H_2 in the model presented in Chapter 5. See also Section 5.4 for a discussion.

6.2 Reproduction of Model Fits to Observations in Previous Work

In order to reproduce the fits of Weiler (2006) to the C_3 and C_2 observations of the comets NEAT, LINEAR and Tempel 1, the model used in this work was applied with the reaction

network of Weiler (2006). The production rate ratios of common cometary species as used in Weiler (2006) are given in Table 6.2. The fitted production rate ratios of C_3H_4, C_4H_2, C_2H_2 and HC_3N from Weiler (2006) are given in Table 6.2.

The comparison with Weiler (2006) in the Figure 6.3 shows that all fits are reproduced. Slightly higher C_2 column densities are noticeable in this work, since for HC_3N only upper limits are given in Weiler (2006), with the exception of the tailward side of comet C/2001 Q4 **(NEAT)**. Other small differences, e.g. identifiable for the C_3 observations of the comets C/2002 T7 **(LINEAR)** and 9P **(Tempel 1)**, are likely associated with small differences in the conversion factors used for the conversion from the C_3 and C_2 fluxes of the observations to column densities. Additionally, note that this work employed the database ephemeris program of the updated version of the comet database of Rauer et al. (2008), which has slightly different heliocentric distances than in Weiler (2006).

Neglection of the Wavelength Dependence of the Optical Depth

In the model of Weiler (2006) an integrated optical depth has been used for most of the modeled species. For a subset of species a wavelength dependent optical depth has been used. These comprise also some species which produce C_2, e.g. C_2H_2, but not species which produce C_3.

In this work, with the exception of the model validation, this wavelength dependency of the optical depth is neglected and the integrated optical depth is used for all species, as is used e.g. in Rodgers and Charnley (2002). Figure 6.3c shows that the difference in C_2 column densities which arise due to this neglect of wavelength dependence is very small. In this Figure the black profiles result from using the wavelength dependent optical depths as in Weiler (2006) whereas the blue dashed lines result from using an integrated optical depths for all species.

Table 6.1: *Input values for comet Hyakutake to validate the model used in this work with the model of Weiler (2006) and the model of Rodgers and Charnley (1998, 2002). For the validation of the species fluxes in Section 6.1.2, Figure 6.2c, the input values of Rodgers and Charnley (1998) (middle column) are required and for the validation of the temperatures and the common gas velocity in Section 6.1.3, Figure 6.2f, the input values of Rodgers and Charnley (2002) (right column) are required. This table lists the heliocentric distance r_h, the water production rate $Q(H_2O)$, the production rate ratios $c(\text{species}) = Q(\text{species})/Q(H_2O)$ of various known cometary species relative to $Q(H_2O)$, the nucleus radius $r_{nucleus}$, the initial gas temperature T_0 and the initial gas velocity u_0 at the nucleus surface.*

comet	Hyakutake	
reference	Rodgers and Charnley (1998)	Rodgers and Charnley (2002)
r_h [AU]	1.1	1.0
$Q(H_2O)$ [molecules s^{-1}]	$1.7 \cdot 10^{29}$ [a]	$1.7 \cdot 10^{29}$ [a]
$c(CO)$	0.06 [a]	0.2 [b,c]
$c(CO_2)$	-	0.06 [d]
$c(CH_4)$	0.007 [a,g]	0.007 [a]
$c(H_2CO)$	0.002 [i]	0.01 [b,c]
$c(CH_3OH)$	0.01 [i]	0.02 [b,c]
$c(NH_3)$	0.003 [j]	0.01 [e]
$c(HCN)$	0.0016 [f,i]	0.001 [b,c,k]
$c(C_2H_2)$	0.003 [h]	0.001 [d]
$c(C_2H_6)$	0.004 [a]	0.004 [a]
r_{nucleus} [km]	2.2 [k]	2.2 [k]
u_0 [m/s]	500 [‡]	325.1 (250) [†]
T_0 [K]	200 [‡]	171.6 (100) [†]

(a) Mumma et al. (1996), (b) Biver et al. (1999), (c) Lis et al. (1997), (d) Bockelée-Morvan et al. (2000), (e) Bird et al. (1997), (f) Irvine et al. (1996), (g) Weaver et al. (1997), (h) Brooke et al. (1996a), (i) Womack et al. (1996), (j) Palmer et al. (1996), (k) Sarmecanic et al. (1997), Lisse et al. (1999).

(†) T_0, u_0 calculated as described in Section 3.1.7 and used in this work as in Weiler (2006), whereas values in parenthesis were used in Rodgers and Charnley (2002).

(‡) used in Rodgers and Charnley (1998).

Table 6.2: *Production rate ratios $c(\text{species}) = Q(\text{species})/Q(H_2O)$ of C_3H_4, C_4H_2, C_2H_2 and HC_3N determined in Weiler (2006) from fits to the tailward and sunward part of the C_3 and C_2 column densities of the comets NEAT, LINEAR and Tempel 1, respectively.*

comet	NEAT		LINEAR		Tempel 1	
$Q(H_2O)$	$1.9 \cdot 10^{29}$		$6.9 \cdot 10^{28}$		$3.4 \cdot 10^{27}$	
parent molecule	production rate ratio sunward / tailward [%]					
$c(C_3H_4)$	$3.56^{+0.74}_{-0.81}$	$3.51^{+0.18}_{-0.23}$	$0.56^{+0.40}_{-0.37}$	$0.45^{+0.22}_{-0.20}$	$8.19^{+0.98}_{-1.23}$	$3.52^{+1.07}_{-1.09}$
$c(C_4H_2)$	$0.192^{+0.056}_{-0.045}$	$0.161^{+0.024}_{-0.020}$	$0.248^{+0.018}_{-0.018}$	$0.242^{+0.008}_{-0.013}$	$0.146^{+0.010}_{-0.009}$	$0.138^{+0.008}_{-0.015}$
$c(C_2H_2)$	0.85	$0.66^{+0.15}_{-0.11}$	0.64	0.56	1.13	1.07
$c(HC_3N)$	< 2.6	$7.7^{+2.9}_{-3.0}$	< 4.0	< 4.4	< 2.8	< 2.4

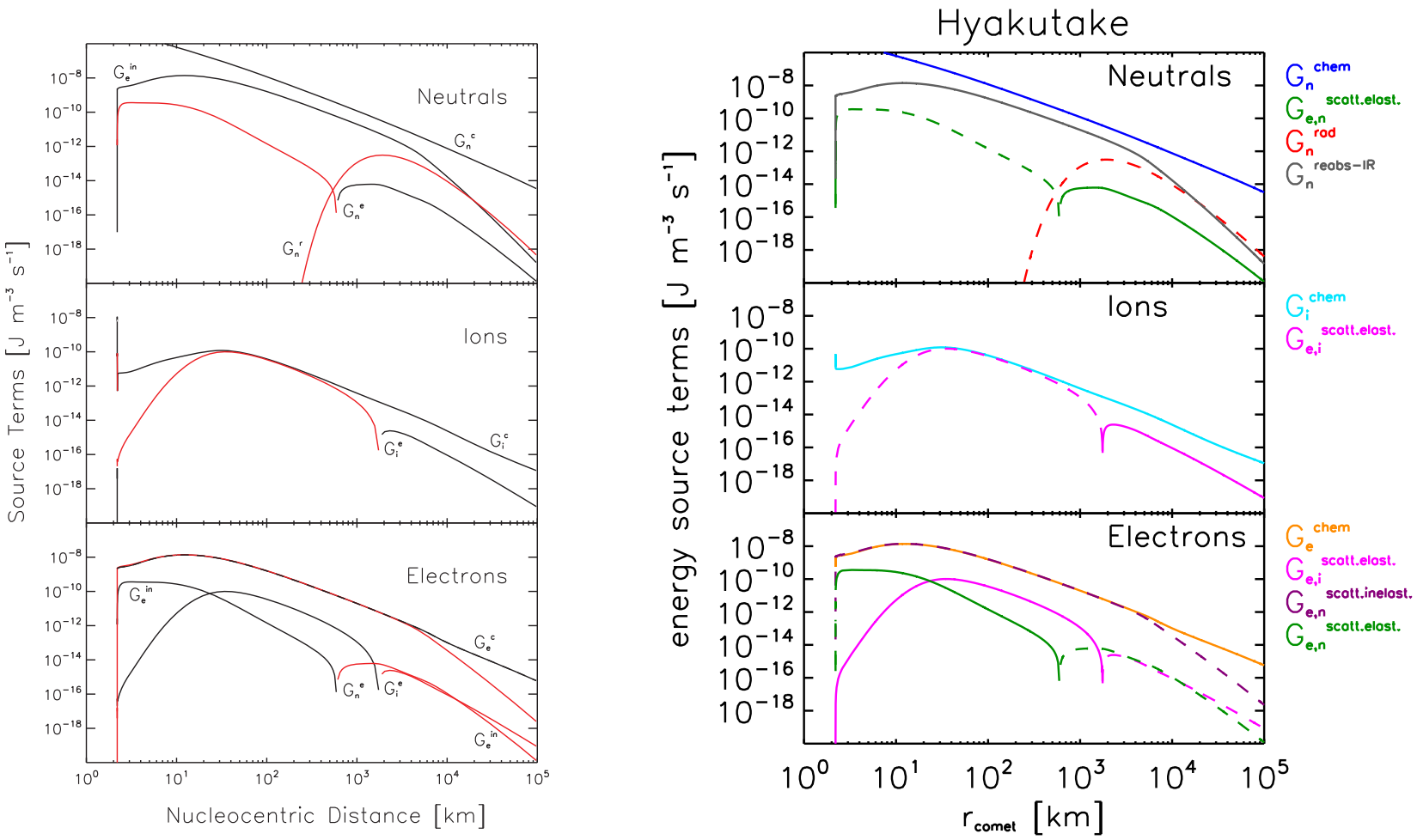

(a) *Weiler (2006)* **(b)** *This work*

Figure 6.1: *Comparison of the energy source terms of comet Hyakutake as computed in (a) Weiler (2006) and (b) this work using the input parameters from Table 6.1 from Rodgers and Charnley (2002). In (a) the red color indicates energy loss, whereas black indicates energy gain. In (b) each source term has a different color and energy loss is indicated by a dashed line.* G_n^c, G_e^{in}, G_n^e, G_n^r, G_i^e, G_i^c, G_e^c *in (a) correspond to* G_n^{chem}, $G_{e,n}^{scatt.inelast.}$, $G_{e,n}^{scatt.elast.}$, G_n^{rad}, $G_{e,i}^{scatt.elast.}$, G_i^{chem}, G_e^{chem} *in (b), see Section 6.1.1 for information about the energy source terms. The indices* n, i, e *denote neutrals, ions and electrons, respectively.*

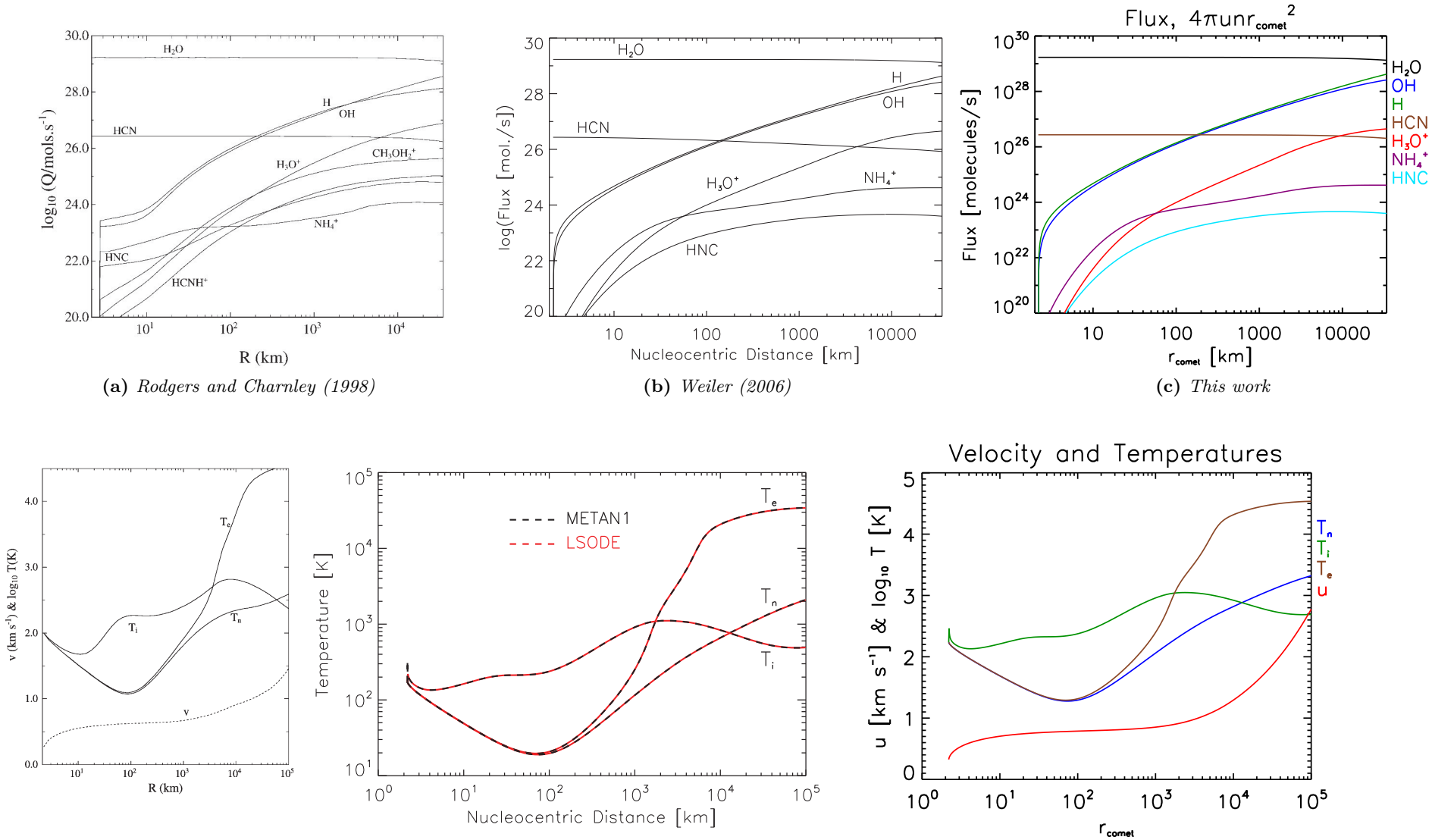

(a) *Rodgers and Charnley (1998)* **(b)** *Weiler (2006)* **(c)** *This work*

(d) *Rodgers and Charnley (2002)* **(e)** *Weiler (2006)* **(f)** *This work*

Figure 6.2: *Figures (a), (b) and (c) show the gas fluxes f of common coma species computed in the work of Rodgers and Charnley (1998), Weiler (2006) and in this work, respectively. Figures (d), (e) and (f) show the temperatures T_n, T_i, T_e of the neutral, ionic and electronic fluid and the common gas velocity u computed in the work of Rodgers and Charnley (2002), Weiler (2006) and in this work.*

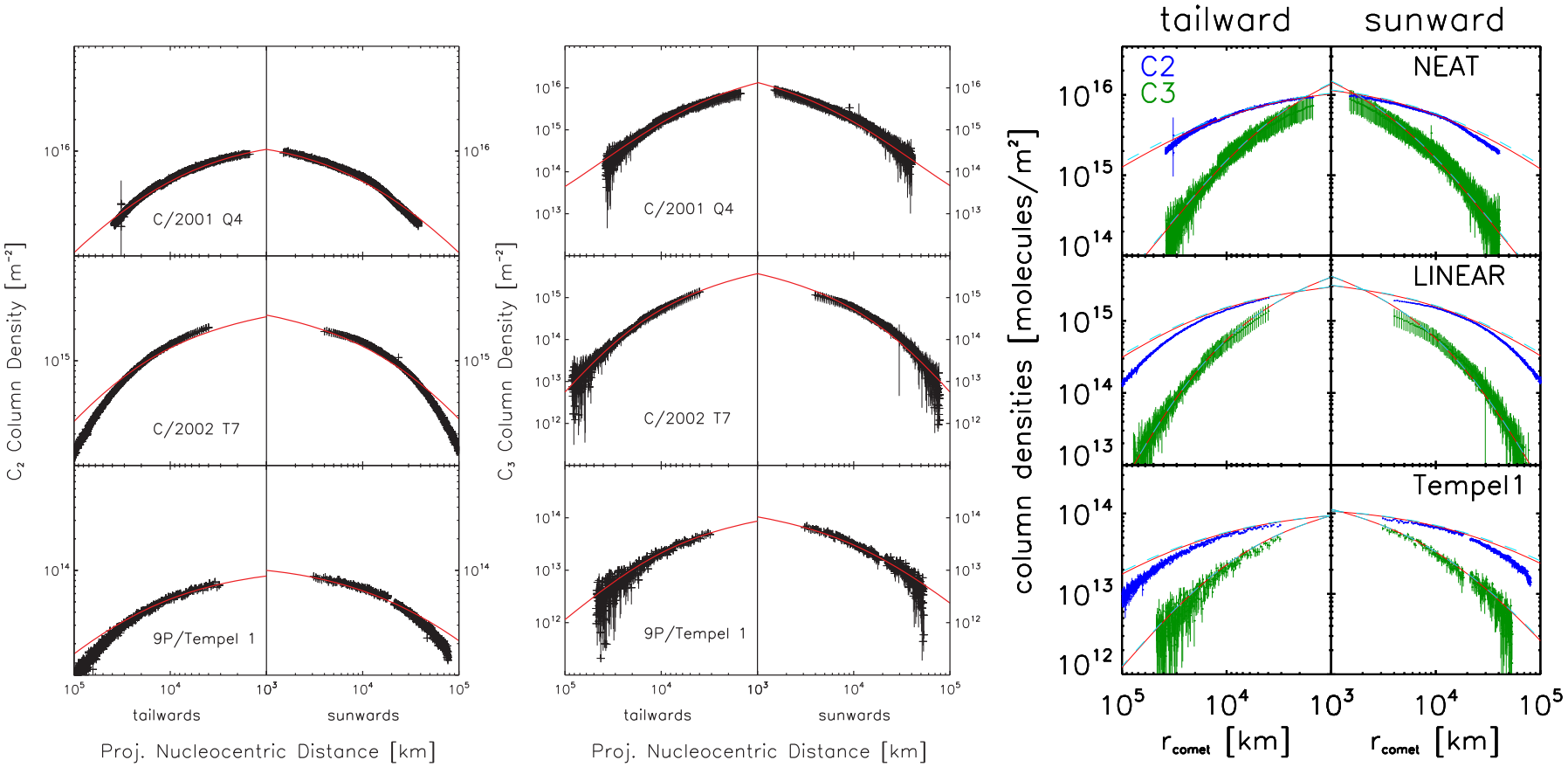

(a) *Weiler (2006):* C_2 **(b)** *Weiler (2006):* C_3 **(c)** *This work:* C_3, C_2

Figure 6.3: C_3 *and* C_2 *column density fit results of Weiler (2006) for the comets NEAT, LINEAR and Tempel 1, shown separately in the panels (a) and (b). The reproduced fit results of the present work, i.e. using the adapted model and the reaction network of Weiler (2006), are shown in panel (c). Panel (c) additionally shows the difference in the* C_2 *profiles when applying an integrated optical depth for all species (blue dashed lines), as used in the present work, instead of a wavelength dependent optical depths for a subset of the species included in the reaction network.*

CHAPTER 7

Update and Uncertainties of Photo Rate Coefficients

This chapter deals with the update of the photochemical part of the reaction network relevant for the C_3 and C_2 formation in comets. This chapter presents the computation of the photodissociation rate coefficients and, for the first time, an computation of their uncertainties which are required for the sensitivity analysis **(SA)** of the coma chemistry model presented in Chapter 8. The numerical computation of the photo rate coefficients is described in Section 7.1. The sources of the uncertainty of the photo rate coefficients are discussed in Section 7.2. The photo rate coefficient distributions are computed with the Monte Carlo **(MC)** method in Section 7.3. A summary is presented in Section 7.4.

7.1 Numerical Computation of Photo Rate Coefficients

7.1.1 Computation Using Absorption Cross Sections σ

Several products can be formed by molecular photodissociation. As described in Section 3.2.2 a photo rate coefficient k_i for reaction i is calculated via

$$k_i(r_h) = \int_0^{\lambda_0^i} \sigma(\lambda)\phi_i(\lambda)F_\odot(\lambda, r_h)\, d\lambda\,, \tag{7.1}$$

assuming a zero optical depth τ, see also Section 5.3.2 of the model description. In Equation (7.1) r_h is the heliocentric distance, λ_0^i the threshold wavelength, $\sigma(\lambda)$ the absorption cross section, $\phi_i(\lambda)$ the quantum yield for dissociation of the regarded molecule, $F_\odot(\lambda, r_h)$ the solar photon flux in units photons cm^{-2} s^{-1} λ-bin^{-1}. In Equation (7.1) the photon flux is assumed to be $F_\odot(\lambda, r_h)$, hence only a function of λ and r_h and its absorption by the cometary coma is neglected. Equation (7.1) can be approximated numerically by (Huebner et al., 1992)

$$k_i = \sum_{j=1}^{J_i} k_{ji} \qquad \text{with} \qquad k_{ji} = F^j_{\odot,\mathrm{int},1\mathrm{AU}} \cdot \bar{\sigma}_j \cdot \bar{\phi}_{ji}\,. \tag{7.2}$$

This is typically done since the quantities to be integrated are not mathematical functions, but are instead binned for a given wavelength resolution. The k_{ji} are summed from the first wavelength bin $j = 1$ to the bin J_i corresponding to the threshold wavelength λ_0^i of reaction path i. In Equation (7.2) $F^j_{\odot,\mathrm{int},1\mathrm{AU}}$ denotes the integrated solar photon flux at $r_h = 1$ AU in

bin j corresponding to a certain wavelength position and bin width. The photon flux can be scaled to other heliocentric distances via

$$F^{j}_{\odot,\mathrm{int},r_h} = F^{j}_{\odot,\mathrm{int},1\mathrm{AU}} \cdot r_h^{-2} \,. \tag{7.3}$$

An example of such a photon flux as presented by Huebner et al. (1992), which is also used in this work, is shown in Figure 7.1 in the wavelength range 0 Å to 8000 Å. $\bar{\sigma}_j$ and $\bar{\phi}_{ji}$ in Equation (7.2) denote the mean of the linear interpolated cross sections σ and quantum yields ϕ_i, respectively, in bin j

$$\bar{\phi}_{ji} = \sum_{l=1}^{L_j} \frac{\phi_{li}}{L_j} \qquad \text{and} \qquad \bar{\sigma}_j = \sum_{l=1}^{L_j} \frac{\sigma_l}{L_j} \,. \tag{7.4}$$

L_j is the number of ϕ_i and σ values in bin j.

7.1.2 Computation Using Electronic Oscillator Strengths f_{ul}

In this work electronic oscillator strengths given in van Hemert and van Dishoeck (2008) are also used to approximate the total rate coefficients k. An introduction to the computation of the f_{ul} and E_{ul} as done in van Hemert and van Dishoeck (2008) is provided in the Appendix C. The photodissociation rate coefficient of each absorption line λ_{ul} (u and l denote the upper and lower electronic state, respectively) is computed via

$$k^{\mathrm{line}}_{\lambda_{ul}}(r_h) = \frac{\pi e^2}{m_e c^2} \lambda_{ul}^2 f_{ul} \phi_u x_l F_\odot(\lambda_{ul}, r_h) \,, \tag{7.5}$$

which has been introduced in Section 3.2.2. $F_\odot(\lambda_{ul}, r_h)$ is approximated via

$$F_\odot(\lambda_{ul}, r_h) \approx \frac{F^{j}_{\odot,\mathrm{int},r_h}}{\Delta\lambda^{j}_{\mathrm{bin}}} \qquad \text{with} \qquad \lambda_{ul} \in [\lambda^{j}_{\mathrm{bin}}, \lambda^{j+1}_{\mathrm{bin}}) \,, \tag{7.6}$$

where $F^{j}_{\odot,\mathrm{int},r_h}$ is the integrated solar photon flux in the j-th wavelength bin $[\lambda^{j}_{\mathrm{bin}}, \lambda^{j+1}_{\mathrm{bin}})$ of width $\Delta\lambda^{j}_{\mathrm{bin}} = \lambda^{j+1}_{\mathrm{bin}} - \lambda^{j}_{\mathrm{bin}}$, in which the absorption line λ_{ul} is located. $F_\odot(\lambda_{ul}, r_h)$ is therefore the mean solar photon flux in the j-th wavelength bin.

To compute each reaction's rate coefficient k_i one requires the branching ratio $br_i(\lambda_{ul})$ and has to sum the contribution at each excitation wavelength $\lambda_{ul} \leq \lambda^i_0$, i.e. $br_i = 0$ when $\lambda_{ul} > \lambda^i_0$,

$$k_i(r_h) = \sum_{u=1}^{N_u} \frac{\pi e^2}{m_e c^2} \lambda_{ul}^2 f_{ul} \underbrace{br_i(\lambda_{ul})\phi_u}_{\phi_{i,ul}} x_l F_\odot(\lambda_{ul}, r_h) \,, \tag{7.7}$$

where N_u is the number of excited electronic states and $u = 1$ is the first excited state.

7.2 Discussion of Parameter Uncertainties

This section discusses the uncertainties of parameters which affect the photo rate coefficients k_i. Section 7.2.1 focuses on the solar photon flux $F_\odot$. Section 7.2.2 deals with the dissociation threshold wavelength λ_0, ionization and dissociative ionization and photodissociation of excited species. Further uncertainties arising in k_i have to be addressed separately, depending on the type of data used to calculate them.

For species with sufficient molecular data in the wavelength space, i.e. for which the required continuous properties $\sigma(\lambda)$, $\phi_i(\lambda)$ or $br_i(\lambda)$ can be approximated by linear interpolation, Equation (7.1) is used. The uncertainties of σ and of ϕ_i and br_i are discussed in Sections 7.2.4 and

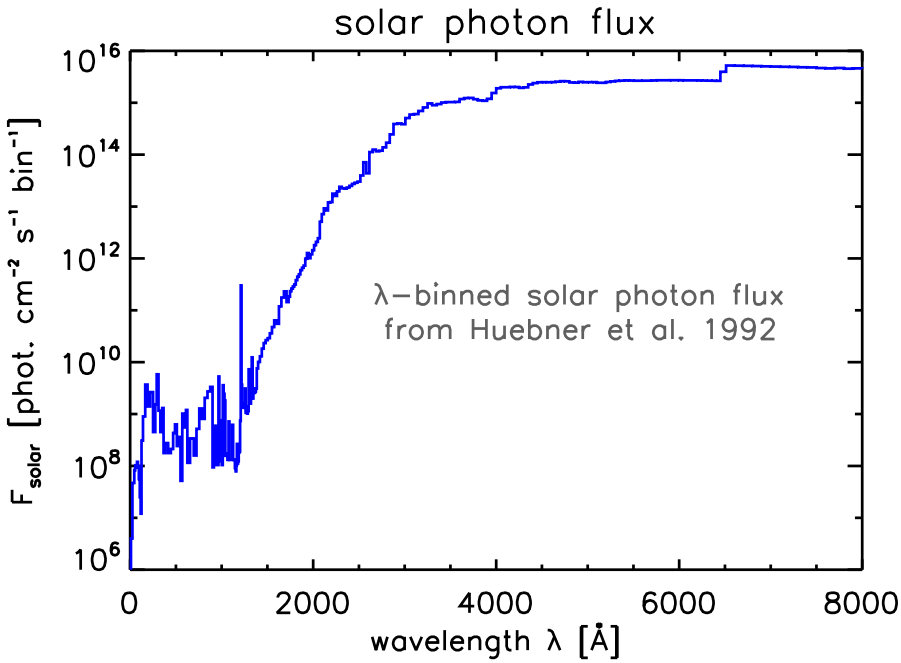

Figure 7.1: *Binned solar photon flux $F^{j}_{\odot,int,1AU}$ for the non-flaring Sun at solar minimum activity in the wavelength range 0 Å to 8000 Å. Source: Huebner et al. (1992).*

7.2.5, respectively. In this work 'molecular data' refers to absorption cross sections σ, quantum yields ϕ_i, branching ratios br_i and threshold wavelengths λ_0.

Little data exist for the σ of the species C_3H_3, C_2H_3, C_2H_5. For C_2H and C_3H_2 data exists only over a very small wavelength range and at a particular wavelength, respectively. An alternative to the limited data is the usage of theoretically determined cross sections or electronic oscillator strengths f_{ul}. For the species C_3H_2, C_3H, C_3, C_4H, C_4 and C_2H this work uses f_{ul} via Equation (7.7) to compute photodissociation rate coefficients. The uncertainties of $\phi_{i,ul} = br_i(\lambda_{ul}) \cdot \phi_u$ and f_{ul}, $E_{ul} = hc/\lambda_{ul}$ are discussed in Sections 7.2.4 and 7.2.5.

To compute the photo rate coefficient uncertainties a MC uncertainty propagation is carried out in Section 7.3.2. The corresponding uncertainty probability distributions of the parameters are defined and discussed in the following sections. Section 7.3.1 provides an overview of the uncertain parameters which are included into the MC uncertainty propagation for the photo rate coefficients.

7.2.1 Solar Photon Flux $F_\odot$

The solar photon flux $F_\odot$ used in this work for the non-flaring Sun at minimum activity as presented in Huebner et al. (1992) is shown in Figure 7.1. The flux data has been compiled and optimized from the data of different publications: 0 Å to 10 Å from Swider (1969); 10 Å to 280 Å from Hinteregger (1970); 270 Å to 1163 Å from Hall and Hinteregger (1970); 1163 Å to 7350 Å from Ackerman (1971) (with corrections from Simon (1974) between 1961 Å and 2299 Å); and from 7350 Å to 140 000 Å from Iqbal (1983). The data is binned: between $\lambda = 0$ Å to 3000 Å, where the bin widths range from 2 Å to 43 Å, between 3000 Å and 6500 Å, where the bins are 50 Å wide and then 100 Å wide between 6500 Å and 8000 Å.

The solar UV flux is subject to long-term and short-term variations, which affect the photodissociation of molecules. The 11 year solar cycle is connected with the number of sunspots and surrounding so-called plages. The plages are regions of higher radiation flux. The monthly

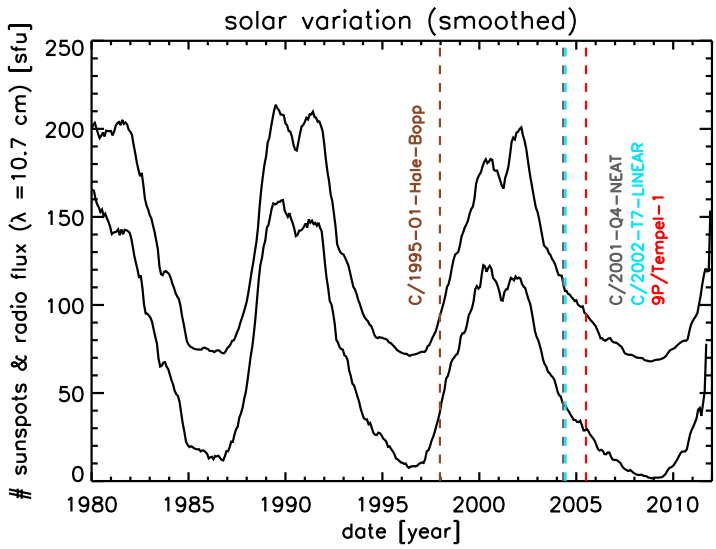

Figure 7.2: *Monthly averaged number of sunspots (lower curve) and the monthly averaged radio flux at $\lambda = 10.7$ cm (upper curve). The radio flux is used as a proxy for the UV flux where the solar flux unit is sfu $= 10^{-22}$ W m^{-2} Hz^{-1}. The sunspot and flux data have been taken from SIDC (2013) and Spaceweather (2013), respectively. The data have been smoothed in this work using a boxcar averaging method and a smoothing width of* 10 *data points (smooth.pro, NASA-IDL-Lib. (2011)). Indicated are the observation dates of the comets Hale-Bopp, LINEAR, NEAT and Tempel 1, which are investigated in this work. Adapted from Weiler (2006).*

averaged number of sunspots (lower curve) and the monthly averaged radio flux at $\lambda = 10.7$ cm (upper curve) in Figure 7.2 is used as a proxy for the UV flux. Figure 7.2 shows the 11 year solar cycle between the years 1980 and 2012 and the dates of observations of the comets Hale-Bopp, NEAT, LINEAR and Tempel 1 investigated in this work. The UV radiation variation between solar minimum and solar maximum activity can reach a factor of $2 - 3$ at Lyman-alpha **(Lα)**. It decreases to $\approx 50\%$ at $\lambda = 1700$ Å, further to < 10 % at $\lambda = 2000$ Å and to less than 1 % at $\lambda = 3000$ Å (Lean, 1987, Figure 17), (Huebner et al., 1992, Figure 3). Additionally, 27-day variations arise due to the rotation of the Sun which implies a change in the number of plages on the Sun disk as viewed from the Earth. The 27-day peak to peak solar photon flux variations are approximately < 10 % at $\lambda = 1700$ Å and much less beyond $\lambda = 2100$ Å. Similar values are obtained in Floyd et al. (2003) for the solar cycles 22 and 23 ($\approx 1986 - 2009$).

Comets investigated in this work were mostly observed close to solar minimum activity. Therefore, the use of $F_\odot$ at minimum activity, as presented in Huebner et al. (1992), is justified. Figure 7.2 suggests the resulting flux change due to not perfectly met solar minimum activity conditions for the comets investigated in this work is < 50 % for the important wavelength range $\lambda > 1700$ Å, since at such wavelengths $\Delta F_\odot / F_\odot < 50$ % between solar minimum and maximum. The 27-day variations are smaller than the 11-year-cycle variations, e.g. $\Delta F_\odot^{\text{27-days}} / F_\odot^{\text{27-days}} \leq 20$ % at $\lambda > 1500$ Å and therefore the effect on the photo rate coefficients is also approximately ≤ 20 % (Lean, 1987).

7.2.2 Threshold Wavelength, Photoionization

Threshold Wavelength

Threshold wavelengths λ_0 reported in the literature typically differ by several tens of Å. In some cases differences between literature values of up to 400 Å, e.g. for HC_3N, can be found. The

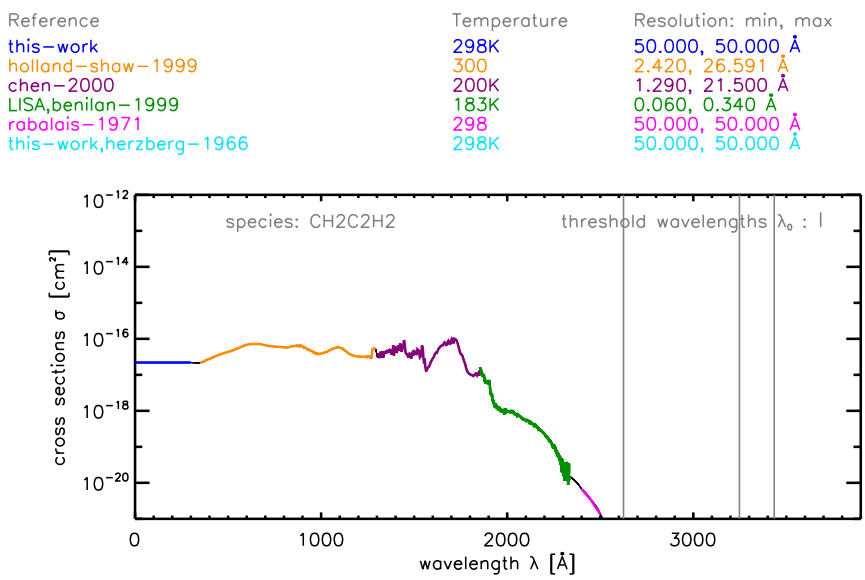

Figure 7.3: *Absorption cross sections σ of* $CH_2C_2H_2$. *Color-coded are the absorption cross sections which correspond to the references at the top left of the Figure. Additionally, each measurement's temperature and the minimum and maximum wavelength resolution are indicated. Three threshold wavelengths are indicated by gray vertical lines, which belong, from left to right, to the reactions* $CH_2C_2H_2 + \gamma \rightarrow C_2H_2 + CH_2$, $CH_2C_2H_2 + \gamma \rightarrow C_3H_3 + H$ *and* $CH_2C_2H_2 + \gamma \rightarrow C_3H_2 + H_2$.

effect of such an uncertainty on the photo rate coefficient uncertainty is now computed using the molecules HC_3N and C_4H_2 as an example. The data used for these computations can be found in the data Appendix D.

For the reaction $C_4H_2 + \gamma \rightarrow C_4H + H$ the $\lambda_0 = 2150$ Å given in Frost et al. (1996) and $\lambda_0 = 2280$ Å given in Glicker and Okabe (1987) lead to a difference in the rate coefficient k_i of ≈ 10 %. For the reaction $HC_3N + \gamma \rightarrow C_3N + H$ the lowest $\lambda_0 = 2067$ Å given in Francisco and Richardson (1994) and the highest $\lambda_0 = 2440$ Å given in Halpern et al. (1988, 1990) lead to a difference in the rate coefficients of ≈ 50 %.

Figure 7.3 shows that in the case of $CH_2C_2H_2$ the σ values fall off to virtually zero before λ_0 is reached. In this case the uncertainty in λ_0 has virtually no effect on the rate coefficient uncertainty, namely when the absorption cross sections approach zero around the threshold wavelength. This is generally the case for reactions which have quite large λ_0 e.g. for reactions involving the species $CH_2C_2H_2$, CH_3C_2H, C_2H_3, C_2H_4, C_2H_5 and C_2H_6.

Generally, the newest threshold wavelengths were used in this work. However, if several recent threshold wavelengths were reported for a reaction the largest threshold wavelength is used so as to obtain the largest possible upper limit of a rate coefficient distribution.

Photo Ionization

Contribution to the Formation of C_3 and C_2 Molecular data for ionization and dissociative ionization are available in the literature only for a subset of the species important for the formation of C_3 and C_2. These are C_3H_3, C_4H_2, C_2H_6, C_2H_5, C_2H_4, C_2H_3, C_2H_2 and C_2. For each species the rate coefficients for ionization and dissociative ionization are at least one order of magnitude smaller compared to the photodissociation rate coefficients. This is due to

the much smaller threshold wavelengths $\lambda_0 \leq 1400$ Å for ionization and dissociative ionization reactions, in comparison to photodissociation reactions having larger λ_0, e.g. $\lambda \geq 1800$ Å, where the solar photon flux is much higher than at $\lambda \leq 1400$ Å, see Figure 7.1.

For some molecules no ionization threshold and also no ionization quantum yields are available in the literature. For such molecules no ionization rate coefficients were computed. Normally, in the ionization wavelength region most photon absorption leads to ionization or dissociative ionization. For such molecules, this work makes the reasonable assumption that photon absorption in the ionization wavelength region leads to photodissociation. As stated above, this simplification affects the photodissociation rate coefficient by up to 10 %, and in most cases much less. This was assumed for the molecules C_6H_6, C_6H_5, CH_3C_2H, $CH_2C_2H_2$, HC_3N and C_3. Rate coefficients for ionization and dissociative ionization could be computed for the molecules C_4H_2, CH_3C_2H, C_2H_6, C_2H_5, C_2H_4, C_2H_3, C_2H_2, C_3H_3 and C_2. For the radicals C_4H, C_4, C_3H_2, C_3H, C_3 and C_2H, for which oscillator strengths and ionization thresholds are available from van Hemert and van Dishoeck (2008), the above simplification was not necessary. In this case only the electronic oscillator strengths at excitation wavelengths above the ionization wavelength range were used to compute photodissociation rate coefficients, see Equation (7.7).

Effect of Hydrocarbon Ions on the C_3 and C_2 Chemistry Beyond the comet's so-called diamagnetic cavity, which is located in the coma between the nucleus and a few 10^3 km away, as described in Section 3.1.2, ions are accelerated to several hundreds of km s^{-1} into the ionic tail. This is much faster than the mean neutral gas velocity of $v \approx 1$ km s^{-1}. In this regard, although ionized radicals are dissociated much faster than neutral species, ionized hydrocarbon products cannot contribute in significant amounts to the formation of C_3 or C_2 in cometary comae at $r_c \gtrapprox 10^3$ km. The value of r_c at which observations of C_3 and C_2 in cometary comae are available for comparison with model outputs as computed in this work, range between $r_c \approx 10^3$ km and $r_c \approx 3 \cdot 10^5$ km.

7.2.3 Photodissociation of Excited Species

Excited molecules, radicals and ions can be easily photodissociated by low energy photons. This is an important point regarding the increased solar photon flux at lower energies, as apparent in Figure 7.1. Excited species are formed by reactions and collisions. Since, however, absorption cross sections of excited species are mostly unknown for hydrocarbons, it is therefore difficult to quantify this effect. This work assumes that the species modeled in this work comprise ground state and excited species. In this way the computed photodissociation rate coefficients represent a lower limit for the excited species.

7.2.4 Absorption Cross Sections and Electronic Oscillator Strengths

This section discusses the temperature-dependence of absorption cross sections σ, the effect of changing the wavelength resolution, measurement uncertainties and the uncertainty effect of data gaps in absorption cross section spectra, for the species for which Equation (7.1) is used. Additionally, this section discusses and estimates the uncertainties of ab initio electronic oscillator strengths f_{ul} for the species for which Equation (7.7) has to be used.

Uncertainties due to Unknown Temperature Dependence of σ

Temperatures across the coma typically range between 200 K (close to the nucleus, outer coma) and < 30 K (inner coma $\sim 10^2$ km) for a comet around 1 AU (Combi et al., 2004). Ideally, absorption cross sections determined at such temperatures should therefore be used but these

are only available for certain species and wavelength ranges, e.g. C_4H_2, HC_3N in Bénilan et al. (1994), Fahr and Nayak (1994), Smith et al. (1998), Ferradaz et al. (2009) or C_2H_2 in Wu et al. (1989), Chen et al. (1991), Smith et al. (1991), Bénilan et al. (1995, 2000). In this work absorption cross sections determined at $T \leq 310$ K were used. Often, measurements close to ambient temperatures are the only available data. Sometimes absorption cross sections determined at much higher temperatures significantly deviate from those measured at ambient temperatures, between $T = 200$ K and $T = 310$ K. The impact upon absorption cross sections however, is usually minor.

In this work measurements at different temperatures below 310 K were used, since data is available over this range. In some cases, a higher wavelength resolution was preferred over a lower temperature to gain a better sampling in the dissociation region. In some cases, the data has been extracted from published graphics with the data extraction program *g3data*. The data is summarized in the Appendix D.

For example Bénilan et al. (2000) report a decrease of the C_2H_2 total photo rate coefficient, calculated over 1850 Å to 2200 Å, of 20 % when using absorption cross sections measured at 173 K compared to 295 K. A continuum is observed underlying the band system between 1900 Å and 2300 Å. The decrease of this continuum is concluded to be caused by fading hot bands (Bénilan et al., 2000). Hot bands are absorption features due to electronic excitation of vibrationally excited ground electronic state molecules. At higher temperatures more molecules populate higher vibrational levels of the electronic ground state, according to the Boltzmann distribution. Absorptions starting from the vibrational ground state are denoted cold bands, whose population is increased at lower temperatures. In summary, lowering (increasing) T leads to enhanced contributions of cold (hot) bands. Additionally, mainly low J value rotational levels are populated at lower temperatures leading to modified band shapes (Bénilan et al., 2000) of hot and cold bands.

Ferradaz et al. (2009) compared HC_3N and C_4H_2 absorption cross sections from $T = 203$ K to $T = 298$ K and from $T = 173$ K to $T = 296$ K, respectively, in the wavelength range 1150 Å to 2250 Å. Between 1150 Å and 1700 Å a significant temperature dependence for HC_3N was observed but only for very sharp peaks and not for predissociation broadened bands. Larger temperature effects were reported for the mid-ultraviolet **(MUV)**, above 2000 Å, where predissociation is less pronounced. This implies that predissociation may be associated with a weakening in T-dependent effects. For C_4H_2 a decrease of continuum and an increase in peaks is observed for lower T, which is due to cold bands. Additionally, in the wavelength range 1660 Å to 1840 Å, a decrease of band continuum and band maxima with temperature decreasing is observed. This arises due to the overlap of cold and hot bands. In this case the hot band contribution decreases more than the cold band contribution increases with decreasing temperature.

The above examples show that understanding temperature effects requires good knowledge of the nature of absorption and photodissociation for each molecule, which is beyond the scope of this thesis. It is not possible to estimate the temperature effect on σ. The only relevant example is C_2H_2. Bénilan et al. (2000) compared the C_2H_2 rate coefficients k computed by using the absorption cross section at $T = 200$ K and $T = 100$ K. The change in k was only 20 %.

Uncertainties due to a Low Wavelength Resolution of σ

Bénilan et al. (2000) calculated the uncertainty of the C_2H_2 photo rate coefficient introduced by low spectral resolution between 1850 Å and 2350 Å. In this wavelength range a continuum is superimposed with relatively small undulations, see Figure 7.6. A change from 0.2 Å to 20 Å wide bins resulted in a 1 % difference in the photo rate coefficient. The wavelength range between 1850 Å and 2350 Å contributes the most to the C_2H_2 photo rate coefficient, which is

due to the increased solar photon flux above 1850 Å, see Figure 7.1.

Measurement Uncertainties of σ

Measurement uncertainties of absorption cross sections are typically ≈ 20 % or less. The uncertainty effect on k_i is therefore at most 20 %. See Appendix D for references of absorption cross section measurements.

Uncertainties due to Data Gaps in Absorption Cross Sections σ

Introduction Clearly, for species, for which absorption cross sections are unknown over small or large wavelength ranges photo rate coefficient uncertainties can be large, even orders of magnitudes, as absorption cross sections may change by orders of magnitudes with wavelength. Such data gaps are exhibited by C_2H_3 as shown in Figure 7.5a. For example for $CH_2C_2H_2$ and C_2H_2 (Figures 7.3, 7.6) the data is however complete.

Motivation of Parameters to Estimate the Uncertainty For the absorption cross sections of C_2H_2, shown in Figure 7.6, a steady increase to smaller wavelengths up to the first ionization threshold $\lambda_0 = 1086$ Å is apparent. This effect is also seen in the spectrum of $CH_2C_2H_2$ in Figure 7.3. For C_2H_3 in Figure 7.5a this effect is still noticeable despite the data gaps between $1500 - 2250$ Å and $2380 - 3855$ Å. For C_2H_2 σ is constant between the first ionization threshold $\lambda_0 = 1086$ Å and the second ionization threshold $\lambda_0 = 697$ Å. Beyond $\lambda_0 = 697$ Å σ decreases.

The increase of σ in the dissociation wavelength region is due to the higher density of electronic states at higher excitation energies, i.e. the number of electronic states per energy interval. This is a generally observed feature of molecules (Schinke, 2002). For C_2H_2 the strongest increase of two orders of magnitudes is apparent between 1510 Å to 1550 Å. Additionally, there are similar but less strong increases at other wavelengths. An example of even higher changes in absorption cross sections than for C_2H_2 is H_2CO between 1800 Å to 2400 Å with a change of about 4 magnitudes, see e.g. (Huebner et al., 2011). Species investigated in this work having data gaps are e.g. C_3N, C_3H_3, C_2H_5 and C_2H_3. For the species C_3H_2, C_3H, C_4H, C_4 and C_3 no absorption cross sections are available, but absorption oscillator strengths. These species are regarded in Section 7.2.4 in more detail.

Monte-Carlo Method To propagate the uncertainty of data gaps in absorption cross section spectra $\sigma(\lambda)$ to the uncertainty of photo rate coefficients k_i an MC method is used in this work, see Section 7.3.2. For this purpose a distribution of absorption cross section spectra is computed for all species having data gaps. The following 4 steps are used to construct the distribution, as exemplified in Figure 7.4:

I) Identify which wavelength ranges have gaps $\lambda > 200$ Å. For each gap $\Delta\lambda = \lambda_r - \lambda_l$ at the position $\{p_l, p_r\} = \{(\lambda_l, \sigma_l), (\lambda_r, \sigma_r)\}$, carry out the following steps:

   II) Define left and right additional wavelength points: $\lambda'_l = \lambda_l + 100$ Å, $\lambda'_r = \lambda_r - 100$ Å.

   III) Repeat the following $10,000$ times: generate a random value α from a uniform distribution $U([0,1])$. Generate at λ'_l and λ'_r log10-uniformly distributed values σ'_l and σ'_r for absorption cross sections in the range $[\sigma_l/10^2, \sigma_l \cdot 10^2]$ and $[\sigma_r/10^2, \sigma_r \cdot 10^2]$,

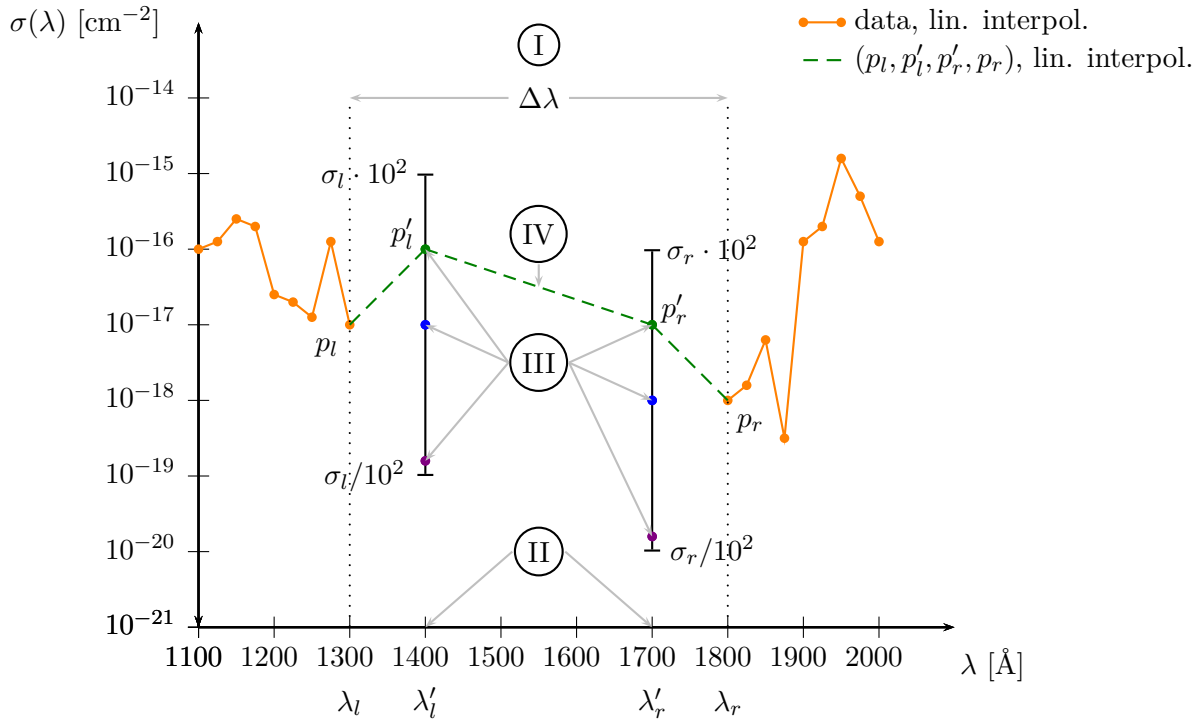

Figure 7.4: *MC method applied for a data gap in absorption cross sections σ. The data gap $\Delta\lambda = \lambda_r - \lambda_l$ is between the points $p_l = (\lambda_l, \sigma_l) = (1300\ \mathring{A}, 10^{-17}\ cm^{-2})$ and $p_r = (\lambda_r, \sigma_r) = (1800\ \mathring{A}, 10^{-18}\ cm^{-2})$.*

respectively:

$$
\begin{aligned}
&\alpha \in U([0,1])\,,\\
&z_l = \mathrm{alog}_{10}\left(\sigma_l/10^2\right) + \left(\mathrm{alog}_{10}\left(\sigma_l \cdot 10^2\right) - \mathrm{alog}_{10}\left(\sigma_l/10^2\right)\right) \cdot \alpha\,,\\
&z_r = \mathrm{alog}_{10}\left(\sigma_r/10^2\right) + \left(\mathrm{alog}_{10}\left(\sigma_r \cdot 10^2\right) - \mathrm{alog}_{10}\left(\sigma_r/10^2\right)\right) \cdot \alpha\,,\\
&\sigma_l' = 10^{z_l}\,, \qquad \sigma_r' = 10^{z_r}\,,\\
&p_l' = (\lambda_l', \sigma_l')\,, \qquad p_r' = (\lambda_r', \sigma_r')\,.
\end{aligned}
\tag{7.8}
$$

Interpolate linearly across p_l, p_l', p_r' and p_r.

IV) Define a distribution of the complete $\sigma(\lambda)$ spectrum, whose $i-th$ spectrum is constructed by combining each gap's $i-th$ interpolated spectrum and the data points. Save all $i = 1, \ldots, 10,000$ spectra.

The left gap of C_2H_3 (Figure 7.5) lies between $p_l = (1683\ \text{Å}, 3.3 \cdot 10^{-17}\ \text{cm}^2)$ and $p_r = (2250\ \text{Å}, 9.6 \cdot 10^{-18}\ \text{cm}^2)$. At $\lambda_l' = 1600$ Å and $\lambda_r' = 2150$ Å the σ_l' and σ_r' are distributed log10-uniformly between $[3.3 \cdot 10^{-19}\ \text{cm}^2, 3.3 \cdot 10^{-15}\ \text{cm}^2]$ and $[9.6 \cdot 10^{-20}\ \text{cm}^2, 9.6 \cdot 10^{-16}\ \text{cm}^2)]$, respectively. Note that the method applied here is defined such as to ensure that the slope between σ_l' and σ_r' is always the same, since the increase or decrease of absorption cross section is usually over a broad wavelength region, see also Figure 7.5b.

For the molecules used in this work data gaps are either smaller than 100 Å or larger than 200 Å. Therefore, assuming a fixed $\Delta\lambda = 200$ Å in this analysis does not lead to a selection effect.

Table 7.1: C_2H *electronic absorption oscillator strengths* f_{ul} *for allowed transitions taken from van Hemert and van Dishoeck (2008). The uncertainty factor of the* f_{ul} *is* $F = 1.3$ *for the first four low-energy electronic states of a symmetry, e.g. the states* $1^2\Pi$, $2^2\Pi$, $3^2\Pi$ *and* $4^2\Pi$. *For these states an uncertainty of the excitation energy* E_{ul} *of* $\Delta E_{ul} = 0.1$ *eV is applied. For the high-energy states* $F = 2$ *and* $\Delta E_{ul} = 0.3$ *eV. The ionization energy for* C_2H *is* $E^{ion} = 11.4$ *eV and the smallest dissociation energy is* $E^{diss} = 4.86$ *eV, therefore state* $1^2\Pi$ *is not included to compute* k_i.

state	E_{ul} [eV]	f_{ul}	$F(f_{ul})$	ΔE_{ul} [eV]
$1^2\Sigma^+$	0.00			
$2^2\Sigma^+$	7.06	$4.0 \cdot 10^{-4}$	1.3	0.1 eV
$3^2\Sigma^+$	8.63	$4.0 \cdot 10^{-5}$	1.3	0.1 eV
$4^2\Sigma^+$	9.28	$3.0 \cdot 10^{-3}$	1.3	0.1 eV
$5^2\Sigma^+$	10.09	$2.8 \cdot 10^{-1}$	2	0.3 eV
$6^2\Sigma^+$	10.28	$1.0 \cdot 10^{-5}$	2	0.3 eV
$1^2\Pi$	0.68	$1.7 \cdot 10^{-3}$	1.3	0.1 eV
$2^2\Pi$	7.63	$1.0 \cdot 10^{-2}$	1.3	0.1 eV
$3^2\Pi$	8.39	$1.0 \cdot 10^{-1}$	1.3	0.1 eV
$4^2\Pi$	9.00	$3.0 \cdot 10^{-2}$	1.3	0.1 eV
$5^2\Pi$	9.47	$3.0 \cdot 10^{-2}$	2	0.3 eV
$6^2\Pi$	9.96	$2.2 \cdot 10^{-2}$	2	0.3 eV
$7^2\Pi$	10.06	$1.1 \cdot 10^{-2}$	2	0.3 eV
$8^2\Pi$	10.33	$4.6 \cdot 10^{-2}$	2	0.3 eV

Electronic Oscillator Strengths f_{ul} and Excitation Energies E_{ul}

van Hemert and van Dishoeck (2008) computed ab initio f_{ul} and vertical excitation energies E_{ul} of electronic states for the species H_2C_3 (l−C_3H_2), (^{3}B)HC_3H, c−C_3H_2, l−C_3H, c−C_3H, l−C_3, l−C_4H, l−C_4 and C_2H. The symbol "c−" is used for species to indicate a cyclic (c) and not a linear (l) structure. (^{3}B)HC_3H is also linear but in contrast to l−C_3H_2 it has one H at each end and it is in a triplet electronic state. For the singlet electronic state species (^{1}A′)HC_3H Mebel et al. (1998) provide f_{ul} and E_{ul}. The present work investigates the C_3 and C_2 formation in comets by modeling C_3H_2, C_3H, C_3 using the species H_2C_3 (l−C_3H_2), l−C_3H and l−C_3, which is further motivated in the data Appendix D.

For the above mentioned species for which photodissociation rate coefficients are computed via Equation (7.7) the uncertainties of the electronic oscillator strengths f_{ul} and the corresponding excitation energies E_{ul} have to be regarded. Figure 7.7 shows the f_{ul} and the vertical excitation wavelengths $\lambda_{ul} = hc/E_{ul}$ for different molecules as computed in van Hemert and van Dishoeck (2008). These authors report estimated uncertainties of f_{ul} of about 30 % (factor $F = 1.3$), or even better, and $\Delta E_{ul} = 0.1$ eV for E_{ul}, for the first four low-energy electronic states of a molecular symmetry. For the electronic states of higher energy they claim that at least the magnitude of the f_{ul} is secure. However, van Dishoeck and van Hemert (2012, pers. comm.) note that the uncertainty factor $F = 2$ is reasonable. For these states they estimate the uncertainty of E_{ul} to be $\Delta E_{ul} = 0.3$ eV. Table 7.1 gives an example of the uncertainties for C_2H, where the lower energy electronic states are $2^2\Sigma^+$, $3^2\Sigma^+$, $4^2\Sigma^+$ and $1^2\Pi$, $2^2\Pi$, $3^2\Pi$, $4^2\Pi$, of the symmetries $^2\Sigma^+$ and $^2\Pi$, respectively. In this work a uniform distribution is defined for each f_{ul} and ΔE_{ul} over $[f_{ul}/F, f_{ul} \cdot F]$ and $[E_{ul} - \Delta E_{ul}, E_{ul} + \Delta E_{ul}]$, respectively, with ΔE_{ul} and F as described above. These uncertainties lead to rate coefficient uncertainties of a factor of $\approx 1.3-2.7$.

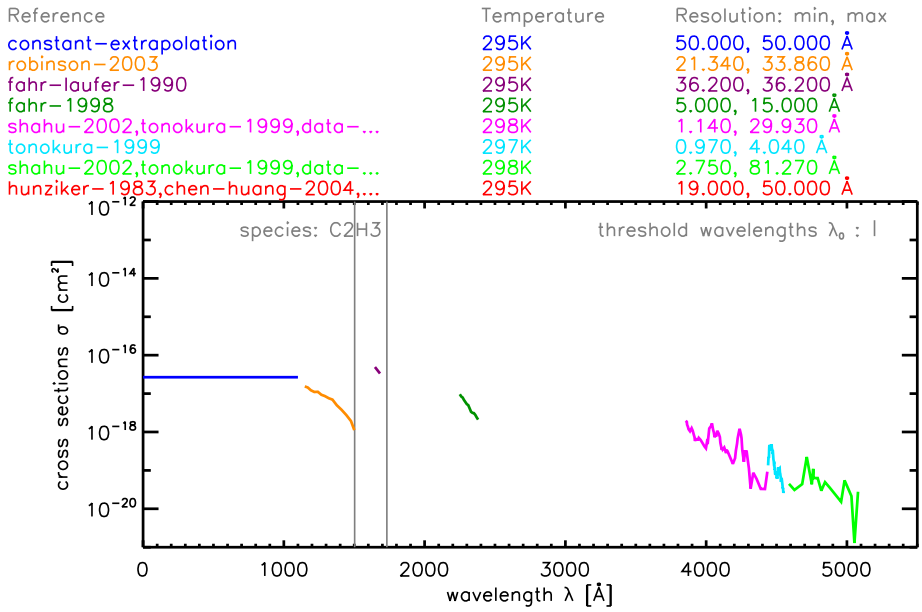

(a) *Absorption cross sections σ of C_2H_3 with large data gaps.*

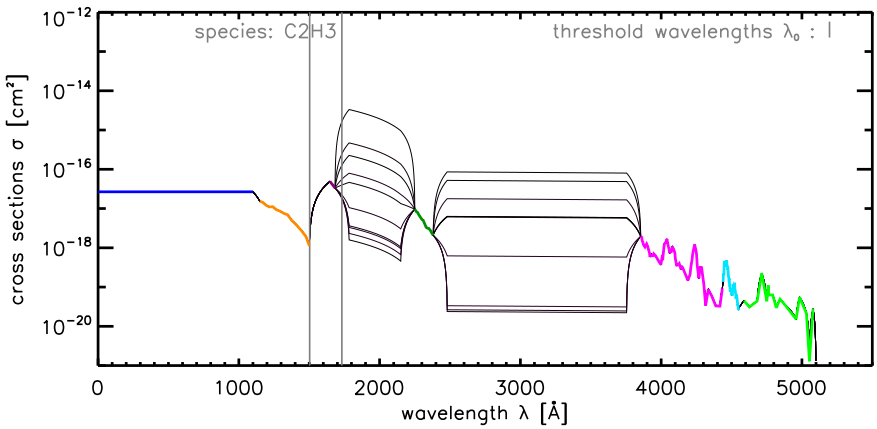

(b) *Filling the σ data gaps with distributions of spectra. Shown are ten samples.*

Figure 7.5: *Illustration of the uncertainty estimation method of data gaps, using C_2H_3 as an example: (a) the spectrum shows two gaps (at $\lambda > \lambda_0^{ion}$) in which σ is undetermined in a range greater than 200 Å. In the ionization region a constant σ value is assumed between 0 Å and 1100 Å in this work. Panel (b) shows ten sample spectra, which are generated by interpolation along the data and respective interpolation points in each data gap. In each of the two gaps the pair of random interpolation points is 100 Å distant to the edge of each gap. Color coded are the measured absorption cross sections from different data sources, the measurement temperature and the minimum and maximum wavelength resolution of the measurements. The threshold wavelengths λ_0 of the photo reactions of C_2H_3 are plotted as grey vertical lines - the corresponding reactions can be found in the data Appendix D.*

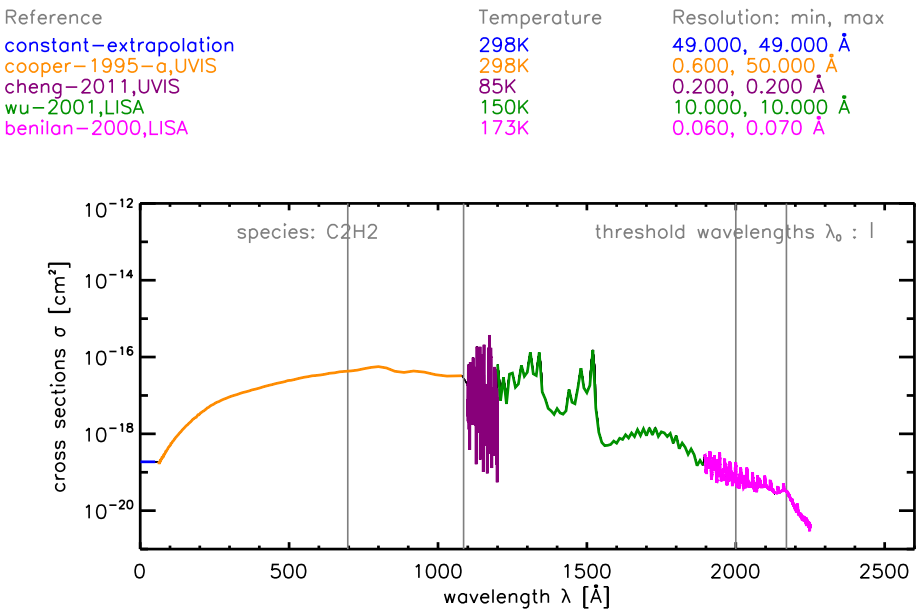

Figure 7.6: *Example of a complete absorption cross sections σ spectrum of* C_2H_2*. Color coded shown are measured absorption cross sections from different data sources, the measurement temperature and the minimum and maximum wavelength resolution of the measurements. The threshold wavelengths λ_0 of the photo reactions of* C_2H_3 *and* C_2H_2 *are plotted as grey vertical lines - the corresponding reactions can be found in the data Appendix D.*

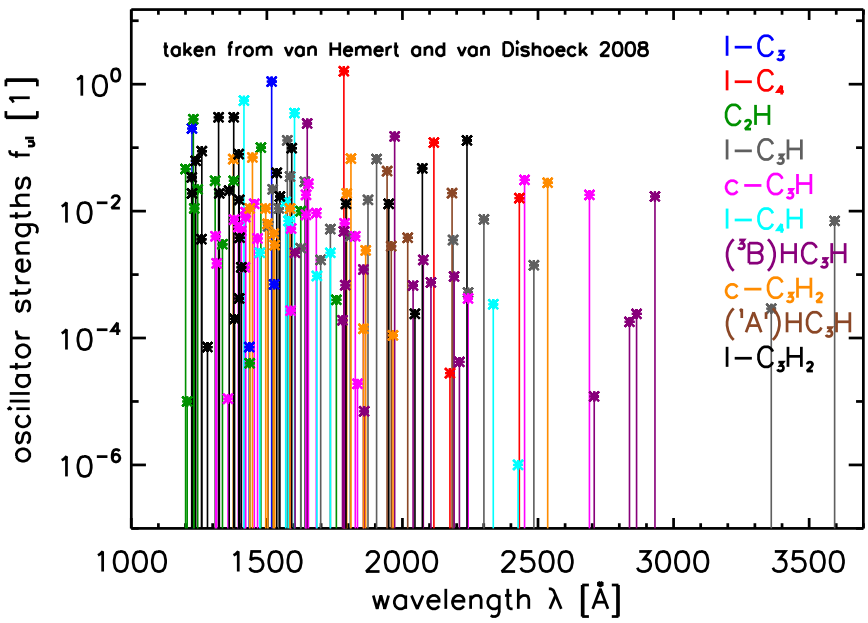

Figure 7.7: *Electronic absorption oscillator strengths f_{ul} of van Hemert and van Dishoeck (2008) of the species* l−C_3, l−C_4, C_2H, l−C_3H, c−C_3H, l−C_4H, (^{3}B)HC_3H, c−C_3H_2, (^{1}A′)HC_3H *and* l−C_3H_2*, used in Equation (7.7). The values for* (^{1}A′)HC_3H *are only available from Mebel et al. (1998). Shown are only those lines which contribute to photodissociation.*

7.2.5 Quantum Yields and Branching Ratios

This section discusses the uncertainty effect of data gaps in quantum yield spectra $\phi_i(\lambda)$ and of using branching ratios br_i in the absence of quantum yields on rate coefficient uncertainties for the species for which Equation (7.1) is used. The measurement uncertainty of these properties is also discussed. Additionally, this section estimates the uncertainty of missing quantum yields $\phi_{i,ul}$ for the species for which Equation (7.7) has to be used, i.e. the oscillator strengths approach.

Measurement Uncertainties of ϕ_i and br_i

Usually the effect of measurement uncertainties of ϕ_i and br_i onto the uncertainty of k_i are $\lessapprox 50$ %. The exceptions are upper limits or estimated values that are small, i.e. in the order of some 0.01 depending on the measurement and estimation method. Usually these uncertainties are in the order of the reported value. For example Glicker and Okabe (1987) report for C_4H_2 $\Delta\phi_i \lessapprox 50$ %. For the upper limit of $\phi_i = 0.06$ at $\lambda = 2280$ Å the uncertainty is reported to be ≈ 0.06. Another example is the photodissociation of CH_3C_2H for which DeSain and Taatjes (2003) report $\phi_i = 0.5 \pm 0.1$ and $\phi_i \approx 0.1$. Generally, the uncertainties of ab initio ϕ_i or br_i are not reported, see e.g. Silva et al. (2008) who computed br_i for the C_4H_2 photodissociation.

Uncertainties due to Data Gaps in $\phi(\lambda)$ Spectra and the Use of br_i

Introduction After absorption of a photon at wavelength λ several fragmentation pathways might be accessible for the excited molecule. Therefore, the quantum yield $\phi_i(\lambda)$, introduced in Section 3.2.2 in Equation (3.27) as the product of total quantum yield ϕ and branching ratio br_i, is required. Most often only branching ratios are reported in the literature, as these are in general easier to determine than quantum yields, which leaves the total quantum yield ϕ, defined as $\phi_i(\lambda) = \phi(\lambda) \cdot br_i(\lambda)$, undetermined. Crovisier (1994) has pointed out the problem of overestimated photo dissociation rate coefficients, e.g. Huebner et al. (1992) has assumed $\phi = 1$ for several reactions where only branching ratios were available. An example is given for the molecule C_4H_2 for which several branching ratios br_i are reported in the literature at the wavelengths $\lambda = 1216$, 1570, 1933, 2120 Å, which are shown in the Figure 7.10a as rectangles. In this Figure $\phi = 1$ was assumed for the br_i. Usage of branching ratios and assuming a ϕ at a particular wavelength introduces a large uncertainty at this wavelength of at least an order of magnitude.

Another shortcoming is the rather incomplete coverage of quantum yields or branching ratios determined by measurements or ab initio calculations. Often these quantities are only known at characteristic laser wavelengths, e.g. at 1570 Å (fluorine), 1933 Å (argon-fluoride) and 2480 Å (neon-copper) lasers. Quantities determined by ab initio calculations are reported also at other wavelengths. An example is shown in Figure 7.10a for C_4H_2. For C_4H_2 five data gaps can be seen, of which two in the range $\approx [1200\ \text{Å}, 1500\ \text{Å}]$ and $\approx [1600\ \text{Å}, 1850\ \text{Å}]$ are very large. A low wavelength coverage of quantum yield data leads on the one hand to orders of magnitude uncertainties in ϕ over a large wavelength range, therefore also in the total photo rate coefficient k and on the other hand to uncertainties in the full branching ratios bf_i, as the branching ratios br_i are not known over a large wavelength range.

Motivation of Parameters to Estimate the Uncertainty This section motivates the parameters chosen when 'filling the data gaps' as discussed in the next paragraph. The total dissociation quantum yield $\phi(\lambda) = \sum_{i=1}^{n} \phi_i$ of a molecule and the dissociation quantum yield $\phi_i(\lambda)$ of each reaction path of a molecule can vary considerably with wavelength λ. There are several ways in which the molecule could fragment. Some examples of quantum yield data are shown in the Figures 7.9a and 7.9b for H_2CO and O_3, respectively, for which data has been

measured relatively continuously over an extensive wavelength range. This is in contrast to the hydrocarbons used in this work, which is partially why we use the species O_3 and H_2CO to derive the estimation parameters.

An example of a varying ϕ_i with λ is shown in Figure 7.9b for H_2CO, where relatively high quantum yields, close to 0.9, have been measured between 2500 Å and 3500 Å. It is known that both dissociation products are produced by unimolecular dissociation, i.e. by internal conversion **(IC)**, see Section 3.2.2, from the higher electronic state S_1 into the vibrational continuum of the ground-state S_0. $H + HCO$ is also produced by intersystem crossing **(ISC)**, see Section 3.2.2, from S_1 into the vibrational continuum of the triplet electronic state T_1, see e.g. Hopkins et al. (2007).

The strong increase and the constancy of the high $\phi_i \approx 0.9$ of reaction $O_3 + \gamma \rightarrow O_2(a^1\Delta_g) + O(^1D)$ shortward of 3000 Å, shown in Figure 7.9a, is due to the Hartley absorption band, shown in e.g. Bogumil et al. (2003), which is due to a repulsive electronic state, since absorptions into repulsive electronic states directly lead to dissociation, i.e. $\phi = 1$. Due to the other dominant reaction $O_3 + \gamma \rightarrow O_2(X^3\Sigma_g^-) + O(^3P)$ shortward of 3000 Å, not shown in Figure 7.9a, with $\phi_i = 0.1$, reaction $O_3 + \gamma \rightarrow O_2(a^1\Delta_g) + O(^1D)$ contributes 90 % of the total dissociation quantum yield ϕ at wavelengths of the Hartley absorption band, i.e. for the latter reaction the branching ratio is $br_i \approx 0.9$. There are also other energetically allowed reactions at $\lambda < 3000$ Å, but these contribute only very small amounts to the dissociation of O_3 (Matsumi et al., 2002). Beyond $\lambda = 3100$ Å $\phi_i = 0.1$ for $O(^1D)$ formation due to the spin-forbidden reaction $O_3 + \gamma \rightarrow O_2(X^3\Sigma_g^-) + O(^1D)$.

In both examples (H_2CO, O_3) strong changes of ϕ_i can appear within 100 Å. The O_3 case suggests that constant and close to one ϕ_i are also likely over relatively large wavelength ranges as well as a nonzero ϕ due to forbidden transitions. The ϕ_i in the case of H_2CO also do not decrease to zero over a relatively long wavelength range. Generally, however, one may assume that quantum yield spectra are more variable, like H_2CO. There are also examples of quantum yield variations within some Å, e.g. ϕ_i for $O(^1D)$ formation from O_2 changes from 1.0 to 0.5 between 1212 Å and 1216 Å (Lacoursière et al., 1999) and from 0 to 0.6 between 1243.5 Å and 1244 Å (Lambert et al., 2004).

On the basis of these examples it was assumed that $\phi \in [0.1, 1]$ for the uncertainty estimation. However, for the branching ratios it was decided to use as the lower limit $br_i = 0$. The upper limit of $br_i = 1.0$ was assumed and motivated by the observations of the br_i of H_2CO and O_3, which can get close to one. This means the other reactions do not contribute. The lower limit of $br_i = 0$ ensures that $br_i \approx 1$ is possible, while the other reactions have a very small br_i, since $\sum_{i=1}^{n} br_i = 1$. Additionally, it is required that $\phi_i(\lambda) = 0$ for all reactions i, for which $\lambda > \lambda_0^i$. This work assumes $\phi_i(\lambda_0^i) = 0$.

Monte-Carlo Method To propagate the uncertainty of data gaps in quantum yield spectra $\phi_i(\lambda)$ to the uncertainty of photo rate coefficients k_i an MC method is used in this work, see Section 7.3.2. For this purpose a distribution of quantum yield spectra is computed for all species having data gaps in their quantum yield spectrum. The following 5 steps are used to construct the distribution as exemplified in Figure 7.8 for C_4H_2.

I) Collect all wavelength positions at which ϕ_i, br_i data and threshold wavelengths λ_0 are located. Identify which wavelength ranges have data gaps $\Delta\lambda = \lambda_b - \lambda_a > 200$ Å.

II) For each gap define $n = \text{Floor}(\Delta\lambda/200 \text{ Å} + 0.5)$ additional wavelength points: $\lambda_j = \lambda_a + j \cdot 100$ Å for $j = 1, \ldots, n-1$ and $\lambda_n = \lambda_b - 100$ Å. If $n = 1$ then $\lambda_n = \lambda_b - 100$ Å. This is performed such as to have approximately every 100 Å an interpolation point for quantum yields similar to H_2CO shown in Figure 7.9b. The λ_j, λ_0 and the wavelength at which br_i are known are denoted $I_1, \ldots, I_m$ in the following.

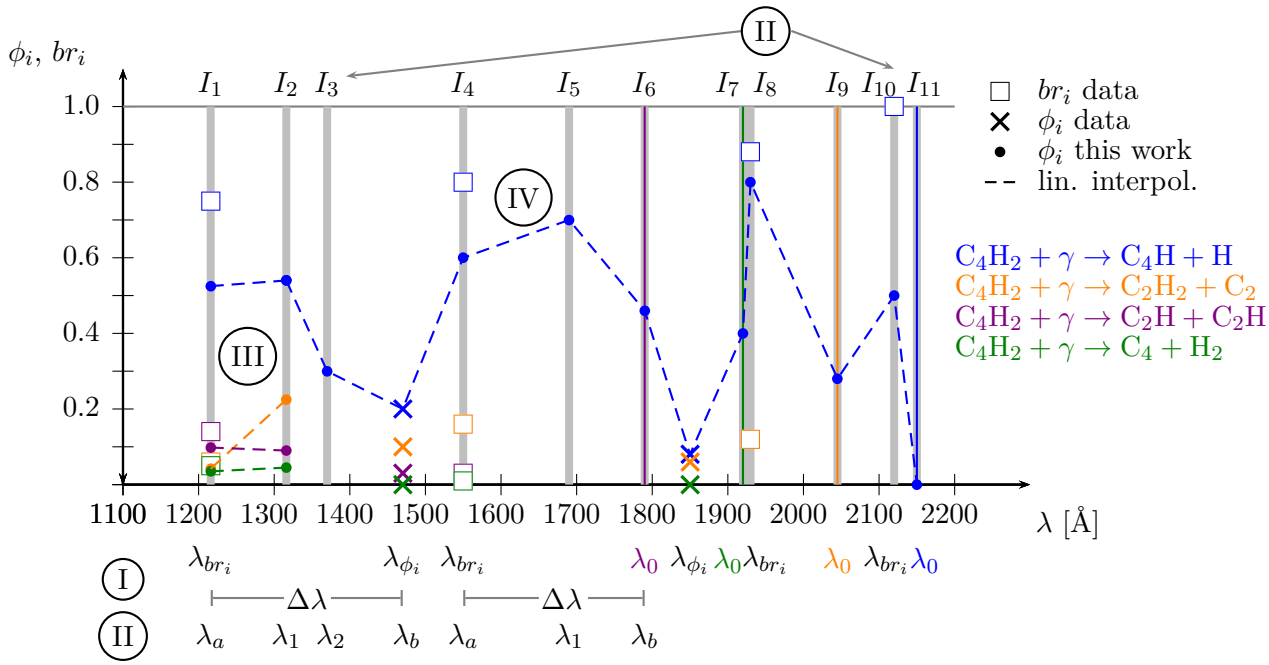

Figure 7.8: *Example for constructing a distribution of ϕ_i spectra for each of the 4 photodissociation reactions of C_4H_2, when there are gaps $\Delta\lambda > 200$ Å. Two data gaps exist having a width of $\Delta\lambda = 1470 - 1216 = 254$ Å and $\Delta\lambda = 1790 - 1570 = 220$ Å.*

III) Repeat the following steps 10,000 times at all I_j:

- Generate a $\phi \in U(0.1, 1)$. Compute for each reaction $\phi_i = \phi \cdot br_i$. Here the br_i are either data or, if unknown, are generated as random numbers via $(br_1, \ldots, br_q) \in \text{Diut}([0, 1], q)$ for the q reactions for which $I_j < \lambda_0$. For all other reactions $br_i = 0$. The 'uniform truncated Dirichlet distribution' **(Diut)** ensures $br_1 + \ldots + br_q = 1$.

IV) One defines a distribution of $p = 1, \ldots, 10,000$ $\phi_i(\lambda)$ spectra for reaction i by interpolation across its data and its additional (I_j, ϕ_i) points generated in step p.

Figure 7.10a shows the linear interpolation across the data for the 4 photodissociation reactions of C_4H_2, thereby assuming $\phi = 1$ to compute $\phi_i = br_i \cdot \phi$ from the br_i data. Figure 7.10b shows the applied uncertainty estimation method including 10 generated $\phi_i(\lambda)$ spectra for each reaction by interpolation across the points (I_j, ϕ_i) and the (λ, ϕ_i) data. Table 7.2 summarizes each reaction's ϕ_i, br_i and λ_0 data and the applied distributions at the 11 interpolation points I_j. 4 are at the threshold wavelengths and 4 at wavelengths where br_i data exists. $n = \text{Floor}(\Delta\lambda/200 \text{ Å} + 0.5) = 2$ I_j are set in the data gap between $\lambda = 1216$ Å and $\lambda = 1470$ Å, where $\Delta\lambda = 254$ Å, and $n = \text{Floor}(\Delta\lambda/200 \text{ Å} + 0.5) = 1$ I_j between $\lambda = 1570$ Å and $\lambda_0 = 1790$ Å, where $\Delta\lambda = 220$ Å. In Figure 7.10b one recognizes the independency of the quantum yield distributions at each interpolation point I_j, which is meant to resemble more closely to the spectrum of H_2CO in Figure 7.9b. If the interpolation points are set at every 10 Å, instead of at every 100 Å in a data gap as done in this work, the k_i uncertainties are changed by at most 20 %.

Quantum Yields $\phi_{i,ul}$ When Using the Electronic Oscillator Strengths f_{ul}

For the species for which photodissociation rate coefficients are computed via Equation (7.7) no quantum yields $\phi_{i,ul} = \phi_u(\lambda_{ul}) \cdot br_i(\lambda_{ul})$ are available. This work uses at each excitation

Table 7.2: *Example for constructing distributions of ϕ_i spectra for each reaction of C_4H_2, required for the MC method applied in Section 7.3.2. The two left columns indicate the interpolation points $I_1, \ldots, I_{11}$ (gray shaded) and the available data, i.e. ϕ_i, br_i and λ_0, respectively. The column 'values' presents the data, or in the case of missing data the values generated from the distributions indicated in the last column. The reactions $R1, \ldots, R4$ are shown in the table notes.*

C_4H_2							
I	data	λ [Å]	values				applied distributions
			R1[a]	R2[b]	R3[c]	R4[d]	
I_1	br_i	1216	$\phi \cdot 0.75$	$\phi \cdot 0.06$	$\phi \cdot 0.14$	$\phi \cdot 0.05$	$\phi \in U([0.1, 1])$
I_2		1316	$\phi \cdot br_1$	$\phi \cdot br_2$	$\phi \cdot br_3$	$\phi \cdot br_4$	$\phi \in U([0.1, 1])$, $(br_1, \ldots, br_4) \in \mathrm{Diut}([0, 1], 4)$
I_3		1370	$\phi \cdot br_1$	$\phi \cdot br_2$	$\phi \cdot br_3$	$\phi \cdot br_4$	$\phi \in U([0.1, 1])$, $(br_1, \ldots, br_4) \in \mathrm{Diut}([0, 1], 4)$
	ϕ_i	1470	0.20	0.10	0.03	0.00	
I_4	br_i	1570	$\phi \cdot 0.80$	$\phi \cdot 0.16$	$\phi \cdot 0.03$	$\phi \cdot 0.01$	$\phi \in U([0.1, 1])$
I_5		1690	$\phi \cdot br_1$	$\phi \cdot br_2$	$\phi \cdot br_3$	$\phi \cdot br_4$	$\phi \in U([0.1, 1])$, $(br_1, \ldots, br_4) \in \mathrm{Diut}([0, 1], 4)$
I_6	λ_0^4	1790	$\phi \cdot br_1$	$\phi \cdot br_2$	$\phi \cdot br_3$	0	$\phi \in U([0.1, 1])$, $(br_1, br_2, br_3) \in \mathrm{Diut}([0, 1], 3)$
	ϕ_i	1849	0.08	0.06	0.00	0.00	
I_7	λ_0^3	1921	$\phi \cdot br_1$	$\phi \cdot br_2$	0	0	$\phi \in U([0.1, 1])$, $(br_1, br_2) \in \mathrm{Diut}([0, 1], 2)$
I_8	br_i	1933	0.88	0.12	0.00	0.00	$\phi \in U([0.1, 1])$
I_9	λ_0^2	2045	$\phi \cdot br_1$	0	0	0	$\phi \in U([0.1, 1])$, $br_1 = 1$
I_{10}	br_i	2120	1.00	0.00	0.00	0.00	$\phi \in U([0.1, 1])$
I_{11}	λ_0^1	2150	0	0	0	0	$\phi = 0$, $br_1 = 0$

[a] R4: $C_4H_2 + \gamma \rightarrow C_2H + C_2H$, $\lambda_0 = 1790$ Å
[b] R3: $C_4H_2 + \gamma \rightarrow C_4 + H_2$, $\lambda_0 = 1921$ Å
[c] R2: $C_4H_2 + \gamma \rightarrow C_2H_2 + C_2$, $\lambda_0 = 2045$ Å
[d] R1: $C_4H_2 + \gamma \rightarrow C_4H + H$, $\lambda_0 = 2150$ Å

wavelength λ_{ul}, as in the case when using Equation (7.2), uniform distributions over the interval $[0.1, 1.0]$ for the total quantum yields ϕ_u (for each upper state u which can contribute to dissociation) and a Dirichlet distribution for the branching ratios $br_i(\lambda_{ul})$, i.e. $(br_1, \ldots, br_q) \in \mathrm{Diut}([0, 1], q)$ for the q reactions for which $\lambda_{ul} < \lambda_0^i$. For the reactions with $\lambda_{ul} > \lambda_0^i$ one has to set $br_i = 0$. The distribution of $\phi_{i,ul}$ is computed via $\phi_{i,ul} = \phi_u \cdot br_i$ for each element of the respective distributions.

It is argued by van Hemert and van Dishoeck (2008) that due to the high density of electronic states in large molecules, internal conversion to a lower dissociative electronic state is typically much faster than the radiative de-excitation processes (Herzberg, 1966). This was used as an argument by van Hemert and van Dishoeck (2008) that the total quantum yield ϕ_u in Equation (7.7) of the upper electronic state is likely to be close to one. However, in this work small total quantum yields are used as the lower limit, i.e. $\phi \in [0.1, 1]$, since ϕ_u is unknown and might be however, very different for each species and also at each individual excitation wavelength λ_{ul}.

The work of Chabot et al. (2010) presents full (integral over λ) branching ratios bf_i for the species C_3H_2, C_3H, C_4H, C_4 and C_2H with which the rate coefficients k_i may be computed as $k_i = k \cdot bf_i$ with k the total photodissociation rate coefficient (integral over λ). However, in their experiments their derived internal energy distribution of the molecules differs strongly from what is expected from species excited by the solar photon flux. This flux features a strong increase, starting at 1500 Å and reaching a plateau at around 3000 Å, see Figure 7.1. The maximum of their internal energy distribution is, however, at $1127 - 954$ Å $(11 - 13$ eV). Their full branching ratios bf_i are therefore not used in this work.

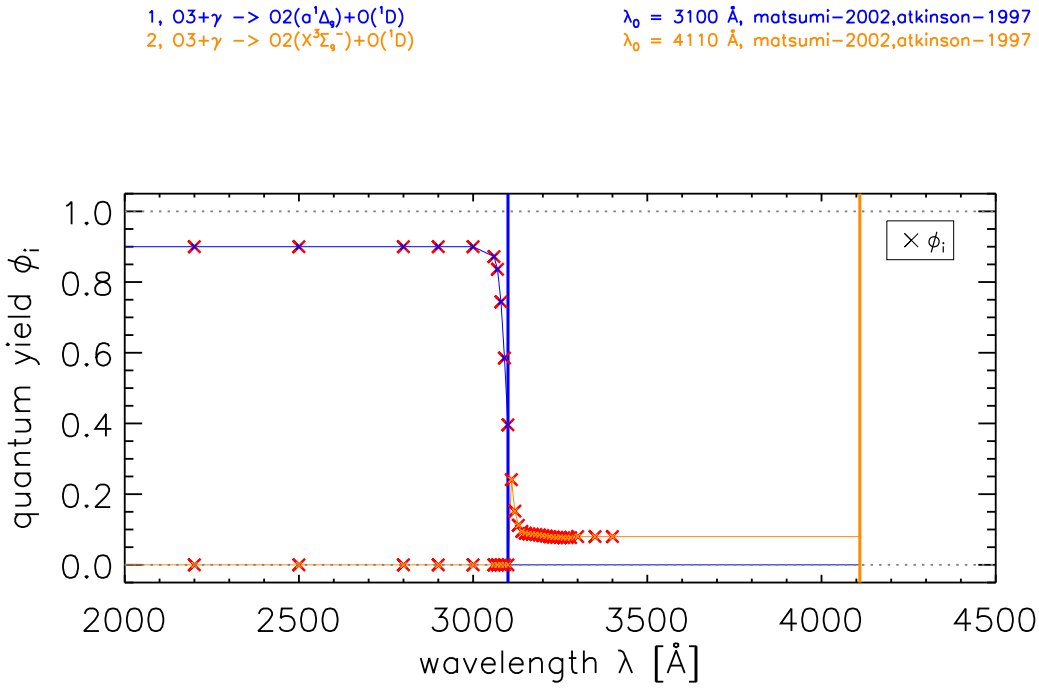

(a) *Photodissociation quantum yield* ϕ_i *for* $O(^1D)$ *formation.*

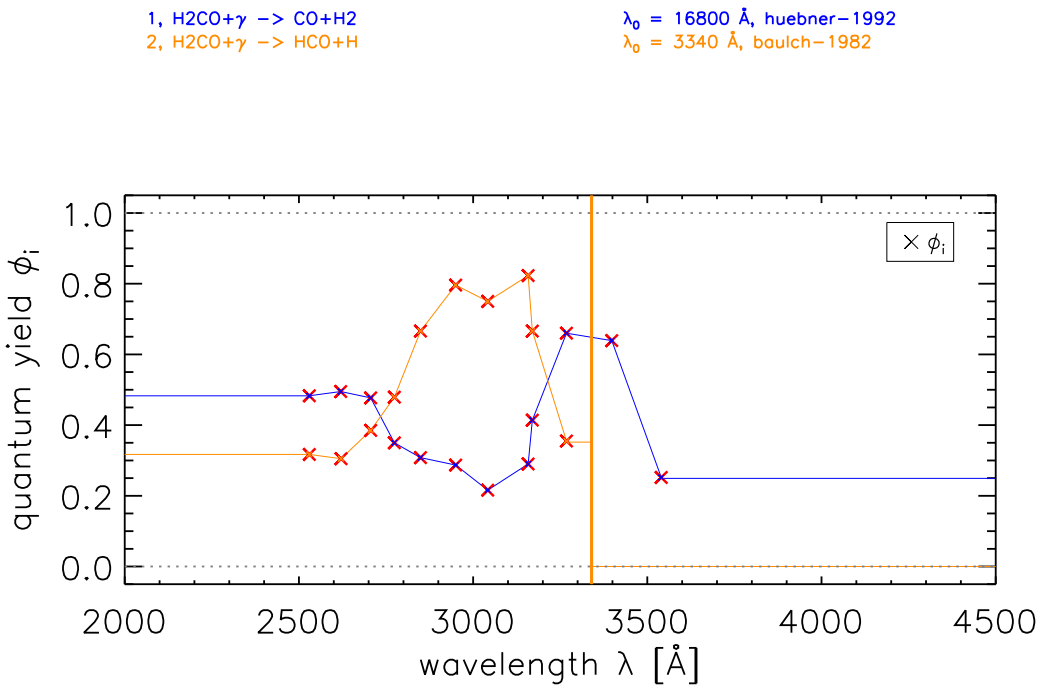

(b) H_2CO *photodissociation quantum yields* ϕ_i.

Figure 7.9: *Examples of quantum yields over wavelength for the species* O_3 *and* H_2CO. *The data is taken from Matsumi et al. (2002,* $T = 203$ *K) for* O_3 *and from Moortgat et al. (1983) for* H_2CO, *both provided by Keller-Rudek and Moortgat (2011). Quantum yield* ϕ_i *(crosses) data points and the threshold wavelengths* λ_0 *(vertical lines) with their reference are plotted in the color of the respective reaction.*

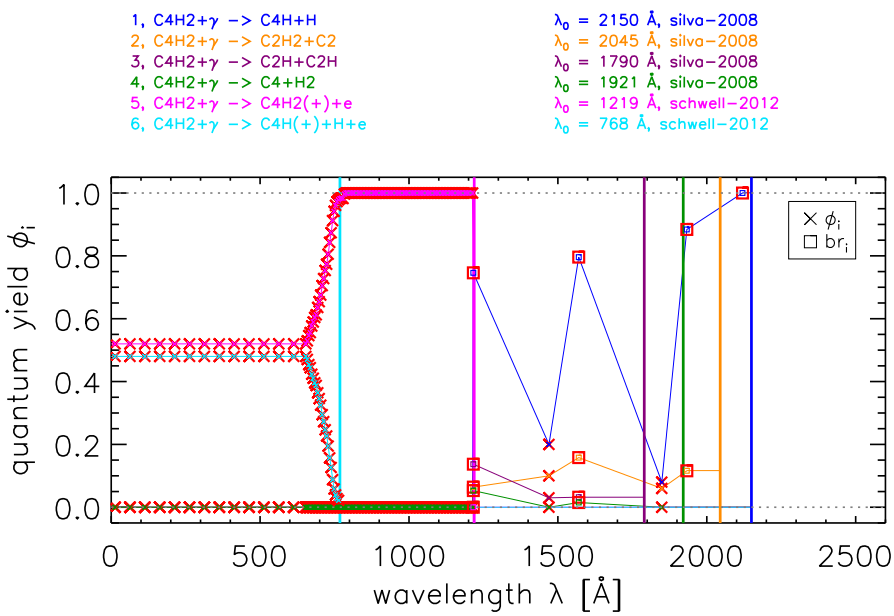

(a) *ϕ_i and br_i (assuming $\phi = 1$) data for C_4H_2 and data gaps.*

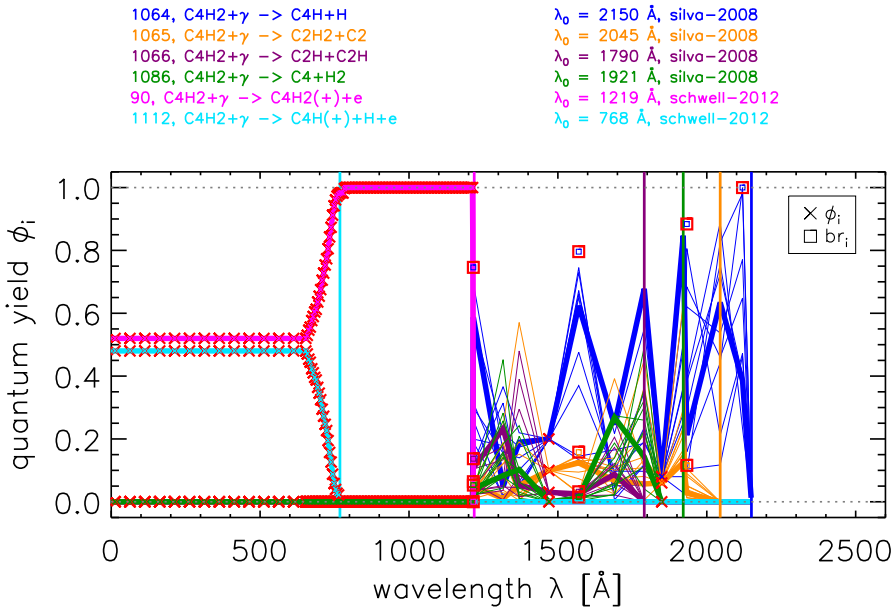

(b) *ϕ_i and br_i data for C_4H_2 with uncertainty estimation.*

Figure 7.10: *Illustration of the estimation of uncertainties from data gaps in the spectrum of ϕ_i of C_4H_2 shown in panel a). The data points of ϕ_i and br_i ($\phi_i = br_i \cdot \phi$, $\phi = 1$) are used for linear interpolation, as is usually done in the literature as ϕ_i is unknown in between the data and ϕ is unknown for the br_i. Data points of ϕ_i (crosses), br_i (rectangles) and the threshold wavelengths λ_0 (vertical lines) are plotted in the color of the respective reaction. Two data gaps $\Delta\lambda$ exist at $1216 - 1470$ Å and $1570 - 1849$ Å. In panel b) the Monte Carlo **(MC)** uncertainty estimation method, as described in the text, has been applied. For each reaction 10 sample spectra (one emphasized in bold) of the distribution of $10,000$ ϕ_i spectra are shown.*

Data Gap Uncertainty Estimation According to Gans et al. (2013) In the literature there exists a different approach to model the uncertainties of k_i resulting from data gaps in ϕ_i, compared to the approach presented in this thesis. In the work of Gans et al. (2013) the trend of the quantum yield curve of CH_4 photodissociation, along the quantum yield measurements and data gaps, is determined with a regression using the measurement uncertainties. An MC approach is used to propagate the uncertainty to the photo rate coefficient. For each sample set of the measurement uncertainty distributions a regression is performed. The results are samples of quantum yield curves, which can be used as inputs to a photochemical model to perform uncertainty analysis. However, that study only investigated one species (CH_4) for a small wavelength range.

7.3 Computation of the Rate Coefficient Distributions via MC

This section presents the computation of photo rate coefficients k_i and their uncertainties using the MC method.

7.3.1 Summary of Included Parameter Uncertainties

Table 7.3 summarizes the discussed sources of uncertainties for the photo rate coefficients k_i. Only those parameters were included into the uncertainty computation, whose uncertainty effect on the rate coefficients k_i is larger than a factor of 1.5 (±50 %).

Hence, for the reactions, for which the k_i have been computed using continuous data, i.e. via Equation (7.1), the included uncertainties are: data gaps in absorption cross section spectra $\sigma(\lambda)$ and in photodissociation quantum yield spectra $\phi_i(\lambda)$, the use of branching ratios br_i, i.e. $\phi_i = \phi \cdot br_i$ cannot be computed since ϕ is unknown.

For the reactions, for which the rate coefficients have been computed using oscillator strengths f_{ul}, i.e. via Equation (7.7), the uncertainties of the following properties have been included into the computation: the f_{ul}, the excitation energies E_{ul}, the quantum yields $\phi_{i,ul}$.

The following (smaller) uncertainties were neglected: the wavelength resolution in measurements of absorption cross sections σ, the temperature effect on σ, the measurement uncertainties of σ, quantum yields ϕ_i, ϕ, branching ratios br_i and λ_0 and the uncertainties regarding the solar photon flux $F_\odot$.

7.3.2 Computation and Results

The k_i uncertainties are computed in this work by propagation of the uncertainties of the included parameter uncertainties, discussed in Section 7.3.1, using the MC method. The 10,000 elements of each reaction's k_i distribution are computed via Equation (7.7) when using the oscillator strengths approach

$$k_i^s = k_i(f_{ul}^s, \phi_{i,ul}^s, \lambda_{ul}^s, \lambda_0^i, F_\odot)\,, \qquad s = 1, \ldots, S = 10,000\,, \tag{7.9}$$

For each of the $s = 1, \ldots, 10,000$ computations the s-th element of the distributions of f_{ul}^s, $\phi_{i,ul}^s$, λ_{ul}^s have to be applied, see the Sections 7.2.5 and 7.2.4.

To compute the k_i distribution using the continuous data approach one has to use Equation (7.1)

$$k_i^s = k_i(\sigma^s(\lambda), \phi_i^s(\lambda), \lambda_0^i, F_\odot)\,, \,, \qquad s = 1, \ldots, S = 10,000\,. \tag{7.10}$$

The $\sigma^s(\lambda)$, $\phi_i^s(\lambda)$ were defined in Sections 7.2.4 and 7.2.5.

Table 7.3: *Overview of the estimated uncertainties of photo rate coefficients k_i. The regarded quantities are the absorption cross section σ, the temperature T effect on σ, the solar photon flux $F_\odot$, the threshold wavelength λ_0, the oscillator strengths f_{ul}, the excitation energies E_{ul}, the branching ratios br_i and the quantum yields ϕ_i. Only those parameters were included into the uncertainty computation via Monte Carlo* ***(MC)****, see Section 7.3.1, whose uncertainty effect onto k_i is larger than a factor of* 1.5*. These parameters are marked with + in the last column.*

type	uncertainty factor $F(k_i)$	Section	included
$F_\odot$	≤ 1.50	7.2.1	-
threshold wavelength λ_0	≤ 1.50	7.2.2	-
σ, ϕ_i, br_i measurement uncertainties	≤ 1.50	7.2.4,7.2.5	-
T effect on σ	≤ 1.20 [a]	7.2.4	-
λ resolution σ	≤ 1.01	7.2.4	-
data gaps in σ	up to orders of magnitudes	7.2.4	+
data gaps in ϕ_i	up to orders of magnitudes	7.2.5	+
use of $br_i(\lambda)$, i.e. unknown $\phi(\lambda)$	up to orders of magnitudes	7.2.5	+
f_{ul} and E_{ul}	factor $\approx 1.3{-}2.7$	7.2.4	+

[a] The only relevant example is C_2H_2 in the temperature range $T = 173 - 295$ K, see Bénilan et al. (2000).

One can compute the distribution of a species' total rate coefficient k and the full branching ratios bf_i of the $i = 1, \ldots, n$ reactions involving the regarded species, by computing in each step $s = 1, \ldots, S$

$$k^s = \sum_{i=1}^{n} k_i^s \,, \qquad bf_i^s = \frac{k_i^s}{k^s} \qquad s = 1, \ldots, S = 10,000 \,. \tag{7.11}$$

Figure 7.11a shows the distributions of the rate coefficients k_i of each of the six C_4H_2 photo reactions plotted in the logarithmic space. The logarithmic space was used since the distributions are asymmetric in the real space, as a result of the Dirichlet distribution used in the uncertainty estimation, which conserve $\sum_{i=1}^{n} br_i(\lambda) = 1$ (combinatorial constraint) at all wavelengths λ. In the logarithmic representation the most likely value, i.e. the mode, is close to the median. The mode was approximated by fitting a Gaussian function to each distribution in the logarithmic space. This is reasonable since the rate coefficient uncertainties span orders of magnitudes for several reactions.

In Figure 7.11a one can see that the photoionization (purple) and photodissociative ionization (gray) reactions' k_i have no uncertainties, since for these reactions no data gaps for ϕ_i, see Figure 7.10a, and σ exist.

The convergence of each of the four k_i distributions to their underlying distributions, given in the color of the respective reaction, is presented in Figure 7.11b by showing the convergence of the 0.5 (median), 0.001, 0.999 percentiles ($\approx 3\sigma$), denoted here as k^{median}, k_i^{min} and k_i^{max}. When 10,000 elements are reached the effect of statistical fluctuations in the percentiles have become insignificant. Using 30,000 elements instead of 10,000 elements affects the percentiles insignificantly. This is true for all regarded reactions.

Table 7.4 gives an overview of each reaction's k_i^{median}, k_i^{min} and k_i^{max} as well as the square of the uncertainty factor F defined as

$$F^2 = k_i^{\text{max}} / k_i^{\text{min}} \,. \tag{7.12}$$

Additionally, a comparison with literature values is given together with an indication as to whether a reaction has been newly included into the reaction network as part of this work

(N), whether its k_i has been updated (U) or if the reaction was rejected in this work (R), i.e. reactions whose contribution to the formation of C_3 and C_2 in cometary comae are clearly negligible, e.g. due to a very small threshold wavelength λ_0. Lastly, the table indicates which parameters lead to the main uncertainty in the k_i. Figure 7.12 presents the uncertainties in a viewgraph, which are discussed further below together with the reaction network used in this work and in Weiler (2006), see Figure 7.15. The Figures 7.13 and 7.14 present the uncertainties of the total rate coefficient k and the full branching ratios bf_i, respectively.

Discussion of the Rate Coefficient Uncertainties

The computed k_i uncertainties are presented in Figure 7.12. The 0.025 and 0.975 percentiles ($\approx 2\sigma$ uncertainty level) areas are plotted in blue and orange. Additionally, the 0.001 and 0.999 percentiles ($\approx 3\sigma$) are plotted in gray, discernable at the 2σ uncertainty boundaries. The colors here are only used to help guide the eye. In this plot the median values are indicated as green crosses and the literature values as red crosses, which are also shown in Table 7.3. The model internal reaction numbers and the reactions are plotted on the right hand side of each figure.

Most of the k_i have large uncertainties. The exception is C_2 for which ab initio absorption cross sections σ are available and ionization absorption cross sections. In general, the k_i uncertainties of the ionization and dissociative ionization reactions are zero, partly due to available ionization and dissociative ionization absorption cross sections and absorption cross sections, from which quantum yields were computed, and in parts because a constant extrapolation has been applied for missing data at small wavelengths, see e.g. Figure 7.10a for C_4H_2.

For C_4H_2 the reactions $C_4H_2 + \gamma \longrightarrow C_4 + H_2$, $C_4H_2 + \gamma \longrightarrow C_4H_2^+ + e^-$ and $C_4H_2 + \gamma \longrightarrow C_4H^+ + H + e^-$ were introduced into the reaction network as part of this work. The k_i of the reaction $C_4H_2 + \gamma \longrightarrow C_4H + H$ computed in Weiler (2006) is just above the 0.998 percentile region computed in this work. This is likely because Weiler (2006) used the old $\lambda_0 = 2280$ Å (Glicker and Okabe, 1987) instead of the new $\lambda_0 = 2150$ Å (Frost et al., 1996, Silva et al., 2008) used in the present work.

For HC_3N the k_i 0.998 percentile uncertainty range of the reaction $HC_3N + \gamma \longrightarrow C_2H + CN$ does not include the k_i as computed in Weiler (2006), who used $\phi_i = 0.05$ of Halpern et al. (1988) at all wavelengths. For the other reaction Weiler (2006) used a constant quantum yield of 0.3. The present work uses quantum yields and branching ratios at several wavelength from Seki et al. (1996), Clarke and Ferris (1995) and Silva et al. (2009).

The k_i of the isomers CH_3C_2H (propyne) and $CH_2C_2H_2$ (allene) of C_3H_4 are compared with the k_i of the C_3H_4 molecule, which has been computed in Helbert (2002) using absorption cross sections σ and ϕ_i of $CH_2C_2H_2$ and CH_3C_2H. The k_i of CH_3C_2H are an order of magnitude lower compared to $CH_2C_2H_2$, due to the lower absorption cross sections σ. Helbert (2002) only used the ϕ_i reported at 1933 Å from Jackson et al. (1991), probably assuming a constant $\phi_i = 0.89$ and $\phi_i = 0.11$ for the reactions $C_3H_4 + \gamma \rightarrow C_3H_3 + H$ and $C_3H_4 + \gamma \rightarrow C_3H_2 + H_2$, respectively. This possibly resulted in a higher k_i for the reaction producing C_3H_3 compared to the present work. In the present work it is assumed that the CH_3C_2H and $CH_2C_2H_2$ isomers of C_3H_4 produce the H_2C_3H and the $l{-}C_3H_2$ (H_2C_3) isomers of C_3H_3 and C_3H_2, respectively. See the discussion in the data appendix D.

For C_2H_6 the only new reactions added in this work are the dissociative ionization reactions, by including σ for dissociative ionization. The k_i for pure ionization is therefore lower in this work compared to that used in Helbert (2002) and Weiler (2006), since it was assumed in their work that all absorptions at $\lambda < \lambda_0^{\text{ion}}$ lead to pure ionization (Huebner et al., 1992). For C_2H_6 the k_i uncertainty is close to zero, since the coverage of ϕ_i is quite good for the wavelength range, where only dissociation occurs, i.e. absorption cross sections σ between 1060 Å and 1600 Å. The absorption cross sections decrease steeply beyond 1500 Å.

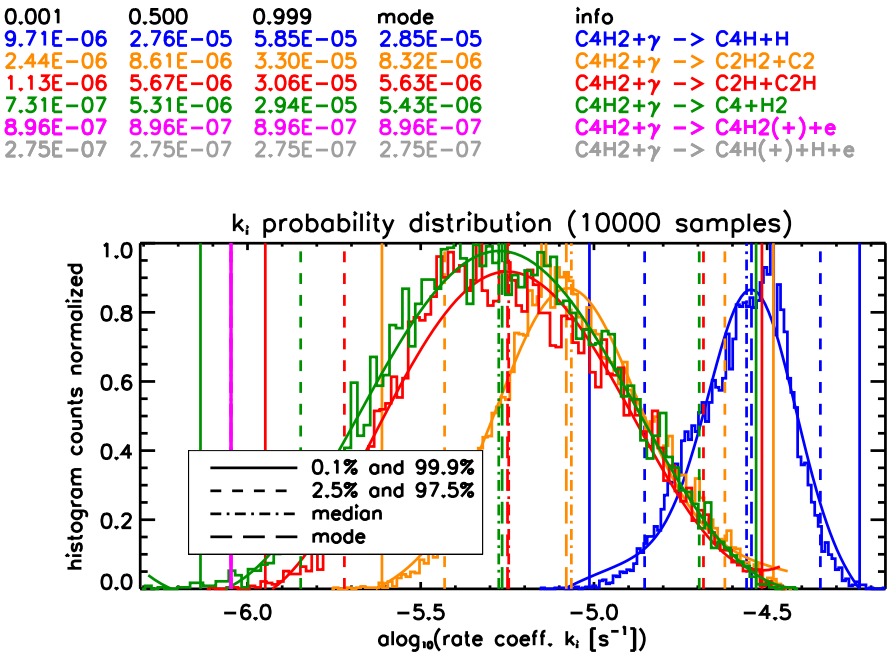

(a) *Probability distribution of* k_i *for* C_4H_2.

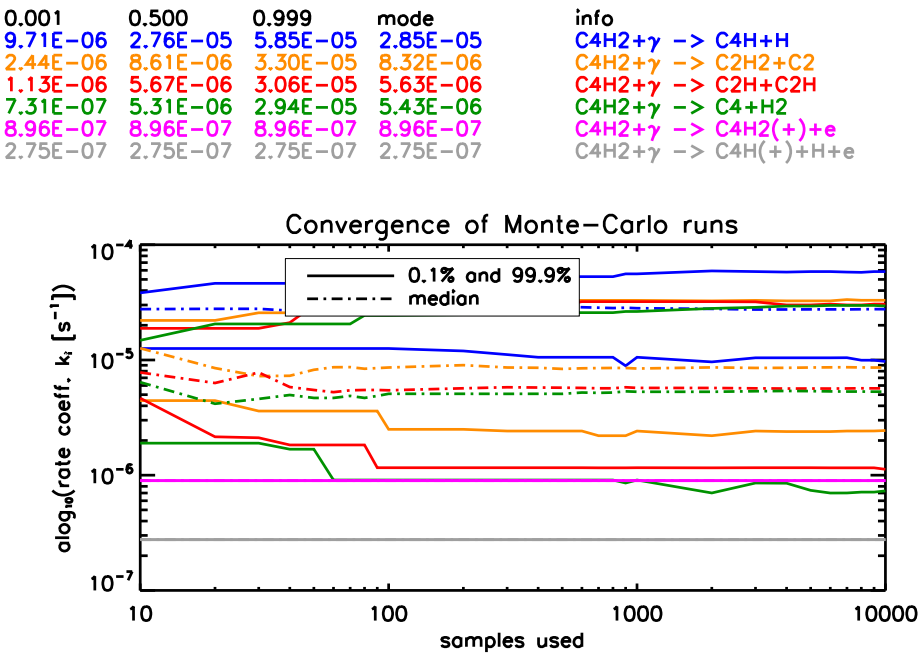

(b) *Convergence of the probability distribution of* k_i *for* C_4H_2.

Figure 7.11: *Probability distributions (panel a) of the photo rate coefficients* k_i *of* C_4H_2 *computed via the MC uncertainty propagation using Equation* (7.10) *and the convergence (panel b) of the* 0.001, 0.999 *and* 0.5 *(median) percentiles. The distributions and the values are shown in the color of the respective reaction.*

Table 7.4: *Overview of the rate coefficient k_i uncertainties computed in this work. The first two columns list the reaction numbers, used in the data Appendix D, and the corresponding reactions. Next, k_i^{min}, k_i^{median} and k_i^{max} are displayed, i.e. the* 0.001, 0.5 *and* 0.999 *percentiles of each reaction's k_i distribution, computed in this work, see e.g. Figure 7.11a. The square of the uncertainty factor, $F^2(k_i)$, was computed via Equation* (7.12)*. The k_i^{median} are compared with the literature k_i used in the work of Helbert (2002) and Weiler (2006). If a reaction, which was used in Helbert (2002), Weiler (2006), but was rejected in this work, this is indicated in the column 'info' by 'R'. All other reactions' k_i are updated in this work (U), whereby reactions newly introduced in this work are indicated by 'N'. The last column gives info on the main uncertainty sources. This work computes k_i individually for each of the C_3H_4 isomers $CH_2C_2H_2$ and CH_3C_2H, in contrast to Helbert (2002) and Weiler (2006), who used k_i of one general C_3H_4 molecule, computed from a combination of absorption cross sections and quantum yields of both isomers. In this table a value $a\,(-b)$ represents $a \cdot 10^{-b}$.*

#	reaction	k_i [s^{-1}] k_i^{min}	k_i^{median}	k_i^{max}	$F(k_i)^2$	literature k_i	info	uncertainty sources
(D.1)	$C_4H_2 + \gamma \rightarrow C_4H + H$	9.7 (−6)	2.8 (−5)	5.8 (−5)	6.0	6.6 (−5) [3]	U	ϕ_i gap, $\phi(br_i)$
(D.3)	$C_4H_2 + \gamma \rightarrow C_2H_2 + C_2$	2.4 (−6)	8.6 (−6)	3.3 (−5)	13.5	1.4 (−5) [3]	U	ϕ_i gap, $\phi(br_i)$
(D.2)	$C_4H_2 + \gamma \rightarrow C_2H + C_2H$	1.1 (−6)	5.7 (−6)	3.1 (−5)	27.1	9.6 (−6) [3]	U	ϕ_i gap, $\phi(br_i)$
(D.4)	$C_4H_2 + \gamma \rightarrow C_4 + H_2$	7.3 (−7)	5.3 (−6)	2.9 (−5)	40.2		N	ϕ_i gap, $\phi(br_i)$
(D.5)	$C_4H_2 + \gamma \rightarrow C_4H_2^+ + e^-$	9.0 (−7)	9.0 (−7)	9.0 (−7)	1.0		N	
(D.6)	$C_4H_2 + \gamma \rightarrow C_4H^+ + H + e^-$	2.8 (−7)	2.8 (−7)	2.8 (−7)	1.0		N	
(D.7)	$C_4H_2 + \gamma \rightarrow C_3 + CH_2$						6.5 (−5) [3]	R
(D.14)	$HC_3N + \gamma \rightarrow C_2H + CN$	2.0 (−6)	6.2 (−6)	1.3 (−5)	6.5	3.4 (−8) [3]	U	ϕ_i gap, $\phi(br_i)$
(D.15)	$HC_3N + \gamma \rightarrow C_3N + H$	3.6 (−6)	9.4 (−6)	1.8 (−5)	4.9	1.0 (−5) [3]	U	ϕ_i gap, $\phi(br_i)$
(D.17)	$CH_3C_2H + \gamma \rightarrow C_3H_3 + H$	5.9 (−6)	1.5 (−5)	3.1 (−5)	5.3	1.3 (−4) [2,3]	U	ϕ_i gap
(D.18)	$CH_3C_2H + \gamma \rightarrow C_3H_2 + H_2$	4.2 (−6)	1.3 (−5)	3.0 (−5)	7.0	3.0 (−5) [2,3]	U	ϕ_i gap
(D.19)	$CH_2C_2H_2 + \gamma \rightarrow C_3H_3 + H$	2.4 (−5)	5.3 (−5)	1.1 (−4)	4.5	1.3 (−4) [2,3]	U	ϕ_i gap, $\phi(br_i)$
(D.20)	$CH_2C_2H_2 + \gamma \rightarrow C_3H_2 + H_2$	1.3 (−5)	4.2 (−5)	9.9 (−5)	7.6	3.0 (−5) [2,3]	U	ϕ_i gap, $\phi(br_i)$
(D.37)	$C_2H_6 + \gamma \rightarrow C_2H_4 + H_2$	3.1 (−6)	3.2 (−6)	3.7 (−6)	1.2	3.7 (−6) [1,2,3]	U	ϕ_i gap, $\phi(br_i)$
(D.38)	$C_2H_6 + \gamma \rightarrow CH_3 + CH_3$	6.4 (−7)	7.1 (−7)	1.2 (−6)	2.0	8.8 (−7) [1,2,3]	U	ϕ_i gap, $\phi(br_i)$
(D.39)	$C_2H_6 + \gamma \rightarrow C_2H_5 + H$	2.6 (−6)	2.6 (−6)	3.2 (−6)	1.2	3.3 (−6) [1,2,3]	U	ϕ_i gap, $\phi(br_i)$
(D.40)	$C_2H_6 + \gamma \rightarrow CH_4 + CH_2$	1.9 (−6)	2.0 (−6)	2.6 (−6)	1.3	2.2 (−6) [1,2,3]	U	ϕ_i gap, $\phi(br_i)$
(D.41)	$C_2H_6 + \gamma \rightarrow C_2H_6^+ + e^-$	2.9 (−7)	2.9 (−7)	2.9 (−7)	1.0	4.9 (−7) [1,2,3]	U	
(D.42)	$C_2H_6 + \gamma \rightarrow C_2H_5^+ + H + e^-$	1.4 (−7)	1.4 (−7)	1.4 (−7)	1.0		N	
(D.43)	$C_2H_6 + \gamma \rightarrow C_2H_4^+ + H_2 + e^-$	6.5 (−7)	6.5 (−7)	6.5 (−7)	1.0		N	
(D.44)	$C_2H_6 + \gamma \rightarrow CH_3^+ + CH_3 + e^-$	2.3 (−8)	2.3 (−8)	2.3 (−8)	1.0		N	
(D.48)	$C_2H_4 + \gamma \rightarrow C_2H_2 + H_2$	2.7 (−6)	9.3 (−6)	2.4 (−5)	9.0	2.4 (−5) [1,2,3]	U	ϕ_i gap, $\phi(br_i)$

Continued on next page

Table 7.4 – *Continued from previous page*

#	reaction	k_i [s^{-1}] k_i^{min}	k_i^{median}	k_i^{max}	$F^2_{k_i}$	literature k_i	info	uncertainty sources
(D.49)	$C_2H_4 + \gamma \rightarrow C_2H_2 + H + H$	2.6 (−6)	8.8 (−6)	2.3 (−5)	9.1	2.3 (−5) [1,2,3]	U	ϕ_i gap, $\phi(br_i)$
(D.50)	$C_2H_4 + \gamma \rightarrow C_2H_3 + H$	7.3 (−7)	4.1 (−6)	1.7 (−5)	23.6		N	ϕ_i gap, $\phi(br_i)$
(D.51)	$C_2H_4 + \gamma \rightarrow C_2H_4^+ + e^-$	5.8 (−7)	5.8 (−7)	5.8 (−7)	1.0	5.8 (−7) [1,2,3]	U	
(D.52)	$C_2H_4 + \gamma \rightarrow C_2H_3^+ + H + e^-$	2.2 (−7)	2.2 (−7)	2.2 (−7)	1.0	2.3 (−7) [1,2,3]	U	
(D.53)	$C_2H_4 + \gamma \rightarrow C_2H_2^+ + H_2 + e^-$	1.8 (−7)	1.8 (−7)	1.8 (−7)	1.0	2.0 (−7) [1,2,3]	U	
(D.55)	$C_2H_4 + \gamma \rightarrow CH_2 + CH_2$						6.0 (−5) [2,3]	R
(D.59)	$C_2H_2 + \gamma \rightarrow C_2H + H$	7.8 (−6)	9.2 (−6)	1.1 (−5)	1.5	1.0 (−5) [1,2,3]	U	ϕ_i gap
(D.60)	$C_2H_2 + \gamma \rightarrow C_2 + H_2$	5.9 (−7)	1.8 (−6)	4.0 (−6)	6.8	2.7 (−6) [1,2,3]	U	ϕ_i gap
(D.61)	$C_2H_2 + \gamma \rightarrow C_2H_2^+ + e^-$	1.0 (−6)	1.0 (−6)	1.0 (−6)	1.0	7.8 (−7) [1,2,3]	U	
(D.62)	$C_2H_2 + \gamma \rightarrow C_2H^+ + H + e^-$	9.8 (−8)	9.8 (−8)	9.8 (−8)	1.0	7.4 (−8) [1,2,3]	U	
(D.8)	$C_4H + \gamma \rightarrow C_4 + H$	2.2 (−6)	1.1 (−5)	3.0 (−5)	13.3	3.0 (−5) [3]	U	ϕ_i gap, f_{ul}, E_{ul}
(D.11)	$C_4H + \gamma \rightarrow C_3 + CH$	2.1 (−7)	2.9 (−6)	1.8 (−5)	82.8		N	ϕ_i gap, f_{ul}, E_{ul}
(D.9)	$C_4H + \gamma \rightarrow C_3H + C$	2.0 (−7)	3.0 (−6)	1.9 (−5)	99.0		N	ϕ_i gap, f_{ul}, E_{ul}
(D.10)	$C_4H + \gamma \rightarrow C_2H + C_2$	2.2 (−7)	3.0 (−6)	1.7 (−5)	79.6	3.0 (−5) [3]	U	ϕ_i gap, f_{ul}, E_{ul}
(D.12)	$C_4 + \gamma \rightarrow C_3 + C$	4.0 (−4)	1.4 (−3)	6.6 (−3)	16.6	1.0 (−4) [3]	U	ϕ_i gap, f_{ul}, E_{ul}
(D.13)	$C_4 + \gamma \rightarrow C_2 + C_2$	5.6 (−7)	2.3 (−4)	1.6 (−3)	2807.7	1.0 (−4) [3]	U	ϕ_i gap, f_{ul}, E_{ul}
(D.25)	$C_3H_3 + \gamma \rightarrow C_3H_2 + H$	2.4 (−4)	9.9 (−4)	1.8 (−2)	75.9	1.8 (−3) [2,3]	U	σ gap, ϕ_i gap, $\phi(br_i)$
(D.26)	$C_3H_3 + \gamma \rightarrow C_3H + H_2$	1.8 (−4)	7.7 (−4)	1.5 (−2)	84.9		N	σ gap, ϕ_i gap, $\phi(br_i)$
(D.27)	$C_3H_3 + \gamma \rightarrow C_3H_3^+ + e^-$	1.0 (−5)	1.0 (−5)	1.0 (−5)	1.0		N	
(D.30)	$C_3H_2 + \gamma \rightarrow C_3 + H_2$	2.8 (−5)	8.8 (−4)	4.6 (−3)	163.2	9.5 (−7) [2,3]	U	ϕ_i gap, f_{ul}, E_{ul}
(D.31)	$C_3H_2 + \gamma \rightarrow C_3H + H$	2.5 (−5)	8.8 (−4)	4.7 (−3)	186.7		N	ϕ_i gap, f_{ul}, E_{ul}
(D.32)	$C_3H_2 + \gamma \rightarrow C_2 + CH_2$	5.0 (−7)	2.8 (−6)	3.8 (−5)	76.4		N	ϕ_i gap, f_{ul}, E_{ul}
(D.33)	$C_3H + \gamma \rightarrow C_3 + H$	2.1 (−3)	1.9 (−2)	6.4 (−2)	30.7		N	ϕ_i gap, f_{ul}, E_{ul}
(D.34)	$C_3H + \gamma \rightarrow C_2H + C$	4.0 (−6)	4.7 (−5)	2.5 (−4)	63.3		N	ϕ_i gap, f_{ul}, E_{ul}
(D.35)	$C_3H + \gamma \rightarrow C_2 + CH$	4.2 (−7)	2.5 (−6)	1.1 (−5)	26.8		N	ϕ_i gap, f_{ul}, E_{ul}
(D.16)	$C_3N + \gamma \rightarrow C_2 + CN$	2.4 (−6)	1.3 (−4)	7.9 (−3)	3362.8	7.2 (−7) [3]	U	σ gap, ϕ_i gap
(D.36)	$C_3 + \gamma \rightarrow C_2 + C$	1.1 (−5)	2.5 (−5)	1.5 (−4)	13.4	2.0 (−5) [2,3]	U	ϕ_i gap, f_{ul}, E_{ul}
(D.45)	$C_2H_5 + \gamma \rightarrow CH_2 + CH_3$	9.0 (−5)	3.6 (−4)	2.0 (−3)	21.9		N	σ gap, ϕ_i gap
(D.46)	$C_2H_5 + \gamma \rightarrow C_2H_4 + H$	9.1 (−5)	3.6 (−4)	1.9 (−3)	21.3		N	σ gap, ϕ_i gap
(D.47)	$C_2H_5 + \gamma \rightarrow C_2H_5^+ + e^-$	2.1 (−6)	2.1 (−6)	2.1 (−6)	1.0		N	
(D.56)	$C_2H_3 + \gamma \rightarrow C_2H_2 + H$	2.8 (−4)	1.7 (−2)	9.9 (−1)	3519.9		N	σ gap, ϕ_i gap

Continued on next page

Table 7.4 – *Continued from previous page*

#	reaction	k_i [s^{-1}] k_i^{min}	k_i^{median}	k_i^{max}	$F^2_{k_i}$	literature k_i	info	uncertainty sources
(D.57)	$C_2H_3 + \gamma \rightarrow CH + CH_2$	3.8 (−9)	3.8 (−6)	5.4 (−5)	14452.9		N	σ gap, ϕ_i gap
(D.58)	$C_2H_3 + \gamma \rightarrow C_2H_3^+ + e^-$	5.5 (−6)	5.5 (−6)	5.5 (−6)	1.0		N	
(D.63)	$C_2H + \gamma \rightarrow C_2 + H$	3.3 (−7)	1.8 (−6)	2.0 (−4)	606.6	3.0 (−5) [2,3]	U	ϕ_i gap, f_{ul}, E_{ul}
(D.64)	$C_2H + \gamma \rightarrow CH + C$	1.0 (−7)	1.4 (−6)	1.9 (−4)	1893.1		N	ϕ_i gap, f_{ul}, E_{ul}
(D.65)	$C_2 + \gamma \rightarrow C + C$	9.7 (−8)	9.7 (−8)	9.7 (−8)	1.0	1.0 (−7) [1,2,3]	U	
(D.66)	$C_2 + \gamma \rightarrow C_2^+ + e^-$	9.0 (−7)	9.0 (−7)	9.0 (−7)	1.0	9.1 (−7) [1,2,3]	U	

1 Huebner et al. (1992)
2 Helbert (2002)
3 Weiler (2006)

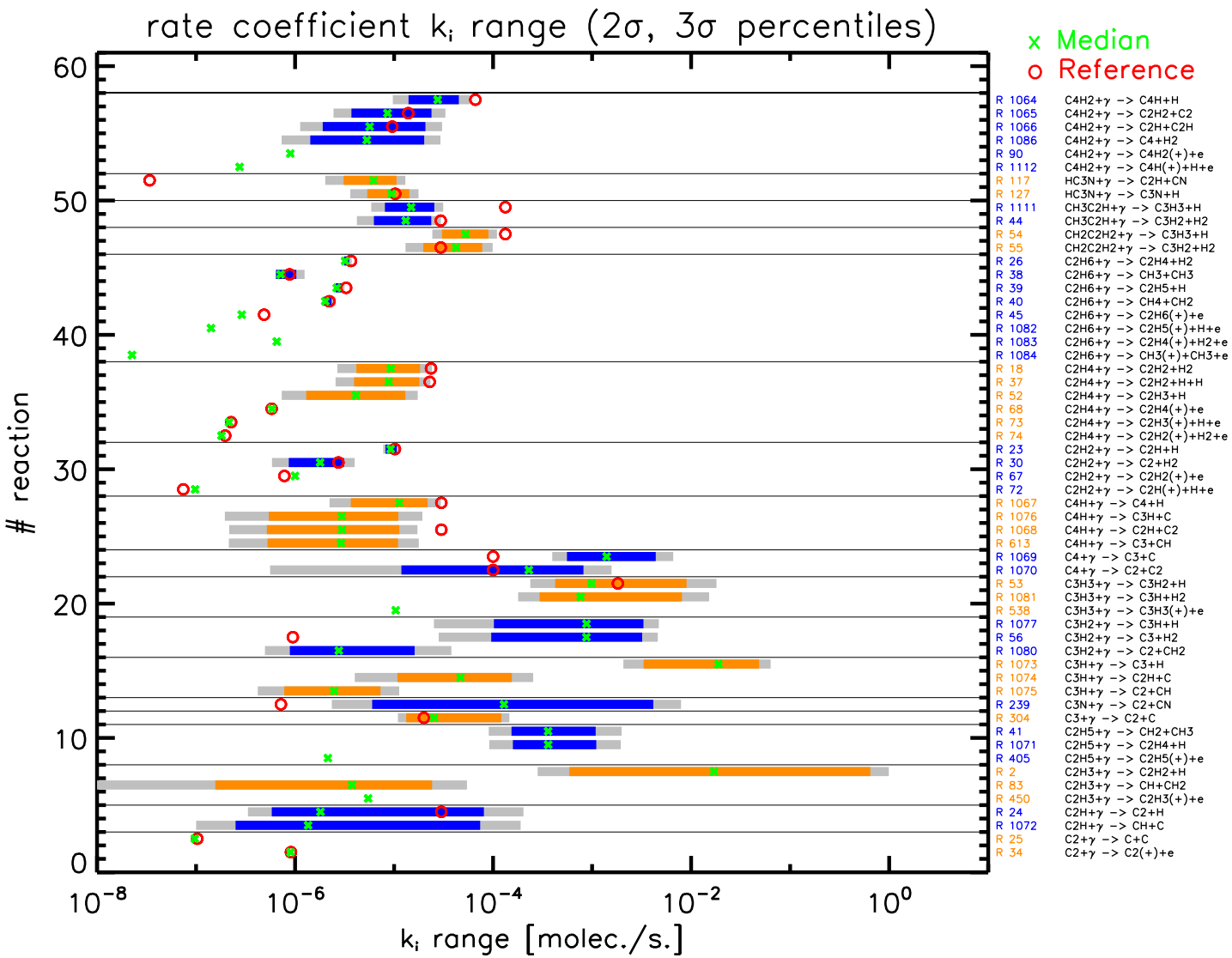

Figure 7.12: *Photo rate coefficient k_i uncertainty ranges. The* 0.025 *and* 0.975 *percentiles* ($\approx \pm 2\sigma$) *are plotted in blue and orange. The colors here are only used to help guide the eye. The* 0.001 *and* 0.999 *percentiles* ($\approx \pm 3\sigma$) *are plotted in gray. The* k_i^{median} (0.500 *percentile) and the literature* k_i *values, see also Table 7.4, are plotted as green crosses and red circles, respectively. Model reaction numbers are indicated on the right hand side together with the reactions, see Appendix F.*

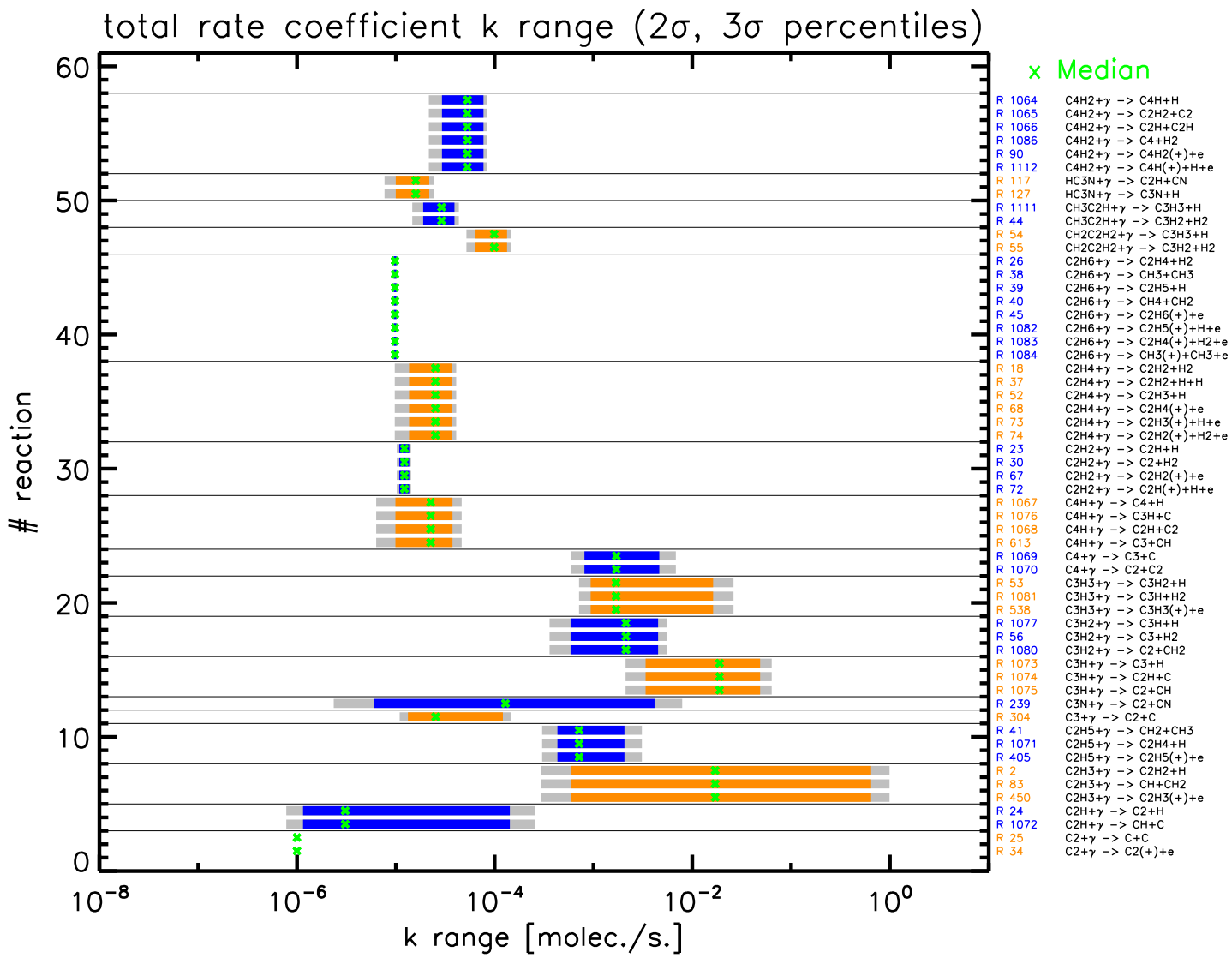

Figure 7.13: *As in Figure 7.12 but for the total rate coefficient k of each species.*

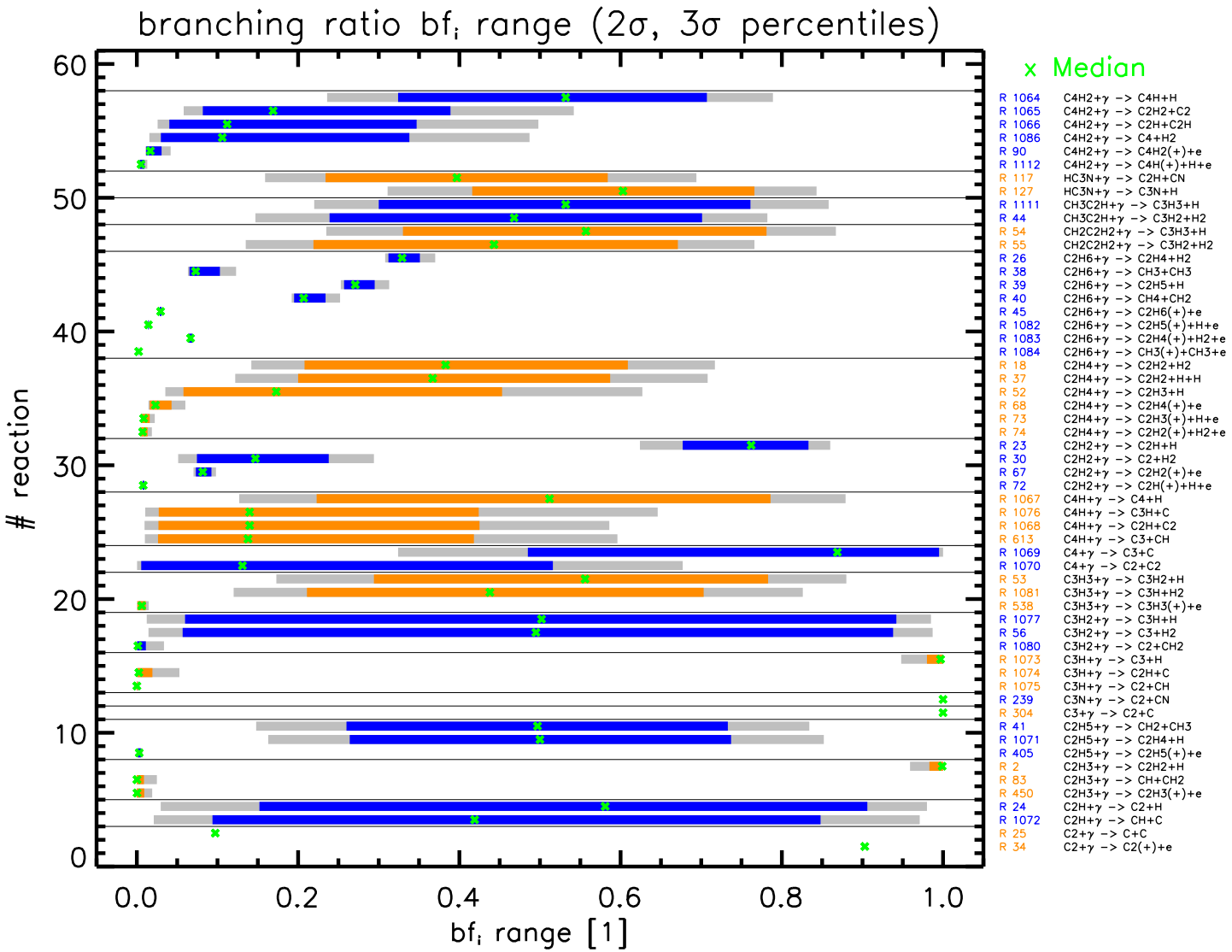

Figure 7.14: *As in Figure 7.12 but for the full branching ratios bf_i.*

In this work the reaction $C_2H_4 + \gamma \rightarrow 2 \cdot CH_2$ is omitted due to its small $\lambda_0 = 1243$ Å, i.e. its k_i is negligible for the C_2 chemistry in cometary comae. Helbert (2002) and Weiler (2006) included this reaction with an estimated $k_i = 6 \cdot 10^{-5}$ s^{-1}, which is twice the k_i of the reaction $C_2H_4 + \gamma \rightarrow C_2H_2 + H_2$ in their work. The photodissociation k_i used in Helbert (2002) and Weiler (2006) are close to the 0.998 percentile of the k_i uncertainty distribution computed in this work.

The uncertainty range of the reaction $C_2H_2 + \gamma \rightarrow C_2 + H_2$ is quite large and a result of two relatively large gaps in the ϕ_i spectrum. Reaction $C_2H_2 + \gamma \rightarrow C_2H + H$ has a larger k_i, as it has a quantum yield close to 1.0 at the two wavelengths $\lambda = 1216$ Å and $\lambda = 1933$ Å. Additionally, $\lambda_0 = 2170$ Å is larger than $\lambda_0 = 2000$ Å of the reaction producing $C_2 + H_2$.

For the radical C_4H two new reactions, leading to $C_3H + C$ and $C_3 + CH$, respectively, are included in this work compared with Weiler (2006). The k_i computed for C_4H and C_4 in this work, using the oscillator strengths f_{ul} reported in van Hemert and van Dishoeck (2008), are quite different to the k_i estimated in Weiler (2006). The exception is reaction $C_4 + \gamma \rightarrow C_2 + C_2$ for which the rate coefficient of Weiler (2006) is close to the median value computed in the present work. For the species C_4H and also for C_4 Weiler (2006) estimated the photodissociation rate coefficients by "comparison with similar reactions for radicals containing two or three carbon atoms" (Weiler, 2006).

In the work of Helbert (2002) the k_i for $C_3H_3 + \gamma \rightarrow C_3H_3 + H$ were taken from Moses et al. (2000), which is in the 2σ uncertainty range. Additionally, the reaction $C_3H_3 + \gamma \rightarrow C_3H + H_2$ has been introduced in this work for the C_3H_3 isomer H_2C_3H used in the present work (Mebel et al., 1998), see the discussion in the data appendix D. Additionally, the reaction $C_3H_3 + \gamma \rightarrow C_3H_3^+ + e^-$ has been introduced into the reaction network as part of this work.

For C_3H_2 Helbert (2002) and Weiler (2006) assumed only one reaction, namely $C_3H_2 + \gamma \rightarrow C_3 + H_2$, whose k_i was fitted in Helbert (2002) to the C_3 column density profiles of Hale-Bopp. This k_i is three orders of magnitudes smaller than the median k_i computed in the present work using the oscillator strengths of van Hemert and van Dishoeck (2008). In total three reactions are possible for the l$-C_3H_2$ isomer of C_3H_2 used in the present work (Mebel et al., 1998).

Photodissociation rate coefficients for C_3H were not estimated in Helbert (2002) and Weiler (2006). Three reactions are reported in Mebel et al. (1998) for the C_3H isomer l$-C_3H$ which is used in the present work. The present work computes the rate coefficients using the oscillator strengths f_{ul} of van Hemert and van Dishoeck (2008).

No ϕ_i data and only one σ value is available for C_3N. This is the reason why this work computes a large uncertainty for the photodissociation rate coefficient of this species. Weiler (2006) assumed a constant $\phi_i = 0.5$ and a mean $\sigma = 10^{-18}$ cm^2. Due to similar reasons as for HC_3N the k_i of Weiler (2006) is not in the 0.999 percentile uncertainty range computed in this work.

The k_i^{median} of C_3, computed using the f_{ul} from van Hemert and van Dishoeck (2008), is very close to that obtained in Helbert (2002) from model fits to Hale-Bopp observations.

New in this work are photo rate coefficients of C_2H_5 and C_2H_3. Both C_2H_5 dissociation rate coefficients have equal uncertainty ranges and median values. This is because ϕ_i is completely unknown and because $\sigma(C_2H_5) \neq 0$ only at $\lambda < 2600$ Å, which is below the λ_0 of both dissociation reactions. For C_2H_3 also ϕ_i is completely unknown and two gaps in σ exist, leading to the high uncertainty of k_i. Reaction $C_2H_3 + \gamma \rightarrow C_2H_2 + H$ has a much higher λ_0 than reaction $C_2H_3 + \gamma \rightarrow CH + CH_2$. As a result the k_i^{median} of the first reaction is much higher.

The k_i for $C_2H + \gamma \rightarrow C_2 + H$ used in Helbert (2002) and Weiler (2006) lies within the 2σ uncertainty range. New in the present work is the reaction $C_2H + \gamma \rightarrow CH + C$. The C_2 photodissociation rate coefficients have no uncertainties as there are no data gaps in the ab initio computed σ and ϕ_i. Also, the rate coefficient for the ionization is quite secure (absorption

cross sections are quite secure). This reaction is the main loss path of C_2.

Reaction Network

Figure 7.15 compares graphically the updated reaction network of this work (panel b), to describe the formation of C_3 and C_2, with the reaction network of Weiler (2006) (panel a). Panel b) in Figure 7.15 features more connections between species producing C_3 and C_2 in contrast to panel a). The present work introduced the reactions and k_i of the C_3H_4 isomers $CH_2H_2H_2$ (allene) and CH_3C_2H (propyne), which were modeled in Helbert (2002) and Weiler (2006) as one molecule by computing the k_i by a combination of data of both isomers. These isomers were included into the present work, because the k_i^{median} of $CH_2C_2H_2$ and CH_3C_2H are different by an order of magnitude, see Figure 7.12, which clearly could be important.

Helbert (2002) noted that C_2H_6 is likely to be only a minor C_2 parent molecule. Weiler (2006) reports that C_2H_6 production rates cannot be constrained from C_2 observations at the cometocentric distances where observations are generally available ($r_c \lessapprox 10^5$ km). The present work investigates also C_2H_6 as a parent molecule, since several updates have been made in the present work regarding the species $C_2H_{(6,5,4,3,2,1)}$. For example, the present work removed the reaction $C_2H_4 + \gamma \rightarrow 2 \cdot CH_2$, since its contribution was overestimated in the previous works, see Section 7.3.2 and Appendix D. This work also included the species C_2H_5 and C_2H_3. Also C_2H_4 is investigated in the present work as a C_2 parent molecule. This allows a complete analysis and classification of the role of each of the (up until now) detected molecules C_2H_2, C_2H_6, HC_3N and the proposed molecules $CH_2C_2H_2$, CH_3C_2H, C_4H_2 and C_2H_4 in the SA in Chapter 8.

7.4 Summary and Conclusion

This chapter has computed for the first time the uncertainties of photodissociation rate coefficients applied in cometary photochemical models. To compute the corresponding distributions the MC method was used. Although, the presented uncertainty estimation method should be regarded as a first approach, where the uncertainty estimation is fixed to a certain level, and which may be improved in future investigations, in summary it should provide reasonable first order uncertainties arising from the lack of quantum yields and absorption cross sections at large parts of the important wavelength ranges (data gaps), from the use of branching ratios in lack of quantum yields as well as from the uncertainties of ab initio electronic absorption oscillator strengths.

The computed uncertainties are large for the majority of the regarded hydrocarbon photodissociation reactions' rate coefficients, i.e. even up to several orders of magnitude. The main sources of these uncertainties are data gaps in the quantum yield and absorption cross section spectra at large parts of the important wavelength ranges.

The computed photo rate coefficient distributions are a prerequisite for a sensitivity analysis **(SA)** of the modeled C_3 and C_2 coma chemistry as done in Chapter 8. These distributions, see Table 7.4, may also be useful for a SA of other models including hydrocarbon photochemistry. The presented uncertainty estimation method may also be used for photo reactions of other species than investigated in this work.

Additionally, the results enable the investigation as to whether the C_3 and C_2 observations of the four comets NEAT, LINEAR, Tempel 1 and Hale-Bopp, observed in the range $r_h = 1 - 3.78$ AU, can be reproduced within the uncertainties of the rate coefficients of the photodissociation reactions. This is done in Chapter 9 by optimizing on the one the hand the production rate ratios of the regarded C_3 and C_2 parent molecules individually for each comet and on the other hand by optimizing a common set of rate coefficients of the regarded photodissociation reactions (within the uncertainties).

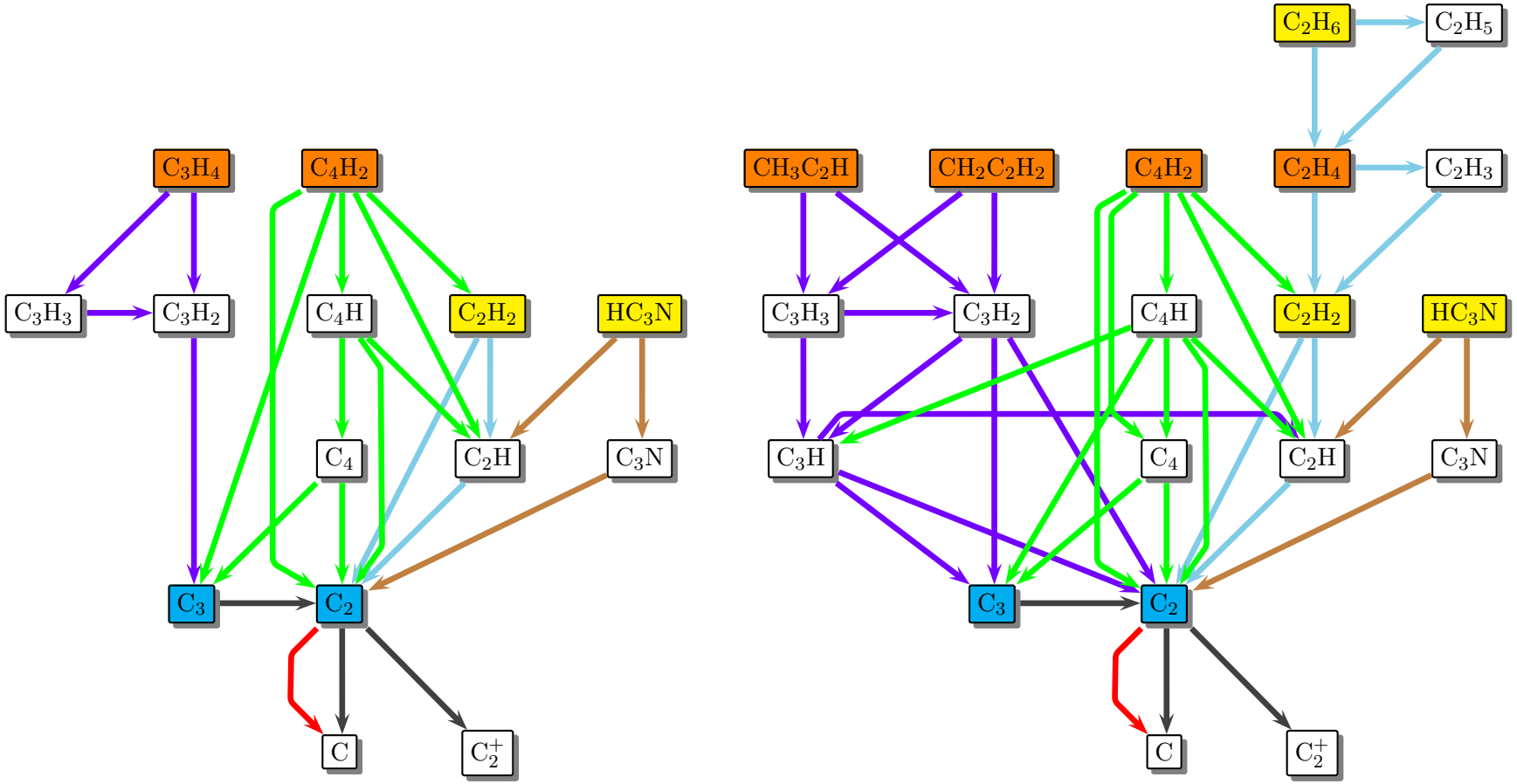

(a) *Reaction network of Weiler (2006)*

(b) *Reaction network used in this work*

Figure 7.15: *Reaction network of the* C_3 *and* C_2 *formation in cometary comae investigated in a) Weiler (2006) and b) this work. The reaction arrows for species containing* C_3, C_4, C_2 *and* C_3N *are colored in lilac, green, light blue and brown, respectively. Reactions removing* C_3 *or* C_2 *are colored in black. The electron impact dissociation of* C_2 *is shown as a red arrow. The molecules* C_4H_2, $CH_2C_2H_2$ *and* CH_3C_2H *are suspected as* C_3 *parent molecules (Crovisier, 1994, Krasnopolsky, 1991, Bockelée-Morvan et al., 2000), and* C_2H_4 *as an additional* C_2 *parent molecule (Kobayashi and Kawakita, 2010). These molecules have not been detected in cometary comae up until now (boxes colored in orange). Only the* C_2 *parent molecules* C_2H_6, C_2H_2 *and* HC_3N *have been detected in comets (boxes colored in yellow). Intermediate and observed species (*C_3 *and* C_2*) are indicated by boxes with background colors of white and blue, respectively. Panel b) features more connections between species producing* C_3 *and* C_2 *in contrast to panel a).*

Part III

Scientific Results

CHAPTER 8

Sensitivity Analyses of the PhotoChemistry

The results of Chapter 7 suggest that significant uncertainties in the photo rate coefficients, used to model the C_3 and C_2 chemistry in cometary comae, may exist. These uncertainties were quantified in order to investigate the impact on the uncertainties of the coma chemistry.

This chapter focuses on the impact of uncertainties of the photodissociation reactions on C_3 and C_2 column densities computed with the model described in Section 5. Reactions significantly involved in the formation of a modeled species and whose uncertainties have a significant influence on the output uncertainty are denoted *key reactions*. Reducing the uncertainty of the key reactions, by future experiments and ab initio computations by chemists, allows an efficient reduction of the model output uncertainty (Dobrijevic et al., 2010). This in turn will allow to determine if a parent molecule is able to account for the observations of C_3 and C_2 in cometary comae or if other new parent molecules have to be proposed. Therefore, identifying such key reactions for C_3 and C_2 is a main motivation of this work.

For such a purpose a sensitivity analysis **(SA)** of the photodissociation reactions involved in the formation of C_3 and C_2 in cometary comae is suitable. Section 8.1 provides an overview of various SA methods applied in the literature. The initial values for the model computations required for the SA are presented in Section 8.2. The results of the SA are shown and discussed in Section 8.3.

8.1 Sensitivity Analysis (SA) Methods

Sensitivity Analysis (SA) methods generally refer to changing one or more particular variables in a system and investigating how the system responds. According to Dobrijevic et al. (2010) SA methods can be split into three main parts, namely production path **(PP)**, local sensitivity analysis **(LSA)** and global sensitivity analysis **(GSA)** as shown in Table 8.1 and described in the following text.

8.1.1 Production Path (PP)

PP methods involve studying the importance of a reaction or a set of reactions (pathway) for the production (and/or loss) of a certain species in a chemical system. Nominal production path (NPP) refers to identifying the relative production P_i^j/P_i of a reaction j or pathway to

the total production of the species i among all related production and loss processes. In the context of NPP those reactions with a significant contribution (production or loss) for species i are called key reactions. The signal flow graph **(SFG)** method identifies all pathways and loops of a chemical system. The relative contribution of each pathway to the production or loss of a species can be calculated, thereby also taking into account the loops. Additionally, the relative importance of each reaction within a regarded pathway can be determined. The nominal production path **(NPP)** method enables an extensive analysis of all pathways, but may be limited computationally to small chemical systems due to the extensive growth in complexity with each additional species. The PP methods are limited in their use due to the negligence of the rate coefficient uncertainties.

8.1.2 Local Sensitivity Analysis (LSA)

LSA refers to calculating the response of a concentration n_i of a species to the change of a chemical rate coefficient k_j, while all other rate coefficients are kept fixed at their nominal value. The one factor at a time **(OAT)** method refers to comparing the model output change when changing a rate coefficient from the nominal to an upper value. Based on the OAT one can compute also the so-called sensitivity coefficients **(SCs)** by multiplying/dividing singly each reaction's rate coefficient by a fixed factor and then comparing the outputs of the modified with the nominal model computation. The SC is defined as

$$S_{ij}^{\text{upper/lower}} = \frac{\log(n_i^{\text{nominal}}) - \log(n_i^{\text{upper/lower}})}{\log(k_j^{\text{nominal}}) - \log(k_j^{\text{upper/lower}})} = \frac{\log(n_i^{\text{nominal}}/n_i^{\text{upper/lower}})}{\log(k_j^{\text{nominal}}/k_j^{\text{upper/lower}})} \tag{8.1}$$

with

$$k_i^{\text{upper}} = k_i^{\text{nominal}} \cdot f\,, \tag{8.2}$$

$$k_i^{\text{lower}} = k_i^{\text{nominal}}/f\,. \tag{8.3}$$

where e.g. $f = 10$. The SCs, which relate the change of a species' concentration to the change of a rate coefficient, allow an intercomparison of the reactions' production/destruction efficiencies. One can also define k_i^{upper} and k_i^{lower} e.g. as the 3σ corresponding percentiles of the rate coefficient distribution (Smith and Nash, 2006).

The local uncertainty propagation **(LUP)** relates the model output uncertainty, i.e. of a concentration c_i of the species i, to the SCs S_{ij} and the variance $\sigma^2(\log k_j)$ of the logarithm of the rate coefficient of reaction j via

$$\sigma^2(\log c_i) = \sum_{j=1}^{J} \sigma_j^2(\log c_i) = \sum_{j=1}^{J} \sigma^2(\log c_i) \cdot (S_{ij})^2\ . \tag{8.4}$$

The SC and the LUP method find different kinds of key reactions, i.e. detecting reactions, which have an impact on a species' concentration or an impact on the uncertainty of a species' concentration (Dobrijevic et al., 2010). All LSA methods are usually limited to linear models or chemical systems with very small uncertainties (typically $\Delta k_i/k_i \leq 10\ \%$), if they are to give the correct key reactions. In such a case and for small chemical systems the number of computations is rather small.

8.1.3 Global Sensitivity Analysis (GSA)

GSA are designed to assess how a chemical system reacts to a simultaneous change of all rate coefficients within the uncertainty range of their probability density function **(PDF)**. There

are the Monte Carlo **(MC)** and the experimental design approach. The basic principle of the MC method is to vary the rate coefficients of all reactions simultaneously so as to retain the nonlinearities and to fully explore all configurations of the chemical reaction network (Dobrijevic et al., 2010). Additionally, a central goal is to compute the probability distribution of the model output for the concentration of one or more species to assess their uncertainty.

A statistically significant number of model runs, depending on the runtime of the model usually between $n_{\mathrm{MC}} = 2,000$ and $n_{\mathrm{MC}} = 10,000$, have to be computed to obtain a representative sample of the probability distribution of each of the regarded species' concentration. An advantage of the MC method is that the variance of the model outputs converges as $1/n_{\mathrm{MC}}$, independent of the number of uncertain model parameters investigated.

$10,000$ statistically independent rate coefficients, see Chapter 7, of each reaction are saved in a list $L(k_i)$ for the GSA. For the first model run the first element of each reaction's list $L(k_i)$, for the second model run the second element of each $L(k_i)$ are used and so on, up to $10,000$ times. The approach is summarized in the following Equation (8.5)

$$(\mathbf{k}_1, \ldots, \mathbf{k}_{n_r}) = \begin{pmatrix} k_1^1 & \ldots & k_{n_r}^1 \\ \vdots & \ddots & \vdots \\ k_1^{n_{\mathrm{MC}}} & \ldots & k_{n_r}^{n_{\mathrm{MC}}} \end{pmatrix} \mapsto \begin{pmatrix} M(k_1^1, \ldots, k_{n_r}^1) \\ \vdots \\ M(k_1^{n_{\mathrm{MC}}}, \ldots, k_{n_r}^{n_{\mathrm{MC}}}) \end{pmatrix} \mapsto \begin{pmatrix} n^1(r_c) \\ \vdots \\ n^{n_{\mathrm{MC}}}(r_c) \end{pmatrix}, \quad (8.5)$$

where $n_{\mathrm{MC}} = 10,000$, $\mathbf{k}_i = (k_i^1, \ldots, k_i^{n_{\mathrm{MC}}}) \in L(k_i)$ is the list of statistically independent rate coefficient values representing the probability distribution of reaction i, n_r the number of reactions for which $L(k_i)$ has been computed, M the model and $n^1(r_c), \ldots, n_{\mathrm{MC}}(r_c)$ a species' MC-computed concentrations at r_c.

To determine the key reactions, i.e. the reactions whose uncertainty have the largest impact on the model output uncertainty, one computes the correlation between a representative sample of each reaction's rate coefficient distribution and the corresponding samples of a species' concentration distribution, e.g. using the rank correlation coefficients **(RCCs)** described in the next Section. Since the model computes a density profile $n^i = n^i(r_c)$, one obtains at each cometocentric distance r_c a probability distribution and one can compute the correlation at each r_c.

The main disadvantage is the large number of computations, which has been reduced in several studies by using e.g. 'Latin Hypercube Sampling' (Zádor et al., 2006, Dobrijevic et al., 2010), which aims at sampling the parameter space more efficiently. The experimental design **(ED)** method aims at drastically reducing the number of required simulations than is needed for the MC approach. This is possible by taking specific values from each distribution of rate coefficients, which are determined by a so-called screening design. With such a screening design, e.g. the Hadamard design, it is possible to reduce the number of computations almost down to the number of rate coefficients investigated. From such a screening a (linear) metamodel

$$Y_j = b_0 + \sum_{i=1}^{n} b_i X_i + \epsilon \quad (8.6)$$

is constructed with Y_j the modeled concentration of species j, n the number of reactions, $X_i = \log k_i$ and ϵ the inaccuracy of the metamodel. The b_i are the metamodel coefficients, determined in a multidimensional regression, which allow to identify the important factors (Dobrijevic et al., 2010).

In this work, it was decided to use a GSA, in particular the MC method, since this allows a full exploration of all configurations of the chemical reaction network.

Table 8.1: *Overview of sensitivity analysis* ***(SA)*** *methods to determine key reactions (Dobrijevic et al., 2010).*

global sensitivity analysis **(GSA)**	**Monte Carlo (MC)** [a]
	experimental design **(ED)**
local sensitivity analysis **(LSA)**	one factor at a time **(OAT)**
	sensitivity coefficient **(SC)**
	local uncertainty propagation **(LUP)**
production path **(PP)**	nominal production path **(NPP)**
	signal flow graph **(SFG)**

[a] used in this work.

Correlation

A correlation is computed by comparing the elements of the probability distribution of the species' concentration and each reaction's rate coefficient k_j, i.e. to determine if in general the species' concentration increases/decreases, when the rate coefficient of a reaction is increased/decreased.

The linear (Pearson's) correlation coefficient is defined as

$$r(k_j, n) = \frac{\text{Mean}((k_j^l - \bar{k}_j) \cdot (n^l - \bar{n}))}{\sigma_{k_j}\sigma_n} = \frac{\sum_{l=1}^{L}(k_j^l - \bar{k}_j) \cdot (n^l - \bar{n})}{\sqrt{\sum_{l=1}^{L}(k_j^l - \bar{k}_j)^2}\sqrt{\sum_{l=1}^{L}(n^l - \bar{n})^2}} \,. \tag{8.7}$$

where σ_{k_j}, σ_n are the standard deviations of the k_j sample distribution and the model output $n(r_c)$ distribution, respectively. $\bar{k}_j$ and $\bar{n}(r_c)$ are the sample means. Equation (8.7) measures the degree of linear dependency between k_j and n. r varies between -1 and 1, where $r = 1$ indicates a completely positive linear correlation, i.e. the data lies on a straight line with slope 1, whereas $r = -1$ indicates a linear negative correlation. $r = 0$ indicates no correlation (Press et al., 2007, Devroye, 1986, Helton et al., 2006). Since the linear correlation coefficient method tends to overlook nonlinear correlations, this work uses the Spearman's RCC, which measures the degree of a monotone relationship instead of a linear relationship. Here, each distribution's n elements are replaced by their ranks, according to their size, from 1 to n. Spearman's rank correlation coefficient r_s is defined as the linear correlation coefficient r from Equation (8.7) of the ranks (Press et al., 2007), where $\bar{R}(x) = \frac{1}{L}\sum_{l=1}^{L} R(x^l)$ (Helton et al., 2006, p.28),

$$r_s(k_j, n) = \frac{\sum_{l=1}^{L}\left(R(k_j^l) - \bar{R}(k_j^l)\right) \cdot \left(R(n^l) - \bar{R}(n)\right)}{\sqrt{\sum_{l=1}^{L}\left(R(k_j^l) - \bar{R}(k_j)\right)^2}\sqrt{\sum_{l=1}^{L}\left(R(n^l) - \bar{R}(n)\right)^2}} \,. \tag{8.8}$$

Knowing the r_s one can determine the reactions with the largest influence on the model outputs, weighted by the uncertainty of the reaction's rate coefficients (Carrasco et al., 2008). The strengths of a correlation can be categorized as shown in Table 8.2. This work computes the RCC r_s and its statistical significance s with the IDL routine `r_correlate.pro` from NASA-IDL-Lib. (2011). The statistical significance of the r_s computed in this work is ensured, since $n_{MC} = 10,000$ model runs are carried out in each MC computation.

Table 8.2: *Correlation strength classification using Spearman's RCC r_s. Source: Dusick (2012).*

r_s range	correlation strength
$\lvert r_s\rvert \in [0.9, 1.0]$	very strong
$\lvert r_s\rvert \in [0.7, 0.9)$	strong
$\lvert r_s\rvert \in [0.5, 0.7)$	moderate
$\lvert r_s\rvert \in [0.3, 0.5)$	low to moderate
$\lvert r_s\rvert \in [0.16, 0.3)$	weak to low
$\lvert r_s\rvert \in [0, 0.16)$	meaningless

8.2 Initial Values and Boundary Conditions

This section now presents the boundary conditions and initial values for the comets C/1995 O1 **(Hale-Bopp)**, C/2001 Q4 **(NEAT)**, C/2002 T7 **(LINEAR)** and 9P **(Tempel 1)**, since these are key quantities for the MC analysis which follows. Table 8.3 shows the boundary conditions of the production rate ratios, $c(\text{species}) = Q(\text{species})/Q(\text{H}_2\text{O})$, of various volatile species with respect to the water production rate $Q(\text{H}_2\text{O})$. The species' initial number densities n_0 are computed using Equation (5.27) and the production rate ratios. This Table also shows the nucleus radius r_0 and the initial gas temperature T_0 and velocity u_0.

8.2.1 Water Production Rates $Q(\text{H}_2\text{O})$

This work applies for comet Hale-Bopp $Q(\text{H}_2\text{O}, 3.78\ \text{AU}) = 4 \cdot 10^{28}$ molecules s^{-1} as computed by Helbert (2002). This work uses for comet NEAT the most up to date water production rate value $Q(\text{H}_2\text{O}, 1.00\ \text{AU}) = 2.6 \cdot 10^{29}$ molecules s^{-1} from Biver et al. (2009). Weaver et al. (1999) reports a slightly different water production rate of $Q(\text{H}_2\text{O}, 1.00\ \text{AU}) = 1.9 \cdot 10^{29}$ molecules s^{-1}. Howell et al. (2004) reports $Q(\text{H}_2\text{O}, 1.20\ \text{AU}) = 6.9 \cdot 10^{28}$ molecules s^{-1} for comet LINEAR, which is used in this work. For comet Tempel 1 two $Q(\text{H}_2\text{O})$ are reported in the literature. This work uses for comet Tempel 1 $Q(\text{H}_2\text{O}, 1.51\ \text{AU}) = 3.4 \cdot 10^{27}$ molecules s^{-1} from Küppers et al. (2005), instead of the water production rate $Q(\text{H}_2\text{O}, 1.51\ \text{AU}) = 1.21 \cdot 10^{28}$ molecules s^{-1} from Mumma et al. (2005), since the effect of the uncertainty of the water production rate onto the model results is not investigated in the present work.

8.2.2 C_3 and C_2 Parent Molecule Production Rate Ratios

C_4H_2, $CH_2C_2H_2$, CH_3C_2H, C_2H_2, C_2H_4, C_2H_6 and HC_3N are investigated in this work as potential parent molecules with a certain contribution to the observed cometary C_3 and C_2. Since many molecules, although present in the model, have not been searched for / detected in the comets investigated in this work, it is required to apply 'educated estimations' for their upper, nominal and lower production rate ratios c^{upper}, c^{nominal} and c^{lower}. These parameters are given in Table 8.4 and are motivated in the following text.

The Molecules C_2H_2, C_2H_6 and HC_3N

Figure 2.1 provides an overview of gas production rate ratios $c(\text{species}) = Q(\text{species})/Q(\text{H}_2\text{O})$, with respect to the water production rate $Q(\text{H}_2\text{O})$, of detected volatile species in cometary comae. Not all of these species are parent molecules, i.e. sublimate directly from the nucleus ices: HNC is mainly produced in the cometary coma, whereas H_2CO and CO are only partly produced there.

Table 8.3: *Boundary values for the comet chemistry model: the production rate ratio* $c(\text{species}) = Q(\text{species})/Q(\text{H}_2\text{O})$ *of various known cometary species, where* Q *is the production rate, the nucleus radius* $r_{nucleus}$*, the initial gas temperature* T_0 *and velocity* u_0*. For the comets NEAT, LINEAR and Tempel 1 these initial values are adopted in parts from Weiler (2006, 2012), as indicated in the table notes by ‡. Initial values for comet Hale-Bopp are from Weiler (2006) and from Helbert (2002), as indicated by † in the table notes. Parts of the initial values given in Weiler (2006) were updated in Weiler (2012). For the reproduction of the Weiler (2006) fits to the comets NEAT, LINEAR and Tempel 1 in the model validation (Chapter 6) the initial values of Weiler (2006) were used, which are also indicated in the table notes.*

comet	Hale-Bopp	NEAT	LINEAR	Tempel 1
r_h [AU]	3.78	1.00	1.20	1.51
$Q(\text{H}_2\text{O})$ [molecules s^{-1}]	$4 \cdot 10^{28}$ [a]	$2.6 \cdot 10^{29}$ [b]	$6.9 \cdot 10^{28}$ [c]	$3.4 \cdot 10^{27}$ [d]
$c(\text{CO})$	2.0175 [e]	0.042 [f]	0.04 [g]	0.147 [h]
$c(\text{CO}_2)$	0.68 [i]	0.04 [g]	0.04 [g]	0.04 [g]
$c(\text{CH}_4)$	0.0284 [j]	0.006 [k]	0.006 [k]	0.006 [k]
$c(\text{H}_2\text{CO})$	0.008 [e]	0.011 [k]	0.016 [l]	0.011 [k]
$c(\text{CH}_3\text{OH})$	0.0114 [e]	0.015 [m]	0.038 [m]	0.048 [d]
$c(\text{H}_2\text{S})$	0.0023 [e]	0.0023 [k]	0.0023 [k]	0.0023 [k]
$c(\text{NH}_3)$	0.0033 [j]	0.007 [k]	0.007 [k]	0.007 [k]
$c(\text{HCN})$	0.0082 [e]	0.00047 [n]	0.0033 [n]	0.006 [d]
$c(\text{HNCO})$	0.001 [k]	0.001 [k]	0.001 [k]	0.001 [k]
$c(\text{CH}_3\text{CN})$	0.00097 [e]	0.0002 [k]	0.0002 [k]	0.0002 [k]
$c(\text{NH}_2\text{CH}_3)$	0.0745 [j]	-	-	-
r_{nucleus} [km]	30.0 [o]	3.75 [p]	52.0 [q]	3.0 [r]
u_0 [m/s]	310.6 [s]	325.1 [s]	322.9 [s]	319.9 [s]
T_0 [K]	165.6 [s]	171.6 [s]	169.3 [s]	166.2 [s]

†: taken from Helbert (2002), Helbert et al. (2005), ‡: taken from Weiler (2006, 2012).
(a)† $Q(\text{H}_2\text{O})$ calculated in Helbert (2002), Helbert et al. (2005) using the sublimation model of Benkhoff and Huebner (1995) and Huebner and Benkhoff (1999), (b)‡ $Q(\text{H}_2\text{O}) = 2.6 \cdot 10^{29}$ molecules s^{-1} is an average of all production rates from 4-29+30-2004 Biver et al. (2009). Weiler (2006) used $Q(\text{H}_2\text{O}) = 1.9 \cdot 10^{29}$ molecules s^{-1} from Weaver et al. (1999), (c)‡ Howell et al. (2004), (d)‡ although this work uses the $Q(\text{H}_2\text{O})$ of Küppers et al. (2005), there is also $Q(\text{H}_2\text{O}) = 1.21 \cdot 10^{28}$ molecules s^{-1} from Mumma et al. (2005), see Section 8.2.1 for more information, (e)† interpolated from Biver et al. (1997), (f)‡ Feldman et al. (2004b), (g)‡ Despois et al. (2005), (h)‡ Feldman et al. (2006), (i)† extrapolation based on Weaver et al. (1999), assuming activity scaling like CO, (j)† extrapolations made by †, (k) based on values of Hale-Bopp at $r_h \approx 1$ AU in Bockelée-Morvan and Crovisier (2002), (l)‡ Milam et al. (2006), H_2CO from parent molecules. Weiler (2006) used $c(\text{H}_2\text{CO}) = 0.011$ based on Bockelée-Morvan and Crovisier (2002), (m)‡ Remijan et al. (2006a), (n)‡ Friedel et al. (2005), (o) Lamy et al. (2004), (p)‡ estimated by Tozzi et al. (2003), (q)‡ upper limit from Weiler et al. (2011), (r)‡ A'Hearn et al. (2005), (s)‡ T_0, u_0 calculated as described in Section 3.1.7. Helbert (2002) calculated $T_0 = 181$ K for Hale-Bopp but the difference to $T_0 = 165.6$ K calculated here does not influence the conclusions, see Weiler (2006).

Figure 2.1 shows that $c(C_2H_2)$ and $c(C_2H_6)$ have been detected in more than ten comets. Summaries of cometary C_2H_2 and C_2H_6 production rate ratios and the corresponding references can be found e.g. in Dello Russo et al. (2006a) and Bockelée-Morvan et al. (2004).

According to Figure 2.1 $c(HC_3N)$ seems to be detected in four comets. However, we found at least two comets with determined production rate ratios in the literature, namely for comet C/2002 X5 (Kudo-Fujikawa) at $r_h = 0.21$ AU $c(HC_3N) = 0.00081$ (Biver et al., 2011) and for Hale-Bopp at $r_h = 1$ AU $c(HC_3N) = 0.0002$ (Bockelée-Morvan et al., 2004). For comet C/2006 P1 (McNaught) a HC_3N production rate was determined but to our knowledge no water production rate (Biver et al., 2011). For several comets upper limits exist: comet 103P (Hartley 2) at $r_h = 1.064$ AU $c(HC_3N) < 0.00015$ (Dello Russo et al., 2011), comet C/2002 V1 (NEAT) ($\neq$ C/2001 Q4 **(NEAT)** used in the present work) at $r_h = 0.12$ AU $c(HC_3N) < 0.00045$ (Biver et al., 2011), C/2001 A2 (LINEAR) ($\neq$ C/2002 T7 **(LINEAR)** used in the present work) at $r_h = 1.1$ AU $c(HC_3N) < 0.0005$ (Biver et al., 2006) and comet 153P (Ikeya-Zhang) at $r_h = 1.0$ AU $c(HC_3N) < 0.0009$ (Biver et al., 2006).

$c(HC_3N)$ appears to be smaller than 0.001, in contrast to $c(C_2H_2)$ and $c(C_2H_6)$, which seem to be smaller than 0.01. The only reported $c(C_2H_6) = 0.016 > c_i^{\text{upper}} = 0.01$ to our knowledge was for comet C/2001 A2 (LINEAR) (Dello Russo et al., 2006b).

Hale-Bopp The production rate ratios of Hale-Bopp at $r_h = 1$ AU were $c(C_2H_2) = 0.002$, $c(C_2H_6) = 0.006$ and $c(HC_3N) = 0.0002$ (Bockelée-Morvan and Crovisier, 2002). However, during the observations of Hale-Bopp at $r_h = 3.78$ AU, investigated in the present work, the production rate ratios $c(C_2H_2)$, $c(C_2H_6)$ and $c(HC_3N)$ are higher due to the much lower production rate (volatility) of water, compared to $r_h = 1$ AU. This is since a species' production rate depends largely on its volatility and the available solar radiation, i.e. depending on r_h. Since water sublimates effectively at $r_h \lessapprox 3$ AU the activity of comet Hale-Bopp at $r_h = 3.78$ AU was then mainly driven by CO. For example, C_2H_6 already sublimates effectively at around $r_h \approx 20$ AU, see Section 3.1.1.

Helbert (2002) fitted a one-dimensional **(1D)** coma chemistry model (ComChem) (Giguere and Huebner, 1978, Boice et al., 1986, 1998, Huebner et al., 1987, Schmidt et al., 1988) to the observations of Hale-Bopp at $r_h = 3.78$ AU and obtained production rate ratios of $c(C_2H_6) \approx 0.033$ and $c(C_2H_2) \approx 0.017$. A factor two higher was reported in Weiler (2006) for C_2H_2, namely $c(C_2H_2) = 0.0265$ (using the reaction network of Helbert (2002), not their updated version with which no fits could be achieved to Hale-Bopp). C_2H_6 was disregarded in Weiler (2006) in contrast to Helbert (2002) as its contribution to C_2 was quoted to be insignificant. However, as stated in Chapter 7 the present work also investigates C_2H_6 in the SA performed in this chapter, since several updates were included for the photodissociation of the species $C_2H_{(6,5,4,3,2,1)}$. Extrapolating the empirical C_2H_6 scaling law $Q(C_2H_6, r_h) = (5.52 \pm 0.20) \cdot 10^{28} \cdot r_h^{(-2.43\pm0.13)}$ molecules s^{-1} of Dello Russo et al. (2001), determined from observations in the infrared **(IR)** over $r_h \approx 1 - 3.0$ AU, to $r_h = 3.78$ AU one obtains $Q(C_2H_6, 3.78\text{ AU}) = 2.18 \cdot 10^{27}$ molecules s^{-1}, i.e. $c(C_2H_6) \approx 0.05$ with $Q(H_2O, 3.78\text{ AU}) = 4 \cdot 10^{28}$ molecules s^{-1}.

Tempel 1 For comet Tempel 1 there have been measurements of C_2H_2 and C_2H_6 production rate ratios, however not at the time of the observations used in this work, i.e. during the night of 3/4 July 2005 close before the *Deep Impact* event. At $r_h = 1.54$ AU on 10 June 2005 Mumma et al. (2005) determined $c(C_2H_6) \approx 0.00194$ and the first detection of C_2H_2 was only after the *Deep Impact* event on 4 July 2005 at $r_h = 1.51$ AU. However, $c(C_2H_2) \approx 0.0013$ and $c(C_2H_6) \approx 0.0035$ are uncertain due to the change of the coma from steady state as assumed in the excitation model of Mumma et al. (2005). $c(HC_3N)$ is unknown.

NEAT and LINEAR For the comets NEAT and LINEAR the production rate ratios of C_2H_2, C_2H_6 and HC_3N are unknown.

The Molecule C_2H_4

For C_2H_4, which is thought to be an intermediate in the formation of C_2H_6 in cometary ices, via hydrogenation of C_2H_2, there exists only one upper limit, namely $c(C_2H_4) < 0.006$ for comet C/2007 N3 **(Lulin)** (Kobayashi, 2012, pers. comm.), see also Kobayashi and Kawakita (2010), Kobayashi et al. (2012). This molecule is investigated as an additional C_2 parent molecule in this work.

The Molecules C_4H_2, $CH_2C_2H_2$, CH_3C_2H

The proposed C_3 parent molecules $CH_2C_2H_2$, CH_3C_2H (C_3H_4 isomers) and C_4H_2 have not been detected in comets up until now. For comet Hale-Bopp at $r_h = 0.9$ AU an upper limit is reported, i.e. $Q(CH_3C_2H) < 4 \cdot 10^{27}$ molecules s^{-1}, which corresponds to a production rate ratio upper limit of $c(CH_3C_2H) < 0.00045$ with the reported water production rate $Q(H_2O, 0.9\text{ AU}) \approx 9 \cdot 10^{30}$ molecules s^{-1} (Crovisier et al., 2004). The comet's production rate ratio $c(CH_3C_2H)$ with respect to water at $r_h = 3.78$ AU is also not known but might be higher than at 0.9 AU since at $r_h = 3.78$ AU the water sublimation is not effective. C_4H_2, $CH_2C_2H_2$ and CH_3C_2H should sublimate effective at $r_h = 3.78$ AU (these species have a smaller sublimation temperature than e.g. CH_3OH (ChemSpider, 2014) which sublimates effectively already at $r_h \lessapprox 5$ AU as shown in Figure 3.1a of Chapter 3). At $r_h = 3.78$ AU the water production rate is $Q(H_2O, 3.78\text{ AU}) = 4 \cdot 10^{28}$ molecules s^{-1}.

Helbert (2002) reports a fitted $c(C_3H_4) \approx 0.014$ for the observations of Hale-Bopp at $r_h = 3.78$ AU. Weiler (2006) reports a factor of three higher $c(C_3H_4) = 0.042$ (using the reaction network of Helbert (2002), not their updated version with which no fits could be achieved to Hale-Bopp). Both studies used C_3H_4 as a representative for both the C_3H_4 isomers CH_3C_2H and $CH_2C_2H_2$.

Summary

For comet Hale-Bopp at $r_h = 3.78$ AU the present work assumes $c^{\text{upper}} = 0.1$, $c^{\text{nominal}} = 0.01$ and $c^{\text{lower}} = 0$ for C_4H_2, $CH_2C_2H_2$ and CH_3C_2H, C_2H_2, C_2H_4 and C_2H_6. For HC_3N an order of magnitude smaller values are assumed. For the comets NEAT, LINEAR and Tempel 1 observed at $1 - 1.5$ AU, where water sublimation is effective, the present work assumes $c^{\text{upper}} = 0.01$, $c^{\text{nominal}} = 0.001$ and $c^{\text{lower}} = 0$. For HC_3N an order of magnitude smaller values are assumed. See Table 8.4 for an overview.

8.3 Results of the Global Sensitivity Analysis (GSA)

This section presents the results obtained by applying a GSA. Discussed are the computed column density distributions and the reactions whose uncertainties most affect the modeled C_3 and C_2 column densities, i.e. the *key reactions* (determined with the help of the RCCs defined in Equation (8.8)).

Section 8.3.1 investigates a 'nominal composition' of the parent molecules C_4H_2, $CH_2C_2H_2$, CH_3C_2H, C_2H_2, C_2H_4, C_2H_6 and HC_3N which are summarized in Table 8.4, i.e. all investigated parent molecule production rate ratios were set to c^{nominal}. Section 8.3.2 extends Section 8.3.1 by investigating also the correlation of each parent molecule's production rate ratio with the

Table 8.4: *Upper c^{upper}, nominal $c^{nominal}$ and lower c^{lower} parent molecule production rate ratios $c(\text{parent}) = Q(\text{parent})/Q(H_2O)$ used in the present work. For the observations of comet Hale-Bopp at $r_h = 3.78$ AU c^{upper} and $c^{nominal}$ of one order of magnitude higher are assumed (see † in the legend) as suggested by observations and as discussed in Section 8.2.2. For* HC_3N *one order of magnitude smaller c^{upper} and $c^{nominal}$ are assumed.*

parent molecules	c_i^{lower}	$c_i^{\text{nominal}\dagger}$	$c_i^{\text{upper}\dagger}$
$CH_2C_2H_2$, CH_3C_2H, C_4H_2,[a] C_2H_6,[b] C_2H_4,[c] C_2H_2	0	0.001	0.01
HC_3N [d]	0	0.0001	0.001

† For the comets NEAT, LINEAR, Tempel 1 observed at $r_h = 1-1.5$ AU. For comet Hale-Bopp observed at $r_h = 3.78$ AU c^{upper} and c^{nominal} of one order of magnitude higher are assumed.

[a] Despois et al. (2005) report $c(C_4H_2) < 0.0005$ taken from the talk of Magee-Sauer et al. (2002) as a tentative upper limit for comet 153P (Ikeya-Zhang). Magee-Sauer (2012, pers. comm.) notes that the C_4H_2 emissions were blended with NH_3 and H_2O emissions. Therefore, this upper limit should not be used.

[b] The only reported $c(C_2H_6) = 0.016 > c_i^{\text{upper}} = 0.01$ to our knowledge was for comet C/2001 A2 LINEAR (Dello Russo et al., 2006b).

[c] There exists only one upper limit estimate, i.e. $c(C_2H_4) < 0.006$, for comet Lulin Kobayashi (2012, pers. comm.), see also Kobayashi and Kawakita (2010), Kobayashi et al. (2012).

[d] The upper limit is based on the low production rate ratios and upper limits determined for several comets.

C_3 and C_2 column densities. Section 8.3.3 regards each parent molecule separately since each comet can have a different composition.

8.3.1 Photodissociation Rate Coefficients

Column Density Histograms

Figure 8.1 shows eight panels split into C_3 (left) and C_2 (right). Shown are the column density probability distributions (shown as a histogram with binsize $\Delta\text{alog}_{10}(\text{col.dens.}) \times \Delta\text{alog}_{10}(r_c) = 0.02 \times 0.02$) of C_3 and C_2 for the comets NEAT (upper panels), LINEAR (first middle panels), Tempel 1 (second middle panels) and Hale-Bopp (bottom panels) computed in the present work. The column density histograms are color coded from black to red, from 0 to 1800 model runs (distributed from the $n_{\text{MC}} = 10,000$ total model runs).

The histograms suggest large uncertainties, from $\approx (0.5-2.0)$ orders of magnitudes, which are larger than the uncertainties of the observations. In the observational range the uncertainties are $\approx (0.5-1.0)$ order of magnitude for C_3 and C_2. Larger uncertainties are observed for C_3 at $r_c > 10^5$ km. For all comets quite similar uncertainties can be seen.

C_3 **Results** The C_3 column density histograms in Figure 8.1 (left panels) suggest that for comet Tempel 1 (third panel) the shape of the most likely column density profile (lightblue area) is quite close, although not similar, to the shape of the observational column densities. For the comets NEAT and Hale-Bopp (top and bottom panels) the profile shapes differ. This feature is even more evident for comet LINEAR (second panel). However, it seems likely that the shape of the C_3 observations can be matched with a specific composition of the investigated parent molecules and a specific set of photodissociation rate coefficients.

C_2 **Results** The C_2 column density histograms in Figure 8.1 (right panels) suggest that the shape of the most likely profile (lightblue) and the observations are similar for comet NEAT and Hale-Bopp (top and bottom panels). For comets LINEAR and Tempel 1 (second and third panels) the observations are steeper at large r_c than the most likely profile. This may have various reasons, e.g. different parent molecules in the cometary ices than investigated in the present work or outgassing variabilities. See Chapter 9 for more details. The present chapter discusses some trends whereas Chapter 9 aims at drawing more detailed conclusions as to whether the the observations can be reproduced with the parent molecules investigated in the present work by optimizing their production rate ratios and the photodissociation reactions' rate coefficients within their uncertainties.

Correlations of C_3 and C_2 With the Photodissociation Rate Coefficients

Figure 8.2 shows the RCCs between column density (top panel C_3 and bottom panel C_2) and rate coefficients. The discussion focuses on comet NEAT, which is taken to be representative for all four comets, since the conclusions for the *key reactions* are mostly similar for all four comets.

The region between the vertical dotted lines is the region where observations are generally available, see also Figure 8.1. The Max(r_s), inside the observational range, is plotted on the right hand side of each plot below 'data'. The reactions are arranged according to these values. The column marked 'total' gives the highest absolute RCC value within the complete range shown. The following discussion also makes use of the correlation strength classification, introduced in Table 8.2. Only reactions with a RCC of $r_s \geq 0.16$ are discussed.

C_3 **Response** The top panel of Figure 8.2 shows that in the observational range the uncertainty is mainly due to reaction

$$C_3 + \gamma \rightarrow C_2 + C \tag{R1}$$

with an absolute correlation of nearly one. The correlation is negative, since C_3 is destroyed in this reaction. The reason for the large uncertainty in the C_3 column densities in the range of the observations (r_{obs}) and at $r_c > r_{\text{obs}}$, see left panels of Figure 8.1, is therefore mainly due to this reaction. The next most important reactions in the observational range are

$$CH_2C_2H_2 + \gamma \rightarrow C_3H_2 + H_2\,, \tag{R2}$$
$$CH_2C_2H_2 + \gamma \rightarrow C_3H_3 + H \tag{R3}$$

with a low to moderate correlation. These reactions also have an effect at $r_c < r_{\text{obs}}$. However, the column density uncertainty at $r_c < r_{\text{obs}}$ is more affected by the reactions

$$C_3H_2 + \gamma \rightarrow C_3 + H_2\,, \tag{R4}$$
$$C_3H_2 + \gamma \rightarrow C_3H + H\,, \tag{R5}$$
$$C_3H + \gamma \rightarrow C_3 + H \tag{R6}$$

and

$$C_3H_3 + \gamma \rightarrow C_3H_2 + H\,, \tag{R7}$$
$$C_3H_3 + \gamma \rightarrow C_3H + H_2\,. \tag{R8}$$

Reaction (R4) has the largest correlation. This is a likely reason that reaction (R2) has a larger uncertainty effect at $r_c < r_{\text{obs}}$ than reaction (R3).

Weak correlations in the observational range are observed for the reactions

$$C_4H_2 + \gamma \rightarrow C_4 + H_2 \tag{R9}$$

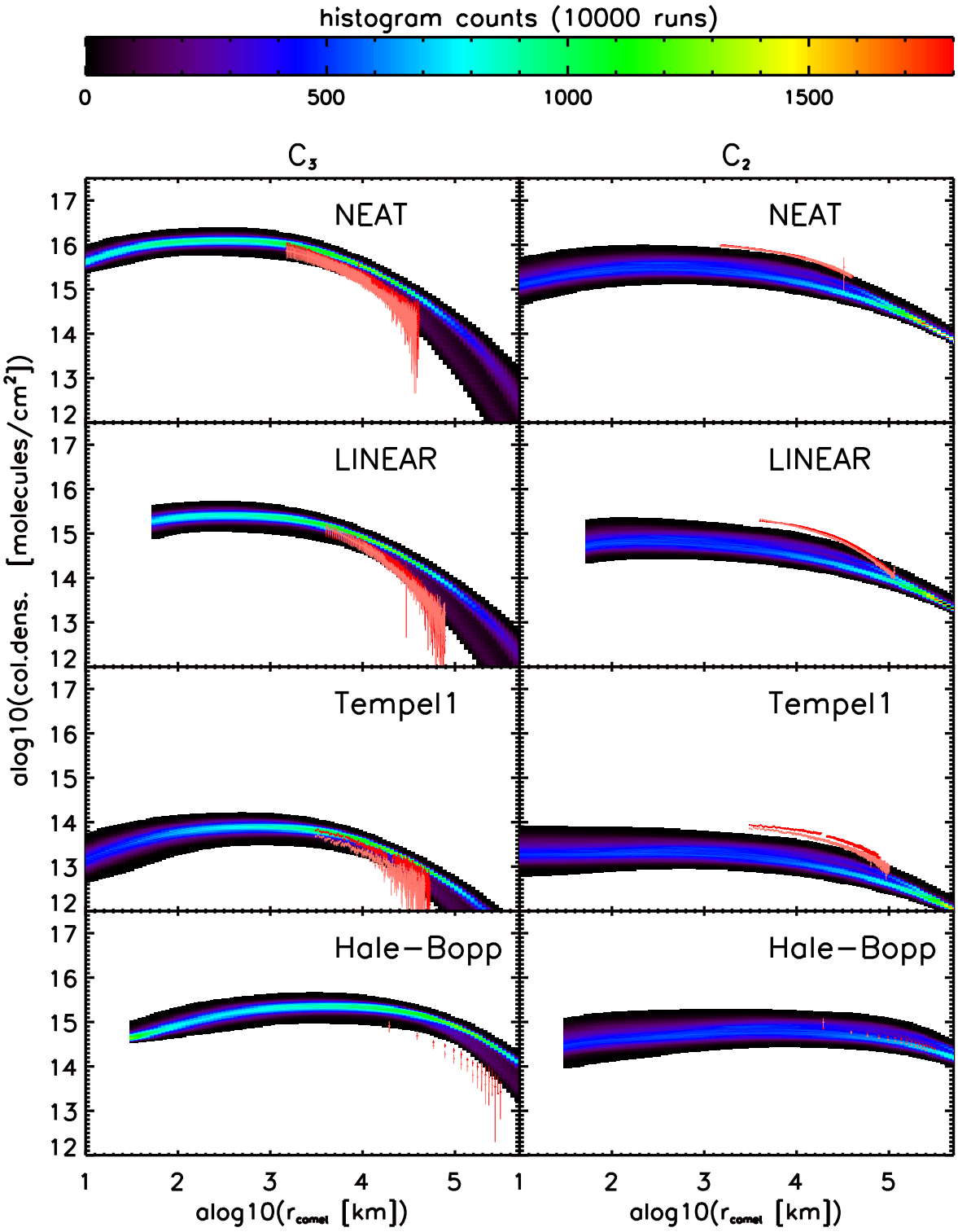

Figure 8.1: *Probability distributions (histograms) of the* C_3 *and* C_2 *column densities for the comets NEAT, LINEAR, Tempel 1 and Hale-Bopp resulting from the propagation of the uncertainties of the rate coefficients via MC. Each parent molecule production rate ratio was set to its nominal value* $c^{nominal}$ *as given in Table 8.4. Red and lightred crosses indicate the sunward and tailward observations, respectively.*

and

$$CH_3C_2H + \gamma \rightarrow C_3H_2 + H_2\,, \tag{R10}$$
$$CH_3C_2H + \gamma \rightarrow C_3H_3 + H\,. \tag{R11}$$

Reactions (R10) and (R13) affect the uncertainty less than the reactions (R2) and (R3), since the median rate coefficients of CH_3C_2H are approximately an order of magnitude smaller than those of $CH_2C_2H_2$, see Figure 7.12. The same is true for reaction (R9) with nearly two orders of magnitude difference between the median rate coefficients. See also Figure 8.5 in Section 8.3.3 in which each parent molecule alone is investigated.

The upper panel of Figure 8.3 depicts the source and loss of the C_3 densities (not column densities) along r_{comet} by the various reactions in the coma chemistry model for the nominal model run, i.e. $k_i = k_i^{\text{median}} \approx k_i^{\text{mode}}$, where k_i^{mode} is the most likely photodissociation rate coefficient value of reaction i (values presented in Section 7.3) for comet NEAT. Additionally, each parent molecule production rate ratio was set to its nominal value c^{nominal} as given in Table 8.4. The source and loss of the densities are shown here, since these are adequate to qualitatively understand the most important source and loss processes for the column densities, see also Section 5.5 for the relation between densities and column densities. The plot indicates that in the observational range up to two orders of magnitude more C_3 is produced from $CH_2C_2H_2$ and CH_3C_2H via reactions (R4) and (R6) (C_3H is mainly produced from $CH_2C_2H_2$ and CH_3C_2H and not from C_4H) than from C_4H_2 via the reactions

$$C_4 + \gamma \rightarrow C_3 + C\,, \tag{R12}$$
$$C_4H + \gamma \rightarrow C_3 + CH\,. \tag{R13}$$

As already mentioned by Helbert (2002) and Weiler (2006) at $r_{\text{comet}} < 10^2$ km C_3 is mainly produced via

$$C_3H_5^+ + e^- \rightarrow C_3 + H_2 + H_2 + H\,, \tag{8.9}$$

which is mainly produced via $H_3O^+ + CH_2C_2H_2\,(CH_3C_2H) \rightarrow C_3H_5^+ + H_2O$.

C_2 **Response** The bottom panel of Figure 8.2 shows that in the observational range reaction (R1) has the largest uncertainty effect. Reaction

$$C_4H_2 + \gamma \rightarrow C_2H_2 + C_2\,, \tag{R14}$$

has a moderate to strong correlation in the observational range and a very strong correlation at $r_c < r_{\text{obs}}$ due to the production of C_2 in one step. The C_2H reactions

$$C_2H + \gamma \rightarrow C_2 + H\,, \tag{R15}$$
$$C_2H + \gamma \rightarrow CH + C \tag{R16}$$

have a small correlation in the outer observational range, since there the uncertainty is dominated by reaction (R1). A moderate correlation is observed at $r_c = 10^5$ km $> r_{\text{obs}}$, however, the model C_2 column density uncertainties are quite small there.

The lower panel of Figure 8.3 depicts the source and loss of the C_2 densities (not column densities) along r_{comet} for the nominal model run for comet NEAT by the various reactions in the coma chemistry model. It indicates e.g. that reaction

$$C_2 + \gamma \rightarrow C_2^+ + e^- \tag{R17}$$

is the main loss of C_2 at $r_c > 10^3$ km, i.e. in the observational range and beyond. Between $r_c = 10^3$ km and $r_c = 10^4$ km reaction (R1) begins to exceed reaction (R14) regarding C_2 production.

The reaction (R16) shows a positive correlation with the C_2 column density uncertainty, because the main uncertainty of the C_2H photodissociation reactions is due to the total rate coefficient k, see Equation (7.11). The Figures 7.13 and 7.14 show that e.g. at 2σ level the k is uncertain by ≈ 2 orders of magnitude whereas the full branching ratios are uncertain by $\lessapprox 1$ order of magnitude, i.e. the k_i of the reactions (R15) and (R16) are coupled to a certain degree despite the branching ratio uncertainties. Additionally, the most likely values of both reactions are nearly identical as indicated by Figure 7.12 (green crosses, third and fourth line).

Relatively small correlations are found for the reactions

$$C_4H_2 + \gamma \rightarrow C_4H + H\,, \tag{R18}$$

$$C_2H_2 + \gamma \rightarrow C_2 + H_2 \tag{R19}$$

at $r_c \neq r_{\text{obs}}$.

Comparison to the Local Sensitivity Analysis

Mostly the same reactions are found in the LSA compared to the GSA (although in a slightly different order of importance in the range of the observations). This is because nearly all reactions have significant uncertainties and so the most efficient reactions, determined in the LSA, appear also as important model uncertainty affecting reactions as determined in the GSA.

The effective C_2 destroying reaction $C_2 + \gamma \rightarrow C_2^+ + e^-$ was more important in the LSA. This is because in the LSA its rate coefficient is varied by a constant factor and in the GSA not, since in Chapter 7 the uncertainty of this reaction was estimated to be very small in comparison to the main uncertainties discussed in that Chapter.

8.3.2 Parent Molecule Production Rate Ratios

The purpose of this section is to investigate which parent molecule's production rate ratio mostly affects the C_3 and C_2 model column densities, i.e. to highlight the importance of each parent molecule with respect to r_{comet}. For this purpose the rate coefficient uncertainties were again propagated via MC. Additionally, for each parent molecule a uniform production rate ratio distribution was included into the MC computation, defined over the interval $[c^{\text{upper}}, c^{\text{nominal}}]$, see Table 8.4, to model a certain production rate ratio uncertainty in order to be able to investigate the correlation of the C_3 and C_2 column densities with the production rate ratios of each parent molecule. All parent molecules were included into the MC computation. Shown are the results for comet NEAT, as the results are mostly similar for all four comets.

Figure 8.4 shows the RCCs between C_3 (left panel) and of C_2 (right panel) with the parent molecule production rate ratios of C_4H_2, $CH_2C_2H_2$, CH_3C_2H, C_2H_2, C_2H_4, C_2H_6 and HC_3N. In this figure the observational range is indicated by the two vertical dotted lines.

C_3 **Response** The left panel of Figure 8.4 shows that $CH_2C_2H_2$ dominates the uncertainty of the C_3 column densities. The reason is that the median rate coefficients of $CH_2C_2H_2$ are at least an order of one magnitude larger than those of CH_3C_2H, see Figure 7.12. C_4H_2 has a smaller effect on the C_3 uncertainty in the region of interest.

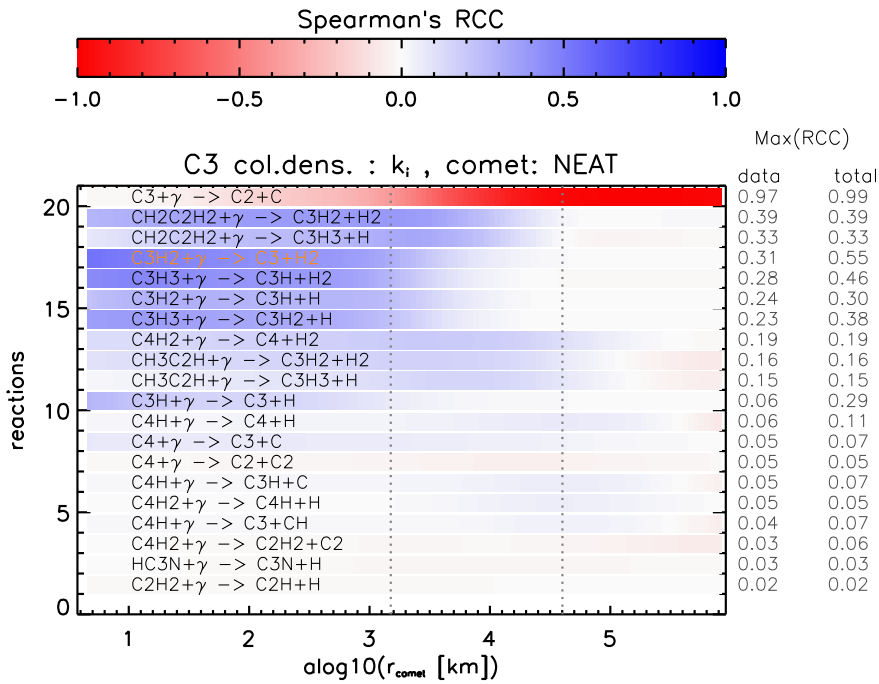

(a) *Correlation of the* C_3 *column densities with the rate coefficients* k_i

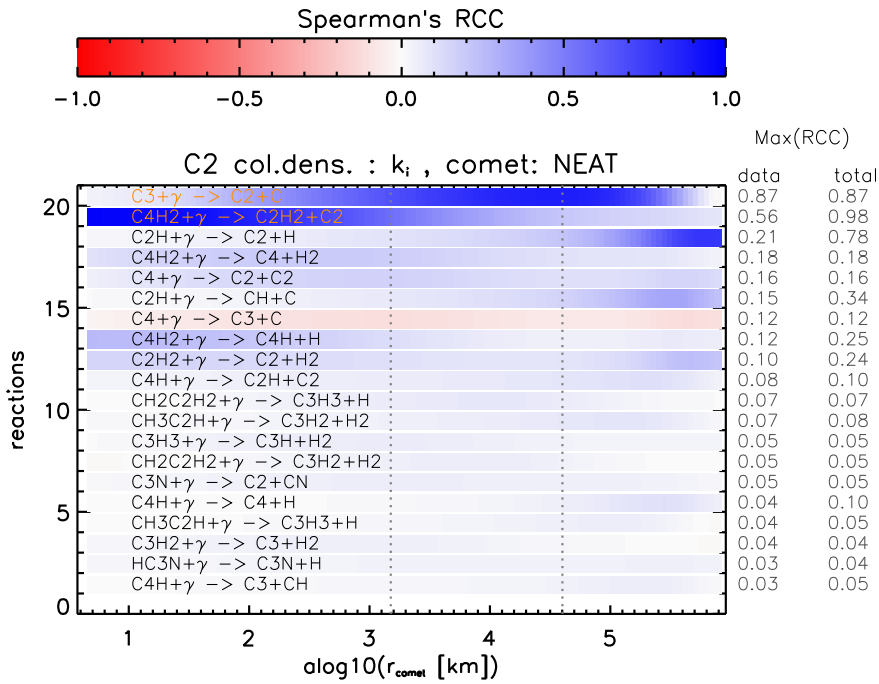

(b) *Correlation of the* C_2 *column densities with the rate coefficients* k_i

Figure 8.2: *Main 20 RCCs* r_s *for comet NEAT, showing the correlation of the* C_3 *(top panel) and* C_2 *column densities (bottom panel) with the rate coefficients* k_i*. All parent molecule production rate ratios were set to the nominal production rate ratio value* $c^{nominal}$*, given in Table 8.4. The vertical dotted lines mark the range of the observations. The column marked 'data' gives the highest absolute RCC value only within the range of the two dotted lines. The column marked 'total' gives the highest absolute RCC value within the complete range shown. Some reactions are colored in red for better reading.*

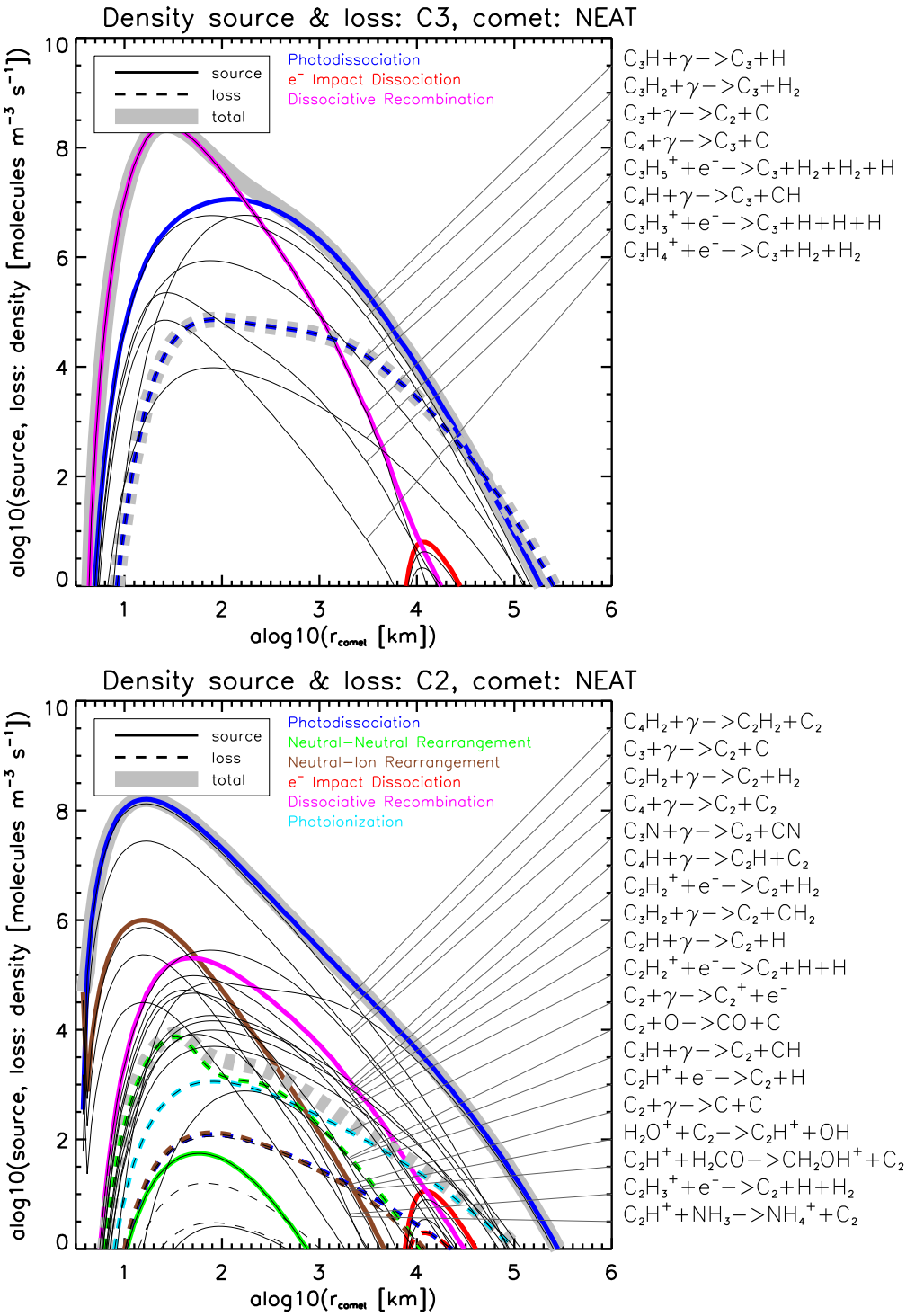

Figure 8.3: *Source (solid lines) and loss (dashed lines) of the* C_3 *(upper panel) and* C_2 *(lower panel) densities by the different types of reactions in the model for the nominal model run, i.e. applying the median photo rate coefficients* $k_i^{median} \approx k_i^{mode}$*, see Table 7.4, for the investigated hydrocarbon photo reactions, for comet NEAT. Each parent molecule production rate ratio was set to its nominal value* $c^{nominal}$ *as given in Table 8.4. The total source and loss of each reaction type is color coded. The solid and dashed thick gray shaded lines indicate the total source and loss from all reactions, respectively. Additionally, sources and sinks due to individual reactions (profiles colored in black) are indicated and marked on the right-hand side.*

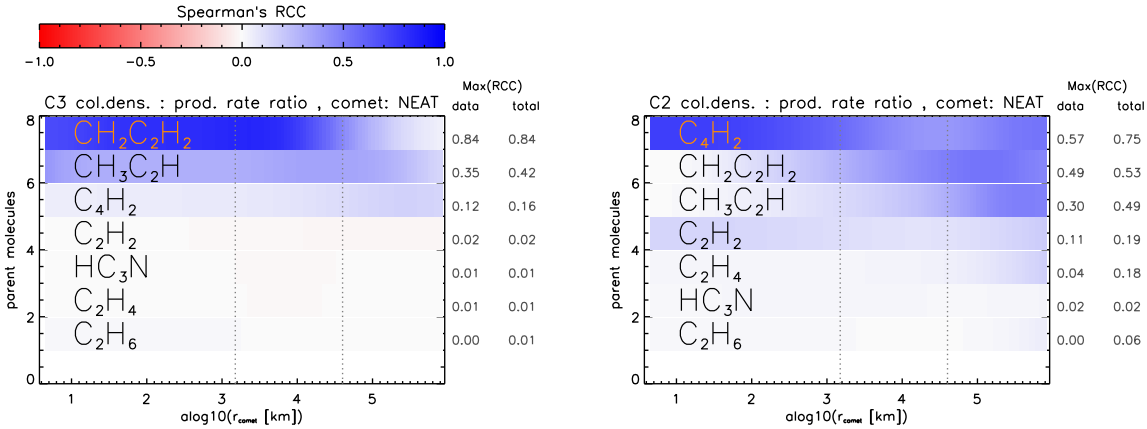

Figure 8.4: *RCCs r_s for comet NEAT, showing the correlation of the* C_3 *(left panel) and* C_2 *(right panel) column densities with the parent molecule production rate ratios* c(parent)*. The vertical dotted lines mark the range of the observations. The column marked with 'data' gives the highest RCC only within the range of the two dotted lines. The column marked with 'total' gives the highest RCC within the complete range shown. Some species are colored in red for better reading.*

C_2 **Response** The right panel of Figure 8.4 shows that C_4H_2 dominates the uncertainty of the C_2 column densities from small to $\text{alog}_{10}(r_c) = 4$ via the reaction (R14) and the other C_4H_2 dissociation reactions as well as via reactions

$$C_4 + \gamma \rightarrow C_2 + C_2 \tag{R20}$$

and (R19), see Figure 8.2b. The strongest correlation at the outer observational range, however, is seen for $CH_2C_2H_2$, which is due to the reaction (R1). CH_3C_2H has a comparable uncertainty effect at even larger r_c due to the smaller median rate coefficients than $CH_2C_2H_2$. C_2H_2 has a low correlation over the entire cometocentric distance. The correlation with C_2H_4 is very low. This is because the reaction path from C_2H_4 to C_2 is larger than e.g. for the path from C_2H_2 to C_2. This is also the reason for the C_2H_6 correlation which is almost zero. HC_3N has also a negligible effect because the production rate ratios c^{upper} and c^{nominal}, see Table 8.4, are an order of magnitude smaller than for the other parent molecules.

8.3.3 Single Parent Molecules

This section investigates singly each of the parent molecules $CH_2C_2H_2$, CH_3C_2H, C_4H_2, C_2H_2, C_2H_4, C_2H_6 and HC_3N. Figure 8.5 shows the C_3 (left panels) and C_2 column densities (right panels) resulting from propagation of the photodissociation rate coefficients via MC resulting from including only one of the following parent molecules, from top to bottom, $CH_2C_2H_2$, CH_3C_2H, C_4H_2, C_2H_2, C_2H_4, C_2H_6 and HC_3N, using $c_i = c^{\text{upper}}$. Additionally, this section reports for each parent molecule the main *key reaction*, in the observational range, with respect to C_3 and C_2. The results are discussed for comet NEAT only, because the conclusions are mostly similar for all four comets.

C_3 Results

It can be seen in the top three left panels of Figure 8.5 that $c_i \leq c^{\text{upper}}$ of either $CH_2C_2H_2$, CH_3C_2H or C_4H_2 can account for the observed C_3.

C_4H_2 gives rise to the largest uncertainty in the C_3 column densities at $r_c \leq 10^5$ km, i.e. nearly two orders of magnitude in comparison to $CH_2C_2H_2$ and CH_3C_2H with at most one order of magnitude. However, the shapes of the C_3 model profiles in the $CH_2C_2H_2$ and the CH_3C_2H cases is still quite uncertain.

For the C_3 cases of C_2H_2, C_2H_4 and C_2H_6 in Figure 8.5 there features neutral-ion rearrangement reactions, such as e.g.

$$C_2H_6 + C_2H_3^+ \longrightarrow C_3H_5^+ + CH_4\,, \tag{R21}$$
$$C_2H_6 + C_2H_2^+ \longrightarrow C_3H_5^+ + CH_3\,, \tag{R22}$$
$$C_2H_4 + C_2H_4^+ \longrightarrow C_3H_5^+ + CH_3\,, \tag{R23}$$
$$CH_4 + C_2H_3^+ \longrightarrow C_3H_5^+ + H_2 \tag{R24}$$

The C_3 containing ions directly produce C_3 via the electron-impact reaction

$$C_3H_5^+ + e^- \longrightarrow C_3 + 2 \cdot H_2 + H\,. \tag{R25}$$

For C_2H_6 these production routes have already been mentioned in Helbert (2002) and Weiler (2006). In the present work the production effectiveness is increased due to the newly included photoionization of C_2H_3 and photodissociative ionization of C_2H_6 to $C_2H_4^+$. However, their contribution to the C_3 in the observational range remains negligible.

C_2 Results

Figure 8.5 suggests that for $CH_2C_2H_2$ (upper right panel), CH_3C_2H (sixth right panel) and C_4H_2 (fifth right panel) $c \leq c^{\text{upper}}$ is sufficient to explain the amount of the observed C_2. The results also suggest that C_2H_2 can explain the amount of observed C_2 only if $c_i = c^{\text{upper}}$ and if C_2H_2 photodissociates very efficiently. C_2H_4 and HC_3N, on the other hand, only produce minor amounts of C_2, when setting $c_i = c_i^{\text{upper}}$. Note that c_i^{upper} of HC_3N is one magnitude lower than for the other parent molecules, see Table 8.4. As already discussed in Helbert (2002) for Hale-Bopp and Weiler (2006) for the comets NEAT, LINEAR and Tempel 1 C_2H_6 contributes only little to the observed C_2 which is also suggested by Figure 8.5.

C_3 and C_2 *Key Reactions* of Each Parent Molecule in the Observational Range

Table 10.1 presents the *key reactions* with RCC $\gtrapprox$ 0.5 for each parent molecule in the observational range, i.e. $r_c \approx 10^3 - 4 \cdot 10^4$ km, $r_c \approx 4 \cdot 10^3 - 10^5$ km, $r_c \approx 3 \cdot 10^3 - 10^5$ km, $r_c \approx 2 \cdot 10^4 - 3 \cdot 10^5$ km, for the comets NEAT, LINEAR, Tempel 1 and Hale-Bopp, respectively, see also Figure 4.2.

Table 10.1 also presents the key reactions for the mixture of the parent molecules C_4H_2, $CH_2C_2H_2$, CH_3C_2H, C_2H_2, C_2H_4, C_2H_6 and HC_3N using a nominal composition, see Table 8.4, as investigated in Section 8.3.1. The key reactions are the same for each comet as in the case of the single parent molecules.

Maximum Production of the C_2 Parent Molecules C_2H_4, HC_3N and C_2H_6

Figure 8.6 compares for each comet the observational C_2 column densities with the 0.999 percentile lines of the C_2 probability distribution produced from the parent molecules C_2H_4, C_2H_6 and HC_3N, when setting $c_i = c_i^{\text{upper}}$, see Table 8.4. This Figure is similar to Figure 8.5 except that data is now shown for all four investigated comets. Each of the four panels shows for the parent molecules C_2H_4, C_2H_6 and HC_3N the value $r = \text{Min}(O/M)$ (on the upper right) defined

Table 8.5: *Overview of the key reactions with a rank correlation coefficient* ***(RCC)*** $r_s \gtrapprox 0.5$ *for the* C_3 *and* C_2 *column densities in the observational range, i.e.* $r_c \approx 10^3 - 4 \cdot 10^4$ *km,* $r_c \approx 4 \cdot 10^3 - 10^5$ *km,* $r_c \approx 3 \cdot 10^3 - 10^5$ *km,* $r_c \approx 2 \cdot 10^4 - 3 \cdot 10^5$ *km, for the comets NEAT, LINEAR, Tempel 1 and Hale-Bopp, respectively, for each of the parent molecules* C_4H_2, $CH_2C_2H_2$, CH_3C_2H, C_2H_2, C_2H_4, C_2H_6 *and* HC_3N *alone (this Section 8.3.3) and for a mixture including all parent molecules* C_4H_2, $CH_2C_2H_2$, CH_3C_2H, C_2H_2, C_2H_4, C_2H_6 *and* HC_3N *with a nominal production rate ratio* $c^{nominal}$ *as provided by Table 8.4, see also Section 8.3.1 and Figure 8.2.*

parent molecule(s)	*key reactions* ($r_s > 0.5$)	
	for C_3	for C_2
C_4H_2	$C_4H_2 \xrightarrow{\gamma} C_4 + H_2$ $C_3 \xrightarrow{\gamma} C_2 + C$	$C_4H_2 \xrightarrow{\gamma} C_2H_2 + C_2$
$CH_2C_2H_2$	$C_3 \xrightarrow{\gamma} C_2 + C$ $CH_2C_2H_2 \xrightarrow{\gamma} C_3H_2 + H_2$	$C_3 \xrightarrow{\gamma} C_2 + C$ $C_3H_2 \xrightarrow{\gamma} C_3 + H_2$
CH_3C_2H	as for $CH_2C_2H_2$	as for $CH_2C_2H_2$
C_2H_2	-	$C_2H_2 \xrightarrow{\gamma} C_2 + H_2$ $C_2H \xrightarrow{\gamma} C_2 + H$
C_2H_4	-	as for C_2H_2
C_2H_6	-	as for C_2H_2
HC_3N	-	$C_3N \xrightarrow{\gamma} C_2 + CN$
mixture of C_4H_2, $CH_2C_2H_2$, CH_3C_2H, C_2H_2, C_2H_4, C_2H_6, HC_3N	$C_3 \xrightarrow{\gamma} C_2 + C$	$C_3 \xrightarrow{\gamma} C_2 + C$ $C_4H_2 \xrightarrow{\gamma} C_2H_2 + C_2$

as the ratio of the column densities between the observations (O, red, orange) and the model (M, colored solid lines), chosen at a value of r_{comet}, such that the ratio (O/M) is a minimum.

For comet NEAT the upper left panel of this Figure shows e.g. that C_2H_6 has a discrepancy of at least a factor of 17 for C_2. C_2H_6 produces (probably) up to an order of magnitude smaller amounts of C_2 than C_2H_4 or HC_3N. The ratio is lower for comet LINEAR and Tempel 1. Note that for comet NEAT the data does not extend to such r_c distances as for the comets LINEAR, Tempel 1 and Hale-Bopp. The results suggest that only a very small part of the observed C_2 of the comets may come from C_2H_6, qualitatively confirming Weiler (2006) for the comets NEAT, LINEAR, Tempel 1 and Helbert (2002) for comet Hale-Bopp. HC_3N also produces only small amounts of C_2 when assuming a maximum production rate ratio c^{upper} an order of magnitude smaller than for the other investigated parent molecules, as suggested by observations.

8.4 Summary and Conclusion

The present chapter has shown that the photodissociation rate coefficient uncertainties lead to significant uncertainties in the modeled C_3 and C_2 column densities. Using a GSA this work determined for the first time the so-called *key reactions*, i.e. the reactions that have the largest effect on the model output uncertainty, for the C_3 and C_2 photochemistry in cometary comae.

The key reactions with RCC $r_s \gtrapprox 0.5$, i.e. a moderate to strong correlation, in the observational range are as follows. For C_3 formation from $CH_2C_2H_2/CH_3C_2H$ these are the reactions $C_3 + \gamma \rightarrow C_2 + C$ and $CH_2C_2H_2/CH_3C_2H + \gamma \rightarrow C_3H_2 + H_2$. For C_4H_2 it is reaction $C_4H_2 + \gamma \rightarrow C_4 + H_2$

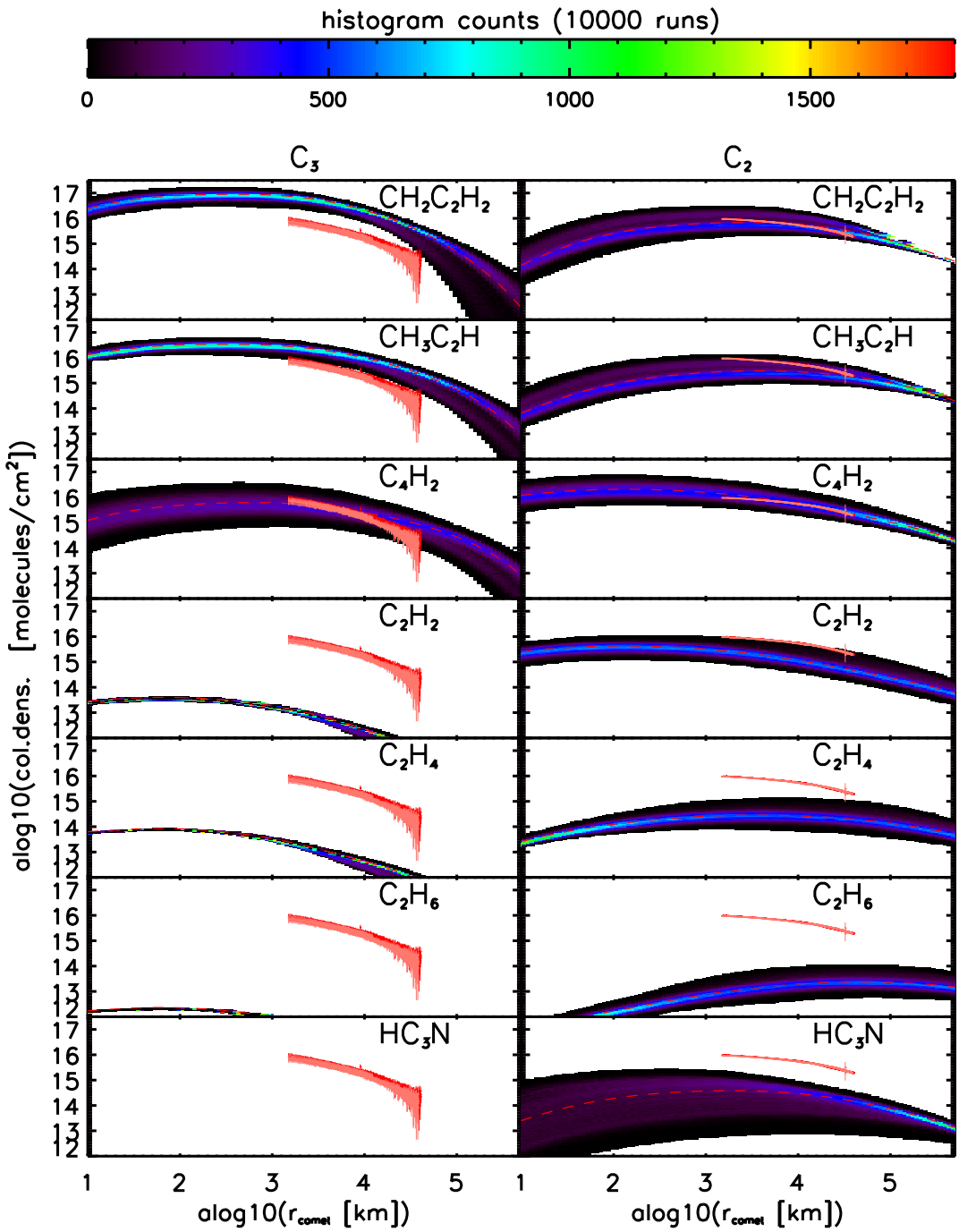

Figure 8.5: *Probability distributions (histograms) of the* C_3 *(left panels) and* C_2 *(right panels) column densities for comet NEAT resulting from the propagation of the uncertainties of the rate coefficients via MC. Results all use* c_i^{upper} *values given in Table 8.4. The red dashed line marks the model profile obtained by applying* $k_i = k_i^{median}$*, see Table 7.4. The sunward and tailward observations are plotted in red and lightred, respectively.*

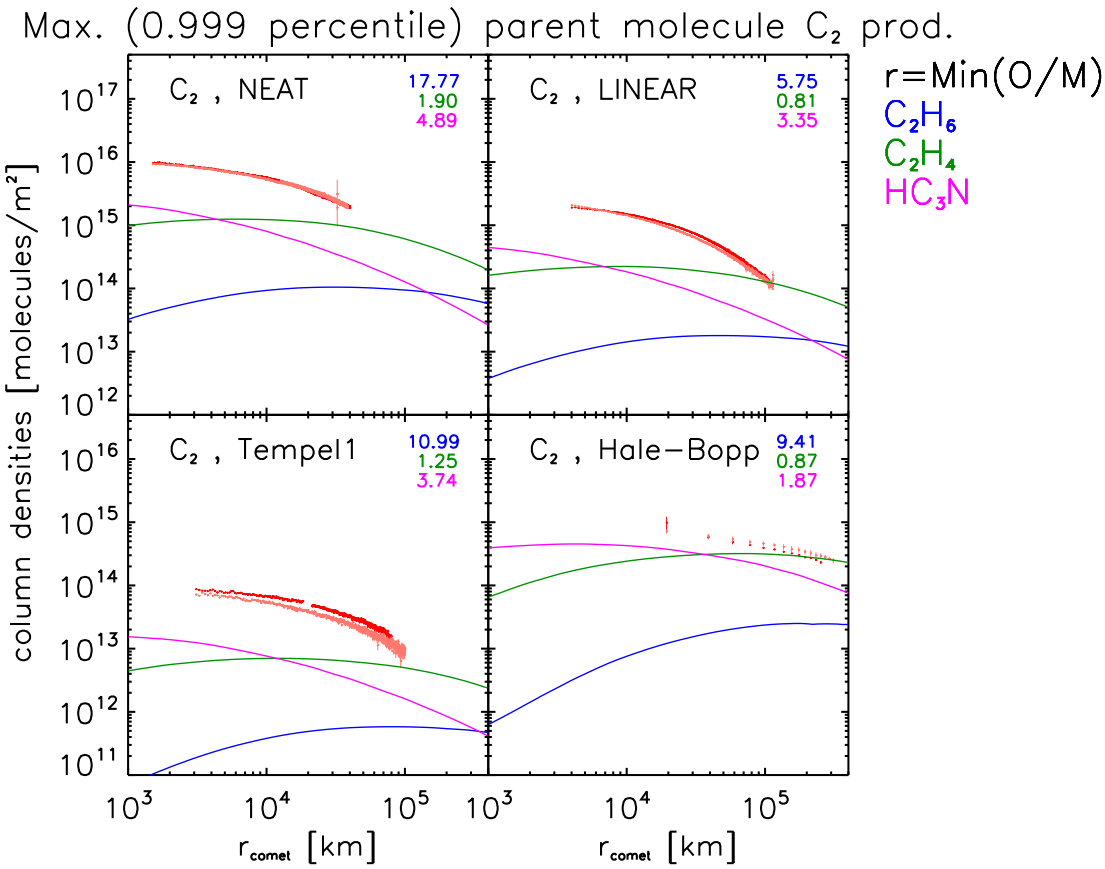

Figure 8.6: *Maximum* C_2 *production (solid lines) of each of the single parent molecules* C_2H_6 *(blue),* C_2H_4 *(green) and* HC_3N *(purple) in comparison to the* C_2 *observations (red), plotted for each comet. The solid lines denote the* 0.999 *percentiles of the probability distributions computed by propagating the uncertainties of the rate coefficients via MC and applying the maximum production rate ratio* c_i^{upper}*, see Table 8.4, for the regarded parent molecule and* $c_i = 0$ *for all others. The value* $r = Min(O/M)$*, depicted in the top right of each panel for* C_2H_6 *(blue),* C_2H_4 *(green) and* HC_3N *(purple), is defined as the ratio of the column densities between the observations (O, red) and the model (M, colored solid lines), chosen at a value of* r_{comet}*, such that the ratio* (O/M) *is a minimum.*

followed by reaction $C_3 + \gamma \rightarrow C_2 + C$. The key reaction for C_2 formation from $CH_2C_2H_2$ and CH_3C_2H is $C_3 + \gamma \rightarrow C_2 + C$. For C_4H_2 it is reaction $C_4H_2 + \gamma \rightarrow C_2H_2 + C_2$. For C_2H_2, C_2H_4 and C_2H_6 these are the reactions $C_2H_2 + \gamma \rightarrow C_2 + H_2$ and $C_2H + \gamma \rightarrow C_2 + H$. For HC_3N it is reaction $C_3N + \gamma \rightarrow C_2 + CN$. For a mixture of these parent molecules (with a nominal composition) the key reaction for the C_3 and C_2 column densities is $C_3 + \gamma \rightarrow C_2 + C$. For the C_2 column densities it is additionally reaction $C_4H_2 + \gamma \rightarrow C_2H_2 + C_2$.

These results now pave the way to effectively increase the accuracy of the coma chemistry model C_3 and C_2 outputs by increasing the accuracy of the key reactions by providing more quantum yields and absorption cross sections by laboratory measurements and quantum chemical computations. This will finally allow to determine if the photodissociation of the investigated known and proposed parent molecules are the main source of the C_3 and C_2 column densities in the comae of individual comets.

It was shown that, despite the changes in the reaction network done in the present work, C_2H_6 still produces only minor amounts of C_2 compared to the observations, which qualitatively confirms the results of Helbert (2002) for Hale-Bopp and Weiler (2006) for the comets NEAT, LINEAR and Tempel 1. C_2H_6 produces $\gtrapprox 1$ order of magnitude less C_2 than the other investigated parent molecules $CH_2C_2H_2$, CH_3C_2H, C_4H_2, C_2H_2, C_2H_4 and HC_3N. C_2H_4 might produce significant amounts of C_2 only in the outer observational ranges of the investigated comets. HC_3N produces only small amounts of C_2 when assuming an upper limit production rate ratio approximately an order of magnitude smaller than for the other parent molecules as suggested in the literature from observations.

CHAPTER 9

Fit of the Coma Chemistry Model to the C_3 and C_2 Observations of Four Comets

This chapter investigates whether one can account for the range of C_3 and C_2 observations of the comets C/2001 Q4 **(NEAT)**, C/2002 T7 **(LINEAR)**, 9P **(Tempel 1)** and C/1995 O1 **(Hale-Bopp)** with various combinations of the known (and in the literature proposed) parent molecules C_4H_2, $CH_2C_2H_2$, CH_3C_2H, C_2H_2, C_2H_4 and HC_3N using the model presented in Chapter 5. For this purpose this work optimizes the parent molecule production rate ratios of each comet (with respect to water) and a common set of photodissociation rate coefficients (within their estimated uncertainties determined in Chapter 7). Appendix E describes the applied harmony search **(HS)** optimization algorithm which optimizes the agreement between model and the observations of four comets and an adjusted χ^2 as a measure of the match. Section 9.1 discusses shortly the optimization parameters. Section 9.2 presents the results.

9.1 Optimization Parameters

The parameters used for the optimization are on the one hand the parent molecule production rate ratios c_i for each comet which are constrained within their upper (c^{upper}) and their lower (c^{lower}) limit as presented in Table 8.4 in Chapter 8. On the other hand one searches for one optimal set of photodissociation rate coefficients k_i for each of the involved species. For each species this work optimizes $k_i = k \cdot bf_i$ by optimizing its total photodissociation rate coefficient k and the full branching ratios bf_i of the reactions in which the species is involved. Besides constraining the k and bf_i within their distribution percentiles $[0.001, 0.999]$ it is also required to constrain the rate coefficients $k_i = k \cdot bf_i$ themselves within their $[0.001, 0.999]$ percentiles, see Appendix E. Section 8.2 presents the boundary conditions and the initial values for each comet.

9.2 Fit of Model to the Observations of Four Comets

This section discusses the modeled C_3 and C_2 column densities obtained for the four comets NEAT, LINEAR, Tempel 1 and Hale-Bopp using different sets of the investigated parent molecules (scenarios) by optimizing the model separately to the tailward and sunward observations. Table 9.1 gives an overview of the four scenarios investigated in this work. The scenarios 1 to 3

Table 9.1: *Overview of the four parent molecule scenarios investigated in this work when optimizing the comet coma chemistry model to the* C_3 *and* C_2 *observations of the comets NEAT, LINEAR, Tempel 1 and Hale-Bopp.*

scenario	parent molecules
1	C_4H_2, C_2H_2
2	$CH_2C_2H_2$, C_2H_2
3	CH_3C_2H, C_2H_2
4	C_4H_2, $CH_2C_2H_2$, CH_3C_2H, C_2H_2, C_2H_4, HC_3N

regard the case in which the comet nucleus ices have only one main C_3 parent molecule, either C_4H_2, $CH_2C_2H_2$ or CH_3C_2H, and one main C_2 parent molecule, namely C_2H_2. Since C_2H_2 is a molecule commonly detected in cometary comae by infrared **(IR)** observations, e.g. Brooke et al. (1996b) and Mumma et al. (2003), it is included as the main C_2 parent molecule in these scenarios. In these three scenarios the production rate ratios of the regarded parent molecules are optimized for each comet to fit the observations of each of the four comets. The production rate ratios of the parent molecules which are disregarded in a given scenario are set to zero.

Scenario 4 includes all parent molecules investigated in this work, with the exception of C_2H_6 which has only a very small contribution to C_2 in the observational range available in this work for the investigated comets in comparison to the other parent molecules as shown in Section 8.3.3.

9.2.1 Intercomparison of the Results for Each Parent Molecule Scenario

Figure 9.1 presents the model fits to the observations of C_3 (green) and C_2 (darkblue) of the comets NEAT, LINEAR, Tempel 1 and Hale-Bopp from top to bottom (left and right panels: tailward and sunward observations, respectively) obtained for the scenarios 1 (lightblue, dashed profiles), 2 (brown profiles), 3 (black profiles) and 4 (red profiles).

For a better comparison between observations and model fits the results for each scenario are depicted in the Figures 9.2 (scenario 1), 9.3 (scenarios 2 and 3 in one plot, since $CH_2C_2H_2$ and CH_3C_2H are isomers of C_3H_4) and 9.4 (scenario 4). The differences in the fit quality between the scenarios are discussed in the following.

Figure 9.1 shows that the best agreement between model and observations are achieved for the comets NEAT (top left and right panels) and Hale-Bopp (bottom panels), although with different quality depending on the regarded scenario and the observational side (tailward, sunward). For comet Tempel 1 the best agreement is obtained for scenario 1 for the tailward observations (blue dashed profile in the third left panel of Figure 9.1, see also Figure 9.2). The observations of comet LINEAR cannot be well reproduced with any of the regarded scenarios (second left and right panels).

C_3 Column Density Results

Figure 9.1 indicates that the C_3 observations (profiles in green) can be reproduced for nearly all comets for the scenarios 1, 2 and 4. The only exception is scenario 3 (profile in black) for comet LINEAR. Additionally, some smaller deviations from the C_3 observations are discernable for the middle part of the tailward observations around $r_c = 10^5$ km of comet Hale-Bopp for all scenarios.

C_2 Column Density Results

Figure 9.1 indicates that in general the C_2 observations are not as well reproduced as the C_3 observations. However, the match between model and observations of the comets NEAT and Hale-Bopp are still reasonably good for all scenarios. For comet Tempel 1 for scenario 1 the tailward observations are reasonably well reproduced (blue dashed profile in the third left panel of Figure 9.1, see also Figure 9.2) whereas a larger discrepancy is seen between the model and the sunward observations. The observations of comet LINEAR cannot be well reproduced with any of the regarded scenarios.

Discussion

The differences between model and observations for the different comets and scenarios may have different reasons:

- The cometary ices may contain parent molecules other than those investigated in this work or so-called extended sources may provide a source of C_3 and/ or C_2, i.e. macromolecules or dust particles that emit C_3 and/ or C_2 directly or species that contain these radicals.
- In the inner coma of comet 1P **(Halley)** (at $\approx$ 2300 km distance to the nucleus) anions were detected (mass peaks at $7-19$, $22-65$, $85-110$ amu) during the Giotto space mission, although with large density uncertainties, (Chaizy et al., 1991). Anions might have an affect on the formation of C_3 and C_2. However, investigation of this effect requires in situ data provided by the ongoing *Rosetta* space mission to comet 67P **(Churyumov-Gerasimenko)**.
- A faster destruction of the species C_4H, C_4, C_3H_2, C_3H, C_3, C_2H and C_2 by forbidden electronic transitions may also be a reason. Such transitions have been neglected in the ab initio computations of absorption oscillator strengths and/ or absorption cross sections for these species in van Hemert and van Dishoeck (2008) and Pouilly et al. (1983) as used in the present work. Estimating the influence of the uncertainty which may be introduced by this difficult effect is beyond the scope of this thesis. Absorption cross sections corresponding to forbidden transitions as well as the corresponding photodissociation quantum yields are usually weak, see e.g. the case of O_3 (Huggins bands, 3000 Å - 3500 Å) (Burrows et al., 1999, Matsumi et al., 2002). However, depending on the wavelength range and the intensity of the solar photon flux, see Figure 7.1, it cannot be ruled out that such transitions may still provide an important contribution to the total photodissociation.

In addition, the model used in this work makes several assumptions (see also model chapter 5), e.g. it assumes a steady-state and a spherically symmetric coma. However, cometary comae are three-dimensional objects which may be more or less asymmetric and non-stationary as a result of the outgassing of the complex aggregates of ices and dust of a comet. This means not all areas of the comet may be active nor may these areas be compositionally similar or homogeneous. Although there has been evidence of chemical similarities between different parts of a comet, e.g. during the break-off of comet 73P **(Schwassmann-Wachmann 3)**, see e.g. Dello Russo et al. (2007), Kobayashi et al. (2007), Schleicher and Bair (2011) as well as chemical similarity between surface and subsurface material, e.g. during the *Deep Impact* mission to comet Tempel 1, see e.g. Cochran et al. (2007), DiSanti et al. (2007), Feldman et al. (2006), Feaga et al. (2007), Feldman et al. (2010), this would not affect the non-stationary character of a cometary coma produced by a rotating comet with sublimation areas with different levels of activity (Crifo et al., 2004). Information upon these effects is however generally not available for comets. Asymmetries in the near nucleus coma due to an irregularly shaped comet nucleus should be evened out at $r_c \gtrapprox 10^3$ km (Crifo et al., 2004). Additionally, the exact size of the comet nucleus, typically

between several hundred meters up to several tens of kilometers, has only a very small effect on the column density profiles (Weiler, 2006). Comets also show large scale variations, i.e. jets.

The smaller slope of the model profiles in comparison to the observations of LINEAR and partly Tempel 1 cannot be explained by an overestimation of the hydrodynamical velocity by the neglection of a treatment of the superthermal species H and H_2 by the model used in this work. These species, especially H, may obtain large excess velocities in the photodissociation of H_2O. With increasing cometocentric distance the gas dilutes and less H share their excess kinetic energy with the bulk gas by collisions, i.e. only a part of this energy leads to a heating of the coma gas and therefore to an increase of the gas expansion velocity. Additionally, the light H require more collisions than heavier species to be thermalized. An inclusion of this effect may result in C_3 and C_2 profiles with a somewhat smaller slope, therefore cannot explain the discrepancy. Additionally, also the excess kinetic energy of the H and H_2 is quite uncertain for H_2O photodissociation (Huebner et al., 1992, Rodgers and Charnley, 2002) and may also have an effect on the profile. However, detailed modelling of this effect needs either application of a Monte Carlo **(MC)** model and/ or a sophisticated parameter study, e.g. of the excess kinetic energy of the H and H_2.

Churyumov et al. (2008a) state that the lightcurve (integrated brightness) of comet LINEAR shows saw-toothed periodic variations, e.g. one to two orders of magnitudes between the beginning of November and the end of December 2005. Variations are also reported at the date of the observations used in this work, i.e. the night from the 12th to the 13th of June 2004 before the perihelion on 23rd of June 2004. These variations are according to Churyumov et al. (2008a) likely effects of a rotating nucleus (e.g. around all three axes). For comet Tempel 1 periodic brightness variations were observed before the *Deep Impact* event, i.e. also at the date of the observations investigated in the present work one day before the impact. For comet Tempel 1 outbursts are reported, approximately one per week, possibly partly related to fresh ice exposed to the Sun (the comet rotated with a period of ≈ 41 hours) (Belton et al., 2006, A'Hearn and Deep Impact Team, 2006). Churyumov et al. (2008b) report for comet Tempel 1 that one strong outburst began on the 22nd of June and another one on the 2nd of July 2005 with the maximum close before the impact at the 4th of July. A variation of the brightness with the rotation period was also detected by Weiler et al. (2007). For comet NEAT Churyumov et al. (2008a) also report brightness variations near the observations used in this work.

A change of the coma gas density at the distances of the observations investigated in this work, i.e. 10^3 km - 10^5 km, require only half an hour to one day to take place, assuming a constant average gas velocity of 1 km s^{-1} throughout the coma. Therefore, observations of C_3 and or C_2 may also capture the change of the coma composition due to a sudden exposure of ice layers of different composition. The outer sunward and tailward C_2 column density profile of comet NEAT might feature such a change, see e.g. the top right and top left panel of the Figures 9.3 and 9.2, respectively. For comet Tempel 1 C_2H_2 was not detected a month before but instead after the *Deep Impact* event, after the coma had relaxed back into an undisturbed state (Mumma et al., 2005). The impact may have exposed ices containing C_2H_2. Note that the observations of Tempel 1 in the present work were taken one day before the impact, i.e. when the coma was undisturbed. No observations for C_2H_2 are available for this date.

In the case of Tempel 1 the sunward C_3 and C_2 observations show a gap at $r_c \approx 2 \cdot 10^4$ km that separates the profiles into two parts which seem to feature a small offset to each other. This may be caused by the fact that during the observations the tailward part was captured only by one of the two CCDs of the FORS2 instrument whereas the sunward part was measured by both CCDs (Weiler, 2006).

9.2.2 Comparison of the Results to Weiler (2006) and Helbert (2002)

Weiler (2006) succeeded in reproducing the C_3 observations of the comets NEAT, LINEAR and Tempel 1 observed at the heliocentric distances $r_h = 1 - 1.5$ AU. Regarding the C_2 column densities that work only reproduced reasonably well the observations of comet NEAT. Neither the C_3 nor the C_2 observations of comet Hale-Bopp could be reproduced for the distance of $r_h = 3.78$ AU. Weiler (2006) used the parent molecules C_4H_2, C_3H_4 (as a representative of its isomers $CH_2C_2H_2$ and CH_3C_2H), C_2H_2 and HC_3N. Weiler (2006) adopted the photodissociation rate coefficients for C_3H_4 and its products from Helbert (2002). The photodissociation rate coefficients of the newly included parent molecules C_4H_2 and HC_3N and their products were estimated. For C_4H_2 and HC_3N these were estimated using absorption cross sections and quantum yields. For the products C_4H, C_4 the photodissociation rate coefficients were estimated by "comparison with similar reactions for radicals containing two or three carbon atoms" (Weiler, 2006). For HC_3N absorption cross sections and quantum yields were used. To estimate the C_3N photodissociation rate coefficient only one absorption cross section data point was available. That work also updated the hydrocarbon electron impact reactions and showed that these have only a small contribution to the formation of C_3 and C_2 in cometary comae. The electron impact reaction rate coefficients are also used in the present work since no new measurements or ab initio computations exist up until now for these reactions.

A comparison between the results of Weiler (2006) shown in Figure 9.5 (panel a: C_3, panel b: C_2, from top to bottom panels: comets NEAT, LINEAR and Tempel 1) and the results of the present work for the scenarios 1 (Figure 9.2), 2 and 3 (Figure 9.3), and 4 (Figure 9.4) shows that the agreement between model and observations is similar for the comets NEAT, LINEAR and Tempel 1. Note that in the plots of Weiler (2006), see the right panel of Figure 9.5, the plot symbols are larger than the actual C_2 uncertainties.

The present work has obtained for the first time reasonably good fits to comets at very different r_h, in the present case for the comets NEAT ($r_h = 1.00$ AU) and Hale-Bopp ($r_h = 3.78$ AU) using the model presented in Chapter 5. Between $r_h = 1.00$ AU and $r_h = 3.78$ AU the solar photon flux differs by approximately an order of magnitude. For comet Tempel 1 at least the tailward observations for scenario 1 can be reproduced reasonably well, observed at $r_h = 1.5$ AU. See also Figure 9.1 for an overview of the results for all comets and scenarios in one plot. Weiler (2006) could not reproduce the observations of comet Hale-Bopp at $r_h = 3.78$ AU. For comparison, the fits to Hale-Bopp obtained in the present work have a similarly good quality as in Helbert (2002), who optimized their model to the tailward and sunward observations together using the parent molecules C_3H_4 (as a representative of the isomers $CH_2C_2H_2$ and CH_3C_2H), C_2H_2 and C_2H_6, see Figure 9.6 (extracted from their Figures 16.9 and 16.10).

A main improvement to Weiler (2006) is that the present work uses realistic parent molecule production rate ratios $c(\text{parent}) \leq 1$ % (relative to water) to obtain reasonable good fits to comet NEAT, observed at $r_h = 1.00$ AU, and fits of similar quality as in Weiler (2006) to Tempel 1, observed at $r_h = 1.51$ AU. Note that at $r_h \lessapprox 3$ AU the solar insolation is high enough that the sublimation is effective for the parent molecules as well as for H_2O the main constituent of the cometary ices (i.e. are a good representation of the nucleus ice abundances), see also Figure 3.1a in Chapter 3. At $r_h \gtrapprox 3$ AU H_2O is less effective in sublimation in comparison to the investigated hydrocarbon molecules due to its higher sublimation temperature. Therefore, for comet Hale-Bopp observed at $r_h = 3.78$ AU, however, c(parent) > 1 % is possible. Realistic production rate ratios $c(\text{parent}) \leq 1$ % have been discussed in Section 8.2, see also Table 8.4, in Chapter 8. Weiler (2006) required C_3H_4 (as a representative of $CH_2C_2H_2$ and CH_3C_2H) production rate ratios for NEAT of ≈ 3.5 % and for Tempel 1 even as high as ≈ 8.2 %. These high values were likely needed to compensate missing C_3 producing reactions in that work for C_3H_4 (the representative in that work for the isomers $CH_2C_2H_2$ and CH_3C_2H), e.g. C_3H photodissociation was not included, and since the reaction $C_3H_2 + \gamma \rightarrow C_3 + H_2$ was modeled

with a three orders of magnitude smaller photodissociation rate coefficient than the best fit value obtained in the present work for the scenarios 2 and 3. For example, Figure 9.8b shows the best fit photodissociation rate coefficient values obtained in the present work (black diamonds) for the scenario 2, whereas the black circles mark the values used in Weiler (2006) and Helbert (2002). Weiler (2006) also determined unrealistically high HC_3N production rate ratios of $2.4 - 7.7$ %. As shown in Table 8.4 realistic HC_3N production rate ratios have $c(HC_3N) \leq 0.1$ % for comets observed at $r_h \lessapprox 3$ AU, i.e. also at the observational distances of the comets NEAT, Tempel 1 and LINEAR as used in the present work.

Additionally, Weiler (2006) was not able to reproduce the C_3 observations of the comets NEAT, LINEAR and Tempel 1 using C_3H_4 as the sole C_3 parent molecule. This was possibly caused by the use of small rate coefficients for the photodissociation reactions of the species C_3H_2 and C_3 as estimated in Helbert (2002). In the work of Helbert (2002) electron impact reactions were quoted as important for the formation of C_3. However, with the updates to the electron impact reaction rate coefficients done by Weiler (2006) it was shown that these reactions are then not important for the formation of C_3 and C_2.

In contrast to Weiler (2006) the present work obtains reasonably good fits to the C_3 and C_2 observations of the comets NEAT and Hale-Bopp using only one of the C_3 parent molecules C_4H_2, $CH_2C_2H_2$ and CH_3C_2H and the C_2 parent molecule C_2H_2. The optimization results of this work indicated that much higher photodissociation rate coefficients are required for the species C_3H_2 and C_3 in scenario 2 and 3 than used in Weiler (2006), see Figure 9.8b. This Figure shows the best fit photodissociation rate coefficients (diamonds) and those used in Weiler (2006) (circles). The gray and light gray shaded bars mark the $[0.025, 0.975]$ ($\approx 2\sigma$) and $[0.001, 0.999]$ ($\approx 3\sigma$) percentiles, respectively, of the photodissociation rate coefficient distributions, as computed in Chapter 7 of the present work. The confidence intervals of the best fit rate coefficients are indicated by green bars. The confidence interval of a parameter p_i ($i = 1, \ldots, n$, n: number of optimized parameters) is defined in this work by the smallest (p_i^{lower}) and the largest value (p_i^{upper}) of the set of parameters which are within $\chi^2_{\text{norm}} = 1$ and $\chi^2_{\text{norm}} = 1.5$. With p_i^{lower} and p_i^{upper} one can estimate the level of constraint of a parameter p_i (relative to the other parameters). The numbers on the right hand side of the Figures 9.7, 9.8, 9.9, 9.10 and 9.11 quantify the level of constraint obtained in the optimization by the ratio $F^2_{\text{conf}} = p_i^{\text{upper}}/p_i^{\text{lower}}$. $F^2_{\text{conf}} < 2$, $F^2_{\text{conf}} \in [2, 10)$ and $F^2_{\text{conf}} \geq 10$ are denoted in this work as well, moderately and poorly constrained, see also Appendix E.3.3.

Weiler (2006) fitted the C_3 observations by including the parent molecule C_4H_2 and assuming the fast C_3 producing reaction $C_4H_2 + \gamma \rightarrow C_3 + CH_2$. This reaction is however not possible for any C_4H_2 isomer according to Silva et al. (2008). In contrast, the optimized photodissociation rate coefficients obtained in the present work for C_4H_2 suggest an effective $C_4 + H_2$ production which could indicate that the HC_4H isomer rapidly isomerizes to H_2C_4 with subsequent dissociation to $C_4 + H_2$. Also important is the isomerization to a rhombic isomer which allows dissociation to $C_2 + C_2H_2$, i.e. C_2 production in one step from C_4H_2. Another interpretation would be that the H_2C_4 and the rhombic C_4H_2 isomer exist in cometary ices beside HC_4H, i.e. regarding the C_4H_2 used in the present work as representative of its isomers, see Section 9.2.3 for more details.

9.2.3 Scenario 1: "C_4H_2, C_2H_2"

Figure 9.7a and 9.7b compile the best fit parent molecule production rate ratios for each comet (sunward and tailward observations separately) and the best fit common set of photodissociation rate coefficients, respectively (shown as black diamonds). The confidence intervals are indicated as colored bars. In Figure 9.7a the confidence intervals are indicated color-coded according to the comet and the observational side (tailward, sunward), e.g. the sunward and tailward results

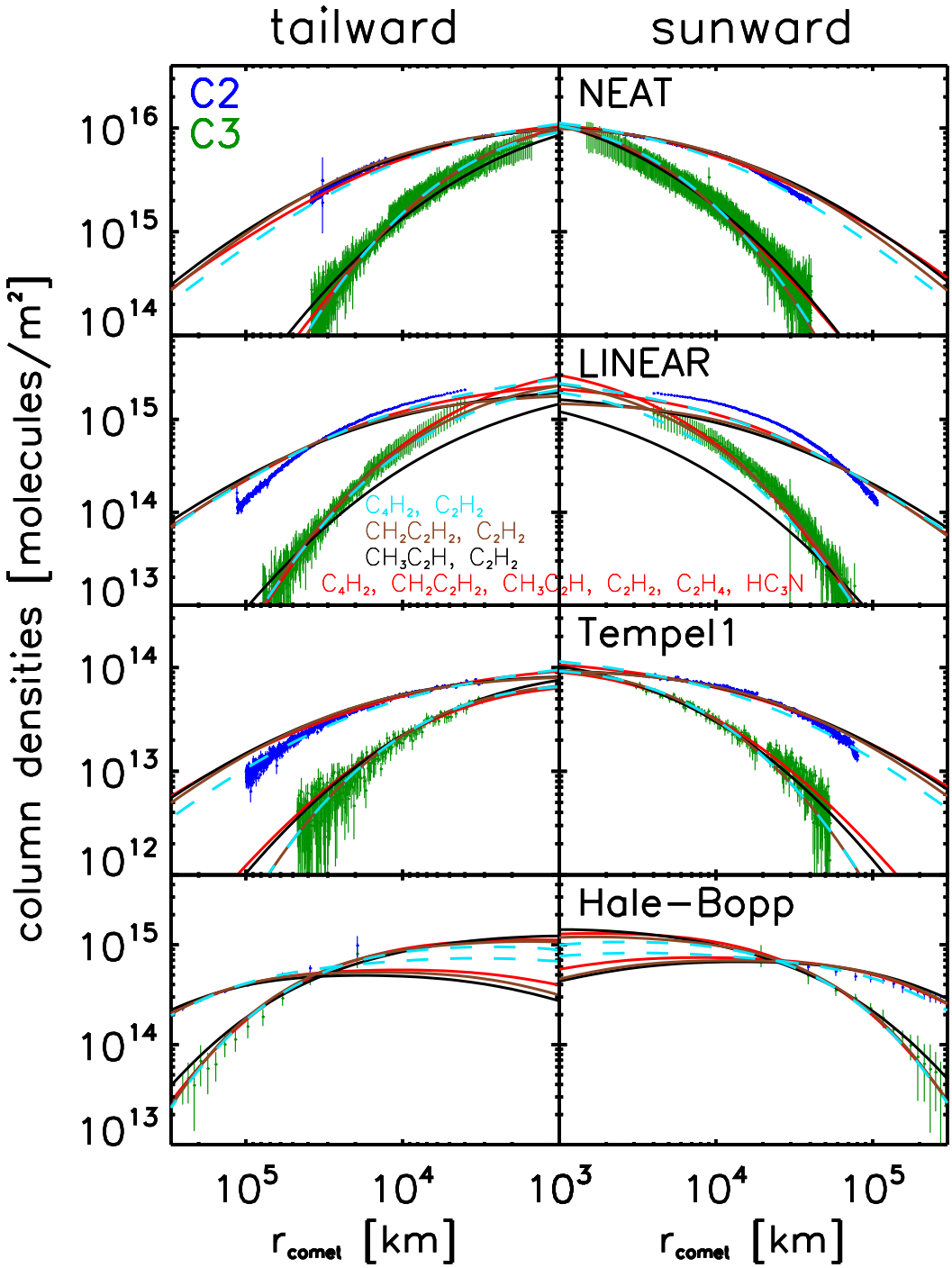

Figure 9.1: *Overview of the best fit results to the* C_3 *(green) and* C_2 *(blue) observations obtained in this work for the four scenarios 1: "*C_4H_2, C_2H_2*" (lightblue, dashed), 2: "*$CH_2C_2H_2$, C_2H_2*" (brown, solid), 3: "*CH_3C_2H, C_2H_2*" (black, solid), and 4: "*C_4H_2, $CH_2C_2H_2$, CH_3C_2H, C_2H_2, C_2H_4, HC_3N*" (red, solid) given in Table 9.1 for the comets C/2001 Q4* ***(NEAT)****, C/2002 T7* ***(LINEAR)****, 9P* ***(Tempel 1)*** *and C/1995 O1* ***(Hale-Bopp)*** *(from top to bottom). The model was fitted separately to the tailward (left) and sunward (right) observations by optimizing for each scenario a common set of rate coefficients of the involved photodissociation reactions (see Figures 9.7b, 9.8b, 9.9b, 9.11) and by optimizing the parent molecule production rate ratios* c_i *for each comet and observational side (see Figures 9.7a, 9.8a, 9.9a, 9.10).*

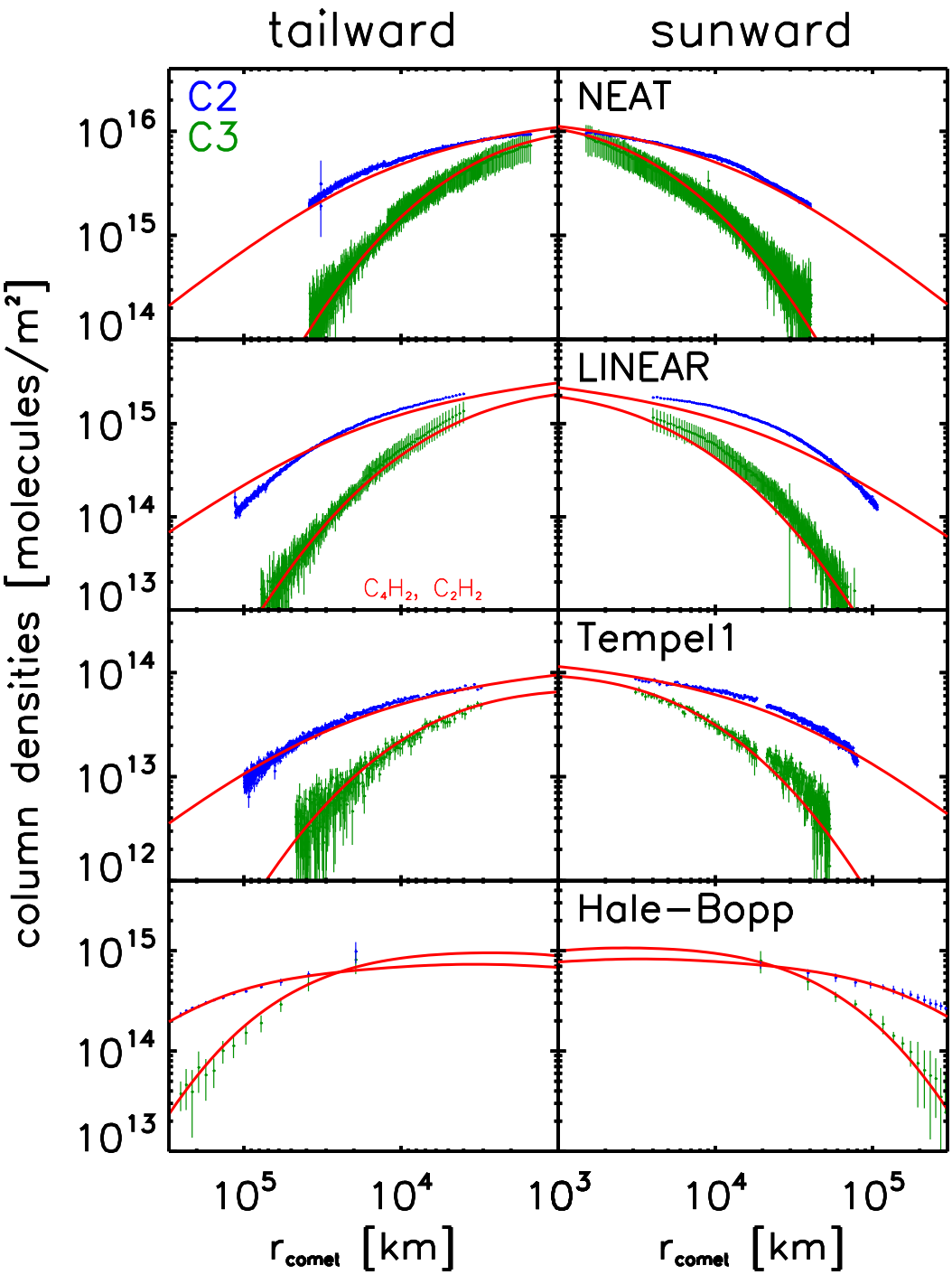

Figure 9.2: *Overview of the best fit results to the* C_3 *(green) and* C_2 *(blue) observations obtained in this work for the scenario "*C_4H_2*,* C_2H_2*" for the comets NEAT, LINEAR, Tempel 1 and Hale-Bopp (from top to bottom). The model was fitted separately to the tailward (left) and sunward (right) observations by optimizing for each scenario a common set of rate coefficients of the involved photodissociation reactions (see Figure 9.7b) and by optimizing the parent molecule production rate ratios* c_i *for each comet and observational side (see Figure 9.7a*

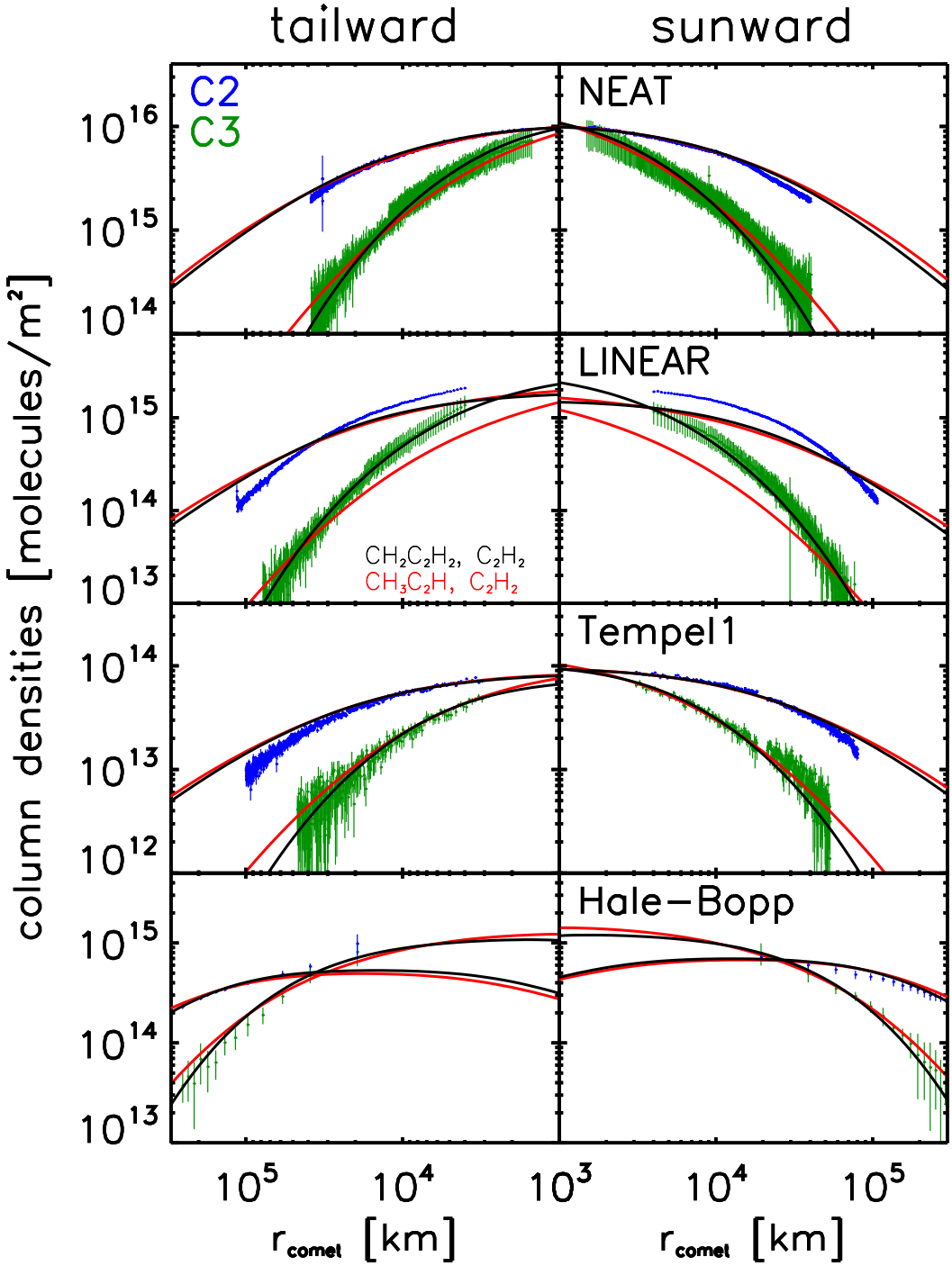

Figure 9.3: *Overview of the best fit results to the* C_3 *(green) and* C_2 *(blue) observations obtained in this work for the scenario 2: "*$CH_2C_2H_2$, C_2H_2*" (black) and 3: "*CH_3C_2H, C_2H_2*" (red) for the comets NEAT, LINEAR, Tempel 1 and Hale-Bopp (from top to bottom). The model was fitted separately to the tailward (left) and sunward (right) observations by optimizing for each scenario a common set of rate coefficients of the involved photodissociation reactions (see Figures 9.8b and 9.9b) and by optimizing the parent molecule production rate ratios* c_i *for each comet and observational side (see Figures 9.8a and 9.9a)*

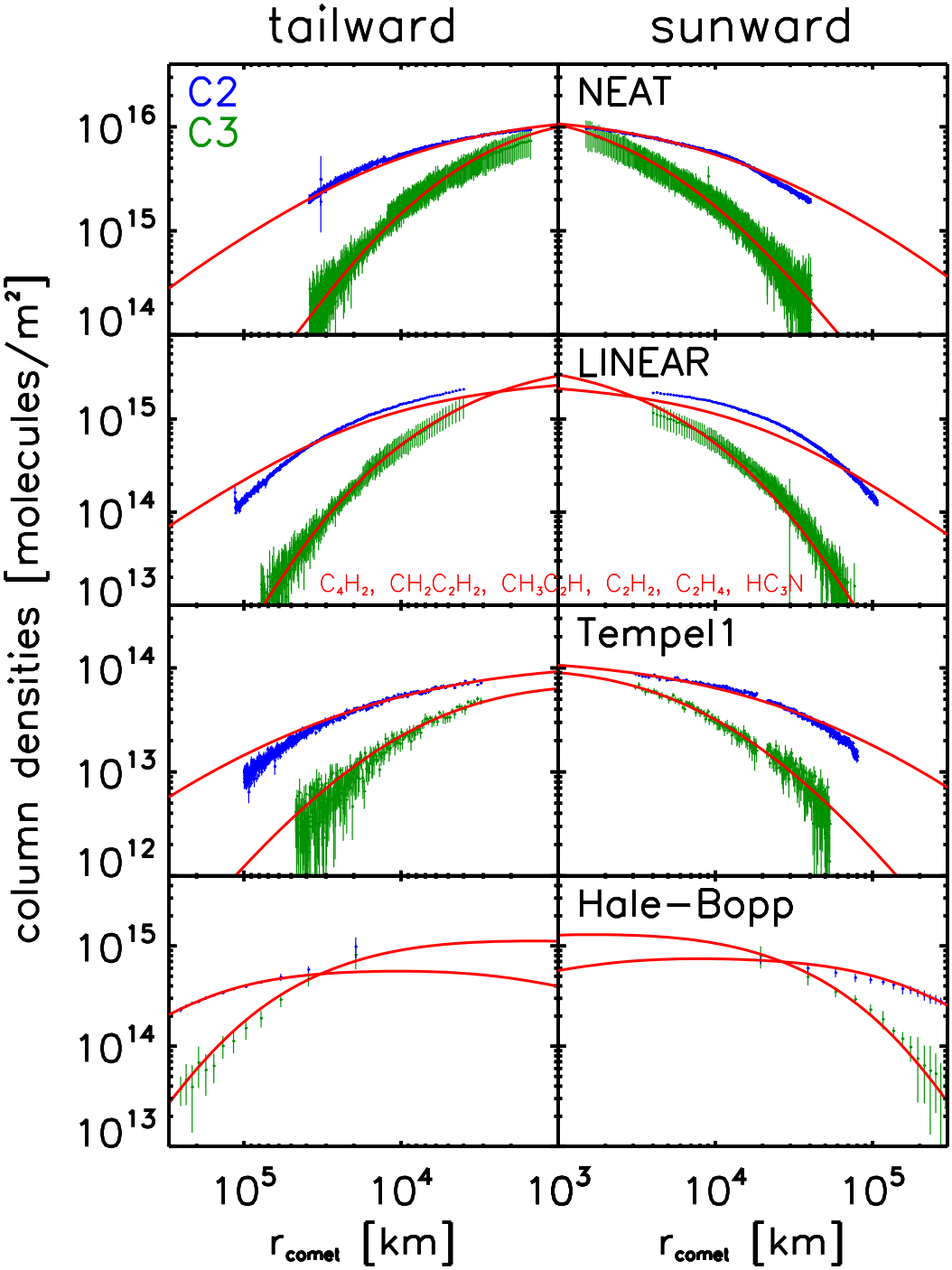

Figure 9.4: *Overview of the best fit results to the* C_3 *(green) and* C_2 *(blue) observations obtained in this work for the scenario 4: "*C_4H_2, $CH_2C_2H_2$, CH_3C_2H, C_2H_2, C_2H_4, HC_3N*" for the comets NEAT, LINEAR, Tempel 1 and Hale-Bopp (from top to bottom). The model was fitted separately to the tailward (left) and sunward (right) observations by optimizing for each scenario a common set of rate coefficients of the involved photodissociation reactions (see Figure 9.11) and by optimizing the parent molecule production rate ratios* c_i *for each comet and observational side (see Figure 9.10*

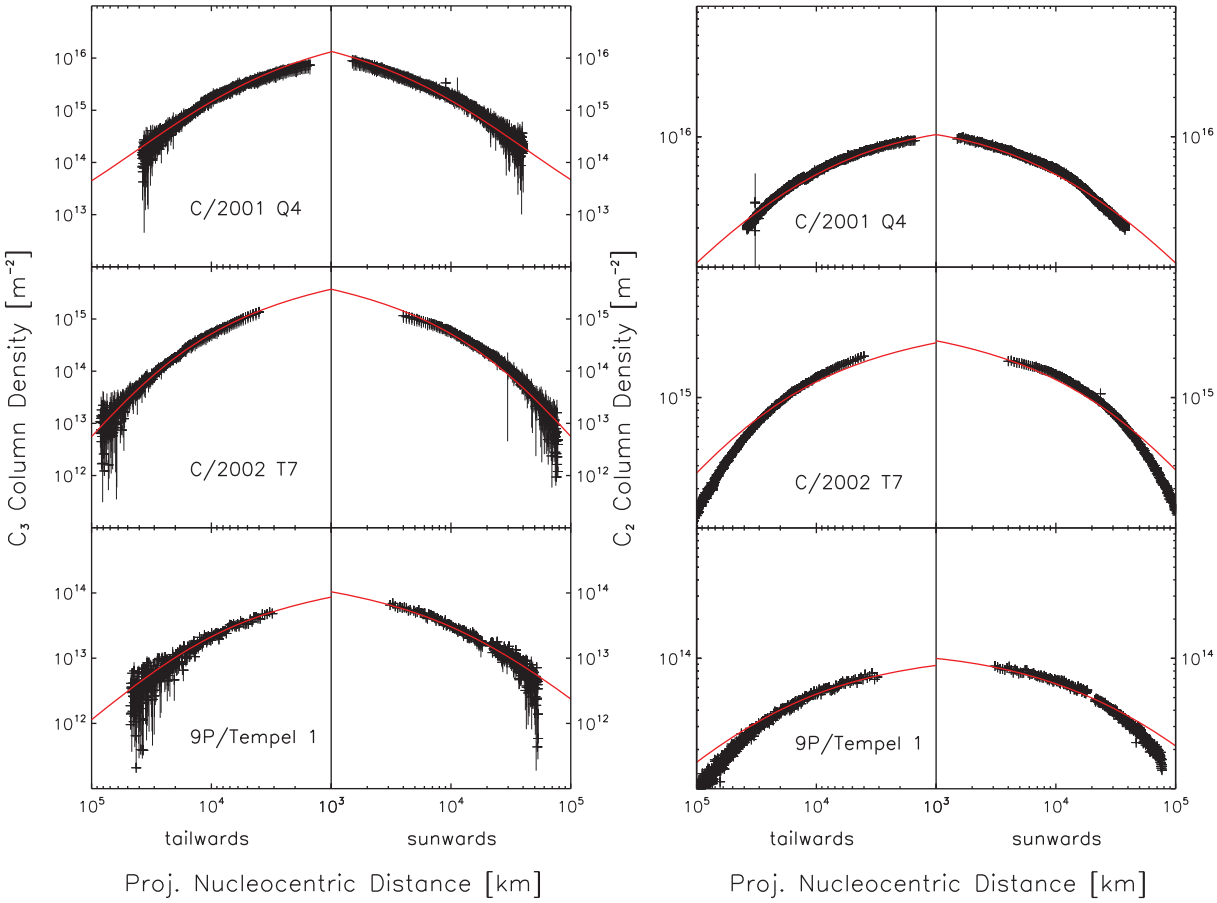

(a) C_3 **(b)** C_2

Figure 9.5: *Best fit results obtained in Weiler (2006) for a)* C_3 *and b)* C_2 *for the comets NEAT, LINEAR and Tempel 1 (their Figures 35 and 37).*

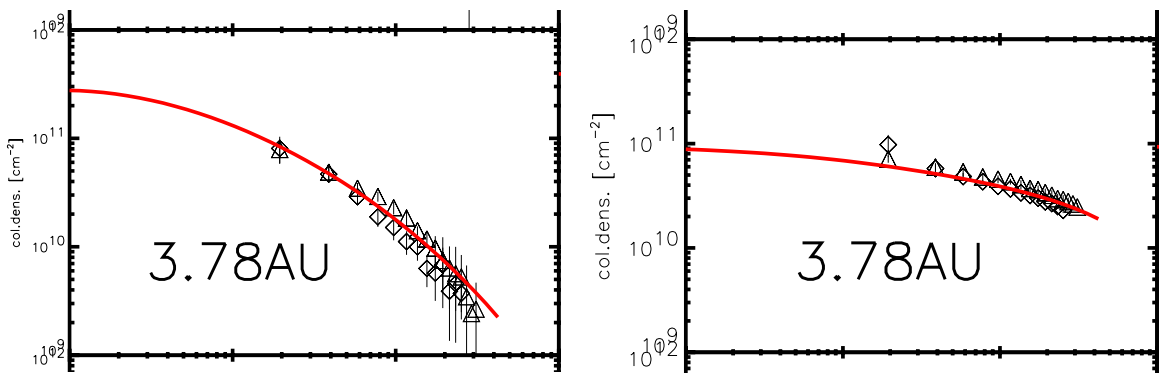

(a) C_3 **(b)** C_2

Figure 9.6: *Best fit results to the* C_3 *(panel a) and* C_2 *(panel b) observations (1σ errors) to comet Hale-Bopp at* $r_h = 3.78$ *AU obtained in Helbert (2002) using their 1D ComChem model (Giguere and Huebner, 1978, Boice et al., 1986, 1998, Huebner et al., 1987, Schmidt et al., 1988). These figures are an excerpt from their figures 16.9 and 16.10, respectively, in which the x-axis and the y-axis are represented in logarithmic scales of the cometocentric distance (from* 10^3 *km left to* 10^6 *km right) and the column densities (from* 10^9 *cm*$^{-2}$ *to* 10^{12} *cm*$^{-2}$*). Note that in Helbert (2002) their model was fitted to the tailward (diamonds) and sunward (triangles) observations together.*

for comet NEAT in lightblue and blue, respectively. In Figure 9.7a the confidence intervals of the optimized rate coefficients are plotted in green. The confidence interval is defined in this work by parameter values for which $\chi^2_{\mathrm{norm}} \in [1, 1.5]$. The numbers on the right hand side of each panel quantify the corresponding level of constraint obtained in the optimization, i.e. the ratio of the upper and lower value of the parameters with $\chi^2_{\mathrm{norm}} \in [1, 1.5]$, denoted F^2_{conf}. $F^2_{\mathrm{conf}} < 2$, $F^2_{\mathrm{conf}} \in [2, 10)$ and $F^2_{\mathrm{conf}} \geq 10$ are denoted in this work as well constrained, moderately constrained and poorly constrained, see also Appendix E.3.3.

Figure 9.7a shows that the production rate ratios $c(C_4H_2)$ and $c(C_2H_2)$ are mostly well and moderately constrained, respectively. For comet Hale-Bopp $c(C_2H_2)$ is poorly constrained. This could be due to the relatively high production rate ratio of C_4H_2 which directly produces C_2 and C_2H_2. For comet Hale-Bopp observed at $r_h = 3.78$ AU a production rate ratio of $c(C_4H_2) > 1$ % is possible since sublimation of water is only efficient at $r_h \lessapprox 3$ AU, i.e. the ratio of the C_4H_2 and the H_2O production rate does not reflect the ice abundance in the nucleus ices at $\mathrm{r_h} = 3.78$ AU.

Figure 9.7b shows that the rate coefficients of the C_4H_2 reactions

$$C_4H_2 + \gamma \rightarrow C_4H + H\,, \tag{R26}$$
$$C_4H_2 + \gamma \rightarrow C_2H + C_2H\,, \tag{R27}$$
$$C_4H_2 + \gamma \rightarrow C_2H_2 + C_2\,, \tag{R28}$$
$$C_4H_2 + \gamma \rightarrow C_4 + H_2\,, \tag{R29}$$

the C_3 reaction

$$C_3 + \gamma \rightarrow C_2 + C\,, \tag{R30}$$

and the C_2H_2 reactions

$$C_2H_2 + \gamma \rightarrow C_2 + H_2\,, \tag{R31}$$
$$C_2H_2 + \gamma \rightarrow C_2H + H\,, \tag{R32}$$

are well constrained ($F^2_{\mathrm{conf}} < 2$). The rate coefficients of the reactions (R26), (R29), (R30), (R31) and (R32) are optimized close to their largest possible value (0.999 percentile).

Moderately constrained ($F^2_{\mathrm{conf}} \in [2, 10)$) are the reactions of C_4H and reaction

$$C_4 + \gamma \rightarrow C_3 + C\,. \tag{R33}$$

All other reactions, on the other hand, including

$$C_2H + \gamma \rightarrow C_2 + H\,, \tag{R34}$$
$$C_2H + \gamma \rightarrow CH + C \tag{R35}$$

are only constrained to an interval of one to two orders of magnitude, however, smaller than the uncertainty as computed in Chapter 7 (lightgray shaded bars in Figure 9.7b). The optimized rate coefficient of reaction (R34) is quite close to the value as used by Helbert (2002) and Weiler (2006). In these works reaction (R35) was not included.

Figure 9.7b shows that the rate coefficients of C_3H are poorly constrained ($F^2_{\mathrm{conf}} > 10$). This is since the optimized rate coefficients suggest that the only C_3H producing reaction

$$C_4H + \gamma \rightarrow C_3H + C\,. \tag{R36}$$

in the regarded scenario has a relatively small rate coefficient and therefore does not contribute significantly to C_3H production.

The favored formation pathway of C_3 from the optimization is

$$C_4H_2 \rightarrow C_4 \rightarrow C_3\,. \tag{R37}$$

The favored formation pathways of C_2 from the optimization are

$$C_4H_2 \rightarrow C_2\,, \tag{R38}$$
$$C_3 \rightarrow C_2\,, \tag{R39}$$
$$C_4H_2 \rightarrow C_2H_2 \rightarrow C_2 + H_2\,, \tag{R40}$$
$$C_2H_2 \rightarrow C_2 + H_2\,. \tag{R41}$$

Discussion of the Rate Coefficient Results for the C_4H_2 Molecule for Scenario 1: The results for the optimized rate coefficients of C_4H_2 for scenario 1, i.e. the including only the parent molecules C_4H_2 and C_2H_2, see black diamonds in Figure 9.7b, can be interpreted in two ways. Firstly, this work models C_4H_2 using the absorption cross sections of HC_4H (diacetylene) since only these are available. This isomer can directly photodissociate to $C_4H + H$ and $C_2H + C_2H$. However, isomerization to the carbene H_2C_4 (butatrienylidene) and a rhombic C_4H_2 allow photodissociation via the reactions (R29) and (R28), respectively (Silva et al., 2008). The present work includes these isomerizations for HC_4H to show that the best agreement between model and observations of the comets Hale-Bopp (tailward, sunward), Tempel 1 (tailward) and NEAT (sunward) is achieved only when these isomerizations and the subsequent dissociations are effective at several wavelengths, i.e. where no measurements and quantum yields are available. HC_4H with only the reactions (R26) and (R27) does not reproduce the C_3 column densities within the rate coefficient uncertainties, i.e. the model profiles have a much smaller slope than the observations (not shown).

Reaction (R29) may involve a strong bending of HC≡C−C≡CH between the two singly bonded C_2H after photo-excitation and subsequent dissociation to C_4 and H_2. Reaction (R28) has a relatively small rate coefficient in comparison to reaction (R29), therefore the rate of isomerization to the rhombic C_4H_2 would be smaller, however, also important. See Silva et al. (2008) for an overview of the C_4H_2 isomers and the possible isomerization paths. For these processes to occur requires that competitive processes like radiative and collisional de-excitation are slower than the isomerization and the subsequent dissociation. It is therefore desirable to determine the photodissociation quantum yields of HC_4H at the undetermined wavelengths (in the laboratory and/ or by ab initio computations), see Appendix D.

Secondly, the results for the optimized rate coefficients for C_4H_2 could also be interpreted as that the above mentioned C_4H_2 isomers are present in the comet nucleus ices. Although the absorption cross sections of the H_2C_4 and the rhombic isomer of C_4H_2 are not available, the rate coefficients of the reactions (R29) and (R28) computed for HC_4H may be regarded as lower limits for the corresponding photodissociation reactions of the H_2C_4 and the rhombic isomer, since these isomers require lower energies for photodissociation than the ground state molecule, i.e. HC_4H (44.7 kcal/mol and 70.8 kcal/mol higher in energy than HC_4H, respectively). For comparison the dissociation threshold of reaction (R26) of HC_4H is 133.1 kcal/mol (Silva et al., 2008). To our knowledge the rhombic isomer has not been detected in the interstellar matter **(ISM)**. The C_4H_2 isomer H_2C_4 was first detected in the Taurus molecular cloud 1 **(TMC-1)** by Kawaguchi et al. (1991). The diacetylene isomer HC_4H was first detected in the ISM by Cernicharo et al. (2001) in the protoplanetary nebula **(PPN)** CRL 618. The results indicate that it is important to search for C_4H_2 and its isomers in cometary comae by direct observations.

9.2.4 Scenario 2: "$CH_2C_2H_2$, C_2H_2" and Scenario 3: "CH_3C_2H, C_2H_2"

The Figures 9.8a and 9.9a show that the production rate ratios $c(CH_2C_2H_2)$ and $c(CH_3C_2H)$ are well constrained. This is likely since the photodissociation reactions of these two C_3 parent molecules were found in Chapter 8 as one of the important *key reactions* in the observational range. The C_2 parent molecule $c(C_2H_2)$ is well to moderately constrained for both scenarios, since $CH_2C_2H_2$ and CH_3C_2H do produce too little C_2 to explain both C_3 and C_2 alone.

The Figures 9.8b and 9.9b show that in the scenario 2 the rate coefficients of the reactions

$$CH_2C_2H_2 + \gamma \rightarrow C_3H_3 + H\,, \tag{R42}$$
$$CH_2C_2H_2 + \gamma \rightarrow C_3H_2 + H_2 \tag{R43}$$

are optimized to values nearly an order of magnitude higher than for the reactions

$$CH_3C_2H + \gamma \rightarrow C_3H_3 + H\,, \tag{R44}$$
$$CH_3C_2H + \gamma \rightarrow C_3H_2 + H_2\,. \tag{R45}$$

in scenario 3.

In both scenarios the rate coefficients of C_3H_3 and C_3H_2 are poorly constrained, although constrained over a range obviously smaller than the uncertainty. Only in the scenario 3 reaction

$$C_3H_2 + \gamma \rightarrow C_3 + H_2 \tag{R46}$$

is constrained to less than an order of magnitude. As found in the sensitivity analysis **(SA)** Chapter 8, the photodissociation reactions of the species C_3H_3, C_3H_2 and C_3H have their main effect on the model output uncertainty at small cometocentric distances r_c of the comet observations and smaller (e.g. $r_c \lessapprox 10^3$ km for comet NEAT in Figure 8.2a) in contrast to the photodissociation reactions of the parent molecules $CH_2C_2H_2$ and $CH_2C_2H_2$ which have a large effect in the observational range.

In contrast to scenario 2 (Figure 9.8b) in scenario 3 (Figure 9.9b) reaction (R35) is better (moderately) constrained to higher values, i.e. C_2H is required to be destroyed faster (although the confidence intervals overlap). This is possibly because more C_2H is produced via the path

$$C_3H_2 \rightarrow C_3H \rightarrow C_2H\,, \tag{R47}$$

since the rate coefficient of reaction

$$C_3H_2 + \gamma \rightarrow C_3H + H\,. \tag{R48}$$

is higher by an order of magnitude in scenario 3.

Besides this small difference, in both scenarios a similar 'mixture' of several C_3 formation pathways optimally fits the observations. These pathways also produce C_2 via C_3 photodissociation additionally to the reactions

$$C_2H_2 \rightarrow C_2H \rightarrow C_2\,, \tag{R49}$$
$$C_2H_2 \rightarrow C_2\,. \tag{R50}$$

9.2.5 Scenario "C_4H_2, $CH_2C_2H_2$, CH_3C_2H, C_2H_2, C_2H_4, HC_3N"

For comet NEAT (lightblue and blue bars in Figure 9.10) the production rate ratios c_i of the parent molecule $CH_2C_2H_2$ is well constrained and that of C_4H_2 is well to moderately constrained.

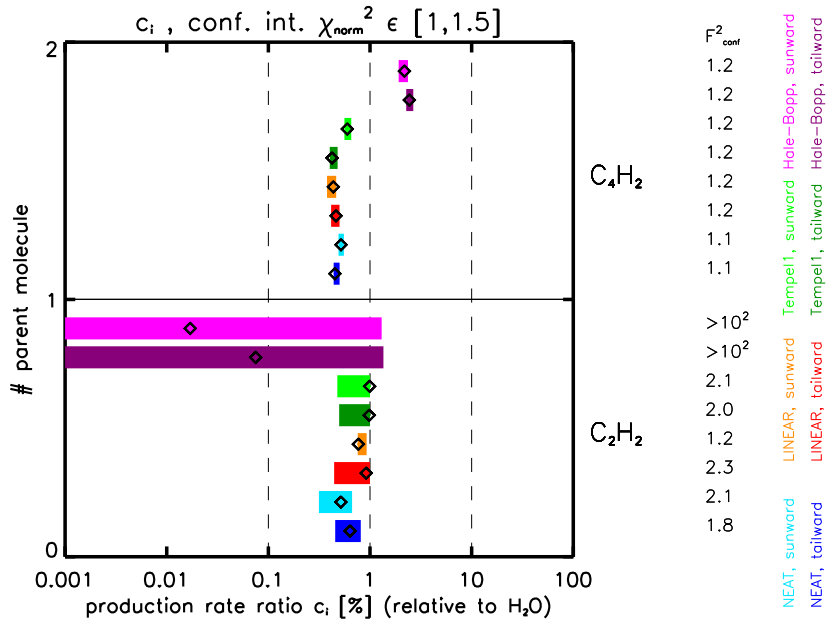

(a) *Production rate ratios $c(C_4H_2)$ and $c(C_2H_2)$ for the sunward (pink) and tailward (violet) observations of comet Hale-Bopp, respectively, up to the sunward (lightblue) and tailward (darkblue) observations of comet NEAT, respectively.*

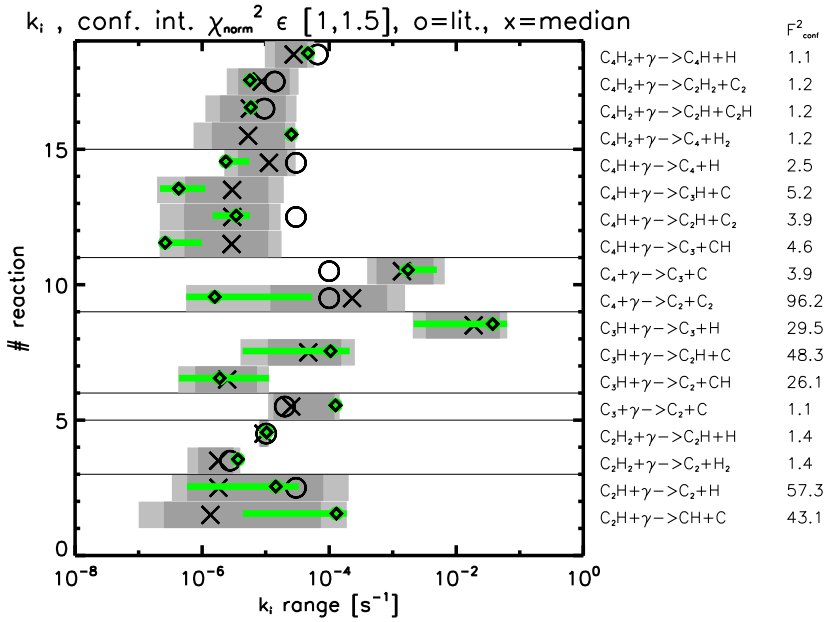

(b) *Photo rate coefficients k_i.*

Figure 9.7: *Overview of the best fit (diamond) parameter values obtained for the scenario 1: (a) the production rate ratios $c(C_4H_2)$ and $c(C_2H_2)$, optimized for each comet and observational side (sunward, tailward), and (b) the photodissociation rate coefficients $\{k_i\}_{i=1}^n$ of the reactions indicated on the right hand side. In panel (a) the confidence interval is color coded for each comet and observational side (see rightmost information). In panel (b) the confidence interval is colored in green for the common set of photodissociation rate coefficients (k_i). The numbers on the right hand side of each panel quantify the level of constraint F^2_{conf} obtained in the optimization, see beginning of Section 9.2.3 or Appendix E.3.3. The gray and light gray shaded bars mark the $[0.025, 0.975]$ ($\approx 2\sigma$) and $[0.001, 0.999]$ ($\approx 3\sigma$) percentiles, respectively, of the k_i distributions (computed in Chapter 7). Black crosses and circles, respectively, mark each distributions' median value and the values used in Weiler (2006).*

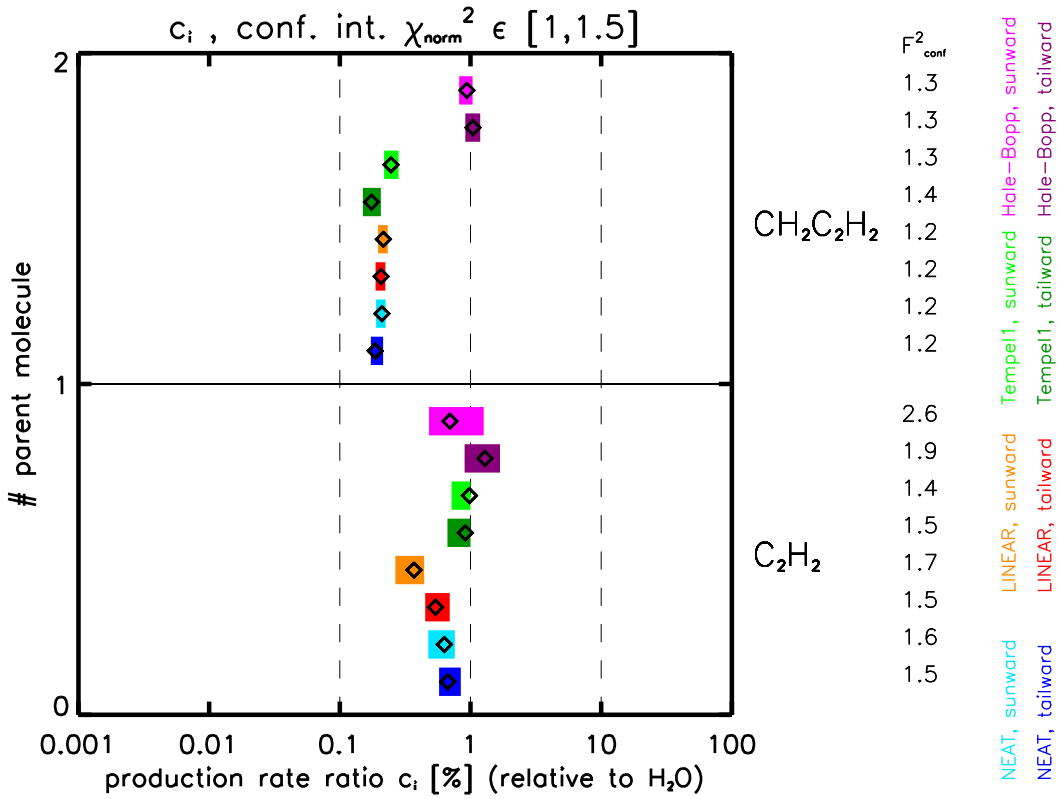

(a) *Production rate ratios c_i.*

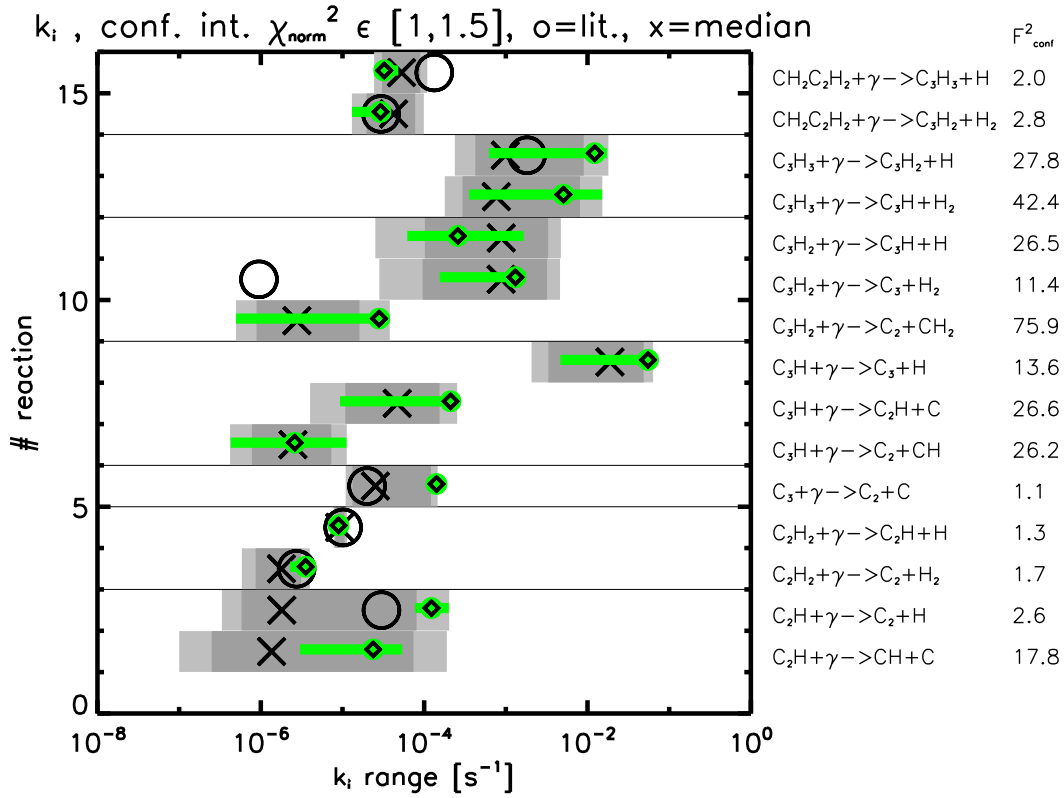

(b) *Photo rate coefficients k_i.*

Figure 9.8: *As in Figure 9.7 but for scenario 2.*

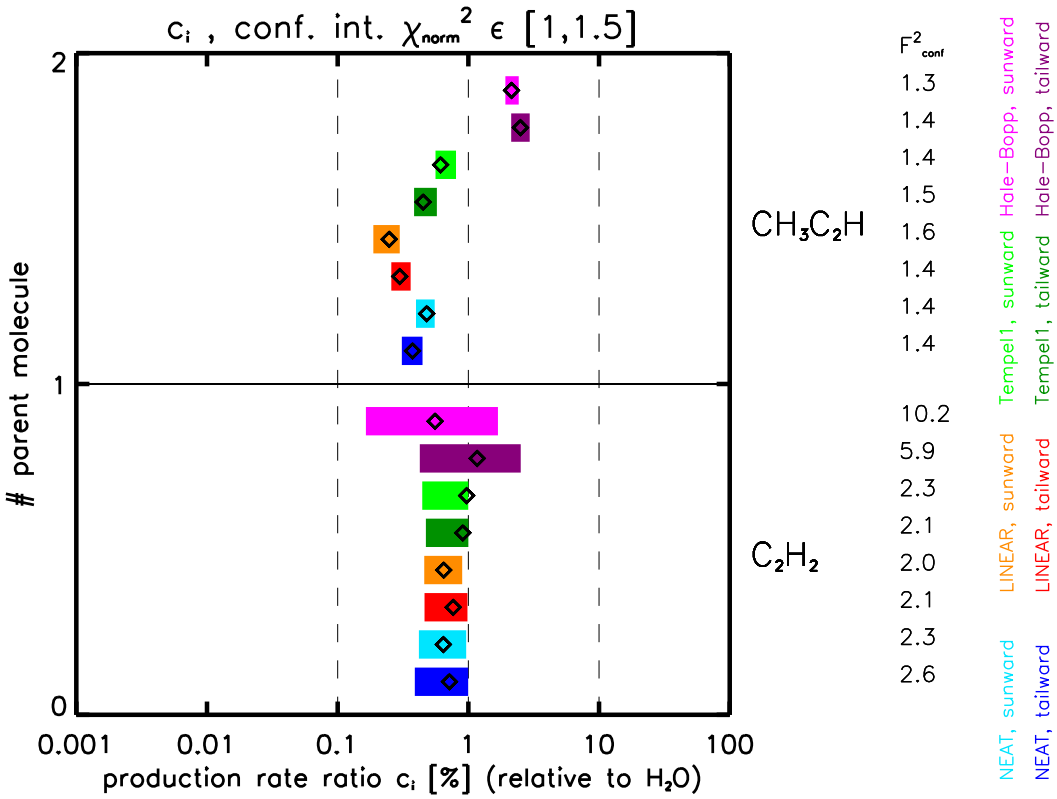

(a) *Production rate ratios c_i.*

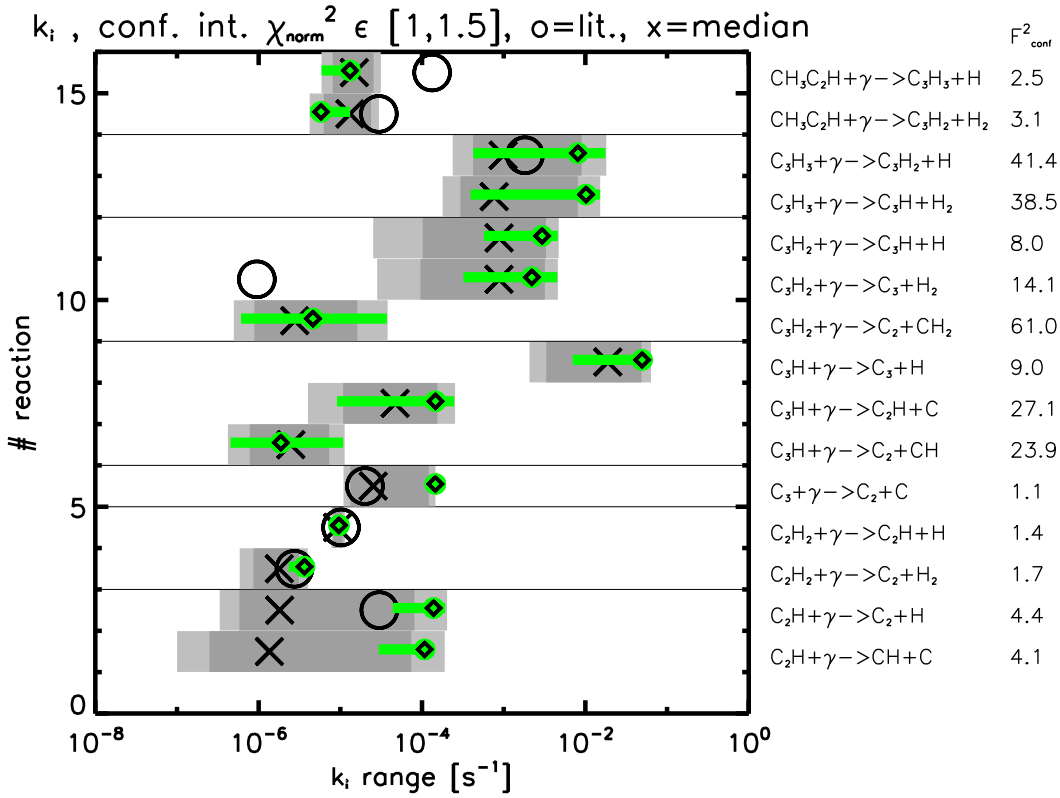

(b) *Photo rate coefficients k_i.*

Figure 9.9: *As in Figure 9.7 but for scenario 3.*

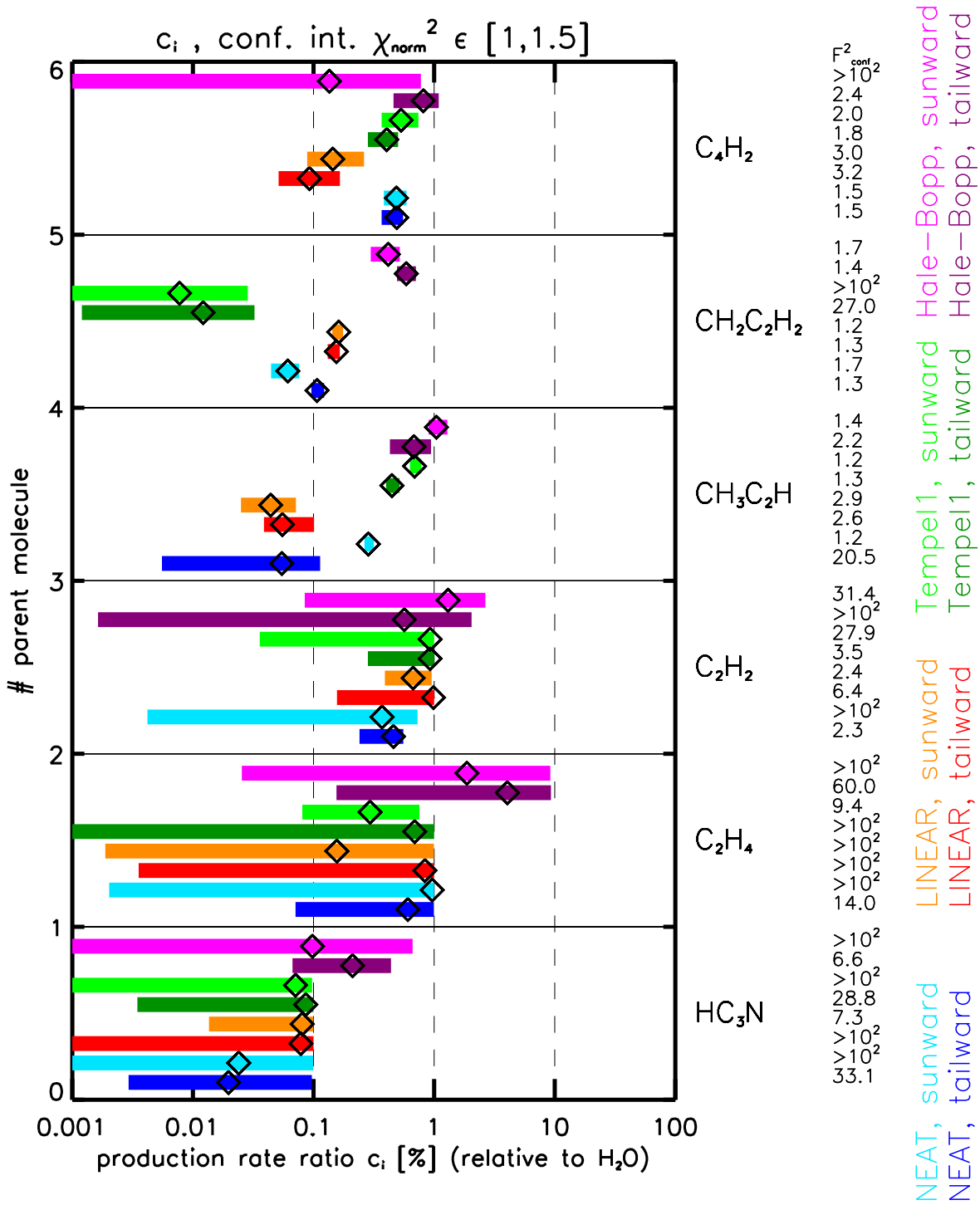

Figure 9.10: *As in Figure 9.7a but for scenario 4.*

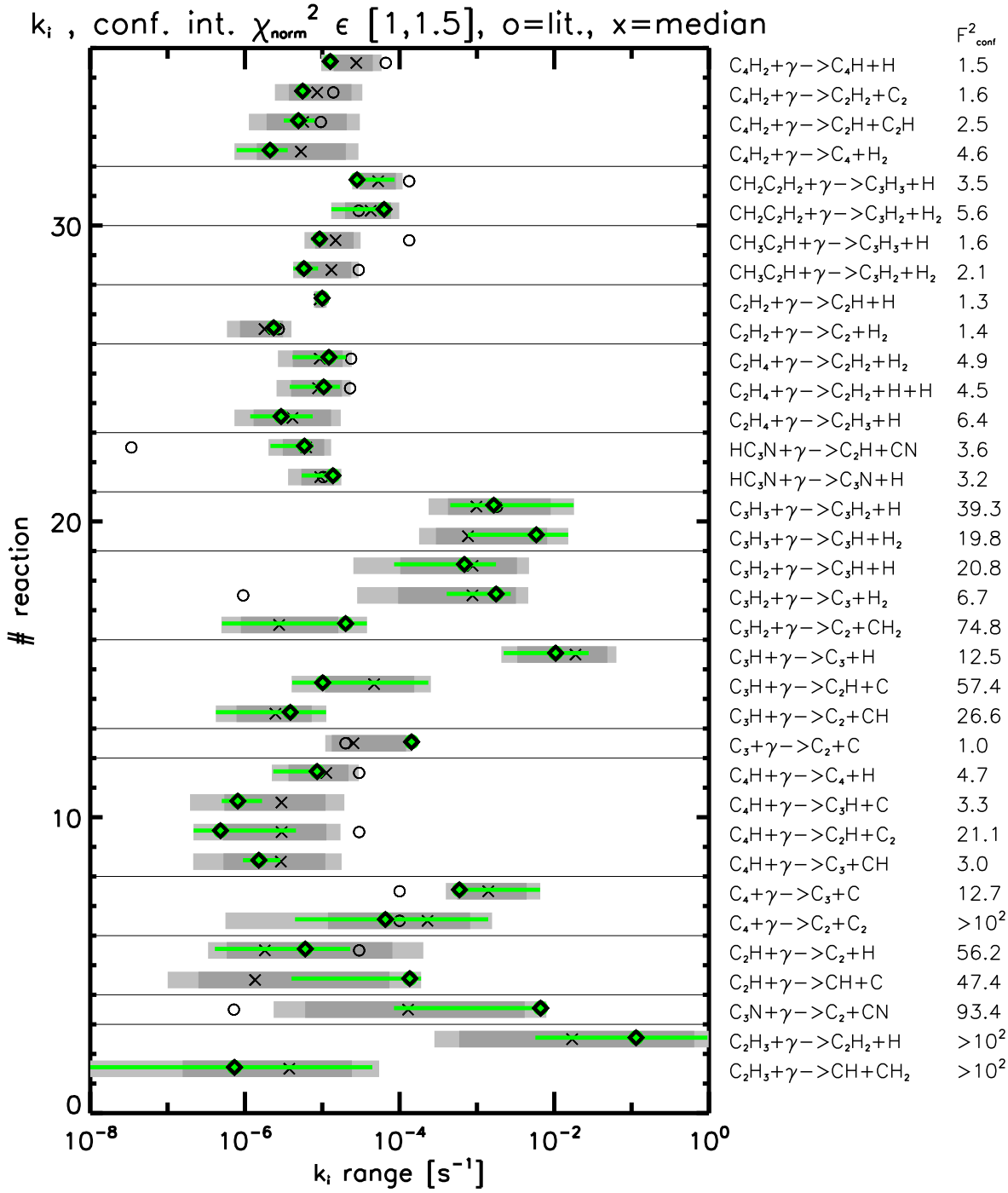

Figure 9.11: *As in Figure 9.7b but for scenario 4.*

For comet Tempel 1 (lightgreen, green bars) the c_i of both parent molecules are well constrained and for comet Hale-Bopp those of $CH_2C_2H_2$. The c_i of C_2H_2 is at most moderately constrained. The c_i for C_2H_4 and HC_3N are poorly constrained for all comets, except Tempel 1 (sunward) and Hale-Bopp (tailward), whereas for comet Hale-Bopp also the c_i of C_4H_2 and C_2H_2 are poorly constrained. This difference in degree of constrainted is since different parent molecules are used to fit the observations of each comet.

In this scenario the optimized rate coefficients are very different for some species in comparison to the scenarios "C_4H_2, C_2H_2", "$CH_2C_2H_2$, C_2H_2" and "CH_3C_2H, C_2H_2", see Figure 9.11. In scenario "C_4H_2, $CH_2C_2H_2$, CH_3C_2H, C_2H_2, C_2H_4, HC_3N", the parent molecule C_4H_2 mainly contributes to C_2 and not to C_3 production, since the rate coefficients of the reactions (R26), (R28) and (R27) are approximately one to two orders of magnitudes larger than that for reaction (R29) (see the discussion of scenario "C_4H_2, C_2H_2"). Reaction (R26) simply does not allow to fit the C_3 observations as discussed for the parent molecule scenario in which C_4H_2 is the sole C_3 parent molecule. However, the pathway for C_3 production seems to be similar in comparison to the scenario "$CH_2C_2H_2$, C_2H_2" or "CH_3C_2H, C_2H_2". The photodissociation rate coefficients of CH_3C_2H are smaller than in scenario "CH_3C_2H, C_2H_2". For C_2H_2 similar photodissociation rate coefficients are obtained. All other reactions are poorly constrained, i.e. $F^2_{\text{conf}} > 10$.

9.3 Summary and Conclusion

This chapter discussed different combinations (scenarios) of C_3 and C_2 parent molecules that have been observed (C_2H_2, HC_3N) and proposed in the literature (C_4H_2, CH_2C_2, CH_3C_2H, C_2H_4) to reproduce the C_3 and C_2 observations of four comets within the uncertainties of the photodissociation reaction's uncertainties using the coma chemistry model described in Chapter 5. To fit the observations of the comets NEAT, LINEAR, Tempel 1 and Hale-Bopp, observed at the heliocentric distances $r_h = 1$, 1.2, 1.5, 3.78 AU, respectively, the present work optimized the parent molecules' production rate ratios (with respect to H_2O) for each comet as well as a common set of rate coefficients of the investigated photodissociation rate coefficients (within their uncertainties).

The results suggest that it is possible to reasonably reproduce the observations of two out of four comets, i.e. NEAT and Hale-Bopp, by the four different parent molecules scenarios: 1) C_4H_2 and C_2H_2, 2) $CH_2C_2H_2$ and C_2H_2, 3) CH_3C_2H and C_2H_2, 4) C_4H_2, $CH_2C_2H_2$, CH_3C_2H, C_2H_2, C_2H_4 and HC_3N when taking the uncertainties of the photodissociation rate coefficients into account. The agreement between model and observations for the comets NEAT, LINEAR and Tempel 1 is similar to the previous work of Weiler (2006). However, the present work requires only one C_3 parent molecule instead of two as used in Weiler (2006).

For the first time it was possible to reproduce reasonably well the observations of two comets observed at very different heliocentric distances, i.e. NEAT and Hale-Bopp observed at $r_h =$ 1.00 AU and $r_h = 3.78$ AU, respectively, for which distances the solar photon flux differs by approximately an order of magnitude.

An important result of the present work is that realistic parent molecule production rate ratios $c_i \leq 1$ % are used to reproduce reasonably well C_3 and C_2 observations at small heliocentric distances, i.e. for comet NEAT observed at $r_h = 1.00$ AU. For comet Hale-Bopp also realistic production rate ratios are obtained. These are, however, higher than 1 % since the comet was observed at $r_h = 3.78$ AU. At such distances from the Sun the sublimation of water is less efficient than that of the investigated hydrocarbon parent molecules due to the smaller insolation.

The observations of the comets LINEAR and Tempel 1 cannot be reasonably reproduced with the investigated parent molecules, even when using all parent molecules. The results might indicate a compositional difference in comparison to the other comets. However, it cannot be

ruled out that the discrepancies between model and observations may be due to outgassing variabilities at the date of the investigated observations. Clearly, a larger set of comets and observations spanning more than one day should be investigated to further constrain the C_3 and C_2 chemistry in comets. Such a larger set of observations would provide a statistically more significant set of observations to deal with possible outgassing variabilities affecting the C_3 and C_2 column densities. Additionally, it is required to reduce the uncertainties of the rate coefficients of the key reactions as determined in Chapter 8. Moreover, ground-truth is required, which will hopefully be provided by the currently running *Rosetta* space mission to comet Churyumov-Gerasimenko, to further calibrate the chemical and physical properties of the cometary nucleus and comae.

In the case of the parent molecule scenario C_4H_2, C_2H_2 it is required that HC_4H isomerizes very efficiently to H_2C_4 after photo-excitation so that it can dissociate into C_4+H_2 and finally C_3 to reproduce the observations of the comets NEAT and Hale-Bopp. Additionally, isomerization to a rhombic C_4H_2 after photo-excitation of HC_4H allows dissociation to $C_2H_2 + C_2$, i.e. a very early C_2 production. The findings could also be explained by the presence of these isomers in cometary ices. Results of this work for the parent molecule scenarios $CH_2C_2H_2$, C_2H_2 and CH_3C_2H, C_2H_2 suggest that a mixture of several C_3 producing reaction paths via C_3H_3, C_3H_2 and C_3H is important.

Strong constraints on the photodissociation rate coefficients, i.e. similar results for all parent molecule scenarios (and well constrained), are obtained for C_3 and C_2H_2 photodissociation. The best fit C_3 photodissociation rate coefficient is an order of magnitude larger than in the previous works of Helbert (2002) and Weiler (2006) whereas the photodissociation rate coefficients for C_2H_2 are similar to those previous works.

Additional constraints on the photodissociation rate coefficients, however depending on the parent molecule scenario, are obtained for the parent molecules C_4H_2, $CH_2C_2H_2$ and CH_3C_2H as well as the species C_4 and C_2H. The best fit photodissociation rate coefficient of the reaction $C_3H_2 + \gamma \rightarrow C_3 + H_2$ (moderately constrained) is two to three orders of magnitude larger in comparison to those previous works. The optimized reaction networks of the present work (photodissociation rate coefficients, parent molecule scenarios) could be tested to investigate the C_3 and C_2 observations of other comets as e.g. the observations of comet Churyumov-Gerasimenko, the target of the ongoing *Rosetta* space mission.

CHAPTER 10

Summary and Outlook

Generally, important constraints to the formation of the Solar System can be deduced by identifying the C_3 and C_2 parent molecules and determining their compositional distribution in each comet population, i.e. the nearly isotropic comets from the Oort cloud and the ecliptic comets from the trans-Neptunian objects. This work investigated the formation of C_3 and C_2 in the coma of the three nearly isotropic comets C/2001 Q4 **(NEAT)**, C/2002 T7 **(LINEAR)** and C/1995 O1 **(Hale-Bopp)** and the one ecliptic comet 9P **(Tempel 1)** by photodissociation of hydrocarbon parent molecules, i.e. molecules that sublimate from the comet nucleus. The present work investigated the parent molecules C_4H_2, $CH_2C_2H_2$, CH_3C_2H, C_2H_2, C_2H_4, C_2H_6 and HC_3N. So far three C_2 parent molecules: C_2H_2, C_2H_6 and HC_3N have been identified by direct measurements. C_2H_4 is prosposed in the literature as an additional C_2 parent molecule, see e.g. Kobayashi and Kawakita (2010), Kobayashi et al. (2013). However, for C_3 no parent molecule has been identified up until now. The molecules C_4H_2, $CH_2C_2H_2$ and CH_3C_2H are proposed in the literature as C_3 parent molecules (Mumma and Charnley, 2011).

For this purpose the present work improved and applied the multifluid hydrodynamical coma chemistry model of Weiler (2006). The present work updated the photochemical part of the reaction network relevant for the formation of C_3 and C_2. The present work investigated photodissociation reactions of the parent molecules C_4H_2, $CH_2C_2H_2$, CH_3C_2H, C_2H_6, C_2H_4, C_2H_2, HC_3N and their product species C_4H, C_4, C_3H_3, C_3H_2, C_3H, C_3, C_2H_5, C_2H_3, C_2H, C_3N and C_2. In the present work a Monte Carlo method was developed and applied to compute, for the first time, the uncertainties of the involved photodissociation rate coefficients. This method computes rate coefficient distributions via the Monte Carlo method using distributions of quantum yield and absorption cross section spectra in the wavelength ranges where no data is available. Also uncertainties in absorption oscillator strengths, computed in the literature by ab initio quantum chemical computations, were estimated as well as uncertainties introduced by the use of fragmentation branching ratios, i.e. when the total quantum yield is unknown. The effect of the uncertainties of the photodissociation reactions on the C_3 and C_2 model column densities was then investigated.

An important scientific question in comet science is to determine whether combinations of the so far observed, i.e. C_2H_2, HC_3N, and proposed hydrocarbon parent molecules, i.e. C_4H_2, $CH_2C_2H_2$, CH_3C_2H, C_2H_4, (parent molecule scenarios) can reproduce the C_3 and C_2 observations in comets and by this to constrain their production rate ratios with respect to water (composition). For this purpose one has to reduce the uncertainties of the rate coefficients of

the involved photodissociation reactions by further laboratory measurements and by performing ab initio quantum chemical computations. To reduce the model output uncertainties efficiently the present work performed a sensitivity analysis to identify the so-called *key reactions*, i.e. the reactions which have the largest effect on the uncertainty of the C_3 and C_2 model column densities. In other words the key reactions are the important reactions weighted by their uncertainty (Carrasco et al., 2008).

In addition, it was investigated whether specific combinations of the observed and proposed parent molecules may reproduce the C_3 and C_2 observational column densities of the comets NEAT, LINEAR, Tempel 1 and Hale-Bopp within the photodissociation rate coefficient uncertainties. Therefore, alternately, the production rate ratios of selected parent molecules were set to zero or optimized. This was done by optimizing the production rate ratios of the investigated parent molecules for each comet and the photodissociation rate coefficients within their uncertainties.

10.1 Aim of This Thesis

In Chapter 1 the aim of this thesis was defined. In the following it is summarized.

Which photodissociation reactions' rate coefficient uncertainties have to be reduced primarily in order to determine if the observed and proposed parent molecules can account for the observed C_3 and C_2?

It was found that the rate coefficients of the investigated hydrocarbon photodissociation reactions have substantial uncertainties, for some reactions even more than two orders of magnitudes (at 3σ level). Large uncertainties are introduced by the lack of quantum yield and absorption cross section values for the important wavelength ranges as well as by an uncertain total quantum yield, i.e. when only the fragmentation branching ratios are reported in the literature. These uncertainties have a significant effect on the modeled C_3 and C_2 column densities. With the sensitivity analysis the responsible key reactions were determined.

Table 10.1 provides an overview of the main key reactions (rank correlation coefficient **(RCC)** $r_s \gtrapprox 0.5$) for each of the investigated parent molecules alone and a mixture of these molecules (nominal composition, see Chapter 8) for the cometocentric distances at which observations are available for the comets investigated in this work.

It was found that, even with the updates for the photodissociation reactions of the species $C_2H_{(6,5,4,3,2,1,0)}$ applied in the present work, C_2H_6 does only produce very small amounts of C_2 in the cometocentric distance range of the observations for the comets Hale-Bopp, qualitatively confirming Helbert (2002), and NEAT, LINEAR and Tempel 1, qualitatively confirming Weiler (2006), when using realistic parent molecule production rate ratios (with respect to water). C_2H_6 produces $\gtrapprox 1$ order of magnitude less C_2 than the other investigated parent molecules $CH_2C_2H_2$, CH_3C_2H, C_4H_2, C_2H_2, C_2H_4 and HC_3N. C_2H_4 might produce significant amounts of C_2 only in the outer observational cometocentric distance ranges of the investigated comets. HC_3N produces only small amounts of C_2 when assuming an upper limit of the production rate ratio approximately an order of magnitude smaller than for the other parent molecules, as suggested in the literature from observations.

Can one account for the C_3 and C_2 observations with the investigated parent molecules within the uncertainties of the photodissociation rate coefficients?

The results suggest that one can reasonably well reproduce the C_3 and C_2 observations of two out of the four comets investigated, namely NEAT and Hale-Bopp using the parent molecule

Table 10.1: *Overview of the main key reactions (rank correlation coefficient* ***(RCC)*** $r_s \gtrapprox 0.5$*) for each of the investigated parent molecules alone and a mixture of these molecules (nominal composition, see Chapter 8) at cometocentric distances of the observations available for the comets investigated in this work.*

parent molecule(s)	*most important key reactions* ($r_s > 0.5$)	
	for C_3	for C_2
C_4H_2	$C_4H_2 \xrightarrow{\gamma} C_4 + H_2$ $C_3 \xrightarrow{\gamma} C_2 + C$	$C_4H_2 \xrightarrow{\gamma} C_2H_2 + C_2$
$CH_2C_2H_2$ or CH_3C_2H	$C_3 \xrightarrow{\gamma} C_2 + C$ $CH_2C_2H_2 \xrightarrow{\gamma} C_3H_2 + H_2$	$C_3 \xrightarrow{\gamma} C_2 + C$ $C_3H_2 \xrightarrow{\gamma} C_3 + H_2$
C_2H_2 or C_2H_4 or C_2H_6	-	$C_2H_2 \xrightarrow{\gamma} C_2 + H_2$ $C_2H \xrightarrow{\gamma} C_2 + H$
HC_3N	-	$C_3N \xrightarrow{\gamma} C_2 + CN$
mixture of C_4H_2, $CH_2C_2H_2$, CH_3C_2H, C_2H_2, C_2H_4, C_2H_6, HC_3N	$C_3 \xrightarrow{\gamma} C_2 + C$	$C_3 \xrightarrow{\gamma} C_2 + C$ $C_4H_2 \xrightarrow{\gamma} C_2H_2 + C_2$

combinations 1) C_4H_2, C_2H_2, 2) $CH_2C_2H_2$, C_2H_2, 3) CH_3C_2H, C_2H_2 and 4) C_4H_2, $CH_2C_2H_2$, CH_3C_2H, C_2H_2, C_2H_4, HC_3N when taking the uncertainties of the photodissociation rate coefficients into account. The agreement between model and observations of the comets NEAT, LINEAR and Tempel 1 is similar to the previous work of Weiler (2006).

The present work uses for the first time realistic parent molecule production rate ratios $c_i \leq 1\,\%$ to reasonably well reproduce C_3 and C_2 observations at small heliocentric distances for comet NEAT ($r_h = 1.00$ AU). For comet Hale-Bopp this work also uses realistic parent molecule production rate ratios as in the previous study of Helbert (2002). Additionally the present work reproduced for the first time observations of the comets NEAT and Hale-Bopp at the very different heliocentric distances $r_h = 1.00$ AU and $r_h = 3.78$ AU, i.e. at distances where the insolation differs by approximately an order of magnitude.

To reproduce the observations of the two comets NEAT and Hale-Bopp with the parent molecules C_4H_2 and C_2H_2 it is required to assume that isomerization to C_4H_2 isomers is efficient, especially the CH_2C_3 isomer, with subsequent dissociation to $C_4 + H_2$. C_4 then photodissociates into $C_3 + C$. The isomerization to a rhombic C_4H_2 isomer allows the formation of $C_2 + C_2H_2$, i.e. the formation of C_2 in one step. Another interpretation than these isomerizations could be that these C_4H_2 isomers are present in the comet nucleus' ices. To fit the C_3 observations using either $CH_2C_2H_2$ or CH_3C_2H requires much higher photodissociation rate coefficients for the product species C_3H_2 and C_3.

The observations of comet LINEAR and comet Tempel 1 could not be reproduced within the uncertainties of the rate coefficients of the photodissociation reactions with the investigated parent molecule combinations. This may indicate a different chemical composition. However, also other effects cannot be ruled out such as e.g. outgassing variations by rotation of the comet nucleus and surface areas with different levels of activity or the sudden exposure of ices of different composition.

10.2 Outlook

10.2.1 Model Improvements

A comparison between a one-dimensional **(1D)** and a 3D coma chemistry model (including rotation by the comet nucleus) would allow to investigate the effect of a rotating nucleus with outgassing surface areas of different strength and composition on the C_3 and C_2 column density profiles, see e.g. Crifo et al. (2004).

Future laboratory measurements and ab initio computations should determine quantum yields and absorption cross sections for the key reactions as determined in the present work. For example for the reaction $C_3 + \gamma \rightarrow C_2 + C$.

Future work has to investigate the impact of an update on the photochemistry by including various isomers, e.g. of C_4H_2, C_4H, C_3H_3, C_3H_2, C_3H, when quantum yields and/ or absorption cross sections become available for the so far undetermined wavelength ranges.

An investigation of the formation of CN (cyanide) radicals in the cometary coma from parent molecules such as e.g. HCN and CH_3CN will provide clues as to whether using different CN parent molecules lead to significant differences in the CN column density profiles, i.e. to see if these parent molecules can be distinguished. To model the formation of CN it is important to include an additional hydrodynamical fluid for the superthermal species such as H (with a separate H fluid temperature), since these superthermal species can drive chemical reactions with HCN species (to produce HNC) depending on their kinetic energy (Rodgers and Charnley, 1998). Also for such an investigation the uncertainties of the involved photodissociation rate coefficients have to be computed by using the method developed in the present work. Also for the collisional reactions the uncertainties have to be investigated. On including such a treatment for superthermal species one could also investigate the effect on the hydrodynamics, i.e. the influence on the common hydrodynamical velocity of the model used in this work. This study should also comprise an investigation of the uncertainty of the excess kinetic energy in the photodissociation of H_2O. Additionally, a comparison with a Monte Carlo **(MC)** model could complement this study.

In the inner coma of comet 1P **(Halley)** at ≈ 2300 km distance to the nucleus anions were detected during the Giotto space mission with mass peaks at $7-19$, $22-65$ and $85-110$ amu (Chaizy et al., 1991), although with large density uncertainties. A possible effect on the formation of C_3 and C_2 by anions in the inner coma and maybe at larger distances should be investigated. However, modelling efforts in this area of research face the problem that the rate coefficients of many anion forming and destroying reactions are highly uncertain or unconstrained as discussed by Chaizy et al. (1991) and Cordiner and Charnley (2013). Therefore, additional laboratory measurements and ab initio calculations are required to model anion chemistry. The ongoing *Rosetta* space mission to comet 67P **(Churyumov-Gerasimenko)** will investigate whether and which hydrocarbon anions are present.

10.2.2 Future Investigation of the Coma Chemistry

When quantum yields and absorption cross sections become available for the so far undetermined wavelength ranges for the investigated molecules, which is required to compute photodissociation rate coefficients with sufficiently small uncertainty, it can be investigated if parent molecules can be distinguished by C_3 and C_2 observations or if these produce similar C_3 and C_2 column density profiles. This may also provide hints to understand the so-called carbon-chain depleted comets, i.e. comets with low or even undetectable C_3 and/or C_2 coma densities, see e.g. A'Hearn et al. (1995) and Schleicher (2008). The observed depletion might be due to the lack of specific hydrocarbon molecules. Such possibly existing sub-groups of depleted comets would provide

further constraints to Solar System formation by investigating compositional correlations with other various chemical components (ices, dust).

One has to reinvestigate the formation of C_3 and C_2 using the data set of Hale-Bopp (Rauer et al., 2003, Helbert, 2002) using the improved model of this work. This data set comprises observations between $r_h = 2.86$ AU and $r_h = 4.74$ AU (pre-perihelion and post-perihelion observations). This study may be combined with the study of the comets NEAT, LINEAR and Tempel 1, observed at $r_h = 1.00$, 1.20, 1.51 AU, respectively, as investigated in the present work. Additional observations (comets and nights) will provide a larger, statistically more significant, data set to further constrain the chemistry in comets.

A direct search in the IR and at radio wavelengths for the molecules C_4H_2, $CH_2C_2H_2$, CH_3C_2H, C_2H_2, C_2H_4 and HC_3N would provide constraints to the C_3 and C_2 formation in comets. Also important would be to search in cometary comae for even larger hydrocarbon molecules which have already been detected in the interstellar matter **(ISM)**, e.g. in the Taurus molecular cloud 1 **(TMC-1)** Remijan et al. (2006b) detected the methylpolyynes CH_3C_4H (methyldiacetylene) and CH_3C_6H (methyltriacetylene) and Lovas et al. (2006) detected CH_2CCHCN (cyanoallene).

The ongoing *Rosetta* space mission to comet 67P **(Churyumov-Gerasimenko)** will provide the composition of the cometary nucleus' ices and the dust as well as the composition of the coma gas. The Cometary Second Ion Mass Analyser **(COSIMA)** experiment onboard the Rosetta orbiter searches for the molecules C_2H_4, C_3H_3, C_3H_7 and C_4H_8 via a time of fly **(TOF)** and a second ion mass spectrometer **(SIMS)** experiment (Kissel et al., 2007). The Visible and Infrared Thermal Imaging Spectrometer **(VIRTIS)** experiment analyses solid material and hydrocarbon ices such as e.g. C_2H_n ($n = 2, 4, 6$) and C_3H_8 on the nucleus surface (reflectance spectra) (Coradini et al., 2007). The Rosetta Orbiter Spectrometer for Ion and Neutral Analysis **(ROSINA)** instrument is capable of analysing ionic and neutral species, as e.g. C_2, C_3, C_2H, both C_2H_2 isomers, C_4H, HC_3N, C_2H_4, C_2H_6 and C_3H_8, using two mass spectrometers with different resolution (Balsiger et al., 2007), see also Gulkis and Alexander (2008) for an overview. Important is also the COSAC instrument onboard the lander *Philae* which analyses comet nucleus samples with a gas chromatograph and a mass spectrometer (Goesmann et al., 2007). The investigations of the Rosetta spacecraft and the Philae lander provide the basis to better constrain the hydrocarbon chemistry in cometary comae by the coma chemistry model used in the present work by comparing also the intermediate photodissociation product species.

Part IV

Appendix

APPENDIX A

Modelling Branching Ratio Uncertainties Using Dirichlet Distributions

A.1 The Dirichlet Distribution

To model uncertainties of properties $b_1, \ldots, b_n \in [0, 1]$ that are constrained by

$$\sum_{i=1}^{n} b_i = 1 \tag{A.1}$$

the Dirichlet distribution

$$(b_1, ..., b_n) \sim \text{Dirichlet}(\gamma_1, ..., \gamma_n) \tag{A.2}$$

can be used. Its probability density function **(PDF)** is defined as

$$p(b_1, \ldots, b_n; \gamma_1, \ldots, \gamma_n) = \frac{1}{B(\gamma_1, \ldots, \gamma_n)} \prod_{i=1}^{n} b_i^{\gamma_i - 1}\,, \tag{A.3}$$

with B the beta and Γ the gamma function

$$B(\gamma_1, \ldots, \gamma_n) = \frac{\prod_{i=1}^{n} \Gamma(\gamma_i)}{\Gamma(\gamma)}\,, \tag{A.4}$$

$$\gamma = \sum_{i=1}^{n} \gamma_i\,. \tag{A.5}$$

The Dirichlet distribution is a special multidimensional version of the Beta distribution

$$b \sim \text{Beta}(\alpha_1, \alpha_2)\,, \tag{A.6}$$

$$p(b; \alpha_1, \alpha_2) = \frac{1}{B(\alpha_1, \alpha_2)} b^{\alpha_1 - 1}(1 - b)^{\alpha_2 - 1}\,. \tag{A.7}$$

It is defined over $b \in [0, 1]$ with the concentration parameters $(\alpha_1, \alpha_2) > (0, 0)$. E.g. $(\alpha_1, \alpha_2) = (0.5, 0.5)$ is a u-shaped distribution, $(\alpha_1, \alpha_2) = (1, 1)$ is a uniform distribution, whereas $(\alpha_1, \alpha_2) = (2, 1)$ is a distribution having a higher probability concentration for b closer to 1.

The so-called marginal distributions of the Dirichlet distribution, i.e. the distribution for each element b_i from Equation (A.2), are beta distributions of the form

$$b_i \sim \mathrm{Beta}(\gamma_i, \gamma - \gamma_i)\,. \tag{A.8}$$

Equation (A.3) measures the likelyhood of the occurrence of a set of parameters $(b_1, \ldots, b_n)$. For example, $\gamma_1 = \ldots = \gamma_n = 1$, then all possible realizations of $(b_1, \ldots, b_n)$ are equally probable. However, the $\mathrm{Beta}(\gamma_i, \gamma - \gamma_i)$ are not uniform over $[0, 1]$, since $(\alpha_1, \alpha_2) \neq (1, 1)$ for $n > 2$. This is a consequence of the Dirichlet distribution's property (A.1).

A.2 The Truncated Uniform Dirichlet Distribution

Sometimes one needs to model branching ratio uncertainties, where all branching ratios are allowed to be distributed over the same interval $b_i \in [b^{\min}, b^{\max}]$, $i = 1, \ldots, n$, and the Dirichlet distribution being uniform, i.e. all combinations of branching ratios $(b_i, \ldots, b_n)$ from the distribution are equally probable. This is achieved, as described before, by setting $\{\gamma_i = 1\}_{i=1}^{n}$ in Equation (A.2) and by additionally rejecting those $(b_i, \ldots, b_n)$ of which some elements are outside the desired branching ratio uncertainty interval. The resulting distribution is denoted 'uniform truncated Dirichlet distribution' **(Diut)** (Carrasco et al., 2007).

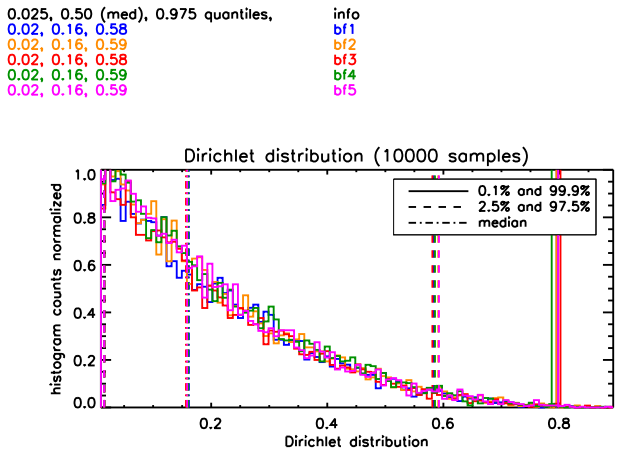

Figure A.1: *Five branching ratio marginal distributions (different colors) of the Diut*$([0.0001, 1.0], 5)$ *distribution defined over the interval* $[0.0001, 1.0]$. *The solid, dashed and dash-dotted vertical lines mark the* $[0.001, 0.999]$ *(*$\approx 3\sigma$*),* $[0.025, 0.975]$ *(*$\approx 2\sigma$*) and the* 0.5 *(median) percentiles, respectively.*

The rejection method is very inefficient when the number of reactions (of a species) is large and when their uncertainty intervals are very different in size and location. An efficient algorithm for such cases is the number-theoretic method of Fang and Yang (2000, experimental design) used in Plessis et al. (2010). However, in this work it was decided to define the branching ratio distribution over the range $[0.0, 1.0]$, see Chapter 7, i.e. $\mathrm{Diut}([0.0, 1.0], n)$ with n reactions, so that the rejection method was not required.

An example distribution is given in Figure A.1 with $\mathrm{Diut}([0.0001, 1.0], 5)$. The marginal distributions are evidently not uniform, i.e. there are conditional probabilities due to the constrain (A.1). This is because e.g. for very high branching ratio uncertainties, sampling a very high b_i demands very low b_j for $j \neq i$. Because this correlation is true for all branching ratios, triangular shaped marginal distributions are the result.

A.3 Sampling From a Dirichlet Distribution

For the estimation of branching ratio uncertainties, samples from a Dirichlet distribution are drawn with the Interactive Data Language **(IDL)** function `RANDOMDIR.pro` from NASA-IDL-

Lib. (2011) This program uses the algorithm

$$(b_1, ..., b_n) = (g_1, ..., g_n) \Big/ \sum_{i=1}^{n} g_i \sim \text{Dirichlet}(\gamma_1, ..., \gamma_n)\,, \tag{A.9}$$

to generate Dirichlet distributed random variables $(b_1, ..., b_n)$. Therein, the $g_i \sim \text{Gamma}(\gamma_i)$ are Gamma-distributed random variables. The normalization by their sum ensures the constrain of Equation (A.1). The random variables of each Gamma distribution were generated in `RANDOMDIR.pro` by using the IDL procedure `RANDOMU.pro` with the keyword `GAMMA` $= \gamma_i$.

APPENDIX B

Absorption Parameters

The absorption cross sections σ used in this work are calculated from different expressions of absorption used in the literature. The relevant parameters are absorption cross section σ, absorption coefficient K and, molar extinction coefficient and base ten (decadic) molar extinction coefficient ϵ. Their relation to each other is described in the following text.

The ability of a substance to absorb light can be quantified by comparing the transmitted reduced light intensity I_{L} by propagation through an absorption cell of length L with the reference initial light intensity I_0. At each infinitesimal length dl the intensity is reduced by dI. The strength of reduction depends on the absorbing substance expressed by the absorption coefficient K

$$dI = -K\, I(l)\, dl\,. \tag{B.1}$$

Integration of (B.1) leads to the Beer-Lambert law

$$\int_{I_0}^{I_{\mathrm{L}}} \frac{1}{I'}\, dI' = \int_0^L -K\, dl \qquad \Leftrightarrow \qquad \ln(I_{\mathrm{L}}/I_0) = -KL\,. \tag{B.2}$$

The reduction of the initial intensity can also be related to the base ten (decadic) logarithm with the corresponding decadic absorption coefficient K', where K and K' are related by $K = K' \cdot \ln(10) = K' \cdot 2.303$,

$$\log(I_0/I_{\mathrm{L}}) = -K'L\,. \tag{B.3}$$

K depends on an intrinsic property of the substance and on the amount of that substance

$$K = \sigma \cdot n = \epsilon \cdot C = \varepsilon \cdot p\,. \tag{B.4}$$

The amount of the substance can be expressed either by the number density n or the molar concentration C or the pressure P at a given temperature of the substance present. The intrinsic absorption property can be expressed either by the absorption cross section σ or the molar extinction coefficient (absorptivity) ϵ or the pressure related extinction coefficient ε (Jimenez, 2005, p.8, adapted here). The units are $[\sigma] = \mathrm{cm}^2/\mathrm{molecule}$, ϵ in units per concentration and per length e.g. as $[\epsilon] = (\mathrm{mol/dm}^3)^{-1} \cdot \mathrm{cm}^{-1} = (\mathrm{mol/l})^{-1} \cdot \mathrm{cm}^{-1} = \mathrm{cm}^2 \cdot \mathrm{mmol}^{-1}$, mmol is milli mol, $[\varepsilon] = \mathrm{atm}^{-1} \cdot \mathrm{cm}^{-1}$ and $[n] = \mathrm{molecules/cm}^3$, $[C] = \mathrm{mol/dm}^3 = \mathrm{mol/l}$ (Haken and Wolf, 2000, Metzger and Cook, 1964) and the pressure $[p] = \mathrm{atm}$.

In the literature the absorption coefficient K is sometimes given in units $\mathrm{cm}^{-1} \cdot \mathrm{amg}^{-1}$ instead of cm^{-1}, which is denoted here with K_{amg}. The amagat (amg) is the number density n of the investigated material under the experiment's conditions p, T relative to the density $n_\circ$ at standard conditions $p_\circ = 1013$ mbar and $T_\circ = 273$ K, with $V = const$. The value $n_\circ = 2.687 \cdot 10^{19}\,\mathrm{cm}^{-3}$ is also denoted as the Loschmidt number (Mohr et al., 2008)

$$\mathrm{amg} = \frac{n}{n_\circ} \qquad \text{and} \qquad K_{\mathrm{amg}} = K/\mathrm{amg}. \tag{B.5}$$

The unit amg is variable because it depends on the experimental conditions. It can be calculated by

$$V = \frac{nkT}{p} = \frac{n_\circ k T_\circ}{p_\circ} \qquad \Leftrightarrow \qquad \frac{p}{1013\,\mathrm{mbar}} \frac{273\,\mathrm{K}}{T} = \frac{n}{n_\circ} = \mathrm{amg}\,. \tag{B.6}$$

The absorption cross section σ is therefore, with (B.4) and (B.5), given by

$$\sigma = \frac{K}{n} = K \frac{1}{n} \frac{n_\circ}{n_\circ} = K \frac{1}{\eta} \frac{1}{n_\circ} = \frac{K_{\mathrm{amg}}}{n_\circ}\,. \tag{B.7}$$

Sometimes the absorption coefficient is given in units $\mathrm{cm}^{-1}\,\mathrm{atm}^{-1}$, denoted here as K_{atm}, where the atm $= 1013\,\mathrm{mbar}$. To calculate σ from K_{atm} one uses

$$\sigma = K_{\mathrm{atm}} \cdot 3.72 \cdot 10^{-20} = \frac{K_{\mathrm{atm}}}{n_\circ}\,, \tag{B.8}$$

which is analogous to calculating σ from K_{amg}. See also Gericke (2012) for a summary on absorption parameters and their relation to each other or Okabe (1981), Glicker and Okabe (1987) for sample calculation at $\lambda = 1470$ Å.

For example to calculate σ from the molar decadic extinction coefficient ϵ_{mol} in units $\mathrm{cm}^2 \cdot \mathrm{mol}^{-1}$ multiply by $\ln(10)/N_A = 3.82 \cdot 10^{-18}\,\mathrm{mol}$. Absorption cross sections σ can also be defined in Megabarns (Mb). These are simply defined as $\sigma(\lambda) = 10^{-18}\mathrm{cm}^2 = 1\,\mathrm{Mb}$.

APPENDIX C

Computation of Oscillator Strengths

This thesis investigates the formation of C_3 and C_2 in cometary comae via photodissociation of hydrocarbons. Therefore, photodissociation rate coefficients are required for all investigated hydrocarbon species. van Hemert and van Dishoeck (2008) provide ab initio electronic absorption oscillator strengths for the hydrocarbon species C_4H, C_4, HC_3H, C_3H, C_3 and C_2H. No continuous absorption cross sections are available for these species. A short overview of the computation and the simplifications applied in van Hemert and van Dishoeck (2008) shall now be given, see also van Dishoeck and Visser (2011).

At the beginning of all quantum computations the Schrödinger equation is required

$$H\Psi(\mathbf{r},\mathbf{R}) = E\Psi(\mathbf{r},\mathbf{R})\,, \tag{C.1}$$

where the wavefunction Ψ contains all information for a given molecule being in a state with the total energy E, $\mathbf{r}$ denotes the spatial and spin coordinates of the n electrons in the molecule and $\mathbf{R}$ the coordinates of the N nuclei in the molecule. H consists of the potential energies due to mutual interactions between the nuclei and the electrons (V) and the respective sum of the kinetic energy operators of the electrons and of the nuclei (T), i.e. the Hamilton operator is $H = T + V$.

In the approach used by van Hemert and van Dishoeck (2008) the time-independent Schrödinger equation is simplified by the Born-Oppenheimer approximation, in which the motion of the nuclei and the electrons is separated by

$$\Psi(\mathbf{r},\mathbf{R}) = \Psi^{\mathrm{el}}(\mathbf{r};\mathbf{R}) \cdot \Psi^{\mathrm{nuc}}(\mathbf{r},\mathbf{R})\,. \tag{C.2}$$

In Equation (C.2) the semicolon indicates that $\mathbf{R}$ is a parameter in $\Psi^{\mathrm{el}}(\mathbf{r};\mathbf{R})$. The Born-Oppenheimer approximation is justified by the fact that the electrons move much faster than the nuclei and therefore the nuclei's location, i.e. $\mathbf{R}$, and momentum do not change significantly during an electronic transition, i.e. a change of $\mathbf{r}$. The electronic potential energy curves $E^{\mathrm{el}}(\mathbf{R})$ and the electronic wave functions $\Psi^{\mathrm{el}}(\mathbf{r};\mathbf{R})$ are determined by solving

$$H^{\mathrm{el}}\Psi^{\mathrm{el}}(\mathbf{r};\mathbf{R}) = E^{\mathrm{el}}(\mathbf{R})\Psi^{\mathrm{el}}(\mathbf{r};\mathbf{R}) \tag{C.3}$$

at a fixed position of the nuclei, i.e. now considering $\mathbf{R}$ as a parameter. Putting Equation (C.2) into Equation (C.1), applying Equation (C.3) and using $\nabla^2_\alpha \Psi^{\mathrm{el}}\Psi^{\mathrm{nuc}} = \nabla^2_\alpha \Psi^{\mathrm{nuc}}\Psi^{\mathrm{el}}$ (Born-

Oppenheimer approximation) one obtains

$$\left[-\sum_{\alpha}\left(\frac{1}{2}M_{\alpha}\right)\nabla_{\alpha}^{2}+E^{\mathrm{el}}(R)-E\right]\Psi^{\mathrm{nuc}}(R)=0\,, \tag{C.4}$$

where α denotes nucleus α and M_α its mass. In the above equations atomic units ($a.u.$) have been used: $\hbar = m_e = e = 1$. Then, the units of distance and energy become: $a.u. = a_0 = 0.52918$ Å, i.e. Bohr radius a_0, and $a.u. = 27.21$ eV, i.e. energy in Hartrees, respectively (van Dishoeck and Visser, 2011).

For simplicity, a diatomic molecule with internuclear distance R is henceforth regarded. For a diatomic molecule the transition dipole moment $\mu(R)$ between a lower state l and an upper state u is computed via

$$\mu_{ul}(R) = \langle \Psi_u^{\mathrm{el}}(r;R)|d|\Psi_l^{\mathrm{el}}(r;R)\rangle \tag{C.5}$$

where the integration is over all electronic coordinates r and d is the electric dipole moment in atomic units. This equation expresses that the transition is the more likely the more the lower state's and the excited state's electronic orbitals overlap. The dipole moment operators for linear molecules are given by

$$d = -\sum z_j \qquad \text{for } \Delta\Lambda = 0\,, \tag{C.6}$$

$$d = -\sum \left(x_j + i\cdot y_j\right)/\sqrt{2} \qquad \text{for } \Delta\Lambda = \pm 1\,, \tag{C.7}$$

where x_j, y_j and z_j are the position operators and $\Delta\Lambda$ the change of the projected orbital angular momentum Λ [1].

If the electronic energies are determined for several nuclear distances R the electronic potential curves can be constructed. An example of the electronic potential energy surfaces for the OH radical are shown in Figure C.1, which were computed in van Dishoeck and Dalgarno (1983). Similar computations can be found in the literature for diatomic molecules and in some cases for larger molecules, e.g. Engel et al. (1992) for H_2O or Klossika et al. (1997) for HNCO.

One can compute the absorption cross section for the excitation from the electronic ground state's bound vibrational level v'' into the upper electronic state's vibrational continuum k' via

$$\sigma_{v''} = 2.69\cdot 10^{-18}\cdot g\cdot \Delta E\cdot \left|\langle \Psi_{k'}^{\mathrm{nuc}}(R)|\mu(R)|\Psi_{v''}^{\mathrm{nuc}}(R)\rangle\right|^2\,. \tag{C.8}$$

or the absorption oscillator strength f for a transition into the vibrational level v' of an upper bound electronic state via

$$f_{v'v''} = \frac{2}{3}\cdot g\cdot \Delta E_{v'v''}\cdot \left|\langle \Psi_{v'}^{\mathrm{nuc}}(R)|\mu(R)|\Psi_{v''}^{\mathrm{nuc}}(R)\rangle\right|^2\,, \tag{C.9}$$

where g_{ul} is the degeneracy factor. For $\Sigma \to \Pi$ transitions $g_{ul} = 2$ and for for all other transitions ($\Sigma \to \Sigma$, $\Pi \to \Sigma$, $\Pi \to \Pi$, $\Pi \to \Delta$, $\Delta \to \Pi$ and $\Delta \to \Delta$) $g_{ul} = 1$. $\Delta E_{ul}(R)$ is the energy difference in Hartrees at internuclear distance R (van Dishoeck and Dalgarno, 1984).

[1] Molecular term symbol of electronic state with general form ${}^{2S+1}\Lambda_{\Omega(\mathrm{g/u})}^{(+/-)}$. S: total spin multiplicity, i.e. number of unpaired e^- times spin 1/2, Λ: projection of orbital angular momentum ($\Sigma, \Pi, \Delta, \ldots = 0, 1, 2, \ldots$), Ω: projection of total angular momentum, onto internuclear distance, respectively, g/u: parity (only for homonuclear diatomics), +/-: symmetry along an arbitrary plane containing internuclear axis. Example: C_2 ground state $X^1\Sigma_g$. An empirical notation of an electronic transition is $\tilde{X}^1A_1 \to \tilde{B}^1A_1$, which means ${}^1A_1 = {}^{2S+1}A_\Omega$, $\tilde{X}$: electronic ground state, all electronically excited states with the same Λ are denoted B, C, etc., ordered by energy above $\tilde{X}$. $\sim$ is added for polyatomics ($\neq$ diatomics). For states with different Λ than the ground state one uses a, b, c. Examples: C_3 excited state to ground state transition: $\tilde{A}^1\Pi_u - \tilde{X}^1\Sigma_g^+$, C_2 excited state to excited state transition $d^3\Pi_g - a^3\Pi_u$ (Demtröder, 2003, chapter 2.4).

In van Hemert and van Dishoeck (2008) electric dipole allowed transitions for molecules containing up to six atoms, e.g. the linear radical l−C_5H, were investigated. These authors limited their computations to electronic transitions to states above the lowest dissociation threshold energy and below $E = 13.6$ eV. Additionally, only transitions in the Franck-Condon region, i.e. at the equilibrium geometry $\mathbf{R} = \mathbf{R}_{\text{equil}}$ of the molecule in the electronic ground state, were evaluated, since photo rate coefficients are mainly determined by these so-called vertical excitations. For the example of OH in Figure C.1 this at $R \approx 1.9\ a_0$

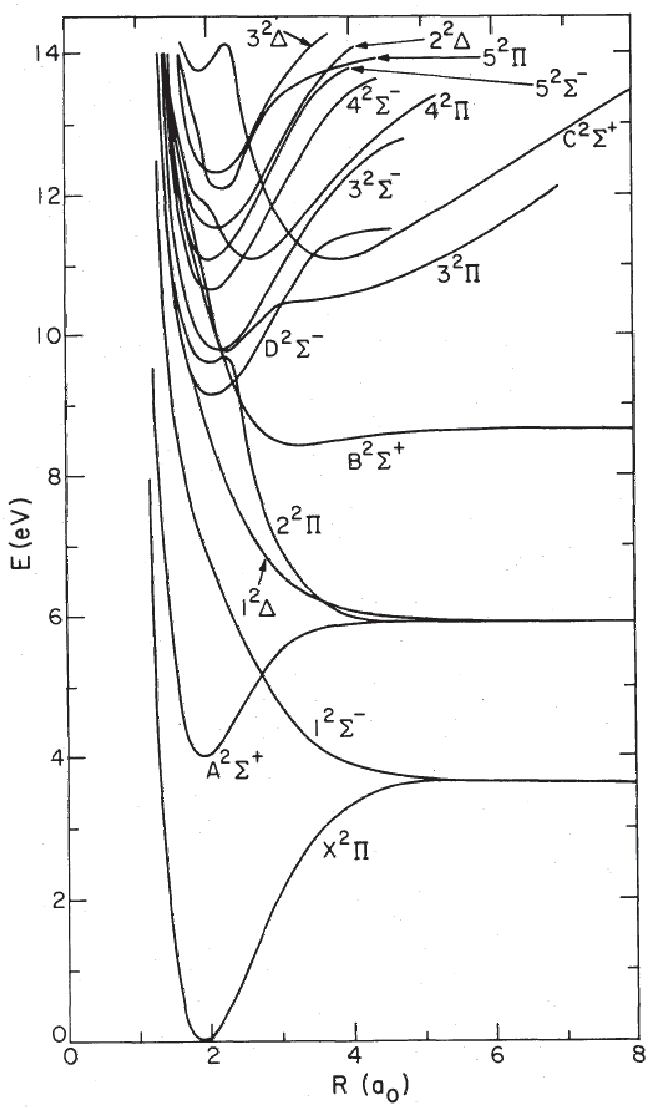

Figure C.1: *Full electronic potential energy surfaces of the* OH *radical. The Franck-Condon region is at the minimum of the ground electronic state* $X^2\Pi$, $R \approx 1.9\ a_0$. *Source: van Dishoeck and Visser (2011).*

The transition dipole moments $\mu_{ul}(\mathbf{R}_{\text{equil}})$ were used to determine the electronic absorption oscillator strengths for transitions from the ground electronic state l to each upper electronic state u via

$$f_{ul}(\mathbf{R}) = \frac{2}{3} \cdot g_{ul} \cdot \Delta E_{ul}(\mathbf{R}) \cdot \mu_{ul}(\mathbf{R})^2 \,. \tag{C.10}$$

These electronic absorption oscillator strengths include transitions to both bound and repulsive states. To obtain continuous cross sections for dissociative states, molecular dynamics calculations would have to be performed, not done in van Hemert and van Dishoeck (2008), which is therefore also beyond the scope of this work. It is therefore unknown which of the oscillator strengths correspond to repulsive (absorption continuum) or to (possibly predissociated) bound states (absorption peaks). To conclude, the total rate coefficient k includes contributions from direct and indirect dissociation processes. To approximate the total photodissociation rate coefficient k for a species via Equations (3.23) and (3.24) one also requires the dissociation quantum yield ϕ_u of each upper electronic state.

APPENDIX D

Molecular Data Used to Compute Photo Rate Coefficients

This appendix chapter summarizes the included reactions of each investigated parent molecule and their products. It also gives an overview on the molecular data, i.e. absorption cross sections σ or oscillator strengths f_{ul}, quantum yields ϕ_i, branching ratios br_i and threshold wavelengths λ_0, used to calculate the photo rate coefficients in Chapter 7. Table D.1 in Section D.1 gives an overview of the used data. Section D.2 shortly introduces how the present work deals with the various isomers of the involved species. The Sections D.3 - D.19 give detailed information about the data used for the individual molecules.

D.1 Table Overview of Used Molecular Data

Table D.1: *This table gives an overview of the molecular data, i.e. absorption cross sections σ, oscillator strengths f_{ul}, quantum yields ϕ_i, branching ratios br_i and threshold wavelengths λ_0 used in this work to compute the photo rate coefficients k_i. The following properties are listed successively: the species, its photo reactions (R) and their λ_0. It follows a summary of ϕ_i or br_i data, separated for each wavelength and each reaction (R). The mean absorption cross sections $\bar{\sigma}$ at the measured wavelength range is given in the last data block of each species and the corresponding references are given in the last row. If oscillator strengths were available and used for the computation of photodissociation rate coefficients of certain species is indicated by f_{ul}. The f_{ul} values and the corresponding excitation energies are presented in Figure 7.7. For ionization reactions the mean quantum yield $\bar{\phi}_i$ is listed.*

reactions / parameters	λ [Å]	values						reference
C_4H_2 isomer: HC_4H (diacetylene)								
R1) $C_4H_2 + \gamma \rightarrow C_4H + H$	$\lambda_0 = 2150$							Silva et al. (2008)
R2) $C_4H_2 + \gamma \rightarrow C_2H_2 + C_2$	$\lambda_0 = 2045$							Silva et al. (2008)
R3) $C_4H_2 + \gamma \rightarrow C_2H + C_2H$	$\lambda_0 = 1790$							Silva et al. (2008)
R4) $C_4H_2 + \gamma \rightarrow C_4 + H_2$	$\lambda_0 = 1921$							Silva et al. (2008)
R5) $C_4H_2 + \gamma \rightarrow C_4H_2^+ + e^-$	$\lambda_0 = 1219$							Schwell et al. (2012)
R6) $C_4H_2 + \gamma \rightarrow C_4H^+ + H + e^-$	$\lambda_0 = 768$							Schwell et al. (2012)
		R1	R2	R3	R4	R5	R6	
$\bar{\phi}_i$ ionization region	13 – 613	0.00	0.00	0.00	0.00	0.52	0.48	this work [6]
$\bar{\phi}_i$ ionization region	654 – 1216	0.01	0.00	0.00	0.00	0.94	0.05	Schwell et al. (2012)
br_i	1216	0.75	0.06	0.14	0.05	0.00	0.00	Silva et al. (2008)
ϕ_i	1470	0.20	0.10	0.03	0.00	0.00	0.00	Glicker and Okabe (1987)
br_i	1570	0.80	0.16	0.03	0.01	0.00	0.00	Silva et al. (2008)
ϕ_i	1849	0.08	0.06	0.00	0.00	0.00	0.00	Glicker and Okabe (1987)
br_i	1933	0.88	0.12	0.00	0.00	0.00	0.00	Silva et al. (2008)
br_i	2120	1.00	0.00	0.00	0.00	0.00	0.00	Silva et al. (2008)
$\bar{\sigma}$	0 - 650	$2.2 \cdot 10^{-17}$ cm^2						this work [4]
$\bar{\sigma}$	654 - 1198	$1.9 \cdot 10^{-17}$ cm^2						Schwell et al. (2012)
$\bar{\sigma}$	1200 - 1600	$8.3 \cdot 10^{-17}$ cm^2						Kloster-Jensen et al. (1974) [1]
$\bar{\sigma}$	1610 - 1950	$3.8 \cdot 10^{-17}$ cm^2						Fahr and Nayak (1994) [1]
$\bar{\sigma}$	1950 - 2500	$2.8 \cdot 10^{-19}$ cm^2						Smith et al. (1998) [1]

Continued on next page

Table D.1 – *Continued from previous page*

reactions / parameters	λ [Å]			values	reference
C_4H isomer: l−C_4H (butadiynyl)					
R1) $C_4H + \gamma \rightarrow C_4 + H$	$\lambda_0 = 2546$				Tuna et al. (2008), Pan et al. (2003)
R2) $C_4H + \gamma \rightarrow C_3H + C$	$\lambda_0 = 1797$				Tuna et al. (2008), Pan et al. (2003)
R3) $C_4H + \gamma \rightarrow C_2H + C_2$	$\lambda_0 = 1876$				Tuna et al. (2008), Pan et al. (2003)
R4) $C_4H + \gamma \rightarrow C_3 + CH$	$\lambda_0 = 1848$				Tuna et al. (2008), Pan et al. (2003)
f_{ul}					van Hemert and van Dishoeck (2008)
C_4 isomer: l−C_4					
R1) $C_4 + \gamma \rightarrow C_3 + C$	$\lambda_0 = 2632$				van Hemert and van Dishoeck (2008), Choi et al. (2000)
R2) $C_4 + \gamma \rightarrow C_2 + C_2$	$\lambda_0 = 2091$				Cao et al. (2002)
f_{ul}					van Hemert and van Dishoeck (2008)
HC_3N isomer: HCCCN (cyanoacetylene)					
R1) $HC_3N + \gamma \rightarrow C_2H + CN$	$\lambda_0 = 1904$				Silva et al. (2009)
R2) $HC_3N + \gamma \rightarrow C_3N + H$	$\lambda_0 = 2138$				Silva et al. (2009)
		R1	R2		
br_i	1216	0.43	0.57		Silva et al. (2009)
br_i	1570	0.43	0.57		Silva et al. (2009)
ϕ_i	1850	0.04	0.09		Clarke and Ferris (1995)
ϕ_i	1933	0.00	0.30		Seki et al. (1996)
br_i	2120	0.00	1.00		Silva et al. (2009)
$\bar{\sigma}$	1 - 800			$1.3 \cdot 10^{-17}$ cm^2	Barfield et al. (1972), Huebner et al. (1992)
$\bar{\sigma}$	803 - 1838			$4.0 \cdot 10^{-17}$ cm^2	Ferradaz et al. (2009)
$\bar{\sigma}$	1840 - 2299			$1.9 \cdot 10^{-19}$ cm^2	Bénilan et al. (1994) [1]
C_3N isomer: CCCN (cyanoethynyl)					
R1) $C_3N + \gamma \rightarrow C_2 + CN$	$\lambda_0 = 2219$				Francisco (2000)
$\bar{\sigma}$	1930 - 1931			$2.5 \cdot 10^{-18}$ cm^2	Halpern et al. (1988), Halpern et al. (1990)

Continued on next page

Table D.1 – *Continued from previous page*

reactions / parameters	λ [Å]	values			reference
C_3H_4 isomer: CH_3C_2H (propyne, methylacetylene)					
R1) $CH_3C_2H + \gamma \rightarrow C_3H_3 + H$	$\lambda_0 = 3222$				Mebel et al. (1998)
R2) $CH_3C_2H + \gamma \rightarrow C_3H_2 + H_2$	$\lambda_0 = 2249$				Mebel et al. (1998)
		R1	R2		
ϕ_i	1933	0.90	0.10		Robinson et al. (2005), Jackson et al. (1991)
$\bar{\sigma}$	0 - 400			$2.6 \cdot 10^{-17}$ cm^2	this work [4]
$\bar{\sigma}$	413 - 1590			$5.1 \cdot 10^{-17}$ cm^2	Ho et al. (1998) [2]
$\bar{\sigma}$	1600 - 1850			$6.3 \cdot 10^{-18}$ cm^2	Fahr and Nayak (1996)
$\bar{\sigma}$	1851 - 2150			$3.8 \cdot 10^{-19}$ cm^2	LISA (2011), Bénilan et al. (1999)
$\bar{\sigma}$	2200 - 3250			0 cm^2	Herzberg (1966) [5]
C_3H_4 isomer: $CH_2C_2H_2$ (allene)					
R1) $CH_2C_2H_2 + \gamma \rightarrow C_3H_3 + H$	$\lambda_0 = 3255$				Mebel et al. (1998)
R2) $CH_2C_2H_2 + \gamma \rightarrow C_3H_2 + H_2$	$\lambda_0 = 3093$				Mebel et al. (1998)
		R1	R2		
ϕ_i	1933	0.90	0.10		Robinson et al. (2005), Jackson et al. (1991)
$\bar{\sigma}$	0 - 300			$2.2 \cdot 10^{-17}$ cm^2	this work [4]
$\bar{\sigma}$	348 - 1293			$4.9 \cdot 10^{-17}$ cm^2	Holland and Shaw (1999)
$\bar{\sigma}$	1302 - 1852			$4.6 \cdot 10^{-17}$ cm^2	Chen et al. (2000)
$\bar{\sigma}$	1854 - 2333			$2.9 \cdot 10^{-18}$ cm^2	LISA (2011), Bénilan et al. (1999)
$\bar{\sigma}$	2400 - 2550			$2.8 \cdot 10^{-21}$ cm^2	Rabalais et al. (1971)
$\bar{\sigma}$	2600 - 3450			0 cm^2	Herzberg (1966) [5]
C_3H_3 isomer: H_2C_3H (propargyl)					
R1) $C_3H_3 + \gamma \rightarrow C_3H_2 + H$	$\lambda_0 = 2968$				Mebel et al. (1998)
R2) $C_3H_3 + \gamma \rightarrow C_3H + H_2$	$\lambda_0 = 3012$				Mebel et al. (1998)
R3) $C_3H_3 + \gamma \rightarrow C_3H_3^+ + e^-$	$\lambda_0 = 1430$				Robinson et al. (2003)
		R1	R2	R3	

Continued on next page

Table D.1 – *Continued from previous page*

reactions / parameters	λ [Å]	values				reference
$\bar{\phi}_i$ ionization region	$0 - 1150$	0.00	0.00	1.00		this work [6]
$\bar{\phi}_i$ ionization region	$1175 - 1426$	0.00	0.00	1.00		Savee et al. (2012)
br_i	1933	0.96	0.04	0.00		Jackson et al. (1991)
br_i	2480	0.98	0.02	0.00		Goncher et al. (2008)
$\bar{\sigma}$	0 - 1150				$2.7 \cdot 10^{-17}$ cm^2	this work [4]
$\bar{\sigma}$	1175 - 1431				$2.1 \cdot 10^{-17}$ cm^2	Savee et al. (2012)
$\bar{\sigma}$	2300 - 2800				$5.3 \cdot 10^{-18}$ cm^2	Fahr et al. (1997)
$\bar{\sigma}$	2850 - 2950				$2.5 \cdot 10^{-19}$ cm^2	Fahr et al. (1997), Fahr and Laufer (2005) [3]
$\bar{\sigma}$	3000 - 3000				$1.1 \cdot 10^{-19}$ cm^2	Fahr et al. (1997)
$\bar{\sigma}$	3050 - 3300				$2.3 \cdot 10^{-18}$ cm^2	Atkinson and Hudgens (1999), Fahr and Laufer (2005) [3]
$\bar{\sigma}$	3325 - 3325				$4.1 \cdot 10^{-18}$ cm^2	Atkinson and Hudgens (1999)
C_3H_2 isomer: H_2C_3 (vinylidenecarbene, propadienylidene, l−C_3H_2)						
R1) $C_3H_2 + \gamma \rightarrow C_3 + H_2$	$\lambda_0 = 3347$					Mebel et al. (1998)
R2) $C_3H_2 + \gamma \rightarrow C_3H + H$	$\lambda_0 = 3201$					Mebel et al. (1998)
R3) $C_3H_2 + \gamma \rightarrow C_2 + CH_2$	$\lambda_0 = 1755$					Mebel et al. (1998)
f_{ul}						van Hemert and van Dishoeck (2008)
C_3H isomer: HC_3 (propynylidyne, l−C_3H)						
R1) $C_3H + \gamma \rightarrow C_3 + H$	$\lambda_0 = 4026$					Tuna et al. (2008)
R2) $C_3H + \gamma \rightarrow C_2H + C$	$\lambda_0 = 2214$					Tuna et al. (2008)
R3) $C_3H + \gamma \rightarrow C_2 + CH$	$\lambda_0 = 1782$					Tuna et al. (2008)
f_{ul}						van Hemert and van Dishoeck (2008)
C_3 isomer: CCC (linear tricarbon)						
R1) $C_3 + \gamma \rightarrow C_2 + C$	$\lambda_0 = 2678$					van Hemert and van Dishoeck (2008), Kim et al. (1997)
f_{ul}						van Hemert and van Dishoeck (2008)
C_2H_6 (ethane)						

Continued on next page

Table D.1 – *Continued from previous page*

reactions / parameters	λ [Å]	values								reference
R1) $C_2H_6 + \gamma \rightarrow C_2H_4 + H_2$	$\lambda_0 = 8743$									Huebner et al. (1992)
R2) $C_2H_6 + \gamma \rightarrow CH_3 + CH_3$	$\lambda_0 = 3172$									Blanksby and Ellison (2003)
R3) $C_2H_6 + \gamma \rightarrow C_2H_5 + H$	$\lambda_0 = 2827$									Blanksby and Ellison (2003)
R4) $C_2H_6 + \gamma \rightarrow CH_4 + CH_2$	$\lambda_0 = 2726$									Huebner et al. (1992)
R5) $C_2H_6 + \gamma \rightarrow C_2H_6^+ + e^-$	$\lambda_0 = 1064$									Schoen (1962)
R6) $C_2H_6 + \gamma \rightarrow C_2H_5^+ + H + e^-$	$\lambda_0 = 950$									Schoen (1962)
R7) $C_2H_6 + \gamma \rightarrow C_2H_4^+ + H_2 + e^-$	$\lambda_0 = 1040$									Schoen (1962)
R8) $C_2H_6 + \gamma \rightarrow CH_3^+ + CH_3 + e^-$	$\lambda_0 = 890$									Schoen (1962)
		R1	R2	R3	R4	R5	R6	R7	R8	
$\bar{\phi}_i$ ionization region	10 – 460	0.00	0.00	0.00	0.00	0.10	0.00	0.03	0.00	this work [6]
$\bar{\phi}_i$ ionization region	491 – 1058	0.00	0.00	0.00	0.00	0.13	0.10	0.36	0.02	Schoen (1962)
ϕ_i	1240	0.40	0.07	0.31	0.26	0.00	0.00	0.00	0.00	Lias et al. (1970)
ϕ_i	1476	0.85	0.01	0.12	0.02	0.00	0.00	0.00	0.00	Lias et al. (1970)
$\bar{\sigma}$	10 - 30	$2.6 \cdot 10^{-19}$ cm^2								this work [4]
$\bar{\sigma}$	56 - 135	$5.1 \cdot 10^{-19}$ cm^2								Au et al. (1993) [2]
$\bar{\sigma}$	138 - 1199	$6.0 \cdot 10^{-17}$ cm^2								Kameta et al. (1996) [2]
$\bar{\sigma}$	1200 - 1499	$1.4 \cdot 10^{-17}$ cm^2								Chen and Wu (2004)
$\bar{\sigma}$	1500 - 1600	$2.2 \cdot 10^{-19}$ cm^2								Lee et al. (2001), Chen and Wu (2004) [2]
$\bar{\sigma}$	1601 - 8743	0 cm^2								Rabalais and Katrib (1974), Lu et al. (2004), Huebner et al. (1992) [5]
C_2H_5 (alkyl)										
R1) $C_2H_5 + \gamma \rightarrow CH_2 + CH_3$	$\lambda_0 = 2875$									Blanksby and Ellison (2003)
R2) $C_2H_5 + \gamma \rightarrow C_2H_4 + H$	$\lambda_0 = 8006$									Blanksby and Ellison (2003)
R3) $C_2H_5 + \gamma \rightarrow C_2H_5^+ + e^-$	$\lambda_0 = 1528$									Blanksby and Ellison (2003)
		R1	R2	R3						
$\bar{\phi}_i$ ionization region	0 – 1050	0.00	0.00	1.00						this work [6]
$\bar{\phi}_i$ ionization region	1083 – 1523	0.00	0.00	1.00						Gans et al. (2011)
$\bar{\sigma}$	0 - 1000	$5.6 \cdot 10^{-18}$ cm^2								this work [4]
$\bar{\sigma}$	1083 - 1524	$3.3 \cdot 10^{-18}$ cm^2								Gans et al. (2011)

Continued on next page

Table D.1 – *Continued from previous page*

reactions / parameters	λ [Å]	values						reference
$\bar{\sigma}$	2000 - 2600	$3.9 \cdot 10^{-18}$ cm^2						Munk et al. (1986)
$\bar{\sigma}$	2601 - 3500	0 cm^2						Wendt and Hunziker (1984)
$\bar{\sigma}$	3551 - 8006	0 cm^2						Blomberg and Liu (1985), Knopp et al. (2002) [5]
C_2H_4 isomer: $H_2C_2H_2$ (ethylene)								
R1) $C_2H_4 + \gamma \rightarrow C_2H_2 + H_2$	$\lambda_0 = 7200$							Benson (1976), Huebner et al. (1992)
R2) $C_2H_4 + \gamma \rightarrow C_2H_2 + H + H$	$\lambda_0 = 1960$							Benson (1976), Huebner et al. (1992)
R3) $C_2H_4 + \gamma \rightarrow C_2H_3 + H$	$\lambda_0 = 2582$							Blanksby and Ellison (2003)
R4) $C_2H_4 + \gamma \rightarrow C_2H_4^+ + e^-$	$\lambda_0 = 1180$							Zelikoff and Watanabe (1953), Huebner et al. (1992)
R5) $C_2H_4 + \gamma \rightarrow C_2H_3^+ + H + e^-$	$\lambda_0 = 898$							Botter et al. (1966), Huebner et al. (1992)
R6) $C_2H_4 + \gamma \rightarrow C_2H_2^+ + H_2 + e^-$	$\lambda_0 = 945$							Botter et al. (1966), Huebner et al. (1992)
		R1	R2	R3	R4	R5	R6	
$\bar{\phi}_i$ ionization region	11 – 511	0.00	0.00	0.00	0.26	0.36	0.24	this work [6]
$\bar{\phi}_i$ ionization region	550 – 1180	0.00	0.00	0.00	0.27	0.09	0.07	Schoen (1962)
br_i	1570	0.46	0.52	0.02	0.00	0.00	0.00	Lee et al. (2004)
br_i	1634	0.49	0.46	0.05	0.00	0.00	0.00	Hara and Tanaka (1973)
br_i	1849	0.53	0.33	0.14	0.00	0.00	0.00	Hara and Tanaka (1973)
ϕ_i	1933	0.37	0.05	0.16	0.00	0.00	0.00	Giroux et al. (1989)
$\bar{\sigma}$	23 - 39	$1.1 \cdot 10^{-18}$ cm^2						Henke et al. (1982)
$\bar{\sigma}$	43 - 60	$4.1 \cdot 10^{-18}$ cm^2						Henke et al. (1982), Kempgens et al. (1995)
$\bar{\sigma}$	89 - 497	$1.7 \cdot 10^{-17}$ cm^2						Cooper et al. (1995)
$\bar{\sigma}$	510 - 1178	$4.5 \cdot 10^{-17}$ cm^2						Holland et al. (1997)
$\bar{\sigma}$	1183 - 1856	$2.6 \cdot 10^{-17}$ cm^2						Wu et al. (2004)
$\bar{\sigma}$	1873 - 1973	$6.8 \cdot 10^{-20}$ cm^2						Zelikoff and Watanabe (1953), Huebner et al. (1992)
$\bar{\sigma}$	2001 - 2001	$2.0 \cdot 10^{-21}$ cm^2						Wilkinson and Mulliken (1955), Zelikoff and Watanabe (1953)
$\bar{\sigma}$	2001 - 8000	0 cm^2						Lu et al. (2004), Wilkinson and Mulliken (1955), Zelikoff and Watanabe (1953), Platt et al. (1949), Huebner et al. (1992) [5]
C_2H_3 isomer: H_2C_2H (vinyl)								

Continued on next page

Table D.1 – *Continued from previous page*

reactions / parameters	λ [Å]	values				reference
R1) $C_2H_3 + \gamma \rightarrow C_2H_2 + H$	$\lambda_0 = 8074$					Blanksby and Ellison (2003)
R2) $C_2H_3 + \gamma \rightarrow CH + CH_2$	$\lambda_0 = 1732$					Blanksby and Ellison (2003)
R3) $C_2H_3 + \gamma \rightarrow C_2H_3^+ + e^-$	$\lambda_0 = 1503$					Robinson et al. (2003)
		R1	R2	R3		
$\bar{\phi}_i$ ionization region	$0 - 1100$	0.00	0.00	1.00		this work [6]
$\bar{\phi}_i$ ionization region	$1149 - 1503$	0.00	0.00	1.00		Robinson et al. (2003)
$\bar{\sigma}$	0 - 1100				$2.7 \cdot 10^{-17}$ cm^2	this work [4]
$\bar{\sigma}$	1149 - 1501				$7.9 \cdot 10^{-18}$ cm^2	Robinson et al. (2003)
$\bar{\sigma}$	1647 - 1683				$4.1 \cdot 10^{-17}$ cm^2	Fahr and Laufer (1990)
$\bar{\sigma}$	2250 - 2380				$5.0 \cdot 10^{-18}$ cm^2	Fahr et al. (1998)
$\bar{\sigma}$	3855 - 4435				$6.8 \cdot 10^{-19}$ cm^2	Shahu et al. (2002), Tonokura et al. (1999) [3]
$\bar{\sigma}$	4440 - 4550				$1.7 \cdot 10^{-19}$ cm^2	Tonokura et al. (1999)
$\bar{\sigma}$	4589 - 5200				$4.5 \cdot 10^{-20}$ cm^2	Shahu et al. (2002), Tonokura et al. (1999) [3]
$\bar{\sigma}$	5231 - 8074				0 cm^2	Hunziker et al. (1983), Chen and Huang (2004) [5]
C_2H_2 isomer: HC_2H (acetylene)						
R1) $C_2H_2 + \gamma \rightarrow C_2H + H$	$\lambda_0 = 2170$					Zhang et al. (2010)
R2) $C_2H_2 + \gamma \rightarrow C_2 + H_2$	$\lambda_0 = 2000$					Zhang et al. (2010)
R3) $C_2H_2 + \gamma \rightarrow C_2H_2^+ + e^-$	$\lambda_0 = 1086$					Herzberg (1966)
R4) $C_2H_2 + \gamma \rightarrow C_2H^+ + H + e^-$	$\lambda_0 = 697$					Metzger and Cook (1964)
		R1	R2	R3	R4	
$\bar{\phi}_i$ ionization region	$12 - 562$	0.00	0.00	0.69	0.31	this work [6]
$\bar{\phi}_i$ ionization region	$600 - 1085$	0.00	0.00	0.76	0.05	Schoen (1962)
ϕ_i	1216	1.00	0.00	0.00	0.00	Läuter (2002)
ϕ_i	1470	0.30	0.10	0.00	0.00	Okabe (1981)
ϕ_i	1849	0.06	0.10	0.00	0.00	Okabe (1983)
ϕ_i	1933	0.94	0.06	0.00	0.00	Läuter (2002)
$\bar{\sigma}$	1 - 50				$1.9 \cdot 10^{-19}$ cm^2	this work [4]
$\bar{\sigma}$	62 - 1080				$1.1 \cdot 10^{-17}$ cm^2	Cooper et al. (1995) [2]
$\bar{\sigma}$	1100 - 1200				$2.2 \cdot 10^{-17}$ cm^2	Cheng et al. (2011) [2]

Continued on next page

Table D.1 – *Continued from previous page*

reactions / parameters	λ [Å]			values	reference
$\bar{\sigma}$	1200 - 1890			$1.5 \cdot 10^{-17}$ cm^2	Wu et al. (2001) [1]
$\bar{\sigma}$	1897 - 2250			$6.4 \cdot 10^{-20}$ cm^2	Bénilan et al. (2000) [1]
C_2H (ethynyl)					
R1) $C_2H + \gamma \rightarrow C_2 + H$	$\lambda_0 = 2531$				van Hemert and van Dishoeck (2008)
R2) $C_2H + \gamma \rightarrow CH + C$	$\lambda_0 = 1604$				Blanksby and Ellison (2003)
f_{ul}					van Hemert and van Dishoeck (2008)
C_2 (dicarbon)					
R1) $C_2 + \gamma \rightarrow C + C$	$\lambda_0 = 1436$				Huebner et al. (1992)
R2) $C_2 + \gamma \rightarrow C_2^+ + e^-$	$\lambda_0 = 1000$				Huebner et al. (1992)
		R1	R2		
$\bar{\phi}_i$ ionization	1 - 1000	0.00	1.00		Huebner et al. (1992)
$\bar{\phi}_i$	1000 - 1210	1.00	0.00		Huebner et al. (1992)
$\bar{\sigma}$	1 - 248			$9.2 \cdot 10^{-19}$ cm^2	Barfield et al. (1972), Huebner et al. (1992)
$\bar{\sigma}$	261 - 1210			$1.5 \cdot 10^{-17}$ cm^2	Padial et al. (1985), Pouilly et al. (1983), Huebner et al. (1992)
$\bar{\sigma}$	1210 - 1436			0 cm^2	Huebner et al. (1992) [5]

1) Downloaded from the webpage of LISA (2011).
2) Downloaded from the webpage of Keller-Rudek and Moortgat (2011).
3) Data is combined from these authors.
4) σ has been extrapolated in this work with a constant value in the ionization wavelength range.
5) σ has been set to zero in this work, due to reported missing absorption of the species in this wavelength range.
6) ϕ_i has been extrapolated in this work with a constant value in the ionization wavelength range.

D.2 Discussion of Used Isomers

Each molecule can have several isomers in different excited states. However, the absorption cross sections are not known for all these isomers and excited states. Additionally, quantum yields or branching ratios are also not known for most of the isomers. The occurrence of isomers in the cometary comae depend on their presence in cometary ices, which is unknown, and the photodissociation behavior. The internal energy of the molecules and their products determines if isomerizations and therefore additional reaction paths are energetically possible. There are species for which absorption cross sections or oscillator strength are available for one isomer, namely HC_4H (C_4H_2), HC_2H (C_2H_2), $H_2C_2H_2$ (C_2H_4), C_2H_6, H_2C_3H (C_3H_3), l−C_4H, l−C_4, l−C_3, H_2C_2H (C_2H_3), C_2H and C_2. For the species C_3H_2 and C_3H oscillator strengths are available for several isomers. However, this work assumes that for C_3H_2 and C_3H the isomers H_2C_3 and HC_3 are used. For more information see the individual sections of each species. Especially for $C_4H_{(2,1,0)}$ and $C_3H_{(4,3,2,1,0)}$ this is discussed in the Sections D.3.1 and D.8.1, respectively.

D.3 C_4H_2 isomer: HC_4H (diacetylene, HC≡C−C≡CH)

$$C_4H_2 + \gamma \longrightarrow C_4H + H \qquad \lambda_0 = 2150 \text{ Å} \tag{D.1}$$

$$C_2H + C_2H \qquad \lambda_0 = 1790 \text{ Å} \tag{D.2}$$

$$C_2H_2 + C_2 \qquad \lambda_0 = 2045 \text{ Å} \tag{D.3}$$

$$C_4 + H_2 \qquad \lambda_0 = 1921 \text{ Å} \tag{D.4}$$

$$C_4H_2^+ + e^- \qquad \lambda_0 = 1219 \text{ Å} \tag{D.5}$$

$$C_4H^+ + H + e^- \qquad \lambda_0 = 768 \text{ Å} \tag{D.6}$$

D.3.1 Discussion of the $C_4H_{(2,1,0)}$ Isomers

For HC_4H it was decided to include a reaction forming directly $C_4 + H_2$ because it was found in this work, see Chapter 9, that C_4 must be produced very fast to be able to reproduce the C_3 and C_2 observations of the investigated comets. C_4 formation may be possible by fast isomerization to H_2C_4 after photoexcitation which then dissociates immediately to $C_4 + H_2$. Isomerization to a rhombic C_4H_2 after photoexcitation allows the formation of $C_2H_2 + C_2$. Isomerizations of HC_4H to H_2C_4 and a rhombic C_4H_2 were observed to be possible by Silva et al. (2008) at least in small proportions at some of the four investigated wavelengths. Another interpretation of the findings of Chapter 9 for C_4H_2 would be that different C_4H_2 isomers have to be present in cometary ices. For C_4H and C_4 there are oscillator strengths available only for the linear species. Therefore, this work only includes these isomers.

Cross sections

This work uses the cross sections from the compilation given at the webpage LISA (2011), which is described in the paper Jolly and Bénilan (2008). The sources are Kloster-Jensen et al. (1974) between 1200 Å and 1600 Å $T = 300$ K, Fahr and Nayak (1994) between 1600 Å and 1950 Å at $T = 223$ K and Smith et al. (1998) between 1950 Å and 2500 Å at $T = 195$ K.

In addition, data is available from the recent measurements of Ferradaz et al. (2009) between 1115 Å and 2250 Å show a difference to Fahr and Nayak (1994) of only 2% and are very similar to Smith et al. (1998) between 1950 Å and 2225 Å. Other absorption cross sections measurements are given in Glicker and Okabe (1987) between 1470 Å and 2540 Å at $T = 300$ K, Okabe (1981)

between 1200 Å and 1800 Å at $T = 300$ K, which values are much lower than in Ferradaz et al. (2009) mainly due to saturation effects by acetone impurities in the older work (Shemansky et al., 2005, Jolly and Bénilan, 2008).

This work also uses the ionization cross sections for the reactions (D.5) and (D.6) reported in Schwell et al. (2012).

Threshold wavelengths

This work uses the threshold wavelengths given in Silva et al. (2008). Silva et al. (2008) state that the thermochemical thresholds were erroneous at the time Glicker and Okabe (1987) published their experimental results on the photodissociation of C_4H_2. The threshold for hydrogen elimination in reaction (D.1) should now be 2150 Å or 133 kcal/mol (Frost et al., 1996) instead of 2280 Å from Glicker and Okabe (1987).

For reaction (D.2) Silva et al. (2008) calculated $\lambda_0 = 1790$ Å (159.7 kcal/mol) which is significantly lower than $\lambda_0 = 2020$ Å from Glicker and Okabe (1987). Reaction (D.3) has $\lambda_0 = 2045$ Å (139.8 kcal/mol) also given in Silva et al. (2008) for which Glicker and Okabe (1987) reported 2050 Å. Reaction (D.4) requires 148.8 kcal/mol equivalent to $\lambda_0 = 1921$ Å (Silva et al., 2008).

The thresholds for the reactions (D.5) and (D.6) are $\lambda_0 = 1219$ Å (10.17 eV) and $\lambda = 768$ Å (16.15 eV), respectively (Schwell et al., 2012).

Reaction

$$C_4H_2 + \gamma \longrightarrow C_3 + CH_2 \qquad \lambda_0 = 1680 \text{ Å} \tag{D.7}$$

as assumed in Weiler (2006) and in Krasnopolsky (1991) is not possible for HC_4H and also not for its isomers according to Silva et al. (2008). This reaction is therefore not used in the present work.

Quantum yields

This work uses the branching ratios and quantum yields of Glicker and Okabe (1987) at 1849 Å, 1470 Å and Silva et al. (2008) at 2120 Å, 1933 Å, 1570 Å and at 1216 Å, respectively. Glicker and Okabe (1987) report quantum yields for the reactions (D.1), (D.2) and (D.3) at the wavelengths 1470 Å, 1849 Å, 2288 Å and 2537 Å of which those at 1470 Å are 0.2, 0.035, 0.1 and at 1849 Å are 0.08, 0.01 and 0.06. However, for reaction (D.2) $\phi = 0$ at 1849 Å since the new $\lambda_0 = 1790$ Å. The reported ϕ_i at 2288 Å and 2537 Å, i.e. above all thresholds, are therefore also not used. Glicker and Okabe (1987) did not consider reaction (D.4).

Silva et al. (2008) investigated the C_4H_2 photodissociation experimentally (detection of H) at 2430 Å, 2120 Å and at 1216 Å and by the theoretical computations at the wavelengths 2120 Å, 1933 Å, 1570 Å and at 1216 Å. From the experiments they suggested statistical dissociation from the ground state and computed branching ratios using Rice-Ramsperger-Kassel-Marcus **(RRKM)** computations for one-photon dissociations (at 2430 Å and 2120 Å they suggested a two-photon process to occur in their experiments). At 2120 Å, 1933 Å, 1570 Å and 1216 Å reaction (D.1) was dominant. The reactions (D.1) and (D.2) are accessible from the ground state C_4H_2, whereas the reactions (D.3) and (D.4) require isomerization to a rhombic C_4H_2 and H_2C_4, respectively. The branching ratios for the linear $C_4H + H$ are a summary from the production from the ground state and the H_2C_4 isomer.

This work includes ionization quantum yields between 654 Å - 1214 Å from Schwell et al. (2012). At $\lambda < 654$ Å a constant quantum yield is assumed.

D.4 C_4H isomer: $l{-}C_4H$ (butadiynyl, $\dot{C}{\equiv}C{-}C{\equiv}CH$)

$$C_4H + \gamma \longrightarrow C_4 + H \qquad \lambda_0 = 2546 \text{ Å} \tag{D.8}$$
$$C_3H + C \qquad \lambda_0 = 1797 \text{ Å} \tag{D.9}$$
$$C_2H + C_2 \qquad \lambda_0 = 1876 \text{ Å} \tag{D.10}$$
$$C_3 + CH \qquad \lambda_0 = 1848 \text{ Å} \tag{D.11}$$

Cross sections

Ab initio photodissociation oscillator strengths calculated by van Hemert and van Dishoeck (2008) are used in this work.

Threshold wavelengths

This work uses the threshold wavelengths $\lambda_0 = 2546$ Å (4.87 eV), $\lambda_0 = 1797$ Å (6.9 eV), $\lambda_0 = 1876$ Å (6.61 eV) and 1848 Å (6.71 eV) for the reactions (D.8), (D.9), (D.10) and (D.11), respectively (Tuna et al., 2008, Pan et al., 2003). This reaction is forbidden for electronic ground state to electronic ground state dissociation (Tuna et al., 2008). However, dissociation involving electronically excited parent and/or products is allowed. As the present work assumes that the ground state species in the reaction network represent also excited species, see Section 7.2.3, reaction (D.11) is taken into account.

Quantum yields

No quantum yields and branching ratios are available, therefore the present work computes the rate coefficients via the Monte Carlo **(MC)** approach as described in Section 7.2.5.

D.5 C_4 isomer: $l{-}C_4$ ($\ddot{C}{=}C{=}C{=}\ddot{C}$)

$$C_4 + \gamma \longrightarrow C_3 + C \qquad \lambda_0 = 2632 \text{ Å} \tag{D.12}$$
$$C_2 + C_2 \qquad \lambda_0 = 2091 \text{ Å} \tag{D.13}$$

Cross sections

Ab initio photodissociation oscillator strengths calculated by van Hemert and van Dishoeck (2008) are used in this work.

Threshold wavelengths

This work uses $\lambda_0 = 2632$ Å (4.71 eV) (van Hemert and van Dishoeck, 2008, Choi et al., 2000) and 2091 Å (5.93 eV) (Cao et al., 2002) for the reactions (D.12) and (D.13), respectively. For (D.12) and (D.13) Díaz-Tendero et al. (2006) report ≈ 5.3 eV and ≈ 6.8 eV, respectively.

Quantum yields

No quantum yields and branching ratios are available, therefore the present work computes the rate coefficients via the MC approach as described in Section 7.2.5.

D.6 HC_3N (cyanoacetylene, HC≡C−C≡N)

$$HC_3N + \gamma \longrightarrow C_2H + CN \qquad \lambda_0 = 1904 \text{ Å} \tag{D.14}$$

$$C_3N + H \qquad \lambda_0 = 2138 \text{ Å} \tag{D.15}$$

Cross sections

This work uses the cross sections given in the compilation of Huebner et al. (1992) from 0 Å to 800 Å as the sum of the atomic cross sections from Barfield et al. (1972), 800 Å to 1840 Å. Also used are the cross sections from Ferradaz et al. (2009) extracted from their Figure 2 at $T = 298$ K and from Bénilan et al. (1994) between 1840 Å and 2300 Å at $T = 213$ K prepared by LISA (2011).

In addition, cross sections are available, with a lower resolution or at $T \geq 298$ K, from Seki et al. (1996) between 1900 Å and 2500 Å, $T = 300$ K, from Connors et al. (1974) between 1058 Å and 1632 Å, $T = 300$ K, from Bruston et al. (1989) between 1840 Å and 2540 Å, $T = 300$ K, from Andrieux et al. (1995) at 1850 Å to 2000 Å, $T = 298$ K, Halpern et al. (1988) at 1850 Å to 2350 Å, $T = 300$ K.

Threshold wavelengths

This work uses the newest threshold wavelengths from the most recent publication of Silva et al. (2009) with $\lambda_0 = 1904$ Å (150.1 kcal/mol) for (D.14) and 2138 Å (133.7 kcal/mol) for (D.15).

Note that other values for the threshold wavelengths are given in older publications. For (D.14) several thresholds are given in the literature: 1844 Å, 2000 Å, 1924 Å, 1946 Å (146.9 kcal/mol) and 2046 Å (133.7 kcal/mol) from the references Monks et al. (1993), Halpern et al. (1988), Yung et al. (1984), Francisco and Richardson (1994), Yang et al. (2006, ab initio), respectively. Thresholds for (D.15) are 2195 Å (5.65 eV) , 2067 Å (138.3 kcal/mol), 2244 Å (127.4 kcal/mol) and 2440 Å from Luo et al. (2008), Francisco and Richardson (1994), Yang et al. (2006, ab initio) and Halpern et al. (1988, 1990), respectively.

Quantum yields

This work uses the values given in Silva et al. (2009), Seki et al. (1996) and Clarke and Ferris (1995) with some exceptions described in the following.

For reaction (D.14) at 1933 Å Halpern et al. (1988) determine $\phi_i = 0.05$ and Seki et al. (1996) $\phi \leq 0.02$. However, due to the newly revised $\lambda_0 = 1904$ Å for (D.14) however, which is widely different to previously measured λ_0, $\phi_i(HC_3N \rightarrow C_2H + CN) = 0$ at $\lambda > \lambda_0$. For reaction (D.15) at 1933 Å Seki et al. (1996) determine $\phi = 0.3$. At 1850 Å Clarke and Ferris (1995) find $\phi = 0.09$ for this reaction. There the quantum yield of (D.14) should lie between $\phi_i = 0.01$ and $\phi_i = 0.06$, the mean $\phi_i = 0.035$ is used. Additionally, Silva et al. (2009) report branching ratios at the wavelength 2120, 1933, 1570, 1216 Å from ab initio computations assuming statistical dissociation.

D.7 C_3N (cyanoethynyl, $\dot{C}$≡C−C≡N)

$$C_3N + \gamma \longrightarrow C_2 + CN \qquad \lambda_0 = 2219 \text{ Å} \tag{D.16}$$

Cross sections

There exists only one absorption cross section value of C_3N which was estimated at 1930 Å by Halpern et al. (1988) to be $\sigma \approx 10^{-17}\text{cm}^2$ and between $\sigma = 0.5 \cdot 10^{-17}\text{cm}^2$ and $\sigma = 10^{-18}\text{cm}^2$ in Halpern et al. (1990, p.1872). The mean value $\sigma = 0.25 \cdot 10^{-17}\text{cm}^2$ is used in this work at $\lambda = 1930$ Å.

Threshold wavelengths

Titarchuk and Halpern (2000) determined $\lambda_0 = 1930$ Å according to the heats of formation given in Halpern et al. (1988). A calculation and extrapolation done in Francisco (2000) gives $\lambda_0 = 2219$ Å (128.8 kcal/mol,). This value is used in this work in view of the better consistency between several theoretical works, as discussed in Francisco (2000).

Quantum yields

The only path is the formation of C_2 + CN since the triple bond between C and N is much stronger than the single bond between C_2 and CN. A branching ratio of one is therefore used for reaction (D.16).

D.8 C_3H_4 isomers: CH_3C_2H (propyne or methylacetylene, $H_3C{-}C{\equiv}CH$) and $CH_2C_2H_2$ (allene, $H_2C{=}C{=}CH_2$)

$$\begin{aligned} CH_3C_2H + \gamma &\longrightarrow C_3H_3 + H & \lambda_0 &= 3222\ \text{Å} & \text{(D.17)} \\ & C_3H_2 + H_2 & \lambda_0 &= 2249\ \text{Å} & \text{(D.18)} \end{aligned}$$

$$\begin{aligned} CH_2C_2H_2 + \gamma &\longrightarrow C_3H_3 + H & \lambda_0 &= 3255\ \text{Å} & \text{(D.19)} \\ & C_3H_2 + H_2 & \lambda_0 &= 3093\ \text{Å} & \text{(D.20)} \end{aligned}$$

D.8.1 Motivation of the Used $C_3H_{(4,3,2,1,0)}$ Isomers

This work investigates the C_3H_4 isomers $CH_2C_2H_2$ and CH_3C_2H as potential parent molecules. This is possible since their absorption cross sections are available. Additionally, their upper limit total photodissociation rate coefficients differ by nearly an order of magnitude. This work introduces the simplification that CH_3C_2H and $CH_2C_2H_2$ mainly dissociate to the C_3H_3 isomer H_2C_3H and mainly to the C_3H_2 isomer H_2C_3. It is also assumed that isomerization between the different $C_3H_{(4,3,2,1,0)}$ isomers is negligible.

For C_3H_3 this is done since only absorption cross sections for H_2C_3H are available. $CH_2C_2H_2$ can only dissociate to H_2C_3H and H_2C_3, whereas CH_3C_2H is additionally able to dissociate to H_3C_3 and HC_3H.

For C_3H_2 there are absorption oscillator strengths available for the isomers H_2C_3, HC_3H and the cyclic form $c{-}C_3H_2$. For HC_3H oscillator strengths are available for the singlet and the triplet state species, i.e. $(^1A')HC_3H$ and $(^3B)HC_3H$. No quantum yields or branching ratios are available regarding the photodissociation of the C_3H_2 and C_3H isomers. The reasons to assume that mainly H_2C_3 is formed is that this isomer can dissociate to the linear HC_3 and to $l{-}C_3$. This is also possible for $(^1A')HC_3H$, however, the rate coefficients of this isomer are similar to those of H_2C_3 and no additional information is obtained regarding the formation of C_3 and

C_2 when including a second molecule showing a very similar behavior regarding C_3 and C_3H formation.

c$-C_3H_2$ only dissociates to c$-C_3H$ which in turn only dissociates to c$-C_3$ (Mebel et al., 1998, Mebel and Kaiser, 2002). c$-C_3$, however, requires an additional isomerization step to rearrange to l$-C_3$ or an additional photon to break the cyclic structure. This makes this path less likely to explain l$-C_3$ in comets (no quantum yields are available for the latter two mentioned processes). This is why this work also assumes that mainly HC_3 is formed although oscillator strengths are also available for c$-C_3H$.

(^{3}B)HC_3H is not produced by the C_3H_4 isomers $CH_2C_2H_2$ and CH_3C_2H although it may well be produced by the C_3H_3 isomers H_2C_3H and H_3C_3 (Mebel et al., 1998). However, it requires isomerization and intersystem crossing **(ISC)** to produce singlet l$-C_3$ (Mebel et al., 1998). Nevertheless, it can dissociate to HC_3 (Leonori et al., 2008) which upper limit total rate coefficient is only a factor of three higher compared to H_2C_3.

There are publications reporting contradicting results regarding the main C_3H_2 isomer formed in the photodissociation of H_2C_3H. The one states that mainly (^{3}B)HC_3H is formed the other that mainly c$-C_3H_2$ is formed. Despite that their results are contradictory the results are only reported for a specific and short wavelength range. The present work assumes that formation of C_3H_2 isomers different than H_2C_3 is negligible.

One purpose of this work is to investigate if a C_3 and C_2 parent molecule can be precluded despite the large uncertainties of the photodissociation rate coefficients, see Chapter 1. This is not possible for the C_3H_4 isomers with the above assumptions, at least for three of the four investigated comets, as shown in Section 9. The present work therefore discusses these questions under the above mentioned assumptions. Future work may investigate the photochemistry of the $C_3H_{(4,3,2,1,0)}$ species in more detail when more absorption cross sections and also quantum yields are available which indicate which isomers are predominantly formed.

Cross sections of CH_3C_2H

Absorption cross sections used in this work are taken from Ho et al. (1998) between 442 Å and 1600 Å at $T = 298$ K, from Fahr and Nayak (1996) between 1600 Å and 1850 Å at $T = 295$ K and Bénilan et al. (1999) between 1851 Å and 2150 Å at $T = 183$ K downloaded from LISA (2011). According to (Herzberg, 1966, p.542) propyne starts to absorb around 2000 Å. Therefore, the absorption is set to zero in this work at $\lambda > 2150$ Å, where the absorption cross sections have decreased to around $10^{-21}\,\mathrm{cm}^2$ in comparison to $10^{-19}\,\mathrm{cm}^2$ at $\lambda = 2000$ Å (LISA, 2011, Bénilan et al., 1999).

Cross sections of $CH_2C_2H_2$

This work uses cross sections taken from Holland and Shaw (1999) from 350 Å to 1300 Å (likely measured at room temperature), from Chen et al. (2000) between 1302 Å and 1852 Å at $T = 200$ K and from Bénilan et al. (1999), see LISA (2011), between 1854 Å and 2333 Å at $T = 183$ K. From 2400 Å to 2550 Å the data from Rabalais et al. (1971) is used. This continuum absorption region is the region where allene dissociates from its lowest excited electronic states (Chen et al., 2000) and the absorption decreases to zero with increasing wavelength, see also Seki and Okabe (1992). In this work the absorption cross sections are therefore set to zero longwards of 2550 Å, where the cross sections reported in Rabalais et al. (1971) are as low as $10^{-21}\,\mathrm{cm}^2$, to the highest threshold wavelength $\lambda_0 = 3435$ Å. Cross sections are also available in Sutcliffe and Walsh (1952), Holland and Shaw (1999), Seki and Okabe (1992) but at lower resolution or higher temperatures.

Threshold wavelengths of CH_3C_2H and $CH_2C_2H_2$

This work uses the thresholds reported in Mebel et al. (1998) for the reactions (D.17), (D.18), (D.19) and (D.20), i.e. 3222 Å (88.7 kcal/mol), 2249 Å (127.1 kcal/mol), 3255 Å (88.7 − 0.9 kcal/mol) and 3093 Å (93.3 − 0.9 kcal/mol), respectively, for H_2C_3H (C_3H_3) and for H_2C_3 (C_3H_2).

Following Mebel et al. (1998) the present work does not take into account the follwing reactions

$$CH_3C_2H + \gamma \longrightarrow C_2H_2 + CH_2\,, \tag{D.21}$$
$$C_2H + CH_3\,, \tag{D.22}$$
$$CH_2C_2H_2 + \gamma \longrightarrow C_2H_2 + CH_2\,, \tag{D.23}$$
$$C_2H + CH_3\,. \tag{D.24}$$

The reactions (D.21) and (D.23) require isomerization to the cyclic c−C_3H_4 (Walch, 1995). The reaction (D.24) requires isomerization to CH_3C_2H and the reactions (D.24) and (D.22) seem to be of minor importance according to Mebel et al. (1998), see also the discussion in the following quantum yield section. In case one would like to include these reactions, the thresholds of the reactions (D.21) and (D.22) are 2575 Å (111 kcal/mol) and 2305 Å (124 kcal/mol), respectively, and the thresholds of the reactions (D.23) and (D.24) are 2596 Å (111.0 − 0.9 kcal/mol) and 2322 Å (124.0 − 0.9 kcal/mol), respectively (Mebel et al., 1998, Kiefer et al., 1997).

Quantum yields of CH_3C_2H and $CH_2C_2H_2$

Used Fragmentation Data

The present work uses the branching ratios of Robinson et al. (2005) at 1933 Å for both CH_3C_2H and $CH_2C_2H_2$ for the included reactions (D.21), (D.22), (D.23) and (D.24), since the present work assumes according to Jackson et al. (1991) and Mebel et al. (1998) that these are the main reaction paths at all wavelengths. Therefore, quantum yield and branching ratio data is not used from publications in which small amounts of C_2H and C_2H_2 are detected.

2033, 2090 and 2133 Å:

Qadiri et al. (2002) suggest that both CH_3C_2H and $CH_2C_2H_2$ isomerize on the ground state and that dissociation takes place after isomerization.

1933 Å:

Jackson et al. (1991) detected at 1933 Å for $CH_2C_2H_2$ the dissociation reactions (D.19) and (D.20) with branching ratios of 0.81 and 0.19, respectively. They did not detect C_2H_2 products as a primary channel of $CH_2C_2H_2$.

For CH_3C_2H dissociation at 1933 Å Seki and Okabe (1992) quote 0.7 ± 0.1 and 0.11 ± 0.01 for (D.17) (mainly H_3C_3 instead of H_2C_3H) and (D.21), respectively. For reaction (D.22) they quote $\phi_i < 0.05$.

At 1933 Å Song et al. (1994) argued that CH_3C_2H and $CH_2C_2H_2$ dissociate from the ground state to $C_3H_2 + H_2$. They argue that formation of C_2H_2 requires rearrangement of CH_3C_2H, being a reason for the lower quantum yield determined in Seki and Okabe (1992).

Ni et al. (1999) found for both CH_3C_2H and $CH_2C_2H_2$ that H loss is the dominant channel at 1933 Å with small amounts of C_3H_2 and C_2H_2 being formed. They suggest that the isomerization between CH_3C_2H and $CH_2C_2H_2$ is slower than the dissociation. They state that their determined

fragmentation branching ratios of H and H_2 formation from $CH_2C_2H_2$ are similar to Jackson et al. (1991). Whereas for CH_3C_2H only 0.5 % H_2 formation is observed.

DeSain and Taatjes (2003) detected H_2C_3H and C_2H_2 formation at 1933 Å for CH_3C_2H with $\phi_i = 0.49$ and $\phi_i = 0.1$, respectively.

Qadiri et al. (2003) report at 1933 Å that dissociation of CH_3C_2H and $CH_2C_2H_2$ occurs via internal conversion **(IC)** to the ground state and that isomerization of the highly vibrationally excited molecules seems to be faster than unimolecular dissociation. They state that the main C_3H_3 isomer is H_2C_3H as used in the present work.

At 1933 Å Robinson et al. (2005) have clearly identified experimentally that H_2C_3H formation is dominant for both CH_3C_2H and $CH_2C_2H_2$. They tentatively suggested formation of different C_3H_2 isomers, HC_3H (propargylene) from CH_3C_2H (propyne) and H_2C_3 (propadienylidene) from $CH_2C_2H_2$ (allene) at 1933 Å. They estimated that the formation of H and H_2 has a branching ratio of 90 : 10 for both propyne and allene. The paper of Sun et al. (1999), which found branching ratios of 56 : 44, in contradiction to Jackson et al. (1991), was retracted by Robinson et al. (2005).

1570 Å:

At 1570 Å Harich et al. (2000b) report for CH_3C_2H besides H and H_2 dissociation also the formation of C_2H and C_2H_2. Ground state isomerization is reported to be significant before dissociation takes place. Reaction (D.21) might be associated with prior isomerization to c$-C_3H_4$ or isomerization to $CH_2C_2H_2$, although this path would involve several isomerization steps and is therefore less likely according to Harich et al. (2000b). They report only branching ratios between H and H_2 formation, which are 0.91 and 0.09 (9.6 : 1) and formation of CH_3 and CH_2 with a ratio of 2.2 : 1.

Harich et al. (2000a) report for $CH_2C_2H_2$ that the reactions (D.19), (D.20) and (D.23) are the main channels with branching ratios of 0.70, 0.11, 0.19 (1.0 : 0.15 : 0.27). The dissociation seems to be from the ground electronic state.

1470 Å:

At 1470 Å quantum yields for H and H_2 decomposition have been measured in Stief et al. (1971) for CH_3C_2H to be ≥ 0.4 for H and 0.15 for H_2.

D.9 C_3H_3 isomer: H_2C_3H (propargyl, $H_2\dot{C}-C\equiv CH$)

$$C_3H_3 + \gamma \longrightarrow C_3H_2 + H \qquad \lambda_0 = 2968 \text{ Å} \tag{D.25}$$

$$C_3H + H_2 \qquad \lambda_0 = 3012 \text{ Å} \tag{D.26}$$

$$C_3H_3^+ + e^- \qquad \lambda_0 = 1430 \text{ Å} \tag{D.27}$$

Cross sections

This work uses values from Fahr et al. (1997) between 2300 Å and 3000 Å, which have a very low resolution of 25 Å to 50 Å and a gap between 2800 Å and 3000 Å. On the one hand Eisfeld (2006) suggested that the absorption maximum around 2400 Å cannot be due to propargyl. On the other hand several other authors, Castiglioni et al. (2010), Zheng et al. (2009), Crider et al. (2009), Goncher et al. (2008), Deyerl et al. (1999), agree that the absorption bands in Fahr et al. (1997) are due to propargyl.

Absorption features reported in Fahr and Laufer (2005), Atkinson and Hudgens (1999) are similar in shape and show a shallow peak starting at 3000 Å in direction to longer wavelengths. Atkinson and Hudgens (1999) determined $\sigma(3325\ \text{Å}) = 4.13 \cdot 10^{-18}\ \text{cm}^2$ which is in agreement with the absorption peak detected by Fahr and Laufer (2005) around 3200 Å.

As mentioned above Fahr et al. (1997) does not report absorption cross sections between 2800 Å and 3000 Å. Absorbance spectra in Fahr and Laufer (2005) however, show a linear decrease in this region. Therefore, in this work interpolated absorption cross sections are set at 2850 Å, 2900 Å and 2950 Å determined from the values at 2800 Å and 3000 Å in Fahr et al. (1997). Additionally, the absorbance between 3000 Å and 3325 Å from Fahr and Laufer (2005) is converted to absorption cross sections with the absorption cross sections at 3000 Å (Fahr et al., 1997) and 3325 Å (Atkinson and Hudgens, 1999) and then interpolated linearly in 50 Å steps.

Used are also the ionization cross sections between approximately 8.6 eV and 10.5 eV, i.e. approximately from 1175 Å to 1431 Å, for $C_3H_3^+$ formation reported by Savee et al. (2012), extracted with g3data. Note that the cross sections of Robinson et al. (2003) are lower than those reported in Savee et al. (2012). Additionally, Robinson et al. (2003) report that dissociative ionization is only possible at energies higher than 13 eV, i.e. $\lambda_0 = 954$ Å, therefore no other ionization paths are accessible in the above mentioned wavelength range. In direction to lower wavelengths a constant cross section is assumed in this work, having the cross section value of $2.7 \cdot 10^{-17}\ \text{cm}^2$ at $\lambda = 1175$ Å, because the contribution of this wavelength range to the rate coefficients is very small.

Threshold wavelength

This work uses for photodissociation of H_2C_3H into propadienylidene, i.e. reaction (D.25), $\lambda_0 =$ 2968 Å (96.3 kcal/mol) and for photodissociation into HC_3, i.e. reaction (D.26), $\lambda_0 = 3012$ Å (94.9 kcal/mol) (Mebel et al., 1998). The dissociation reactions

$$C_3H_3 + \gamma \longrightarrow C_2H_2 + CH \tag{D.28}$$

$$C_2 + CH_3 \tag{D.29}$$

are only accessible directly from the isomers c$-C_3H_3$ and CH_3C_2, respectively, to which H_2C_3H would have to rearrange (Mebel et al., 1998). These isomers are disregarded in the present work.

Quantum yields

2400 Å - 2650 Å:

Deyerl et al. (1999) report c$-C_3H_2$ formation to be dominant between 2400 Å and 2650 Å, which is energetically the most favorable isomer of C_3H_2 (Mebel et al., 1998). These results have been obtained theoretically by assuming IC to and dissociation from the ground state (RRKM computations). Their experiments give evidence for the formation of c$-C_3H_2$. Zheng et al. (2009) performed measurements between 2300 Å and 2500 Å and report that the dissociation is from the ground state. Dominant C_3H_2 formation is also found by Goncher et al. (2008) at 2480 Å (isomers were not determined in their work).

At 2420 Å Nguyen et al. (2001) computed branching ratios for H_2C_3H photodissociation assuming IC to and dissociation from the ground state and found: 90.2 % $HC_3H(^3B) + H$, 5.1 % c$-C_3H_2(^1A_1) + H$, 3.0 % $HC_3(^2A') + H_2$, 1.6 % $H_2C_3(^1A_1) + H$ and 0.1 % $C_2H_2 + CH(^2\Pi)$.

The results from Nguyen et al. (2001) and from Deyerl et al. (1999) at 2420 Å disagree on which C_3H_2 isomer is dominantly produced. The photodissociation at these wavelengths is therefore still insecure and one may assume that H_2C_3 may be the dominant isomer at 2400 Å - 2650 Å which is done in the present work.

1933 Å:

Jackson et al. (1991) report branching ratios for C_3H_3 dissociation (formed from $CH_2C_2H_2$), which are 0.96 and 0.04 for the reactions (D.25) and (D.26) (product isomers were not determined).

At 1933 Å Nguyen et al. (2001) found: 86.5 % $HC_3H(^3B)+H$, 3.6 % c−$C_3H_2(^1A_1)+H$, 5.5 % $HC_3(^2A')+H_2$, 3.5 % $H_2C_3(^1A_1)+H$ and 0.9 % $C_2H_2+CH(^2\Pi)$, which are in agreement with the branching ratios of Jackson et al. (1991) with respect to the $C_3H_3 : C_3H_2$ ratio.

0 Å - 1431 Å:

Between 1175 Å to 1431 Å, where reaction (D.27) dominates, a constant unity quantum yield is assumed as no dissociative ionization paths are accessible in this wavelength range, see the explanations for the absorption cross sections above. For simplicity this is also assumed for $\lambda < 1175$ Å. However, the contribution from this wavelength range is very small to the ionization rate coefficient, due to the low solar photon flux in this wavelength range.

D.10 C_3H_2 isomer: H_2C_3 (vinylidenecarbene or propadienylidene, l−C_3H_2, $H_2C{=}C{=}\ddot{C}$)

$$C_3H_2+\gamma \longrightarrow C_3+H_2 \qquad \lambda_0 = 3347 \text{ Å} \tag{D.30}$$

$$C_3H+H \qquad \lambda_0 = 3201 \text{ Å} \tag{D.31}$$

$$C_2+CH_2 \qquad \lambda_0 = 1755 \text{ Å} \tag{D.32}$$

Cross sections

Oscillator strengths are reported in van Hemert and van Dishoeck (2008) for the three isomers H_2C_3, c−C_3H_2 and $(^3B)HC_3H$. Mebel et al. (1998) also reports oscillator strength for the singlet $(^1A')HC_3H$. The present work models C_3H_2 assuming that only H_2C_3 is formed.

Threshold wavelength

This work uses the threshold wavelengths given in Mebel et al. (1998) for the reactions (D.30), (D.31) (which forms HC_3) and (D.32), which are 3347 Å (85.4 kcal/mol, 3.7 eV), 3201 Å ($102.8 - 13.5 = 89.3$ kcal/mol, 3.87 eV) and 1755 Å ($176.4 - 13.5 = 162.9$ kcal/mol, 7.06 eV), respectively. These are the only directly accessible reactions for H_2C_3. All other paths require isomerization of H_2C_3 to the other isomers (Mebel et al., 1998).

Quantum yields

No quantum yields and branching ratios are available, therefore the present work computes the rate coefficients via the MC approach as described in Section 7.2.5.

D.11 C_3H isomer: HC_3 (propynylidyne, l−C_3H, $H\dot{C}{=}C{=}\ddot{C}$)

$$C_3H+\gamma \longrightarrow C_3+H \qquad \lambda_0 = 4026 \text{ Å} \tag{D.33}$$

$$C_2H+C \qquad \lambda_0 = 2214 \text{ Å} \tag{D.34}$$

$$C_2+CH \qquad \lambda_0 = 1782 \text{ Å} \tag{D.35}$$

Cross sections

Oscillator strengths for dissociation computed by van Hemert and van Dishoeck (2008) are reported for the two isomers HC_3 and c$-C_3H$. The present work assumes that only HC_3 is formed.

Threshold wavelengths

This work uses the threshold wavelengths reported in Tuna et al. (2008) as computed by Mebel and Kaiser (2002), which are 4026 Å (3.08 eV), 2214 Å (5.6 eV) and 1782 Å (6.96 eV) for the reactions (D.33), (D.34) and (D.35), respectively. These are used since these correspond to higher threshold wavelengths and allow to estimate higher upper limit photodissociation rate coefficients than when using those reported by Pan et al. (2003, computed), see also Chapter 7. Pan et al. (2003) report for the above reactions 3.46 eV, 6.21 eV and 7.57 eV (Tuna et al., 2008).

Quantum yields

No quantum yields and branching ratios are available, therefore the present work computes the rate coefficients via the MC approach as described in Section 7.2.5.

D.12 C_3 isomer l$-C_3$ (tricarbon, $\ddot{C}$=C=$\ddot{C}$)

$$C_3 + \gamma \longrightarrow C_2 + C \qquad \lambda_0 = 2678 \text{ Å} \tag{D.36}$$

Cross sections

This work uses the oscillator strengths reported in van Hemert and van Dishoeck (2008).

Threshold wavelength

For reaction (D.36) ($(a^3\Pi_u)C_2 + C(^3P)$ formation) 4.63 eV has been determined in Kim et al. (1997), used by van Hemert and van Dishoeck (2008), corresponding to $\lambda_0 = 2678$ Å. Díaz-Tendero et al. (2006) report ≈ 7.6 eV. However, the only state of van Hemert and van Dishoeck (2008) above 7.6 eV is at 3.1 eV and does not lead to photodissociation for both thresholds of 7.6 eV and 4.63 eV.

Quantum yields

No quantum yields are available, therefore the present work computes the rate coefficients via the MC approach as described in Section 7.2.5.

D.13 C_2H_6 (ethane, $H_3C{-}CH_3$)

$$C_2H_6 + \gamma \longrightarrow C_2H_4 + H_2 \qquad \lambda_0 = 8743 \text{ Å} \tag{D.37}$$
$$CH_3 + CH_3 \qquad \lambda_0 = 3172 \text{ Å} \tag{D.38}$$
$$C_2H_5 + H \qquad \lambda_0 = 2827 \text{ Å} \tag{D.39}$$
$$CH_4 + CH_2 \qquad \lambda_0 = 2726 \text{ Å} \tag{D.40}$$
$$C_2H_6^+ + e^- \qquad \lambda_0 = 1064 \text{ Å} \tag{D.41}$$
$$C_2H_5^+ + H + e^- \qquad \lambda_0 = 950 \text{ Å} \tag{D.42}$$
$$C_2H_4^+ + H_2 + e^- \qquad \lambda_0 = 1040 \text{ Å} \tag{D.43}$$
$$CH_3^+ + CH_3 + e^- \qquad \lambda_0 = 890 \text{ Å} \tag{D.44}$$

Cross sections

Absorption cross sections are taken in this work in the range 56 Å to 135 Å and in the range 138 Å to 1200 Å from Au et al. (1993) and Kameta et al. (1996) at $T = 298$ K, respectively, which were downloaded from the webpage Keller-Rudek and Moortgat (2011). From 1200 Å to 1500 Å the cross sections from Chen and Wu (2004) at 150 K are used. From 1500 Å to 1600 Å cross sections from Lee et al. (2001) are used, published in Chen and Wu (2004), were downloaded from Keller-Rudek and Moortgat (2011). Above 1700 Å the cross sections become negligibly small (Rabalais and Katrib, 1974, Lu et al., 2004, Huebner et al., 1992) hence are set to zero in this work.

The older values from Barfield et al. (1972), Koch and Skibowski (1971), Lombos et al. (1967) used in Huebner et al. (1992) are not used in this work, because the first publication reports only atomic absorption cross sections and the last two have a lower resolution.

Threshold wavelengths

λ_0 are adopted in this work from Huebner et al. (1992), except for the reactions (D.38) and (D.39) for which $\lambda_0 = 3172$ Å and $\lambda_0 = 2827$ Å are used, respectively (Blanksby and Ellison, 2003). For the ionization reactions (D.41), (D.42), (D.43) and (D.44) the thresholds are taken to be the onsets of contribution of these reactions.

Quantum yields

This work uses the quantum yields from Lias et al. (1970). In the literature, e.g. Lavvas et al. (2008) or Wilson and Atreya (2004), estimated contributions from reactions forming C_2H_4+H+H and $C_2H_2 + H_2 + H_2$. Since no measurements to our knowledge are reported for such dissociation behavior these reactions are not taken into account in this work. Schoen (1962) measured ionization cross sections to produce $C_2H_6^+$, $C_2H_5^+$, $C_2H_4^+$ and CH_3^+ which can be converted to ionization quantum yields with the total absorption cross sections. These are used in this work.

D.14 C_2H_5 (alkyl, $H_2\dot{C}{-}CH_3$)

$$C_2H_5 + \gamma \longrightarrow CH_2 + CH_3 \qquad \lambda_0 = 2875 \text{ Å} \tag{D.45}$$
$$C_2H_4 + H \qquad \lambda_0 = 8006 \text{ Å} \tag{D.46}$$
$$C_2H_5^+ + e^- \qquad \lambda_0 = 1528 \text{ Å} \tag{D.47}$$

Cross sections

This work uses the absorption cross sections given in Munk et al. (1986) between 2000 Å and 2600 Å downloaded from Keller-Rudek and Moortgat (2011). Other cross sections are also reported in Keller-Rudek and Moortgat (2011) but are older. The cross sections from e.g. Adachi et al. (1979) are a factor of two lower compared to Munk et al. (1986). Wendt and Hunziker (1984, Figure 1) measured the absorption cross sections between 2000 Å and 3500 Å with some impurities, with almost zero absorption between 2600 Å and 3500 Å. This is consistent with the view that the lowest accessible electronic state lies in the ultraviolet **(UV)** starting absorption around 2650 Å (Knopp et al., 2002, Blomberg and Liu, 1985). Therefore, in this work the cross sections are set to zero from 2600 Å to $\lambda_0 = 8006$ Å.

The ionization cross sections for reaction (D.47) are taken from Gans et al. (2011), determined between approximately 1083 Å and 1523 Å. It is assumed that only ionization takes place in the ionization wavelength range, since no dissociation or dissociative ionization quantum yields are known. Moreover, their contribution to the total dissociation is negligible.

Threshold wavelengths

This work uses $\lambda_0 = 2875$ Å and $\lambda_0 = 8006$ Å, respectively, for the reactions (D.45) and (D.46) (Blanksby and Ellison, 2003). The ionization threshold $\lambda_0 = 1528$ Å for reaction (D.47) used in this work is taken from Ruscic et al. (1989).

Quantum yields

No quantum yields or branching ratios are reported in the literature. In the ionization wavelength range the quantum yield is one for reaction (D.47) and zero for the pure dissociation reactions, since only ionization cross sections for (D.47) are known.

D.15 C_2H_4 (ethylene, $H_2C{=}CH_2$)

$$C_2H_4 + \gamma \longrightarrow C_2H_2 + H_2 \qquad \lambda_0 = 7200 \text{ Å} \tag{D.48}$$

$$C_2H_2 + H + H \qquad \lambda_0 = 1960 \text{ Å} \tag{D.49}$$

$$C_2H_3 + H \qquad \lambda_0 = 2582 \text{ Å} \tag{D.50}$$

$$C_2H_4^+ + e^- \qquad \lambda_0 = 1180 \text{ Å} \tag{D.51}$$

$$C_2H_3^+ + H + e^- \qquad \lambda_0 = 898 \text{ Å} \tag{D.52}$$

$$C_2H_2^+ + H_2 + e^- \qquad \lambda_0 = 945 \text{ Å} \tag{D.53}$$

$$\tag{D.54}$$

Cross sections

This work uses absorption cross sections from Henke et al. (1982), 23 Å to 38 Å, Henke et al. (1982), Kempgens et al. (1995), 43 Å to 60 Å, Cooper et al. (1995), 89 Å to 497 Å, Holland et al. (1997), 510 Å to 1178 Å, Zelikoff and Watanabe (1953), 1183 Å to 1973 Å, measured all at $T = 298$ K, and from Wu et al. (2004) measured at $T = 140$ K. Although the cross sections reported by Wu et al. (2004) and Zelikoff and Watanabe (1953) are in reasonable agreement, the values in peaks and valleys between 1600 Å and 1700 Å of Wu et al. (2004) are larger by 15-20 % than those reported in Zelikoff and Watanabe (1953). At $\lambda > 2000$ Å the cross sections become negligibly small (Lu et al., 2004, Wilkinson and Mulliken, 1955, Zelikoff and Watanabe,

1953, Platt et al., 1949, Huebner et al., 1992) hence are set to zero in this work as is done in Huebner et al. (1992) and Huebner et al. (2011).

Threshold wavelengths

For the reaction (D.50) a threshold of 2582 Å is used, $DH_{298}(H_2CCH - H) = 110.7$ kcal/mol (Blanksby and Ellison, 2003). All other λ_0 are adopted from Huebner et al. (1992): dissociation thresholds from heats of formation (Benson, 1976), for ionization from Zelikoff and Watanabe (1953) and for dissociative ionization from Botter et al. (1966).

Reaction

$$C_2H_4 + \gamma \longrightarrow CH_2 + CH_2 \qquad \lambda_0 = 1243 \text{ Å} \tag{D.55}$$

together with its $\lambda_0 = 1243$ Å (Blanksby and Ellison, 2003) is shown here for information only, since this reaction is omitted in this work, as it has only a very small rate coefficient due to its small λ_0. This reaction was used in the work of Helbert (2002) and Weiler (2006) with a rate coefficient approximately three times the rate coefficient of the reaction (D.48) or (D.49).

Quantum yields

Used in this work are the dissociation quantum yields from Giroux et al. (1989) at 1933 Å. Branching ratios from Hara and Tanaka (1973) at 1849 Å and 1634 Å and from Lee et al. (2004) at 1570 Å are also used in this work. This is the only information available for pure dissociation, to our knowledge.

From 550 Å to 1180 Å ionization quantum yields are used in this work, calculated by dividing ionization cross sections of each species by the total absorption cross sections of Schoen (1962). In this work no neutral fragmentation branching ratios or quantum yields were estimated for the ionization wavelength region, in contrast to Huebner et al. (1992), because these have a negligible contribution to the neutral photodissociation rate coefficients.

D.16 C_2H_3 (vinyl, $H\dot{C}{=}CH_2$)

$$C_2H_3 + \gamma \longrightarrow C_2H_2 + H \qquad \lambda_0 = 8074 \text{ Å} \tag{D.56}$$

$$CH + CH_2 \qquad \lambda_0 = 1732 \text{ Å} \tag{D.57}$$

$$C_2H_3^+ + e^- \qquad \lambda_0 = 1503 \text{ Å} \tag{D.58}$$

Cross sections

This work uses absorption cross sections from Fahr and Laufer (1990) between 1647 Å and 1683 Å and Fahr et al. (1998) between 2250 Å and 2380 Å. The absorption cross sections from (Tonokura et al., 1999, g3data extracted) in the range 4440 Å, to 4550 Å are used in this work to convert the absorbance reported in Shahu et al. (2002), between approximately 3850 Å and 5080 Å to absorption cross sections. Between 4440 Å and 4550 Å values from Tonokura et al. (1999) are used.

Used in this work are also the ionization cross sections between 7.8 eV and 10.8 eV for $C_2H_3^+$ formation reported by Robinson et al. (2003). These are extrapolated from $\lambda = 1149$ Å to $\lambda = 0$ Å with the cross section value $\sigma = 1.5 \cdot 10^{-17}$ cm^2 for ionization at $\lambda = 1149$ Å. They also report that dissociative ionization is only possible at energies higher than 13 eV, i.e. $\lambda = 954$ Å. This choice has little effect on the rate coefficient of the reaction (D.58).

Threshold wavelengths

Ahmed et al. (1999) observed the formation of H_2C_2 (vinylidene) and HC_2H (acetylene) at 2430 Å. The formation of acetylene HC_2H has the largest $\lambda_0 = 8074$ Å (35.4 kcal/mol) whereas the formation of H_2C_2 has $\lambda_0 = 3444$ Å (83.0 kcal/mol) (Blanksby and Ellison, 2003). This work uses $\lambda_0 = 8074$ Å. For reaction (D.57) this work uses $\lambda_0 = 1732$ Å (165.0 kcal/mol) from Blanksby and Ellison (2003). The threshold for reaction (D.58) used in this work is taken from Robinson et al. (2003), which is $\lambda_0 = 1503$ Å (8.25 eV).

Quantum yields

No quantum yields were found in the literature for pure dissociation as in the case of C_2H_5. This work assumes that in the ionization region only (D.58) takes place for which ionization absorption cross sections are reported in Robinson et al. (2003).

D.17 C_2H_2 isomer: HC_2H (acetylene, HC≡CH)

$$C_2H_2 + \gamma \longrightarrow C_2H + H \qquad \lambda_0 = 2170 \text{ Å} \tag{D.59}$$

$$C_2 + H_2 \qquad \lambda_0 = 2000 \text{ Å} \tag{D.60}$$

$$C_2H_2^+ + e^- \qquad \lambda_0 = 1086 \text{ Å} \tag{D.61}$$

$$C_2H^+ + H + e^- \qquad \lambda_0 = 697 \text{ Å} \tag{D.62}$$

Cross sections

This work uses absorption cross sections from Cooper et al. (1995) between 62 Å an 1080 Å at $T = 295$ K, downloaded from the webpage Keller-Rudek and Moortgat (2011). The values from Huebner et al. (1992) are omitted, who have used from 0 Å to 500 Å Barfield et al. (1972, cross sections of the atomic constituents) and from 600 Å to 1000 Å the values from Metzger and Cook (1964) at a lower resolution but at the same temperature. Between 1100 Å and 1200 Å the values from Cheng et al. (2011) measured at $T = 85$ K are used as apposed to those measured at $T = 298$ K from Nakayama and Watanabe (1964) at $T = 298$ K, see Huebner et al. (1992, 2011). From 1200 Å to 1890 Å the cross sections from Wu et al. (2001) at $T = 150$ K and from 1890 Å to 2250 Å from Bénilan et al. (2000) at $T = 173$ K are used, downloaded from LISA (2011). Additional absorption cross sections, determined by Smith et al. (1991), were not used due to acetone impurities, reported by Wu et al. (2001), see also Smith (2012).

Threshold wavelengths

This work uses $\lambda_0 = 2170$ and $\lambda_0 = 2000$ Å for the reactions (D.59) and (D.60), respectively (Zhang et al., 2010). From these only the first value is much different in comparison to the older values 2306 Å and 2006 Å in Huebner et al. (1992) from Okabe (1975). The ionization thresholds are $\lambda_0 = 1086$ Å for (D.61) (Herzberg, 1966) and $\lambda_0 = 697$ Å for (D.62) (Schoen, 1962).

Quantum yields

Relatively low quantum yields were found for reaction (D.59) $(0.1 - 0.3)$ at 1933 Å by Satyapal and Bersohn (1991), Shin and Michael (1991) and Seki and Okabe (1993). The new measurements of Läuter (2002) at 1216 Å and at 1933 Å found the quantum yields 0.94 and 1,

respectively. The present work uses the quantum yields of Läuter (2002) at 1216 Å and at 1933 Å and assumes that at 1216 Å $\phi_{\text{total}} - \phi_{C_2H_2 \rightarrow C_2H+H} = 1 - 0.94 = 0.06$ is the quantum yield of reaction (D.60). Additionally, this work uses the quantum yields at 1849 Å from Okabe (1983) and at 1470 Å from Okabe (1981).

Ionization quantum yields are calculated by dividing ionization by absorption cross sections (Schoen, 1962).

D.18 C_2H (ethynyl, $\dot{C}{\equiv}CH$)

$$C_2H + \gamma \longrightarrow C_2 + H \qquad \lambda_0 = 2531 \text{ Å} \tag{D.63}$$

$$CH + C \qquad \lambda_0 = 1604 \text{ Å} \tag{D.64}$$

Cross sections

Ab initio photodissociation oscillator strengths from van Hemert and van Dishoeck (2008) are used in this work.

Threshold wavelengths

This work uses the threshold wavelengths $\lambda_0 = 2531$ Å (4.9 eV) (van Hemert and van Dishoeck, 2008) and 1604 Å (178.2 kcal/mol, 7.73 eV) (Blanksby and Ellison, 2003) for the reactions (D.63) and (D.64), respectively. For reaction (D.63) Pan et al. (2003) report 5.01 eV.

Quantum yields

No quantum yields and branching ratios are available, therefore the present work computes the rate coefficients via the MC approach as described in Section 7.2.5.

D.19 C_2 (dicarbon, $\dot{C}{\equiv}\dot{C}$)

$$C_2 + \gamma \longrightarrow C + C \qquad \lambda_0 = 2030 \text{ Å} \tag{D.65}$$

$$C_2^+ + e^- \qquad \lambda_0 = 1000 \text{ Å} \tag{D.66}$$

Cross sections

Values used in this work are adopted from Huebner et al. (1992). The latter study used for the wavelength range 0 Å to 248 Å, two times the cross sections of C given in Barfield et al. (1972). Huebner et al. (1992) combined calculated ionization cross sections from 248 Å to 954 Å of Padial et al. (1985) with computed dissociation cross sections of Pouilly et al. (1983) from 918 Å to 1210 Å. Huebner et al. (1992) report excellent agreement between Barfield et al. (1972) and Padial et al. (1985) above 248 Å and assume the total cross sections as the sum of the ionization and dissociation cross sections in the 918 to 954 Å overlap region. Between 1210 to 2030 Å the cross sections are very small or zero as reported in Huebner et al. (1992).

Pouilly et al. (1983) calculated oscillator strengths for several transitions from which the two electronic transitions $F(=2)^1\Pi_u \leftarrow X^1\Sigma_g^+$ (at 10.03 eV) and $3^1\Pi_u \leftarrow X^1\Sigma_g^+$ were used to compute the corresponding absorption cross sections between $E = 10.03$ eV and $E \approx 13.5$ eV or 1236 Å and 918 Å shown in their Figure 6. Bruna and Grein (2001) calculated a five times

higher oscillator strength $f = 0.1$ for $F(=2)^1\Pi_u \leftarrow X^1\Sigma_g^+$ in contrast to $f = 0.02$ from Pouilly et al. (1983). The value of Bruna and Grein (2001) is equal to the semi-empirical derivation of Chaffee et al. (1980, p.479) from astronomical data. However, these values have no significant effect on the photodissociation rate coefficient.

Threshold wavelengths

Okabe (1978) calculated the wavelength equivalent dissociation energy to be $\lambda_0 = 1436$ Å and $\lambda_0 = 2030$ Å for the reactions $C_2 + \gamma \rightarrow C(^1d) + C(^1d)$ and $C_2 + \gamma \rightarrow C(^3p) + C(^3p)$, respectively. $C(^1d)$ and $C(^3p)$ are combined into C in the present work. $\lambda_0 = 2007$ Å is reported in Blanksby and Ellison (2003) as the threshold calculated from heats of formation which, however, makes no difference since the absorption cross sections are zero beyond $\lambda = 1210$ Å.

The ionization threshold is $\lambda_0 = 1000$ Å (12.4 eV) reported from Okabe (1978) or $\lambda_0 = 1055$ Å (11.75 eV) reported in Bruna and Grein (2001). The threshold as used in Huebner et al. (1992, 2011), i.e. 2030 Å and 1000 Å, are adopted in this work because the new thresholds have no or only a very small influence on the results.

Quantum yields

This work also adopts the quantum yields used in Huebner et al. (1992). These are calculated in this work from the total absorption cross sections and the partial cross sections (cross sections for each reaction) given on the webpage Huebner et al. (2011). Therein ionization quantum yields were calculated from ionization and absorption cross sections. The remaining absorption is assumed to lead to dissociation in the ionization region. At larger wavelengths Huebner et al. (1992, 2011) used $\phi_i = 1$ for reaction (D.65), since mainly direct photodissociation occurs in the electronic states of C_2 for which absorption cross sections have been computed in Pouilly et al. (1983).

APPENDIX E

The HS Algorithm, the clr Transformation and the Adjusted χ^2

This part of the appendix describes the harmony search **(HS)** algorithm, the centred-logratio **(clr)** transformation and the adjustments to the χ^2 required in this work.

E.1 The HS Algorithm

As the rate coefficients of the hydrocarbon photodissociation reactions and the parent molecule production rate ratios are a large parameter space for the optimization of the model to reproduce the observations of C_3 and C_2, a search algorithm is required, which has shown its suitability in many large scale optimization problems. One of the advantages of the HS algorithm is that it generally converges faster than the genetic, the simulated annealing and other heuristic algorithms. It generally, finds more often the global or a near global solution in comparison to other heuristic algorithms (Shukla and Anand, 2011, Geem, 2009). In this work the harmony search **(HS)** algorithm is used, which was first developed by Geem et al. (2001). It is based on the music harmony improvisation process of jazz musicians.

When improvising a new music piece a musician can either play a famous music piece from his memory, attune it to a different pitch or the musician can combine parts of known music pieces with parts of other known music pieces or with new or random notes. The components required for HS are therefore the harmony memory **(HM)**, the pitch adjustment and the randomization. The harmony memory

$$\mathbf{HM} = \begin{pmatrix} x_1^1, \ldots, x_n^1 \\ \vdots \\ x_1^{\mathrm{HMS}}, \ldots, x_n^{\mathrm{HMS}} \end{pmatrix} \in \mathbb{R}^{\mathrm{HMS}\,\mathrm{x}\,n}, \tag{E.1}$$

saves the current HMS (harmony memory size) best solutions $\mathbf{x}^j = (x_1^j, x_2^j, \ldots, x_n^j)^T$. This is similar to the best-fit individuals in a genetic algorithm. Indeed, the HS algorithm is an improved version of the genetic algorithm. After each optimization round the worst solution of the HM is exchanged by the best new found solution.

A HM accepting rate $r_{\mathrm{accept}} \in [0, 1]$ controls the rate of taking the HM into consideration when generating new harmonies for testing of fitness. It is typically between $r_{\mathrm{accept}} \in [0.7, 0.95]$,

since a too low rate can result in a slow convergence, whereas a value near one means that harmonies outside the HM are not considered. In this work r_{accept} is generated randomly in each optimization step as $r_{\text{HM}} = 0.05 + 0.95 \cdot \epsilon_1$, with ϵ_1 a uniformly distributed random number. The pitch adjustment rate r_{pitch} is the rate of generating a new harmony by slightly adjusting one or more parameters of the harmony via

$$x_i^{\text{new}} = x_i^{\text{HM}} + b_{\text{range}} \cdot \epsilon_2 \,. \tag{E.2}$$

$\epsilon_2 \in [-1, 1]$ is a normally distributed random number, independent of ϵ_1, and b_{range} is the bandwidth. As one can generate and evaluate several new harmonies in one round so that one has a population of m test parameter arrays, in this work b_{range} is defined as the standard deviation of the regarded parameter from the population members. The pitch adjusting rate r_{pitch} has an equivalent in genetic algorithms, i.e. the mutation operator. Ideally, one uses $r_{\text{pitch}} \in [0.1, 0.5]$ and a medium band width b_{range} to avoid on the one hand a slow convergence when only a subspace is evaluated by using small r_{pitch} and b_{range} and on the other hand a scattering in the search space around a global optimum by using large r_{pitch} and b_{range}. The pitch adjustment corresponds to a local search, whereas a global search is realized everytime when not taking a harmony from the HM. This means

$$P_{\text{random}} = 1 - r_{\text{accept}} \,, \tag{E.3}$$

$$P_{\text{pitch}} = r_{\text{accept}} \cdot r_{\text{pitch}} \tag{E.4}$$

are the probabilities of randomization and pitch adjustment, respectively (Yang, 2010). The HS algorithm is shown in Figure E.2 in a flowchart and in Table E.1 as a pseudo code.

This work performs the HS on a computer cluster, where several model computations can be carried out at one time. This 'population' of, e.g. $m = 24$, parallel running model computations (individuals) is used to update the HM. Therefore, in Figure E.2 one performs '*Improvise a new harmony*' and '*Add new harmony to HM? ... Update HM*' for each of the m individuals. The HS code has been provided by Csizmadia (2013, pers. comm.), see e.g. Cabrera et al. (2010).

Finally, the HS algorithm used in this work does a random global search, after initialization of the HM, evaluates these random parameter sets to get an idea where parameters may be located globally that give model outputs close to the observations. This search is required to feed the HM with globally good parameters. After this initial phase the actual HS starts. In addition, with a low rate of $r_{\text{random}} = 0.001$ for each element of a new improvised parameter vector, i.e. if $rand < 0.001$, the HS includes a random value from the allowed parameter space, instead of improvising a new parameter value as described above. Figure E.1 shows for example the parameter search for production rate ratios of the parent molecules C_4H_2 and C_2H_2 and the involved photodissociation rate coefficients. In this figure the red crosses, the upper and lower green solid horizontally aligned lines and the green dashed horizontally aligned lines mark the best fit parameters, the upper and lower limit of the production rate ratios and photodissociation rate coefficient uncertainties ([0.001,0.999] percentiles) and the median value, respectively.

Stopping Criteria

An optimization run is stopped, when the minimum and maximum $\hat{\chi}^2$, see Equation (E.14) in Appendix E.3, of the m individuals is less than 1 %. Therefore,

$$\frac{\text{Max}\left(\{\hat{\chi}_1^2, \ldots, \hat{\chi}_m^2\}\right)}{\text{Min}\left(\{\hat{\chi}_1^2, \ldots, \hat{\chi}_m^2\}\right)} < 1.01 \,, \tag{E.5}$$

is a criterion for the convergence of the optimization process to a global optimum. $\hat{\chi}^2$, see Equation (E.14), is the adjusted χ^2 as described in Section E.3.2.

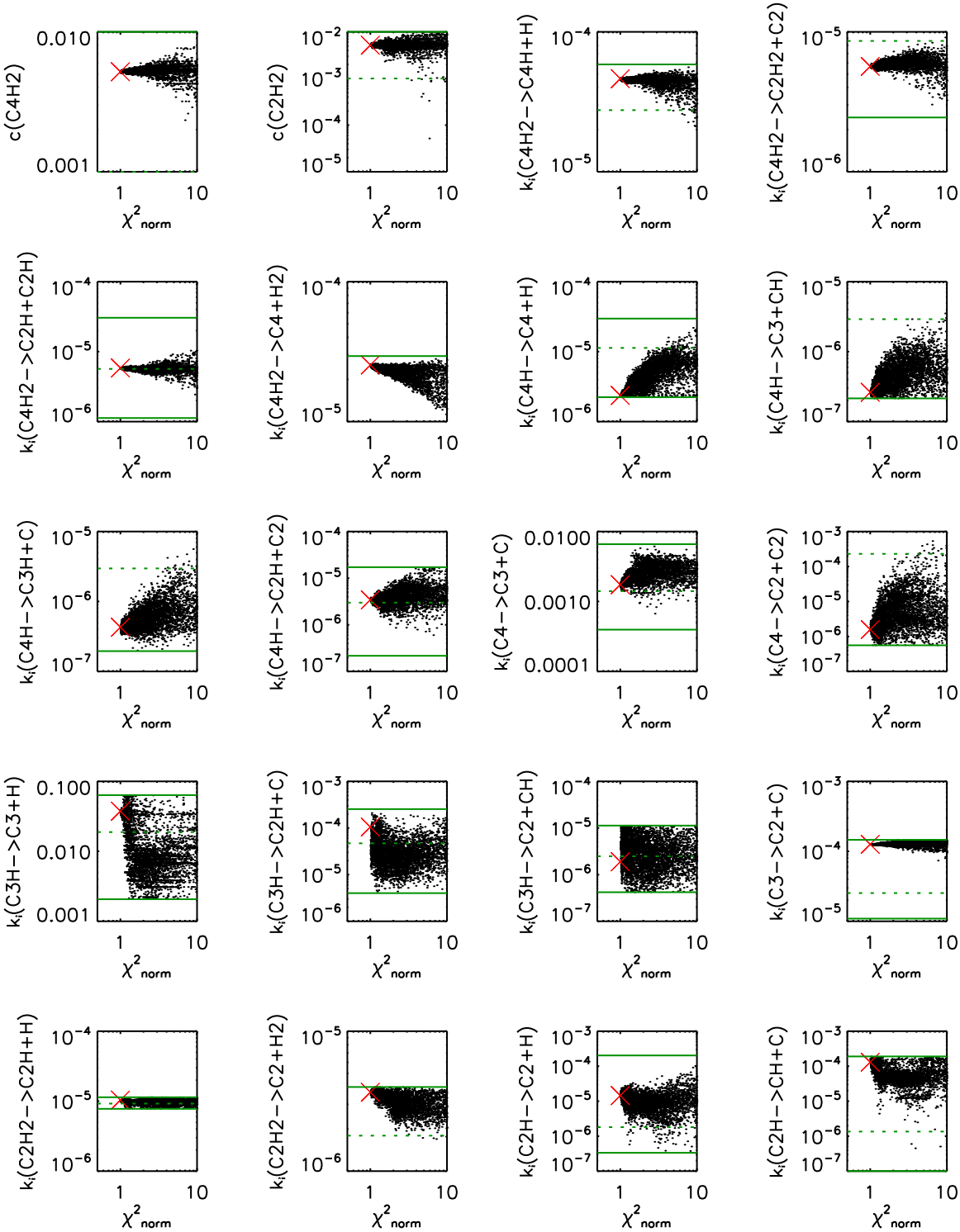

Figure E.1: *Overview of tested parameters within the HS optimization for the scenario* "C_4H_2, C_2H_2"*. The best fit values are marked with a red cross. The first two panels show the results for* $c(C_4H_2)$ *and* $c(C_2H_2)$ *for the sunward side of the NEAT observations. The subsequent panels show the results for the optimized common set of rate coefficients for all comets and data sides (tailward, sunward). The solid horizontally aligned green lines mark the* 0.999 *and* 0.001 *percentiles and the dashed green line the median of the rate coefficient* k_i *and production rate ratio* c_i *distributions, respectively. The x-axis depicts the* χ^2_{norm}*, see Equation* (E.18)*. Only parameters with* $\chi^2_{norm} \in [1, 10]$ *are shown.*

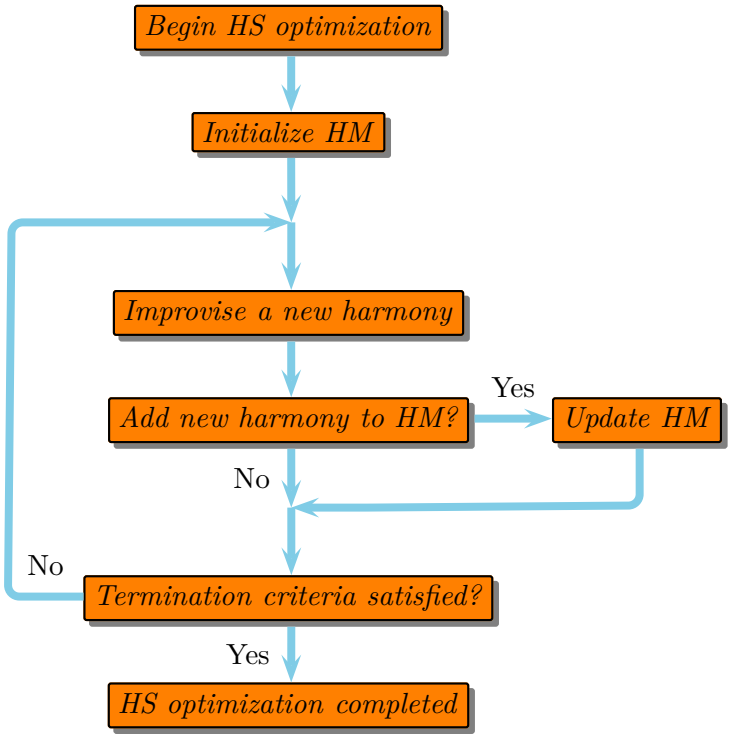

Figure E.2: *Flowchart of the harmony search* ***(HS)*** *algorithm. HM is the harmony memory. Adapted from: Geem (2009).*

Table E.1: *Pseudo code of the HS algorithm. HM is the harmony memory and rand*(1) *and rand*(2) *are independent random numbers. f is in this work $\hat{\chi}^2$ as defined in Equation* (E.14)*. f_{min} and f_{max} are the smallest and the largest f value in the HM. tol is a tolerance factor, e.g. tol* $= 0.01$*. See text for more information. Source: Geem (2009).*

Harmony Search
begin
Define objective function $f(\mathbf{x})$, $\mathbf{x} = (x_1, x_2, \ldots, x_n)^T$
Define HM accepting rate r_{accept}
Define pitch adjusting rate r_{pitch}, pitch limits and bandwidth b_{range}
Generate HM with random harmonies (real number arrays)
while $t <$ max number of iterations **or** $f_{\max}/f_{\min} < 1 + tol$ **do**
while $i <$ max number of variables **do**
if $rand(1) < r_{\text{accept}}$ **then** choose a value from HM for the variable i
if $rand(2) < r_{\text{pitch}}$ **then** adjust the value by adding a certain amount
endif
else choose a random value
endif
endwhile
Accept the new harmony (solution) if better
endwhile
Find the current best solution
end

E.2 The Centered Logratio Transformation (clr)

In order to respect the constraint $\sum_{i=1}^{n} bf_i = 1$ of the full branching ratios $\mathbf{bf} = (bf_1, \ldots, bf_n)$ (compositional data) within the optimization process, one needs to transform the bf_i from the standard simplex $\mathbb{S}^n := \{(x_1, \ldots, x_n) \in \mathbb{R}^n \,|\, x_i \geq 0, \sum_{i=1}^{n} x_i\}$ into the real space $\mathbb{R}^{n-1}$ via the clr transformation. It is defined as

$$\begin{aligned} \mathrm{clr} \,:\, \mathbb{S}^n \longrightarrow \mathbb{R}^{n-1}\,, \quad \mathbf{x} = (x_1, \ldots, x_n) \longmapsto \mathbf{z} = (z_1, \ldots, z_{n-1}) \\ z_i = \ln\left(\frac{x_i}{g(\mathbf{x})}\right)\,, \quad g(\mathbf{x}) = \sqrt[n]{\prod_{j=1}^{n} x_j}\,, \quad z_n = -\sum_{j=1}^{n-1} z_j\,, \quad \sum_{j=1}^{n} z_j = 0\,, \end{aligned} \tag{E.6}$$

with $g(\mathbf{x})$ the geometric mean of the n elements of the composition $\mathbf{x}$. Since this compositional data only contains relative information it is adequate to use logs of ratios to analyze the data (Tsagris et al., 2011). The clr transformation is a common transformation to do statistics (defined in the real space) and then back-transform into the simplex space $\mathbb{S}^n$ of compositional data. The clr transformation is only a special case of several other logratio transformations, e.g. the additive-logratio **(alr)** (Aitkison, 1986) and the isometric-logratio **(ilr)** transformation (Jarauta-Bragulat et al., 2003). Only $z_1, \ldots, z_{n-1}$ are required for the optimization. The corresponding $bf_1, \ldots, bf_n$ are transformed back from the z_i via (Aitkison, 1986)

$$x_i = \frac{\exp(z_i)}{\sum_{j=1}^{n} \exp(z_j)}\,, \tag{E.7}$$

with $z_n = 1 - \sum_{j=1}^{n-1} z_j$. See e.g. Benneke and Seager (2012) and Gans et al. (2013) for applications of the clr transformation.

Figure E.3 (upper panel) shows the $[0.001, 0.999]$ percentile area of the three bf_i of the photodissociation reactions of the species C_2H_4, C_3H_2 and C_3H in a ternary plot and (lower panel) the corresponding *clr* transformed values $\mathbf{z} = (z_1, \ldots, z_{n-1})$ with $n = 3$. One recognizes that the boundaries of the areas in the $\mathbb{R}^{n-1}$, denoted here as A_{species}, are irregular. In this work the tested z_i parameters are kept within their A_{species} by sampling $\mathbf{z}$ values in a box surrounding A_{species} and rejecting those outside. The boundaries of each A_{species} surrounding box are estimated via

$$\begin{aligned} \mathbf{z}^{\max} &= (z^{\max}, \ldots, z^{\max})\,, \\ \mathbf{z}^{\min} &= \left(z^{\min}, \ldots, z^{\min}\right) \end{aligned} \tag{E.8}$$

with

$$\begin{aligned} z^{\max} &= \mathrm{clr}\left(\left[\mathrm{Max}\{bf_i^{\max}\}_{i=1}^{n}, \mathrm{Min}\{bf_i^{\min}\}_{i=1}^{n}\right] \Big/ \left(\mathrm{Max}\{bf_i^{\max}\}_{i=1}^{n} + \mathrm{Min}\{bf_i^{\min}\}_{i=1}^{n}\right)\right)\,, \\ z^{\min} &= \mathrm{clr}\left(\left[\mathrm{Min}\{bf_i^{\min}\}_{i=1}^{n}, \mathrm{Max}\{bf_i^{\max}\}_{i=1}^{n}\right] \Big/ \left(\mathrm{Max}\{bf_i^{\max}\}_{i=1}^{n} + \mathrm{Min}\{bf_i^{\min}\}_{i=1}^{n}\right)\right) \\ &= -z^{\max}\,. \end{aligned} \tag{E.9}$$

$bf_i^{\min}$ and $bf_i^{\max}$ are the 0.001 and 0.999 percentiles, respectively, of the uncertainty distributions of each bf_i, enclosing the 99.8 % probability area. This rejection method is required in the HS algorithm when initializing the HM and when improvising new harmonies.

E.3 Adjusted χ^2

Generally, the likelihood of a set of parameters of a model given the observations can be estimated using the χ^2 statistic, described in the following. The most likely set of parameters, obtained in an optimization process, are the so-called 'maximum likelihood estimators'.

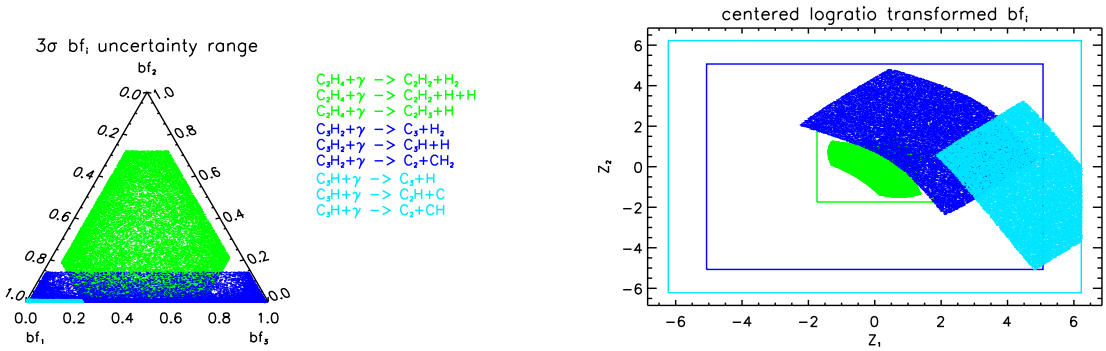

(a) *Ternary plot of* $\boldsymbol{bf} = (bf_1, bf_2, bf_3)$ *example uncertainty areas in the simplex* $\mathbb{S}^3$

(b) *Uncertainty areas* $A_{species}$ *of the* $\boldsymbol{z} = (z_1, z_2) = clr((bf_1, bf_2, bf_3))$ *values in the* $\mathbb{R}^2$

Figure E.3: *Visualization of the centred-logratio* ***(clr)*** *transformation. In (a) a ternary (simplex) plot depicts example* 99.8 *% uncertainty areas of the branching ratios* $\boldsymbol{bf} = (bf_1, bf_2, bf_3)$ *of the depicted specie's photodissociation reactions (ionization reactions omitted). In (b) the clr transformed uncertainty areas* $A_{species}$ *(dotted) are shown in the color of each species. To make visible* $A_{species}$*, for each species* $3 \cdot 10^4$ $\boldsymbol{z} = (z_1, z_2)$ *values were generated uniformly via sampling from the surrounding boxes, which boundaries were computed via Equation* (E.9)*, and then collecting values* $\boldsymbol{z} = (z_1, z_2)$ *which corresponding* bf_i *fulfill their constraints. In (a) the number density is larger at the borders of the simplex due to the constant sum (combinatorial) constraint.*

E.3.1 χ^2 and goodness-of-fit (*g.o.f.*)

In order to optimize the model to the observations one has to minimize their deviation. For this purpose the χ^2 statistic of $\nu = n - m - 1$ degrees of freedom is used

$$\chi^2 = \sum_{i=1}^{n} \left(\frac{O_i - M_i(\mathbf{x})}{\sigma_i} \right)^2 , \qquad \mathbf{x} = (x_1, \ldots, x_m) , \tag{E.10}$$

where $M_i(\mathbf{x})$ are the model values, when applying the model parameter vector $\mathbf{x}$, O_i the observation with the uncertainty σ_i and n and m the number of data points and parameters, respectively. Reducing χ^2 corresponds to increasing the likelihood of M_i being a correct representation of the observation O_i, which are assumed in Equation (E.10) to be normally distributed, i.e. the probability that O_i is nature's (most likely) correct value $\bar{O}_i$ is $P(O_i) = \frac{1}{\sigma_i \sqrt{2\pi}} \exp\left(-\frac{1}{2} \left(\frac{O_i - \bar{O}_i}{\sigma_i} \right)^2 \right)$.

Usually, fits having a $\chi^2 \approx \nu$ are considered 'moderately' good fits, since the χ^2 distribution has the mean ν and the standard deviation $\sqrt{2\nu}$, converging to a normal distribution for large ν. Often one uses the reduced χ^2 defined as

$$\chi^2_{\text{red}} = \frac{\chi^2}{\nu} , \tag{E.11}$$

so that moderately good fits have $\chi^2_{\text{red}} \approx 1$.

The *goodness-of-fit* (*g.o.f.*) is the probability $Q(\chi^2|\nu)$ of obtaining a worse χ^2 than the correct one, due to chance fluctuations in the observations, i.e. the observational data points may not be nature's correct values. As Equation (E.10) assumes normally distributed data, $\chi^2 > \nu$ and very small Q can be obtained, when this assumption is not met. In this case often fits with $Q > 0.001$ are considered good fits (Press et al., 2007). Other reasons may be underestimated uncertainties. Too good fits, i.e. fits with relatively high Q, may be caused by overestimated uncertainties. Q decreases with increasing ν, i.e. the effect of statistical fluctuations on χ^2 decreases. To compute $Q(\chi^2, \nu) = 1 - P(\chi^2, \nu)$, P is computed using `chisqr_pdf.pro` (NASA-IDL-Lib., 2011).

E.3.2 χ^2 Adjustments to Simultaneously Optimize C_3 and C_2

Distance Weight

For the purposes of this work a distance weight has to be included into the χ^2 measure as (Weiler, 2006)

$$\tilde{\chi}^2 = \sum_{i=1}^{n} \left(\frac{O_i - M_i}{\sigma_i} \cdot \frac{1}{r_{\mathrm{c},i}} \right)^2 . \tag{E.12}$$

This is required on the one hand because the inner data points determine most the final production rate ratio of each parent molecule after the optimization and on the other hand because these data points are smaller in number in comparison to the bulk of data points reaching up to approximately $\approx 10^5$ km, which dominate the χ^2 in Equation (E.10).

For the purposes of this chapter it is required to optimize the model simultaneously to the observational C_3 and C_2 column densities of the four comets C/2001 Q4 **(NEAT)**, C/2002 T7 **(LINEAR)**, 9P **(Tempel 1)** and C/1995 O1 **(Hale-Bopp)** with the coma chemistry model described in Chapter 5.

Simultaneous Optimization In Previous Works

Helbert (2002) optimized their model to the C_3 and C_2 observations simultaneously with the following approach. Helbert (2002) first optimized to C_3 by varying the C_3H_4 production rate $Q(C_3H_4)$ until the fit with the best χ^2 value was determined. $Q(C_3H_4)$ is then fixed to the best fit value. In the next step the model is optimized to C_2 on the one hand by varying the ratio $Q(C_2H_6)/Q(C_2H_2)$, which determines the shape of the model profile, and on the other hand by varying the absolute value of $Q(C_2H_2)$, which determines the height of the C_2 model profile. From this two-dimensional parameter space the parameter set with the best χ^2 is determined. Weiler (2006) made use of the same approach, but taking the ratio $Q(C_3H_4)/Q(C_4H_2)$, i.e. additionally C_4H_2 as a C_3 parent molecule, and the absolute value $Q(C_4H_2)$ to optimize to the C_3 observations and the $Q(C_2H_2)/Q(HC_3N)$ ratio together with the absolute value $Q(HC_3N)$ to optimize to the C_2 observations.

Simultaneous Optimization Applied in This Work

Since in this work the C_3 and the C_2 model column density profiles are optimized simultaneously, one has to define a total χ^2 as

$$\tilde{\chi}^2 = \tilde{\chi}^2_{C_3} + \tilde{\chi}^2_{C_2} = \sum_{i=1}^{m} \left(\frac{O_i - M_i}{\sigma_i} \cdot \frac{1}{r_{\mathrm{c},i}} \right)^2_{C_3} + \sum_{j=1}^{n} \left(\frac{O_j - M_j}{\sigma_j} \cdot \frac{1}{r_{\mathrm{c},j}} \right)^2_{C_2} , \tag{E.13}$$

As the observational column density uncertainties of C_3 are much higher than those of C_2, the $\tilde{\chi}^2$ is dominated by $\tilde{\chi}^2_{C_2}$, leading the HS algorithm to mainly optimize the model to the C_2 observations. To avoid this, a normalization between $\tilde{\chi}^2_{C_3}$ and $\tilde{\chi}^2_{C_2}$ is required, which can either be a mean normalization factor $\alpha(C_2, C_3)$ defined via

$$\hat{\chi}^2 = \alpha(C_2, C_3) \cdot \tilde{\chi}^2_{C_3} + \tilde{\chi}^2_{C_2} \qquad \text{as} \qquad \alpha(C_2, C_3) = \frac{\sum_{j=1}^{n} \left(\frac{O_j^{C_2}}{\sigma_j^{C_2} r_{\mathrm{c},j}^{C_2}} \right)^2}{\sum_{i=1}^{m} \left(\frac{O_i^{C_3}}{\sigma_i^{C_3} r_{\mathrm{c},i}^{C_3}} \right)^2} , \tag{E.14}$$

or it is chosen as a normalization for each data point via

$$\hat{\chi}^2 = \sum_{i=1}^{m} \alpha_i \left(\frac{O_i - M_i}{\sigma_i} \cdot \frac{1}{r_{\mathrm{c},i}} \right)^2_{\mathrm{C}_3} + \tilde{\chi}^2_{\mathrm{C}_2} \qquad \text{as} \qquad \alpha_i = \frac{\left(\frac{O_j^{\mathrm{C}_2}}{\sigma_j^{\mathrm{C}_2} r_{\mathrm{c},i}^{\mathrm{C}_2}} \right)^2}{\left(\frac{O_i^{\mathrm{C}_3}}{\sigma_i^{\mathrm{C}_3} r_{\mathrm{c},i}^{\mathrm{C}_3}} \right)^2}, \tag{E.15}$$

provided that for the C_3 and C_2 observations $r_{c,i}^{\mathrm{C}_3} = r_{c,j}^{\mathrm{C}_2}$ and $n = m$.

This work applies the approach of Equation (E.14) as it preserves the uncertainties within a data profile. The effect of the normalization constant α can be visualized if one assumes that the observations and the model only differ by a constant value, i.e. $O_i - M_i = const$. Then $\tilde{\chi}^2_{\mathrm{C}_3}$ and $\tilde{\chi}^2_{\mathrm{C}_2}$ differ by α of Equation (E.14), which is computed in the beginning of the optimization from the data and its uncertainties. If observations of several comets are to be optimized in one optimization run, using the production rate ratios of each comet and a common set of rate coefficients as parameters, one has to extend the approach of Equation (E.14) to

$$\begin{aligned} \hat{\chi}^2 &= \alpha({\mathrm{C}_2}^{(1)}, {\mathrm{C}_3}^{(1)}) \cdot \tilde{\chi}^2_{{\mathrm{C}_3}^{(1)}} + \tilde{\chi}^2_{{\mathrm{C}_2}^{(1)}} + \dots \\ &\dots + \alpha({\mathrm{C}_2}^{(1)}, {\mathrm{C}_3}^{(M)}) \cdot \tilde{\chi}^2_{{\mathrm{C}_3}^{(M)}} + \alpha({\mathrm{C}_2}^{(1)}, {\mathrm{C}_2}^{(M)}) \cdot \tilde{\chi}^2_{{\mathrm{C}_2}^{(M)}} \end{aligned} \tag{E.16}$$

in which $(1), \dots, (M)$ denote the data of each of the $1, \dots, M$ comets included in the optimization process, i.e. in Equation (E.16) all $\tilde{\chi}^2$ of all C_3 and C_2 observations of all comets (except that of C_2 of comet 1) are normalized to the $\tilde{\chi}^2$ of the C_2 observations of comet 1. The normalization may also be done with respect to any other comet and with respect to C_3 instead of C_2. In this work this approach is extended to optimize the model separately to the tailward and sunward sides of the observations of each comet.

E.3.3 Confidence Intervals and Level of Constraint

The HS algorithm performs a global optimization, it stops when reaching the optimum parameter vector $\mathbf{x} = (x_1, \dots, x_n)$. To provide confidence intervals, one has to obtain a significant number of $\mathbf{x}$ adjacent to $\mathbf{x}$.

Confidence Intervals

The confidence interval C_i of the parameter x_i is defined as

$$\begin{aligned} C_i &= [\mathrm{Min}(x_i), \mathrm{Max}(x_i)] = [x_i^{\mathrm{upper}}, x_i^{\mathrm{lower}}], \\ \mathbf{x} &= (x_1, \dots, x_n), \quad \hat{\chi}^2_{\mathrm{norm}}(\mathbf{x}) \in [1, 1+\delta] \end{aligned} \tag{E.17}$$

with e.g. $\delta = 0.5$. The normalized $\hat{\chi}^2$ is defined as

$$\hat{\chi}^2_{\mathrm{norm}}(\mathbf{x}) = \frac{\hat{\chi}^2(\mathbf{x})}{\mathrm{Min}\left(\{\hat{\chi}^2(\mathbf{x})\}_{\mathbf{x} \in X}\right)}, \tag{E.18}$$

where X is the set of tested parameter vectors by the optimization algorithm. This χ^2_{norm} was used e.g. in Helbert (2002) to remove the effect that each observation's individual data quality has on χ^2.

A sufficient number of $\approx 1,000 - 1,500$ tested parameter vectors is obtained with the HS algorithm within the parameter confidence interval defined by $\chi^2_{\mathrm{norm}} \in [1, 1.5]$ as used in this work.

The so-called simulated annealing algorithm (code provided by Csizmadia (2013, pers.comm.)), see also Press et al. (2007), was also tested in this work to generate test parameters around the

best fit parameter vector by starting the search at this parameter vector. This algorithm, however, generally only found parameter vectors with a worse χ^2 than the best fit parameter found by the HS algorithm.

Level of Constraint

The level of constraint of a parameter can be estimated by the dispersion of the tested parameter values with $\chi^2_{\text{norm}} \in [1, 1.5]$, see e.g. Figure E.1. This work defines the level of parameter constraint via, see Equation (E.17),

$$F^2_{i,\text{conf}} = \frac{x_i^{\text{upper}}}{x_i^{\text{lower}}} \,. \tag{E.19}$$

with which a parameter is defined to be well, moderately and poorly constrained if $F^2_{i,\text{conf}} < 2$ ($F_{i,\text{conf}} \lessapprox 40$ %), $F^2_{i,\text{conf}} \in [2, 10)$ and $F^2_{i,\text{conf}} \geq 10$, respectively. This is similar to F^2 of Equation (7.12) in Chapter 7 used to describe the level of uncertainty of a rate coefficient. In Chapter 7, only uncertainties of parameters were included to compute each reaction's rate coefficient distribution, which result in $F(k_i) > 50$ % (close to 40 % used here).

APPENDIX F

Reaction Network

This Appendix chapter presents the complete reaction network of the coma chemistry model used in this work, sorted by the type of reaction. The following tables display the reaction, the Arrhenius coefficients A, B, C with respect to Equation (3.17), the mean total excess energy ΔE of a reaction and the model internal reaction number. In the following tables A has units [10^{-6} s^{-1}] for photo reactions and [10^{-6} cm^3 s^{-1}] for all other reaction types. ΔE has units [eV]. Very large or small numbers are written in exponential form, where e.g. 1E04 represents 10^4. For the updated photo rate coefficients and newly introduced photo reactions, see Chapter 7, the median rate coefficients k_i^{median} are reported, see Table 7.4. All other rate coefficients and excess energies are adopted from the reaction network used in Weiler (2006) which comprises updates applied in that work as well as values adopted from Helbert (2002) and Huebner et al. (1992).

The present work includes the photodissociation reactions of the C_3H_4 isomers $CH_2C_2H_2$ and CH_3C_2H. The corresponding C_3H_4 reactions used in the former works were updated in the present work by including the same set of reactions for $CH_2C_2H_2$ as well as for CH_3C_2H. The reactions including $C_3H_4^+$ were not updated to include the C_3H_4 isomers, since no photoionization reactions of these isomers are included into this work. This assumption is reasonable since all reactions besides photodissociation do not contribute significantly to C_3 and C_2.

F.1 Photodissociation

Photodissociation	A	B	C	ΔE	#
$C_2 + \gamma \rightarrow C + C$	0.0973	0.0	0.0	7.4100	25
$C_2H + \gamma \rightarrow C + CH$	1.3544	0.0	0.0	3.0000	1072
$C_2H + \gamma \rightarrow C_2 + H$	1.8103	0.0	0.0	3.8200	24
$C_2H_2 + \gamma \rightarrow C_2 + H_2$	1.7920	0.0	0.0	3.0000	30
$C_2H_2 + \gamma \rightarrow C_2H + H$	9.2422	0.0	0.0	1.8400	23
$C_2H_3 + \gamma \rightarrow C_2H_2 + H$	1.7E+04	0.0	0.0	0.0	2
$C_2H_3 + \gamma \rightarrow CH + CH_2$	3.7507	0.0	0.0	0.0	83
$C_2H_4 + \gamma \rightarrow C_2H_2 + H + H$	8.8497	0.0	0.0	5.2900	1152
$C_2H_4 + \gamma \rightarrow C_2H_2 + H_2$	9.3017	0.0	0.0	3.0300	1151
$C_2H_4 + \gamma \rightarrow C_2H_3 + H$	4.1214	0.0	0.0	5.1000	1154
$C_2H_5 + \gamma \rightarrow C_2H_4 + H$	360.2080	0.0	0.0	3.7400	1153
$C_2H_5 + \gamma \rightarrow CH_2 + CH_3$	360.0860	0.0	0.0	14.0000	37
$C_2H_6 + \gamma \rightarrow C_2H_4 + H_2$	3.1984	0.0	0.0	3.1600	18
$C_2H_6 + \gamma \rightarrow C_2H_5 + H$	2.6392	0.0	0.0	1.2700	52

Continued on next page

Table F.1 – *Continued from previous page*

Photodissociation	A	B	C	ΔE	#
$C_2H_6 + \gamma \rightarrow CH_3 + CH_3$	0.7140	0.0	0.0	0.4500	1071
$C_2H_6 + \gamma \rightarrow CH_4 + CH_2$	2.0184	0.0	0.0	6.7600	41
$C_3 + \gamma \rightarrow C_2 + C$	25.3407	0.0	0.0	1.0000	1156
$C_3H + \gamma \rightarrow C_2 + CH$	2.4814	0.0	0.0	0.0	1155
$C_3H + \gamma \rightarrow C_2H + C$	46.8734	0.0	0.0	0.0	26
$C_3H + \gamma \rightarrow C_3 + H$	1.9E+04	0.0	0.0	7.1500	39
$C_3H_2 + \gamma \rightarrow C_2 + CH_2$	2.7713	0.0	0.0	0.0	38
$C_3H_2 + \gamma \rightarrow C_3 + H_2$	876.6910	0.0	0.0	30.2000	40
$C_3H_2 + \gamma \rightarrow C_3H + H$	879.2670	0.0	0.0	0.0	1171
$C_3H_3 + \gamma \rightarrow C_3H + H_2$	766.6920	0.0	0.0	0.0	304
$C_3H_3 + \gamma \rightarrow C_3H_2 + H$	986.1380	0.0	0.0	4.0500	1075
$C_3N + \gamma \rightarrow C_2 + CN$	128.8330	0.0	0.0	6.5200	1074
$C_4 + \gamma \rightarrow C_2 + C_2$	229.6550	0.0	0.0	7.9000	1073
$C_4 + \gamma \rightarrow C_3 + C$	1402.6899	0.0	0.0	8.6400	1080
$C_4H + \gamma \rightarrow C_2H + C_2$	2.9870	0.0	0.0	1.0000	1079
$C_4H + \gamma \rightarrow C_3 + CH$	2.9152	0.0	0.0	10.2300	1078
$C_4H + \gamma \rightarrow C_3H + C$	2.9685	0.0	0.0	0.0	56
$C_4H + \gamma \rightarrow C_4 + H$	11.2970	0.0	0.0	3.0000	1077
$C_4H_2 + \gamma \rightarrow C_2H + C_2H$	5.6746	0.0	0.0	0.0	116
$C_4H_2 + \gamma \rightarrow C_2H_2 + C_2$	8.6077	0.0	0.0	4.0000	634
$C_4H_2 + \gamma \rightarrow C_4 + H_2$	5.3126	0.0	0.0	0.0	1085
$C_4H_2 + \gamma \rightarrow C_4H + H$	27.5828	0.0	0.0	6.0400	1081
$CH + \gamma \rightarrow C + H$	9200.0000	0.0	0.0	2.1000	53
$CH + \gamma \rightarrow C(^1d) + H$	5.1200	0.0	0.0	11.2000	239
$CH_2 + \gamma \rightarrow CH + H$	20.0000	0.0	0.0	3.0000	1070
$CH_2C_2H_2 + \gamma \rightarrow C_3H_2 + H_2$	42.2922	0.0	0.0	9.9800	1069
$CH_2C_2H_2 + \gamma \rightarrow C_3H_3 + H$	52.8231	0.0	0.0	0.0	1068
$CH_3C_2H + \gamma \rightarrow C_3H_2 + H_2$	13.1348	0.0	0.0	7.3800	613
$CH_3C_2H + \gamma \rightarrow C_3H_3 + H$	14.8690	0.0	0.0	0.0	1076
$CH_3CN + \gamma \rightarrow CH_3 + CN$	50.0000	0.0	0.0	0.7500	1067
$CH_3OH + \gamma \rightarrow CH_3 + OH$	0.5580	0.0	0.0	0.3900	1066
$CH_3OH + \gamma \rightarrow H_2CO + H_2$	10.2000	0.0	0.0	2.0700	1065
$CH_4 + \gamma \rightarrow CH + H_2 + H$	0.6390	0.0	0.0	19.1000	1086
$CH_4 + \gamma \rightarrow CH_2 + H + H$	2.1400	0.0	0.0	7.9000	1064
$CH_4 + \gamma \rightarrow CH_2 + H_2$	3.9600	0.0	0.0	3.0000	1150
$CH_4 + \gamma \rightarrow CH_3 + H$	0.2640	0.0	0.0	9.8000	1110
$CN + \gamma \rightarrow C + N$	3.1700	0.0	0.0	0.0	1109
$CO + \gamma \rightarrow C + O$	0.2810	0.0	0.0	2.5600	1158
$CO + \gamma \rightarrow C(^1d) + O(^1d)$	0.0346	0.0	0.0	0.0	1157
$CO(^3p) + \gamma \rightarrow C + O$	72.0000	0.0	0.0	3.6000	1108
$CO_2 + \gamma \rightarrow CO + O$	0.0171	0.0	0.0	2.1400	1107
$CO_2 + \gamma \rightarrow CO + O(^1d)$	0.9240	0.0	0.0	5.4500	1106
$CO_2 + \gamma \rightarrow CO(^3p) + O$	0.2820	0.0	0.0	0.0	1097
$CS_2 + \gamma \rightarrow CS + S$	2030.0000	0.0	0.0	7.4500	1096
$CS_2 + \gamma \rightarrow CS + S(^1d)$	892.0000	0.0	0.0	0.0	1098
$H_2 + \gamma \rightarrow H + H$	0.0480	0.0	0.0	0.0	1091
$H_2CO + \gamma \rightarrow CO + H + H$	32.0000	0.0	0.0	1.6900	1090
$H_2CO + \gamma \rightarrow CO(^1p) + H_2$	1.6300	0.0	0.0	6.3500	1165
$H_2CO + \gamma \rightarrow CO(^3d) + H_2$	1.6300	0.0	0.0	13.1000	1166
$H_2CO + \gamma \rightarrow CO(^3p) + H_2$	1.6300	0.0	0.0	15.9000	1164
$H_2CO + \gamma \rightarrow CO(^3s) + H_2$	1.6300	0.0	0.0	12.4000	1163
$H_2CO + \gamma \rightarrow H + HCO$	66.4000	0.0	0.0	12.0000	1161
$H_2CO + \gamma \rightarrow H_2 + CO$	116.0000	0.0	0.0	6.8600	1162
$H_2CO_2 + \gamma \rightarrow CO_2 + H_2$	316.0000	0.0	0.0	8.0100	1160
$H_2CO_2 + \gamma \rightarrow OH + HCO$	564.0000	0.0	0.0	19.6000	1159
$H_2CS + \gamma \rightarrow CS + H_2$	1.0E-05	0.0	0.0	0.0	1105
$H_2O + \gamma \rightarrow H + H + O$	0.7550	0.0	0.0	0.7000	1104
$H_2O + \gamma \rightarrow H + OH$	10.3000	0.0	0.0	3.4100	1103
$H_2O + \gamma \rightarrow O(^1d) + H_2$	0.5970	0.0	0.0	5.0600	1102
$H_2S + \gamma \rightarrow HS + H$	320.0000	0.0	0.0	4.9600	1101
$HC_3N + \gamma \rightarrow C_2H + CN$	6.2037	0.0	0.0	0.0	1100
$HC_3N + \gamma \rightarrow C_3N + H$	9.4354	0.0	0.0	0.0	1099
$HCN + \gamma \rightarrow CN + H$	12.6000	0.0	0.0	6.2100	1094
$HCO + \gamma \rightarrow CO + H$	40.0000	0.0	0.0	3.6200	1093
$HNC + \gamma \rightarrow CN + H$	20.0000	0.0	0.0	7.2600	1092
$HNCO + \gamma \rightarrow H + NCO$	13.8000	0.0	0.0	1.6700	1095
$HNCO + \gamma \rightarrow NH + CO$	14.9000	0.0	0.0	16.9000	1089
$N_2 + \gamma \rightarrow N + N$	0.6610	0.0	0.0	0.0	1088
$NH + \gamma \rightarrow N + H$	10.0000	0.0	0.0	6.3800	1087
$NH_2 + \gamma \rightarrow NH + H$	2.1500	0.0	0.0	1.7200	32
$NH_2CH_3 + \gamma \rightarrow NH_2 + CH_3$	30.0000	0.0	0.0	0.0	64
$NH_3 + \gamma \rightarrow NH + H + H$	1.9900	0.0	0.0	8.9600	27

Continued on next page

Table F.1 – *Continued from previous page*

Photodissociation	A	B	C	ΔE	#
$NH_3 + \gamma \rightarrow NH + H_2$	3.9500	0.0	0.0	1.5200	771
$NH_3 + \gamma \rightarrow NH_2 + H$	170.0000	0.0	0.0	0.0	316
$NO + \gamma \rightarrow N + O$	2.2000	0.0	0.0	2.0000	55
$O_2 + \gamma \rightarrow O + O$	0.1450	0.0	0.0	0.0	54
$O_2 + \gamma \rightarrow O + O(^1d)$	4.0500	0.0	0.0	0.8300	705
$O_2 + \gamma \rightarrow O(^1s) + O(^1s)$	0.0390	0.0	0.0	1.7200	1143
$OCS + \gamma \rightarrow CO + S$	15.3000	0.0	0.0	0.0	44
$OCS + \gamma \rightarrow CO + S(^1d)$	49.9000	0.0	0.0	0.0	1111
$OCS + \gamma \rightarrow CO + S(^1s)$	30.1000	0.0	0.0	0.0	65
$OCS + \gamma \rightarrow CS + O$	0.0692	0.0	0.0	0.0	10
$OCS + \gamma \rightarrow CS + O(^1d)$	6.3400	0.0	0.0	0.0	9
$OH + \gamma \rightarrow O + H$	6.5400	0.0	0.0	3.0700	63
$OH + \gamma \rightarrow O(^1d) + H$	0.6350	0.0	0.0	6.1400	62
$OH + \gamma \rightarrow O(^1s) + H$	0.0671	0.0	0.0	6.7800	31
$SO + \gamma \rightarrow S + O$	620.0000	0.0	0.0	27.0000	57
$SO_2 + \gamma \rightarrow S + O_2$	50.9000	0.0	0.0	0.0	22
$SO_2 + \gamma \rightarrow SO + O$	159.0000	0.0	0.0	0.0	4

F.2 Photoionization

Photoionization	A	B	C	ΔE	#
$C + \gamma \rightarrow C^+ + e^-$	0.4100	0.0	0.0	1.6900	393
$C(^1d) + \gamma \rightarrow C^+ + e^-$	3.5800	0.0	0.0	6.3800	394
$C_2 + \gamma \rightarrow C_2^+ + e^-$	0.9031	0.0	0.0	3.4100	34
$C_2H_2 + \gamma \rightarrow C_2H_2^+ + e^-$	0.9998	0.0	0.0	2.0700	67
$C_2H_3 + \gamma \rightarrow C_2H_3^+ + e^-$	5.4773	0.0	0.0	7.3800	450
$C_2H_4 + \gamma \rightarrow C_2H_4^+ + e^-$	0.5841	0.0	0.0	0.3900	68
$C_2H_5 + \gamma \rightarrow C_2H_5^+ + e^-$	2.1469	0.0	0.0	8.9600	405
$C_2H_6 + \gamma \rightarrow C_2H_6^+ + e^-$	0.2896	0.0	0.0	2.5600	45
$C_3H_3 + \gamma \rightarrow C_3H_3^+ + e^-$	10.3877	0.0	0.0	6.7800	538
$C_4H_2 + \gamma \rightarrow C_4H_2^+ + e^-$	0.8960	0.0	0.0	2.1400	90
$CH + \gamma \rightarrow CH^+ + e^-$	0.7580	0.0	0.0	1.5200	71
$CH_2 + \gamma \rightarrow CH_2^+ + e^-$	1.0000	0.0	0.0	4.9600	70
$CH_4 + \gamma \rightarrow CH_4^+ + e^-$	0.3580	0.0	0.0	7.4500	1167
$CO + \gamma \rightarrow CO^+ + e^-$	0.3800	0.0	0.0	0.0	69
$CO(^3p) + \gamma \rightarrow CO^+ + e^-$	8.5800	0.0	0.0	7.4100	35
$CO_2 + \gamma \rightarrow CO_2^+ + e^-$	0.6550	0.0	0.0	0.7000	401
$CS_2 + \gamma \rightarrow CS_2^+ + e^-$	0.5500	0.0	0.0	1.6700	36
$H + \gamma \rightarrow H^+ + e^-$	0.0731	0.0	0.0	1.7200	416
$H_2 + \gamma \rightarrow H_2^+ + e^-$	0.0541	0.0	0.0	1.8400	392
$H_2CO + \gamma \rightarrow H_2CO^+ + e^-$	0.4030	0.0	0.0	3.0000	399
$H_2CO_2 + \gamma \rightarrow H_2CO_2^+ + e^-$	0.9110	0.0	0.0	2.1000	407
$H_2O + \gamma \rightarrow H_2O^+ + e^-$	0.3310	0.0	0.0	3.6200	408
$H_2S + \gamma \rightarrow H_2S^+ + e^-$	0.5640	0.0	0.0	6.7600	404
$HCN + \gamma \rightarrow HCN^+ + e^-$	0.4510	0.0	0.0	12.0000	413
$N + \gamma \rightarrow N^+ + e^-$	0.1850	0.0	0.0	3.0300	50
$N_2 + \gamma \rightarrow N_2^+ + e^-$	0.3520	0.0	0.0	3.1600	395
$NH_3 + \gamma \rightarrow NH_3^+ + e^-$	0.6100	0.0	0.0	3.0000	402
$NO + \gamma \rightarrow NO^+ + e^-$	1.2800	0.0	0.0	3.0000	406
$O + \gamma \rightarrow O^+ + e^-$	0.2120	0.0	0.0	0.0	403
$O(^1d) + \gamma \rightarrow O^+ + e^-$	0.1820	0.0	0.0	6.2100	396
$O(^1s) + \gamma \rightarrow O^+ + e^-$	0.1960	0.0	0.0	0.0	397
$O_2 + \gamma \rightarrow O_2^+ + e^-$	0.4640	0.0	0.0	3.8200	398
$OCS + \gamma \rightarrow OCS^+ + e^-$	0.2370	0.0	0.0	14.0000	400
$OH + \gamma \rightarrow OH^+ + e^-$	0.2470	0.0	0.0	6.8600	414
$S + \gamma \rightarrow S^+ + e^-$	1.0700	0.0	0.0	3.0700	49
$S(^1d) + \gamma \rightarrow S^+ + e^-$	1.0800	0.0	0.0	0.4500	409
$S(^1s) + \gamma \rightarrow S^+ + e^-$	1.0500	0.0	0.0	5.2900	411
$SO + \gamma \rightarrow SO^+ + e^-$	0.8700	0.0	0.0	1.2700	410
$SO_2 + \gamma \rightarrow SO_2^+ + e^-$	1.0600	0.0	0.0	16.9000	412

F.3 Photodissociative Ionization (2 Product Species)

Photodissociative Ionization (2 Product Species)	A	B	C	ΔE	#
$C_2H_2 + \gamma \rightarrow C_2H^+ + H + e^-$	0.0980	0.0	0.0	2.5600	72
$C_2H_4 + \gamma \rightarrow C_2H_2^+ + H_2 + e^-$	0.1810	0.0	0.0	12.0000	74
$C_2H_4 + \gamma \rightarrow C_2H_3^+ + H + e^-$	0.2158	0.0	0.0	6.8600	73
$C_2H_6 + \gamma \rightarrow C_2H_4^+ + H_2 + e^-$	0.6547	0.0	0.0	6.1400	1083
$C_2H_6 + \gamma \rightarrow C_2H_5^+ + H + e^-$	0.1417	0.0	0.0	6.7800	1082
$C_2H_6 + \gamma \rightarrow CH_3^+ + CH_3 + e^-$	0.0226	0.0	0.0	0.0	1084
$C_4H_2 + \gamma \rightarrow C_4H^+ + H + e^-$	0.2755	0.0	0.0	5.1000	1112
$CH_4 + \gamma \rightarrow CH_2^+ + H_2 + e^-$	0.0208	0.0	0.0	0.3900	1170
$CH_4 + \gamma \rightarrow CH_3^+ + H + e^-$	0.1980	0.0	0.0	2.0700	1169
$CH_4 + \gamma \rightarrow H^+ + CH_3 + e^-$	0.0091	0.0	0.0	7.4500	1168
$CO + \gamma \rightarrow C^+ + O + e^-$	0.0294	0.0	0.0	1.7200	76
$CO + \gamma \rightarrow O^+ + C + e^-$	0.0242	0.0	0.0	1.6900	75
$CO(^3p) + \gamma \rightarrow C^+ + O + e^-$	0.0240	0.0	0.0	6.3800	78
$CO(^3p) + \gamma \rightarrow O^+ + C + e^-$	0.0210	0.0	0.0	3.0300	354
$CO_2 + \gamma \rightarrow C^+ + O_2 + e^-$	0.0289	0.0	0.0	0.7000	355
$CO_2 + \gamma \rightarrow CO^+ + O + e^-$	0.0502	0.0	0.0	7.4100	356
$CO_2 + \gamma \rightarrow O^+ + CO + e^-$	0.0638	0.0	0.0	3.1600	357
$CS_2 + \gamma \rightarrow C^+ + S_2 + e^-$	0.0012	0.0	0.0	7.3800	46
$CS_2 + \gamma \rightarrow CS^+ + S + e^-$	0.0077	0.0	0.0	16.9000	363
$CS_2 + \gamma \rightarrow S^+ + CS + e^-$	0.0119	0.0	0.0	14.0000	364
$CS_2 + \gamma \rightarrow S_2^+ + C + e^-$	0.0003	0.0	0.0	1.6700	382
$H_2 + \gamma \rightarrow H^+ + H + e^-$	0.0095	0.0	0.0	4.9600	380
$H_2CO + \gamma \rightarrow CHO^+ + H + e^-$	0.1960	0.0	0.0	3.0000	379
$H_2CO + \gamma \rightarrow CO^+ + H_2 + e^-$	0.1210	0.0	0.0	3.6200	381
$H_2CO_2 + \gamma \rightarrow CHO^+ + OH + e^-$	0.2820	0.0	0.0	2.1000	351
$H_2O + \gamma \rightarrow H^+ + OH + e^-$	0.0131	0.0	0.0	3.8200	366
$H_2O + \gamma \rightarrow O^+ + H_2 + e^-$	0.0058	0.0	0.0	1.8400	367
$H_2O + \gamma \rightarrow OH^+ + H + e^-$	0.0554	0.0	0.0	0.0	373
$H_2S + \gamma \rightarrow HS^+ + H + e^-$	0.0726	0.0	0.0	0.0	362
$H_2S + \gamma \rightarrow S^+ + H_2 + e^-$	0.1470	0.0	0.0	3.4100	361
$N_2 + \gamma \rightarrow N^+ + N + e^-$	0.0150	0.0	0.0	1.5200	360
$NH_3 + \gamma \rightarrow H^+ + NH_2 + e^-$	0.0033	0.0	0.0	3.0000	6
$NH_3 + \gamma \rightarrow NH^+ + H_2 + e^-$	0.0069	0.0	0.0	3.0000	5
$NH_3 + \gamma \rightarrow NH_2^+ + H + e^-$	0.1770	0.0	0.0	8.9600	352
$NO + \gamma \rightarrow N^+ + O + e^-$	0.0318	0.0	0.0	6.2100	372
$NO + \gamma \rightarrow O^+ + N + e^-$	0.0018	0.0	0.0	0.0	370
$O_2 + \gamma \rightarrow O^+ + O + e^-$	0.1100	0.0	0.0	2.1400	369
$OCS + \gamma \rightarrow C^+ + SO + e^-$	0.0006	0.0	0.0	6.7600	359
$OCS + \gamma \rightarrow CO^+ + S + e^-$	0.0020	0.0	0.0	5.2900	358
$OCS + \gamma \rightarrow CS^+ + O + e^-$	0.0003	0.0	0.0	0.4500	353
$OCS + \gamma \rightarrow O^+ + CS + e^-$	0.0002	0.0	0.0	1.2700	378
$OCS + \gamma \rightarrow S^+ + CO + e^-$	0.0087	0.0	0.0	3.0700	375

F.4 Photodissociative Ionization (3 Product Species)

Photodissociative Ionization (3 Product Species)	A	B	C	ΔE	#
$CH_4 + \gamma \rightarrow CH^+ + H_2 + H + e^-$	0.0042	0.0	0.0	3.4100	77
$CO_2 + \gamma \rightarrow C^+ + O + O + e^-$	0.0289	0.0	0.0	0.0	365
$NH_3 + \gamma \rightarrow N^+ + H_2 + H + e^-$	0.0033	0.0	0.0	0.7000	371

F.5 Neutral-Neutral Rearrangement

Neutral-Neutral Rearrangement	A	B	C	ΔE	#
$C + CH_2C_2H_2 \rightarrow C_4H_2 + H_2$	0.0004	0.0	0.0	0.0	1142

Continued on next page

Table F.5 – *Continued from previous page*

Neutral-Neutral Rearrangement	A	B	C	ΔE	#
$C + CH_3C_2H \rightarrow C_4H_2 + H_2$	0.0004	0.0	0.0	12.0000	288
$C + NO \rightarrow CN + O$	6.0E-05	-0.1600	0.0	0.0	497
$C + O_2 \rightarrow CO + O$	3.3E-05	0.0	0.0	6.5200	496
$C + OH \rightarrow CO + H$	0.0001	0.0	0.0	5.1000	480
$C(^1d) + CH_4 \rightarrow C_2H_2 + H_2$	3.2E-05	0.0	0.0	2.0700	289
$C(^1d) + H_2 \rightarrow CH + H$	4.1E-05	0.0	0.0	6.3500	510
$C(^1d) + H_2O \rightarrow C + H_2O$	0.0002	0.0	0.0	1.8400	334
$C(^1d) + NO \rightarrow CN + O$	9.2E-05	0.0	0.0	15.9000	511
$C_2 + O \rightarrow CO + C$	3.0E-05	0.0	0.0	3.6000	503
$C_2H_3 + H \rightarrow C_2H_2 + H_2$	3.3E-05	0.0	0.0	0.0	284
$C_2H_3 + H_2 \rightarrow C_2H_4 + H$	5.0E-06	0.0	3200.0000	3.4100	283
$CH + C \rightarrow C_2 + H$	6.6E-05	0.0	0.0	1.7200	502
$CH + CH_4 \rightarrow C_2H_4 + H$	0.0001	-1.0400	36.0000	6.8600	287
$CH + H \rightarrow C + H + H$	0.0060	0.0	4.0E+04	7.4100	418
$CH + H \rightarrow C + H_2$	0.0001	0.0	80.0000	1.0000	505
$CH + H_2 \rightarrow C + H + H_2$	0.0060	0.0	4.0E+04	1.2700	429
$CH + N \rightarrow CN + H$	0.0002	-0.0900	0.0	0.0	491
$CH + O \rightarrow CO + H$	4.0E-05	0.0	0.0	0.8300	501
$CH + S \rightarrow CS + H$	5.0E-05	0.0	0.0	12.4000	513
$CH_2 + CH_2 \rightarrow C_2H_2 + H_2$	0.0026	0.0	6013.0000	0.7000	285
$CH_2 + CH_3 \rightarrow C_2H_4 + H$	5.0E-05	0.0	0.0	2.5600	286
$CH_2 + N \rightarrow HCN + H$	3.9E-05	0.1700	0.0	0.3900	290
$CH_3 + S \rightarrow H_2CS + H$	0.0001	0.0	0.0	0.0	520
$CH_4 + H \rightarrow CH_3 + H + H$	0.3300	0.0	4.4E+04	1.5200	295
$CH_4 + H_2 \rightarrow CH_3 + H + H_2$	0.3300	0.0	4.4E+04	4.9600	294
$CN + O_2 \rightarrow NCO + O$	1.9E-05	-0.1300	-40.0000	2.0000	504
$CO + H \rightarrow C + O + H$	0.0060	0.0	1.3E+05	3.1600	419
$CO + H_2 \rightarrow C + O + H_2$	0.0060	0.0	1.3E+05	6.7600	430
$CO + OH \rightarrow CO_2 + H$	2.8E-07	0.0	176.0000	0.0	500
$CO(^3p) + H_2O \rightarrow CO + H_2O$	0.0002	0.0	0.0	0.0	333
$CS + O \rightarrow CO + S$	0.0002	-0.6500	783.0000	27.0000	517
$H_2 + H \rightarrow H + H + H$	0.4670	-1.0000	5.5E+04	3.0000	423
$H_2CO + H \rightarrow HCO + H + H$	0.6000	0.0	4.4E+04	5.2900	427
$H_2CO + H_2 \rightarrow HCO + H + H_2$	0.0060	0.0	4.4E+04	0.0	437
$H_2O + H \rightarrow OH + H + H$	0.0058	0.0	5.3E+04	3.0000	424
$H_2O + H_2 \rightarrow OH + H + H_2$	0.0058	0.0	5.3E+04	7.3800	434
$HCO + H \rightarrow CO + H + H$	0.0010	0.0	8350.0000	2.1000	425
$HCO + H \rightarrow CO + H_2$	0.0002	0.0	0.0	7.9000	487
$HCO + H_2 \rightarrow CO + H + H_2$	0.0010	0.0	8350.0000	6.7800	435
$HS + N \rightarrow NS + H$	0.0001	0.0	0.0	27.8000	516
$HS + O \rightarrow SO + H$	8.3E-05	0.1700	-254.0000	19.6000	515
$N + NH \rightarrow N_2 + H$	5.0E-05	0.0	0.0	11.2000	489
$N + OH \rightarrow NO + H$	5.8E-05	0.0	0.0	0.0	498
$N_2 + H \rightarrow N + N + H$	6700.0000	-1.6000	1.1E+05	3.6200	421
$N_2 + H_2 \rightarrow N + N + H_2$	6700.0000	-1.6000	1.1E+05	16.9000	432
$NH + C \rightarrow CN + H$	0.0001	0.5000	0.0	0.7500	490
$NH + O \rightarrow NO + H$	0.0001	0.0	0.0	0.0	492
$NH_2 + O \rightarrow HNO + H$	4.6E-05	0.0	-10.0000	0.0	494
$NH_2 + O \rightarrow OH + NH$	1.4E-05	0.0	40.0000	0.0	493
$NH_3 + H \rightarrow NH_2 + H + H$	0.0150	0.0	4.2E+04	3.0700	426
$NH_3 + H_2 \rightarrow NH_2 + H + H_2$	0.0150	0.0	4.2E+04	6.1400	436
$NO + H \rightarrow N + O + H$	670.0000	-1.5000	7.6E+04	3.0000	420
$NO + H_2 \rightarrow N + O + H_2$	670.0000	-1.5000	7.6E+04	14.0000	431
$NO + N \rightarrow N_2 + O$	3.8E-05	0.0	26.0000	0.0	495
$O + CH_2 \rightarrow CH + OH$	0.0005	0.0	6000.0000	0.0	482
$O + CH_2 \rightarrow HCO + H$	5.0E-05	0.0	0.0	9.9800	483
$O + CH_3 \rightarrow H_2CO + H$	0.0001	0.0	0.0	4.0500	481
$O + HCO \rightarrow CO + OH$	5.0E-05	0.0	0.0	30.2000	485
$O + HCO \rightarrow CO_2 + H$	5.0E-05	0.0	0.0	9.8000	486
$O + OH \rightarrow H + O_2$	4.1E-05	0.0	0.0	19.1000	488
$O(^1d) + CH_4 \rightarrow CH_3 + OH$	0.0001	0.0	0.0	7.4500	291
$O(^1d) + CH_4 \rightarrow H_2CO + H_2$	0.0001	0.0	0.0	7.2600	507
$O(^1d) + CO \rightarrow CO + O$	0.0005	0.0	625.0000	1.7200	327
$O(^1d) + CO_2 \rightarrow CO_2 + O$	0.0001	0.0	0.0	2.1400	326
$O(^1d) + H_2 \rightarrow OH + H$	0.0001	0.0	0.0	0.0	509
$O(^1d) + H_2O \rightarrow OH + OH$	0.0002	0.0	0.0	5.4500	508
$O(^1d) + N_2 \rightarrow N_2 + O$	2.3E-05	0.0	0.0	1.6900	328
$O(^1d) + NH_3 \rightarrow NH_2 + OH$	0.0003	0.0	0.0	5.0600	506
$O(^1d) + O_2 \rightarrow O_2 + O$	5.3E-05	0.0	0.0	6.3800	329
$O(^1s) + N_2 \rightarrow N_2 + O$	1.0E-11	0.0	0.0	0.0	331
$O(^1s) + O \rightarrow O + O$	2.0E-08	0.0	0.0	6.2100	332

Continued on next page

Table F.5 – *Continued from previous page*

Neutral-Neutral Rearrangement	A	B	C	ΔE	#
$O(^1s) + O_2 \rightarrow O_2 + O$	4.9E-06	0.0	870.9000	3.0300	330
$O_2 + H \rightarrow O + O + H$	0.0060	0.0	5.2E+04	3.8200	417
$O_2 + H_2 \rightarrow O + O + H_2$	0.0060	0.0	5.2E+04	0.4500	428
$OH + H \rightarrow O + H + H$	0.0060	0.0	5.1E+04	8.9600	422
$OH + H_2 \rightarrow O + H + H_2$	0.0060	0.0	5.1E+04	1.6700	433
$OH + OH \rightarrow O + H_2O$	1.6E-06	1.1400	50.0000	0.0	499
$OH + S \rightarrow SO + H$	6.6E-05	0.0	0.0	8.0100	514
$S + O_2 \rightarrow SO + O$	4.7E-07	1.4100	-439.0000	13.1000	512
$SO + C \rightarrow CO + S$	3.5E-05	0.0	0.0	0.0	521
$SO + C \rightarrow CS + O$	3.5E-05	0.0	0.0	0.0	522
$SO + N \rightarrow NO + S$	1.7E-05	0.5000	750.0000	0.0	518
$SO + OH \rightarrow SO_2 + H$	8.6E-05	0.5000	0.0	0.0	519

F.6 Neutral-Ion Rearrangement (2 Product Species)

Neutral-Ion Rearrangement (2 Product Species)	A	B	C	ΔE	#
$C^+ + C_2H \rightarrow C_3^+ + H$	0.0010	0.0	0.0	0.0	213
$C^+ + CH \rightarrow C_2^+ + H$	0.0004	0.0	0.0	0.0	743
$C^+ + CH \rightarrow CH^+ + C$	0.0004	0.0	0.0	5.2900	130
$C^+ + CH_2 \rightarrow C_2H^+ + H$	0.0005	0.0	0.0	0.0	211
$C^+ + CH_2C_2H_2 \rightarrow C_2H_2^+ + C_2H_2$	0.0002	0.0	0.0	0.0	1134
$C^+ + CH_2C_2H_2 \rightarrow C_2H_3^+ + C_2H$	0.0002	0.0	0.0	0.0	1136
$C^+ + CH_2C_2H_2 \rightarrow C_3H_3^+ + CH$	0.0004	0.0	0.0	0.0	1135
$C^+ + CH_2C_2H_2 \rightarrow C_3H_4^+ + C$	0.0006	0.0	0.0	3.0000	1118
$C^+ + CH_2C_2H_2 \rightarrow C_4H_2^+ + H_2$	0.0006	0.0	0.0	0.0	1137
$C^+ + CH_3 \rightarrow C_2H_2^+ + H$	0.0013	0.0	0.0	0.0	212
$C^+ + CH_3C_2H \rightarrow C_2H_2^+ + C_2H_2$	0.0002	0.0	0.0	0.0	205
$C^+ + CH_3C_2H \rightarrow C_2H_3^+ + C_2H$	0.0002	0.0	0.0	0.0	207
$C^+ + CH_3C_2H \rightarrow C_3H_3^+ + CH$	0.0004	0.0	0.0	0.0	206
$C^+ + CH_3C_2H \rightarrow C_3H_4^+ + C$	0.0006	0.0	0.0	8.9600	124
$C^+ + CH_3C_2H \rightarrow C_4H_2^+ + H_2$	0.0006	0.0	0.0	0.0	208
$C^+ + CH_4 \rightarrow C_2H_2^+ + H_2$	0.0004	0.0	0.0	0.0	210
$C^+ + CH_4 \rightarrow C_2H_3^+ + H$	0.0011	0.0	0.0	0.0	209
$C^+ + CO_2 \rightarrow CO^+ + CO$	0.0011	0.0	0.0	2.2900	734
$C^+ + CS \rightarrow CS^+ + C$	0.0016	0.0	0.0	0.0	678
$C^+ + H_2CO \rightarrow CH_2^+ + CO$	0.0023	0.0	0.0	3.0000	744
$C^+ + H_2CO \rightarrow CHO^+ + CH$	0.0009	0.0	0.0	4.3400	745
$C^+ + H_2CO \rightarrow H_2CO^+ + C$	0.0008	0.0	0.0	0.0	604
$C^+ + H_2CS \rightarrow CH_2^+ + CS$	0.0015	0.0	0.0	-6.5000	922
$C^+ + H_2O \rightarrow CHO^+ + H$	0.0018	0.0	0.0	8.2300	733
$C^+ + H_2S \rightarrow H_2S^+ + C$	0.0006	0.0	0.0	0.0	681
$C^+ + H_2S \rightarrow HCS^+ + H$	0.0014	0.0	0.0	-4.5000	924
$C^+ + HCN \rightarrow C_2N^+ + H$	0.0032	0.0	0.0	2.1000	748
$C^+ + HS \rightarrow CS^+ + H$	0.0011	0.0	0.0	-11.4600	915
$C^+ + NH \rightarrow CN^+ + H$	0.0008	0.0	0.0	0.7400	738
$C^+ + NH \rightarrow H^+ + CN$	0.0010	0.0	0.0	1.3300	737
$C^+ + NH_2 \rightarrow H^+ + HCN$	0.0010	0.0	0.0	2.2000	739
$C^+ + NH_2 \rightarrow HCN^+ + H$	0.0011	0.0	0.0	1.8400	740
$C^+ + NH_3 \rightarrow H_2CN^+ + H$	0.0011	0.0	0.0	4.3900	736
$C^+ + NH_3 \rightarrow HCN^+ + H_2$	7.0E-05	0.0	0.0	3.3800	735
$C^+ + NH_3 \rightarrow NH_3^+ + C$	0.0051	0.0	0.0	0.0	624
$C^+ + NO \rightarrow NO^+ + C$	0.0005	0.0	0.0	0.0	596
$C^+ + NS \rightarrow CS^+ + N$	0.0008	0.0	0.0	-4.8000	923
$C^+ + NS \rightarrow NS^+ + C$	0.0008	0.0	0.0	0.0	680
$C^+ + O_2 \rightarrow CO^+ + O$	0.0004	0.0	0.0	1.9900	746
$C^+ + O_2 \rightarrow O^+ + CO$	0.0006	0.0	0.0	2.1000	747
$C^+ + OCS \rightarrow CO^+ + CS$	0.0009	0.0	0.0	-5.5400	919
$C^+ + OCS \rightarrow CS^+ + CO$	0.0016	0.0	0.0	-3.7000	920
$C^+ + OH \rightarrow CO^+ + H$	0.0008	0.0	0.0	0.0	741
$C^+ + OH \rightarrow H^+ + CO$	0.0010	0.0	0.0	3.8400	742
$C^+ + S \rightarrow S^+ + C$	0.0015	0.0	0.0	0.0	677

Continued on next page

Table F.6 – *Continued from previous page*

Neutral-Ion Rearrangement (2 Product Species)	A	B	C	ΔE	#
$C^+ + SO \rightarrow CO^+ + S$	0.0003	0.0	0.0	-4.4300	918
$C^+ + SO \rightarrow CS^+ + O$	0.0003	0.0	0.0	-5.1100	917
$C^+ + SO \rightarrow S^+ + CO$	0.0003	0.0	0.0	-7.0000	916
$C^+ + SO \rightarrow SO^+ + C$	0.0003	0.0	0.0	0.0	679
$C^+ + SO_2 \rightarrow SO^+ + CO$	0.0023	0.0	0.0	-4.5000	921
$C_2^+ + CH_4 \rightarrow C_2H^+ + CH_3$	0.0002	0.0	0.0	3.0000	200
$C_2^+ + CH_4 \rightarrow C_2H_2^+ + CH_2$	1.8200	0.0	0.0	0.0	203
$C_2^+ + CH_4 \rightarrow C_3H_2^+ + H_2$	0.0006	0.0	0.0	3.7400	199
$C_2^+ + CH_4 \rightarrow C_3H_3^+ + H$	0.0002	0.0	0.0	7.1500	201
$C_2^+ + H_2 \rightarrow C_2H^+ + H$	0.0011	0.0	0.0	0.0	204
$C_2^+ + S \rightarrow CS^+ + C$	0.0006	0.0	0.0	0.0	937
$C_2^+ + S \rightarrow S^+ + C_2$	0.0006	0.0	0.0	0.0	687
$C_2H^+ + CH_4 \rightarrow C_2H_2^+ + CH_3$	0.0004	0.0	0.0	6.0400	192
$C_2H^+ + CH_4 \rightarrow C_3H_3^+ + H_2$	0.0004	0.0	0.0	4.0000	193
$C_2H^+ + CH_4 \rightarrow C_3H_4^+ + H$	0.0001	0.0	0.0	0.0	194
$C_2H^+ + H_2 \rightarrow C_2H_2^+ + H$	0.0011	0.0	0.0	7.9000	198
$C_2H^+ + H_2CO \rightarrow CH_2OH^+ + C_2$	0.0010	0.0	0.0	1.0000	196
$C_2H^+ + HCN \rightarrow H_2CN^+ + C_2$	0.0010	0.0	0.0	8.6400	197
$C_2H^+ + NH_3 \rightarrow NH_4^+ + C_2$	0.0005	0.0	0.0	3.0000	195
$C_2H^+ + S \rightarrow S^+ + C_2H$	0.0012	0.0	0.0	6.3800	111
$C_2H_2^+ + C_2H_2 \rightarrow C_4H_2^+ + H_2$	0.0005	0.0	0.0	0.0	179
$C_2H_2^+ + C_2H_2 \rightarrow C_4H_3^+ + H$	0.0009	0.0	0.0	0.0	180
$C_2H_2^+ + C_2H_4 \rightarrow C_2H_4^+ + C_2H_2$	0.0004	0.0	0.0	4.9600	106
$C_2H_2^+ + C_2H_4 \rightarrow C_3H_3^+ + CH_3$	0.0005	0.0	0.0	0.0	187
$C_2H_2^+ + C_2H_4 \rightarrow C_4H_5^+ + H$	0.0003	0.0	0.0	10.2300	188
$C_2H_2^+ + C_2H_6 \rightarrow C_2H_4^+ + C_2H_4$	0.0003	0.0	0.0	0.0	181
$C_2H_2^+ + C_2H_6 \rightarrow C_2H_5^+ + C_2H_3$	0.0001	0.0	0.0	0.0	182
$C_2H_2^+ + C_2H_6 \rightarrow C_3H_5^+ + CH_3$	0.0008	0.0	0.0	0.0	184
$C_2H_2^+ + C_2H_6 \rightarrow C_4H_7^+ + H$	0.0001	0.0	0.0	0.0	186
$C_2H_2^+ + CH_2C_2H_2 \rightarrow C_3H_4^+ + C_2H_2$	0.0005	0.0	0.0	6.2000	1116
$C_2H_2^+ + CH_2C_2H_2 \rightarrow C_5H_4^+ + H_2$	0.0005	0.0	0.0	0.0	1132
$C_2H_2^+ + CH_2C_2H_2 \rightarrow C_5H_5^+ + H$	0.0005	0.0	0.0	0.0	1133
$C_2H_2^+ + CH_3C_2H \rightarrow C_3H_4^+ + C_2H_2$	0.0005	0.0	0.0	1.5200	107
$C_2H_2^+ + CH_3C_2H \rightarrow C_5H_4^+ + H_2$	0.0005	0.0	0.0	27.0000	177
$C_2H_2^+ + CH_3C_2H \rightarrow C_5H_5^+ + H$	0.0005	0.0	0.0	0.0	178
$C_2H_2^+ + CH_4 \rightarrow C_3H_4^+ + H_2$	0.0002	0.0	0.0	8.7900	190
$C_2H_2^+ + CH_4 \rightarrow C_3H_5^+ + H$	0.0007	0.0	0.0	0.0	191
$C_2H_2^+ + H_2CO \rightarrow C_2H_4^+ + CO$	0.0003	0.0	0.0	17.8000	844
$C_2H_2^+ + H_2CO \rightarrow C_3H_3O^+ + H$	6.5E-05	0.0	0.0	2.2000	843
$C_2H_2^+ + H_2CO \rightarrow CH_2OH^+ + C_2H$	0.0004	0.0	0.0	15.9000	842
$C_2H_2^+ + H_2CO \rightarrow H_2CO^+ + C_2H_2$	0.0009	0.0	0.0	1.7200	109
$C_2H_2^+ + H_2CO \rightarrow HCO^+ + C_2H_3$	0.0005	0.0	0.0	10.0000	189
$C_2H_2^+ + H_2O \rightarrow H_3O^+ + C_2H$	0.0002	0.0	0.0	18.9000	840
$C_2H_2^+ + H_2S \rightarrow C_2H_3^+ + HS$	4.6E-05	0.0	0.0	6.9400	1006
$C_2H_2^+ + H_2S \rightarrow H_2S^+ + C_2H_2$	0.0022	0.0	0.0	1.6900	110
$C_2H_2^+ + H_2S \rightarrow H_3S^+ + C_2H$	4.6E-05	0.0	0.0	4.0000	1007
$C_2H_2^+ + HCN \rightarrow C_3H_2N^+ + H$	3.1E-05	0.0	0.0	12.4000	846
$C_2H_2^+ + HCN \rightarrow H_2CN^+ + C_2H$	2.2E-05	0.0	0.0	8.2300	845
$C_2H_2^+ + NH_3 \rightarrow NH_3^+ + C_2H_2$	0.0021	0.0	0.0	2.1400	108
$C_2H_2^+ + NH_3 \rightarrow NH_4^+ + C_2H$	0.0010	0.0	0.0	6.5600	841
$C_2H_3^+ + C_2H_2 \rightarrow C_4H_3^+ + H_2$	0.0007	0.0	0.0	6.3500	170
$C_2H_3^+ + C_2H_4 \rightarrow C_2H_5^+ + C_2H_2$	0.0009	0.0	0.0	0.0	169
$C_2H_3^+ + C_2H_6 \rightarrow C_2H_5^+ + C_2H_4$	0.0003	0.0	0.0	5.0600	166
$C_2H_3^+ + C_2H_6 \rightarrow C_3H_5^+ + CH_4$	0.0002	0.0	0.0	7.2600	167
$C_2H_3^+ + C_2H_6 \rightarrow C_4H_7^+ + H_2$	8.1E-05	0.0	0.0	5.4500	168
$C_2H_3^+ + CH_2C_2H_2 \rightarrow C_3H_5^+ + C_2H_2$	0.0005	0.0	0.0	0.0	1130
$C_2H_3^+ + CH_2C_2H_2 \rightarrow C_5H_5^+ + H_2$	0.0005	0.0	0.0	0.0	1131
$C_2H_3^+ + CH_3C_2H \rightarrow C_3H_5^+ + C_2H_2$	0.0005	0.0	0.0	2.0000	164
$C_2H_3^+ + CH_3C_2H \rightarrow C_5H_5^+ + H_2$	0.0005	0.0	0.0	1.0000	165
$C_2H_3^+ + CH_4 \rightarrow C_3H_5^+ + H_2$	0.0002	0.0	0.0	27.8000	176
$C_2H_3^+ + H_2CO \rightarrow CH_2OH^+ + C_2H_2$	0.0010	0.0	0.0	12.4000	173
$C_2H_3^+ + H_2O \rightarrow H_3O^+ + C_2H_2$	0.0011	0.0	0.0	15.9000	171

Continued on next page

Table F.6 – *Continued from previous page*

Neutral-Ion Rearrangement (2 Product Species)	A	B	C	ΔE	#
$C_2H_3^+ + H_2S \rightarrow H_3S^+ + C_2H_2$	0.0008	0.0	0.0	19.6000	175
$C_2H_3^+ + HCN \rightarrow H_2CN^+ + C_2H_2$	0.0010	0.0	0.0	8.0100	174
$C_2H_3^+ + NH_3 \rightarrow NH_4^+ + C_2H_2$	0.0025	0.0	0.0	13.1000	172
$C_2H_4^+ + C_2H_2 \rightarrow C_3H_3^+ + CH_3$	0.0006	0.0	0.0	0.8300	161
$C_2H_4^+ + C_2H_2 \rightarrow C_4H_5^+ + H$	0.0002	0.0	0.0	1.7200	162
$C_2H_4^+ + C_2H_4 \rightarrow C_3H_5^+ + CH_3$	0.0007	0.0	0.0	0.0	159
$C_2H_4^+ + C_2H_4 \rightarrow C_4H_7^+ + H$	7.9E-05	0.0	0.0	0.0	160
$C_2H_4^+ + CH_2C_2H_2 \rightarrow C_4H_5^+ + CH_3$	0.0008	0.0	0.0	0.0	1129
$C_2H_4^+ + CH_3 \rightarrow CH_3^+ + C_2H_4$	0.0010	0.0	0.0	7.4500	105
$C_2H_4^+ + CH_3C_2H \rightarrow C_4H_5^+ + CH_3$	0.0008	0.0	0.0	0.0	158
$C_2H_4^+ + H \rightarrow C_2H_3^+ + H_2$	0.0003	0.0	0.0	0.0	847
$C_2H_4^+ + NH_3 \rightarrow NH_3^+ + C_2H_4$	0.0018	0.0	0.0	0.3900	104
$C_2H_4^+ + NH_3 \rightarrow NH_4^+ + C_2H_3$	0.0019	0.0	0.0	3.6000	163
$C_2H_5^+ + C_2H_2 \rightarrow C_3H_3^+ + CH_4$	6.8E-05	0.0	0.0	0.7500	150
$C_2H_5^+ + C_2H_2 \rightarrow C_4H_5^+ + H_2$	0.0001	0.0	0.0	0.0	151
$C_2H_5^+ + C_2H_4 \rightarrow C_3H_5^+ + CH_4$	0.0004	0.0	0.0	0.0	152
$C_2H_5^+ + CH_3 \rightarrow C_2H_4^+ + CH_4$	0.0005	0.0	0.0	0.0	157
$C_2H_5^+ + H_2CO \rightarrow CH_2OH^+ + C_2H_4$	0.0010	0.0	0.0	0.0	155
$C_2H_5^+ + H_2O \rightarrow H_3O^+ + C_2H_4$	0.0014	0.0	0.0	0.0	153
$C_2H_5^+ + HCN \rightarrow H_2CN^+ + C_2H_4$	0.0010	0.0	0.0	6.5200	156
$C_2H_5^+ + NH_3 \rightarrow NH_4^+ + C_2H_4$	0.0021	0.0	0.0	0.0	154
$C_2H_6^+ + C_2H_2 \rightarrow C_2H_5^+ + C_2H_3$	0.0002	0.0	0.0	30.2000	145
$C_2H_6^+ + C_2H_2 \rightarrow C_3H_5^+ + CH_3$	0.0008	0.0	0.0	0.0	143
$C_2H_6^+ + C_2H_2 \rightarrow C_4H_7^+ + H$	0.0001	0.0	0.0	9.9800	144
$C_2H_6^+ + C_2H_4 \rightarrow C_2H_4^+ + C_2H_6$	0.0012	0.0	0.0	6.8600	101
$C_2H_6^+ + C_2H_6 \rightarrow C_3H_8^+ + CH_4$	8.0E-06	0.0	0.0	4.0500	142
$C_2H_6^+ + CH_3 \rightarrow CH_3^+ + C_2H_6$	0.0010	0.0	0.0	2.0700	103
$C_2H_6^+ + H \rightarrow C_2H_5^+ + H_2$	0.0001	0.0	0.0	5.7700	848
$C_2H_6^+ + H_2CO \rightarrow CH_2OH^+ + C_2H_5$	0.0010	0.0	0.0	19.1000	148
$C_2H_6^+ + H_2O \rightarrow H_3O^+ + C_2H_5$	0.0030	0.0	0.0	9.8000	146
$C_2H_6^+ + HCN \rightarrow H_2CN^+ + C_2H_5$	0.0010	0.0	0.0	11.2000	149
$C_2H_6^+ + NH_3 \rightarrow NH_3^+ + C_2H_6$	0.0006	0.0	0.0	12.0000	102
$C_2H_6^+ + NH_3 \rightarrow NH_4^+ + C_2H_5$	0.0016	0.0	0.0	7.9000	147
$C_3^+ + H_2 \rightarrow C_3H^+ + H$	0.0002	0.0	0.0	5.1000	141
$C_3H_2^+ + CH_2C_2H_2 \rightarrow C_3H_3^+ + C_3H_3$	0.0003	0.0	0.0	3.0000	1127
$C_3H_2^+ + CH_2C_2H_2 \rightarrow C_6H_4^+ + H_2$	0.0003	0.0	0.0	6.0000	1128
$C_3H_2^+ + CH_3C_2H \rightarrow C_3H_3^+ + C_3H_3$	0.0003	0.0	0.0	6.1400	139
$C_3H_2^+ + CH_3C_2H \rightarrow C_6H_4^+ + H_2$	0.0003	0.0	0.0	0.0	140
$C_3H_3^+ + CH_2C_2H_2 \rightarrow C_6H_5^+ + H_2$	0.0010	0.0	0.0	7.0000	1126
$C_3H_3^+ + CH_3C_2H \rightarrow C_6H_5^+ + H_2$	0.0010	0.0	0.0	6.7800	138
$C_3H_4^+ + CH_2C_2H_2 \rightarrow C_6H_7^+ + H$	0.0008	0.0	0.0	5.0000	1120
$C_3H_4^+ + CH_3C_2H \rightarrow C_6H_7^+ + H$	0.0008	0.0	0.0	1.2700	132
$C_3H_5^+ + C_6H_6 \rightarrow C_6H_7^+ + CH_2C_2H_2$	0.0001	0.0	0.0	3.0000	1119
$C_3H_5^+ + C_6H_6 \rightarrow C_6H_7^+ + CH_3C_2H$	0.0001	0.0	0.0	0.4500	131
$C_4H^+ + CH_2C_2H_2 \rightarrow C_7H_4^+ + H$	0.0012	0.0	0.0	2.7600	1121
$C_4H^+ + CH_3C_2H \rightarrow C_7H_4^+ + H$	0.0012	0.0	0.0	6.7600	133
$C_4H_2^+ + CH_2C_2H_2 \rightarrow C_7H_4^+ + H_2$	0.0010	0.0	0.0	8.3400	1122
$C_4H_2^+ + CH_3C_2H \rightarrow C_7H_4^+ + H_2$	0.0010	0.0	0.0	14.0000	134
$C_4H_3^+ + CH_2C_2H_2 \rightarrow C_7H_5^+ + H_2$	0.0010	0.0	0.0	2.3300	1123
$C_4H_3^+ + CH_3C_2H \rightarrow C_7H_5^+ + H_2$	0.0010	0.0	0.0	16.9000	135
$C_5H_2^+ + CH_2C_2H_2 \rightarrow C_8H_4^+ + H_2$	0.0010	0.0	0.0	6.3700	1124
$C_5H_2^+ + CH_3C_2H \rightarrow C_8H_4^+ + H_2$	0.0010	0.0	0.0	1.6700	136
$C_6H_2^+ + CH_2C_2H_2 \rightarrow C9H_4^+ + H_2$	0.0011	0.0	0.0	1.0000	1125
$C_6H_2^+ + CH_3C_2H \rightarrow C9H_4^+ + H_2$	0.0011	0.0	0.0	7.3800	137
$CH^+ + C_2H_2 \rightarrow C_2H_3^+ + C$	0.0010	0.0	0.0	0.0	247
$CH^+ + C_2H_4 \rightarrow C_2H_5^+ + C$	0.0010	0.0	0.0	0.0	248
$CH^+ + CH_4 \rightarrow C_2H_3^+ + H_2$	0.0011	0.0	0.0	0.0	243
$CH^+ + CH_4 \rightarrow C_2H_4^+ + H$	6.5E-05	0.0	0.0	0.0	242
$CH^+ + CO_2 \rightarrow HCO^+ + CO$	0.0016	0.0	0.0	0.0	238
$CH^+ + H_2 \rightarrow CH_2^+ + H$	0.0012	0.0	0.0	0.0	251
$CH^+ + H_2CO \rightarrow CH_2OH^+ + C$	0.0010	0.0	0.0	0.0	245
$CH^+ + H_2O \rightarrow H_2CO^+ + H$	0.0006	0.0	0.0	0.0	236

Continued on next page

Table F.6 – *Continued from previous page*

Neutral-Ion Rearrangement (2 Product Species)	A	B	C	ΔE	#
$CH^+ + H_2O \rightarrow H_3O^+ + C$	0.0006	0.0	0.0	0.0	237
$CH^+ + H_2O \rightarrow HCO^+ + H_2$	0.0029	0.0	0.0	0.0	235
$CH^+ + H_2S \rightarrow HCS^+ + H_2$	0.0015	0.0	0.0	0.0	941
$CH^+ + HCN \rightarrow H_2CN^+ + C$	0.0018	0.0	0.0	0.0	246
$CH^+ + HCO \rightarrow H_2CO^+ + C$	0.0010	0.0	0.0	0.0	249
$CH^+ + N \rightarrow CN^+ + H$	0.0002	0.0	0.0	2.1000	749
$CH^+ + NH_2 \rightarrow NH_3^+ + C$	0.0010	0.0	0.0	0.0	250
$CH^+ + NH_3 \rightarrow H_2CN^+ + H_2$	0.0018	0.0	0.0	0.0	240
$CH^+ + NH_3 \rightarrow NH_3^+ + CH$	0.0005	0.0	0.0	0.0	614
$CH^+ + NH_3 \rightarrow NH_4^+ + C$	0.0004	0.0	0.0	0.0	241
$CH^+ + O \rightarrow CO^+ + H$	0.0003	0.0	0.0	2.1000	750
$CH^+ + O_2 \rightarrow CHO^+ + O$	0.0010	0.0	0.0	4.7500	751
$CH^+ + O_2 \rightarrow CO^+ + OH$	1.0E-05	0.0	0.0	0.0	753
$CH^+ + O_2 \rightarrow O^+ + HCO$	1.0E-05	0.0	0.0	1.7600	752
$CH^+ + S \rightarrow CS^+ + H$	0.0005	0.0	0.0	0.0	940
$CH^+ + S \rightarrow HS^+ + C$	0.0005	0.0	0.0	0.0	939
$CH^+ + S \rightarrow S^+ + CH$	0.0005	0.0	0.0	0.0	691
$CH_2^+ + CH_4 \rightarrow C_2H_4^+ + H_2$	0.0008	0.0	0.0	0.0	232
$CH_2^+ + CH_4 \rightarrow C_2H_5^+ + H$	0.0004	0.0	0.0	0.0	231
$CH_2^+ + CO_2 \rightarrow H_2CO^+ + CO$	0.0016	0.0	0.0	2.7200	755
$CH_2^+ + H_2 \rightarrow CH_3^+ + H$	0.0016	0.0	0.0	0.1300	758
$CH_2^+ + H_2O \rightarrow CH_2OH^+ + H$	0.0012	0.0	0.0	0.6200	754
$CH_2^+ + H_2S \rightarrow H_3CS^+ + H$	0.0018	0.0	0.0	1.0000	971
$CH_2^+ + NH_3 \rightarrow CH_4N^+ + H$	0.0015	0.0	0.0	2.1300	757
$CH_2^+ + NH_3 \rightarrow NH_4^+ + CH$	0.0013	0.0	0.0	1.9600	756
$CH_2^+ + O \rightarrow CHO^+ + H$	0.0010	0.0	0.0	0.8500	759
$CH_2^+ + O_2 \rightarrow CHO^+ + OH$	0.0009	0.0	0.0	0.4400	760
$CH_2^+ + O_2 \rightarrow H_2CO^+ + O$	0.0002	0.0	0.0	0.5000	761
$CH_2^+ + S \rightarrow HCS^+ + H$	0.0014	0.0	0.0	4.0700	970
$CH_2OH^+ + CH \rightarrow CH_2^+ + H_2CO$	0.0010	0.0	0.0	-12.6000	892
$CH_2OH^+ + CH_2 \rightarrow CH_3^+ + H_2CO$	0.0010	0.0	0.0	-10.1600	893
$CH_2OH^+ + H_2O \rightarrow H_3O^+ + H_2CO$	0.0020	0.0	648.8000	-12.0600	889
$CH_2OH^+ + HCN \rightarrow H_2CN^+ + H_2CO$	0.0010	0.0	0.0	-13.7900	891
$CH_2OH^+ + NH_2 \rightarrow NH_3^+ + H_2CO$	0.0010	0.0	0.0	0.0	895
$CH_2OH^+ + NH_3 \rightarrow NH_4^+ + H_2CO$	0.0023	0.0	0.0	-14.0100	890
$CH_3^+ + C \rightarrow C_2H^+ + H_2$	0.0012	0.0	0.0	0.0	230
$CH_3^+ + C_2H_2 \rightarrow C_3H_3^+ + H_2$	0.0012	0.0	0.0	0.0	221
$CH_3^+ + C_2H_4 \rightarrow C_2H_3^+ + CH_4$	0.0003	0.0	0.0	2.6500	222
$CH_3^+ + C_2H_4 \rightarrow C_3H_5^+ + H_2$	0.0005	0.0	0.0	0.0	224
$CH_3^+ + C_2H_6 \rightarrow C_2H_5^+ + CH_4$	0.0015	0.0	0.0	0.0	225
$CH_3^+ + CH_4 \rightarrow C_2H_5^+ + H_2$	0.0012	0.0	0.0	0.0	227
$CH_3^+ + H_2CO \rightarrow HCO^+ + CH_4$	0.0016	0.0	0.0	0.0	229
$CH_3^+ + H_2S \rightarrow H_3CS^+ + H_2$	0.0013	0.0	0.0	1.0000	1005
$CH_3^+ + HS \rightarrow H_2CS^+ + H_2$	0.0010	0.0	0.0	8.0000	1003
$CH_3^+ + N \rightarrow H_2CN^+ + H$	3.4E-05	0.0	0.0	0.0	763
$CH_3^+ + N \rightarrow HCN^+ + H_2$	3.4E-05	0.0	0.0	0.0	764
$CH_3^+ + NH_3 \rightarrow CH_4N^+ + H_2$	0.0013	0.0	0.0	0.0	762
$CH_3^+ + NH_3 \rightarrow NH_4^+ + CH_2$	0.0003	0.0	0.0	0.0	228
$CH_3^+ + NO \rightarrow NO^+ + CH_3$	0.0010	0.0	0.0	0.0	615
$CH_3^+ + O \rightarrow CHO^+ + H_2$	0.0004	0.0	0.0	0.0	765
$CH_3^+ + O_2 \rightarrow CHO^+ + H_2O$	4.3E-05	0.0	0.0	0.0	766
$CH_3^+ + S \rightarrow HCS^+ + H_2$	0.0014	0.0	0.0	5.0000	1002
$CH_3^+ + SO \rightarrow HOCS^+ + H_2$	0.0010	0.0	0.0	5.8200	1004
$CH_4^+ + C_2H_2 \rightarrow C_2H_2^+ + CH_4$	0.0011	0.0	0.0	3.0300	112
$CH_4^+ + C_2H_2 \rightarrow C_2H_3^+ + CH_3$	0.0012	0.0	0.0	0.0	215
$CH_4^+ + C_2H_4 \rightarrow C_2H_4^+ + CH_4$	0.0014	0.0	0.0	0.0	113
$CH_4^+ + C_2H_4 \rightarrow C_2H_5^+ + CH_3$	0.0004	0.0	0.0	0.0	217
$CH_4^+ + CH_4 \rightarrow CH_5^+ + CH_3$	0.0015	0.0	0.0	0.0	220
$CH_4^+ + CO \rightarrow CH_3CO^+ + H$	7.0E-05	0.0	0.0	-6.0000	774
$CH_4^+ + CO \rightarrow CHO^+ + CH_3$	0.0007	0.0	0.0	-6.9000	775
$CH_4^+ + CO_2 \rightarrow CO_2H^+ + CH_3$	0.0012	0.0	0.0	0.0	768
$CH_4^+ + H_2 \rightarrow CH_5^+ + H$	4.1E-05	0.0	0.0	0.0	772

Continued on next page

Table F.6 – *Continued from previous page*

Neutral-Ion Rearrangement (2 Product Species)	A	B	C	ΔE	#
$CH_4^+ + H_2O \rightarrow H_3O^+ + CH_3$	0.0026	0.0	0.0	0.0	767
$CH_4^+ + H_2S \rightarrow CH_5^+ + HS$	9.0E-05	0.0	0.0	1.0000	1009
$CH_4^+ + H_2S \rightarrow H_2S^+ + CH_4$	0.0009	0.0	0.0	0.0	711
$CH_4^+ + H_2S \rightarrow H_3S^+ + CH_3$	0.0012	0.0	0.0	2.9000	1010
$CH_4^+ + NH_3 \rightarrow CH_5^+ + NH_2$	6.4E-05	0.0	0.0	0.0	769
$CH_4^+ + NH_3 \rightarrow NH_3^+ + CH_4$	0.0016	0.0	0.0	6.2100	114
$CH_4^+ + NH_3 \rightarrow NH_4^+ + CH_3$	0.0012	0.0	0.0	0.0	770
$CH_4^+ + O \rightarrow H_2CO^+ + H_2$	0.0010	0.0	0.0	-8.1000	773
$CH_4^+ + O_2 \rightarrow O_2^+ + CH_4$	0.0004	0.0	0.0	0.0	115
$CH_5^+ + CH_3 \rightarrow C_2H_6^+ + H_2$	0.0005	0.0	0.0	0.0	214
$CH_5^+ + CO \rightarrow CHO^+ + CH_4$	0.0010	0.0	0.0	0.0	778
$CH_5^+ + H_2O \rightarrow H_3O^+ + CH_4$	0.0037	0.0	0.0	-7.7000	776
$CH_5^+ + NH_3 \rightarrow NH_4^+ + CH_4$	0.0025	0.0	0.0	0.0	777
$CH_5^+ + S \rightarrow HS^+ + CH_4$	0.0013	0.0	0.0	6.1700	1011
$CHO^+ + C \rightarrow CH^+ + CO$	0.0010	0.0	0.0	0.0	881
$CHO^+ + CH \rightarrow CH_2^+ + CO$	0.0010	0.0	0.0	0.0	879
$CHO^+ + CH_2 \rightarrow CH_3^+ + CO$	0.0010	0.0	0.0	0.0	878
$CHO^+ + CS \rightarrow HCS^+ + CO$	0.0012	0.0	0.0	5.7300	982
$CHO^+ + H_2CO \rightarrow CH_2OH^+ + CO$	0.0010	0.0	0.0	0.0	875
$CHO^+ + H_2CS \rightarrow H_3CS^+ + CO$	0.0011	0.0	0.0	0.0	987
$CHO^+ + H_2O \rightarrow H_3O^+ + CO$	0.0032	0.0	0.0	0.0	870
$CHO^+ + H_2S \rightarrow H_3S^+ + CO$	0.0011	0.0	0.0	3.0000	985
$CHO^+ + HCN \rightarrow H_2CN^+ + CO$	0.0011	0.0	0.0	0.0	876
$CHO^+ + HCO \rightarrow H_2CO^+ + CO$	0.0010	0.0	0.0	0.0	877
$CHO^+ + HS \rightarrow H_2S^+ + CO$	0.0008	0.0	0.0	9.0000	981
$CHO^+ + NH \rightarrow NH_2^+ + CO$	0.0010	0.0	1007.0000	0.0	880
$CHO^+ + NH_2 \rightarrow NH_3^+ + CO$	0.0010	0.0	0.0	0.0	874
$CHO^+ + NH_3 \rightarrow NH_4^+ + CO$	0.0026	0.0	0.0	0.0	871
$CHO^+ + NS \rightarrow HNS^+ + CO$	0.0011	0.0	0.0	4.6200	983
$CHO^+ + OCS \rightarrow HOCS^+ + CO$	0.0013	0.0	0.0	6.0000	986
$CHO^+ + OH \rightarrow CO_2H^+ + H$	0.0010	0.0	0.0	0.0	872
$CHO^+ + OH \rightarrow H_2O^+ + CO$	0.0010	0.0	0.0	0.0	873
$CHO^+ + SO \rightarrow HSO^+ + CO$	0.0008	0.0	0.0	1.7300	984
$CN^+ + CH_4 \rightarrow CH_2CN^+ + H_2$	0.0010	0.0	0.0	-9.2500	896
$CN^+ + H_2 \rightarrow HCN^+ + H$	0.0010	0.0	0.0	-24.2900	897
$CN^+ + S \rightarrow S^+ + CN$	0.0011	0.0	0.0	0.0	695
$CO^+ + CH_4 \rightarrow CH_3CO^+ + H$	5.2E-05	0.0	0.0	0.0	866
$CO^+ + CH_4 \rightarrow CH_4^+ + CO$	0.0008	0.0	0.0	2.1000	128
$CO^+ + CH_4 \rightarrow CHO^+ + CH_3$	0.0002	0.0	0.0	0.0	865
$CO^+ + CO_2 \rightarrow CO_2^+ + CO$	0.0010	0.0	0.0	0.0	652
$CO^+ + H \rightarrow H^+ + CO$	0.0008	0.0	0.0	0.0	661
$CO^+ + H_2 \rightarrow CHO^+ + H$	0.0008	0.0	0.0	0.0	869
$CO^+ + H_2CO \rightarrow CHO^+ + HCO$	0.0010	0.0	0.0	0.0	867
$CO^+ + H_2CO \rightarrow H_2CO^+ + CO$	0.0014	0.0	0.0	0.0	654
$CO^+ + H_2CO_2 \rightarrow H_2CO_2^+ + CO$	0.0030	0.0	0.0	0.0	655
$CO^+ + H_2O \rightarrow CHO^+ + OH$	0.0009	0.0	0.0	0.0	863
$CO^+ + H_2O \rightarrow H_2O^+ + CO$	0.0017	0.0	0.0	0.0	651
$CO^+ + HCN \rightarrow CHO^+ + CN$	0.0005	0.0	0.0	0.0	868
$CO^+ + HCN \rightarrow HCN^+ + CO$	0.0034	0.0	0.0	0.0	656
$CO^+ + NH_3 \rightarrow CHO^+ + NH_2$	4.2E-05	0.0	0.0	0.0	864
$CO^+ + NH_3 \rightarrow NH_3^+ + CO$	0.0020	0.0	0.0	0.0	653
$CO^+ + NO \rightarrow NO^+ + CO$	0.0003	0.0	0.0	0.0	658
$CO^+ + O \rightarrow O^+ + CO$	0.0001	0.0	0.0	0.0	660
$CO^+ + O_2 \rightarrow O_2^+ + CO$	0.0001	0.0	0.0	0.0	659
$CO^+ + OH \rightarrow OH^+ + CO$	0.0003	0.0	0.0	0.0	657
$CO^+ + S \rightarrow S^+ + CO$	0.0011	0.0	0.0	0.0	694
$CO^+ + SO_2 \rightarrow SO^+ + CO_2$	0.0017	0.0	0.0	0.0	947
$CO_2^+ + CH_4 \rightarrow CH_4^+ + CO_2$	0.0005	0.0	0.0	3.0700	129
$CO_2^+ + CH_4 \rightarrow CO_2H^+ + CH_3$	0.0005	0.0	0.0	-18.1200	902
$CO_2^+ + H \rightarrow CHO^+ + O$	0.0003	0.0	0.0	-20.5300	904
$CO_2^+ + H \rightarrow H^+ + CO_2$	0.0001	0.0	0.0	0.0	663
$CO_2^+ + H_2 \rightarrow CO_2H^+ + H$	0.0010	0.0	0.0	-18.7200	903
$CO_2^+ + H_2O \rightarrow CO_2H^+ + OH$	0.0008	0.0	0.0	-19.4700	901

Continued on next page

Table F.6 – *Continued from previous page*

Neutral-Ion Rearrangement (2 Product Species)	A	B	C	ΔE	#
$CO_2^+ + H_2O \rightarrow H_2O^+ + CO_2$	0.0020	0.0	0.0	0.0	664
$CO_2^+ + NH_3 \rightarrow NH_3^+ + CO_2$	0.0019	0.0	0.0	0.0	665
$CO_2^+ + NO \rightarrow NO^+ + CO_2$	0.0001	0.0	0.0	0.0	669
$CO_2^+ + O \rightarrow O^+ + CO_2$	9.6E-05	0.0	0.0	0.0	667
$CO_2^+ + O \rightarrow O_2^+ + CO$	0.0002	0.0	0.0	-18.6500	905
$CO_2^+ + O_2 \rightarrow O_2^+ + CO_2$	5.3E-05	0.0	0.0	0.0	668
$CO_2^+ + OH \rightarrow OH^+ + CO_2$	0.0003	0.0	0.0	0.0	666
$CO_2H^+ + CH_2 \rightarrow CH_3^+ + CO_2$	0.0010	0.0	0.0	-5.1200	911
$CO_2H^+ + CH_4 \rightarrow CH_5^+ + CO_2$	0.0008	0.0	0.0	-4.4800	908
$CO_2H^+ + CO \rightarrow CHO^+ + CO_2$	0.0010	0.0	0.0	-5.4500	912
$CO_2H^+ + H_2CO \rightarrow CH_2OH^+ + CO_2$	0.0010	0.0	0.0	-6.1100	909
$CO_2H^+ + H_2O \rightarrow H_3O^+ + CO_2$	0.0023	0.0	0.0	-21.2900	906
$CO_2H^+ + HCN \rightarrow H_2CN^+ + CO_2$	0.0010	0.0	0.0	-9.7600	910
$CO_2H^+ + NH_3 \rightarrow NH_4^+ + CO_2$	0.0010	0.0	0.0	-27.9900	907
$CS^+ + H_2 \rightarrow HCS^+ + H$	0.0004	0.0	0.0	0.0	959
$CS^+ + O \rightarrow CO^+ + S$	6.0E-05	0.0	0.0	0.0	958
$H^+ + CH_2C_2H_2 \rightarrow C_3H_4^+ + H$	0.0020	0.0	0.0	8.3000	1117
$H^+ + CH_3C_2H \rightarrow C_3H_4^+ + H$	0.0020	0.0	0.0	3.0000	122
$H^+ + CH_4 \rightarrow CH_3^+ + H_2$	0.0023	0.0	0.0	0.0	276
$H^+ + CH_4 \rightarrow CH_4^+ + H$	0.0015	0.0	0.0	3.6200	123
$H^+ + CO_2 \rightarrow CHO^+ + O$	0.0030	0.0	0.0	0.0	712
$H^+ + CS \rightarrow CS^+ + H$	0.0049	0.0	0.0	0.0	672
$H^+ + H_2CO \rightarrow H_2CO^+ + H$	0.0030	0.0	0.0	0.0	601
$H^+ + H_2CS \rightarrow H_2CS^+ + H$	0.0047	0.0	0.0	0.0	676
$H^+ + H_2O \rightarrow H_2O^+ + H$	0.0069	0.0	0.0	0.0	594
$H^+ + H_2S \rightarrow H_2S^+ + H$	0.0053	0.0	0.0	0.0	675
$H^+ + HS \rightarrow HS^+ + H$	0.0016	0.0	0.0	0.0	671
$H^+ + HS \rightarrow S^+ + H_2$	0.0016	0.0	0.0	-11.0900	913
$H^+ + NH_3 \rightarrow NH_3^+ + H$	0.0037	0.0	0.0	0.0	595
$H^+ + NO \rightarrow NO^+ + H$	0.0029	0.0	0.0	0.0	599
$H^+ + NS \rightarrow NS^+ + H$	0.0047	0.0	0.0	0.0	673
$H^+ + O \rightarrow O^+ + H$	0.0008	-0.1550	215.0000	0.0	598
$H^+ + O_2 \rightarrow O_2^+ + H$	0.0020	0.0	0.0	0.0	600
$H^+ + OCS \rightarrow HS^+ + CO$	0.0021	0.0	0.0	-13.5500	914
$H^+ + OH \rightarrow OH^+ + H$	0.0021	0.0	0.0	0.0	597
$H^+ + S \rightarrow S^+ + H$	0.0013	0.0	0.0	0.0	670
$H^+ + SO \rightarrow SO^+ + H$	0.0032	0.0	0.0	0.0	674
$H_2^+ + C \rightarrow CH^+ + H$	0.0024	0.0	0.0	0.0	275
$H_2^+ + C_2H_2 \rightarrow C_2H_2^+ + H_2$	0.0048	0.0	0.0	7.4100	120
$H_2^+ + C_2H_2 \rightarrow C_2H_3^+ + H$	0.0005	0.0	0.0	0.0	258
$H_2^+ + C_2H_4 \rightarrow C_2H_4^+ + H_2$	0.0022	0.0	0.0	3.8200	119
$H_2^+ + C_2H_6 \rightarrow C_2H_6^+ + H_2$	0.0003	0.0	0.0	1.8400	118
$H_2^+ + CH_4 \rightarrow CH_4^+ + H_2$	0.0014	0.0	0.0	3.1600	121
$H_2^+ + CH_4 \rightarrow CH_5^+ + H$	0.0001	0.0	0.0	0.0	265
$H_2^+ + CO \rightarrow CHO^+ + H$	0.0022	0.0	0.0	0.0	717
$H_2^+ + CO \rightarrow CO^+ + H_2$	0.0006	0.0	0.0	0.0	605
$H_2^+ + H_2 \rightarrow H_3^+ + H$	0.0021	0.0	0.0	0.0	714
$H_2^+ + H_2O \rightarrow H_2O^+ + H_2$	0.0039	0.0	0.0	0.0	602
$H_2^+ + H_2O \rightarrow H_3O^+ + H$	0.0034	0.0	0.0	0.0	713
$H_2^+ + H_2S \rightarrow H_2S^+ + H_2$	0.0027	0.0	0.0	0.0	686
$H_2^+ + N \rightarrow NH^+ + H$	0.0019	0.0	0.0	0.0	715
$H_2^+ + N_2 \rightarrow N_2H^+ + H$	0.0020	0.0	0.0	0.0	719
$H_2^+ + NH_3 \rightarrow NH_3^+ + H_2$	0.0057	0.0	0.0	0.0	603
$H_2^+ + O \rightarrow OH^+ + H$	0.0015	0.0	0.0	0.0	716
$H_2^+ + O_2 \rightarrow O_2^+ + H_2$	0.0008	0.0	0.0	0.0	606
$H_2^+ + O_2 \rightarrow O_2H^+ + H$	0.0019	0.0	0.0	0.0	718
$H_2CN^+ + NH_3 \rightarrow NH_4^+ + HCN$	0.0011	0.0	0.0	-19.0700	900
$H_2CN^+ + NH_3 \rightarrow NH_4^+ + HNC$	0.0011	0.0	0.0	-22.3500	899
$H_2CO^+ + C_2 \rightarrow C_2H^+ + HCO$	0.0008	0.0	0.0	0.0	278
$H_2CO^+ + C_2H_4 \rightarrow C_2H_5^+ + HCO$	0.0010	0.0	0.0	0.0	277
$H_2CO^+ + CH \rightarrow CH_2^+ + HCO$	0.0003	0.0	0.0	-14.5300	886
$H_2CO^+ + CH_2 \rightarrow CH_3^+ + HCO$	0.0004	0.0	0.0	-15.5800	887
$H_2CO^+ + CO \rightarrow H_2CO^+ + CO$	0.0001	0.5000	0.0	0.0	385

Continued on next page

Table F.6 – *Continued from previous page*

Neutral-Ion Rearrangement (2 Product Species)	A	B	C	ΔE	#
$H_2CO^+ + CO_2 \rightarrow H_2CO^+ + CO_2$	0.0001	0.5000	0.0	0.0	368
$H_2CO^+ + H_2CO \rightarrow CH_2OH^+ + HCO$	0.0010	0.0	0.0	-15.4300	883
$H_2CO^+ + H_2O \rightarrow H_3O^+ + HCO$	0.0026	0.0	0.0	-13.6000	882
$H_2CO^+ + H_2S \rightarrow H_2S^+ + H_2CO$	0.0005	0.0	0.0	0.0	710
$H_2CO^+ + HCN \rightarrow H_2CN^+ + HCO$	0.0014	0.0	0.0	-12.4000	885
$H_2CO^+ + NH_2 \rightarrow NH_3^+ + HCO$	0.0009	0.0	0.0	-13.6200	888
$H_2CO^+ + NH_3 \rightarrow NH_3^+ + H_2CO$	0.0004	0.0	0.0	0.0	662
$H_2CO^+ + NH_3 \rightarrow NH_4^+ + HCO$	0.0013	0.0	0.0	-11.2600	884
$H_2CO^+ + S \rightarrow HS^+ + HCO$	0.0005	0.0	0.0	3.0000	1001
$H_2O^+ + C \rightarrow CH^+ + OH$	0.0011	0.0	0.0	0.0	831
$H_2O^+ + C_2 \rightarrow C_2H^+ + OH$	0.0005	0.0	0.0	0.0	256
$H_2O^+ + C_2H_2 \rightarrow C_2H_3^+ + OH$	0.0010	0.0	0.0	0.0	254
$H_2O^+ + C_2H_4 \rightarrow C_2H_5^+ + OH$	0.0010	0.0	0.0	0.0	255
$H_2O^+ + CH \rightarrow CH_2^+ + OH$	0.0003	0.0	0.0	0.0	830
$H_2O^+ + CH_2 \rightarrow CH_3^+ + OH$	0.0005	0.0	0.0	0.0	829
$H_2O^+ + CH_4 \rightarrow H_3O^+ + CH_3$	0.0014	0.0	0.0	48.4000	823
$H_2O^+ + CO \rightarrow CHO^+ + OH$	0.0003	0.3090	180.0000	0.0	826
$H_2O^+ + H_2 \rightarrow H_3O^+ + H$	0.0006	0.0	0.0	0.0	832
$H_2O^+ + H_2CO \rightarrow CH_2OH^+ + OH$	0.0007	0.0	0.0	50.2000	824
$H_2O^+ + H_2CO \rightarrow H_2CO^+ + H_2O$	0.0014	0.0	0.0	0.0	638
$H_2O^+ + H_2O \rightarrow H_3O^+ + OH$	0.0021	0.0	0.0	53.4000	821
$H_2O^+ + H_2S \rightarrow H_2S^+ + H_2O$	0.0010	0.0	0.0	0.0	702
$H_2O^+ + H_2S \rightarrow H_3O^+ + HS$	0.0005	0.0	0.0	9.3400	980
$H_2O^+ + H_2S \rightarrow H_3S^+ + OH$	0.0008	0.0	0.0	7.0000	979
$H_2O^+ + HCN \rightarrow H_2CN^+ + OH$	0.0010	0.0	0.0	0.0	825
$H_2O^+ + HCO \rightarrow H_2CO^+ + OH$	0.0003	0.0	0.0	0.0	827
$H_2O^+ + NH_2 \rightarrow NH_3^+ + OH$	0.0005	0.0	0.0	0.0	828
$H_2O^+ + NH_3 \rightarrow NH_3^+ + H_2O$	0.0022	0.0	0.0	0.0	637
$H_2O^+ + NH_3 \rightarrow NH_4^+ + OH$	0.0009	0.0	0.0	51.3000	822
$H_2O^+ + O_2 \rightarrow O_2^+ + H_2O$	0.0005	0.0	0.0	0.0	639
$H_2O^+ + S \rightarrow HS^+ + OH$	0.0004	0.0	0.0	3.0000	978
$H_2O^+ + S \rightarrow HSO^+ + H$	0.0004	0.0	0.0	5.0000	977
$H_2O^+ + S \rightarrow S^+ + H_2O$	0.0004	0.0	0.0	0.0	703
$H_2S^+ + C \rightarrow HCS^+ + H$	0.0010	0.0	0.0	1.0000	992
$H_2S^+ + H_2O \rightarrow H_3O^+ + HS$	0.0008	0.0	0.0	6.2900	996
$H_2S^+ + H_2S \rightarrow H_3S^+ + HS$	0.0010	0.0	0.0	5.2400	997
$H_2S^+ + HCO \rightarrow CHO^+ + H_2S$	0.0007	0.0	0.0	0.0	708
$H_2S^+ + N \rightarrow NS^+ + H_2$	0.0008	0.0	0.0	1.0000	993
$H_2S^+ + NH_3 \rightarrow NH_3^+ + H_2S$	0.0003	0.0	0.0	0.0	709
$H_2S^+ + NH_3 \rightarrow NH_4^+ + HS$	0.0014	0.0	0.0	3.0000	998
$H_2S^+ + NO \rightarrow NO^+ + H_2S$	0.0004	0.0	0.0	0.0	707
$H_2S^+ + O \rightarrow HS^+ + OH$	0.0003	0.0	0.0	5.0000	994
$H_2S^+ + O \rightarrow SO^+ + H_2$	0.0003	0.0	0.0	0.0	995
$H_2S^+ + S \rightarrow S^+ + H_2S$	0.0011	0.0	0.0	0.0	706
$H_3^+ + C \rightarrow CH^+ + H_2$	0.0020	0.0	0.0	0.0	273
$H_3^+ + C_2H_2 \rightarrow C_2H_3^+ + H_2$	0.0035	0.0	0.0	0.0	267
$H_3^+ + C_2H_4 \rightarrow C_2H_5^+ + H_2$	0.0012	0.0	0.0	0.0	268
$H_3^+ + CH_2C_2H_2 \rightarrow C_3H_5^+ + H_2$	0.0068	0.0	0.0	0.0	1140
$H_3^+ + CH_3C_2H \rightarrow C_3H_5^+ + H_2$	0.0068	0.0	0.0	0.0	272
$H_3^+ + CH_4 \rightarrow CH_5^+ + H_2$	0.0024	0.0	0.0	0.0	274
$H_3^+ + CN \rightarrow HCN^+ + H_2$	0.0020	0.0	0.0	0.0	732
$H_3^+ + CO \rightarrow CHO^+ + H_2$	2.7E-05	0.0	0.0	0.0	725
$H_3^+ + CO_2 \rightarrow CO_2H^+ + H_2$	0.0020	0.0	0.0	0.0	721
$H_3^+ + CS \rightarrow HCS^+ + H_2$	0.0029	0.0	0.0	0.0	964
$H_3^+ + H_2CO \rightarrow CH_2OH^+ + H_2$	0.0020	0.0	0.0	0.0	727
$H_3^+ + H_2CS \rightarrow H_3CS^+ + H_2$	0.0028	0.0	0.0	0.0	969
$H_3^+ + H_2O \rightarrow H_3O^+ + H_2$	0.0059	0.0	0.0	0.0	720
$H_3^+ + H_2S \rightarrow H_3S^+ + H_2$	0.0037	0.0	0.0	0.0	967
$H_3^+ + HCN \rightarrow H_2CN^+ + H_2$	0.0080	0.0	0.0	0.0	728
$H_3^+ + HCO \rightarrow H_2CO^+ + H_2$	0.0017	0.0	0.0	0.0	729
$H_3^+ + HS \rightarrow H_2S^+ + H_2$	0.0019	0.0	0.0	0.0	963
$H_3^+ + N_2 \rightarrow N_2H^+ + H_2$	0.0017	0.0	0.0	0.0	731
$H_3^+ + NH_3 \rightarrow NH_4^+ + H_2$	0.0044	0.0	0.0	0.0	722

Continued on next page

Table F.6 – *Continued from previous page*

Neutral-Ion Rearrangement (2 Product Species)	A	B	C	ΔE	#
$H_3^+ + NO \rightarrow HNO^+ + H_2$	0.0011	0.0	0.0	0.0	730
$H_3^+ + NS \rightarrow HNS^+ + H_2$	0.0028	0.0	0.0	0.0	965
$H_3^+ + O \rightarrow OH^+ + H_2$	0.0008	0.0	0.0	0.0	723
$H_3^+ + O_2 \rightarrow O_2H^+ + H_2$	0.0009	0.0	100.0000	0.0	726
$H_3^+ + OCS \rightarrow HOCS^+ + H_2$	0.0019	0.0	0.0	0.0	968
$H_3^+ + OH \rightarrow H_2O^+ + H_2$	0.0013	0.0	0.0	0.0	724
$H_3^+ + S \rightarrow HS^+ + H_2$	0.0026	0.0	0.0	0.0	962
$H_3^+ + SO \rightarrow HSO^+ + H_2$	0.0019	0.0	0.0	0.0	966
$H_3O^+ + C \rightarrow CHO^+ + H_2$	0.0020	0.0	0.0	21.6000	839
$H_3O^+ + C_2H_3 \rightarrow C_2H_4^+ + H_2O$	0.0020	0.0	0.0	0.0	252
$H_3O^+ + CH \rightarrow CH_2^+ + H_2O$	0.0007	0.0	0.0	21.6000	838
$H_3O^+ + CH_2 \rightarrow CH_3^+ + H_2O$	0.0009	0.0	0.0	14.9000	837
$H_3O^+ + CH_2C_2H_2 \rightarrow C_3H_5^+ + H_2O$	0.0018	0.0	0.0	0.0	1138
$H_3O^+ + CH_3C_2H \rightarrow C_3H_5^+ + H_2O$	0.0018	0.0	0.0	0.0	253
$H_3O^+ + CO \rightarrow H_3O^+ + CO$	0.0001	0.5000	0.0	2.5600	61
$H_3O^+ + CO_2 \rightarrow H_3O^+ + CO_2$	0.0001	0.5000	0.0	0.7000	60
$H_3O^+ + H_2CO \rightarrow CH_2OH^+ + H_2O$	0.0011	0.0	0.0	3.5000	834
$H_3O^+ + H_2O \rightarrow H_3O^+ + H_2O$	0.0001	0.5000	0.0	0.0	59
$H_3O^+ + HCN \rightarrow H_2CN^+ + H_2O$	0.0010	0.0	0.0	5.9000	835
$H_3O^+ + NH_2 \rightarrow NH_3^+ + H_2O$	0.0010	0.0	0.0	1.0000	836
$H_3O^+ + NH_3 \rightarrow NH_4^+ + H_2O$	0.0022	0.0	0.0	0.0	833
$HCN^+ + H_2 \rightarrow H_2CN^+ + H$	0.0009	0.0	0.0	-21.1900	898
$HCN^+ + S \rightarrow HS^+ + CN$	0.0006	0.0	0.0	8.9700	988
$HCN^+ + S \rightarrow S^+ + HCN$	0.0006	0.0	0.0	0.0	704
$HCO^+ + C_2H \rightarrow C_2H_2^+ + CO$	0.0008	0.0	0.0	0.0	282
$HCO^+ + C_2H_2 \rightarrow C_2H_3^+ + CO$	0.0014	0.0	0.0	0.0	279
$HCO^+ + C_2H_4 \rightarrow C_2H_5^+ + CO$	0.0014	0.0	0.0	0.0	280
$HCO^+ + CH_2C_2H_2 \rightarrow C_3H_5^+ + CO$	0.0014	0.0	0.0	0.0	1141
$HCO^+ + CH_3C_2H \rightarrow C_3H_5^+ + CO$	0.0014	0.0	0.0	0.0	281
$HCS^+ + O \rightarrow CHO^+ + S$	0.0010	0.0	0.0	6.3500	1012
$HCS^+ + O \rightarrow OCS^+ + H$	5.0E-06	0.0	0.0	1.0000	1013
$HNO^+ + S \rightarrow HS^+ + NO$	0.0011	0.0	0.0	7.4900	989
$HS^+ + C \rightarrow CS^+ + H$	0.0010	0.0	0.0	0.0	948
$HS^+ + CH \rightarrow CH_2^+ + S$	0.0006	0.0	0.0	0.0	952
$HS^+ + CH_4 \rightarrow H_3CS^+ + H_2$	0.0002	0.0	0.0	0.0	957
$HS^+ + H_2O \rightarrow H_3O^+ + S$	0.0008	0.0	0.0	0.0	953
$HS^+ + H_2S \rightarrow H_2S^+ + HS$	0.0004	0.0	0.0	0.0	697
$HS^+ + H_2S \rightarrow H_3S^+ + S$	0.0005	0.0	0.0	1.3000	955
$HS^+ + HCN \rightarrow H_2CN^+ + S$	0.0009	0.0	0.0	0.0	954
$HS^+ + N \rightarrow NS^+ + H$	0.0007	0.0	0.0	0.0	949
$HS^+ + NH_3 \rightarrow NH_3^+ + HS$	0.0005	0.0	0.0	0.0	698
$HS^+ + NH_3 \rightarrow NH_4^+ + S$	0.0010	0.0	0.0	0.0	956
$HS^+ + O \rightarrow S^+ + OH$	0.0003	0.0	0.0	0.0	951
$HS^+ + O \rightarrow SO^+ + H$	0.0003	0.0	0.0	0.0	950
$HS^+ + S \rightarrow S^+ + HS$	0.0010	0.0	0.0	0.0	696
$N^+ + CH_4 \rightarrow CH_4^+ + N$	2.8E-05	0.0	0.0	0.0	618
$N^+ + CO \rightarrow CO^+ + N$	0.0008	0.0	0.0	0.0	619
$N^+ + CO \rightarrow NO^+ + C$	0.0001	0.0	0.0	0.0	783
$N^+ + CO_2 \rightarrow CO_2^+ + N$	0.0008	0.0	0.0	0.0	617
$N^+ + H_2 \rightarrow NH^+ + H$	0.0010	0.0	85.0000	0.0	782
$N^+ + H_2O \rightarrow H_2O^+ + N$	0.0028	0.0	0.0	0.0	616
$N^+ + NH \rightarrow N_2^+ + H$	0.0004	0.0	0.0	0.0	784
$N^+ + NO \rightarrow N_2^+ + O$	7.9E-05	0.0	0.0	0.0	787
$N^+ + NO \rightarrow NO^+ + N$	0.0005	0.0	0.0	0.0	621
$N^+ + O \rightarrow O^+ + N$	1.0E-06	0.0	0.0	0.0	622
$N^+ + O_2 \rightarrow NO^+ + O$	0.0003	0.0	0.0	0.0	786
$N^+ + O_2 \rightarrow O^+ + NO$	3.7E-05	0.0	0.0	0.0	785
$N^+ + O_2 \rightarrow O_2^+ + N$	0.0003	0.0	0.0	0.0	620
$N_2^+ + CH_4 \rightarrow CH_4^+ + N_2$	0.0002	0.0	0.0	3.0000	125
$N_2^+ + CO \rightarrow CO^+ + N_2$	7.4E-05	0.0	0.0	0.0	643
$N_2^+ + CO_2 \rightarrow CO_2^+ + N_2$	0.0008	0.0	0.0	0.0	641
$N_2^+ + H \rightarrow H^+ + N_2$	0.0001	0.0	0.0	0.0	645
$N_2^+ + H_2 \rightarrow N_2H^+ + H$	0.0017	0.0	0.0	6.3000	851

Continued on next page

Table F.6 – *Continued from previous page*

Neutral-Ion Rearrangement (2 Product Species)	A	B	C	ΔE	#
$N_2^+ + H_2O \rightarrow H_2O^+ + N_2$	0.0023	0.0	0.0	0.0	640
$N_2^+ + H_2O \rightarrow N_2H^+ + OH$	0.0005	0.0	0.0	3.1900	849
$N_2^+ + NH_3 \rightarrow N_2H^+ + NH_2$	2.1E-05	0.0	0.0	3.8900	850
$N_2^+ + NH_3 \rightarrow NH_3^+ + N_2$	0.0019	0.0	0.0	0.0	642
$N_2^+ + NO \rightarrow NO^+ + N_2$	0.0004	0.0	0.0	0.0	647
$N_2^+ + O \rightarrow NO^+ + N$	0.0001	0.0	0.0	5.4200	852
$N_2^+ + O \rightarrow O^+ + N_2$	1.0E-05	0.0	0.0	0.0	644
$N_2^+ + O_2 \rightarrow O_2^+ + N_2$	5.0E-05	0.0	0.0	0.0	646
$N_2^+ + S \rightarrow S^+ + N_2$	0.0011	0.0	0.0	0.0	688
$N_2H^+ + CH_4 \rightarrow CH_5^+ + N_2$	0.0009	0.0	0.0	1.5000	858
$N_2H^+ + CO \rightarrow CHO^+ + N_2$	0.0009	0.0	0.0	12.0000	859
$N_2H^+ + CO_2 \rightarrow CO_2H^+ + N_2$	0.0009	0.0	0.0	9.8000	856
$N_2H^+ + H_2O \rightarrow H_3O^+ + N_2$	0.0026	0.0	0.0	6.2100	855
$N_2H^+ + NH_3 \rightarrow NH_4^+ + N_2$	0.0023	0.0	0.0	2.1800	857
$N_2H^+ + O \rightarrow OH^+ + N_2$	0.0001	0.0	0.0	2.4100	860
$N_2H^+ + S \rightarrow HS^+ + N_2$	0.0011	0.0	0.0	3.6300	990
$NH^+ + H_2 \rightarrow NH_2^+ + H$	0.0013	0.0	0.0	0.0	791
$NH^+ + H_2O \rightarrow H_3O^+ + N$	0.0010	0.0	0.0	0.0	789
$NH^+ + NH_3 \rightarrow NH_3^+ + NH$	0.0018	0.0	0.0	0.0	623
$NH^+ + NH_3 \rightarrow NH_4^+ + N$	0.0006	0.0	0.0	0.0	790
$NH^+ + S \rightarrow HS^+ + N$	0.0007	0.0	0.0	0.0	943
$NH^+ + S \rightarrow NS^+ + H$	0.0007	0.0	0.0	3.2000	942
$NH^+ + S \rightarrow S^+ + NH$	0.0007	0.0	0.0	0.0	692
$NH_2^+ + H_2 \rightarrow NH_3^+ + H$	0.0003	0.0	0.0	26.4000	796
$NH_2^+ + H_2O \rightarrow H_3O^+ + NH$	0.0028	0.0	0.0	0.0	792
$NH_2^+ + H_2O \rightarrow NH_3^+ + OH$	0.0001	0.0	0.0	28.9000	794
$NH_2^+ + H_2O \rightarrow NH_4^+ + O$	0.0001	0.0	0.0	24.8000	793
$NH_2^+ + H_2S \rightarrow H_2S^+ + NH_2$	0.0007	0.0	0.0	0.0	701
$NH_2^+ + H_2S \rightarrow H_3S^+ + NH$	0.0003	0.0	0.0	11.0000	976
$NH_2^+ + NH_3 \rightarrow NH_3^+ + NH_2$	0.0007	0.0	0.0	0.0	625
$NH_2^+ + NH_3 \rightarrow NH_4^+ + NH$	0.0016	0.0	0.0	23.8000	795
$NH_2^+ + S \rightarrow HNS^+ + H$	0.0004	0.0	0.0	10.9500	974
$NH_2^+ + S \rightarrow HS^+ + NH$	0.0004	0.0	0.0	6.0000	975
$NH_2^+ + S \rightarrow S^+ + NH_2$	0.0004	0.0	0.0	0.0	700
$NH_3^+ + CH_2 \rightarrow CH_3^+ + NH_2$	0.0010	0.0	0.0	36.5000	803
$NH_3^+ + CH_4 \rightarrow NH_4^+ + CH_3$	0.0005	0.0	0.0	32.6000	799
$NH_3^+ + H_2 \rightarrow NH_4^+ + H$	1.0E-07	0.0	0.0	25.2000	801
$NH_3^+ + H_2CO \rightarrow NH_4^+ + HCO$	0.0011	0.0	0.0	18.6000	802
$NH_3^+ + H_2O \rightarrow NH_4^+ + OH$	0.0001	0.0	0.0	26.0000	797
$NH_3^+ + H_2S \rightarrow H_3S^+ + NH_2$	0.0001	0.0	0.0	7.0000	1000
$NH_3^+ + H_2S \rightarrow NH_4^+ + HS$	0.0013	0.0	0.0	5.0000	999
$NH_3^+ + NH_3 \rightarrow NH_4^+ + NH_2$	0.0022	0.0	0.0	32.0000	798
$NH_3^+ + OH \rightarrow NH_4^+ + O$	0.0007	0.0	0.0	18.6000	800
$NH_4^+ + CO \rightarrow NH_4^+ + CO$	0.0001	0.5000	0.0	0.0	292
$NH_4^+ + CO_2 \rightarrow NH_4^+ + CO_2$	0.0001	0.5000	0.0	0.0	306
$NH_4^+ + H_2O \rightarrow NH_4^+ + H_2O$	0.0001	0.5000	0.0	3.4100	58
$NS^+ + O \rightarrow NO^+ + S$	0.0006	0.0	0.0	0.0	961
$O^+ + CH_4 \rightarrow CH_3^+ + OH$	0.0001	0.0	0.0	27.1000	805
$O^+ + CH_4 \rightarrow CH_4^+ + O$	0.0009	0.0	0.0	0.0	628
$O^+ + CO_2 \rightarrow O_2^+ + CO$	0.0009	0.0	0.0	25.0000	804
$O^+ + H \rightarrow H^+ + O$	0.0006	0.3600	-8.6000	0.0	631
$O^+ + H_2 \rightarrow OH^+ + H$	0.0017	0.0	0.0	27.9000	806
$O^+ + H_2O \rightarrow H_2O^+ + O$	0.0032	0.0	0.0	0.0	626
$O^+ + H_2S \rightarrow H_2S^+ + O$	0.0014	0.0	0.0	0.0	682
$O^+ + N_2 \rightarrow NO^+ + N$	1.2E-06	-1.0000	0.0	7.3400	808
$O^+ + NH_3 \rightarrow NH_3^+ + O$	0.0012	0.0	0.0	0.0	627
$O^+ + O_2 \rightarrow O_2^+ + O$	1.9E-05	0.0	0.0	0.0	630
$O^+ + OH \rightarrow H^+ + O_2$	2.7E-05	0.1300	0.0	30.2000	807
$O^+ + OH \rightarrow OH^+ + O$	0.0004	0.0	0.0	0.0	629
$O_2^+ + C \rightarrow C^+ + O_2$	5.2E-05	0.0	0.0	0.0	650
$O_2^+ + H_2S \rightarrow H_2S^+ + O_2$	0.0014	0.0	0.0	0.0	690
$O_2^+ + N \rightarrow NO^+ + O$	0.0002	0.0	0.0	0.0	861
$O_2^+ + NH_3 \rightarrow NH_3^+ + O_2$	0.0020	0.0	0.0	0.0	648

Continued on next page

Table F.6 – *Continued from previous page*

Neutral-Ion Rearrangement (2 Product Species)	A	B	C	ΔE	#
$O_2^+ + NO \rightarrow NO^+ + O_2$	0.0005	0.0	0.0	0.0	649
$O_2^+ + S \rightarrow S^+ + O_2$	0.0005	0.0	0.0	0.0	689
$O_2^+ + S \rightarrow SO^+ + O$	0.0005	0.0	0.0	0.0	938
$O_2H^+ + H_2 \rightarrow H_3^+ + O_2$	0.0006	0.0	0.0	0.0	862
$O_2H^+ + S \rightarrow HS^+ + O_2$	0.0011	0.0	0.0	5.6000	991
$OH^+ + C \rightarrow CH^+ + O$	0.0012	0.0	0.0	61.0000	820
$OH^+ + C \rightarrow CO^+ + H$	0.0010	0.0	0.0	61.6000	819
$OH^+ + C_2H_5 \rightarrow C_2H_6^+ + O$	0.0010	0.0	0.0	0.0	257
$OH^+ + CH_4 \rightarrow CH_4^+ + OH$	0.0010	0.0	0.0	3.0000	126
$OH^+ + CH_4 \rightarrow H_3O^+ + CH_2$	0.0013	0.0	0.0	11.3000	811
$OH^+ + CO \rightarrow CHO^+ + O$	2.0E-05	0.0	0.0	21.4000	815
$OH^+ + CO_2 \rightarrow CO_2H^+ + O$	0.0014	0.0	0.0	29.5000	813
$OH^+ + H_2 \rightarrow H_2O^+ + H$	0.0010	0.0	0.0	56.6000	818
$OH^+ + H_2CO \rightarrow CH_2OH^+ + O$	0.0011	0.0	0.0	26.2000	812
$OH^+ + H_2CO \rightarrow H_2CO^+ + OH$	0.0007	0.0	0.0	0.0	635
$OH^+ + H_2O \rightarrow H_2O^+ + OH$	0.0016	0.0	0.0	0.0	632
$OH^+ + H_2O \rightarrow H_3O^+ + O$	0.0013	0.0	0.0	28.5000	809
$OH^+ + H_2S \rightarrow H_3S^+ + O$	0.0008	0.0	0.0	0.7000	946
$OH^+ + HCN \rightarrow H_2CN^+ + O$	0.0010	0.0	0.0	20.3000	814
$OH^+ + N_2 \rightarrow N_2H^+ + O$	0.0002	0.0	0.0	57.5000	816
$OH^+ + NH_3 \rightarrow NH_3^+ + OH$	0.0012	0.0	0.0	0.0	633
$OH^+ + NH_3 \rightarrow NH_4^+ + O$	0.0012	0.0	0.0	0.0	810
$OH^+ + O_2 \rightarrow O_2^+ + OH$	0.0006	0.0	0.0	0.0	636
$OH^+ + OH \rightarrow H_2O^+ + O$	0.0007	0.0	0.0	62.1000	817
$OH^+ + S \rightarrow HS^+ + O$	0.0004	0.0	0.0	0.0	945
$OH^+ + S \rightarrow S^+ + OH$	0.0004	0.0	0.0	0.0	693
$OH^+ + S \rightarrow SO^+ + H$	0.0004	0.0	0.0	0.0	944
$S^+ + C_2 \rightarrow CS^+ + C$	0.0008	0.0	0.0	0.0	925
$S^+ + CH \rightarrow CS^+ + H$	0.0006	0.0	0.0	0.0	926
$S^+ + CH_2 \rightarrow HCS^+ + H$	1.0E-05	0.0	0.0	0.0	929
$S^+ + CH_3 \rightarrow H_2CS^+ + H$	1.0E-05	0.0	0.0	0.7000	933
$S^+ + CH_4 \rightarrow H_3CS^+ + H$	0.0004	0.0	0.0	0.0	934
$S^+ + H_2CO \rightarrow H_2S^+ + CO$	0.0003	0.0	0.0	0.0	931
$S^+ + HCO \rightarrow CHO^+ + S$	0.0004	0.0	0.0	0.0	684
$S^+ + HCO \rightarrow HS^+ + CO$	0.0004	0.0	0.0	0.0	930
$S^+ + NH \rightarrow NS^+ + H$	0.0006	0.0	0.0	0.0	927
$S^+ + NH_3 \rightarrow NH_2^+ + HS$	7.0E-05	0.0	0.0	0.0	932
$S^+ + NH_3 \rightarrow NH_3^+ + S$	0.0014	0.0	0.0	0.0	685
$S^+ + NO \rightarrow NO^+ + S$	0.0004	0.0	0.0	0.0	683
$S^+ + O_2 \rightarrow O^+ + SO$	2.0E-05	0.0	0.0	6.0000	1014
$S^+ + OH \rightarrow SO^+ + H$	0.0006	0.0	0.0	0.0	928
$SO^+ + N \rightarrow NS^+ + O$	5.0E-05	0.0	0.0	0.0	960
$SO^+ + NH_3 \rightarrow NH_3^+ + SO$	0.0013	0.0	0.0	0.0	699

F.7 Neutral-Ion Rearrangement (3 Product Species)

Neutral-Ion Rearrangement (3 Product Species)	A	B	C	ΔE	#
$C_2^+ + CH_4 \rightarrow C_3H^+ + H_2 + H$	0.0002	0.0	0.0	0.7000	202
$C_2H_2^+ + C_2H_6 \rightarrow C_3H_3^+ + CH_3 + H_2$	8.8E-05	0.0	0.0	3.4100	183
$C_2H_2^+ + C_2H_6 \rightarrow C_4H_5^+ + H_2 + H$	7.3E-05	0.0	0.0	0.0	185
$CH^+ + CH_4 \rightarrow C_2H_2^+ + H_2 + H$	0.0001	0.0	0.0	1.5200	244
$CH_2^+ + CH_4 \rightarrow C_2H_2^+ + H_2 + H_2$	0.0001	0.0	0.0	4.9600	234
$CH_2^+ + CH_4 \rightarrow C_2H_3^+ + H_2 + H$	0.0003	0.0	0.0	7.4500	233
$CH_2^+ + H_2S \rightarrow HCS^+ + H_2 + H$	0.0002	0.0	0.0	3.0000	973
$CH_3^+ + C_2H_4 \rightarrow C_3H_3^+ + H_2 + H_2$	4.6E-05	0.0	0.0	2.0700	223
$CH_3^+ + C_2H_6 \rightarrow C_3H_5^+ + H_2 + H_2$	0.0002	0.0	0.0	0.3900	226
$CH_4^+ + C_2H_2 \rightarrow C_3H_3^+ + H_2 + H$	0.0002	0.0	0.0	2.5600	216
$CH_4^+ + C_2H_4 \rightarrow C_3H_5^+ + H_2 + H$	5.5E-05	0.0	0.0	6.8600	218
$CH_4^+ + C_2H_6 \rightarrow C_2H_4^+ + CH_4 + H_2$	0.0019	0.0	0.0	12.0000	219
$H_2^+ + C_2H_4 \rightarrow C_2H_2^+ + H_2 + H_2$	0.0009	0.0	0.0	1.7200	260

Continued on next page

Table F.7 – *Continued from previous page*

Neutral-Ion Rearrangement (3 Product Species)	A	B	C	ΔE	#
$H_2^+ + C_2H_4 \rightarrow C_2H_3^+ + H_2 + H$	0.0018	0.0	0.0	2.1400	259
$H_2^+ + C_2H_6 \rightarrow C_2H_4^+ + H_2 + H_2$	0.0023	0.0	0.0	6.3800	262
$H_2^+ + C_2H_6 \rightarrow C_2H_5^+ + H_2 + H$	1.4E-09	0.0	0.0	1.6900	261
$H_2^+ + CH_4 \rightarrow CH_3^+ + H_2 + H$	0.0023	0.0	0.0	3.0300	266
$H_2^+ + H_2S \rightarrow HS^+ + H + H_2$	0.0009	0.0	0.0	3.6200	935
$H_2^+ + H_2S \rightarrow S^+ + H_2 + H_2$	0.0008	0.0	0.0	8.9600	936
$H_3^+ + C_2H_4 \rightarrow C_2H_3^+ + H_2 + H_2$	0.0012	0.0	0.0	0.0	269
$H_3^+ + C_2H_6 \rightarrow C_2H_5^+ + H_2 + H_2$	0.0034	0.0	0.0	6.2100	270
$H_3^+ + CH_2C_2H_2 \rightarrow C_3H_3^+ + H_2 + H_2$	0.0022	0.0	0.0	3.0000	1139
$H_3^+ + CH_3C_2H \rightarrow C_3H_3^+ + H_2 + H_2$	0.0022	0.0	0.0	0.0	271
$N^+ + CH_4 \rightarrow CH_3^+ + N + H$	0.0005	0.0	0.0	1.8400	779
$N^+ + CH_4 \rightarrow H_2CN^+ + H + H$	0.0004	0.0	0.0	3.8200	780
$N^+ + CH_4 \rightarrow HCN^+ + H_2 + H$	5.6E-05	0.0	0.0	7.4100	781
$N_2^+ + CH_4 \rightarrow CH_2^+ + H_2 + N_2$	7.0E-05	0.0	0.0	3.0000	854
$N_2^+ + CH_4 \rightarrow CH_3^+ + H + N_2$	0.0009	0.0	0.0	3.1600	853

F.8 Neutral-Ion Rearrangement (4 Product Species)

Neutral-Ion Rearrangement (4 Product Species)	A	B	C	ΔE	#
$H_2^+ + C_2H_6 \rightarrow C_2H_2^+ + H_2 + H_2 + H_2$	0.0002	0.0	0.0	0.0	264
$H_2^+ + C_2H_6 \rightarrow C_2H_3^+ + H_2 + H_2 + H$	0.0007	0.0	0.0	3.4100	263

F.9 Ionizative Association

Ionizative Association	A	B	C	ΔE	#
$CH + O \rightarrow CHO^+ + e^-$	2.0E-05	0.4400	0.0	3.4100	19

F.10 e^- Impact Dissociation

e^- Impact Dissociation	A	B	C	ΔE	#
$C_2 + e^- \rightarrow C + C + e^-$	0.0009	0.5000	7.1E+04	6.8600	464
$C_2H + e^- \rightarrow C + C + H + e^-$	0.0040	0.5980	1.2E+05	2.1000	1018
$C_2H_2 + e^- \rightarrow C_2 + H + H + e^-$	0.0045	0.5954	1.2E+05	8.9600	612
$C_2H_2 + e^- \rightarrow C_2H + H + e^-$	0.0190	0.5000	6.2E+04	0.0	80
$C_2H_3 + e^- \rightarrow C_2 + H_2 + H + e^-$	0.0032	0.5900	1.2E+05	3.0000	1016
$C_2H_4 + e^- \rightarrow C_2 + H_2 + H_2 + e^-$	0.0077	0.3625	1.2E+05	3.0000	1015
$C_3H + e^- \rightarrow C + C + C + H + e^-$	0.0062	0.5911	1.2E+05	3.6200	611
$C_3H_2 + e^- \rightarrow C_3H + H + e^-$	0.0065	0.5958	1.2E+05	3.0000	610
$C_3H_3 + e^- \rightarrow C_3H + H + H + e^-$	0.0098	0.3690	1.2E+05	3.1600	609
$C_3H_3 + e^- \rightarrow C_3H_2 + H + e^-$	0.0046	0.5948	1.2E+05	7.4100	608
$CH_2C_2H_2 + e^- \rightarrow C_3 + H_2 + H_2 + e^-$	0.0103	0.3690	1.2E+05	3.0700	1113
$CH_2C_2H_2 + e^- \rightarrow C_3H_3 + H + e^-$	0.0048	0.5950	1.2E+05	5.2900	1144
$CH_3C_2H + e^- \rightarrow C_3 + H_2 + H_2 + e^-$	0.0103	0.3688	1.2E+05	3.4100	79
$CH_3C_2H + e^- \rightarrow C_3H_3 + H + e^-$	0.0048	0.5949	1.2E+05	3.8200	607
$CH_3CN + e^- \rightarrow CH_3 + CN + e^-$	0.0380	0.5000	5.6E+04	0.0	478
$CH_4 + e^- \rightarrow CH_3 + H + e^-$	0.0009	0.5000	5.2E+04	0.7000	82
$CO + e^- \rightarrow C + O + e^-$	0.0009	0.5000	1.3E+05	7.4500	468
$CO_2 + e^- \rightarrow CO + O + e^-$	0.0009	0.5000	6.3E+04	0.3900	467
$CO_2 + e^- \rightarrow CO(^1p) + O + e^-$	0.0009	0.5000	1.6E+05	4.9600	469
$CO_2 + e^- \rightarrow CO(^3p) + O + e^-$	0.0009	0.5000	1.3E+05	1.5200	470
$H_2 + e^- \rightarrow H + H + e^-$	0.0032	0.3500	1.0E+05	2.5600	463
$H_2CO + e^- \rightarrow CO + H + H + e^-$	0.0190	0.5000	5.2E+04	0.0	476
$H_2CO + e^- \rightarrow HCO + H + e^-$	0.0190	0.5000	4.3E+04	3.0300	475

Continued on next page

Table F.10 – *Continued from previous page*

e^- Impact Dissociation	A	B	C	ΔE	#
$H_2O + e^- \rightarrow H_2 + O(^1d) + e^-$	0.0009	0.5000	8.1E+04	2.1400	471
$H_2O + e^- \rightarrow OH + H + e^-$	0.0009	0.5000	5.9E+04	1.7200	472
$HCN + e^- \rightarrow CN + H + e^-$	0.0380	0.5000	7.5E+04	6.2100	477
$N_2 + e^- \rightarrow N + N + e^-$	0.0001	1.0000	1.2E+05	12.0000	465
$NH_2CH_3 + e^- \rightarrow NH_2 + CH_3 + e^-$	0.0380	0.5000	5.2E+04	1.8400	479
$NH_3 + e^- \rightarrow H_2 + NH + e^-$	0.0009	0.5000	6.4E+04	6.3800	474
$NH_3 + e^- \rightarrow NH_2 + H + e^-$	0.0009	0.5000	5.1E+04	1.6900	473
$O_2 + e^- \rightarrow O + O + e^-$	0.0009	0.5000	5.9E+04	2.0700	466

F.11 e^- Impact Ionization

e^- Impact Ionization	A	B	C	ΔE	#
$C + e^- \rightarrow C^+ + e^- + e^-$	0.0003	0.4000	1.3E+05	2.5600	440
$C_2 + e^- \rightarrow C_2^+ + e^- + e^-$	0.0009	0.5000	1.4E+05	6.8600	441
$C_2H + e^- \rightarrow C_2H^+ + e^- + e^-$	0.0003	0.7540	1.2E+05	6.3800	1042
$C_2H_2 + e^- \rightarrow C_2H_2^+ + e^- + e^-$	0.0004	0.7541	1.2E+05	3.0000	1051
$C_2H_3 + e^- \rightarrow C_2H_3^+ + e^- + e^-$	0.0001	0.7713	1.2E+05	3.1600	1050
$C_2H_4 + e^- \rightarrow C_2H_4^+ + e^- + e^-$	0.0001	0.7734	1.2E+05	7.4100	1049
$C_2H_5 + e^- \rightarrow C_2H_5^+ + e^- + e^-$	0.0001	0.7703	1.2E+05	3.8200	1048
$C_2H_6 + e^- \rightarrow C_2H_6^+ + e^- + e^-$	0.0002	0.7650	1.2E+05	1.8400	1047
$C_3H + e^- \rightarrow C_3H^+ + e^- + e^-$	0.0007	0.7685	1.2E+05	0.0	1046
$C_3H_2 + e^- \rightarrow C_3H_2^+ + e^- + e^-$	0.0005	0.7631	1.2E+05	6.2100	1045
$C_3H_3 + e^- \rightarrow C_3H_3^+ + e^- + e^-$	0.0002	0.7667	1.2E+05	0.0	1044
$CH_2C_2H_2 + e^- \rightarrow C_3H_4^+ + e^- + e^-$	0.0002	0.7700	1.2E+05	3.6200	1145
$CH_3C_2H + e^- \rightarrow C_3H_4^+ + e^- + e^-$	0.0002	0.7703	1.2E+05	3.0300	1043
$CH_4 + e^- \rightarrow CH_4^+ + e^- + e^-$	3.8E-07	1.9100	6.6E+04	3.4100	84
$CO + e^- \rightarrow CO^+ + e^- + e^-$	0.0007	0.7200	1.7E+05	4.9600	446
$CO_2 + e^- \rightarrow CO_2^+ + e^- + e^-$	5.1E-06	1.2400	1.1E+05	1.5200	447
$H + e^- \rightarrow H^+ + e^- + e^-$	5.8E-05	0.5000	1.6E+05	0.0	438
$H_2 + e^- \rightarrow H_2^+ + e^- + e^-$	0.0009	0.5000	1.8E+05	0.7000	439
$H_2O + e^- \rightarrow H_2O^+ + e^- + e^-$	5.3E-05	0.9700	9.0E+05	2.1400	448
$N + e^- \rightarrow N^+ + e^- + e^-$	0.0001	0.4400	1.7E+05	12.0000	442
$N_2 + e^- \rightarrow N_2^+ + e^- + e^-$	4.0E-07	1.3400	1.1E+05	2.0700	443
$NH_3 + e^- \rightarrow NH_3^+ + e^- + e^-$	0.0009	0.5000	1.2E+05	1.7200	449
$NO + e^- \rightarrow NO^+ + e^- + e^-$	5.9E-05	1.1000	1.1E+05	1.6900	451
$O + e^- \rightarrow O^+ + e^- + e^-$	0.0013	0.5700	1.6E+05	0.3900	444
$O_2 + e^- \rightarrow O_2^+ + e^- + e^-$	0.0003	0.7900	1.6E+05	7.4500	445

F.12 Recombination

Recombination	A	B	C	ΔE	#
$C^+ + e^- \rightarrow C$	3.5E-06	-0.7000	0.0	0.7000	384
$CH^+ + e^- \rightarrow CH$	0.0001	0.0	0.0	3.4100	293
$H^+ + e^- \rightarrow H$	3.5E-06	-0.7000	0.0	0.0	383
$H_2CS^+ + e^- \rightarrow H_2CS$	0.0001	-0.7000	0.0	7.4500	391
$H_2S^+ + e^- \rightarrow H_2S$	0.0001	-0.7000	0.0	0.3900	390
$N^+ + e^- \rightarrow N$	3.5E-06	-0.7000	0.0	2.5600	386
$O^+ + e^- \rightarrow O$	3.5E-06	-0.7000	0.0	6.8600	387
$O_2^+ + e^- \rightarrow O_2$	4.0E-06	-0.7000	0.0	12.0000	388
$S^+ + e^- \rightarrow S$	3.9E-06	-0.6300	0.0	2.0700	389

F.13 Dissociative Recombination (2 Product Species)

Dissociative Recombination (2 Product Species)	A	B	C	ΔE	#
$C_2^+ + e^- \rightarrow C + C$	0.3000	-0.5000	0.0	2.1000	547
$C_2H^+ + e^- \rightarrow C_2 + H$	0.1160	-0.7600	0.0	12.0000	92
$C_2H^+ + e^- \rightarrow CH + C$	0.2890	-0.5000	0.0	5.0600	1029
$C_2H_2^+ + e^- \rightarrow C_2 + H_2$	0.2950	-0.5000	0.0	3.0700	548
$C_2H_2^+ + e^- \rightarrow C_2H + H$	0.0900	-0.5000	0.0	6.8600	91
$C_2H_2^+ + e^- \rightarrow CH + CH$	0.1410	-0.5000	0.0	1.0000	1027
$C_2H_3^+ + e^- \rightarrow C_2H + H_2$	0.0575	-1.3800	0.0	0.8300	1020
$C_2H_3^+ + e^- \rightarrow C_2H_2 + H$	0.2780	-1.3800	0.0	1.7200	1023
$C_2H_3^+ + e^- \rightarrow CH_2 + CH$	0.0029	-1.3800	0.0	2.0000	1025
$C_2H_3^+ + e^- \rightarrow CH_3 + C$	0.0058	-1.3800	0.0	3.6000	1024
$C_2H_4^+ + e^- \rightarrow C_2H_2 + H_2$	0.0336	-0.7600	0.0	2.5600	89
$C_2H_5^+ + e^- \rightarrow C_2H_3 + H_2$	0.3000	-0.5000	0.0	0.0	1019
$C_2H_6^+ + e^- \rightarrow C_2H_4 + H_2$	0.3080	-0.5000	0.0	0.7000	87
$C_3^+ + e^- \rightarrow C_2 + C$	0.3000	-0.5000	0.0	5.2900	549
$C_3H^+ + e^- \rightarrow C_2H + C$	0.2280	-0.5000	0.0	27.8000	1039
$C_3H^+ + e^- \rightarrow C_3 + H$	0.1500	-0.5000	0.0	0.3900	94
$C_3H_2^+ + e^- \rightarrow C_2 + CH_2$	0.0300	-0.5000	0.0	15.9000	1034
$C_3H_2^+ + e^- \rightarrow C_2H + CH$	0.3420	-0.5000	0.0	19.6000	1038
$C_3H_2^+ + e^- \rightarrow C_2H_2 + C$	0.0300	-0.5000	0.0	12.4000	1036
$C_3H_2^+ + e^- \rightarrow C_3 + H_2$	0.0600	-0.5000	0.0	13.1000	1035
$C_3H_2^+ + e^- \rightarrow C_3H + H$	0.3420	-0.5000	0.0	8.0100	1037
$C_3H_3^+ + e^- \rightarrow C_3H + H_2$	0.3420	-0.5000	0.0	6.3500	1033
$C_3H_3^+ + e^- \rightarrow C_3H_2 + H$	0.3420	-0.5000	0.0	0.0	1032
$C_3H_4^+ + e^- \rightarrow C_3H_2 + H_2$	0.3420	-0.5000	0.0	5.4500	1031
$C_3H_4^+ + e^- \rightarrow C_3H_3 + H$	0.3420	-0.5000	0.0	7.2600	1030
$C_3H_5^+ + e^- \rightarrow CH_2C_2H_2 + H$	0.1500	0.5000	0.0	0.0	1115
$C_3H_5^+ + e^- \rightarrow CH_3C_2H + H$	0.1500	-0.5000	0.0	2.0700	93
$C_4H_2^+ + e^- \rightarrow C_2H + C_2H$	0.2500	-0.5000	0.0	0.0	86
$C_4H_5^+ + e^- \rightarrow CH_2C_2H_2 + CH$	0.1500	0.5000	0.0	27.0000	1114
$C_4H_5^+ + e^- \rightarrow CH_3C_2H + CH$	0.1500	-0.5000	0.0	3.4100	85
$CH^+ + e^- \rightarrow C + H$	0.1500	-0.4200	0.0	1.7200	100
$CH_2^+ + e^- \rightarrow CH + H$	0.1600	-0.6000	0.0	3.0300	528
$CH_2OH^+ + e^- \rightarrow H_2CO + H$	0.3200	-0.5000	0.0	6.7800	563
$CH_3^+ + e^- \rightarrow CH + H_2$	0.1950	-0.5000	0.0	0.0	529
$CH_3^+ + e^- \rightarrow CH_2 + H$	0.0775	-0.5000	0.0	2.1400	99
$CH_4^+ + e^- \rightarrow CH_2 + H_2$	0.1200	-0.5000	0.0	1.5200	97
$CH_4^+ + e^- \rightarrow CH_3 + H$	0.1750	-0.5000	0.0	4.9600	96
$CH_5^+ + e^- \rightarrow CH_4 + H$	0.0140	-0.5200	0.0	7.4500	95
$CHO^+ + e^- \rightarrow CO + H$	0.1100	-1.0000	0.0	16.9000	559
$CN^+ + e^- \rightarrow C + N$	0.1800	-0.5000	0.0	6.1400	565
$CO^+ + e^- \rightarrow C + O$	0.2000	-0.4800	0.0	1.6700	560
$CO^+ + e^- \rightarrow C(^1d) + O(^1d)$	0.2500	-0.5000	0.0	7.3800	561
$CO_2^+ + e^- \rightarrow CO + O$	0.3800	-0.5000	0.0	9.9800	571
$CO_2^+ + e^- \rightarrow CO + O(^1d)$	0.2920	-0.5000	0.0	9.8000	573
$CO_2^+ + e^- \rightarrow CO(^3p) + O$	0.0879	-0.5000	0.0	30.2000	572
$CO_2H^+ + e^- \rightarrow CO_2 + H$	0.0600	-0.6400	0.0	7.9000	574
$CS^+ + e^- \rightarrow C + S$	0.2000	-0.5000	0.0	11.2000	579
$H_2^+ + e^- \rightarrow H + H$	0.0160	-0.4300	0.0	1.6900	525
$H_2CN^+ + e^- \rightarrow HCN + H$	0.2130	-0.5000	0.0	5.1000	567
$H_2CN^+ + e^- \rightarrow HNC + H$	0.2130	-0.5000	0.0	4.0500	568
$H_2O^+ + e^- \rightarrow O + H_2$	0.0390	-0.5000	0.0	3.6200	541
$H_2O^+ + e^- \rightarrow O(^1d) + H_2$	0.0760	-0.5000	0.0	8.9600	542
$H_2O^+ + e^- \rightarrow OH + H$	0.0860	-0.5000	0.0	3.0000	540
$H_2S^+ + e^- \rightarrow HS + H$	0.1500	-0.5000	0.0	0.0	583
$H_3^+ + e^- \rightarrow H_2 + H$	0.0234	-0.5200	0.0	6.3800	526
$H_3CS^+ + e^- \rightarrow H_2CS + H$	0.3000	-0.5000	0.0	0.0	593
$H_3O^+ + e^- \rightarrow H_2O + H$	0.1080	-0.5000	0.0	3.0000	543
$H_3O^+ + e^- \rightarrow OH + H_2$	0.0602	-0.5000	0.0	3.0000	544
$H_3S^+ + e^- \rightarrow H_2S + H$	0.1850	-0.5000	0.0	6.5200	587
$HCN^+ + e^- \rightarrow CN + H$	0.2000	-0.5000	0.0	0.0	566
$HCS^+ + e^- \rightarrow CS + H$	0.1840	-0.5700	0.0	0.0	584
$HNS^+ + e^- \rightarrow NS + H$	0.3000	-0.5000	0.0	0.0	586
$HOCS^+ + e^- \rightarrow OCS + H$	0.2000	-0.5000	0.0	0.0	590

Continued on next page

Table F.13 – *Continued from previous page*

Dissociative Recombination (2 Product Species)	A	B	C	ΔE	#
$HOCS^+ + e^- \rightarrow OH + CS$	0.2000	-0.5000	0.0	0.0	589
$HS^+ + e^- \rightarrow S + H$	0.2000	-0.5000	0.0	19.1000	578
$HSO^+ + e^- \rightarrow SO + H$	0.2000	-0.5000	0.0	0.0	585
$N_2^+ + e^- \rightarrow N + N$	0.1700	-0.3000	0.0	0.4500	555
$N_2H^+ + e^- \rightarrow N_2 + H$	0.7600	-0.5000	0.0	1.2700	556
$NH^+ + e^- \rightarrow N + H$	0.0460	-0.5000	0.0	6.2100	531
$NH_2^+ + e^- \rightarrow NH + H$	0.3000	-0.5000	0.0	0.0	532
$NH_3^+ + e^- \rightarrow NH + H_2$	0.1000	-0.5000	0.0	3.8200	534
$NH_3^+ + e^- \rightarrow NH_2 + H$	0.1550	-0.5000	0.0	1.8400	533
$NH_4^+ + e^- \rightarrow NH_3 + H$	0.1170	-0.5000	0.0	7.4100	536
$NO^+ + e^- \rightarrow N + O$	0.4300	-0.3700	0.0	0.0	570
$NS^+ + e^- \rightarrow N + S$	0.2000	-0.5000	0.0	0.0	581
$O_2^+ + e^- \rightarrow O + O$	0.1950	-0.7000	0.0	6.7600	557
$O_2H^+ + e^- \rightarrow O_2 + H$	0.3000	-0.5000	0.0	14.0000	558
$OH^+ + e^- \rightarrow O + H$	0.0375	-0.5000	0.0	3.1600	539
$SO^+ + e^- \rightarrow S + O$	0.2000	-0.5000	0.0	0.7500	580

F.14 Dissociative Recombination (3 Product Species)

Dissociative Recombination (3 Product Species)	A	B	C	ΔE	#
$C_2H^+ + e^- \rightarrow C + C + H$	0.2890	-0.5000	0.0	3.0000	1028
$C_2H_2^+ + e^- \rightarrow C_2 + H + H$	0.1410	-0.5000	0.0	3.1600	1026
$C_2H_3^+ + e^- \rightarrow C_2 + H + H_2$	0.0287	-1.3800	0.0	7.4100	1022
$C_2H_3^+ + e^- \rightarrow C_2H + H + H$	0.5650	-1.3800	0.0	3.8200	1021
$C_2H_5^+ + e^- \rightarrow C_2H_2 + H_2 + H$	0.0812	-0.7900	0.0	3.4100	88
$C_3H^+ + e^- \rightarrow CH + C + C$	0.2280	-0.5000	0.0	3.6200	1040
$C_3H_2^+ + e^- \rightarrow C_3 + H + H$	0.0600	-0.5000	0.0	7.4500	550
$C_3H_4^+ + e^- \rightarrow C_3 + H_2 + H_2$	0.5000	-0.5000	0.0	4.9600	552
$CH_3^+ + e^- \rightarrow CH + H + H$	0.2000	-0.4000	0.0	6.8600	530
$CH_4^+ + e^- \rightarrow CH + H_2 + H$	0.1200	-0.5000	0.0	0.7000	523
$CH_4^+ + e^- \rightarrow CH_2 + H + H$	0.1750	-0.5000	0.0	0.0	98
$CH_4N^+ + e^- \rightarrow CN + H_2 + H_2$	0.0300	-0.5000	0.0	3.0300	577
$CH_4N^+ + e^- \rightarrow HCN + H_2 + H$	0.3000	-0.5000	0.0	6.3800	576
$CO_2H^+ + e^- \rightarrow CO + O + H$	0.8100	-0.6400	0.0	1.6900	575
$H_2CN^+ + e^- \rightarrow CN + H + H$	0.2130	-0.5000	0.0	1.7200	569
$H_2CO^+ + e^- \rightarrow CO + H + H$	0.5000	-0.5000	0.0	2.1400	562
$H_2CO_2^+ + e^- \rightarrow CO + OH + H$	0.2000	-0.5000	0.0	1.5200	554
$H_2CS^+ + e^- \rightarrow CS + H + H$	0.3000	-0.5000	0.0	0.0	591
$H_2S^+ + e^- \rightarrow S + H + H$	0.1500	-0.5000	0.0	0.0	582
$H_3^+ + e^- \rightarrow H + H + H$	0.0436	-0.5200	0.0	2.5600	527
$H_3CS^+ + e^- \rightarrow CS + H + H_2$	0.3000	-0.5000	0.0	1.8400	592
$H_3O^+ + e^- \rightarrow OH + H + H$	0.2580	-0.5000	0.0	0.3900	545
$H_3S^+ + e^- \rightarrow HS + H + H$	0.1850	-0.5000	0.0	6.2100	588
$NH_3^+ + e^- \rightarrow NH + H + H$	0.1550	-0.5000	0.0	12.0000	535
$NH_4^+ + e^- \rightarrow NH_2 + H + H$	0.1300	-0.5000	0.0	2.0700	537

F.15 Dissociative Recombination (4 Product Species)

Dissociative Recombination (4 Product Species)	A	B	C	ΔE	#
$C_3H^+ + e^- \rightarrow C + C + C + H$	0.2280	-0.5000	0.0	6.8600	1041
$C_3H_3^+ + e^- \rightarrow C_3 + H + H + H$	0.5000	-0.5000	0.0	0.0	551
$C_3H_5^+ + e^- \rightarrow C_3 + H_2 + H_2 + H$	0.2500	-0.5000	0.0	0.7000	553
$CH_2OH^+ + e^- \rightarrow CO + H + H + H$	0.3200	-0.5000	0.0	2.5600	564
$CH_4^+ + e^- \rightarrow CH + H + H + H$	0.1200	-0.5000	0.0	3.4100	524

F.16 e^- Impact Excitation

e^- Impact Excitation	A	B	C	ΔE	#
$CO + e^- \rightarrow CO(^1p) + e^-$	0.0045	0.2030	9.5E+04	3.4100	335
$CO + e^- \rightarrow CO(^3d) + e^-$	0.0008	-0.0400	1.0E+05	2.5600	338
$CO + e^- \rightarrow CO(^3p) + e^-$	0.1630	-0.4180	8.4E+04	0.0	336
$CO + e^- \rightarrow CO(^3s) + e^-$	0.0029	0.1070	9.1E+04	0.7000	337

F.17 Dissociative e^- Impact Ionization

Dissociative e^- Impact Ionization	A	B	C	ΔE	#
$C_2H_2 + e^- \rightarrow C_2H^+ + H + e^- + e^-$	0.0003	0.7385	1.4E+05	6.3800	1055
$C_2H_3 + e^- \rightarrow C_2H^+ + H_2 + e^- + e^-$	0.0006	0.7250	1.4E+05	3.0300	1056
$C_2H_3 + e^- \rightarrow C_2H_2^+ + H + e^- + e^-$	0.0001	0.7313	1.4E+05	0.0	1057
$C_2H_4 + e^- \rightarrow C_2H_2^+ + H_2 + e^- + e^-$	0.0006	0.7266	1.4E+05	6.2100	1058
$C_2H_4 + e^- \rightarrow C_2H_3^+ + H + e^- + e^-$	0.0001	0.7335	1.4E+05	0.0	1059
$C_2H_5 + e^- \rightarrow C_2H_3^+ + H_2 + e^- + e^-$	0.0006	0.7378	1.4E+05	1.8400	1060
$C_2H_5 + e^- \rightarrow C_2H_4^+ + H + e^- + e^-$	0.0001	0.7298	1.4E+05	3.8200	1061
$C_2H_6 + e^- \rightarrow C_2H_4^+ + H_2 + e^- + e^-$	0.0007	0.7355	1.4E+05	7.4100	1062
$C_2H_6 + e^- \rightarrow C_2H_5^+ + H + e^- + e^-$	0.0001	0.7286	1.4E+05	3.1600	1063
$C_3H_2 + e^- \rightarrow C_3H^+ + H + e^- + e^-$	0.0004	0.7349	1.4E+05	2.1400	1052
$C_3H_3 + e^- \rightarrow C_3H_2^+ + H + e^- + e^-$	0.0001	0.7301	1.4E+05	1.7200	1053
$CH_2C_2H_2 + e^- \rightarrow C_3H_3^+ + H + e^- + e^-$	0.0002	0.7290	1.4E+05	3.0000	1146
$CH_3C_2H + e^- \rightarrow C_3H_3^+ + H + e^- + e^-$	0.0002	0.7287	1.4E+05	1.6900	1054
$CO + e^- \rightarrow C^+ + O + e^- + e^-$	3.5E-06	1.0550	7.3E+04	0.7000	454
$CO_2 + e^- \rightarrow CO^+ + O + e^- + e^-$	9.0E-06	1.0900	2.7E+05	6.8600	456
$CO_2 + e^- \rightarrow O^+ + CO + e^- + e^-$	9.0E-06	1.0900	2.7E+05	2.5600	455
$H_2O + e^- \rightarrow H^+ + OH + e^- + e^-$	1.1E-07	2.0200	1.0E+05	2.0700	458
$H_2O + e^- \rightarrow H_2^+ + O + e^- + e^-$	1.6E-06	0.6300	1.2E+05	0.3900	459
$H_2O + e^- \rightarrow O^+ + H_2 + e^- + e^-$	8.5E-10	2.0000	9.7E+04	7.4500	460
$H_2O + e^- \rightarrow OH^+ + H + e^- + e^-$	5.0E-07	1.4500	1.1E+05	12.0000	457
$N_2 + e^- \rightarrow N^+ + N + e^- + e^-$	2.3E-09	2.3400	1.3E+05	3.4100	452
$NO + e^- \rightarrow N^+ + O + e^- + e^-$	1.0E-06	1.4200	2.5E+05	4.9600	461
$NO + e^- \rightarrow O^+ + N + e^- + e^-$	1.0E-06	1.4200	2.5E+05	1.5200	462
$O_2 + e^- \rightarrow O^+ + O + e^- + e^-$	1.6E-08	2.0900	9.8E+05	0.0	453

F.18 Radiative De-Excitation

Radiative De-Excitation	A	B	C	ΔE	#
$C(^1d) \rightarrow C + \gamma$	340.0000	0.0	0.0	12.0000	344
$CO(^1p) \rightarrow CO + \gamma$	9.7E+13	0.0	0.0	2.0700	345
$CO(^3d) \rightarrow CO + \gamma$	10.0000	0.0	0.0	4.9600	348
$CO(^3d) \rightarrow CO(^3p) + \gamma$	2.4E+11	0.0	0.0	2.1400	350
$CO(^3p) \rightarrow CO + \gamma$	1.3E+08	0.0	0.0	0.3900	346
$CO(^3s) \rightarrow CO + \gamma$	1.0E+11	0.0	0.0	7.4500	347
$CO(^3s) \rightarrow CO(^3p) + \gamma$	1.0E+11	0.0	0.0	1.5200	349
$O(^1d) \rightarrow O + \gamma$	6800.0000	0.0	0.0	3.4100	339
$O(^1s) \rightarrow O(^1d) + \gamma$	1.3E+06	0.0	0.0	0.0	340
$S(^1d) \rightarrow S + \gamma$	3.6E+04	0.0	0.0	0.7000	341
$S(^1s) \rightarrow S + \gamma$	3.6E+05	0.0	0.0	6.8600	343
$S(^1s) \rightarrow S(^1d) + \gamma$	1.8E+06	0.0	0.0	2.5600	342

Bibliography

Ackerman, M. (**1971**): Ultraviolet Solar Radiation Related to Mesospheric Processes, in: **G. Fiocco** (Editor), Mesospheric Models and Related Experiments, vol. 25 of *Astrophysics and Space Science Library*, 149–+.

Adachi, H., Basco, N., and James, D. G. L. (**1979**): A quantitative study of alkyl radical reactions by kinetic spectroscopy III. Absorption spectrum and rate constants of mutual interaction for the ethyl radical, International Journal of Chemical Kinetics, 11(9):995–1005.

A'Hearn, M. and Cowan, J. (**1980**): Vaporization in Comets: The icy grain halo of Comet West, The Moon and the Planets, 23:41 – 52.

A'Hearn, M. and Millis, R. (**1980**): Abundance correlation among Comets, The Astronomical Journal, 85:1528 – 1537.

A'Hearn, M., Millis, R., Schleicher, D., and Osip, D. (**1995**): The ensemble properties of comets: Results from narrow-band photometry of 85 Comets, 1976-1992, Icarus, 118:223 – 270.

A'Hearn, M. F. (**2011**): Comets as Building Blocks, ARA&A, 49:281–299.

A'Hearn, M. F., Belton, M. J. S., Delamere, W. A., Kissel, J. et al. (**2005**): Deep Impact: Excavating Comet Tempel 1, Science, 310:258–264.

A'Hearn, M. F. and Deep Impact Team (**2006**): Deep Impact: Excavating Comet Tempel 1, in: **Mackwell, S. and Stansbery, E.** (Editors), 37th Annual Lunar and Planetary Science Conference, vol. 37 of *Lunar and Planetary Inst. Technical Report*, 1978.

Ahmed, M., Peterka, D. S., and Suits, A. G. (**1999**): The photodissociation of the vinyl radical (C_2H_3) at 243 nm studied by velocity map imaging, J. Chem. Phys., 110:4248–4253.

Aitkison, J. (**1986**): The Statistical Analysis of Compositional Data, 416 p.

Alexander, C. M. O., Cody, G. D., Fogel, M., and Yabuta, H. (**2008**): Organics in meteorites - Solar or interstellar?, Proceedings of the International Astronomical Union, 4(Symposium S251):293–298.

Alman, D. A., Ruzic, D. N., and Brooks, J. N. (**2000**): A hydrocarbon reaction model for low temperature hydrogen plasmas and an application to the Joint European Torus, Physics of Plasmas, 7:1421–1432.

Altwegg, K. (**2009**): Rapporteur Paper on the Composition of Comets, 291.

Altwegg, K., Balsiger, H., and Geiss, J. (**1999**): Composition of the Volatile Material in Halley's Coma from In Situ Measurements, Space Sci. Rev., 90:3–18.

Andrieux, D., Bénilan, Y., de Vanssay, E., Paillous, P. et al. (**1995**): Absorption coefficient of propynenitrile in the mid-UV range for the study of Titan's atmosphere: Solution to sample contaminations, J. Geophys. Res., 100:9455–9460.

Ashihara, O. (**1975**): The electron energy loss rates by polar molecules, Tokyo University Institute of Space and Aeronautical Science Report, 40:257–275.

Atkinson, D. B. and Hudgens, J. W. (**1999**): Rate Coefficients for the Propargyl Radical Self-Reaction and Oxygen Addition Reaction Measured Using Ultraviolet Cavity Ring-down Spectroscopy, The Journal of Physical Chemistry A, 103(21):4242–4252.

Au, J., Cooper, G., Burton, G., Olney, T., and Brian, C. (**1993**): The valence shell photoabsorption of the linear alkanes, C_nH_{2n+2} (n = 18): absolute oscillator strengths (7-220 eV), Chemical Physics, 173:209–239.

Balsiger, H., Altwegg, K., Bochsler, P., Eberhardt, P. et al. (**2007**): Rosina - Rosetta Orbiter Spectrometer for Ion and Neutral Analysis, Space Science Reviews, 128(1-4):745–801.

Barfield, W., Koontz, G., and Huebner, W. (**1972**): Fits to new calculations of photoionization cross sections for low-Z elements, J. Quant. Spec. Radiat. Transf., 12:1409–1433.

Becker, L., Poreda, R. J., and Bunch, T. E. (**2000**): Fullerenes: An extraterrestrial carbon carrier phase for noble gases, Proceedings of the National Academy of Science, 97:2979–2983.

Belton, M. J. S., Thomas, P. C., Carcich, B., Crockett, C. J., and Deep Impact Science Team (**2006**): The Spin State of 9P/Tempel 1, in: **Mackwell, S. and Stansbery, E.** (Editors), 37th Annual Lunar and Planetary Science Conference, vol. 37 of *Lunar and Planetary Inst. Technical Report*, 1487.

Bénilan, Y., Andrieux, D., and Bruston, P. (**1995**): Mid-UV acetylene cross-sections revisited: Sample contamination risk in source data, Geophys. Res. Lett., 22:897–900.

Bénilan, Y., Bruston, P., Raulin, F., Cossart-Magos, C., and Guillemin, J. (**1994**): Mid-UV spectroscopy of propynenitrile at low temperature: consequences on expected results from observations of Titan's atmosphere., J. Geophys. Res., 99:17–+.

Bénilan, Y., Jolly, A., and Raulin, F. (**1999**): Comparative UV and IR spectroscopic studies of allene and methylacetylene: implications for observations and modeling of Titan atmosphere., in: Bulletin of the American Astronomical Society, vol. 31 of *Bulletin of the American Astronomical Society*, 1169.

Bénilan, Y., Smith, N., Jolly, A., and Raulin, F. (**2000**): The long wavelength range temperature variations of the mid-UV acetylene absorption coefficient, Planet. Space Sci., 48:463–471.

Benkhoff, J. and Huebner, W. F. (**1995**): Influence of the vapor flux on temperature, density, and abundance distributions in a multicomponent, porous, icy body, Icarus, 114:348–354.

Benneke, B. and Seager, S. (**2012**): Atmospheric Retrieval for Super-Earths: Uniquely Constraining the Atmospheric Composition with Transmission Spectroscopy, ApJ, 753:100.

Benson, S. (**1976**): Thermochemical Kinetics: Methods for the Estimation of Thermo-chemical Data and Rate Parameters, John Wiley & Sons, Inc.

Bergin, E. A., Goldsmith, P. F., Snell, R. L., and Ungerechts, H. (**1994**): CH_3C_2H as a temperature probe in dense giant molecular cloud cores, ApJ, 431:674–688.

Bird, M. K., Huchtmeier, W. K., Gensheimer, P., Wilson, T. L. et al. (**1997**): Radio detection of ammonia in comet Hale-Bopp., A&A, 325:L5–L8.

Biver, N., Bockelée-Morvan, D., Colom, P., Crovisier, J. et al. (**1997**): Long-term Evolution of the Outgassing of Comet Hale-Bopp From Radio Observations, Earth Moon and Planets, 78:5–11.

Biver, N., Bockelée-Morvan, D., Colom, P., Crovisier, J. et al. (**2009**): Periodic variation in the water production of comet C/2001 Q4 (NEAT) observed with the Odin satellite, A&A, 501:359–366.

Biver, N., Bockelée-Morvan, D., Colom, P., Crovisier, J. et al. (**2011**): Molecular investigations of comets C/2002 X5 (Kudo-Fujikawa), C/2002 V1 (NEAT), and C/2006 P1 (McNaught) at small heliocentric distances, A&A, 528:A142.

Biver, N., Bockelée-Morvan, D., Crovisier, J., Colom, P. et al. (**2002**): Chemical Composition Diversity Among 24 Comets Observed At Radio Wavelengths, Earth Moon and Planets, 90:323–333.

Biver, N., Bockelée-Morvan, D., Crovisier, J., Davies, J. et al. (**1999**): Spectroscopic monitoring of Comet C/1996 B2 (Hyakutake) with the JCMT and IRAM Radio Telescopes, The Astronomical Journal, 118:1850 – 1872.

Biver, N., Bockelée-Morvan, D., Crovisier, J., Lis, D. et al. (**2006**): Radio wavelength molecular observations of comets C/1999 T1 (McNaught-Hartley), C/2001 A2 (LINEAR), C/2000 WM1 (LINEAR) and 153P/Ikeya-Zhang, Astronomy and Astrophysics, 449:1255 – 1270.

Blanksby, S. and Ellison, G. (**2003**): Bond Dissociation Energies of Organic Molecules, Accounts of Chemical Research, 36(4):255–263.

Blomberg, M. R. A. and Liu, B. (**1985**): A theoretical investigation of the UV spectrum of ethyl radical, J. Chem. Phys., 83:3995–4000.

Bockelée-Morvan, D. (**2011**): An Overview of Comet Composition, in: IAU Symposium, vol. 280 of *IAU Symposium*, 261–274.

Bockelée-Morvan, D. and Crovisier, J. (**2002**): Lessons of Comet Hale-Bopp for Coma Chemistry: Observations and Theory, Earth Moon and Planets, 89:53–71.

Bockelée-Morvan, D., Crovisier, J., Mumma, M. J., and Weaver, H. A. (**2004**): The composition of cometary volatiles, 391–423.

Bockelée-Morvan, D., Gautier, D., Hersant, F., Huré, J.-M., and Robert, F. (**2002**): Turbulent radial mixing in the solar nebula as the source of crystalline silicates in comets., A&A, 384:1107–1118.

Bockelée-Morvan, D., Lis, D. C., Wink, J. E., Despois, D. et al. (**2000**): New molecules found in comet C/1995 O1 (Hale-Bopp). Investigating the link between cometary and interstellar material, A&A, 353:1101–1114.

Bogumil, K., Orphal, J., Homann, T., Voigt, S. et al. (**2003**): Measurements of molecular absorption spectra with the SCIAMACHY pre-flight model: instrument characterization and reference data for atmospheric remote-sensing in the 230-2380 nm region, Journal of Photochemistry and Photobiology A: Chemistry, 157(2-3):167 – 184.

Boice, D. C., Huebner, W. F., Keady, J. J., Schmidt, H. U., and Wegmann, R. (**1986**): A model of Comet P/Giacobini-Zinner, Geophys. Res. Lett., 13:381–384.

Boice, D. C., Huebner, W. F., Keady, J. J., Schmidt, H. U., and Wegmann, R. (**1998**): A Model of Comet P / Giacobini-Zinner (GRL 13(4) 1986), 206.

Botter, R., Dibeler, V. H., Walker, J. A., and Rosenstock, H. M. (**1966**): Mass-Spectrometric Study of Photoionization. IV. Ethylene and 1,2-Dideuteroethylene, J. Chem. Phys., 45:1298–1301.

Brooke, T., Tokunaga, A., Weaver, H., Crovisier, J. et al. (**1996**a): Bulletin of the American Astronomical Society, 28.

Brooke, T., Tokunaga, A., Weaver, H., Crovisier, J. et al. (**1996**b): Detection of Acetylene in the infrared spectrum of Comet Hyakutake, Nature, 383:606 – 608.

Brownlee, D., Tsou, P., Aléon, J., Alexander, C. M. O. . et al. (**2006**): Comet 81P/Wild 2 Under a Microscope, Science, 314:1711–.

Bruna, P. J. and Grein, F. (**2001**): Spectroscopy of the C_2 molecule: Valence and Rydberg states in the 7-10 eV region. An ab initio study, Canadian Journal of Physics, 79:653–671.

Bruston, P., Poncet, H., Raulin, F., Cossart-Magos, C., and Courtin, R. (**1989**): UV Spectroscopy of Titan's Atmosphere, Planetary Organic Chemistry, and Prebiological Synthesis, Icarus, 78:38–53.

Burrows, J., Richter, A., Dehn, A., Deters, B. et al. (**1999**): Atmospheric remote-sensing reference data from GOME: Part 2. Temperature-dependent absorption cross-sections of O3 in the 231-794 nm range, J. Quant. Spectrosc. Radiat. Transfer, (61):509–517.

Cabrera, J., Bruntt, H., Ollivier, M., Díaz, R. F. et al. (**2010**): Transiting exoplanets from the CoRoT space mission . XIII. CoRoT-13b: a dense hot Jupiter in transit around a star with solar metallicity and super-solar lithium content, A&A, 522:A110.

Cami, J., Bernard-Salas, J., Peeters, E., and Malek, S. E. (**2010**): Detection of C_{60} and C_{70} in a Young Planetary Nebula, Science, 329:1180–.

Cao, Z., Mühlhäuser, M., Hanrath, M., and Peyerimhoff, S. (**2002**): Study of possible photodissociation channels in linear carbon clusters C_n ($n = 4-6$), Chemical Physics Letters, 351(3-4):327 – 334.

Carrasco, N., Hébrard, E., Banaszkiewicz, M., Dobrijevic, M., and Pernot, P. (**2007**): Influence of neutral transport on ion chemistry uncertainties in Titan ionosphere, Icarus, 192:519–526.

Carrasco, N., Plessis, S., Dobrijevic, M., and Pernot, P. (**2008**): Toward a reduction of the bimolecular reaction model for titan's ionosphere, International Journal of Chemical Kinetics, 40(11):699–709.

Castiglioni, L., Vukovic, S., Crider, P. E., Lester, W. A., and Neumark, D. M. (**2010**): Intramolecular competition in the photodissociation of C_3D_3 radicals at 248 and 193 nm, Physical Chemistry Chemical Physics (Incorporating Faraday Transactions), 12:10714.

Cernicharo, J., Guélin, M., Agündez, M., Kawaguchi, K. et al. (**2007**): Astronomical detection of C_4H^-, the second interstellar anion, A&A, 467:L37–L40.

Cernicharo, J., Heras, A. M., Tielens, A. G. G. M., Pardo, J. R. et al. (**2001**): Infrared Space Observatory's Discovery of C_4H_2, C_6H_2, and Benzene in CRL 618, ApJ, 546:L123–L126.

Chabot, M., Tuna, T., Béroff, K., Pino, T. et al. (**2010**): Statistical universal branching ratios for cosmic ray dissociation, photodissociation, and dissociative recombination of the $C_{n=2-10}$, $C_{n=2-4}H$ and C_3H_2 neutral and cationic species, A&A, 524:A39+.

Chaffee, F. H., Jr., Lutz, B. L., Black, J. H., Vanden Bout, P. A., and Snell, R. L. (**1980**): Rotational fine-structure lines of interstellar C_2 toward Zeta Persei, ApJ, 236:474–480.

Chaizy, P., Reme, H., Sauvaud, J. A., D'Uston, C. et al. (**1991**): Negative ions in the coma of Comet Halley, Nature, 349:393–396.

ChemSpider (**2014**): ChemSpider, `http://www.chemspider.com`.

Chen, B.-Z. and Huang, M.-B. (**2004**): Dissociation reactions of the vinyl radical in the A^2A'' state, Chemical Physics, 300(1-3):325 – 334.

Chen, F., Judge, D., and Wu, C. (**2000**): Temperature dependent photoabsorption cross sections of allene and methylacetylene in the VUV-UV region, Chemical Physics, 260:215–223.

Chen, F., Judge, D. L., Wu, C. Y. R., Caldwell, J. et al. (**1991**): High-resolution, low-temperature photoabsorption cross sections of C_2H_2, PH_3, AsH_3, and GeH_4, with application to Saturn's atmosphere, J. Geophys. Res., 961:17519–+.

Chen, F. Z. and Wu, C. Y. R. (**2004**): Temperature-dependent photoabsorption cross sections in the VUV-UV region. I. Methane and ethane, J. Quant. Spec. Radiat. Transf., 85:195–209.

Cheng, B.-M., Chen, H.-F., Lu, H.-C., Chen, H.-K. et al. (**2011**): Absorption Cross Section of Gaseous Acetylene at 85 K in the Wavelength Range 110-155 nm, ApJS, 196:3.

Cheng, B.-M., Lu, H.-C., Chen, H.-K., Bahou, M. et al. (**2006**): Absorption Cross Sections of NH_3, NH_2D, NHD_2, and ND_3 in the Spectral Range 140-220 nm and Implications for Planetary Isotopic Fractionation, ApJ, 647:1535–1542.

Chin, Y.-N., Kaiser, R. I., Lemme, C., and Henkel, C. (**2006**): Detection of Interstellar Cyanoallene and its Implications for Astrochemistry, in: **Kaiser, R. I., Bernath, P., Osamura, Y., Petrie, S., and Mebel, A. M.** (Editors), Astrochemistry - From Laboratory Studies to Astronomical Observations, vol. 855 of *American Institute of Physics Conference Series*, 149–153.

Choi, H., Bise, R. T., Hoops, A. A., Mordaunt, D. H., and Neumark, D. M. (**2000**): Photodissociation of Linear Carbon Clusters C_n (n = 4-6), The Journal of Physical Chemistry A, 104(10):2025–2032.

Churyumov, K. I., Filonenko, V. S., and Chubko, L. S. (**2008**a): Light curves and photometric parameters of the comets C/1999 S4 (LINEAR), C/2001 Q4 (NEAT), C/2002 T7 (LINEAR), C/2002 V1 (NEAT), C2004 Q2 (Machholz), and 153P/2002 C1 (Ikeya-Zhang), Kinematics and Physics of Celestial Bodies, 24:105–111.

Churyumov, K. I., Filonenko, V. S., and Chubko, L. S. (**2008**b): The light curve of the comet 9P/Tempel 1: Temporal evolution from 1867 till 2005, Kinematics and Physics of Celestial Bodies, 24:327–330.

Clarke, D. W. and Ferris, J. P. (**1995**): Photodissociation of cyanoacetylene: Application to the atmospheric chemistry of Titan, Icarus, 115:119–125.

Clemett, S. J., Sandford, S. A., Nakamura-Messenger, K., Hörz, F., and McKay, D. S. (**2010**): Complex aromatic hydrocarbons in Stardust samples collected from comet 81P/Wild 2, Meteoritics & Planetary Science, 45(5):701–722.

Cochran, A. (**1985**): A re-evaluation of the Haser Model scale length for Comets, The Astronomical Journal, 90:2609 – 2614.

Cochran, A., Barker, E., Ramseyer, T., and Storrs, A. (**1992**): The McDonald Observatory Faint Comet Survey: Gas production in 17 Comets, Icarus, 98:151 – 162.

Cochran, A. L., Barker, E. S., and Gray, C. L. (**2012**): Thirty years of cometary spectroscopy from McDonald Observatory, Icarus, 218:144–168.

Cochran, A. L., Jackson, W. M., Meech, K. J., and Glaz, M. (**2007**): Observations of Comet 9P/Tempel 1 with the Keck 1 HIRES instrument during Deep Impact, Icarus, 187:156–166.

Cody, G. D., Alexander, C. M. O., Kilcoyne, A. L. D., and Yabuta, H. (**2008**): Unraveling the chemical history of the Solar System as recorded in extraterrestrial organic matter, Proceedings of the International Astronomical Union, 4(Symposium S251):277–284.

Combi, M. (**2000**): Hale-Bopp: What Makes a Big Comet Different? Coma Dynamics: Observations and Theory, Earth Moon and Planets, 89:73–90.

Combi, M., Reinard, A., Bertaux, J.-L., Quémerais, E., and Mäkinen, T. (**2000**): SOHO/SWAN observations of the structure and evolution of the Hydrogen Lyman-α coma of Comet Hale-Bopp (1995 O1), Icarus, 144:191 – 202.

Combi, M. R. and Feldman, P. D. (**1993**): Water production rates in Comet P/Halley from IUE observations of H I Lyman-alpha, Icarus, 105:557.

Combi, M. R. and Fink, U. (**1997**): A Critical Study of Molecular Photodissociation and CHON Grain Sources for Cometary C_2, ApJ, 484:879.

Combi, M. R., Harris, W. M., and Smyth, W. H. (**2004**): Gas dynamics and kinetics in the cometary coma: theory and observations, 523–552.

Connors, K. (**1990**): Chemical Kinetics, VCH, Weinheim.

Connors, R. E., Roebber, J. L., and Weiss, K. (**1974**): Vacuum Ultraviolet Spectroscopy of Cyanogen and Cyanoacetylenes, J. Chem. Phys., 60:5011–5024.

Cooper, G., Burton, G. R., and Brion, C. E. (**1995**): Absolute UV and soft X-ray photoabsorption of acetylene by high resolution dipole (e,e) spectroscopy, Journal of Electron Spectroscopy and Related Phenomena, 73(2):139 – 148, a Collection of Invited Papers in Honour of the Late Professor W.C. (Bill) Price.

Cooper, G., Olney, T. N., and Brion, C. E. (**1995**): Absolute UV and Soft X-ray photoabsorption of ethylene by high resolution dipole (e,e) spectroscopy, Chemical Physics, 194:175–184.

Coradini, A., Capaccioni, F., Drossart, P., Arnold, G. et al. (**2007**): Virtis: An Imaging Spectrometer for the Rosetta Mission, Space Science Reviews, 128(1-4):529–559.

Cordiner, M. A. and Charnley, S. B. (**2012**): Gas-Grain Models for Interstellar Anion Chemistry, ApJ, 749:120.

Cordiner, M. A. and Charnley, S. B. (**2013**): Negative ion chemistry in the coma of comet 1p/halley, Meteoritics & Planetary Science.

Cordiner, M. A., Charnley, S. B., Buckle, J. V., Walsh, C., and Millar, T. J. (**2011**): Discovery of Interstellar Anions in Cepheus and Auriga, ApJ, 730:L18.

Cordiner, M. A. and Millar, T. J. (**2009**): Density-Enhanced Gas and Dust Shells in a New Chemical Model for IRC+10216, ApJ, 697:68–78.

Cottin, H. and Fray, N. (**2008**): Distributed Sources in Comets, Space Sci. Rev., 138:179–197.

Cravens, T. E. and Gombosi, T. I. (**2004**): Cometary magnetospheres: a tutorial, Advances in Space Research, 33:1968–1976.

Cravens, T. E. and Korosmezey, A. (**1986**): Vibrational and rotational cooling of electrons by water vapor, Planet. Space Sci., 34:961–970.

Crider, P. E., Castiglioni, L., Kautzman, K. E., and Neumark, D. M. (**2009**): Photodissociation of the propargyl and propynyl (C_3D_3) radicals at 248 and 193 nm, J. Chem. Phys., 130(4):044310.

Crifo, J. F. (**1991**): Hydrodynamic models of the collisional coma, in: **Newburn, R. L., Jr., Neugebauer, M., and Rahe, J.** (Editors), IAU Colloq. 116: Comets in the post-Halley era, vol. 167 of *Astrophysics and Space Science Library*, 937–989.

Crifo, J. F., Fulle, M., Kömle, N. I., and Szego, K. (**2004**): Nucleus-coma structural relationships: lessons from physical models, 471–503.

Crovisier, J. (**1994**): Photodestruction rates for cometary parent molecules, J. Geophys. Res., 3777–3781.

Crovisier, J. (**2007**): Cometary diversity and cometary families, ArXiv Astrophysics e-prints.

Crovisier, J., Biver, N., Bockelée-Morvan, D., Boissier, J. et al. (**2009**a): The Chemical Diversity of Comets: Synergies Between Space Exploration and Ground-based Radio Observations, Earth Moon and Planets, 105:267–272.

Crovisier, J., Biver, N., Bockelée-Morvan, D., and Colom, P. (**2009**b): Radio observations of Jupiter-family comets, Planet. Space Sci., 57:1162–1174.

Crovisier, J., Bockelée-Morvan, D., Colom, P., Biver, N. et al. (**2004**): The composition of ices in comet C/1995 O1 (Hale-Bopp) from radio spectroscopy. Further results and upper limits on undetected species, A&A, 418:1141–1157.

Crovisier, J. and Encrenaz, T. (**2000**): Comet Science. The study of remnants from the birth of the solar system, Cambridge University Press.

Csizmadia, S. (**2013**): Personal communication.

Dello Russo, N., Mumma, M., DiSanti, M., Magee-Sauer, K., and Novak, R. (**2001**): Ethane production and release in Comet C/1995 O1 Hale-Bopp, Icarus, 153:162 – 179.

Dello Russo, N., Mumma, M. J., Disanti, M. A., Magee-Sauer, K. et al. (**2006**a): A high-resolution infrared spectral survey of Comet C/1999 H1 Lee, Icarus, 184:255–276.

Dello Russo, N., Vervack, R. J., Jr., Lisse, C. M., Weaver, H. A. et al. (**2011**): The Volatile Composition and Activity of Comet 103P/Hartley 2 During the EPOXI Closest Approach, ApJ, 734:L8.

Dello Russo, N., Vervack Jr., R., Weaver, H., Biver, N. et al. (**2007**): Compositional homogeneity in the fragmented Comet 73P/Schwassmann-Wachmann 3, Nature, 448:172 – 175.

Dello Russo, N., Weaver Jr., H., Lisse, C., and Vervack Jr., R. (**2006**b): Comet Chemistry: Obtaining Clues to the Formation and Evolution of the Solar System with High-Resolution Infrared Spectroscopy, Johns Hopkins APL Technical Digest, 27(2):121–132.

Demtröder, W. (**2003**): Molekülphysik, Oldenbourg Verlag München Wien.

DeSain, J. D. and Taatjes, C. A. (**2003**): Infrared Laser Absorption Measurements of the Kinetics of Propargyl Radical Self-Reaction and the 193 nm Photolysis of Propyne, The Journal of Physical Chemistry A, 107(24):4843–4850.

Despois, D., Biver, N., Bockelée-Morvan, D., and Crovisier, J. (**2005**): Observations of Molecules in Comets, in: **D. C. Lis, . E. H., G. A. Blake** (Editor), Astrochemistry: Recent Successes and Current Challenges, vol. 231 of *IAU Symposium*, 469–478.

Despois, D. and Cottin, H. (**2005**): Comets: Potential sources of prebiotic molecules for the early earth, in: **Gargaud, M., Barbier, B., Martin, H., and Reisse, J.** (Editors), Lectures in Astrobiology, Advances in Astrobiology and Biogeophysics, 289–352, Springer Berlin Heidelberg.

Devroye, L. (**1986**): Non- Uni form Random Variate Generation, Springer-Verlag New York Inc.

Deyerl, H.-J., Fischer, I., and Chen, P. (**1999**): Photodissociation dynamics of the propargyl radical, J. Chem. Phys., 111:3441–3448.

Díaz-Tendero, S., Sánchez, G., Alcamí, M., Martín, F. et al. (**2006**): Fragmentation of small neutral carbon clusters, International Journal of Mass Spectrometry, 252:126–132.

DiSanti, M., Villanueva, G., Bonev, B., Magee-Sauer, K. et al. (**2007**): Temporal evolution of parent volatiles and dust in Comet 9P/Tempel 1 resulting from the Deep Impact experiment, Icarus, 187:240 – 252.

Disanti, M. A. and Mumma, M. J. (**2008**): Reservoirs for Comets: Compositional Differences Based on Infrared Observations, Space Sci. Rev., 138:127–145.

Dobrijevic, M., Hébrard, E., Plessis, S., Carrasco, N. et al. (**2010**): Comparison of methods for the determination of key reactions in chemical systems: Application to Titan's atmosphere, Advances in Space Research, 45:77–91.

Donati, G. B. (**1864**): Schreiben des Herrn Prof. Donati an den Herausgeber, Astronomische Nachrichten, 62:375.

Douglas, A. E. (**1951**): Laboratory Studies of the λ 4050 Group of Cometary Spectra., ApJ, 114:466.

Draine, B. T. (**1980**): Interstellar shock waves with magnetic precursors, ApJ, 241:1021–1038.

Draine, B. T. (**1986**): Multicomponent, reacting MHD flows, MNRAS, 220:133–148.

Drake, G. W. F. (Editor) (**2006**): Handbook of Atomic, Molecular and Optical Physics, Springer.

Dusick, D. (**2012**): BOLD Educational Software digital textbook, Introduction to Inferential Statistics, `http://bold-ed.com/statsbook.htm`.

Eisfeld, W. (**2006**): Calculation of the Vibrationally Resolved Electronic Absorption Spectrum of the Propargyl Radical (H_2CCCH), The Journal of Physical Chemistry A, 110(11):3903–3910.

Engel, V., Staemmler, V., Vander Wal, R. L., Crim, F. F. et al. (**1992**): Photodissociation of water in the first absorption band: a prototype for dissociation on a repulsive potential energy surface, The Journal of Physical Chemistry, 96(8):3201–3213.

Fahr, A., Hassanzadeh, P., and Atkinson, D. (**1998**): Ultraviolet absorption spectrum and cross-sections of vinyl (C_2H_3) radical in the 225-238 nm region, Chemical Physics, 236:43–51.

Fahr, A., Hassanzadeh, P., Laszlo, B., and Huie, R. (**1997**): Ultraviolet absorption and cross sections of propargyl (C_3H_3) radicals in the 230-300 nm region, Chemical Physics, 215:59–66.

Fahr, A. and Laufer, A. (**1990**): Direct measurements of the combination and disproportion of vinyl radicals, J. Phys. Chem., (94):726–729.

Fahr, A. and Laufer, A. H. (**2005**): UV-Absorption Spectra of the Radical Transients Generated from the 193 nm Photolysis of Allene, Propyne, and 2-Butyne, The Journal of Physical Chemistry A, 109(11):2534–2539.

Fahr, A. and Nayak, A. (**1994**): Temperature dependent ultraviolet absorption cross sections of 1,3-butadiene and butadiyne, Chemical Physics, 189:725–731.

Fahr, A. and Nayak, A. (**1996**): Temperature dependent ultraviolet absorption cross sections of propylene, methylacetylene and vinylacetylene, Chemical Physics, 203:351–358.

Fanale, F. P. and Salvail, J. R. (**1984**): An idealized short-period comet model - Surface insolation, H_2O flux, dust flux, and mantle evolution, Icarus, 60:476–511.

Fang, K.-T. and Yang, Z.-H. (**2000**): On uniform design of experiments with restricted mixtures and generation of uniform distribution on some domains, Statistics & Probability Letters, 46(2):113 – 120.

Feaga, L. M., A'Hearn, M. F., Sunshine, J. M., Groussin, O., and Farnham, T. L. (**2007**): Asymmetries in the distribution of H_2O and CO_2 in the inner coma of Comet 9P/Tempel 1 as observed by Deep Impact, Icarus, 190:345–356.

Feldman, P., A'Hearn, M., and Millis, R. (**1984**): Temporal and spatial behavior of the ultrviolet emission of Comet Iras-Araki-Alcock 1983d, The Astrophysical Journal, 282:799 – 802.

Feldman, P., Weaver, H., and Burgh, E. (**2002**): Far Ultraviolet Spectroscopic Explorer Observations of CO and H_2 emission in Comet C/2001 A2 (LINEAR), The Astrophysical Journal, 576:91 – 94.

Feldman, P. D., Cochran, A. L., and Combi, M. R. (**2004**a): Spectroscopic investigations of fragment species in the coma, 425–447.

Feldman, P. D., Lupu, R. E., McCandliss, S. R., Weaver, H. A. et al. (**2006**): Carbon Monoxide in Comet 9P/Tempel 1 before and after the Deep Impact Encounter, ApJ, 647:L61–L64.

Feldman, P. D., McCandliss, S. R., Morgenthaler, J. P., Lisse, C. M. et al. (**2010**): Galaxy Evolution Explorer Observations of CS and OH Emission in Comet 9P/Tempel 1 During Deep Impact, ApJ, 711:1051–1056.

Feldman, P. D., Weaver, H. A., Christian, D., Combi, M. R. et al. (**2004**b): FUSE Observations of Comet C/2001 Q4 (NEAT), in: AAS/Division for Planetary Sciences Meeting Abstracts #36, vol. 36 of *Bulletin of the American Astronomical Society*, 1121.

Ferradaz, T., Bénilan, Y., Fray, N., Jolly, A. et al. (**2009**): Temperature-dependent photoabsorption cross-sections of cyanoacetylene and diacetylene in the mid- and vacuum-UV: Application to Titan's atmosphere, Planet. Space Sci., 57:10–22.

Fink, U. (**1992**): Comet Yanaka (1988r) - A new class of carbon-poor Comet, Science, 257:1926–1929.

Fink, U. (**2009**): A taxonomic survey of comet composition 1985-2004 using CCD spectroscopy, Icarus, 201:311 – 334.

Flower, D. R., Pineau des Forets, G., and Hartquist, T. W. (**1985**): Theoretical studies of interstellar molecular shocks. I - General formulation and effects of the ion-molecule chemistry, MNRAS, 216:775–794.

Floyd, L., Rottman, G., Deland, M., and Pap, J. (**2003**): 11 years of solar UV irradiance measurements from UARS, in: **Wilson, A.** (Editor), Solar Variability as an Input to the Earth's Environment, vol. 535 of *ESA Special Publication*, 195–203.

Francisco, J. (**2000**): Determination of the CC bond dissociation energy in C_3N radical, Chemical Physics Letters, 324(4):307–310.

Francisco, J. S. and Richardson, S. L. (**1994**): Determination of the heats of formation of CCCN and HCCCN, J. Chem. Phys., 101:7707–7711.

Fray, N., Bénilan, Y., Biver, N., Bockelée-Morvan, D. et al. (**2006**): Heliocentric evolution of the degradation of polyoxymethylene: Application to the origin of the formaldehyde (H_2CO) extended source in Comet C/1995 O1 (Hale Bopp), Icarus, 184:239–254.

Friedel, D., Remijan, A., Snyder, L., A'Hearn, M. et al. (**2005**): BIMA Array detections of HCN in Comets LINEAR (C/2002 T7) and NEAT (C/2001 Q4), The Astrophysical Journal, 630:623 – 630.

Frost, R. K., Arrington, C. A., Ramos, C., and Zwier, T. S. (**1996**): Ultraviolet Photochemistry of Diacetylene: The Metastable $C_4H_2^*$ Reaction with Ethene, Propene, and Propyne, Journal of the American Chemical Society, 118(18):4451–4461.

Gail, H.-P. (**2002**): Radial mixing in protoplanetary accretion disks. III. Carbon dust oxidation and abundance of hydrocarbons in comets, A&A, 390:253–265.

Gans, B., Garcia, G. A., Boyé-Péronne, S., Loison, J.-C. et al. (**2011**): Absolute photoionization cross section of the ethyl radical in the range 8-11.5 ev: Synchrotron and vacuum ultraviolet laser measurements, The Journal of Physical Chemistry A, 115(21):5387–5396.

Gans, B., Peng, Z., Carrasco, N., Gauyacq, D. et al. (**2013**): Impact of a new wavelength-dependent representation of methane photolysis branching ratios on the modeling of Titans atmospheric photochemistry, Icarus, 223(1):330 – 343.

Geem, Z., Kim, J., and Loganathan, G. (**2001**): A new heuristic optimization algorithm: harmony search, Simulation, 76(2):60–68.

Geem, Z. W. (**2009**): Music-Inspired Harmony Search Algorithm: Theory and Applications, Springer Publishing Company, Incorporated, 1st ed.

Gehrz, R. D., Becklin, E. E., de Pater, I., Dunham, E. W. et al. (**2008**): SOFIA Observations of Stellar Occultations, Extra-solar Planets, Asteroids, and Comets, in: European Planetary Science Congress 2008, 817.

Geiss, J., Altwegg, K., Balsiger, H., and Graf, S. (**1999**): Rare Atoms, Molecules and Radicals in the Coma of P/Halley, Space Sci. Rev., 90:253–268.

Gericke, K.-H. (**2012**): WICHTIGE KONSTANTEN UND UMRECHNUNGEN, TU Braunschweig, `http://www.pci.tu-bs.de/aggericke/Konstanten.html`.

Giguere, P. T. and Huebner, W. F. (**1978**): A model of comet comae. I - Gas-phase chemistry in one dimension, ApJ, 223:638–654.

Giroux, L., Back, M., and Back, R. (**1989**): The Photolysis of ethylene at 193 nm, Can. J. Chem., 67:1166–1173.

Glicker, S. and Okabe, H. (**1987**): Photochemistry of Diacetylene, J.Phys.Chem., 91:437–440.

Goesmann, F., Rosenbauer, H., Roll, R., Szopa, C. et al. (**2007**): Cosac, The Cometary Sampling and Composition Experiment on Philae, Space Sci. Rev., 128:257–280.

Gomes, R., Levison, H. F., Tsiganis, K., and Morbidelli, A. (**2005**): Origin of the cataclysmic Late Heavy Bombardment period of the terrestrial planets, Nature, 435:466–469.

Goncher, S. J., Moore, D. T., Sveum, N. E., and Neumark, D. M. (**2008**): Photofragment translational spectroscopy of propargyl radicals at 248 nm, J. Chem. Phys., 128(11):114303–+.

Gounelle, M., Morbidelli, A., Bland, P. A., Spurny, P. et al. (**2008**): Meteorites from the Outer Solar System?, 525–541.

Graf, S., Geiss, J., and Leutwyler, S. (**2001**): Ab initio calculations of excited states in C_4H and implications for ultraviolet photodissociation, J. Chem. Phys., 114:4542–4551.

Greenstein, J. L. (**1958**): High-resolution spectra of Comet MRKOS (1957d), ApJ, 128:106–106.

Grunenberg, J. (Editor) (**2010**): Computational Spectroscopy: Methods, Experiments and Applications, Wiley-VCH.

Gulkis, S. and Alexander, C. (**2008**): Composition Measurements of a Comet from the Rosetta Orbiter Spacecraft, in: **Balsiger, H., Altwegg, K., Huebner, W., Owen, T., and Schulz, R.** (Editors), Origin and Early Evolution of Comet Nuclei, vol. 28 of *Space Sciences Series of ISSI*, 259–274, Springer New York.

Gupta, H., Gottlieb, C. A., McCarthy, M. C., and Thaddeus, P. (**2009**): A Survey of C_4H, C_6H, and C_6H^- With the Green Bank Telescope, ApJ, 691:1494–1500.

Haken, H. and Wolf, H. (**2000**): Atom- und Quantenphysik, Springer Verlag Berlin Heidelberg, 7th ed.

Haken, H. and Wolf, H. (**2005**): Molekülphysik und Quantenchemie, Springer Verlag Berlin Heidelberg, 5th ed.

Hall, L. A. and Hinteregger, H. E. (**1970**): Solar radiation in the extreme ultraviolet and its variation with solar rotation., J. Geophys. Res., 75:6959–6965.

Halpern, J. B., Miller, G. E., Okabe, H., and Nottingham, W. (**1988**): The UV photochemistry of cyanoacetylene, J.Photochem.Photobiol., 42:63–72.

Halpern, J. B., Petway, L., Lu, R., Jackson, W. M., and McCrary, V. R. (**1990**): Photochemistry of cyano- and dicyanoacetylene at 193 nm, Journal of Physics Conference Series, 94:1869–1873.

Hanner, M. S. and Bradley, J. P. (**2004**): Composition and mineralogy of cometary dust, 555–564.

Hara, H. and Tanaka, I. (**1973**): Photolysis of the Ethylene at 1634 Å and 1849 Å, Bulletin of the Chemical Society of Japan, 46:3012–3015.

Harada, N. and Herbst, E. (**2008**): Modeling Carbon Chain Anions in L1527, ApJ, 685:272–280.

Harich, S., Lee, Y. T., and Yang, X. (**2000**a): Photodissociation dynamics of allene at 157 nm, Physical Chemistry Chemical Physics (Incorporating Faraday Transactions), 2:1187–1191.

Harich, S., Lin, J. J., Lee, Y. T., and Yang, X. (**2000**b): Photodissociation dynamics of propyne at 157 nm, J. Chem. Phys., 112:6656–6665.

Harker, D. E., Wooden, D. H., Woodward, C. E., and Lisse, C. M. (**2002**): Grain Properties of Comet C/1995 O1 (Hale-Bopp), ApJ, 580:579–597.

Harker, D. E., Wooden, D. H., Woodward, C. E., and Lisse, C. M. (**2004**): Erratum: "Grain Properties of Comet C/1995 O1 (Hale-Bopp)" (ApJ, 580, 579 [2002]), ApJ, 615:1081–1081.

Hartogh, P., Crovisier, J., de Val-Borro, M., Bockelée-Morvan, D. et al. (**2010**): HIFI observations of water in the atmosphere of comet C/2008 Q3 (Garradd), A&A, 518:L150.

Hartogh, P., Lis, D. C., Bockelée-Morvan, D., de Val-Borro, M. et al. (**2011**): Ocean-like water in the Jupiter-family comet 103P/Hartley 2, Nature, 478:218–220.

Helbert, J. (**2002**): Studying the longterm evolution of gas activity in the coma of Comet C/1995 O1 (Hale-Bopp), with a special focus on the chemistry of carbon bearing molecules, Ph.D. thesis, Freie Universität Berlin.

Helbert, J., Rauer, H., Boice, D. C., and Huebner, W. F. (**2005**): The chemistry of C_2 and C_3 in the coma of Comet C/1995 O1 (Hale-Bopp) at heliocentric distances $r_h \geq 2.9$ AU, A&A, 442:1107–1120.

Helton, J., Johnson, J., Sallaberry, C., and Storlie, C. (**2006**): Survey of sampling-based methods for uncertainty and sensitivity analysis, Reliability Engineering & System Safety, 91(10-11):1175 – 1209, the Fourth International Conference on Sensitivity Analysis of Model Output (SAMO 2004) - SAMO 2004.

Henke, B. L., Lee, P., Tanaka, T. J., Shimabukuro, R. L., and Fujikawa, B. K. (**1982**): Low-energy X-ray interaction coefficients: Photoabsorption, scattering, and reflection: E = 100-2000 eV, Z = 1-94, Atomic Data and Nuclear Data Tables, 27(1):1 – 144.

Herbst, E. and Leung, C. M. (**1989**): Gas-phase production of complex hydrocarbons, cyanopolyynes, and related compounds in dense interstellar clouds, ApJS, 69:271–300.

Herzberg, G. (**1966**): Molecular Spectra and Molecular Structure. III. Electronic Spectra and Electronic Structure of Polyatomic Molecules, New York.

Hills, J. G. (**1981**): Comet showers and the steady-state infall of comets from the Oort cloud, AJ, 86:1730–1740.

Hinteregger, H. E. (**1970**): The extreme ultraviolet solar spectrum and its variation during a solar cycle., Annales de Geophysique, 26:547–554.

Hiraoka, K. and Sato, T. (**2001**): Laboratory simulation of tunneling reactions in interstellar ices, Radiation Physics and Chemistry, 60:389–393.

Ho, G. H., Lin, M. S., Wang, Y. L., and Chang, T. W. (**1998**): Photoabsorption and photoionization of propyne, J. Chem. Phys., 109:5868–5879.

Holland, D. and Shaw, D. (**1999**): A study of the valence-shell photoabsorption, photodissociation and photoionisation cross-sections of allene, Chemical Physics, 243:333–339.

Holland, D. M. P., Shaw, D. A., Hayes, M. A., Shpinkova, L. G. et al. (**1997**): A photoabsorption, photodissociation and photoelectron spectroscopy study of C_2H_4 and C_2D_4, Chemical Physics, 219(1):91 – 116.

Hopkins, S., Loock, H.-P., Cronin, B., Nix, M. G. D. et al. (**2007**): State-selective photodissociation dynamics of formaldehyde: Near threshold studies of the H+HCO product channel, J. Chem. Phys., 127(6):064301.

Howell, E. S., Lovell, A. J., and Schloerb, F. P. (**2004**): Comet C/2002 T7 (LINEAR), IAU Circ., 8329:2.

Hsieh, H. H. and Jewitt, D. (**2006**): A Population of Comets in the Main Asteroid Belt, Science, 312:561–563.

Huebner, W. (**1990**): Physics and Chemistry of Comets, Astronomy and Astrophysics Library, Springer.

Huebner, W., Keady, J., and Lyon, S. (**2011**): Photoionization/Dissociation Rates, `http://phidrates.space.swri.edu/`.

Huebner, W. F. and Benkhoff, J. (**1999**): From Coma Abundances to Nucleus Composition, Space Sci. Rev., 90:117–130.

Huebner, W. F., Benkhoff, J., Capria, M.-T., Coradini, A. et al. (Editors) (**2006**): Heat and Gas Diffusion in Comet Nuclei.

Huebner, W. F., Keady, J. J., Boice, D. C., Schmidt, H. U., and Wegmann, R. (**1987**): Chemico-Physical Models of Cometary Atmospheres, in: **Vardya, M. S. and Tarafdar, S. P.** (Editors), Astrochemistry, vol. 120 of *IAU Symposium*, 431.

Huebner, W. F., Keady, J. J., and Lyon, S. P. (**1992**): Solar photo rates for planetary atmospheres and atmospheric pollutants, Ap&SS, 195:1–289.

Huggins, W. (**1867**): Note on the Spectrum of Comet II. 1867, MNRAS, 27:288.

Hunziker, H., Kneppe, H., McLean, A., Siegbahn, P., and Wendt, H. (**1983**): Visible electronic absorption-spectrum of vinyl radical, Can. J. Chem., (61):993–995.

Iqbal, M. (**1983**): An introduction to solar radiation.

Irvine, W. M., Bockelée-Morvan, D., Lis, D. C., Matthews, H. E. et al. (**1996**): Spectroscopic evidence for interstellar ices in comet Hyakutake, Nature, 383:418–420.

Jackson, W. (**1976**): The photochemical formation of cometary radicals, Journal of Photochemistry, 5(2):107–118.

Jackson, W. M., Anex, D. S., Continetti, R. E., Balko, B. A., and Lee, Y. T. (**1991**): Molecular beam studies of the photolysis of allene and the secondary photodissociation of the C_3H_x fragments, J. Chem. Phys., 95:7327–7336.

Jarauta-Bragulat, E., P., B., and C., H. (**2003**): An algebraic method to compute isometric logratio transformation and back transformation of compositional data, IAMG annual edition.

Jewitt, D. (**2012**): The Active Asteroids, AJ, 143:66.

Jewitt, D., Morbidelli, A., and Rauer, H. (**2008**): Trans-Neptunian Objects and Comets.

Jimenez, J.-L. (**2005**): Lecture 6: Spectroscopy and Photochemistry II, `http://cires.colorado.edu/jimenez/AtmChem/CHEM-5151_S05_L6.pdf`.

Jolly, A. and Bénilan, Y. (**2008**): Review of quantitative spectroscopy of polyynes, J. Quant. Spec. Radiat. Transf., 109:963–973.

Kameta, K., Machida, S., Kitajima, M., Ukai, M. et al. (**1996**): Photoabsorption, photoionization, and neutral-dissociation cross sections of C_2H_6 and C_3H_8 in the extreme-UV region, Journal of Electron Spectroscopy and Related Phenomena, 79:391 – 393, proceedings of the 11th International Conference on Vacuum Ultraviolet Radiation Physics.

Kawaguchi, K., Kaifu, N., Ohishi, M., Ishikawa, S.-I. et al. (**1991**): Observations of cumulene carbenes, H2CCCC and H2CCC, in TMC-1, PASJ, 43:607–619.

Keenan, J., Chao, J., and Kaye, J. (**1983**): Gas tables: International version, second edition (si units), AIChE Journal.

Keller, H. U., Britt, D., Buratti, B. J., and Thomas, N. (**2004**): In situ observations of cometary nuclei, 211–222.

Keller, L. P., Bajt, S., Baratta, G. A., Borg, J. et al. (**2006**): Infrared Spectroscopy of Comet 81P/Wild 2 Samples Returned by Stardust, Science, 314:1728–.

Keller-Rudek, H. and Moortgat, G. (**2011**): MPI-Mainz-UV-VIS Spectral Atlas of Gaseous Molecules, `http://satellite.mpic.de/spectral_atlas`.

Kemper, F., Vriend, W. J., and Tielens, A. G. G. M. (**2004**): The Absence of Crystalline Silicates in the Diffuse Interstellar Medium, ApJ, 609:826–837.

Kemper, F., Vriend, W. J., and Tielens, A. G. G. M. (**2005**): Erratum: "The Absence of Crystalline Silicates in the Diffuse Interstellar Medium" (ApJ, 609, 826 [2004]), ApJ, 633:534–534.

Kempgens, B., Itchkawitz, B. S., Randall, K. J., Feldhaus, J. et al. (**1995**): Dynamic effects in the C 1s excitation spectra of ethene isotopomers, Chemical Physics Letters, 246(3):347 – 352.

Kiefer, J. H., Mudipalli, P. S., Sidhu, S. S., Kern, R. D. et al. (**1997**): Unimolecular Dissociation in Allene and Propyne: The Effect of Isomerization on the Low-Pressure Rate, The Journal of Physical Chemistry A, 101(22):4057–4071.

Kim, S., Lee, Y., Nordlander, P., and Tomanek, D. (**1997**): Disintegration of finite carbon chains in electric fields, Chemical Physics Letters, 264(3-4):345–350.

Kislov, V. V., Nguyen, T. L., Mebel, A. M., Lin, S. H., and Smith, S. C. (**2004**): Photodissociation of benzene under collision-free conditions: An ab initio/Rice-Ramsperger-Kassel-Marcus study, J. Chem. Phys., 120:7008–7017.

Kissel, J., Altwegg, K., Clark, B. C., Colangeli, L. et al. (**2007**): Cosima High Resolution Time-of-Flight Secondary Ion Mass Spectrometer for the Analysis of Cometary Dust Particles onboard Rosetta, Space Sci. Rev., 128:823–867.

Klossika, J.-J., Flöthmann, H., Beck, C., Schinke, R., and Yamashita, K. (**1997**): The topography of the hnco(s1) potential energy surface and its implications for photodissociation dynamics, Chemical Physics Letters, 276(5-6):325 – 333.

Kloster-Jensen, E., Haink, H.-J., and Christen, H. (**1974**): The Electronic Spectra of Unsubstituted Mono- to Pentaacetylene in the Gas Phase and in Solution in the Range 1100 to 4000 Å, Helvetica Chimica Acta, 57(6):1731–1744.

Knollenberg, J. (**1993**): Modellrechnungen zur Staubverteilung in der inneren Koma von Kometen unter spezieller Berücksichtigung der HMC-Daten der Giotto-Mission, Ph.D. thesis, Georg-August-Universität zu Göttingen (1993).

Knopp, G., Beaud, P., Radi, P., Tulej, M., and Gerber, T. (**2002**): Femtosecond photodissociation of the ethyl radical C_2H_5, World Scientific, Singapore.

Kobayashi, H. (**2012**): Personal communication.

Kobayashi, H. and Kawakita, H. (**2010**): Fluorescence Excitation Model And Mixing Ratios Of Ethylene (C_2H_4) In Comets, in: AAS/Division for Planetary Sciences Meeting Abstracts #42, vol. 42 of *Bulletin of the American Astronomical Society*, 961.

Kobayashi, H., Kawakita, H., Mumma, M., Bonev, B. et al. (**2007**): Organic volatiles in Comet 73P-B/Schwassmann-Wachmann 3 observed during its outburst: A clue to the formation region of the jupiter-family Comets, The Astrophysical Journal, 668:75 – 78.

Kobayashi, H., Watanabe, N., and Kawakita, H. (**2012**): Grain-surface reactions related to cometary hydrocarbons (ethane, ethylene, and acetylene), no. 6210 in Asteroids, Comets, Meteors (2012).

Kobayashi, H., Watanabe, N., Watanabe, Y., Fukushima, T., and Kawakita, H. (**2013**): Hydrogen addition reactions of aliphatic hydrocarbons in comets, in: AAS/Division for Planetary Sciences Meeting Abstracts, vol. 45 of *AAS/Division for Planetary Sciences Meeting Abstracts*.

Koch, E. E. and Skibowski, M. (**1971**): Optical absorption of gaseous methane, ethane, propane and butane and reflection of solid methane and ethane in the vacuum ultraviolet, Chemical Physics Letters, 9:429–432.

Korth, A., Marconi, M. L., Mendis, D. A., Krueger, F. R. et al. (**1989**): Probable detection of organic-dust-borne aromatic $C_3H_3^+$ ions in the coma of Comet Halley, Nature, 337:53–55.

Krasnopolsky, V. A. (**1991**): C_3 and CN parents in Comet P/Halley, A&A, 245:310–315.

Küppers, M., Bertini, I., Fornasier, S., Gutierrez, P. J. et al. (**2005**): A large dust/ice ratio in the nucleus of comet 9P/Tempel 1, Nature, 437:987–990.

Körösmezey, A., Cravens, T. E., Gombosi, T. I., Nagy, A. F. et al. (**1987**): A new model of cometary ionospheres, Journal of Geophysical Research: Space Physics, 92(A7):7331–7340.

Lacoursière, J., Meyer, S. A., Faris, G. W., Slanger, T. G. et al. (**1999**): The $O(^1D)$ yield from O_2 photodissociation near H Lyman-α (121.6 nm), J. Chem. Phys., 110:1949–1958.

Lambert, H., Dixit, A., Davis, E., and Houston, P. (**2004**): Quantum yields for product formation in the 120-133 nm photodissociation of O_2, The Journal of Chemical Physics, 121(21):10437–10446.

Lamy, P. L., Toth, I., Fernandez, Y. R., and Weaver, H. A. (**2004**): The sizes, shapes, albedos, and colors of cometary nuclei, 223–264.

Landau, L. and Lifschitz, E. (**1991**): VI.Hydrodynamik.

Langland-Shula, L. E. and Smith, G. H. (**2011**): Comet classification with new methods for gas and dust spectroscopy, Icarus, 213:280–322.

Läuter, A. (**2002**): Absolute primary H atom quantum yield measurements in the 193.3 and 121.6 nm photodissociation of acetylene, Chemical Physics Letters, 358:314–319.

Lavvas, P. P., Coustenis, A., and Vardavas, I. M. (**2008**): Coupling photochemistry with haze formation in Titan's atmosphere, Part I: Model description, Planet. Space Sci., 56:27–66.

Lean, J. (**1987**): Solar ultraviolet irradiance variations - A review, J. Geophys. Res., 92:839–868.

Lee, A. Y. T., Yung, Y. L., Cheng, B., Bahou, M. et al. (**2001**): Enhancement of Deuterated Ethane on Jupiter, ApJ, 551:L93–L96.

Lee, H.-H., Herbst, E., Pineau des Forets, G., Roueff, E., and Le Bourlot, J. (**1996**): Photodissociation of H_2 and CO and time dependent chemistry in inhomogeneous interstellar clouds., A&A, 311:690–707.

Lee, S., Lee, Y. T., and Yang, X. (**2004**): Dynamics of photodissociation of ethylene and its isotopomers at 157 nm: Branching ratios and kinetic-energy distributions, J. Chem. Phys., 120:10983–10991.

Leonori, F., Petrucci, R., Hickson, K. M., Segoloni, E. et al. (**2008**): Crossed molecular beam study of gas phase reactions relevant to the chemistry of planetary atmospheres: The case of C_2+C_2H_2, Planet. Space Sci., 56:1658–1673.

Levison, H. F. (**1996**): Comet taxonomy, ASP conference series, 107:173 – 191.

Levison, H. F., Duncan, M. J., Brasser, R., and Kaufmann, D. E. (**2010**): Capture of the Sun's Oort Cloud from Stars in Its Birth Cluster, Science, 329(5988):187–190.

Lias, S. G., Collin, G. J., Rebbert, R. E., and Ausloos, P. (**1970**): Photolysis of Ethane at 11.6-11.8 eV, J. Chem. Phys., 52:1841–1851.

Lis, D., Keene, J., Young, K., Phillips, T. et al. (**1997**): Spectroscopic observations of Comet C/1996 B2 (Hyakutake) with the Caltech Submillimeter Observatory, ICARUS, 130:355 – 372.

LISA (**2011**): Titan's spectroscopic database, Laboratoire Inter-Universitaire des Système Atmosphérique, see Jolly and Bénilan et al. 2008, `http://www.lisa.univ-paris12.fr/GPCOS/SCOOPweb/`, `http://www.lisa.univ-paris12.fr/GPCOS/SCOOPweb/lesmoleculesdeSCOOP.htm`, `http://losno.lisa.univ-paris-diderot.fr/services/DiffuseUVdata/`.

Lisse, C. M., Fernández, Y. R., Kundu, A., A'Hearn, M. F. et al. (**1999**): The Nucleus of Comet Hyakutake (C/1996 B2), Icarus, 140:189–204.

Lockerby, D. A., Reese, J. M., and Struchtrup, H. (**2009**): Switching criteria for hybrid rarefied gas flow solvers, Proceedings of the Royal Society A: Mathematical, Physical and Engineering Science, 465(2105):1581–1598.

Lombos, B. A., Sauvageau, P., and Sandorfy, C. (**1967**): The electronic spectra of n-alkanes, Journal of Molecular Spectroscopy, 24:253–269.

Lovas, F. J., Remijan, A. J., Hollis, J. M., Jewell, P. R., and Snyder, L. E. (**2006**): Hyperfine Structure Identification of Interstellar Cyanoallene toward TMC-1, ApJ, 637:L37–L40.

Lu, H.-C., Chen, H.-K., and Cheng, B.-M. (**2004**): Analysis of C_2H_4 in C_2H_6 and C_2H_5D with VUV Absorption Spectroscopy and a Method to Remove C_2H_4 from C_2H_6 and C_2H_5D, Analytical Chemistry, 76(19):5965–5967.

Luo, C., Du, W., Duan, X., and Li, Z. (**2008**): A Theoretical Study of the Photodissociation Mechanism of Cyanoacetylene in its Lowest Singlet and Triplet Excited States, ApJ, 687:726–730.

Magee-Sauer, K. (**2012**): Personal communication.

Magee-Sauer, K., Dello Russo, N., DiSanti, M. A., Gibb, E., and Mumma, M. J. (**2002**): CSHELL Observations of Comet C/2002 C1 (Ikeya-Zhang) in the 3.0-Micron Region, in: AAS/Division for Planetary Sciences Meeting Abstracts #34, vol. 34 of *Bulletin of the American Astronomical Society*, 868.

Marconi, M. L., Korth, A., Mendis, D. A., Lin, R. P. et al. (**1989**): On the possible detection of organic dust-borne $C_3H^{(}+)$ ions in the coma of Comet Halley, ApJ, 343:L77–L79.

Marconi, M. L. and Mendis, D. A. (**1983**): The atmosphere of a dirty-clathrate cometary nucleus - A two-phase, multifluid model, ApJ, 273:381–396.

Marconi, M. L. and Mendis, D. A. (**1986**): The electron density and temperature in the tail of Comet Giacobini-Zinner, Geophys. Res. Lett., 13:405–+.

Matsumi, Y., Comes, F. J., Hancock, G., Hofzumahaus, A. et al. (**2002**): Quantum yields for production of $O(^1D)$ in the ultraviolet photolysis of ozone: Recommendation based on evaluation of laboratory data, Journal of Geophysical Research (Atmospheres), 107:4024.

McCarthy, M. C., Gottlieb, C. A., Gupta, H., and Thaddeus, P. (**2006**): Laboratory and Astronomical Identification of the Negative Molecular Ion C_6H^-, ApJ, 652:L141–L144.

Mebel, A. M., Jackson, W. M., Chang, A. H. H., and Lin, S. H. (**1998**): Photodissociation Dynamics of Propyne and Allene: A View from ab Initio Calculations of the C_3H_n (n = 1-4) Species and the Isomerization Mechanism for C_3H_2, Journal of the American Chemical Society, 120(23):5751–5763.

Mebel, A. M. and Kaiser, R. I. (**2002**): An ab initio study on the formation of interstellar tricarbon isomers $l-C_3$ ($X^1\Sigma_g^+$) and $c-C_3$ (X^3A_2'), Chemical Physics Letters, 360:139–143.

Meech, K. J., Ageorges, N., A'Hearn, M. F., Arpigny, C. et al. (**2005**): Deep Impact: Observations from a Worldwide Earth-Based Campaign, Science, 310:265–269.

Meech, K. J. and Svoren, J. (**2004**): Using cometary activity to trace the physical and chemical evolution of cometary nuclei, 317–335.

Metzger, P. H. and Cook, G. R. (**1964**): On the Continuous Absorption, Photoionization, and Fluorescence of H_2O, NH_3, CH_4, C_2H_2, C_2H_4, and C_2H_6 in the 600-to-1000-Å Region, J. Chem. Phys., 41:642–648.

Milam, S., Remijan, A., Womack, M., Abrell, L. et al. (**2006**): Formaldehyde in Comets C/1995 O1 (Hale-Bopp), C/2002 T7 (LINEAR), and C/2001 Q4 (NEAT): Investigating the Cometary origin of H_2CO, The Astrophysical Journal, 649:1169 – 1177.

Millar, T. J., Walsh, C., Cordiner, M. A., Ní Chuimín, R., and Herbst, E. (**2007**): Hydrocarbon Anions in Interstellar Clouds and Circumstellar Envelopes, ApJ, 662:L87–L90.

Milone, E. F. and Wilson, W. J. (**2008**): Solar System Astrophysics: Planetary Atmospheres and the Outer Solar System, Astronomy and Astrophysics Library, Springer, New York, NY.

Mohr, P. J., Taylor, B. N., and Newell, D. B. (**2008**): CODATA recommended values of the fundamental physical constants: 2006, Rev. Mod. Phys., 80(2):633–730.

Monks, P. S., Romani, P. N., Nesbitt, F. L., Scanlon, M., and Stief, L. J. (**1993**): The kinetics of the formation of nitrile compounds in the atmospheres of Titan and Neptune, J. Geophys. Res., 98:17115–17122.

Moortgat, G. K., Seiler, W., and Warneck, P. (**1983**): Photodissociation of HCHO in air - CO and H_2 quantum yields at 220 and 300 K, J. Chem. Phys., 78:1185–1190.

Morbidelli, A., Levison, H. F., Tsiganis, K., and Gomes, R. (**2005**): Chaotic capture of Jupiter's Trojan asteroids in the early Solar System, Nature, 435:462–465.

Morbidelli, A., Lunine, J. I., O'Brien, D. P., Raymond, S. N., and Walsh, K. J. (**2012**): Building Terrestrial Planets, Annual Review of Earth and Planetary Sciences, 40:251–275.

Moses, J. I., Bézard, B., Lellouch, E., Gladstone, G. R. et al. (**2000**): Photochemistry of Saturn's Atmosphere. I. Hydrocarbon Chemistry and Comparisons with Observations, Icarus, 143:244–298.

Mulliken, R. S. (**1927**): Electronic States and Band Spectrum Structure in Diatomic Molecules. IV. Hund's Theory. Second Positive Nitrogen and Swan Bands. Alternating Intensities, Physical Review, 29:637–649.

Mumma, M., DiSanti, M., Dello Russo, N., Fomenkova, M. et al. (**1996**): Detection of abundant Ethane and Methane, along with Carbon Monoxide and Water, in Comet C/1996 B2 Hyakutake: Evidence for interstellar origin, Science, 272:1310 – 1314.

Mumma, M., DiSanti, M., Magee-Sauer, K., Bonev, B. et al. (**2005**): Parent volatiles in Comet 9P/Tempel 1: Before and after impact, Science, 310:270 – 274.

Mumma, M. J. and Charnley, S. B. (**2011**): The Chemical Composition of Comets - Emerging Taxonomies and Natal Heritage, ARA&A, 49:471–524.

Mumma, M. J., DiSanti, M. A., Dello Russo, N., Magee-Sauer, K. et al. (**2003**): Remote infrared observations of parent volatiles in comets: A window on the early solar system, Advances in Space Research, 31:2563–2575.

Munk, J., Pagsberg, P., Ratajczak, E., and Sillesen, A. (**1986**): Spectrokinetic studies of ethyl and ethylperoxy radicals, The Journal of Physical Chemistry, 90(12):2752–2757.

Murakami, H., Baba, H., Barthel, P., Clements, D. L. et al. (**2007**): The Infrared Astronomical Mission AKARI, PASJ, 59:369.

Nakayama, T. and Watanabe, K. (**1964**): Absorption and Photoionization Coefficients of Acetylene, Propyne and 1-Butyne, J. Chem. Phys., 40:558–561.

NASA-IDL-Lib. (**2011**): The IDL Astronomy User's Library, `http://idlastro.gsfc.nasa.gov/`.

Newburn Jr., R. and Spinrad, H. (**1984**): Spectrophotometry of 17 Comets I. The emission features, The Astronomical Journal, 97:289 – 309.

Nguyen, T. L., Mebel, A. M., Lin, S. H., and Kaiser, R. I. (**2001**): Product Branching Ratios of the $C(^3P) + C_2H_3(^2A')$ and $CH(^2\Pi) + C_2H_2(^1\Sigma_g^+)$ Reactions and Photodissociation of $H_2CC{\equiv}CH(^2B_1)$ at 193 and 242 nm: an ab Initio/RRKM Study, The Journal of Physical Chemistry A, 105(51):11549–11559.

Ni, C., Huang, J. D., Chen, Y. T., Kung, A. H., and Jackson, W. M. (**1999**): Photodissociation of propyne and allene at 193 nm with vacuum ultraviolet detection of the products, J. Chem. Phys., 110:3320–3325.

Ni, C.-K., Tseng, C.-M., Lin, M.-F., and Dyakov, Y. A. (**2007**): Photodissociation Dynamics of Small Aromatic Molecules Studied by Multimass Ion Imaging, The Journal of Physical Chemistry B, 111(44):12631–12642.

Nieto-Gligorovski, L., Gligorovski, S., Romano, R., Vedova, C. D., and Zetzsch, C. (**2009**): UV absorption cross-sections of a series of vinyl ethers, Journal of Photochemistry and Photobiology A: Chemistry, 204(1):46 – 51.

Okabe, H. (**1975**): Photodissociation of acetylene and bromoacetylene in the vacuum ultraviolet: Production of electronically excited C_2H and C_2, J. Chem. Phys., 62:2782–2787.

Okabe, H. (**1978**): Photochemistry of Small Molecules, John Wiley & Sons, Inc., New York.

Okabe, H. (**1981**): Photochemistry of acetylene at 1470 Å, J. Chem. Phys., 75:2772–2778.

Okabe, H. (**1983**): Photochemistry of acetylene at 1849 Å, J. Chem. Phys., 78:1312–1317.

Oort, J. H. (**1950**): The structure of the cloud of comets surrounding the Solar System and a hypothesis concerning its origin, Bull. Astron. Inst. Netherlands, 11:91–110.

Ootsubo, T., Kawakita, H., Hamada, S., Kobayashi, H. et al. (**2012**): AKARI Near-infrared Spectroscopic Survey for CO_2 in 18 Comets, ApJ, 752:15.

Padial, N. T., Collins, L. A., and Schneider, B. I. (**1985**): Photoionization of ground-state molecular carbon C_2, ApJ, 298:369–374.

Palmer, P., Wootten, A., Butler, B., Bockelée-Morvan, D. et al. (**1996**): Bulletin of the American Astronomical Society, 188.

Pan, L., Rao, B. K., Gupta, A. K., Das, G. P., and Ayyub, P. (**2003**): H-substituted anionic carbon clusters C_nH^- ($n \leq 10$): Density functional studies and experimental observations, J. Chem. Phys., 119:7705–7713.

Peach, D. (**2014**): Damion Peach's view of the Solar System, `http://www.damianpeach.com`.

Pizzarello, S., Cooper, G. W., and Flynn, G. J. (**2006**): The Nature and Distribution of the Organic Material in Carbonaceous Chondrites and Interplanetary Dust Particles, 625–651.

Platt, J. R., Klevens, H. B., and Price, W. C. (**1949**): Absorption Intensities of Ethylenes and Acetylenes in the Vacuum Ultraviolet, J. Chem. Phys., 17:466–469.

Plessis, S., Carrasco, N., and Pernot, P. (**2010**): Knowledge-based probabilistic representations of branching ratios in chemical networks: The case of dissociative recombinations, J. Chem. Phys., 133(13):134110–+.

Pouilly, B., Robbe, J. M., Schamps, J., and Roueff, E. (**1983**): Photodissociation and radiative processes in interstellar C_2, Journal of Physics B Atomic Molecular Physics, 16:437–448.

Press, W. H., Teukolsky, S. A., Vetterling, W. T., and Flannery, B. P. (**2007**): Numerical Recipes 3rd Edition: The Art of Scientific Computing, Cambridge University Press, 3rd ed.

Prialnik, D., Benkhoff, J., and Podolak, M. (**2004**): Modeling the structure and activity of comet nuclei, 359–387.

Prialnik, D., Sarid, G., Rosenberg, E. D., and Merk, R. (**2008**): Thermal and Chemical Evolution of Comet Nuclei and Kuiper Belt Objects, Space Sci. Rev., 138:147–164.

Qadiri, R. H., Feltham, E. J., Cottrill, E. E. H., Taniguchi, N., and Ashfold, M. N. R. (**2002**): Near ultraviolet photodissociation of allene and propyne, J. Chem. Phys., 116:906–912.

Qadiri, R. H., Feltham, E. J., Hendrik Nahler, N., Pérez García, R., and Ashfold, M. N. R. (**2003**): Propyne and allene photolysis at 193.3 nm and at 121.6 nm, J. Chem. Phys., 119:12842–12851.

Rabalais, J., McDonald, J., Scherr, V., and McGlynn, S. (**1971**): Electronic spectoscopy of isoelectronic molecules. II. Linear triatomic groupings containing sixteen valence electrons, Chemical Reviews, 71(1):73–108, listed as McGlynn et al. 1971.

Rabalais, J. W. and Katrib, A. (**1974**): Electronic states of C_2H_6, Molecular Physics, 27:923–931.

Radhakrishnan, K. and Hindmarsh, A. (**1993**): Description and Use of LSODE, the Livermore Solver for Ordinary Differential Equations, nASA Reference Publication 1327, Lawrence Livermore National Laboratory Report UCRL-ID-113855.

Rauer, H., Arpigny, C., Boehnhardt, H., Colas, F. et al. (**1997**): Optical observations of comet Hale-Bopp (C/1995 O1) at large heliocentric distances before perihelion., Science, 275:1909–1912.

Rauer, H., Helbert, J., Arpigny, C., Benkhoff, J. et al. (**2003**): Long-term optical spectrophotometric monitoring of comet C/1995 O1 (Hale-Bopp), A&A, 397:1109–1122.

Rauer, H., Hoelscher, A., and Weiler, M. (**2008**): Gaseous composition of comets: ensemble properties of comets from the DLR comet data base, in: European Planetary Science Congress 2008.

Remijan, A., Friedel, D., de Pater, I., Hogerheijde, M. et al. (**2006**a): A BIMA Array survey of molecules in Comets LINEAR (C/2002 T7) and NEAT (C/2001 Q4), The Astrophysical Journal, 643:567 – 572.

Remijan, A. J., Hollis, J. M., Lovas, F. J., Cordiner, M. A. et al. (**2007**): Detection of C_8H^- and Comparison with C_8H toward IRC +10 216, ApJ, 664:L47–L50.

Remijan, A. J., Hollis, J. M., Snyder, L. E., Jewell, P. R., and Lovas, F. J. (**2006**b): Methyltriacetylene (ch_3c_6h) toward tmc-1: The largest detected symmetric top, The Astrophysical Journal Letters, 643(1):L37.

Robinson, J. C., Sveum, N. E., Goncher, S. J., and Neumark, D. M. (**2005**): Photofragment translational spectroscopy of allene, propyne, and propyne-d3 at 193 nm, Molecular Physics, 103(13):1765–1783.

Robinson, J. C., Sveum, N. E., and Neumark, D. M. (**2003**): Determination of absolute photoionization cross sections for vinyl and propargyl radicals, J. Chem. Phys., 119:5311–5314.

Rodgers, S. D. and Charnley, S. B. (**1998**): HNC and HCN in Comets, ApJ, 501:L227.

Rodgers, S. D. and Charnley, S. B. (**2002**): A model of the chemistry in cometary comae: deuterated molecules, MNRAS, 330:660–674.

Rodgers, S. D., Charnley, S. B., Huebner, W. F., and Boice, D. C. (**2004**): Physical processes and chemical reactions in cometary comae, 505–522.

Rousselot, P., Hill, S. M., Burger, M. H., Brain, D. A. et al. (**2000**): Theoretical Modeling of the C_2 Fluorescence Spectrum in Comet Hale-Bopp, Icarus, 146:263–269.

Ruscic, B., Berkowitz, J., Curtiss, L. A., and Pople, J. A. (**1989**): The ethyl radical - Photoionization and theoretical studies, J. Chem. Phys., 91:114–121.

Sandford, S. A., Aléon, J., Alexander, C. M. O. ., Araki, T. et al. (**2006**): Organics Captured from Comet 81P/Wild 2 by the Stardust Spacecraft, Science, 314:1720–.

Sarmecanic, J., Fomenkova, M., Jones, B., and Lavezzi, T. (**1997**): Constraints on the Nucleus and Dust Properties from Mid-Infrared Imaging of Comet Hyakutake, The Astrophysical Journal Letters, 483(1):L69.

Satyapal, S. and Bersohn, R. (**1991**): Photodissociation of acetylene at 193.3 nm, J. Phys. Chem., 95:8004–8006.

Savee, J. D., Soorkia, S., Welz, O., Selby, T. M. et al. (**2012**): Absolute photoionization cross-section of the propargyl radical, J. Chem. Phys., 136(13):134307.

Schinke, R. (**1993**): Photodissociation dynamics, Cambridge University Press.

Schinke, R. (**2002**): Photodissociation Dynamics. Encyclopedia of Computational Chemistry., Wiley.

Schleicher, D. (**2008**): The extremely anomalous molecular abundances of comet 96P/Machholz 1 from narrowband photometry, The Astronomical Journal, 136:2204 – 2213.

Schleicher, D. G. (**2010**): The Fluorescence Efficiencies of the CN Violet Bands in Comets, AJ, 140:973–984.

Schleicher, D. G. and Bair, A. N. (**2011**): The Composition of the Interior of Comet 73P/Schwassmann-Wachmann 3: Results from Narrowband Photometry of Multiple Components, AJ, 141:177.

Schleicher, D. G., Bus, S. J., and Osip, D. J. (**1993**): The anomalous molecular abundances of Comet P/Wolf-Harrington, Icarus, 104:157–166.

Schmidt, H. U., Wegmann, R., Huebner, W. F., and Boice, D. C. (**1988**): Cometary gas and plasma flow with detailed chemistry., Computer Physics Communications, 49:17–59.

Schoen, R. I. (**1962**): Absorption, Ionization and Ion-Fragmentation Cross Sections of Hydrocarbon Vapors under Vacuum-Ultraviolet Radiation, J. Chem. Phys., 37:2032–2041.

Schulz, R. (**2009**): Rosetta - one comet rendezvous and two asteroid fly-bys, Solar System Research, 43:343–352.

Schwamb, M. (**2014**): Solar System: Stranded in no-man's-land, Nature, 7493:435–436.

Schwell, M., Bénilan, Y., Fray, N., Gazeau, M.-C. et al. (**2012**): Ionization photophysics and Rydberg spectroscopy of diacetylene, Molecular Physics, 0(0):1–14.

Seki, K., He, M., Liu, R., and Okabe, H. (**1996**): Photochemistry of Cyanoacetylene at 193.3 nm, J.Phys.Chem., 100:5349–5353.

Seki, K. and Okabe, H. (**1992**): Photodissociation of methylacetylene at 193 nm, The Journal of Physical Chemistry, 96(8):3345–3349.

Seki, K. and Okabe, H. (**1993**): Photochemistry of acetylene at 193.3 nm, J. Phys.Chem., 97:5284–5290.

Semenov, D. and Wiebe, D. (**2011**): Chemical Evolution of Turbulent Protoplanetary Disks and the Solar Nebula, ApJS, 196:25.

Senay, M. C. and Jewitt, D. (**1994**): Coma formation driven by carbon monoxide release from comet Schwassmann-Wachmann 1, Nature, 371:229–231.

Shahu, M., Yang, C.-H., Pibel, C. D., McIlroy, A. et al. (**2002**): Vinyl radical visible spectroscopy and excited state dynamics, J. Chem. Phys., 116:8343–8352.

Shemansky, D. E., Stewart, A. I. F., West, R. A., Esposito, L. W. et al. (**2005**): The Cassini UVIS Stellar Probe of the Titan Atmosphere, Science, 308:978–982.

Shin, K. and Michael, J. (**1991**): Rate constants (296-1700 K) for the reactions $C_2H + C_2H_2 \rightarrow C_4H_2 + H$ and $C_2D + C_2D_2 \rightarrow C_4D_2 + D$, J.Phys.Chem., 95:5864–5869.

Shukla, S. and Anand, A. (**2011**): Multi-objective optimization of an industrial styrene reactor using Harmony Search Algorithm, International Journal of Computer and communication Technology, (2):1–7.

SIDC (**2013**): SIDC, `http://sidc.oma.be/sunspot-data/`.

Silva, R., Gichuhi, W. K., Huang, C., Doyle, M. B. et al. (**2008**): Chemical Dynamics Special Feature: H elimination and metastable lifetimes in the UV photoexcitation of diacetylene, Proceedings of the National Academy of Science, 105:12713–12718.

Silva, R., Gichuhi, W. K., Kislov, V. V., Landera, A. et al. (**2009**): UV Photodissociation of Cyanoacetylene: A Combined Ion Imaging and Theoretical Investigation, Journal of Physical Chemistry A, 113:11182–11186.

Simon, P. (**1974**): Balloon Measurements of Solar Fluxes Between 1960 Å and 2300 Å, in: **A. J. Broderick & T. M. Hard** (Editor), Proceedings of the Third Conference on the Climatic Impact Assessment, 137–+.

Smith, G. P. and Nash, D. (**2006**): Local sensitivity analysis for observed hydrocarbons in a Jupiter photochemistry model, Icarus, 182:181–201.

Smith, N., Bénilan, Y., and Bruston, P. (**1998**): The temperature dependent absorption cross sections of C_4H_2 at mid ultraviolet wavelengths, Planetary and Space Science, 46(9-10):1215–1220.

Smith, P. (**2012**): Detected impurities in the C_2H_2 gas for absorption cross section measurements published in smith et al. 1991, AMP - Atomic and Molecular Physics, Center for Astrophyics, Harvard-Smithsonian, `http://www.cfa.harvard.edu/amp/ampdata/c2h2/c2h2.html`.

Smith, P. L., Yoshino, K., Parkinson, W. H., Ito, K., and Stark, G. (**1991**): High-resolution, VUV (147-201 nm) photoabsorption cross sections for C_2H_2 at 195 and 295 K, J. Geophys. Res., 96:17529–+.

Snyder, L. E. and Buhl, D. (**1973**): Interstellar Methylacetylene and Isocyanic Acid, Nature Physical Science, 243:45–46.

Song, X., Bao, Y., Urdahl, R. S., Gosine, J. N., and Jackson, W. M. (**1994**): Laser-induced flourescence studies of C_3 formation and isomerization in the 193 nm photolysis of allene and propyne, Chemical Physics Letters, 217:216–221.

Spaceweather (**2013**): Spaceweather, `http://www.spaceweather.gc.ca/sx-5-eng.php`.

Stern, S. A. (**2003**): The evolution of comets in the Oort cloud and Kuiper belt, Nature, 424:639–642.

Stief, L. J. (**1972**): Origin of C_3 in Comets, Nature, 237:29–+.

Stief, L. J., de Carlo, V. J., and Payne, W. A. (**1971**): Photolysis of Propyne at 1470 Å, J. Chem. Phys., 54:1913–1918.

Stief, L. J., Decarlo, V. J., and Mataloni, R. J. (**1965**): Vacuum-Ultraviolet Photolysis of Acetylene, J. Chem. Phys., 42:3113–3121.

Sun, W., Yokoyama, K., Robinson, J. C., Suits, A. G., and Neumark, D. M. (**1999**): Discrimination of product isomers in the photodissociation of propyne and allene at 193 nm, J. Chem. Phys., 110:4363–4368.

Sutcliffe, L. H. and Walsh, A. D. (**1952**): 162. the absorption spectrum of allene in the vacuum ultra-violet, J. Chem. Soc., 899–905.

Swider, W., Jr. (**1969**): Ionization rates due to the attenuation of 1-100 Å nonflare solar X-rays in the terrestrial atmosphere., Reviews of Geophysics and Space Physics, 7:573–594.

Swings, P. (**1941**): Complex structure of cometary bands tentatively ascribed to the contour of the solar spectrum, Lick Observatory Bulletin, 19:131–136.

Swings, P. (**1965**): Cometary Spectra, QJRAS, 6:28–+.

Thomas, N., Alexander, C., and Keller, H. U. (**2008**): Loss of the Surface Layers of Comet Nuclei, 165.

Tielens, A. G. G. M. (**2008**): Interstellar Polycyclic Aromatic Hydrocarbon Molecules, ARA&A, 46:289–337.

Titarchuk, T. and Halpern, J. (**2000**): The excitation spectrum of cyanoacetylene (HC_3N) and emission from C_3N fragments, Chemical Physics Letters, 323:305–311.

Tokunaga, A. T., Brooke, T. Y., Weaver, H. A., Crovisier, J., and Bockelée-Morvan, D. (**1996**): Interstellar molecules in comets, IAU Circ., 1:6378.

Tonokura, K., Marui, S., and Koshi, M. (**1999**): Absorption cross-section measurements of the vinyl radical in the 440-460 nm region by cavity ring-down spectroscopy, Chemical Physics Letters, 313(5-6):771 – 776.

Tozzi, G. P., Boehnhardt, H., and Lo Curto, G. (**2003**): Imaging and spectroscopy of comet C/2001 Q4 (NEAT) at 8.6 AU from the Sun, A&A, 398:L41–L44.

Tsagris, M. T., Preston, S., and Wood, A. T. A. (**2011**): A data-based power transformation for compositional data, ArXiv e-prints.

Tsai, S.-T., Huang, C.-L., Lee, Y. T., and Ni, C.-K. (**2001**): Ring opening dissociation of d_6-benzene, J. Chem. Phys., 115:2449–2455.

Tsiganis, K., Gomes, R., Morbidelli, A., and Levison, H. F. (**2005**): Origin of the orbital architecture of the giant planets of the Solar System, Nature, 435:459–461.

Tuna, T., Chabot, M., Pino, T., Désesquelles, P. et al. (**2008**): Fragmentation branching ratios of highly excited hydrocarbon molecules C_nH and their cations C_nH^+ ($n \leq 4$), J. Chem. Phys., 128(12):124312.

van Dishoeck, E. and van Hemert, M. (**2012**): Personal communication.

van Dishoeck, E. F. and Dalgarno, A. (**1983**): Photodissociation processes in the OH molecule, J. Chem. Phys., 79:873–888.

van Dishoeck, E. F. and Dalgarno, A. (**1984**): Photodissociation of OH in Interstellar Clouds, ApJ, 277:576.

van Dishoeck, E. F. and Visser, R. (**2011**): Molecular photodissociation, ArXiv e-prints.

van Hemert, M. and van Dishoeck, E. (**2008**): Photodissociation of small carbonaceous molecules of astrophysical interest, Chemical Physics, 343(2-3):292 – 302, theoretical Spectroscopy and its Impact on Experiment - (in honour of Sigrid D. Peyerimhoff).

Walch, S. (**1995**): "characterization of the minimum energy paths for the reactions of $CH(X^2\pi)$ and $^1ch_2$ with c_2h_2", The Journal of Chemical Physics, 103(16):7064–7071.

Walsh, K. J., Morbidelli, A., Raymond, S. N., O'Brien, D. P., and Mandell, A. M. (**2011**): A low mass for Mars from Jupiter's early gas-driven migration, Nature, 475:206–209.

Weaver, H., Brooke, T., DiSanti, M., Mumma, M. et al. (**1997**): Bulletin of the American Astronomical Society, 29.

Weaver, H., Feldman, P., A'Hearn, M., Arpigny, C. et al. (**1999**): Post-perihelion HST observations of Comet Hale-Bopp (C/1995 O1), Icarus, 141:1 – 12.

Weaver, H. A. and Feldman, F. D. (**1992**): Probing the Nature of Comets with the Hubble Space Telescope, in: **Benvenuti, P. and Schreier, E.** (Editors), European Southern Observatory Conference and Workshop Proceedings, vol. 44 of *European Southern Observatory Conference and Workshop Proceedings*, 475.

Weiler, M. (**2006**): Study of the Gas and Dust Activity of Recent Comets, Ph.D. thesis, Technische Universität Berlin.

Weiler, M. (**2012**): The chemistry of C_3 and C_2 in cometary comae. I. Current models revisited, A&A, 538:A149.

Weiler, M., Rauer, H., Knollenberg, J., and Sterken, C. (**2007**): The gas production of Comet 9P/Tempel 1 around the Deep Impact date, Icarus, 190:423–431.

Weiler, M., Rauer, H., and Sterken, C. (**2011**): Cometary nuclear magnitudes from sky survey observations, Icarus, 212:351–366.

Wendt, H. R. and Hunziker, H. E. (**1984**): The UV spectra of primary, secondary, and tertiary alkyl radicals, J. Chem. Phys., 81:717–723.

Westphal, A. J., Fakra, S. C., Gainsforth, Z., Marcus, M. A. et al. (**2009**): Mixing Fraction of Inner Solar System Material in Comet 81P/Wild2, ApJ, 694:18–28.

Wilkinson, P. G. and Mulliken, R. S. (**1955**): Far Ultraviolet Absorption Spectra of Ethylene and Ethylene-d_4, J. Chem. Phys., 23:1895–1907.

Wilson, E. H. and Atreya, S. K. (**2004**): Current state of modeling the photochemistry of Titan's mutually dependent atmosphere and ionosphere, Journal of Geophysical Research (Planets), 109(E18):6002–+.

Womack, M., Festou, M., and Stern, S. (**1996**): Bulletin of the American Astronomical Society, 188.

Woodall, J., Agúndez, M., Markwick-Kemper, A. J., and Millar, T. J. (**2007**): The UMIST database for astrochemistry 2006, A&A, 466:1197–1204, `http://www.udfa.net/`.

Wooden, D., Desch, S., Harker, D., Gail, H.-P., and Keller, L. (**2007**): Comet Grains and Implications for Heating and Radial Mixing in the Protoplanetary Disk, Protostars and Planets V, 815–833.

Woon, D. (**2013**): Astrochymist, `http://www.astrochymist.org/astrochymist_comet.html`.

Wu, C. Y. R., Chen, F. Z., and Judge, D. L. (**2001**): Measurements of temperature-dependent absorption cross sections of C_2H_2 in the VUV-UV region, J. Geophys. Res., 106.

Wu, C. Y. R., Chen, F. Z., and Judge, D. L. (**2004**): Temperature-dependent photoabsorption cross sections in the VUV-UV region: Ethylene, Journal of Geophysical Research (Planets), 109(E18):7–+.

Wu, C. Y. R., Chien, T. S., Liu, G. S., Judge, D. L., and Caldwell, J. J. (**1989**): Photoabsorption and direct dissociation cross sections of C_2H_2 in the 1530-1930 Å region - A temperature dependent study, J. Chem. Phys., 91:272–280.

Yamamoto, T. (**1981**): On the photochemical formation of CN, C_2, and C_3 radicals in cometary comae, Moon and Planets, 24:453–463.

Yang, X., Maeda, S., and Ohno, K. (**2006**): Global analysis of reaction pathways on the potential energy surface of cyanoacetylene by the scaled hypersphere search method, Chemical Physics Letters, 418:208–216.

Yang, X.-S. (**2010**): Harmony Search as a Metaheuristic Algorithm, ArXiv e-prints.

Yokoyama, A., Zhao, X., Hintsa, E. J., Continetti, R. E., and Lee, Y. T. (**1990**): Molecular beam studies of the photodissociation of benzene at 193 and 248 nm, J. Chem. Phys., 92:4222–4233.

Yung, Y. L., Allen, M., and Pinto, J. P. (**1984**): Photochemistry of the atmosphere of Titan - Comparison between model and observations, ApJS, 55:465–506.

Zádor, J., Zsély, I., and Turányi, T. (**2006**): Local and global uncertainty analysis of complex chemical kinetic systems, Reliability Engineering and System Safety, 91(10 - 11):1232 – 1240, the Fourth International Conference on Sensitivity Analysis of Model Output (SAMO 2004) {SAMO} 2004 The Fourth International Conference on Sensitivity Analysis of Model Output (SAMO 2004).

Zelikoff, M. and Watanabe, K. (**1953**): Absorption coefficients of ethylene in the vacuum ultraviolet, Journal of the Optical Society of America (1917-1983), 43:756–+.

Zhang, Y., Yuan, K., Yu, S., Parker, D. H., and Yang, X. (**2010**): Photodissociation dynamics of acetylene via the $\widetilde{C}^1\Pi_u$ electronic state, J. Chem. Phys., 133(1):014307–+.

Zheng, X., Song, Y., and Zhang, J. (**2009**): Ultraviolet Photodissociation Dynamics of the Propargyl Radical, The Journal of Physical Chemistry A, 113(16):4604–4612.

Zolensky, M., Nakamura-Messenger, K., Rietmeijer, F., Leroux, H. et al. (**2008**): Comparing Wild 2 particles to chondrites and IDPs, Meteoritics and Planetary Science, 43:261–272.

Zolensky, M. E., Zega, T. J., Yano, H., Wirick, S. et al. (**2006**): Mineralogy and Petrology of Comet 81P/Wild 2 Nucleus Samples, Science, 314:1735–.

Danksagung

Ich möchte mich bei Prof. Dr. Heike Rauer dafür bedanken, dass Sie es mir ermöglicht hat in diesem interessanten Gebiet der Astrophysik und Astrochemie zu promovieren. Ich danke ihr für das entgegengebrachte Vertrauen und die Betreuung meiner Arbeit. Prof. Dr. Otto Dopfer danke ich sehr für sein Interesse und die hilfreichen und interessanten Diskussionen über die Chemie.

Ein großer Dank geht auch an Dr. Jörg Knollenberg für die vielen Diskussionen, Tipps und Ideen, ohne die diese Arbeit nicht möglich gewesen wäre, und natürlich für die interessanten und lustigen Gespräche in der Kaffeepause. Ich danke Dr. Szilard Csizmadia für die Optimierungscodes und vielen hilfreichen Diskussionen, die für die Arbeit sehr wichtig waren. Ein großer Dank geht an Dr. Lee Grenfell, Dr. Mareike Godolt, Dr. Jörg Knollenberg, Thomas Pasternacki, Dr. Barbara Stracke, Dr. Jörn Helbert und Dr. Anders Erikson für die vielen wichtigen Kommentare zu meiner Arbeit. Thomas Pasternacki danke ich für die etlichen unterhaltsamen, motivierenden und erhellenden Diskussionen und Pausen. Barbara Stracke danke ich für ihre vielen Tipps, Diskussionen und die tolle Arbeitsatmosphäre. Ein weiterer Dank sei auch Beate Patzer ausgesprochen, für wichtige Diskussionen über die Photochemie. Ich danke allen Leuten, die sich in den Atmosphären-Meetings und auch nebenbei Zeit genommen haben mit mir über meine Arbeit zu diskutieren: Dr. Joachim Stock, Dr. Philipp von Paris, Dr. Daniel Kitzmann, Dr. Stefanie Gebauer und viele andere. Uwe Bolick danke ich für die Hilfe am TU-Cluster und für etliche sehr hilfreiche Tipps und Tricks. Allen anderen Mitarbeitern der Arbeitsgruppe sei für die tolle Arbeitsatmosphäre gedankt.

Ich möchte mich bei meiner Familie für die Unterstütztung und Motivierung wärend meiner Arbeit bedanken. Mein größter Dank gebührt meiner Freundin Katrin, für ihre Liebe, ihr Verständnis und dass sie immer für mich da war.